Anodized ZnO Nanostructures for Next-Generation Photovoltaics

Miles, David

Award date:
2016

Awarding institution:
University of Bath

Anodized ZnO Nanostructures for Next-Generation Photovoltaics

David Oliver Miles

A thesis submitted for the degree of Doctor of Philosophy

University of Bath
Department of Chemical Engineering

November 2015

Acknowledgements

First and foremost, I must thank both of my supervisors, Davide Mattia and Petra Cameron, for their support and guidance throughout the PhD. Being such an interdisciplinary project, it really couldn't have worked without both supervisors being heavily involved. I would also like to thank Davide for his continued confidence in letting me manage various aspects of this project. I believe this has made me a much better researcher as a result.

I must also thank all the members of both research groups I have been working in. I have always felt like a full member of both groups and that has made my three years much more enjoyable. In particular, I would like to thank Anyela Ramirez-Canon and Maria De La Luz Medina Llamas for always keeping me smiling on long days in the lab and trying to improve my terrible Spanish. I would also like to thank Adam Pockett for always lending a helping hand, particularly when I have needed to quiz him about electrochemistry.

I would like to extend a big thank you to Professor Jong Hak Kim, who kindly hosted me during my placement at Yonsei University. This was an excellent experience and I learnt a great deal from it. I would also like to thank all of his group for making me feel welcome and especially to Chang Soo Lee who has worked extremely hard as part of our collaboration.

For use of the near infrared rapid annealing apparatus I would like to thank my industrial partner SPECIFIC and Dr Trystan Watson, who has been my point of contact. For use of the TEM and XPS facilities I would also like to thank the Leeds EPSRC Nanoscience and Nanotechnology Research Equipment Facility (LENNF).

I must extend a very big thank you to John Mitchels and Ursula Potter for all of the help I received at the Microscopy and Analysis Suite over the years. The advice I have received on materials preparation and characterisation from John has been invaluable and in many ways he has acted like a third supervisor to me. Similarly, for all the help and advice offered to me over the course of my PhD, I would like to thank the technical staff within both chemical engineering and chemistry.

I must thank the EPSRC for funding my research through the Centre for Sustainable Chemical Technologies. I also thank both the Royal Society of Chemistry and Santander for providing me with funding to attend some excellent conferences around the world.

The Centre for Sustainable Chemical Technologies has provided me with many excellent opportunities to develop my skills in ways not typically open to PhD students, and for this I am extremely grateful. I would particularly like to thank Janet Scott, for all of her hard work and for

pushing us to make the most of the opportunities provided. I would also like to thank Sheila Apps for always being incredibly helpful with everything administrative.

Thank you to all of the students, both within the CSCT and within my two departments, who have made this PhD so much more enjoyable. Starting my PhD within a cohort of like-minded individuals has been an excellent experience and I continue to consider them as some of my closest friends. I would also like to thank Rhodri Jenkins, Lisa Sargeant, Anyela Ramirez-Canon, Jess Sharpe and all of the newcomers (you know who you are) for being such excellent office mates. You will all be sorely missed.

Finally, I need to thank all of my friends outside of university and especially my family for always being supportive of whatever I do and being there when I need them the most.

Abstract

Emerging photovoltaic technologies, such as dye-sensitized solar cells and perovskite solar cells, offer huge potential for providing large-scale and affordable renewable energy to meet our growing power requirements. Central to the success of these technologies is the development of low cost production techniques and materials, often with control of morphological features at the nanoscale. Electrochemical anodization is one example of a technique that can meet these criteria. The aim of this PhD project is to develop ZnO nanostructures using electrochemical anodization and apply them as electron transport materials within dye-sensitized and perovskite solar cells.

Aligned arrays of ZnO nanowires were produced by the anodization of zinc foil under mild reaction conditions. A systematic study of the influence of various reaction parameters on the growth of nanowires was conducted and subsequently used to optimise nanowire growth rates. Extremely high growth rates of over 3 μm min^{-1} were achieved, allowing high aspect ratio nanowires to be produced with lengths in excess of 100 μm. Annealing the nanowire arrays led to the production of polycrystalline ZnO nanowires with an average diameter of 160 nm and a radial slit-type pore structure along their length. Further synthetic modification of these nanowires led to the production of high surface area hierarchical structures.

Direct application of the nanowire arrays in back-illuminated dye-sensitized solar cells was found to be unsuccessful due to issues with cracking. However, through the preparation of various pastes using these nanowires, it was possible to produce a range of front-illuminated dye-sensitized solar cell architectures. Whilst the anodic nanowires were found to reduce the efficiency of cells when incorporated within mesoporous ZnO films, they were found to increase the power conversion efficiencies from 1.4 % to 1.9 % when applied as light scattering layers above the mesoporous films. Furthermore, hierarchical core-shell nanostructures, derived from the anodic nanowires, were found to greatly increase the efficiency of quasi-solid state dye-sensitized solar cells with TiO_2 photoanodes. Maximum power conversion efficiencies of 7.5 % were achieved through the incorporation of small quantities of these nanostructures. These are amongst the highest reported efficiencies for cells featuring ZnO and quasi-solid state cells in general.

The use of ZnO nanostructures, including anodic nanowires, was compared with the use of TiO_2 nanoparticles as electron transport materials within perovskite solar cells. Maximum power conversion efficiencies were 50 % lower for cells featuring ZnO rather than TiO_2 mesoporous layers. Furthermore, no obvious advantage of using nanowires rather than nanoparticles could be observed. The lower performance of the cells based on ZnO was related to the detrimental thermal degradation of the perovskite material in contact with ZnO. This casts doubt over the use of ZnO nanostructures within perovskite solar cells.

Declaration of Authorship

All work presented within this thesis is my own, except where a clear acknowledgment is made within the text. Experimental work performed in collaboration with other researchers is as follows:

Chapter 5, Section 5.3: Modification of the nanowires shown in Figure 5.16 was performed by Chang Soo Lee, a PhD student at Yonsei University, as part of a collaborative project. The electron micrographs and XPS measurements reported within this section were recorded on behalf of myself by Chang Soo Lee, using equipment at Yonsei University.

Chapter 6, Section 6.3.3: Fabrication and characterisation of the dye-sensitized solar cells within this section was conducted by Chang Soo Lee at Yonsei University. Analysis of the data, including the equivalent circuit analysis of the electrochemical impedance spectroscopy measurements was conducted by myself.

Contents

Acknowledgements ..... **i**
Abstract ..... **iii**
Declaration of Authorship ..... **iv**
List of Figures ..... **viii**
List of Tables ..... **xxi**
Abbreviations ..... **xxii**
Nomenclature ..... **xxv**
Chapter 1 – Introduction **2**
1.1 Aims and Scope **6**
1.2 Thesis Structure **7**
Chapter 2 – Literature Review **9**
2.1 Photovoltaics **9**
2.1.1 The three generations of photovoltaics 9
2.1.2 Analysis of photovoltaic performance 13
2.2 Dye-Sensitized Solar Cells **15**
2.2.1 Operating principles of DSCs 15
2.2.2 Major breakthroughs in DSCs 17
2.2.3 Three main components: dye, electrolyte and semiconductor 18
2.2.4 ZnO in DSCs 27
2.2.5 Future prospects for DSCs 33
2.3 Perovskite Solar Cells **35**
2.3.1 Perovskite materials 35
2.3.2 Evolution from the DSC 36
2.3.3 Remaining challenges and current focus 41
2.3.4 ZnO within perovskite solar cells 45
2.4 ZnO Nanostructures from Anodization **60**
2.4.1 A short background to anodization 61
2.4.2 ZnO nanostructures from anodization 62
2.5 Implications of the Literature **67**
Chapter 3 – Materials and Methods **68**
3.1 Materials **70**
3.2 Anodization **72**
3.2.1 Electrode preparation 72
3.2.2 Anodization in $KHCO_{3(aq)}$ 72
3.2.3 Anodization in $NaHCO_{3(aq)}$ or $NH_3HCO_{3(aq)}$ 74
3.2.4 Anodization of larger substrates 75

3.3 Modification of Nanowires 77
3.3.1 Nanowire film annealing 77
3.3.2 Secondary growth on nanowires 78
3.4 Dye-Sensitized Solar Cell Fabrication 80
3.4.1 Back-illuminated dye-sensitized solar cells 80
3.4.2 Front-illuminated dye-sensitized solar cells 81
3.4.3 Solid-state dye-sensitized solar cells 86
3.5 Perovskite Solar Cell Fabrication 92
3.5.1 Substrate and blocking layer preparation 92
3.5.2 Planar cell configurations 96
3.5.3 Mesoscopic cell configurations 99
3.6 Characterisation 102
3.6.1 Materials characterisation 102
3.6.2 Solar cell characterisation 104
Chapter 4 – Controlled Growth of ZnO Nanowires Using Anodization 106
4.1 Understanding the Growth Process 107
4.1.1 Growth initiation 107
4.1.2 Alignment of nanowires 109
4.1.3 Formation of layered films 110
4.1.4 Branching of nanowires 111
4.2 Control of Growth through Reaction Conditions 112
4.2.1 Controlled growth in $KHCO_{3(aq)}$ electrolytes 112
4.2.2 Growth in other bicarbonate electrolytes 118
4.3 Conversion to ZnO 131
4.3.1 Thermal degradation of nanowires 131
4.3.2 Formation of a slit-type pore structure 137
4.3.3 Alternative conversion methods 142
4.3.4 Crack formation during heating 145
4.4 Chapter Summary 147
Chapter 5 – Modification of the Nanowire Structure 148
5.1 Structure Modification through Controlled Heating 150
5.1.1 Effect of heating time 150
5.1.2 Control of heating temperature 152
5.1.3 Modelling the influence of annealing on nanowire surface area 156
5.2 Solution Based Structure Modifications 158
5.2.1 Attempts at surface passivation 158
5.2.2 Formation of hierarchical ZnO structures 160

5.3 Core-Shell Structures via Solution Based Growth **164**
5.4 Chapter Summary **171**
Chapter 6 – Application of ZnO Nanowires in Dye-Sensitized Solar Cells **172**
6.1 Back-Illuminated Dye-Sensitized Solar Cells **174**
6.1.1 Dye-adsorption on the nanowire films 174
6.1.2 Cell fabrication and measurement 177
6.2 Front-Illuminated Dye-Sensitized Solar Cells **180**
6.2.1 Formation of ZnO pastes 181
6.2.2 ZnO films by doctor blading 181
6.2.3 Optimizing device performance 184
6.2.4 Addition of nanowires to the mesoporous films 194
6.2.5 Use of nanowires as light scattering layers 198
6.3 Quasi-Solid State Dye-Sensitized Solar Cells **201**
6.3.1 Formation of mixed ZnO and TiO_2 films 201
6.3.2 Device performance 207
6.3.3 Incorporation of hierarchical core-shell ZNW@TNS structures 211
6.4 Chapter Summary **222**
Chapter 7 – Application of ZnO Nanowires in Perovskite Solar Cells **223**
7.1 Planar Perovskite Solar Cells **225**
7.2 Mesoscopic Perovskite Solar Cells **235**
7.2.1 Porous layer preparation 235
7.2.2 Fabrication and testing of mesoscopic perovskite solar cells 239
7.2.3 Mesoscopic cell preparation under controlled humidity 243
7.2.4 Effect of perovskite annealing time on device performance 249
7.3 Chapter Summary **255**
Chapter 8 – Conclusions and Future Work **257**
8.1 Conclusions **257**
8.2 Future Work **261**
Dissemination **265**
Journal Publications **265**
Conference Presentations **265**
Prizes **266**
References **267**
Appendix 1 – Estimation of the Specific Surface Area of Hexagonal Nanowires **277**
Appendix 2 – Estimation of the Specific Surface Area of Spheroidal ZnO Nanoparticles **279**

List of Figures

Figure 1.1. Carbon dioxide concentrations (in parts per million) for the last 1100 years, measured from air trapped in ice cores (blue) and directly from atmospheric measurements in Hawaii (red).[2-4] 3

Figure 1.2. Comparison of the estimated theoretical total global resources of different renewable power sources using spheres with volumes corresponding to their relative magnitude.[8] 4

Figure 1.3. A schematic summary of the contents and research focus of each results chapter of the thesis. 8

Figure 2.1. Simplified cross-section of a typical crystalline silicon photovoltaic device. 9

Figure 2.2. Simplified cross-sections of typical second generation photovoltaic technologies, including amorphous silicon (*a*-Si) (a), CdTe (b) and CIGS (c). ITO = indium tin oxide and FTO = fluorine-doped tin oxide. 11

Figure 2.3. Simplified cross-sections of typical third generation photovoltaic technologies including CZTSSe (a) and organic bulk heterojunction (BH) (b) solar cells..... 12

Figure 2.4. A typical *J-V* curve of a solar cell (red line) showing the associated parameters measured from it (a) and the corresponding plot of power *vs*. voltage from which the maximum power point (P_{max}) is obtained (b). 14

Figure 2.5. Schematic diagram of the mechanism of current generation in DSCs (TCO = transparent conducting oxide, CB = conduction band, and NHE = normal hydrogen electrode). 16

Figure 2.6. Cross-section of a DSC, similar to the one originally reported by Grätzel *et al*.[27] .. 16

Figure 2.7. Plot of record power conversion efficiency of DSC devices over time according to publication date. Efficiencies were obtained from the references within this section.[27, 34-41]..... 17

Figure 2.8. Chemical structures of notable or commonly used Ru-based dyes for application in DSCs. 20

Figure 2.9. Chemical structures of notable non Ru-based dyes for application in DSCs. 21

Figure 2.10. Chemical structures of the two dyes used for co-sensitization in the current record efficiency DSC devices. 22

Figure 2.11. Chemical structure of the organic hole conductor Spiro-OMeTAD..... 24

Figure 2.12. Simplified representation of electron transport through a mesoporous (a) and a one-dimensional nanostructured (b) semiconductor support. 30

Figure 2.13. Crystalline structure of $CH_3NH_3PbI_3$ in the cubic phase (temperatures above 330 K). The methylammonium ion occupies the central site, surrounded by octahedra of iodine (purple) and lead (green).[116] 36

Figure 2.14. Schematic showing the change in perovskite cell structure from a DSC type structure (a) to a planar perovskite cell (d and e). 37

Figure 2.15. Number of publications each year containing the combination of words "perovskite*" and "solar", or "CH_3NH_3Pb*" and "solar" within the title, based on a Web of Science search (08/10/2015). 38
Figure 2.16. A plot of published maximum power conversion efficiencies over time for perovskite solar cells. Current record certified efficiencies of crystalline silicon solar cells and CdTe solar cells are shown for comparison.[26] Values for perovskite solar cells were obtained from the references within this section. 40
Figure 2.17. *J-V* curve demonstrating hysteresis in the measurements undertaken backwards from forward bias (FB) to short circuit (SC) and forwards from SC to FB. 44
Figure 2.18. Simplified cross-sections of the three main types of perovskite cell structures used with ZnO. HTM = hole transport material, TCO = transparent conducting oxide and ETM = electron transport material. In the case of the bilayer structure, the ETM is typically an organic n-type semiconductor or TiO_2. 46
Figure 2.19. Maximum reported power conversion efficiencies *vs.* publication date for all reports to date (11/10/2015) featuring ZnO within perovskite solar cells (black "+" symbols). The dashed line is a linear fit of all values and the main types of device structure are highlighted by the coloured circles. All values were obtained from the references within this section. 56
Figure 2.20. The three different processes controlling anodization: Field assisted oxide growth (1), field assisted dissolution of metal oxide (2) and chemical dissolution of metal oxide (3)... 61
Figure 3.1. Schematic demonstrating the range of nanomaterials and photovoltaic devices produced and the respective sections of Chapter 3 in which the details of production are discussed. 68
Figure 3.2. Dimensions and picture of the one-hole anode holder used for anodization. 73
Figure 3.3. Experimental setup for the anodization of electropolished zinc foils. 73
Figure 3.4. Dimensions (left) and picture (right) of the front plate of the Teflon® sample holder used to expose three circular areas (12 mm diameter) of the zinc foil. 74
Figure 3.5. Picture of a zinc foil in a rectangular Kapton® mask for anodization of large substrates. 75
Figure 3.6. Picture demonstrating the potential to anodize intricate shapes into the zinc foil using a Kapton® mask. 76
Figure 3.7. Pictures of the NIR rapid annealing system before (left) and during use (right). 77
Figure 3.8. A picture of the anodic nanowire films used for ZnO nanowire powder production. 79
Figure 3.9. Scheme depicting the key stages of back-illuminated DSC production. 80
Figure 3.10. Schematic representation of the cross-section of a typical front-illuminated DSC. 81

Figure 3.11. Pictures of the main cell preparation stages including after sintering (a), re-sizing (b), dyeing (c), counter electrode preparation (d) and sealing (e). 84
Figure 3.12. Picture of the finished front-illuminated DSCs. 85
Figure 3.13. Scheme demonstrating the main stages of front-illuminated DSC preparation. 85
Figure 3.14. Picture of the PVC-g-POEM graft copolymer. 86
Figure 3.15. Picture of the final solid-state DSCs. 90
Figure 3.16. Picture of the chromatography sprayer and heating block used for spray pyrolysis. 93
Figure 3.17. Experimental setup used for the spray pyrolysis of ZnO on conducting glass substrates. 94
Figure 3.18. Diagram and picture of the electrodeposition experimental setup. 96
Figure 3.19. Cross-section of a planar perovskite cell structure. 97
Figure 3.20. Picture of the finished perovskite solar cells consisting of 10 separate measurement areas on one substrate. 98
Figure 3.21. Picture of the gold evaporation mask. 99
Figure 3.22. Scheme demonstrating the main stages of planar perovskite cell preparation for both one and two-step depositions. 99
Figure 3.23. Cross-section of the mesoscopic perovskite cells. 100
Figure 3.24. Typical cell making stages for mesoscopic perovskite cells. 101
Figure 3.25. Example of a typical *J*-*V* curve recorded for either a dye-sensitized or perovskite solar cell and the cell parameters that are extracted from it. 105
Figure 4.1. FESEM micrographs of multiple (a) and a single nanoflower (b) formed in the early growth stages and a graphical representation of the initial stages of nanowire growth (c). The stages show: (1) formation of pits within the Zn foil, (2) growth of nanoflower structures in regions of close proximity to the pits, (3) increase in both the quantity and size of nanoflowers, (4) full surface coverage of nanoflowers, and (5) inhibition of radial growth resulting in nanowire alignment. 108
Figure 4.2. Plots of recorded anodization current over time, showing the initial surge in current (inset) followed by a gradual decay over time. 109
Figure 4.3. FESEM surface morphology (a) and cross-section (b) showing the complete coverage of the zinc surface with nanoflowers (5 min), eventually forming an array of aligned nanowires (c) (15 min). 110
Figure 4.4. FESEM cross-sections and surface morphologies showing the initial (up to 5 min reaction time) formation of thin nanowires (a), the development of a layered structure with large hexagonal wires (b & c) and the formation of hierarchical structures (d-f). 111
Figure 4.5. Photo of a zinc foil before and after anodization. 113

Figure 4.6. Image of an anodic film produced with stirring (a) and an anodic film produced under the same anodization conditions without stirring (b). 113
Figure 4.7. FESEM micrographs showing the effect of changing the anodization voltage (a-c), time (d-f), concentration (g-i) and temperature (j-l) on the surface morphology of the anodic films. Unless otherwise stated, the anodization conditions used were 10 V, 15 min, 50 mM $KHCO_{3(aq)}$ electrolyte concentration and 10 °C. The peak currents measured during anodization are shown in brackets. 114
Figure 4.8. Image of the delamination of a film produced at 10 V. 115
Figure 4.9. The diameters and packing density of nanowires formed at different anodization voltages (a, b), times (c, d), electrolyte concentrations (e, f), and temperatures (g, h) for films formed in a $KHCO_{3(aq)}$ electrolyte. Errors shown are a standard deviation over 20 (diameter) or 3 (packing density) measurements. Unless otherwise stated the anodization conditions used were 10 V, 15 min, 50 mM $KHCO_{3(aq)}$ electrolyte and 10 °C. 116
Figure 4.10. Low (a) and high (b) magnification FESEM micrographs of cracks in the nanostructured anodic films. 117
Figure 4.11. FESEM micrographs of the surfaces of nanowire films produced via anodization in aqueous $NaHCO_3$ for times of 1 (a), 5 (c) 15 (e), 30 (g), 60 (i) and 120 min (k). The corresponding films produced in aqueous NH_4HCO_3 are also shown (b, d, f, h, j & l). All films were produced under constant reaction conditions of 5 V, 10 °C and 50 mM electrolyte concentration. 119
Figure 4.12. Cross-sectional FESEM micrographs of nanowire films produced via anodization in aqueous $NaHCO_3$ for times of 1 (a), 5 (c) 15 (e), 30 (g), 60 (i) and 120 min (k). The corresponding films produced in aqueous NH_4HCO_3 are also shown (b, d, f, h, j & l). All films were produced under constant reaction conditions of 5 V, 10 °C and 50 mM electrolyte concentration. 120
Figure 4.13. Plots of nanowire film thickness, measured through analysis of the cross-sections via FESEM, for different anodization times (a), voltages (b), temperatures (c) and electrolyte concentrations (d) in $NaHCO_3$ or NH_4HCO_3 electrolytes. Unless otherwise stated, anodizations were carried out under conditions of 5 V, 10 °C, 50 mM electrolyte concentration and for 15 min. The error bars represent the standard deviation based upon five measurements at each condition. 121
Figure 4.14. FESEM surface morphologies of nanowire films produced via anodization in aqueous $NaHCO_3$ at temperatures of 5 (a), 10 (c) and 20 °C (e). The corresponding films produced in aqueous NH_4HCO_3 are also shown (b, d & f). All films were produced under constant reaction conditions of 15 minutes, 5 V and 50 mM electrolyte concentration. 122
Figure 4.15. Cross-sectional FESEM micrographs of nanowire films produced via anodization in aqueous $NaHCO_3$ at temperatures of 5 (a), 10 (c) and 20 °C (e). The corresponding films produced in aqueous NH_4HCO_3 are also shown (b, d & f). All films were produced under constant reaction conditions of 15 minutes, 5 V and 50 mM electrolyte concentration. 123

Figure 4.16. Arrhenius plot of the natural logarithm of the rate constant (inferred from the nanowire film thickness) *vs.* the reciprocal of the anodization temperature for anodizations undertaken in either $NaHCO_3$ or NH_4HCO_3 electrolytes. 124
Figure 4.17. FESEM surface morphologies of nanowire films produced via anodization in aqueous $NaHCO_3$ at applied voltages of 1 (a), 2 (c), 5 (e) and 10 V (g). The corresponding films produced in aqueous NH_4HCO_3 are also shown (b, d, f & h). All films were produced under constant reaction conditions of 30 minutes, 10 °C and 50 mM electrolyte concentration. 125
Figure 4.18. Cross-sectional FESEM micrographs of nanowire films produced via anodization in aqueous $NaHCO_3$ at applied voltages of 1 (a), 2 (c), 5 (e) and 10 V (g). The corresponding films produced in aqueous NH_4HCO_3 are also shown (b, d, f & h). All films were produced under constant reaction conditions of 30 minutes, 10 °C and 50 mM electrolyte concentration. 127
Figure 4.19. FESEM surface morphologies of nanowire films produced via anodization in aqueous $NaHCO_3$ at concentrations of 50 (a), 100 (c) and 200 mM (e). The corresponding films produced in aqueous NH_4HCO_3 are also shown (b, d & f). All films were produced under constant reaction conditions of 5 minutes, 2 V and 10 °C. 129
Figure 4.20. Cross-sectional FESEM micrographs of nanowire films produced via anodization in aqueous $NaHCO_3$ at concentrations of 50 (a), 100 (c) and 200 mM (e). The corresponding films produced in aqueous NH_4HCO_3 are also shown (b, d & f). All films were produced under constant reaction conditions of 5 minutes, 2 V and 10 °C. 130
Figure 4.21. FESEM surface morphologies of the anodic nanowire films before (a) and after (b) annealing at 300 °C for 1 h. 131
Figure 4.22. Flat plate powder XRD patterns for nanowire films obtained directly from anodization (a) and after annealing at 300 °C for 1 h (b). 132
Figure 4.23. XPS survey spectra and C1s region spectra for nanowire films obtained directly from anodization (a & c) and after annealing at 300 °C (b & d) 133
Figure 4.24. FT-IR spectrum of powders produced from nanowire array films before (a) and after (b) a heat treatment at 300 °C for 1 hour in air. 134
Figure 4.25. Raman spectrum of nanowire array films before (a) and after (b) a heat treatment at 300 °C for 1 hour in air. 135
Figure 4.26. UV-Visible reflectance spectrum of a nanowire array film before (blue) and after (red) annealing at 300 °C for 1 hour in air. 136
Figure 4.27. Scheme showing the two-step production of polycrystalline ZnO nanowires with a "slit-pore" structure (a), low magnification TEM micrographs of the nanowires before (b) and after (c) annealing, and high magnification micrographs showing the polycrystalline slit-pore structure after annealing (d & e). 138
Figure 4.29. Nitrogen adsorption-desorption isotherms for the slit-pore type ZnO nanowires (a) and determination of the BET surface area (b). 139

Figure 4.30. TEM micrographs showing the electron beam damage and conversion of the non-annealed nanowires to polycrystalline ZnO (a – c) and the electron diffraction pattern of the resulting ZnO structures (d). 140
Figure 4.31. Nanowire diameter distributions determined by TEM for nanowires before annealing (a) and after annealing (b). 141
Figure 4.32. Photos of the NIR rapid annealing system used for conversion of the anodic nanowires to ZnO during standby (a) and during operation (b)..... 142
Figure 4.33. Flat plate powder x-ray diffraction patterns of the anodic nanowire films after NIR heating at different heating powers. All heating powers shown are for a conveyor belt speed of 2 m min^{-1}. It should be noted that all Zn peaks occur from the substrate. 143
Figure 4.34. Back (a) and front (b) of a nanowire film heated at 50 % power showing signs of substrate melting and nanowire film cracking. 144
Figure 4.35. (a) electropolished films heated at 35 %, 30 % or 0 % power (left to right). (b) the same but for no electropolishing pretreatment. 145
Figure 4.36. FESEM micrograph of a nanowire film surface after annealing at 300 °C for 1 h demonstrating the typical cracking observed as a result of annealing. 146
Figure 4.37. FESEM cross-section of an annealed ZnO nanowire film set inside resin, demonstrating the cracking between sections of nanowire film penetrating to the Zn substrate. 146
Figure 5.1. Schematic summarising the content and structure of Chapter 5, which focusses on the modification of the nanowire structure after anodization. 148
Figure 5.2. Flat plate powder x-ray diffraction patterns of anodic nanowire films annealed at 300 °C for times ranging between 1 and 24 h with ramping at 2 °C min^{-1}. Peaks attributed to the wurtzite form of ZnO (circles) and the Zn substrate (triangles) are shown. 151
Figure 5.3. Crystallite sizes calculated by applying the Scherrer equation to the (100) ZnO peak in the XRD patterns recorded for nanowire films annealed for different times (a) and at different temperatures (b). 152
Figure 5.4. Flat plate powder x-ray diffraction patterns of anodic nanowire films annealed for 1 h at temperatures ranging between 200 and 350 °C with ramping at 2 °C min^{-1}. A diffraction pattern of the nanowire film without heating (WH) is also included for comparison. Peaks attributed to the wurtzite form of ZnO (circles) and the Zn substrate (triangles) are shown. 153
Figure 5.5. TEM micrographs showing the polycrystalline structure of annealed nanowires and the difference in particle size between films annealed at 300 °C (a) and 350 °C (b). 154
Figure 5.6. Particle size distributions over multiple transmission electron micrographs for anodic nanowires annealed at 300 °C (a) or 350 °C (b) for 1 h..... 155

Figure 5.7. Particle sizes determined from TEM analysis overlaid on the values determined by Scherrer analysis of the XRD patterns for nanowires annealed at different temperatures. The error bars show the standard deviation over more than 30 measurements. 155
Figure 5.8. Predicted surface areas for polycrystalline nanowires composed of nanoparticles of different diameters, assuming either isolated perfect spheres (red circles) or sintered spheres with a sintering factor of 0.57 (blue triangles). The specific surface area measured for nanowires consisting of 11.2 nm diameter nanoparticles is shown in as a yellow triangle. 156
Figure 5.9. FESEM micrograph of the porous (a) and nanowire fragment areas (b) present on the dark surface of the film after a double anodization treatment (c). 159
Figure 5.10. Flat plate powder x-ray diffraction patterns of the anodic nanowire films after a second anodization (a), after treatment in a solution of $Zn(NH_3)_4^{2+}$ (b) and after treatment within water (c). 159
Figure 5.11. Low (a) and high (b) magnification FESEM micrographs of the nanowire film surface after three 1 min treatments in a solution containing $Zn(NH_3)_4^{2+}$ at room temperature followed by annealing in air at 300 °C for 1 h. 160
Figure 5.12. Low (a) and high (b) magnification FESEM micrographs of anodic nanowire films after treatment in water for 24 h, followed by annealing in air at 300 °C for 1 h, and FESEM micrograph of the growth on a bare Zn surface after the same treatment in water (c). 161
Figure 5.13. Scheme demonstrating the steps in the production of hierarchical ZnO nanowire arrays (a), TEM micrographs of the polycrystalline ZnO nanowires with a slit-pore structure before water treatment (b-c) and with a hierarchical structure featuring spikes after water treatment (d-e). 162
Figure 5.14. Comparison of the XPS spectrum of the anodic nanowire arrays after annealing (a) and after further treating with water and annealing for a second time (b). 163
Figure 5.15. FESEM micrographs of the resulting structures formed under conditions 1 (a-b), 2 (c-d) and 3 (e-f). 165
Figure 5.16. FESEM micrographs of the resulting structures formed under conditions 4 (a-b), 5 (c-d), 6 (e-f) and 7 (g-h). 167
Figure 5.17. Cartoon demonstrating the transformation of structure from polycrystalline ZnO nanowires (ZNW) to hierarchical core-shell nanowires with TiO_2 nanosheets (ZNW@TNS). 168
Figure 5.18. FESEM (a-c) and TEM (d-f) micrographs of the ZnO nanowires before modification (ZNW) (a and d) and after modification (ZNW@TNS) with separation by either centrifugation (b and e) or precipitation (c and f). 168
Figure 5.19. Powder XRD pattern of the ZNW@TNS nanowires formed from a solvothermal reaction at 200 °C for 24 h under reaction condition 4. 169
Figure 5.20. Comparison of the XPS spectra of the ZNW and ZNW@TNS structures within the Zn 2p (a), Ti 2p (b), O 1s (c) and N 1s (d) region. 170

Figure 6.1. Schematic summarising the chapter contents and layout. 172
Figure 6.2 Schematic showing the cross-sectional structure of a back-illuminated DSC..... 174
Figure 6.3. Photo of anodic nanowire films formed by anodization for different lengths of time (resulting in different thicknesses) and dyeing in an ethanolic N719 dye solution (a) and cross-sectional FESEM micrographs of the films they correspond to, showing an increase in film thickness (b-d)..... 175
Figure 6.4. Calibration curve of absorbance *vs.* N719 dye concentration (a), UV-Vis absorbance of desorbed dye from nanowire films dyed for different lengths of time (b) and the corresponding loading of dye on the nanowire films (c). 176
Figure 6.5. Typical *J-V* curve measured under AM 1.5 solar irradiation for a back-illuminated DSC using an anodic nanowire film. 178
Figure 6.6. Schematic representing the likely route of performance loss within the back-illuminated DSCs (a) and a cross-sectional FESEM micrograph showing cracking in the annealed film (b). 178
Figure 6.7. Schematic representing the three main photoanode architectures investigated in this section. 180
Figure 6.8. Plots of ZnO film thickness *vs.* the number of deposited ZnO layers (a) and the number of tape layers used as a spacer (b) for the thin ZnO paste. The arithmetic mean roughness is shown in the red bars..... 182
Figure 6.9. Plots of ZnO film thickness *vs.* the number of deposited ZnO layers (a) and the number of tape layers used as a spacer (b) for the thick ZnO paste. The arithmetic mean roughness is shown in the red bars. 182
Figure 6.10. Plots of mesoporous film thickness *vs.* the number of tape layers used as a spacer during doctor blading for the optimized ZnO paste (a) and a commercial TiO_2 paste (Dyesol) (b). The arithmetic mean roughness is shown in the red bars..... 183
Figure 6.11. Low (a-b) and high (c-d) magnification FESEM micrographs of the cross-section of a ZnO mesoporous film (optimized ZnO paste) (a and c) and a TiO_2 mesoporous film (Dyesol paste) (b and d)..... 184
Figure 6.12. *J-V* curves for the best performing cells produced using ZnO mesoporous films and different types of blocking layer (a). Average cell parameters for cells produced using different blocking layers (b-e) with the standard deviation of each set of three cells shown in red..... 186
Figure 6.13. Average cell parameters measured for cells using different mesoporous ZnO film thicknesses with the standard deviations for each set of three cells shown in red. 188
Figure 6.14. *J-V* curves (a) and average cell parameters (b-e) measured for cells using different mesoporous TiO_2 film thicknesses (Dyesol paste) with the standard deviations for each set of three cells shown in red..... 190
Figure 6.15. *J-V* curves measured for ZnO mesoporous cells using different electrolytes..... 192

Figure 6.16. Photo of a DSC 2 h after fabrication using a guanidinium thiocyanate containing electrolyte, showing bleaching in the top right corner. 192
Figure 6.17. Effect of dyeing time in an ethanolic N719 dye solution on average device performance for mesoporous ZnO films. Standard deviations based on three cells are shown in red. 193
Figure 6.18. *J-V* curves recorded at AM 1.5 solar irradiation for DSCs produced under equivalent conditions, but using photoanodes composed of either ZnO nanoparticles (**NP**), a mixture of anodic ZnO nanowires and nanoparticles (**A_NW**), or a mixture of commercial ZnO nanowires and nanoparticles (**C_NW**). The top-left plot is a comparison of the best cells of each type... 195
Figure 6.19. Comparison of average short circuit current density (a), open circuit voltage (b), fill factor (c) and power conversion efficiency (d) for DSCs fabricated using different types of photoanodes. The standard deviation over three cells is represented by the red bars. 196
Figure 6.20. Low (a-b) and high (c-d) magnification FESEM micrographs of the cross-section of an A_NW film (a and c) and C_NW film (b and d)..... 197
Figure 6.21. Film thicknesses (black plus symbols) and masses (red triangles) for photoanodes without scattering layers and with scattering layers formed of anodic nanowires (ANW) or commercial nanowires (CNW). 199
Figure 6.22. Comparison of average short circuit current density (a), open circuit voltage (b), fill factor (c) and power conversion efficiency (d) for DSCs fabricated using different types of scattering layers on ZnO nanoparticle photoanodes. The standard deviation over three cells is represented by the red bars. 200
Figure 6.23. Picture of photoanodes prepared with different quantities of ZNW structures added to the OM-TiO_2 film, ranging between 0 and 24 wt.%. 202
Figure 6.24. Picture of photoanodes prepared with different quantities of ZNW structures added to the OM-TiO_2 film, ranging between 0 and 7 wt.%. Films with 5 wt.% commercial nanowires are shown as a comparison. 202
Figure 6.25. FESEM micrographs of the OM-TiO_2 films (a-b), OM-TiO_2 films with 5 wt.% commercial ZnO NWs (c-d) and OM-TiO_2 films with 3 (e-f), 5 (g-h) or 7 wt.% (i-j) ZNW structures. Micrographs shown on the left are of the film surface and cross-sections are shown on the right. 204
Figure 6.26. Photo of photoanodes formed with different quantities of ZNW nanostructures from pastes where the HCl was replaced by H_2O. 205
Figure 6.27. FESEM micrographs of the OM-TiO_2 films (a-b) and OM-TiO_2 films with 3 (c-d), 5 (e-f) or 7 wt.% (g-h) ZNW structures for films prepared from pastes in which the HCl had been replaced with H_2O. Micrographs shown on the left are of the film surface and cross-sections are shown on the right..... 206

Figure 6.28. *J-V* curves recorded under 1 Sun AM 1.5 simulated sunlight for solid-state DSCs produced using 0 (a), 3 (b), 5 (c) or 7 wt.% (d) ZNW structures in the OM-TiO_2 photoanode.207
Figure 6.29. Average cell performance parameters extracted from *J-V* curves, recorded under 1 Sun AM 1.5 simulated sunlight, for solid-state DSCs produced using 0, 3, 5 or 7 wt.% ZNW structures in the OM-TiO_2 photoanode. The red error bars represent the standard deviation over five cells and the stars show the values for the highest efficiency cell of each type. 208
Figure 6.30. *J-V* curves recorded under 1 Sun AM 1.5 simulated sunlight for qssDSCs produced using 0 (a), 3 (b), 5 (c) or 7 wt.% (d) ZNW structures in the OM-TiO_2 photoanode without using HCl in the film preparation. Each plot shows the results of four different cells prepared under the same conditions..... 209
Figure 6.31. Cell performance parameters extracted from *J-V* curves, recorded under 1 Sun AM 1.5 simulated sunlight, for qssDSCs produced using 0, 3, 5 or 7 wt.% ZNW structures in the OM-TiO_2 photoanode without using HCl in the film preparation. The red error bars represent the standard deviation over four cells and the crosses show the values for the highest efficiency cell of each type. 210
Figure 6.32. Surface SEM micrographs of OM-TiO_2 films without HCl (a-b) and with HCl (c-d) at low (left) and high (right) magnification..... 212
Figure 6.33. Surface SEM micrographs of ZNW1 (a-b), ZNW2 (c-d), and ZNW3 (e-f) photoanodes at low (left) and high (right) magnification. 213
Figure 6.34. Surface SEM micrographs of ZNW@TNS1 (a-b), ZNW@TNS2 (c-d), and ZNW@TNS3 (e-f) photoanodes at low (left) and high (right) magnification. 214
Figure 6.35. UV-visible light reflectance spectra (a) and photograph of OM, ZNW, and ZNW@TNS photoanodes (b). 215
Figure 6.36. *J-V* curves (a) and IPCE spectra (b) of qssDSCs with OM, ZNW, and ZNW@TNS photoanodes. 216
Figure 6.37. Nyquist plots recorded from electrochemical impedance spectroscopy at open circuit voltage and 1 Sun illumination for qssDSCs featuring an OM, ZNW or ZNW@TNS photoanode (symbols) and their equivalent circuit fittings (solid lines). The equivalent circuit used for analysis of the data is also shown at the top right of the figure, where R_S is the series resistance, R1 is the charge transfer resistance at the counter electrode, C1 is the capacitance at the counter electrode, R2 is the charge transfer resistance at the semiconductor/electrolyte interface, CPE1 is a constant phase element used to represent the capacitance at the semiconductor/electrolyte interface and Ws1 is a Warburg impedance associated with diffusion of redox species through the electrolyte. 219
Figure 7.1 Schematic summarising the contents and structure of Chapter 7. 224
Figure 7.2. Schematic showing the cross-sectional structure of a planar perovskite solar cell featuring a ZnO blocking layer. 225

Figure 7.3. Photos comparing the perovskite films obtained using the 1-step and 2-step deposition methods on a ZnO blocking layer. 226
Figure 7.4. Average cell performances and standard deviations (30 cells) for planar perovskite cells, produced on ZnO blocking layers deposited by different numbers of spray pyrolysis cycles. The black crosses represent the values corresponding to the highest efficiency device of each type. 227
Figure 7.5. FESEM micrographs of clean FTO (a) and blocking layers deposited by TTIP spin coating (b), TiO_2 spray pyrolysis (c), ZnO electrodeposition (d), spin coating of a zinc acetate solution (e), spin coating of a zinc acetate solution containing ethanolamine (f), spin coating ZnO nanoparticles (~5 nm diameter) (g) and spin coating ZnO nanoparticles (~5 nm diameter) followed by annealing (h). 229
Figure 7.6. TEM micrographs of ZnO nanoparticles, synthesized for deposition of a ZnO blocking layer, on a lacy carbon TEM grid at low (a) and high (b) magnification. 230
Figure 7.7. Average cell performances for planar perovskite cells produced on ZnO blocking layers, deposited by different numbers of nanoparticle spin coating cycles. The black crosses represent the values corresponding to the highest efficiency device of each type and the red bars show the standard deviation over 30 cells. 231
Figure 7.8. Average cell performances for planar perovskite cells produced on ZnO blocking layers using different PbI_2 deposition methods. The black crosses represent the values corresponding to the highest efficiency device of each type and the red bars show the standard deviation over 30 cells. 232
Figure 7.9. FESEM cross-section of a planar perovskite solar cell fabricated on a ZnO NP blocking layer 234
Figure 7.10. Schematic showing the cross-sectional structure of mesoscopic perovskite solar cells featuring either ZnO nanoparticle layers or ZnO nanowire layers 235
Figure 7.11. FESEM micrographs of the initial annealed ZnO nanoparticle (a), TiO_2 nanoparticle (b), anodic ZnO nanowire (c) and commercial ZnO nanowire (d) layers on FTO coated glass. 237
Figure 7.12. Average nanoparticle or nanowire film thicknesses obtained for different spin coating speeds. The error bars show the arithmetic mean roughness of the films calculated from profilometry. For the ZnO NP layers, two sets of thicknesses are shown; one for films deposited on a ZnO nanoparticle blocking layer (Nanoparticle BL, red), and one for films deposited on a ZnO blocking layer formed from spin coating a zinc acetate solution (ZnAc BL, blue). TiO_2 NP layers were deposited on spin coated TiO_2 blocking layers and both nanowire films were deposited on ZnO blocking layer from spin coating a zinc acetate solution. 238

Figure 7.13. FESEM micrographs of annealed ZnO nanoparticle (a), TiO_2 nanoparticle (b), anodic ZnO nanowire (c) and commercial ZnO nanowire (d) layers on FTO coated glass after optimisation of paste preparation. 239
Figure 7.14. *J-V* curves recorded in the backward (red) and forward (blue) scan directions for the highest efficiency pixels for each of the different porous oxide layers. ZnO NW refers to commercial ZnO nanowire layers. All porous layers apart from TiO_2 NP were deposited on ZnO blocking layers. TiO_2 NP layers were deposited on TiO_2 blocking layers..... 240
Figure 7.15. Average cell performances and standard deviations (30 cells each) measured for mesoscopic perovskite cells featuring ZnO nanoparticle (ZNP), commercial ZnO nanowire (CNW) or TiO_2 nanoparticle (TNP) porous layers on ZnO (ZNP, CNW and TNP2) or TiO_2 (TNP1) blocking layers. Forward scans are shown in blue and backward scans are shown in red. The values corresponding to the highest efficiency cell on the backwards scan are shown as black crosses. 241
Figure 7.16. Average cell performances and standard deviations (30 cells each) measured for mesoscopic perovskite cells featuring ZnO nanoparticle (ZNP), commercial ZnO nanowire (CNW), anodic ZnO nanowire (ANW) or TiO_2 nanoparticle (TNP) porous layers on ZnO blocking layers. Forward scans are shown in blue and backward scans are shown in red. The values corresponding to the highest efficiency cell are shown as black crosses..... 244
Figure 7.17. Average cell performances and standard deviations (30 cells each) measured for mesoscopic perovskite cells featuring ZnO nanoparticle (ZnO NP) or TiO_2 nanoparticle (TiO2 NP) porous layers on TiO_2 blocking layers. Forward scans are shown in blue and backward scans are shown in red. The values corresponding to the highest efficiency cell are shown as black crosses. 246
Figure 7.18. Schematic demonstrating the proposed routes of electron transport through mesoscopic perovskite solar cells featuring either TiO_2 or ZnO mesoporous layers..... 247
Figure 7.19. FESEM cross-section of a mesoscopic perovskite solar cell featuring a mesoporous TiO_2 layer and a TiO_2 blocking layer. 248
Figure 7.20. Average cell performances and standard deviations (30 cells each) measured for mesoscopic perovskite cells featuring TiO_2 nanoparticle porous layers of different thicknesses on TiO_2 blocking layers. Forward scans are shown in blue and backward scans are shown in red. The values corresponding to the highest efficiency cell are shown as black crosses..... 249
Figure 7.21. Average cell performances and standard deviations (10 cells each) measured for mesoscopic perovskite cells featuring TiO_2 nanoparticle porous layers on ZnO blocking layers, after annealing the perovskite layer at 70°C for different lengths of time. Forward scans are shown in blue and backward scans are shown in red. The values corresponding to the highest efficiency cell are shown as black crosses. 250

Figure 7.22. Average cell performances and standard deviations (10 cells each) measured for mesoscopic perovskite cells featuring TiO_2 nanoparticle porous layers on TiO_2 blocking layers, after annealing the perovskite layer at 70°C for different lengths of time. Forward scans are shown in blue and backward scans are shown in red. The values corresponding to the highest efficiency cell are shown as black crosses. 251
Figure 7.23. Average cell performances and standard deviations (10 cells each) measured for mesoscopic perovskite cells featuring ZnO nanoparticle porous layers on ZnO blocking layers, after annealing the perovskite layer at 70°C for different lengths of time. Forward scans are shown in blue and backward scans are shown in red. The values corresponding to the highest efficiency cell are shown as black crosses. 252
Figure 7.24. Average cell performances and standard deviations (10 cells each) measured for mesoscopic perovskite cells featuring ZnO nanoparticle porous layers on TiO_2 blocking layers, after annealing the perovskite layer at 70°C for different lengths of time. Forward scans are shown in blue and backward scans are shown in red. The values corresponding to the highest efficiency cell are shown as black crosses. 253
Figure 8.1 Diagram of a possible experimental setup for continuous nanowire production using anodization. 262

List of Tables

Table 2.1. The photovoltaic performance of different perovskite solar cells featuring ZnO nanorods reported in the literature. CBD = chemical bath deposition and CVD = chemical vapour deposition. 48

Table 2.2. The photovoltaic performance of different perovskite solar cells featuring planar ZnO layers reported in the literature. 51

Table 2.3. The photovoltaic performance of different perovskite solar cells featuring a bilayer electron selective contact including ZnO reported in the literature. 54

Table 2.4. The photovoltaic performance of other perovskite solar cell architectures featuring ZnO reported in the literature. CNT = carbon nanotubes. 56

Table 3.1. Reactant quantities used for each titania nanosheet growth attempt. 79

Table 3.2. ZnO nanowire powder mass and equivalent wt.% present within pastes..... 88

Table 5.1. Reagent volumes used for the synthesis of ZNW@TNS under different conditions based on 2-propanol solvent volume of 40 mL..... 164

Table 6.1. ZnO content of nanostructure pastes produced and used within Section 6.2. 181

Table 6.2. Composition of the different electrolytes tested within the front-illuminated DSCs with ZnO photoanodes, where PMII stands for 1-methyl-3-propylimidazolium iodide and 4-*t*BP is 4-*tert*-butylpyridine. 191

Table 6.3. Summary of the DSC performance for different photoanode types. 196

Table 6.4 Dye loading, specific surface area and qssDSC cell performance for different photoanodes. 217

Table 6.5. Calculated values of series and charge transfer resistances obtained from equivalent circuit analysis of qssDSCs based on different photoanodes. 220

Abbreviations

1-D	One-dimensional
2-D	Two-dimensional
3-D	Three-dimensional
4-*t*BP	4-*tert*-butylpyridine
A_NW	Anodic ZnO nanowire/nanoparticle mixture
a-Si	Amorphous silicon
ADEKA-1	A metal-free alkoxysilyl carbazole dye (see Figure 2.12)
ALD	Atomic layer deposition
AM	Air mass
ANW	Anodic ZnO nanowires
BH	Bulk heterojunction
BIPV	Building integrated photovoltaics
C3	A heteroleptic Cu-based dye (see Figure 2.11)
C_NW	Commercial ZnO nanowire/nanoparticle mixture
CB	Conduction band
CBD	Chemical bath deposition
CIGS	$CuIn_xGa_{(1-x)}Se_2$
CNT	Carbon nanotubes
CNW	Commerical ZnO nanowires
CVD	Chemical vapour deposition
CZTSSe	$Cu_2ZnSn(S_{(1-x)}Se_x)_4$
D149	An organic dye (see Figure 2.11)
DC	Direct current
DETA	Diethylenetriamine
DMF	Dimethylformamide
DMSO	Dimethylsulfoxide
DSC	Dye-sensitized solar cell
EIS	Electrochemical impedance spectroscopy
ETM	Electron transport material
FA	Formamidinium
FB	Forward bias
FESEM	Field-emission scanning electron microscopy
FF	Fill factor
FT-IR	Fourier-transform infrared
FTO	Fluorine-doped tin oxide

FWHM	Full width at half maximum
GIXRD	Grazing incidence X-ray diffraction
HC	High concentration electrolyte
HMTETA	1,1,4,7,10,10-Hexamethyltriethyl tetramine
HOMO	Highest occupied molecular orbital
HTM	Hole transport material
IPA	2-Propanol
IPCE	Incident photon-to-current conversion efficiency
ITO	Indium tin oxide
KRICT	Korean research institute of chemical technology
LC	Low concentration electrolyte
LEG4	An organic dye (see Figure 2.12)
LiTFSI	Bis(trifluromethane)sulfonimide lithium salt
LUMO	Lowest unoccupied molecular orbital
MA	Methylammonium
MAI	Methylammonium iodide
N3	A Ru-based dye (see Figure 2.10)
N719	A Ru-based dye (see Figure 2.10)
N749	A Ru-based dye (see Figure 2.10)
NHE	Normal hydrogen electrode
NIR	Near infrared
NMP	1-Methyl-2-pyrrolidone
NP	Nanoparticle
NW	Nanowire
OC	Open circuit
OM	Organised mesoporous
P3HT	Poly(3-hexylthiophene-2,5-diyl)
PCBM	Phenyl-C_{61}-butyric acid methyl ester
PCE	Power conversion efficiency
PEBII	Poly((1-(4-ethenylphenyl)methyl)-3-butyl-imidazolium iodide)
PEDOT:PSS	Poly(3,4-ethylenedioxythiophene)-poly(styrenesulfonate)
PEIE	Polyethylenimine ethoxylated
PEN	Polyethylene naphthalate
PET	Polyethylene terephthalate
PFN-OX	Poly[9,9-bis(6′-(*N*,*N*-diethylamino)propyl)-fluorene-*alt*-9,9-bis-(3-ethyl(oxetane-3-ethyloxy)-hexyl)-fluorene]

PIL	Polymerised ionic liquid
PMII	1-Methyl-3-propylimidazolium iodide
POEM	Poly(ethylene glycol) methyl ether methacrylate
ppm	Parts per million
PSC	Perovskite solar cell
PV	Photovoltaic
PVC	Polyvinyl chloride
p-XRD	Powder X-ray diffraction
QDSC	Quantum dot sensitized solar cell
qssDSC	Quasi-solid state dye-sensitized solar cell
RF	Radio frequency
SC	Short circuit
SEM	Scanning electron microscope
SM315	A porphyrin-based dye (see Figure 2.11)
SNT@TNS	SnO_2 nanotubes coated in TiO_2 nanosheets
Spiro-OMeTAD	$N^2,N^2,N^{2'},N^{2'},N^7,N^7,N^{7'},N^{7'}$-octakis(4-methoxyphenyl)-9,9′-spirobi[9*H*-fluorene]-2,2′,7,7′-tetramine
ssDSC	Solid-state dye-sensitized solar cell
TCO	Transparent conducting oxide
TEM	Transmission electron microscopy
THF	Tetrahydrofuran
TNP	TiO_2 nanoparticles
TTIP	Titanium(IV) isopropoxide
UATR	Universal attenuated total reflectance
UV	Ultraviolet
WH	Without heating
XPS	X-ray photoelectron spectroscopy
XRD	X-ray diffraction
ZNP	ZnO nanoparticles
ZNW	ZnO nanowires
ZNW@TNS	ZnO nanowires coated in TiO_2 nanosheets

Nomenclature

a	Geometric surface area (m^2)
A	Pre-exponential factor
B	Peak width at half maximum
C	Concentration (mol dm^{-3})
D	Dye loading (mol m^{-2})
E_a	Activation energy (kJ mol^{-1})
I	Current (A)
J	Current density (A m^{-2})
J_{sc}	Short-circuit current density (A m^{-2})
k	Rate constant (s^{-1})
K	Scherrer constant
L	Crystallite size (m)
M_n	Molar mass (g mol^{-1})
p	Partial vapour pressure of adsorbate gas in equilibrium with the surface at 77.4 K (Pa)
p_o	Saturated pressure of adsorbate gas (Pa)
P_{in}	Incident light intensity (J s^{-1} m^{-2})
P_{max}	Maximum power output (J s^{-1} m^{-2})
R	Universal gas constant (J K^{-1} mol^{-1})
S_{BET}	Specific surface area from BET analysis (m^2 kg^{-1})
S_{calc}	Calculated specific surface area for a material composed of perfect spheres (m^2 kg^{-1})
t	Time (s)
T	Temperature (K)
v	Volume (m^3)
V	Voltage (V)
V_a	Volume of gas adsorbed at standard temperature and pressure (m^3)
V_{oc}	Open-circuit voltage (V)
Z'	Real component of impedance (Ω)
Z''	Imaginary component of impedance (Ω)
η	Power conversion efficiency (%)
θ	Diffraction angle (°)
λ	Wavelength (m)
φ	Angle of elevation of the sun (°)

Chapter 1 – Introduction

As we progress further into the 21st century the ever growing energy challenge becomes more apparent. The problems related to the use of fossil fuels as our primary energy source are now well known and can be generalized as a three-fold problem of finite resources, security of supply and the impacts of greenhouse gas emissions.

Estimates, based on fossil fuel reserves and current production rates, predict that there is under 56 years' worth of oil and 60 years' worth of natural gas within the world.[1] Although estimates of reserves may increase upon discovery of new sources, these values indicate that production of a sufficient quantity of fossil fuels to meet a growing global energy demand will be a major challenge within our lifetimes. The uneven distribution of these fossil fuels around the world only adds to this problem. Taking the case of Europe for example, it can be estimated that a continuation of current oil production would lead to a depletion of all the known European oil reserves within a period of 20 years.[1] Increasingly, this leads to reliance on fossil fuel production within some of the world's most politically unstable regions, including the Middle-East, which is home to three of the five countries with the biggest oil and gas reserves in the world.[1]

In addition to these two issues of supply, there is the impact of greenhouse gas emissions on the global climate. Since pre-industrial times global CO_2 levels have risen dramatically within the atmosphere and surface oceans. Shown in Figure 1.1 is a collection of data from ice core measurements and direct atmospheric measurements of CO_2 concentrations spanning the last 1100 years.[2-4] The vast majority of this dramatic increase in CO_2 levels is undeniably attributed to the release of CO_2 from the burning of fossil fuels for energy. CO_2 is well known to act as a greenhouse gas, resulting in the gradual warming of the Earth due to the absorption and re-emission of infrared radiation from the Earth. Although the exact extent of global warming is still open to some uncertainty, it is becoming increasingly clear that a significant change to our approach to energy production and usage is required if we are to prevent significant changes to the global climate.[5]

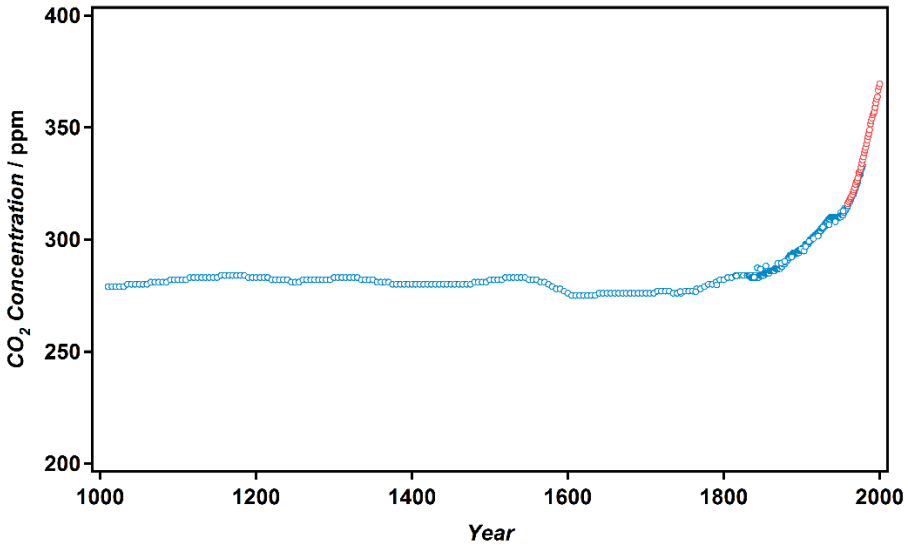

Figure 1.1. Carbon dioxide concentrations (in parts per million) for the last 1100 years, measured from air trapped in ice cores (blue) and directly from atmospheric measurements in Hawaii (red).[2-4]

One proposed way of reducing the impact of fossil fuel technologies is through the use of carbon capture and storage.[6] Another low CO_2 alternative is the use of energy generated from nuclear fission reactors, which can generate a stable base load of energy. However, as a long term solution, renewable energy provides by far the most promise for a sustainable energy future. Renewable energy technologies produce extremely low, or negligible, CO_2 emissions, are more evenly distributed on a global scale and are not finite resources, unlike fossil fuels. As of 2014, renewable energy sources accounted for only 3 % of the total global energy consumption and 6 % of total global power generation, which neglects energy involved in transportation.[7] However, this value is set to increase dramatically in the future, with growth of over 12 % reported in 2014 alone.[7]

Of all of the sources of renewable energy available to us solar energy is by far the largest (Figure 1.2). With approximately 122,000 TW of solar power reaching the surface of the Earth, compared to the current global power consumption of ~16 TW, it is easy to see why it is such an attractive source.[7, 8] Solar energy is now the fastest growing renewable energy technology. In 2014 alone solar power generation grew by 38.2 % compared to the previous year.[7] It is hoped that such rapid growth can continue in order to aid in bridging the gap between our current levels of power consumption and the estimated ~27 TW that we are projected to consume by the middle of the century.[9] This solar energy is typically utilised in three different ways: Solar biomass, solar thermal or solar electric, otherwise known as photovoltaics, the latter of which will form the focus of this thesis.

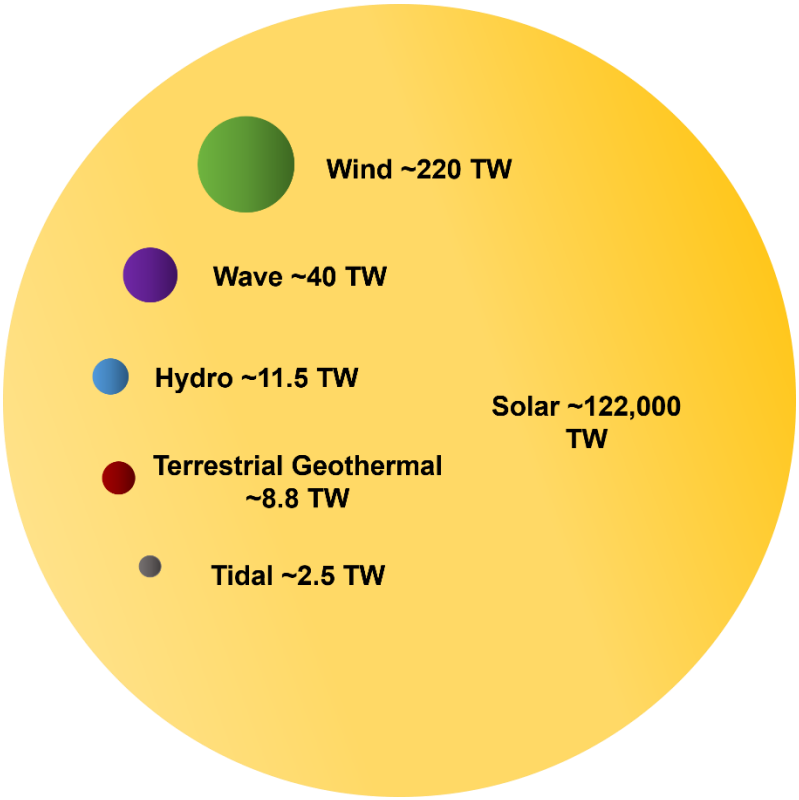

Figure 1.2. Comparison of the estimated theoretical total global resources of different renewable power sources using spheres with volumes corresponding to their relative magnitude.[8]

Solar biomass uses solar energy to drive chemical reactions, where the energy is stored in the chemical bonds. This is the process that plants use during photosynthesis. Solar biomass power in its simplest form could involve a repeated cycle of growing plants and burning them for power. More sophisticated methods include the production of ethanol or biodiesel from plants or algae, which can be used as transport fuels. Although such methods could prove very useful as alternatives for petroleum based transport fuels, their use for global energy production is limited due to the inherently low efficiency of photosynthesis. For instance, in Europe, solar power conversion efficiencies for some of the best crops are less than 1 %.[10] Another problem arises from the competition for agricultural land required to grow most of these crops. This has led to what is known as the "food *vs*. fuel debate".

Solar thermal power involves the conversion of solar energy into thermal energy, usually via the heating of a fluid. The thermal energy can then either be used directly for hot water systems within houses or it can be converted into higher-grade energy, such as electricity. Roof based units typically use sets of pipes coated in a light absorbing material that will heat the pipes and, therefore, the water passing through them. This only produces low-grade heat energy, which is not easy to distribute, but is good for onsite use through water heating. Larger installations use arrays of mirrors, such as parabolic troughs or Fresnel mirror arrangements, to direct and

concentrate light onto a tube through which a liquid is passed. This can then be used to heat water, generating steam to drive a turbine and generate electricity. Solar thermal power can give relatively high power conversion efficiencies, although power losses are experienced upon conversion into electrical power.[11]

Photovoltaics is potentially the most useful of these three types of technology, thanks to the ability to directly produce high grade electrical energy. This allows the generation of electricity at the site of use and requires almost no maintenance owing to there being no moving parts. This also means that no gas emissions are generated at the site of use and they are silent, the latter of which is a common complaint of other renewable energy technologies e.g. wind turbines. Photovoltaics can be integrated into buildings in what is termed building integrated photovoltaics (BIPV), allowing building materials such as windows and roofs to become active components of the building and generate its own power at the site of use. This can, therefore, distribute the power network and allow users to take more control over their power usage, particularly when combined with battery technologies.

Despite the many advantages of photovoltaic technology, it is not without its flaws. As with other renewable energy technologies, the supply of energy is intermittent meaning that it needs to be combined with energy storage to deliver a stable supply of energy. The distribution of solar energy is also relatively diffuse, meaning that large land areas often require covering to gain a sufficient amount of power. However, one of the main drawbacks of photovoltaic technology currently is the cost of generating power in this way. A considerable amount of the cost can be linked to the production and materials price during manufacturing of the panels, which also has a significant energy cost for conventional photovoltaic panels. It is for this reason that there is much research interest in developing new photovoltaic technologies that benefit from cheaper materials and manufacturing processes.

There are now many different photovoltaic technologies, including several emerging technologies, which show great potential for providing us with affordable renewable energy as a replacement to fossil fuels. Many of these technologies will be briefly reviewed in Chapter 2, but the focus of this thesis is on two emerging photovoltaic technologies: dye-sensitized solar cells and perovskite solar cells. Key to the efficient functioning of these devices are materials that can absorb light and materials that can selectively transport photo-generated charges. It is the latter set of materials that will form the main focus of this thesis. More specifically, the use of ZnO as an electron selective charge transport material will be investigated.

1.1 Aims and Scope

Before materials can be tested within photovoltaic devices they first have to be made, therefore, the synthesis of materials will form a large part of this thesis. As will be discussed in detail within Chapter 2, morphological control of materials at the nanoscale is key to gaining high efficiency devices for both dye-sensitized and perovskite solar cells. Fortunately there are many different techniques available for creating nanostructures of ZnO with a variety of different morphologies. The technique chosen for the production of ZnO nanostructures within this thesis is electrochemical anodization, which will be discussed in detail in Chapter 2. This is a scalable and low temperature technique that has been shown to be capable of producing a wide range of ZnO nanostructures.

In particular, this thesis will focus on the production of ZnO nanowires using anodization, as nanowires have many appealing characteristics for application in photovoltaics. The factors that control this anodization process will be examined in detail in order to allow bespoke nanostructures to be produced for application in the two photovoltaic technologies studied in this thesis. It is often necessary to further modify nanomaterials in order to gain the properties required to work effectively in their desired application. The use of simple post-anodization modifications will, therefore, also be explored to tailor the nanomaterial properties towards their applications.

The second half of the thesis will focus on the application of these ZnO nanomaterials within dye-sensitized and perovskite solar cells. A number of different device architectures will be produced in order to establish in which situations, if any, the use of anodic ZnO nanowires can bring benefits to the overall cell performance. In the case of perovskite solar cells, which is a relatively new field, the more general use of ZnO materials, rather than solely nanowires, will also be investigated to assess their suitability for this application.

The specific objectives of this thesis can therefore be summarised as:

- To determine the factors that control the growth of nanowires during anodization and use this knowledge to tailor the nanowire properties towards application in photovoltaics.
- To establish simple post-anodization treatments that allow the nanowire structure to be modified further, thereby, providing properties that are beneficial when applied within the photovoltaic devices.
- To apply the nanowires produced by anodization, and the modified nanowires, within dye-sensitized solar cells as a high surface area electron-selective contact. This will involve producing various device architectures, in which the merits of using nanowires will be assessed.

- To apply ZnO nanomaterials, including nanowires produced from anodization, as electron-selective contacts within perovskite solar cells. This will again involve the production of various different device architectures and comparison of the use of nanowires with simpler nanoparticle morphologies. In addition to this, the general use of ZnO within perovskite solar cells will be assessed against the most commonly used electron selective material, TiO_2.

1.2 Thesis Structure

The thesis is divided into eight chapters. After this introductory chapter, Chapter 2 will introduce and review the literature on the two photovoltaic technologies that are the focus of this thesis. It will then go on to review the production of ZnO nanostructures by electrochemical anodization. In Chapter 3, the full details of all of the experimental procedures and methods of characterisation will be documented. These experimental details support the results reported in Chapters 4 to 7.

The results reported in this thesis are very much split into two halves. Chapters 4 and 5 will focus on the development of ZnO nanomaterials, whilst Chapters 6 and 7 will focus on their application within photovoltaic devices. In Chapter 4, a full systematic study of the factors that control the growth of nanowires during anodization will be presented. Further characterisation of the nanowires is then used to determine the likely mechanisms of nanowire growth during anodization. The modification of these anodic nanowires, through the use of simple synthetic techniques, will then be presented in Chapter 5.

The nanomaterials discussed in Chapters 4 and 5 will then be applied in dye-sensitized solar cells in Chapter 6, followed by perovskite solar cells in Chapter 7. In both cases, multiple different solar cell architectures will be demonstrated and the merits of the various ZnO nanomaterials within them will be discussed. A breakdown of the materials reported and the solar cell architectures tested in each results chapter is shown in Figure 1.3.

Finally, the results of this thesis will be concluded in Chapter 8 and suggestions for possible areas of future work will be proposed.

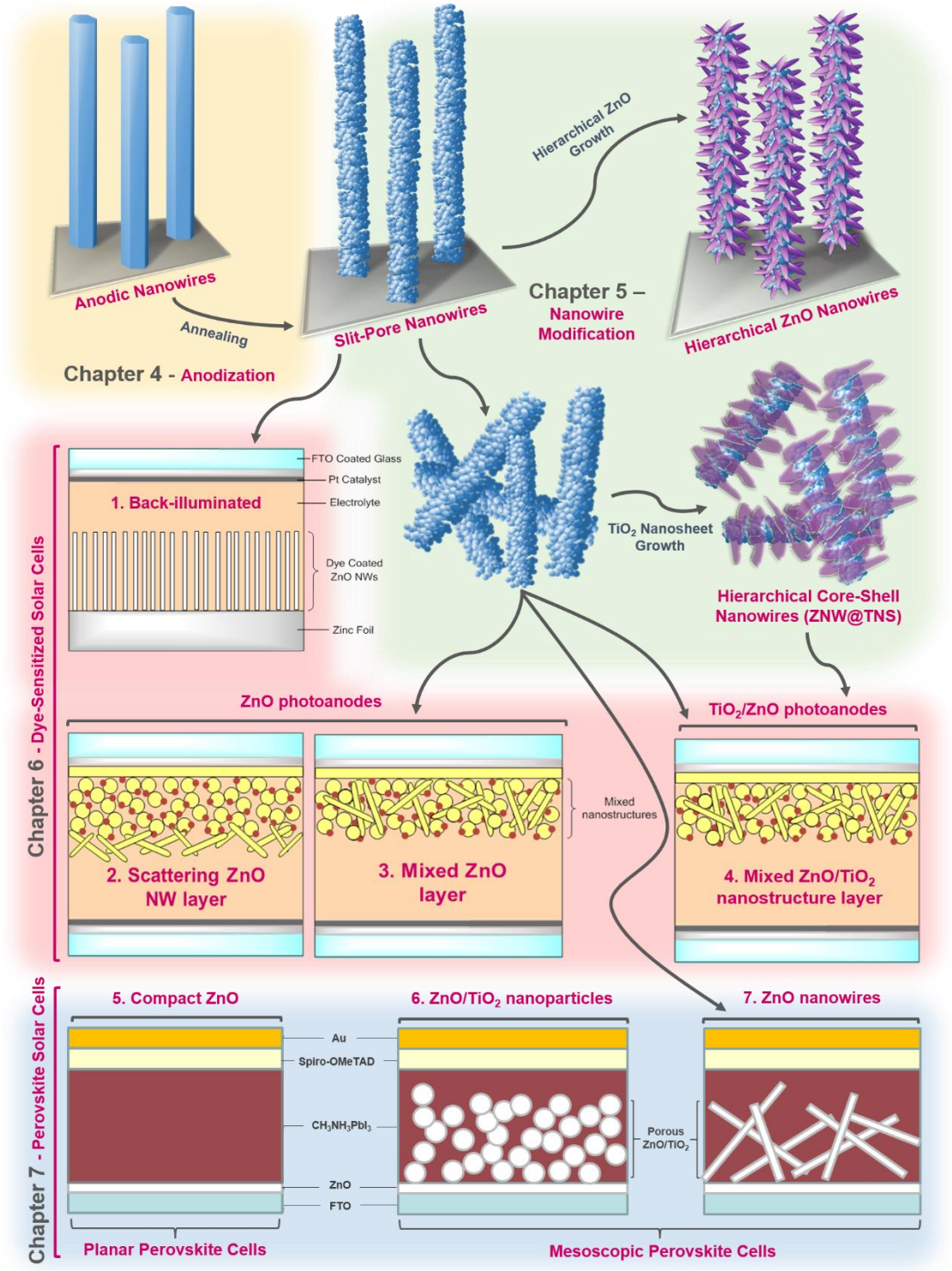

Figure 1.3. A schematic summary of the contents and research focus of each results chapter of the thesis.

Chapter 2 – Literature Review

In this chapter the photovoltaic technologies of interest, as well as the process of anodization, will be introduced and the current literature in these fields is reviewed. The chapter begins by providing a brief background to photovoltaic technologies as a whole before going into more detail on both dye-sensitized solar cells and perovskite solar cells, which are the subject of this thesis. For both of these technologies, a general background to their development and current status will be given, before focussing on previous reports of the use of ZnO within them. The final section of this chapter will review the production of ZnO nanostructures by anodization, which is the primary synthesis technique used in this thesis.

2.1 Photovoltaics

2.1.1 The three generations of photovoltaics

Although the photovoltaic (PV) effect was originally discovered in 1839 by Edmond Becquerel, it was not until the 1950s that modern research into photovoltaics really began.[12] This research was sparked by the invention of the crystalline silicon solar cell, which today remains as the dominant photovoltaic technology.[13] Crystalline silicon solar cells (Figure 2.1) operate on the principle of p-n junctions, which are formed by joining p-type and n-type semiconductors together. Electrons and their corresponding electron holes are generated by the absorption of light at the interface of the p-n junction and then separated by an electrical field that acts across the junction. These charges are then collected through an external circuit, resulting in a current.

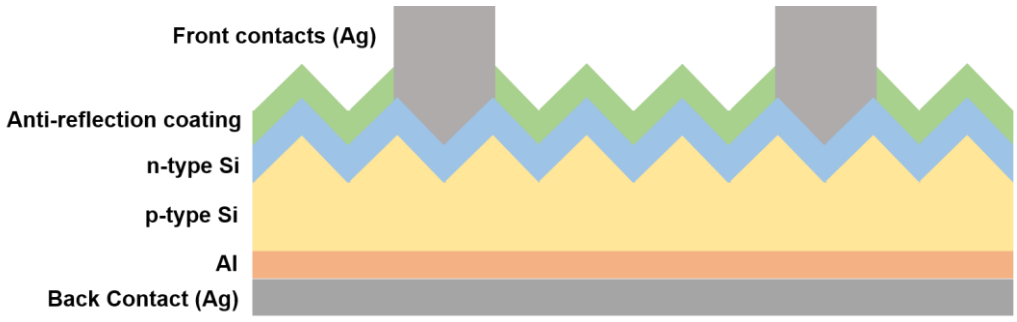

Figure 2.1. Simplified cross-section of a typical crystalline silicon photovoltaic device.

In many ways, crystalline silicon is an extremely hard photovoltaic technology to beat. It is made predominantly from silicon, the second most abundant element in the Earth's crust, so is unlikely to face issues of element abundance or toxicity. It also benefits from a huge wealth of

knowledge and expertise from the well-established semiconductor electronics industry. After over half a century of intensive research on these devices, they can now be produced at record power conversion efficiencies of 25 %, which is not far from the theoretical efficiency maximum of 32 % for a single junction solar cell, known as the Shockley-Queisser limit.[14, 15] Commercial module efficiencies are typically lower, but module efficiencies in the range of 15-18 % are commonplace.[16] Despite these many advantageous characteristics of crystalline photovoltaics, their price is still a major issue in making solar energy competitive with conventional fossil fuels. Recent years have seen the price of crystalline silicon modules drop dramatically to below US$1 per peak Watt, due to the scaling up of production and development of new processing methods.[17] It has also been found that for each doubling of module production volume the module cost is typically reduced by 22 %.[18] How much further this can drop remains an open issue, however, and it is possible that the cost involved with producing the high quality crystalline silicon required for these devices may prove prohibitive.

In an effort to reduce the price of solar energy, a significant amount of research has been focussed on the development of a range of alternative photovoltaic devices. Photovoltaics are now commonly grouped into three different generations of devices, the first generation of these being based on crystalline silicon. The second generation of photovoltaic devices are those that use thin films (typically ~1 μm) of material as the active component of the solar cell. These include cells based on cadmium telluride (CdTe), amorphous silicon (*a*-Si) and copper indium gallium selenide (CIGS).[14] These materials have a much higher light absorbance than crystalline silicon allowing the use of thinner films, which in turn can reduce the fabrication costs associated with raw materials.[19]

Amorphous silicon solar cells (Figure 2.2a) can be produced at lower temperatures than crystalline silicon and deposited on low-cost flexible substrates, such as plastics or metal foils. However, record efficiencies for these devices are currently behind those of crystalline silicon and other second generation technologies (13.6 %).[14] Other second generation technologies, such as CdTe and CIGS solar cells, are typically composed of a 1-2 μm thick absorbing layer of the compound semiconductor onto which a thin (~ 100 nm) "window" layer is deposited (Figure 2.2b and c). These absorbing layers have to exhibit a high absorption coefficient to be effective in the generation of current and a suitable band gap to provide good voltage.[19] CdTe and CIGS have achieved record efficiencies, of 21.5 % and 21.7 % respectively, making them competitive with crystalline silicon technologies.[14] Despite these promising efficiencies, there are multiple concerns about both the scarcity and the toxicity of elements used within these solar cells, which present questions over their widespread use.[19] In the case of CdTe it has been calculated that resource limitations appear to restrict the possible contribution of these cells to less than 1 % of the total additional power required to meet global power needs in 2050.[20]

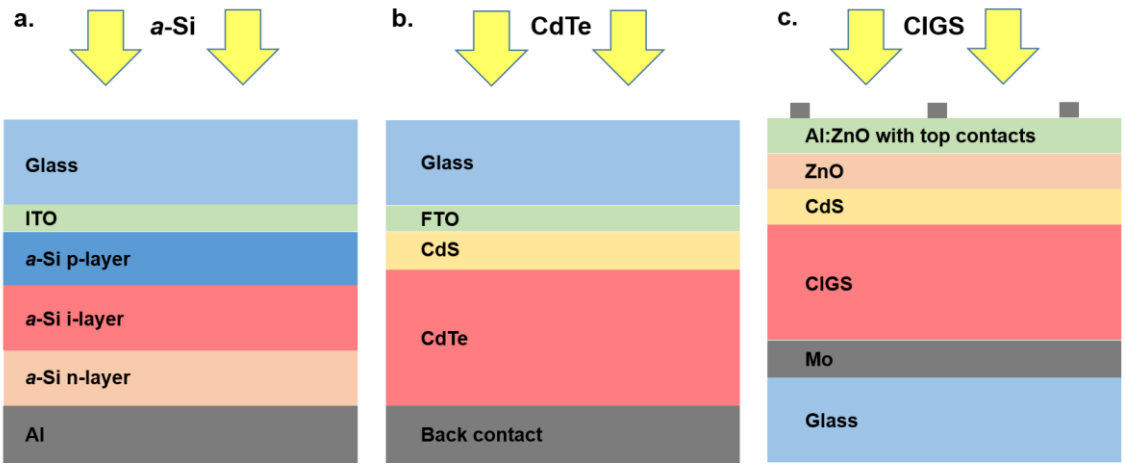

Figure 2.2. Simplified cross-sections of typical second generation photovoltaic technologies, including amorphous silicon (*a*-Si) (a), CdTe (b) and CIGS (c). ITO = indium tin oxide and FTO = fluorine-doped tin oxide.

Third generation photovoltaics are a broad group of emerging technologies that have the potential to avoid many of the shortcomings of the previous generations. Many of the technologies included in this category show promise in providing extremely low cost photovoltaic devices through the use of solution processing, which is compatible with high throughput manufacturing. They also generally use more abundant raw materials, so that fundamental limitations on production capacity can be overcome. In addition to this, some third generation technologies present the opportunity to surpass the theoretical Shockley-Queisser limit of 32 % through the use of processes such as multiple exciton generation, which offers the potential to extract more than one electron from the absorption of a single photon.[15, 21] Example of materials that can demonstrate this ability are quantum dots of PbSe and PbS.[21] Other processes that can be used to surpass this efficiency limit are up-conversion of two or more low energy photons to generate a high energy photon capable of exciting an electron, or down-conversion of a high energy photon into two or more lower energy photons.[22]

Solar cells based upon $Cu_2ZnSn(S_{1-x}Se_x)_4$ (CZTSSe) absorbing layers are an extremely promising alternative to CIGS solar cells.[23] CZTSSe can be used in similar device structures as CIGS (Figure 2.3a), however, the expensive and scarce elements indium and gallium are replaced by a combination of much cheaper zinc and tin. In addition to this, selenium can be replaced to some extent by abundant and cheap sulfur. Significant progress has been made in the fabrication and efficiencies of these devices over the past years. However, their record power efficiencies of 12.6 % are still significantly lower than their less sustainable analogues.[24]

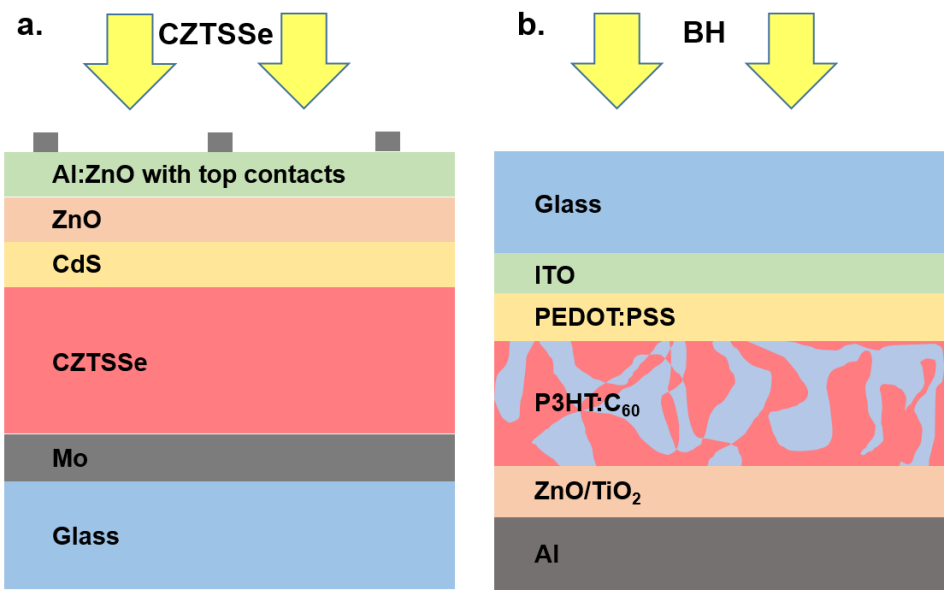

Figure 2.3. Simplified cross-sections of typical third generation photovoltaic technologies including CZTSSe (a) and organic bulk heterojunction (BH) (b) solar cells.

Thin film photovoltaic cells based on organic semiconductors have also attracted significant attention as an alternative to devices based on inorganic materials.[25] Of this class of devices, bulk heterojunction solar cells have been some of the most commonly reported and most successful. These cells are based on the formation of a bulk heterojunction between a fullerene derivative, which acts as an electron acceptor, and a conducting polymer such as poly-3-hexyl thiophene (P3HT), which acts as an electron donor (Figure 2.3b). These materials are typically cast from solution and as the solvent evaporates the two components phase-separate into nanodomains, forming the so-called bulk heterojunction. The indium tin oxide (ITO) electrode substrate is usually coated with a layer of a hole selective polymer, such as poly(3,4-ethylenedioxythiophene) poly(styrenesulfonate) (PEDOT:PSS), whilst transparent oxides such as ZnO are used as electron selective contacts.[25] This type of cell offers many potential advantages including simple roll-to-roll processing on flexible substrates, low weight and semi-transparent devices and short energy payback times.[25] These beneficial properties make organic solar cells very attractive candidates for low cost photovoltaics for a variety of applications, however, it is likely that further advances from their current record efficiency of 11.5 % are required for widespread commercialisation of this technology.[26]

One of the other third generation technologies that has received significant attention is the dye-sensitized solar cell (DSC), which makes use of a molecular dye attached to a high-surface area semiconductor to absorb light.[27] From this technology two further types of photovoltaic device have emerged: the quantum dot-sensitized solar cell (QDSC), which uses semiconductor nanoparticles to absorb light rather than a dye, and more recently, the perovskite solar cell (PSC).

Dye-sensitized solar cells and perovskite solar cells form the area of focus for this thesis and will, therefore, be covered in detail within Sections 2.2 and 2.3 respectively.

2.1.2 Analysis of photovoltaic performance

Before moving on to discuss dye-sensitized and perovskite solar cells in detail it is, perhaps, an ideal moment to briefly explain some of the parameters and methods associated with measurement of photovoltaic cell efficiencies. The efficiency of a solar cell is most commonly assessed by measuring the photocurrent as the voltage is swept from short circuit (SC, 0 V) to some forward bias, at which point the measured current becomes negative, known as open circuit (OC). The plot of current (*I*) *vs*. voltage (*V*) typically resembles a curve and is, therefore, commonly referred to as an *I-V* curve. To account for the different sizes of active cell area that are used this is more commonly displayed as a plot of current density (*J*) *vs.* voltage, which is similarly named a *J-V* curve (Figure 2.4a). During this measurement, the solar cell is typically illuminated by a standardised light source. The most commonly used standard spectrum is called AM 1.5, where AM stands for air mass and can be approximated as:

$$AM = \frac{1}{cos\varphi} \qquad \text{Eq. 2.1}$$

Where φ is the angle of elevation of the sun in the sky. Consequently AM 1.5 corresponds to φ equalling an angle of 42°. This spectrum is then normalised so that the amount of radiant energy received at the solar cell per unit time and per unit area corresponds to 1000 W m^{-2}, which is commonly referred to as 1 Sun. 1 Sun is the most commonly reported light intensity used during solar cell testing, however, some researchers also test cells under lower light intensities, such as 0.1 Sun in order to gain a more accurate assessment of the cell performance under lower light conditions, as would be expected in reality for areas such as northern Europe.

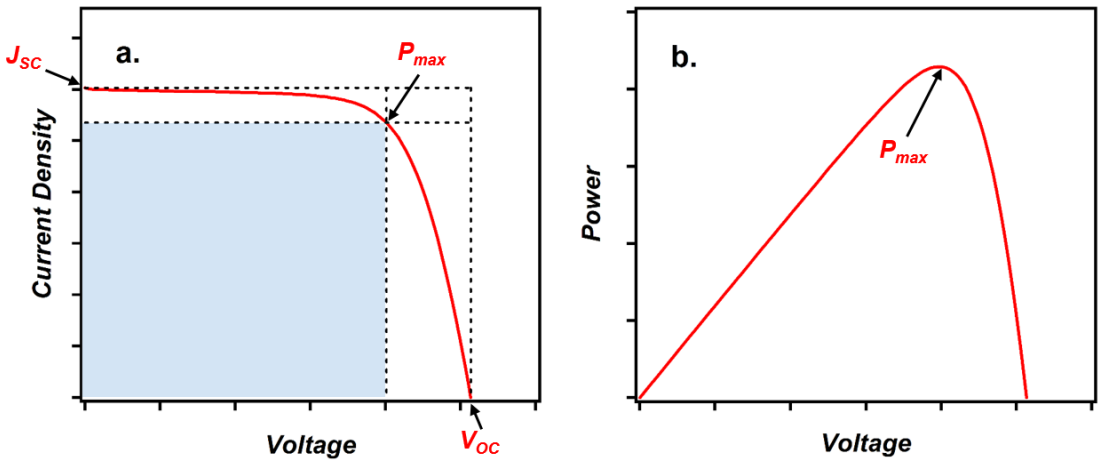

Figure 2.4. A typical *J-V* curve of a solar cell (red line) showing the associated parameters measured from it (a) and the corresponding plot of power *vs*. voltage from which the maximum power point (P_{max}) is obtained (b).

Four parameters are typically extracted from the *J-V* curve. These are the short circuit current density (J_{sc}), which is obtained from the y-axis intercept, the open circuit voltage (V_{oc}), which is obtained from the x-axis intercept, the fill factor (*FF*) and the power conversion efficiency (*PCE*). The fill factor is a measure of how ideal the *J-V* curve is, with a perfect rectangle being the ideal shape. Based on Figure 2.4a the fill factor can be described as being the ratio of the rectangular area denoted by the outer dashed line to the rectangular area highlighted in blue. In order to calculate the fill factor, it is first necessary to calculate the maximum power output (P_{max}) of the cell by multiplying the current and voltage data and plotting as a function of the voltage (Figure 2.4b). The fill factor can then be calculated simply as:

$$FF = \frac{J_{sc} \cdot V_{oc}}{P_{max}} \qquad \text{Eq. 2.2}$$

From these first three parameters the power conversion efficiency can then be calculated as:

$$PCE = \frac{J_{sc} \cdot V_{oc} \cdot FF}{P_{in}} \cdot 100\% \qquad \text{Eq. 2.3}$$

Where P_{in} is the power of the incident light intensity. These four parameters are used extensively within photovoltaics research to compare the performance of solar cells and will, therefore, be used within the discussion of previous research in Sections 2.2 and 2.3.

2.2 Dye-Sensitized Solar Cells

Dye-sensitized solar cells (DSCs) are a type of third generation photovoltaic technology used for the direct conversion of solar energy into electrical energy. These cells do not rely on p-n junctions to absorb light, unlike first and second generation solar cells, and as a result, offer the possibility to exceed the efficiency limits placed on such cell designs.[28] DSCs offer the prospect of very low fabrication cost compared to traditional silicon based p-n junction solar cells, which require large wafers of high purity, high crystallinity silicon that are both costly and energy intensive to produce.[29] The ease of production through roll-to-roll processing and adapting of existing printing techniques provides further possibilities to reduce costs in manufacturing compared to silicon photovoltaics, which rely on batch production methods.[30] Other benefits of DSCs include their aesthetic appeal due to their partial transparency and colour, easy integration into building architecture and short energy payback time, which is the time required to generate an amount of energy equal to the energy embodied within the system during production.[31]

2.2.1 Operating principles of DSCs

The main components of a typical dye-sensitized solar cell are displayed in Figure 2.5. The most characteristic part of the cell is the layer of dye molecules that coats the semiconductor support. The dye molecules are responsible for the absorption of light, which is used to excite an electron from a lower energy level, known as the highest occupied molecular orbital (HOMO), to a higher energy level above the lowest unoccupied molecular orbital (LUMO), thereby producing an exciton. An exciton is a combination of the excited electron and the electron hole left in the HOMO. The excited electron has a negative charge and the electron hole has an equal and opposite positive charge. For a current to be generated the two charges must then be separated, preventing their recombination. The semiconductor support onto which the dye is adsorbed acts as the transport medium for excited electrons, whilst an electrolyte on the opposite side of the dye will act as a transport medium for the electron holes, carrying their charges to the anode and cathode respectively. In this way the circuit is completed and electrons are passed around the circuit by the light absorbing dye molecules.[32]

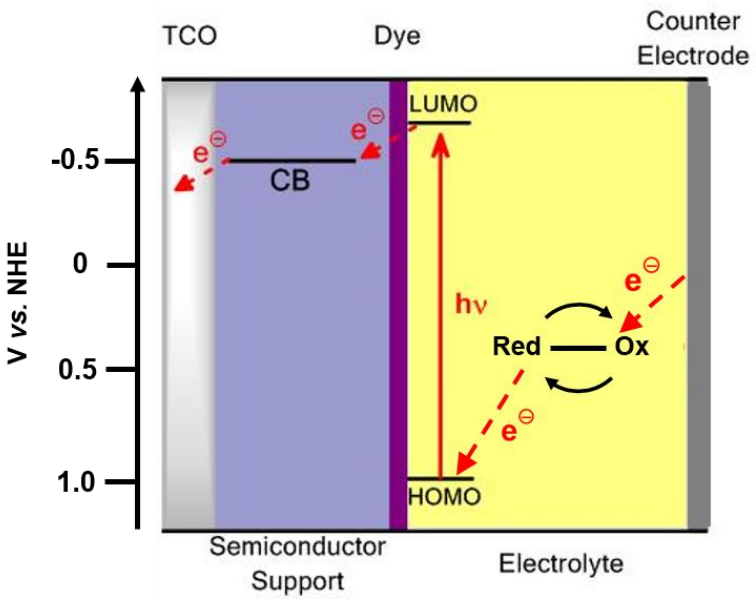

Figure 2.5. Schematic diagram of the mechanism of current generation in DSCs (TCO = transparent conducting oxide, CB = conduction band, and NHE = normal hydrogen electrode).

In all cell designs, at least one of the electrodes must be made from a transparent conducting material, such as fluorine-doped tin oxide (FTO), to allow transmission of light to the dye molecules. The materials chosen for the other electrode can vary depending on the cell design and can be chosen to either transmit light or reflect light back towards the dye to increase light absorption. In the commonly used cell design, developed by Grätzel in 1991 (Figure 2.6),[27] a dye is adsorbed onto a high surface area semiconductor consisting of a mesoporous film of titania nanoparticles. The liquid electrolyte contains a redox mediator, typically the I^-/I^{3-} redox couple, which is regenerated at the platinum coated counter electrode.

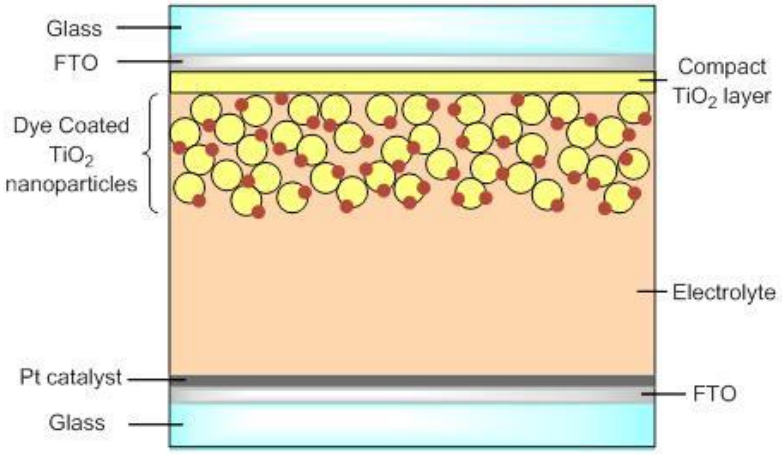

Figure 2.6. Cross-section of a DSC, similar to the one originally reported by Grätzel *et al.*[27]

All of the components within the cell need to be carefully selected in order to correctly align their respective energy levels. The maximum output voltage (the V_{oc}) of the cell is ultimately determined by the difference in potentials between the conduction band edge of the semiconductor support and the redox potential of the electrolyte. These potentials therefore need to be matched as closely as possible to the LUMO and HOMO levels of the dye in order to minimise energy losses.[32]

Dyes with broad absorbance ranges and high extinction coefficients are typically used in DSCs to maximise the amount of light absorbed and, thereby, increasing the overall power conversion efficiency. Commonly used dyes are ruthenium-bipyridyl complexes, such as *cis*-diisothiocyanato-bis(2,2'-bipyridyl-4,4'-dicarboxylato)ruthenium(II) bis(tetrabutylammonium) (N719), which display excellent absorbance intensities over a broad range of wavelengths and have LUMOs that match closely to the conduction band edge of TiO_2 (anatase).[27]

2.2.2 Major breakthroughs in DSCs

Since Grätzel's famous 1991 publication,[27] in which it was shown that high efficiency (7.9 %) DSCs could be produced by using high surface area metal oxides sensitized by a ruthenium-based dye, interest in DSCs has seen continual growth. Much of the decade that followed focussed on the improvement of the Ru-based molecular dye used to sensitize the semiconductor. Notable examples include the N3 dye, which boosted the efficiency to 10 %, and the "black dye", with a broader absorption spectrum, which was used to produce DSCs with efficiencies of 10.4 % (Figure 2.7).[33, 34]

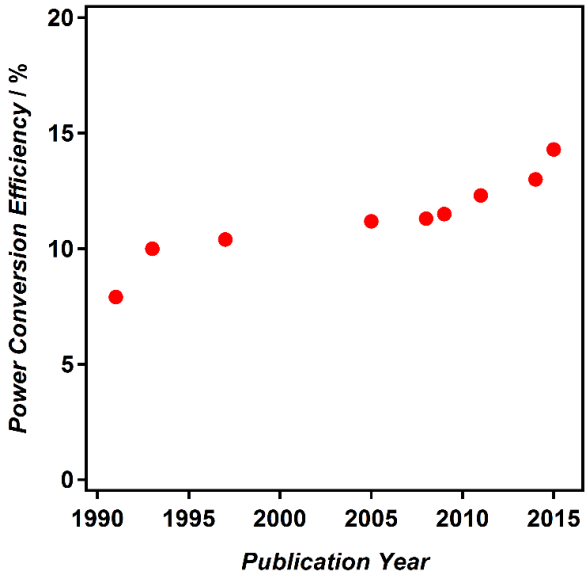

Figure 2.7. Plot of record power conversion efficiency of DSC devices over time according to publication date. Efficiencies were obtained from the references within this section.[27, 34-41]

After 1997, progress in record DSC efficiencies was relatively slow for a whole decade (Figure 2.7), despite significant research efforts into various alternative dyes and cell designs. Some progress was made in the latter half of the last decade through the modification of the commonly used Ru-based dyes. Nazeeruddin *et al*. applied a purification procedure to obtain pure N-bonded isomers of the N3 sensitizers, obtaining an efficiency of 11.18 %.[36] Other researchers developed heteroleptic Ru-complexes with high molar extinction coefficients by extending the π-conjugation of spectator ligands. This allowed efficiencies of 11.3 %, and later 11.5 %, to be reached.[37, 38]

Despite these small advances at the end of the decade, it can be observed that record DSC efficiencies seemed to have plateaued (Figure 2.7). In a recent review the authors highlight that this is, perhaps, not surprising given that Ru-based dyes and I^-/I_3^- based electrolytes continue to be used within cells.[42] Although Ru-based dyes have been successful in demonstrating reasonably broad absorption spectra, their molar extinction coefficients are relatively low (~10^4 M^{-1} cm^{-1}) and with typical absorption onsets of around 780 nm they utilise few photons within the near infrared (NIR) region.[34, 37, 43] This acts to limit the maximum achievable current of DSCs based on Ru-based dyes. Perhaps an even greater barrier to efficiency increases is the I^-/I_3^- redox couple used in the electrolyte. This two-electron redox couple has a significant loss of potential associated with the regeneration of the Ru-based dye which contributes significantly to the total potential loss within the cell. It has been estimated that the lowest possible loss in potential for a cell featuring a Ru-based dye, and the I^-/I_3^- redox couple is 750 mV, which limits the maximum obtainable conversion efficiency of the DSC to 13.8 %.[43] To overcome this limit, it was highlighted that researchers must either use alternative dyes that have absorption spectra into the NIR region, allowing higher currents to be achieved, or use alternative 1-electron redox couples with lower redox potentials to increase the V_{oc} of the cell.[42]

This is indeed what has been done over the past few years, and to a reasonable degree of success. The use of either porphyrin or organic based dyes, with broader absorption spectra, in combination with 1-electron Co-based redox couples has led to the apparent efficiency plateaux being broken.[39, 40] The 13.8 % predicted efficiency limit on Ru-based DSCs was also recently surpassed by Kakiage *et al*., who used two different dyes to co-sensitize the semiconductor surface, in combination with a 1-electron redox couple, to obtain a record efficiency of 14.3 %.[44] It seems likely that further advances in DSC efficiency might be made through similar approaches.

2.2.3 Three main components: dye, electrolyte and semiconductor

This next section will focus on the advancements and areas of focus in the field of DSCs over the past two decades. Due to the enormity of research papers in the field of DSCs, this section will

certainly not provide an exhaustive list of developments, but instead will aim to give a focused overview of the key innovations and open challenges in DSCs. For more exhaustive records of research in the area of DSCs readers are directed to the many review papers in the literature, including an excellent review on the area by Hagfeldt *et al*.[45] Research in the field of DSCs has largely been focussed on one of the three main components of the DSC, namely the dye, electrolyte and semiconductor. Therefore, this section will also be separated in this way to highlight these areas of research.

Dyes

The dye molecule plays a central role in the functioning of a DSC and has, therefore, been the subject of intense research over the past two decades, with hundreds of different dyes being tested. Ideally, an effective dye should provide high light absorption over the whole visible region of the spectrum and also into the NIR to maximise light harvesting. It should feature a suitable anchoring group, such as a carboxylic acid, by which it can be attached to the semiconducting oxide. It should possess a suitable excited and oxidised state energy level to allow effective injection of electrons into the n-type semiconductor and allow regeneration via a redox couple in the electrolyte. Finally, the dye should be stable in order for the cell to maintain its efficiency for the lifetime required of a typical commercial PV device (~25 years).

Molecular dyes based on ruthenium complexes were used in the initial breakthrough paper by Grätzel and O'Regan in 1991 and have remained the most commonly used class of dyes since.[27] This initial report used a trinuclear Ru-complex (Figure 2.8) to sensitize the TiO_2 semiconductor, achieving a power conversion efficiency of 7.9 %. Within two years, the use of mononuclear Ru-complexes was adopted and has been maintained ever since. This first mononuclear Ru-complex, named N3 (Figure 2.8), featured excellent absorbance, long excited state lifetimes and strong binding to the semiconductor surface through up to 4 carboxyl groups, which combined to give 10 % efficient DSCs.[34] The absorbance of this dye was later broadened further into the red end of the spectrum through the use of a terpyridine ligand which has been named N749 (Figure 2.8), or more commonly as the "black dye", owing to its broad range of absorption.[35] It was found by Nazeeruddin *et al*. that deprotonation of the N3 dye could cause a negative shift to both the oxidation and reduction potential.[46] This led to the doubly deprotonated form (N719, Figure 2.8) being used which could achieve higher efficiencies. Both N3 and N719 remain the most commonly used dyes in DSC investigations and are commonly used as benchmarks for other molecular dyes. The development of Ru-complexes for DSCs has been an intensely studied area for the last two decades and many variations to the ligands used in these original complexes have now been reported. For extensive details on these modifications of Ru-complexes for DSCs the reader is pointed towards a comprehensive review in this area.[47]

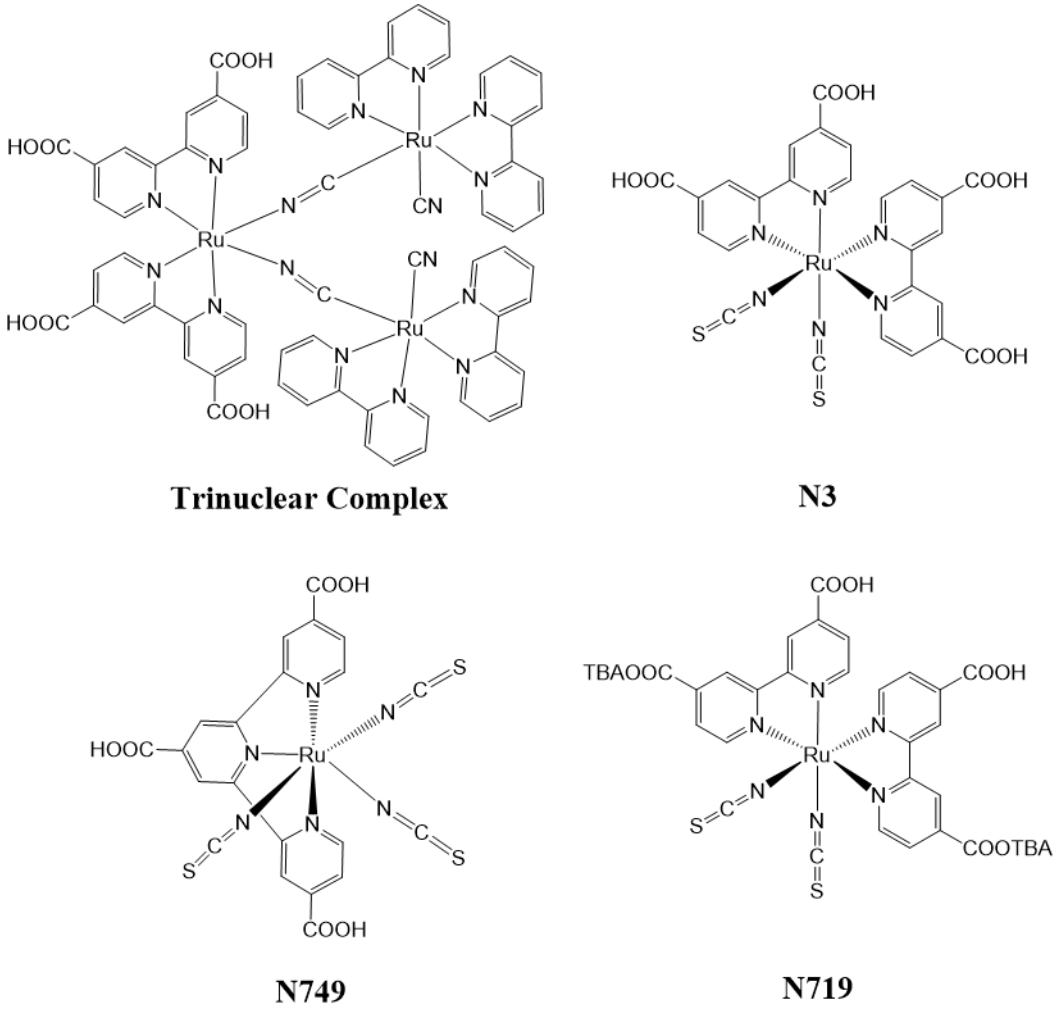

Figure 2.8. Chemical structures of notable or commonly used Ru-based dyes for application in DSCs.

In addition to Ru-complexes, multiple other types of dyes have been investigated for use in DSCs. Complexes based on other metal centres have been investigated to avoid the use of the expensive Ru core. A recent example of this includes the use of a heteroleptic copper(I)–bis(diimine) complex (C3, Figure 2.9) that has achieved a power conversion efficiency of 4.66 %.[48] Porphyrins have also been studied for use in DSCs due to their similarity with the molecules active in the process of photosynthesis. The use of the molecularly engineered porphyrin SM315 (Figure 2.9) has recently led to a 13 % efficient DSC.[40] Hundreds of organic dyes have also been studied for use in DSCs. The vast range of structures available for organic dyes means that there is a huge scope for imagination in dye design and synthesis. They also have the potential to be made cheaply due to the absence of a precious metal centre. In addition to this, they typically possess higher extinction coefficients than Ru-based dyes, which might prove useful in thinner solid state cells. One of the most commonly used and highest efficiency organic dyes used in DSC studies is the indoline based D149 dye (Figure 2.9).[49]

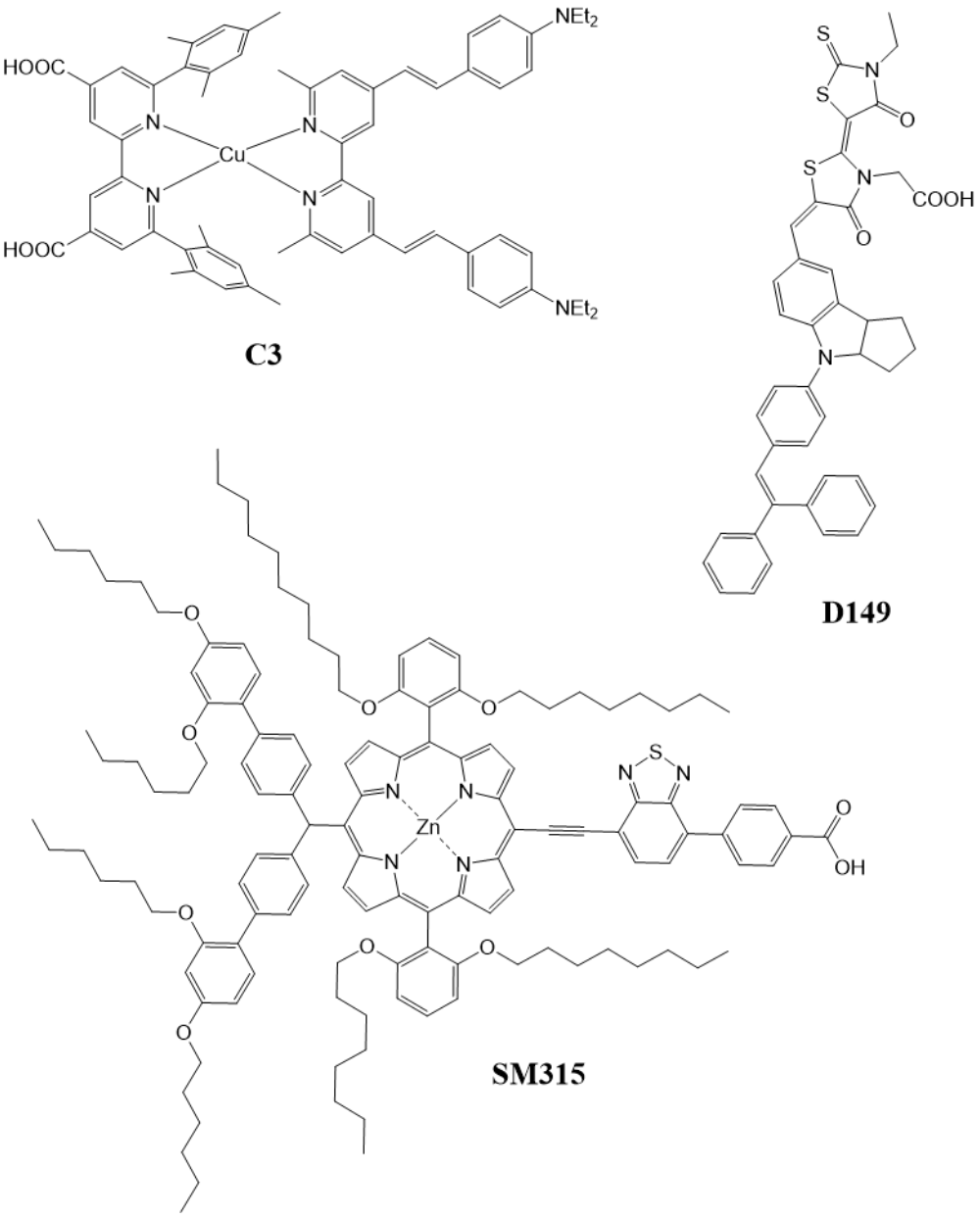

Figure 2.9. Chemical structures of notable non Ru-based dyes for application in DSCs.

The use of two or more dyes, commonly termed co-sensitization, is also a successful route to achieving a broad absorption within both the visible and NIR spectral ranges. Very recently, this method was adopted by Kakiage *et al*. who co-sensitized TiO_2 with an alkoxysilyl anchor dye (ADEKA-1) and a carboxy-anchor organic dye (LEG4) (Figure 2.10).[44] They found that electron transfer occurs from the light excited ADEKA-1 to the co-adsorbent LEG4, followed by immediate electron injection from LEG4 to the conduction band of the TiO_2 with much higher efficiency than the direct electron injection from the light-excited ADEKA-1. They combined this co-sensitization with the use of a Co-based electrolyte and a graphene-based counter electrode to achieve the current maximum reported power conversion efficiency for a DSC (14.3 %).

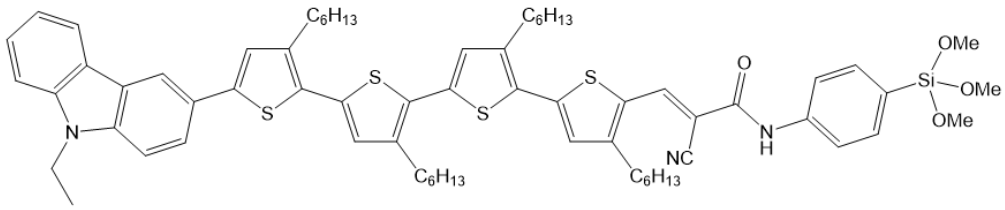

ADEKA-1

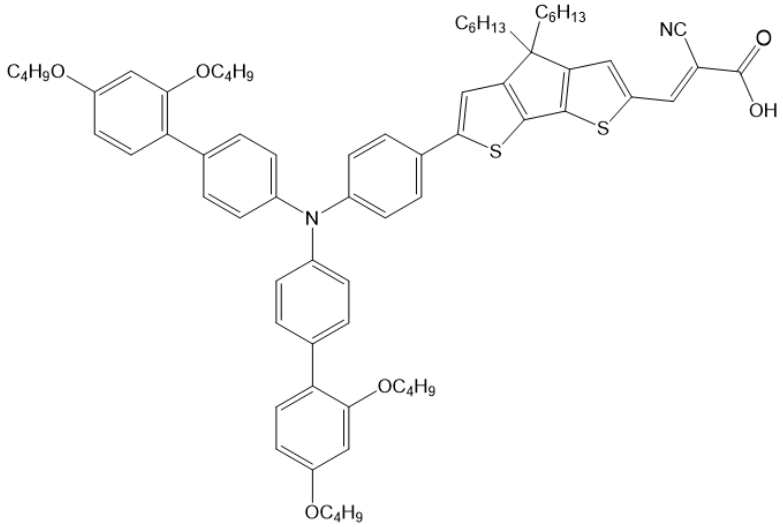

LEG4

Figure 2.10. Chemical structures of the two dyes used for co-sensitization in the current record efficiency DSC devices.

Electrolytes

The electrolytes most commonly used in DSCs are formed of a redox couple dissolved in a suitable solvent and, typically, some additives to boost the cell performance. The electrolyte used in the seminal 1991 paper by Grätzel and O'Regan consisted of 0.5 M tetrapropylammonium iodide and 0.04 M iodine dissolved in an 80:20 solvent mixture of ethylene carbonate and acetonitrile.[27] In this electrolyte the active redox couple is I^-/I_3^-, requiring the transfer of two electrons between the oxidised and reduced states. Remarkably, despite investigations into many alternative redox couples, this still remains the most commonly used redox couple in DSCs. Due to the susceptibility of many sensitizing dyes to hydrolysis, water and other highly protic solvents are typically avoided. Instead reasonably polar organic solvents are the most common choice. Acetonitrile is the solvent of choice for demonstrating record cell efficiencies due to the high diffusion coefficient of the redox couple within this solvent.[45] When high stability devices are required this is replaced with 3-methoxypropionitrile, which has a higher boiling point and viscosity, thereby reducing leakage from the cells.[50]

Many different iodide salts have been tested in DSC electrolytes and the cation used can have a significant effect on the overall cell performance. It has been found that the V_{oc} of DSCs can increase as a function of the cation used in the order $Li^+ < Na^+ < K^+ < Rb^+ < Cs^+$.[51] Whilst the photovoltage drops for cations of smaller radii, the photocurrent is found to increase, therefore LiI is commonly used within DSCs alongside other additives which can raise the V_{oc}. Electrolyte additives are crucial in gaining the highest cell efficiencies and most are based around electron-donating nitrogen containing heterocycles. The most commonly used additive is 4-*tert*-butylpyridine (4-*t*BP), which has been shown to demonstrate significant increases in V_{oc} when combined with LiI.[34]

Although the I^-/I_3^- redox couple remains the most commonly used, several of the most recent record DSC efficiencies have been achieved through the use of a Co^{2+}/Co^{3+} redox couple.[39, 44] This redox couple features a higher reduction potential than that of I^-/I_3^-, providing the possibility of higher voltages that was limiting in previous devices. However, as this is a one-electron redox couple, recombination at the semiconductor/electrolyte interface will be faster, requiring the need to take measures to block the redox couple from reaching the semiconductor surface. This has been achieved through the use of dyes containing long alkyloxy chains to inhibit charge recombination at the semiconductor/electrolyte interface.[39]

Liquid electrolytes are generally undesirable for large-scale manufacture of DSCs and can also lead to some cell sealing and stability issues. Strategies that have been investigated to overcome this problem are the replacement of the liquid electrolyte with a solid state, polymeric, gelled or ionic liquid based electrolyte. To date, Spiro-OMeTAD (2,2(,7,7(-tetrakis-(N,N-dipmethoxyphenylamine)9,9'-spirobifluorene) (Figure 2.11) has been the most commonly used organic hole conductor for solid state dye-sensitized solar cells.[31] It benefits from a small molecular size and high solubility in organic media in addition to a redox potential that is more positive than that of the I^-/I_3^- redox couple, which can result in increased open circuit voltages. Using Spiro-OMeTAD as an organic hole conductor, solid state dye-sensitized solar cells have been created with efficiencies as high as 7.7 %.[52]

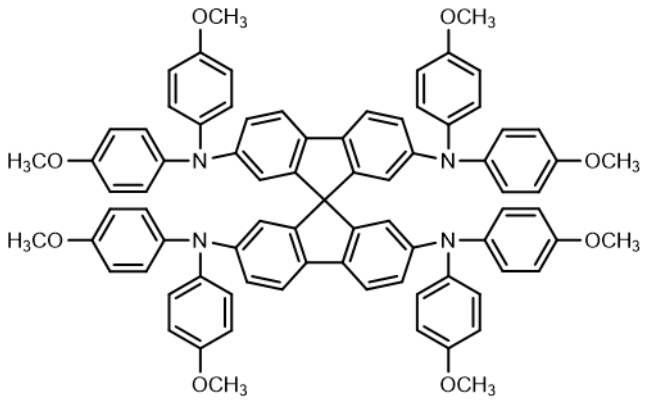

Spiro-OMeTAD

Figure 2.11. Chemical structure of the organic hole conductor Spiro-OMeTAD.

P-type organic semiconductors, such as PEDOT:PSS (poly(3,4-ethylenedioxythiophene) poly(styrenesulfonate)), have also been investigated as liquid electrolyte replacements and benefit from better electrical conductivities compared with Spiro-OMeTAD (500 S cm^{-1} compared to 10^{-3} S cm^{-1}).[31] However, PEDOT:PSS in a secondary or tertiary structure is too large to penetrate through the mesopores of conventional TiO_2 films. This results in incomplete pore filling, producing regions of increased electron-hole recombination.[31]

As an alternative to organic-based solid electrolytes, inorganic p-type semiconductors have also been investigated. CuSCN is an example of a typical inorganic solid electrolyte that has been explored for DSCs. It is relatively stable and provides reasonable energy conversion efficiencies (~2 %).[53] However, the low electric conductivity of CuSCN (~10^{-2} S m^{-1}) prevents further improvement of solid state dye-sensitized solar cells (ssDSCs) based on this material. Recently, Chung *et al.* reported very high efficiency ssDSC using $CsSnI_3$, a new type of p-type inorganic hole conductor. [54] Efficiencies of 10.2 % were obtained using this material, showing that inorganic hole conductors can be competitive with the best liquid electrolytes.

Gel and polymer electrolytes are discerned from organic hole conductors by the fact that a redox mediator (such as the I^-/I^{3-} redox couple) is included, similarly to liquid electrolytes. Another distinction comes from the fact that charge transport occurs mainly by diffusion of molecules rather than the hopping of charges. They are formed by adding gelating or polymeric agents to electrolytes based on organic solvents or ionic liquids and can be thought of as quasi-solid electrolytes.[55] Although these gelled or polymer electrolytes often provide enhanced stability compared to their liquid equivalents, cell efficiencies are usually lower due to limitations in the mobility of the redox mediators within the electrolyte. However, a recent publication reported efficiencies of 9.1 % for a low molecular weight organic gelator-based electrolyte.[56] This efficiency is similar to those of high performance cells using liquid electrolytes.

Ionic liquids have also been investigated extensively as electrolyte replacements and detailed reviews on this area have been published.[57, 58] Ionic liquids have many properties, such as low volatility, electrochemical stability and high conductivity, which make them attractive electrolytes for DSCs. The main drawbacks of ionic liquids is their high viscosity, which leads to mass transport limitations on the photocurrents in the solar cells under full light intensities. The vast majority of ionic liquids that have been investigated are imidazolium-based, but recent advances have come from forming eutectic mixtures which lower melting temperatures and thereby reduce mass transport limitations. Using this method, cell performances of over 8 % have been achieved.[59]

Semiconductors

The high surface area metal oxide semiconductor within a DSC acts as both an electron transport material and a scaffold for the dye to adsorb onto. It is, therefore, desirable for the metal oxide to possess the following properties:

- A wide band gap (>3.0 eV) – this allows transmission of lower energy visible light to the dye layer for absorption.
- Good energy level alignment – the conduction band edge of the semiconductor must be close, but slightly below (100-150 mV), the excited state of the dye to allow efficient charge injection.[60]
- High electron mobility (typically >1 cm^2 V s^{-1}) – this is generally beneficial to ensure the rapid transport of electrons from the light absorber to the working electrode, thereby minimising recombination.
- High surface area (roughness factors – defined as the ratio of the actual surface area to the geometric surface area - of the magnitude of ~1000) – as only an extremely thin layer of the light absorbing material (a monolayer in the case of a dye) is deposited on the metal oxide surface, a high surface area is required to maximise the amount of light absorbed.

In the first cells reported by Grätzel and co-workers, these properties were met by using a layer (~10 μm thick) of TiO_2 nanoparticles (~20 nm diameter) that had been sintered together to form a mesoporous film.[27] TiO_2 exists in three main crystal structures: anatase, brookite and rutile. Anatase is the form most commonly used within DSCs and possesses a band bap of 3.2 eV, with the conduction band edge closely matching the HOMO level of the most commonly used ruthenium-based dyes.[61] The mesoporous structure provides a very high surface area, which can be easily increased or decreased by changing the film thickness. To put this into perspective, a film consisting of 15 nm nanoparticles with a thickness of 10 μm has been demonstrated to have an internal surface area as high as 780 cm^2 for each 1 cm^2 of geometric surface.[27] These

mesoporous TiO_2 films have remained as the standard semiconductor component in DSCs ever since.

It has been commented in previous literature that electron collection in mesoporous TiO_2 films is nearly 100 % efficient in optimized cell setups.[62] So why is there need to further research this component? The answer to this is that although electron collection at the working electrode is nearly 100 % efficient in conventional cells, this is not the case in many of the new cell designs published over recent years. This is particularly true for when new redox species, such as cobalt-based redox couples are used in the electrolyte, which have a lower ionic diffusion rate compared to the I^-/I^{3-} species.[63] When this is the case, a semiconductor support that can more rapidly transport the excited electrons from the dye to the collecting electrode could be preferable in order to reduce the back reaction between the dye and electrolyte species.

Recent years have seen a huge rise in the number of different types of metal oxide material used in DSCs. These have varied in both elemental composition of the material and also the morphology. In terms of morphology, approaches have generally tried to focus on one or more of the areas of: Improvement to electron transport, enhancement of light management, increasing surface areas, or the improvement of pore infiltration, particularly when highly viscous or solid-state electrolytes are used.

Despite the very high surface areas that nanoparticle films possess, they do have some flaws. For instance, if a solid or polymer electrolyte were to be used, rather than a liquid electrolyte, then problems would occur with pore filling due to the very small pore sizes between nanoparticles. Poor pore filling has been reported even for relatively thin mesoporous layers (2.5 μm) when using organic hole conductors such as Spiro-OMeTAD.[64] Other problems include poor light scattering for films of small nanoparticles. Poor scattering within the visible light range is adverse for the uptake of light by dye molecules due to a reduction in the effective path length of the light through the film.[65] Efforts have been made to overcome this by adding a second layer of larger nanoparticles to act as a scattering layer.[66] Another method that has been used to overcome this is through the use of oxide aggregates, which are assemblies of nanoparticles that form submicron-sized spheres.[67] In addition to improving the light scattering and pore structure of metal oxide films, significant effort has also been made to introduce direct pathways for electron transport via the use of 1-dimensional nanostructures.[68] More extensive details on these various modifications of the morphology will be covered in the next section, which focusses on ZnO within DSCs.

The wide band gaps required to meet the criteria for a semiconductor support are almost exclusively found within metal oxides. Within this group of materials, only two metal oxides have received significant attention as alternatives to TiO_2: ZnO and SnO_2. SnO_2 is a chemically stable

wide band gap oxide that has a conduction band edge 0.5 eV lower than TiO_2 (anatase).[45] This lower conduction band edge makes it suitable for use with dyes that have low LUMO levels that inject poorly into TiO_2. This metal oxide has received significantly less interest than ZnO as an alternative DSC material, largely due to its low efficiencies when coupled with commonly used dyes such as N719.[69] The best efficiency achieved to date using SnO_2 is 2.8 %, however higher efficiencies have been achieved when other metal oxides have been deposited on its surface in thin shells. An example of this is ZnO-coated SnO_2, which achieved efficiencies up to 6.3 %.[70] The use of ZnO within DSCs will now be discussed in more detail.

2.2.4 ZnO in DSCs

ZnO has been the most frequently studied alternative to TiO_2 for application as a semiconducting metal oxide in DSCs. At first glance ZnO looks to be an ideal candidate for the replacement of TiO_2 as it possesses a very similar band gap (3.3 eV as opposed to 3.2 eV) and a bulk electron mobility that is over an order of magnitude higher than TiO_2 (205-300 cm^2 V s^{-1} *vs.* 0.1-4 cm^2 V s^{-1}).[71, 72] ZnO also boasts a wide range of easily producible nanostructures, such as nanowires, which are not found to the same extent for TiO_2.[73]

Research in the area of ZnO nanostructures for DSCs has focussed on three main themes: (1.) The use of a wide range of nanostructured morphologies to achieve higher surface areas than simple nanoparticle networks; (2.) the use of novel hierarchical structures to improve light scattering whilst not reducing surface areas; and (3.) the improvement of electron transport within the metal oxide by using nanomaterials with a 1-dimensional structure. There already exist a number of excellent reviews on the use of ZnO and its various nanostructures within DSCs, therefore, this area will not be covered comprehensively herein.[74-76] Instead this section aims to give an overview of the main areas of focus and provide some perspective on where research in this area could move forward to.

Nanoparticle or nanoporous ZnO films

The simplest way to apply ZnO within DSCs is to replace the mesoporous film of TiO_2 nanoparticles with an equivalent film of ZnO nanoparticles. ZnO nanoparticle films have been prepared and applied within DSCs by a number of research groups with varying degrees of success.[77-79] Efficiencies for apparently very similar ZnO nanoparticle films have given rise to devices with power conversion efficiencies ranging all the way from below 1.0 % to 6.6 %, highlighting the sensitivity of the devices' performance to preparation conditions and the importance of optimisation of this preparation procedure for new photoanodes.[77, 80] The highest efficiency devices based on ZnO nanoparticle films were prepared by Saito *et al.* (6.6 %), who

fabricated mesoporous ZnO photoanodes from commercial ZnO nanoparticles and focussed on a stepwise optimisation of the photoanode preparation procedure.[77] Amongst these reports, a method documented by Keis *et al*. involving the formation of nanoparticle films by a compression method appears to be relatively promising.[78] This technique used compression to avoid the high temperature annealing step, which is often seen as a bottleneck in large scale production of DSCs, and achieved an efficiency of 5 % under 0.1 Sun conditions.[78]

In addition to the use of films of nanoparticles, there are many techniques available for the direct fabrication of porous ZnO films from solution. Perhaps one of the most interesting of these techniques, owing to its simplicity, low cost and relatively rapid growth, is electrochemical deposition. A particularly interesting example of the application of this technique for DSCs has been presented by Yoshida and co-workers.[81, 82] They were able to demonstrate that the dye eosin-y can be used as a structure directing agent during electrodeposition to give rise to porous, pre-sensitized ZnO films. The initial efficiencies gained with these photoanodes were found to be low due to the formation of dye aggregates within the pores, however, by desorbing and re-adsorbing the dye they were able to achieve efficiencies of up to 2.7 % with the simple and cheap eosin-y dye.

High efficiencies have also been gained through the use of 3-dimensional (3-D), sponge-like, porous ZnO films.[83] These porous structures were formed from room temperature radio frequency (RF) magnetron sputtering of Zn followed by thermal oxidation to form ZnO. When 18 μm thick films were applied within DSCs, a maximum power conversion efficiency of 6.67 % was achieved, which was attributed to the relatively high surface areas and long electron diffusion length of the photoanodes.

A number of other high surface area nanostructures have also been tested within DSCs, including 2-dimensional sheets and belts of ZnO, achieving reasonable efficiencies of 2.6 % in both cases.[84, 85] 2-dimensional, asymmetric, panel-like structures have also been mixed with ZnO nanoparticles to form effective photoanodes for quasi-solid state DSCs (qssDSCs) with an efficiency of up to 5.6 %.[86] Further increases in efficiency were gained by Mahmood *et al*. who used films of boron-doped ZnO nanosheets to obtain impressive power conversion efficiencies of 6.75 %, over double that of undoped nanosheets.[87] The nanosheets, deposited by electrostatic spray deposition, were found to be porous and contributed towards a higher surface area compared to normal nanosheets.

Hierarchical ZnO structures for light scattering

It has been previously shown experimentally that the inclusion of larger particles as light scattering centres within nanocrystalline films can improve the optical absorption of light within the film.[88] However, the inclusion of these larger particles has the inevitable effect of reducing

the overall surface area of the film, acting to counteract much of the improvement in absorption arising from light scattering. Hierarchical structures that possess high surface areas, whilst still being large enough for effective light scattering, are therefore desirable. Due to the wide range of synthetic techniques available for producing ZnO nanostructures this has been an area of focus. One of the most notable examples of the benefits of hierarchical structures for light scattering enhancement is the use of spherical aggregates of ZnO nanoparticles.[67, 89] Zhang *et al*. were able to demonstrate that aggregates on the scale of 100 to 500 nm, formed from small (15 nm) ZnO nanoparticles, could greatly improve the power conversion efficiency to 5.4 % compared to 2.4 % for simple nanoparticle films. This efficiency increase was due to a greatly improved J_{sc}, originating from improved light absorption.

More recently, the production of hierarchical ZnO nanoparticle aggregates was reported by Memarian *et al*., who achieved a power conversion efficiency of 7.5 %, the current record for photoanodes entirely formed of ZnO.[90] They used a spray deposition setup to produce the ZnO aggregates on a conducting glass substrate and found that significant improvements in performance could be achieved through the inclusion of a compact ZnO layer between the substrate and the aggregates. In addition to gaining higher efficiencies using spray deposition, the process could be completed far more rapidly than if nanoparticles first had to be synthesised from hydrothermal growth, making the process more compatible with large-scale production.

1-Dimensional ZnO structures

An alternative to the use of nanoparticle films is to use more ordered one-dimensional (1-D) nanostructures, such as nanotubes or nanowires, the latter of which will form the focus of this thesis. The use of ZnO nanowires was reported by Law *et al.* for the first time to demonstrate that 1-D nanostructures might provide direct pathways for electron transport in DSCs.[68] They reported that electron transport in a photoelectrode comprised of single crystal nanowires is 100 times faster than that in the case of a nanocrystalline film. In addition to the direct pathways provided (Figure 2.12), enhancements in electron transport can be attributed to high crystallinity and a low number of grain boundaries and surface defects, which can accelerate electron transport and reduce the possibility of interfacial recombination. It has also been proposed that a radial electric field can exist within the nanowire that drives injected electrons toward the nanowire core. This could then combine with an axial electric field to result in efficient electron transport to the conducting substrate.[68]

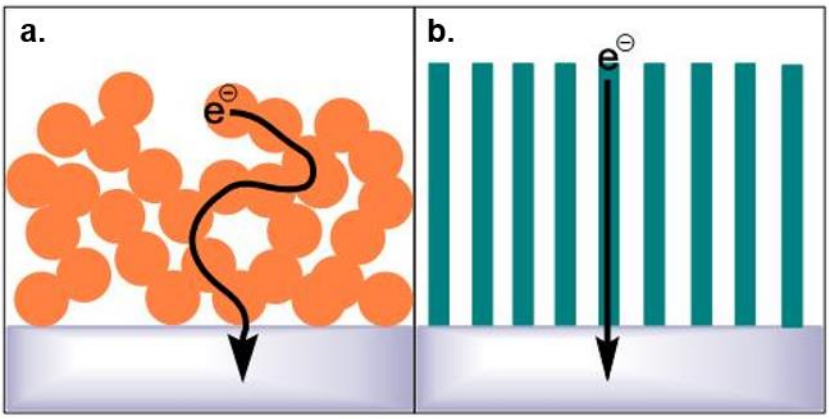

Figure 2.12. Simplified representation of electron transport through a mesoporous (a) and a one-dimensional nanostructured (b) semiconductor support.

Law *et al*. were able to demonstrate further improvements to their nanowire DSCs by coating the ZnO nanowires with a TiO_2 shell.[91] In contrast to an Al_2O_3 shell that acted as an insulating barrier, the TiO_2 shell allowed efficient transport into the ZnO nanowire core and provided an energetic barrier to recombination of the photo-excited electron with the electrolyte. This core-shell structure allowed them to improve the power conversion efficiencies of the DSCs to 2.25 %. It was commented that further improvements would likely be achieved through increasing the surface area of the nanowire arrays.

In addition to enhanced electron transport, 1-D nanostructures can offer improved light scattering over films consisting of small nanoparticles as they are macroscopic in one direction. This enhanced light scattering can result in improved light absorption of dye molecules.[92] However, these enhancements are often overshadowed by the low light absorptions found for dye-sensitized films of 1-D nanostructures. This arises from the low surface areas of 1-D nanostructured films compared to nanoparticle films, which is due to the smoothness of the single crystal surfaces and the relatively large spacing between nanostructures. Because of this, thicker oxide layers are required compared to nanoparticle films to get high enough surface areas.[68] This, however, can be difficult to achieve practically using many synthesis techniques. One example of where high surface area nanowire films have been achieved is the production of multilayer ZnO nanowire arrays, which have given rise to 7 % efficient DSCs.[93] Using multiple cycles of nanowire growth followed by coating of a self-assembled monolayer, it was possible to grow highly ordered nanowire arrays of up to 40 µm in length. Using these long nanowire arrays and a thin TiO_2 coating it was possible to obtain sufficient dye loading to gain these high efficiencies. Despite the demonstration of good performances, the complexity of the multistep synthesis is likely to hinder any potential uptake of this technology for large-scale applications.

To overcome the difficulties of producing high quality arrays of high aspect ratio nanowires, researchers have looked towards creating hierarchical structures from the nanowires. These can combine the efficient electron transport of the 1-D structure with higher surface areas for dye loading. An example of this approach is the growth of ZnO "nanoforests" by Ko *et al*..[94] These "nanoforests" consisted of an array of vertically aligned nanowires onto which a dense covering of thinner nanowires had been grown. These nanowire branches greatly increased the dye loading and, therefore, the light absorption of the sensitized film. After optimisation of the nanowire and branch growth, power conversion efficiencies of 2.63 % were achieved; a significant improvement on the 0.85 % achieved using nanowire arrays without branching.

Another route to overcome the low surface areas of nanowires is to combine them with small nanoparticles. Guerin *et al*. demonstrated that filling the void spaces between electrodeposited nanowires with ZnO nanocrystallites resulted in a significant increase in power conversion efficiency from 0.49 % for bare nanowires to 4.08 %, due to increased dye loading.[95] This value was also higher than the 2.84 % obtained for a thick (12 μm) ZnO nanoparticle film, demonstrating the benefits of this hybrid nanowire/nanoparticle structure. A similar approach was employed by Puyoo *et al*. who used ZnO nanowires grown by ultrasonic spray pyrolysis combined with nanoparticles to obtain efficiencies of 4.7 %.[96] The combination of ZnO nanowires and TiO_2 nanoparticles has yielded even higher efficiencies due to the favourable interactions between the sensitizing dyes and TiO_2.[97] The *in situ* growth of ZnO nanowires within TiO_2 films by Bai *et al.* was shown to give high efficiency DSCs (8.44 % compared to 6.65 % for TiO_2 nanoparticles only) due to the enhanced light scattering effect and the improved electron transport within the films.

Problems with ZnO in DSCs

Despite these attractive characteristics, the highest recorded efficiency for an entirely ZnO-based DSCs to date is 7.5 %, far lower than the record efficiency for TiO_2.[90] One of the main reasons for these lower cell efficiencies is the interaction between the sensitizing dye and the ZnO surface. Almost all of the most successful sensitizing dyes used for DSCs make use of carboxylic acid anchoring groups to bind to the metal oxide surface. ZnO is less stable to acidic conditions than TiO_2 and reactions can occur, leading to the corrosion of the ZnO surface and the formation of Zn^{2+}/dye complexes that can agglomerate on the metal oxide surface.[98, 99] Although these complexes can absorb light, they are not capable of injecting electrons into the ZnO for transport to the electrode, leading to significant losses in photocurrent. Because of this, far shorter dyeing times are required for ZnO photoanodes compared to TiO_2 and care needs to be taken to optimise this dyeing time in order to gain reasonable efficiencies.[78] Alternative dyes to the commonly used

Ru-based dyes can also relieve this problem, examples of which are xanthene based dyes such as eosin-y.[100]

The strength of the dye-ZnO interaction has also been reported to be an issue. The weakness of this interaction compared to the dye-TiO_2 interaction can lead to the detachment of the dye from the surface, either when the electrolyte acts as a good solvent or when there is an electrolyte additive such as 4-*tert*-butylpyridine competes for adsorption sites on the semiconductor surface.[75] As a result, some electrolyte additives that would typically be expected to reduce recombination, thereby increasing the cell voltage, can actually be detrimental on device performance.

Another possible reason for the reduced efficiency of ZnO-based DSCs is highlighted in a recent review by Anta *et al*.[75] Within this review they discuss how the formation of a surface-bound state after excitation of the dye can limit charge separation and cause the build-up of negative charge in the semiconductor, leading to a lowering of both the photocurrent and the fill factor of the cell. This has been linked to the lower dielectric constant of ZnO compared to TiO_2 and could represent a fundamental limitation for ZnO based DSCs.

Outlook for ZnO within DSCs

The use of ZnO presents an almost endless range of morphological possibilities for photoanodes in DSCs. Through thorough control of the morphology it seems likely that photoanodes will be able to be developed that combine high-surface areas, direct electron transport pathways and effective light scattering, which could see rises in cell efficiencies. In addition to this, ZnO presents the opportunity for a range of low temperature and rapid fabrication techniques, such as electrodeposition, that are more compatible with large-scale manufacturing.

Despite this, ZnO-based DSCs currently have a long way to go in order to rival their counterparts based on TiO_2. Although a huge range of interesting morphologies of ZnO have been demonstrated within DSCs, relatively little progress in efficiencies has been made from cells based on simple nanoparticle films. Part of this problem is likely to be related to the fact that the vast majority of studies still make use of the Ru-based dyes and electrolyte systems developed for TiO_2, despite the widely reported issues of sensitization for ZnO. However, with few baseline studies showing efficient devices with alternative dyes, it is difficult to gain a good literature comparison with anything other than Ru-based dyes. It may, therefore, be the case that N719 and N3 dyes will remain as the most commonly used dyes for ZnO until higher efficiencies are demonstrated for alternatives. A thorough systematic study of alternative dyes for ZnO DSCs is, therefore, needed in order to gain significant progress in this field.

In the meantime, it seems that the use of core-shell structures might provide an effective route for the utilisation of ZnO nanostructures within DSCs. In this way, the unique nanostructures that can be formed from ZnO can be combined with the stability and dye compatibility of a shell material, such as TiO_2, in order to improve device efficiencies. These structures may also exhibit added benefits, such as energy barriers to recombination, which could further boost cell performance compared to either of the materials by themselves.

2.2.5 Future prospects for DSCs

Increasing cell efficiencies

Progress in achieving higher power conversion efficiencies is a necessity if DSCs are going to be a serious competitor for more established PV technologies in grid-scale power generation. As discussed in Section 2.2.2, some recent progress in this area has arisen through the use of alternative dyes in combination with Co-based redox couples in the electrolyte.[44] These recent reports appear to have broken the apparent efficiency plateaux that DSCs had faced for over a decade. It is entirely possible that the use of similar strategies will yield even further advances in record efficiencies and further research efforts should be made in this area. Sensitization using two or more dyes appears to be a promising route to gaining a broad absorption spectrum without undertaking significant synthetic effort to create a single broadly absorbing dye.[44] Further efficiency improvements might also be made via controlling recombination at the semiconductor interface and improving diffusion pathways through the semiconductor film, both of which are current problems for the Co-based redox couples used to gain high efficiencies.[101, 102]

Creating affordable technologies

Whilst obtaining higher efficiency devices has an obvious impact on the price per Watt of DSCs, it is certainly not the only factor that needs to be considered in making DSCs a competitive PV technology. Within a recent review it was calculated that for a 10 % efficient DSC module, a production price of US$20-30 m^{-2} would need to be achieved.[42] Whilst there is relatively low materials usage in the active part of the DSC, substrates can represent a significant cost, particularly when two layers of FTO-coated glass are used, as is the case in most research prototypes. At large scale production levels FTO coated glass costs between US$8-12 m^{-2} and would, therefore, account for a vast amount of the overall cell price.

Largely driven by this reason, there have been efforts to replace the use of conducting glass electrodes, such as FTO coated glass. Although these materials offer good transparency and high conductivities, their rigidity also limits the methods in which DSCs can be manufactured. This problem becomes particularly relevant if processes such as roll-to-roll production were to be

used for industrial-scale manufacturing. One of the alternatives is to use metal foils as electrode materials. These electrodes have good conductivity and can be flexible depending on the thickness. Due to the opacity of the metal, what is known as a back-illuminated DSC configuration is used, where light enters the cell via the counter electrode.

Ito *et al.* produced flexible DSCs with efficiencies of 7.2 % by replacing the conducting glass electrode with titanium foil and using a platinum coated tin doped indium oxide/polyethylenenaphthalate (ITO/PEN) counter electrode.[103] This back-illuminated configuration resulted in a slightly lower conversion efficiency than the equivalent front-illuminated cell made using an FTO glass substrate. The lower efficiency could largely be attributed to the light absorption of the platinum layer and the electrolyte. Paulose *et al.* produced back-illuminated solar cells based on 6 μm long highly-ordered TiO_2 nanotube-array films, grown directly on titanium foil by anodization.[104] Using a back-illuminated cell they achieved efficiencies of 4.24 % and gained open circuit voltages higher than those of typical nanocrystalline cells. Many conducting polymer substrates have also been examined, such as FTO coated polyethylene terephthalate (PET), PEN and polyester.[105-109] Although these have the advantage of being transparent, allowing the production of front-illuminated DSCs, their main disadvantage currently is that they cannot be taken up to high temperatures that are commonly used to sinter together the semiconductor films. For this reason, metal substrates are generally more attractive materials. Despite the progress in this area, there is still much work to be done in realising large-scale and affordable DSC modules that can be competitive with conventional PV technologies.

Competitive technologies

Perhaps one of the biggest barriers to the continuation of progress in DSC research is the emergence of new technologies. Although DSCs remain competitive with many other emerging PV technologies, such as CZTS, organic solar cells and QDSCs, a new technology has recently emerged that has drawn a significant amount of attention away from DSCs. This new technology is the perovskite solar cell. This exciting new technology, which has evolved from the DSC over the past few years, has taken with it a significant proportion of the DSC research community. It is this technology that will be covered next in this review.

2.3 Perovskite Solar Cells

Perovskite solar cells are an exciting new class of photovoltaics that have gained the attention of a large proportion of the solar energy research community. Since the first reported use of perovskites within solar cells in 2009, significant improvements in cell efficiencies have been achieved, reaching certified values of 20.1 % in 2015.[110, 111] These high efficiencies place perovskite solar cells as direct competitors for more established thin film photovoltaic technologies, such as CdTe and CIGS, and even as competition for crystalline silicon technology.[26] Such rapid rises in performance have led to researchers from other areas of photovoltaics, particularly within the area of dye-sensitized solar cells to migrate to this field of study. As this shift in research focus occurred during the period of this PhD, perovskite solar cells will be investigated in addition to DSCs within this thesis.

This section aims to give an overview of the rapid development of perovskite solar cells, as well as discussing some of the current understanding behind their operation. Focus will then be placed on the use of different electron transport materials within perovskite solar cells, particularly ZnO, which is the focus of the research in Chapter 7.

2.3.1 Perovskite materials

Perovskite is a name given to a class of materials with a generic structure ABX_3, where both A and B are cations and X is an anion. The perovskite materials that are of interest for application in solar cells are hybrid organic-inorganic materials where A is an organic cation, B is generally Pb^{2+} and X is a halide such as I, Cl or Br.[112] The most commonly reported perovskite for application in solar cells is $CH_3NH_3PbI_3$, which consists of a cage structure of lead and iodine ions with the $CH_3NH_3^+$ ion sitting within the voids (Figure 2.13). The first reports on the structure and physical properties of these materials was made by Weber in 1978 and were originally of potential interest for application as high-temperature superconductors.[113-115] However, it was not until the reports of efficient solar cells using these materials that significant research into their structure and properties was completed.

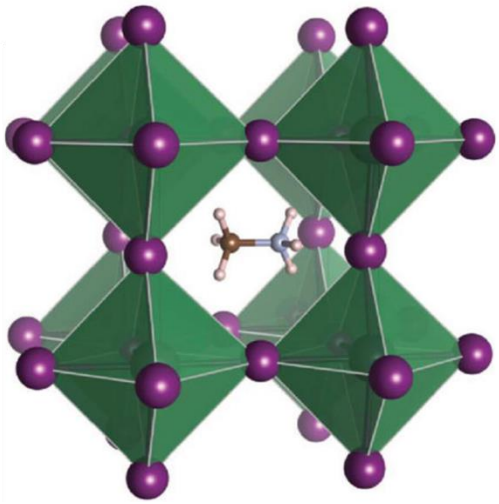

Figure 2.13. Crystalline structure of $CH_3NH_3PbI_3$ in the cubic phase (temperatures above 330 K). The methylammonium ion occupies the central site, surrounded by octahedra of iodine (purple) and lead (green).[116]

The $CH_3NH_3PbX_3$ material has been found to form a tetragonal phase at room temperature, which transitions to cubic at high temperature and orthorhombic at low temperature.[117] Within the cubic and tetragonal phases the organic methylammonium cation can rotate within the cage structure, but is locked in place within the orthorhombic phase. Very high light absorption coefficients of 10^4-10^5 cm^{-1} have been reported for these materials along with a band gap of 1.50-1.55 eV, both of which make them attractive candidates for effective light absorption across the visible spectrum.[118, 119] In addition to the beneficial optical properties, they have been found to possess electron and hole diffusion lengths in excess of 1 μm, making them effective charge transport materials.[120]

It has been found that the band gap of these materials can be tuned, both by substituting the type of halide ions used and also by substituting the metal cation. By substituting different quantities of Pb^{2+} for Sn^{2+} Hao *et al*. were able to tune the band gap between 1.55 and 1.17 eV.[121] Further alternations in the band gap can be achieved through the use of a larger organic cation, such as the formamidinium ion ($HC(NH_2)_2^+$).[122] This tuneable band gap could prove very useful when applying the materials in both multi-junction perovskite devices and in tandem cells with other solar technologies.

2.3.2 Evolution from the DSC

Within the first reported use of hybrid organic-inorganic perovskite materials in 2009, the material was applied in the form of quantum dots as an alternative sensitizer for dye-sensitized type solar

cells (Figure 2.14a). Maximum efficiencies of 3.8 % were achieved using this device architecture, however, it gained little attention due to the efficiencies being lower than those obtained with conventional sensitizing dyes and also due to the very low stability in the liquid electrolyte used.[110] The next report came in 2011 by Im *et al*. who achieved a power conversion efficiency of 6.5 % through optimisation of the quantum dot deposition and cell structure.[123] Despite the higher efficiencies, stability of the cells was still a significant issue with the liquid electrolytes used, rendering them impractical for use.

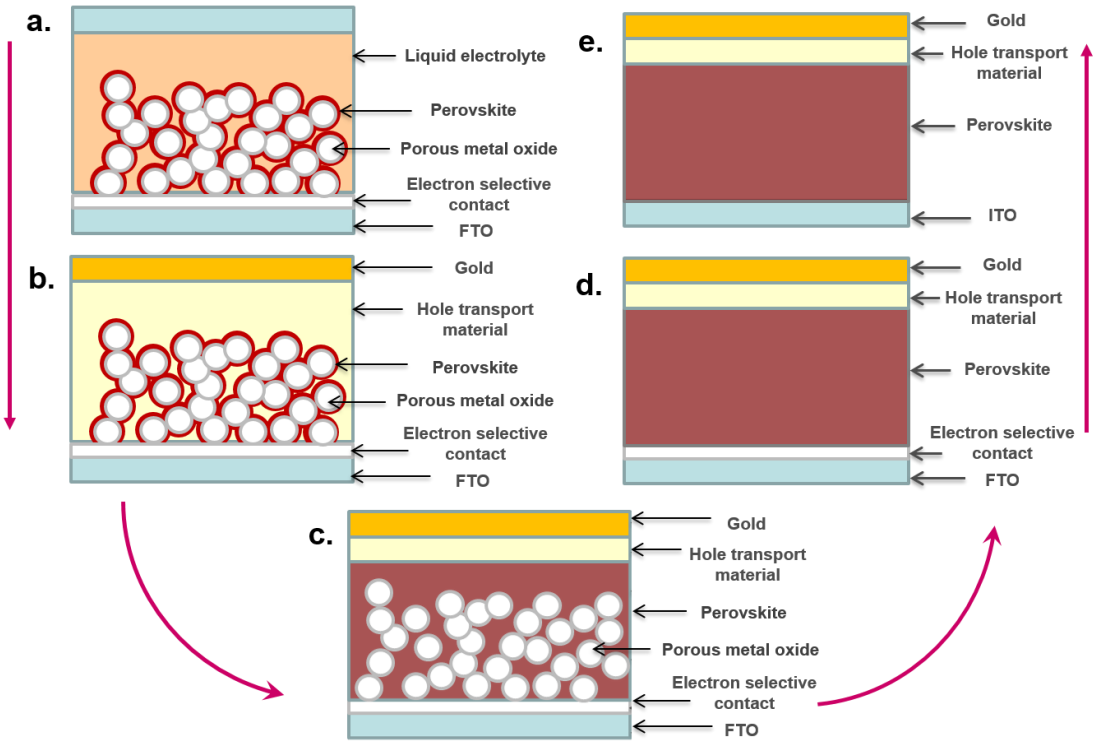

Figure 2.14. Schematic showing the change in perovskite cell structure from a DSC type structure (a) to a planar perovskite cell (d and e).

The first significant breakthrough in perovskite solar cells came in 2012 through the substitution of the liquid electrolyte with the solid-state organic hole conductor Spiro-OMeTAD (Figure 2.14b). This was reported, almost simultaneously, by both Lee *et al*. and Kim *et al*. achieving efficiencies of 10.9 % and 9.7 % respectively.[119, 124] These cells featured a sub-micrometre thick mesoporous oxide layer that had been coated in a thin layer of perovskite material. The solid-state hole conductor was then infiltrated into this structure to produce an all solid-state cell. One of the most important findings to come out of the paper by Lee *et al*. was that the efficiencies of the cells actually increased by replacing the semiconducting mesoporous TiO_2 with Al_2O_3, which is an insulator.[124] This led to the conclusion that electron transport could occur through the perovskite material itself and did not need to be injected into a semiconducting support. This finding was pivotal in opening up the field to new cell designs that digressed further

away from the original DSC device architecture. The cells produced within the report also made use of a mixed halide perovskite, made up of both I^- and Cl^- anions, which was found to be more stable to processing in air.[124]

Soon after, it was found by Etgar *et al*. that the perovskite material could also function without a hole transport material at all, be it at a reduced efficiency.[125] This result indicated that the perovskite material could transport holes as well as electrons. As a result of these two findings, device architectures evolved from a thin coating of perovskite on the mesoscopic support to a fully infiltrated structure (Figure 2.14c).[126-128] Noh *et al*. were able to produce 12.3 % efficient cells using a fully infiltrated TiO_2 mesoporous layer and were also able to tune the band gap of the perovskite through the controlled substitution of I^- with Br^- anions. This gave rise to a range of semi-transparent cells in different colours.[127] At a similar time Ball *et al*. were able to demonstrate fully infiltrated devices based on Al_2O_3 scaffolds, again achieving efficiencies of 12.3 %.[128] They were also able to demonstrate efficient devices when the thickness of the scaffold was significantly reduced, giving rise to a planar over-layer of perovskite.

By this point, perovskite solar cells had caught significant attention from the solar cell community and publication in this area began to increase greatly (Figure 2.15). Improvements to cell efficiencies were introduced through the use of a two-step perovskite deposition technique, which involved first depositing a layer of PbI_2 within the mesoporous scaffold and then converting by submerging in a solution of methylammmonium iodide.[129] Efficiencies of up to 15.0 % were achieved using this method, owing to the improved control of the perovskite morphology.

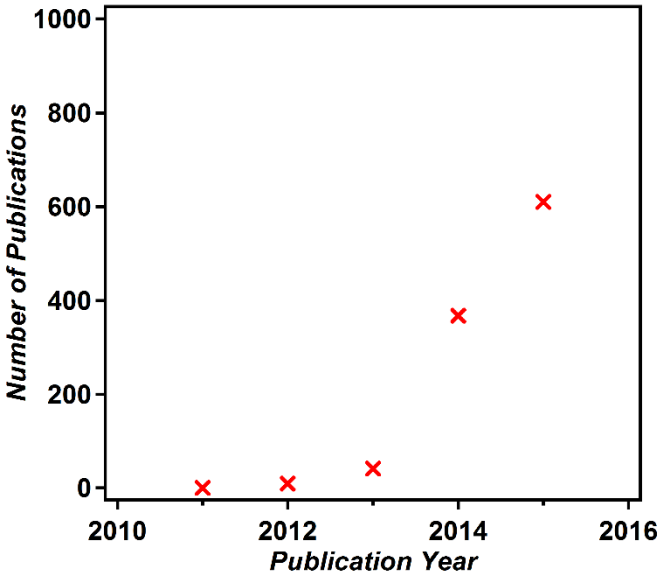

Figure 2.15. Number of publications each year containing the combination of words "perovskite*" and "solar", or "CH_3NH_3Pb*" and "solar" within the title, based on a Web of Science search (08/10/2015).

Not long after this, a drastically different cell architecture emerged, which removed the mesoporous layer from the cell entirely (Figure 2.14d). Using a planar film of perovskite, deposited using a dual source vapour evaporation system, planar perovskite cells with efficiencies of up to 15.4 % were achieved.[130] These results proved that efficient devices could be produced without the need for a mesoporous metal oxide. This planar cell structure allows potentially simpler large-scale fabrication and at lower temperatures, as there is no need to anneal a mesoporous oxide film. Similar device structures were reported by the same group soon after using solution processing, however, slightly lower efficiencies were obtained owing to reduced homogeneity of the perovskite layers compared to when they were vapour deposited.[131] Planar cell structures have also been demonstrated more recently in which the electron transport material is removed entirely, so that the perovskite directly contacts the conducting substrate (Figure 2.14e).[132] Using this approach Liu *et al*. were able to achieve power conversion efficiencies of 13.5 %, only marginally lower than the 13.6 % achieved when using a ZnO blocking layer. This simple cell structure shows how significantly different perovskite solar cells operate compared to their predecessors, dye-sensitized solar cells. It may be the case that further digressions from the commonly adopted architectures will give rise to further improvements in cell performance.

A significant amount of research continues to be published on alterations and improvements to perovskite solar cells, based on both the planar and mesoscopic device architectures, and it is not clear which structure will prove to be the most successful in the long term. Some of the most efficient devices currently make use of an intermediate structure between these two, with a very thin porous metal oxide layer onto which a thick planar layer is deposited.[111, 133-135] In these cases it is likely that the extremely thin porous layer is simply acting to improve adhesion between the perovskite and the substrate. It is, therefore, likely that improving the interactions between the perovskite layer and a compact blocking layer will result in the planar cell configuration being the most successful. In this context, Zhou *et al*. were able to demonstrate highly efficient planar devices through the optimisation of perovskite deposition and careful control of the interfaces within the cell.[136] They used the polymer polyethyleneimine ethoxylated (PEIE) to modify the work function of an ITO substrate and coated this with an yttrium-doped TiO_2 blocking layer, which has a lower resistance than TiO_2. Using this approach, they were able to achieve power conversion efficiencies of up to 19.3 % for planar device architectures.

The most recent advances in perovskite solar cells have come through the judicious control of the perovskite deposition in order to gain smooth, thick films of perovskite with no pin holes and high crystallinity. The most successful attempts at this have been made by the group of Sang Il Seok from the Korean Research Institute of Chemical Technology (KRICT) who currently hold the record power conversion efficiency of 20.1 % (Figure 2.16).[111] Their efforts to improve

the perovskite deposition have involved the use of anti-solvents and growth via intermediate, solvent containing phases. This has allowed them to reduce the speed of perovskite formation and obtain smooth films with high crystallinity.[111, 133, 134] The use of mixed $FAPbI_3$ and $MAPbBr_3$ (where FA is formamidinium and MA is methylammonium) phases has also given rise to efficiency increases due to the broader light absorption range of $FAPbI_3$ compared to the most commonly used $MAPbI_3$ materials.[111, 133]

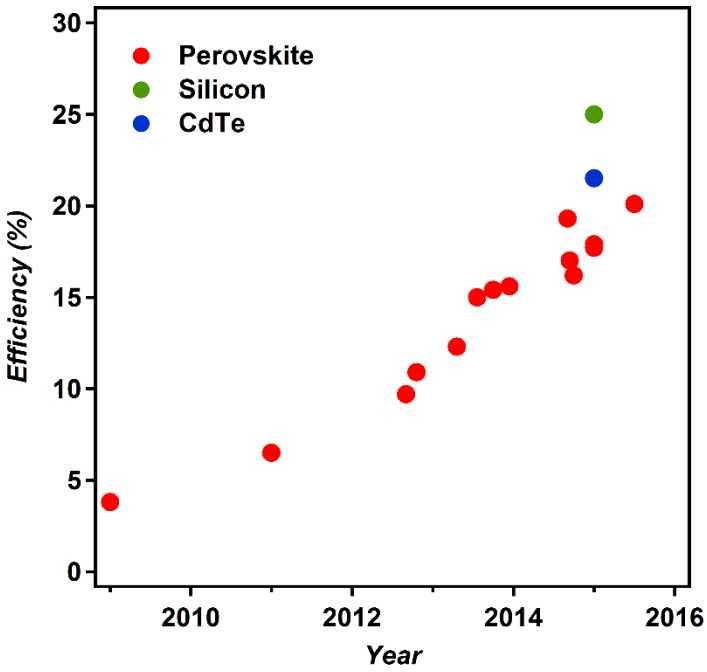

Figure 2.16. A plot of published maximum power conversion efficiencies over time for perovskite solar cells. Current record certified efficiencies of crystalline silicon solar cells and CdTe solar cells are shown for comparison.[26] Values for perovskite solar cells were obtained from the references within this section.

Looking forward, it seems that further increases in cell performance are likely to be achieved through improved crystallization of the perovskite materials, thereby reducing pin holes and grain boundaries within the films. Significant progress in this area is already being made and perovskite films featuring grain sizes of up to 1 mm have been demonstrated through the use of a hot-casting technique.[137] Further progress in this area could lead to highly crystalline films to rival the best crystalline silicon technologies in the future.

2.3.3 Remaining challenges and current focus

Lead toxicity

One of the proposed barriers to the widespread uptake of perovskite technology is the potential risk of lead leaching into the environment. Exposure to lead can lead to severe health effects ranging from cardiovascular and developmental diseases to neurological and reproductive damage.[138] It is, therefore, important to understand the routes to leaching from perovskite solar cell modules and also the quantities that are likely to be leached in the case of encapsulation failure. Hailegnaw *et al*. studied the leaching of Pb from a film of $CH_3NH_3PbI_3$ using simulated rainfall.[138] This study represented a worst case scenario, where the perovskite layer was not encapsulated and completely exposed to the water. They found that the perovskite films were essentially completely removed (~70 % removal) within the space of an hour of simulated rainfall. This decomposition proceeded via the removal of the methylammonium iodide to leave the PbI_2 which has a relatively high solubility in polar solvents such as water. They calculated, however, that even the complete dissolution of all the perovskite within a module would only result in an increase of ~70 ppm of lead within the surrounding surface soil. When compared to the 50-200 ppm of lead typically found in soils in urban areas they argue that the leakage would certainly not be catastrophic.[138]

The relatively low quantities of lead within perovskite cells has also been commented on by Fabini, who calculated that the lead required to produce enough cells to provide the entire US power demand was 160 t $year^{-1}$.[139] It is argued that this value is significantly lower than other sources of lead within the US, such as the production of solder for electronics (6,200 t $year^{-1}$) and lead waste generated through the processing and combustion of coal (5,900-93,000 t $year^{-1}$). It is, therefore, likely that provided cells feature suitable encapsulation, alongside an end-of-life recycling system, then the extent of lead pollution from perovskite solar cells should not be a major issue. A recently published life cycle assessment on perovskite solar cells actually points towards the gold contacts as being the major source of environmental impact, based on current cell making techniques.[140] However, it should be noted that on a commercial, rather than research scale, the excessive use of gold as contacts is unlikely to be common place. The life cycle assessment was also able to show that perovskite solar cells had the potential to achieve the lowest energy payback times amongst all other photovoltaic technologies. Benefits such as these should be balanced against issues such as lead toxicity when considering the future of perovskite cells.

In the meantime, whilst further studies are assessing the toxicity issues associated with lead based perovskites, research efforts are being made to develop Pb-free perovskite structures that can be used in photovoltaics. The most viable alternative metals are the other group 14 metals Ge and Sn. Working Pb-free devices based on Sn have now been demonstrated by both Hao *et al*.

and Noel *et al*. achieving power conversion efficiencies of 5.7 % and 6.4 % respectively.[141, 142] Hao *et al*. produced the solution processed perovskite $CH_3NH_3SnI_3$. This material had a bandgap of 1.3 eV, resulting in a red shifted absorption onset compared to $CH_3NH_3PbI_3$. They then tuned the band gap of the material through the substitution of the I^- ions with Br^-, enabling them to achieve a maximum power conversion efficiency of 5.7 % for the doubly substituted $CH_3NH_3SnIBr_2$. Noel *et al*. reported a $CH_3NH_3SnI_3$ perovskite solar cell, processed on mesoporous TiO_2, with an efficiency of 6.4 % without substitution of the iodide. They found that the materials required encapsulation under an inert atmosphere in order to gain efficient devices due to their instability in ambient atmosphere. Without encapsulation, rapid degradation was observed to occur within seconds in ambient air. They also found that the measured diffusion lengths were considerably shorter than those for Pb-based perovskites. Despite issues of stability, these initial reports of efficiencies for Sn-based perovskites are promising in highlighting that efficient photovoltaic behaviour is not solely found for Pb-based perovskites and could pave the way for exploration of alternative hybrid organic-inorganic structures.

Stability

The stability of devices is another key barrier to commercialisation of perovskite solar cells. As previously discussed, the hybrid organic-inorganic perovskites used within solar cells are easily degraded in contact with water.[138] These materials are also sensitive to moisture in air and can easily degrade to a hydrated form, leading to drastically reduced efficiencies. This causes problems both in fabrication and the long term stability of perovskite solar cells. In the production of high efficiency devices within a research laboratory it is commonplace to undertake cell preparation within a controlled humidity environment, such as a dry box or glove box, to reduce the exposure to moisture. Although possible at laboratory scale, the use of these systems for large scale production is likely to prove difficult and costly. Encapsulation of devices is common practice in many areas of photovoltaics and has also been shown to greatly improve device stabilities for perovskite solar cells.[143]

Degradation of the perovskite material under ultraviolet (UV) light exposure has also been reported when undertaking long-term stability tests under AM 1.5 simulated sunlight.[143] This was found to occur predominantly for encapsulated cells featuring a mesoporous TiO_2 layer and was attributed to the light-induced desorption of surface-adsorbed oxygen. Although a UV filter was successful in reducing some of the performance loss, a 15 % reduction in performance occurred within 5 h. It was found that by substituting the TiO_2 for Al_2O_3 then a much higher stability could be achieved, even in the absence of a UV filter. Using Al_2O_3, encapsulated cells could deliver stable photocurrents over a period of 1,000 h under continuous light exposure.

In addition to moisture and UV instability, reports of thermal degradation of the perovskite have also been made.[144-146] This results in the formation of PbI_2 within the film that can have adverse effects on device performance. As solar cells have to be able to endure high temperatures, which result from prolonged sun exposure, this is a critical issue that would need to be resolved. Thermal degradation has been reported to be much stronger when ZnO is used within the cells rather than TiO_2, due to the basicity of this oxide.[146] This will be explored in more detail within Section 2.3.4 where the use of ZnO within perovskite solar cells is discussed and is also explored experimentally in Chapter 7. It seems likely that the thermal instability is an issue related to the chemistry between the perovskite and the contact layer, rather than an inherent problem of the perovskite. This problem might, therefore, simply be negated through the correct choice of materials.

Hysteresis and cell measurement

As discussed in Section 2.1.3, the performance of a solar cell is typically assessed via the measurement of a *J-V* curve. This involves the sweeping of the applied voltage whilst measuring the current under a standard light source, such as 1 Sun AM 1.5. This measurement is designed to represent, as closely as possible, the steady-state power output from a cell at any given bias and should not be dependent on the scan direction or scan speed. When differences arise in the current measured in the forward scan (short circuit (SC) to forward bias (FB)) and the reverse scan (FB to SC) this is termed hysteresis. Hysteresis in current voltage measurements can be exhibited in DSCs due to their slow response to abrupt changes in voltage when high scan rates are used.[147] In this case, high scan rates typically result in capacitive charging at forward bias which can then be extracted in addition to the photogenerated charge upon sweeping back to short circuit, resulting in hysteresis. This hysteresis can, therefore, be eliminated by reducing the scan speed. This effect is also observed within silicon solar cells when extremely high scan rates are used.[148]

Perovskite solar cells have been shown to exhibit significant hysteresis between forward and backward scans of *J-V* measurements, with improved performances measured on the backward scan (Figure 2.17).[147] However, unlike in the case of DSCs or silicon solar cells, this hysteresis is generally increased upon reducing the scan speed. This indicates that capacitive charging is not the source of hysteresis within perovskite solar cells which has led to this being termed "anomalous hysteresis". At high scan speeds (~0.3 V s^{-1}) this hysteresis is often minimized or not visible at all, but can become significant at slower scan speeds, particularly for planar cell structures.[147] For cells featuring mesoporous films, this effect has been reported to be significantly less pronounced when TiO_2 is used rather than Al_2O_3, likely due to the different routes of charge transport within these cells. Due to this hysteresis, it has been suggested that the measurement of the steady-state power output at a fixed bias should accompany *J-V* curves when reporting results

of record cell efficiencies in order to verify the results. Snaith *et al*. found that in the case of cells featuring mesoporous alumina the steady state power closely matched the maximum power output recorded from the backward scan.[147] This was not found in the case of mesoporous TiO_2 cells and planar cells, which both exhibited lower steady-state power outputs compared to those measured from *J-V* curves.

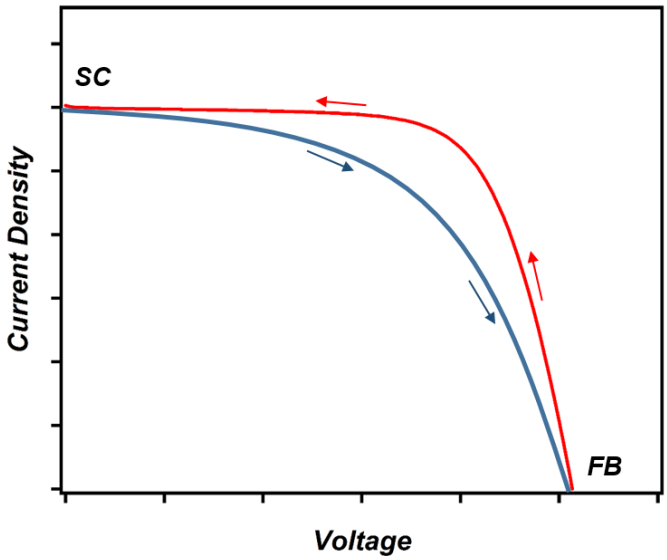

Figure 2.17. *J-V* curve demonstrating hysteresis in the measurements undertaken backwards from forward bias (FB) to short circuit (SC) and forwards from SC to FB.

More recently, highly pronounced hysteresis has been reported when cells featuring no electron selective contacts are used (cell structure shown in Figure 2.14e).[149] The investigation into this type of cell was prompted after the unexpected reports of high efficiencies for these devices.[132] Zhang *et al*. found that whilst these cells gave high efficiencies of over 13 % using a *J-V* measurement from FB to SC, the steady-state power output was almost negligible.[147] These results point towards a polarisation being built up within the perovskite layer under an applied forward bias, likely due to the migration of mobile ions within the perovskite towards the contacts. This polarisation allows the build-up of positive and negative space charge at the respective electrodes that facilitates efficient charge extraction. However, under normal working conditions, this polarisation would relax and the facilitation of charge extraction would only occur in the presence of charge selective contacts. This explanation can likely be linked to the anomalous hysteresis observed within *J-V* measurements due to the facilitation of charge extraction after forward bias has been applied to the cells. This would also explain why the hysteresis is observed to increase at slower scan rates, as there would be more time for relaxation of the polarisation to occur.

The source of anomalous hysteresis is still, however, under much debate. Another theory for the source of hysteresis involves the apparent ferroelectric behaviour of the perovskites.[150] Until the reasons behind this anomalous hysteresis have been clarified, it seems likely that significant uncertainty about the accuracy of reported record efficiencies will remain unless *J-V* curves are reported alongside steady-state power output measurements. Reporting of hysteresis in record cell efficiencies is now commonplace within the field and the majority of the latest high efficiency devices have exhibited very little difference between the forward and backward scans.[111] Despite this, *J-V* curves are still rarely accompanied by steady state power measurements.

2.3.4 ZnO within perovskite solar cells

A huge variety of inorganic materials have now been demonstrated as effective electron selective contacts in perovskite solar cells, including TiO_2,[130] ZnO,[151] $SrTiO_3$ [152] and Zn_2SnO_4 [153] to name but a few. The final part of this section on perovskite solar cells will focus on the use of ZnO as an electron selective material within these devices, which will form the area of investigation within Chapter 7.

In a similar manner to the course of DSC research, ZnO has been one of the first and most commonly explored alternatives to TiO_2 as an electron selective contact in perovskite solar cells. This is not surprising, due to the similar band gap and energy levels of these materials, and also due to the higher bulk electron mobilities in ZnO.[154] The primary drawback of ZnO within DSCs was the incompatibility with acidic dyes, and as this was not likely to be an issue within perovskite cells, ZnO was a natural alternative.

Perovskite solar cells based on ZnO nanorods

The first two reports of the use of ZnO within perovskite solar cells came in close proximity to each other and both involved the use of ZnO nanorods as electron selective contacts (Figure 2.18a).[155, 156] Bi *et al*. grew ZnO nanorods on FTO coated glass substrates using hydrothermal growth and applied them within solid-state perovskite cells, featuring a Spiro-OMeTAD hole conductor and gold contacts.[155] Different nanorod lengths were investigated and lengths of 1000 nm were found to give optimal power conversion efficiencies of 5.0 %. They found that ZnO shows lower performance compared to TiO_2 due to increased recombination losses within this cell design. The stability of these cells over 500 hours in air was reported to be good, even without any sealing. Kumar *et al*. employed a similar device structure, but with shorter nanorods (~500 nm), through electrodeposition of a ZnO compact layer which was coated in a layer of ZnO nanorods by chemical bath deposition.[156] Conversion efficiencies of up to 8.90 % were obtained

on rigid substrates and 2.62 % for flexible substrates. Power conversion efficiencies for the nanorod devices were found to be significantly higher than planar devices (5.54 % for planar).

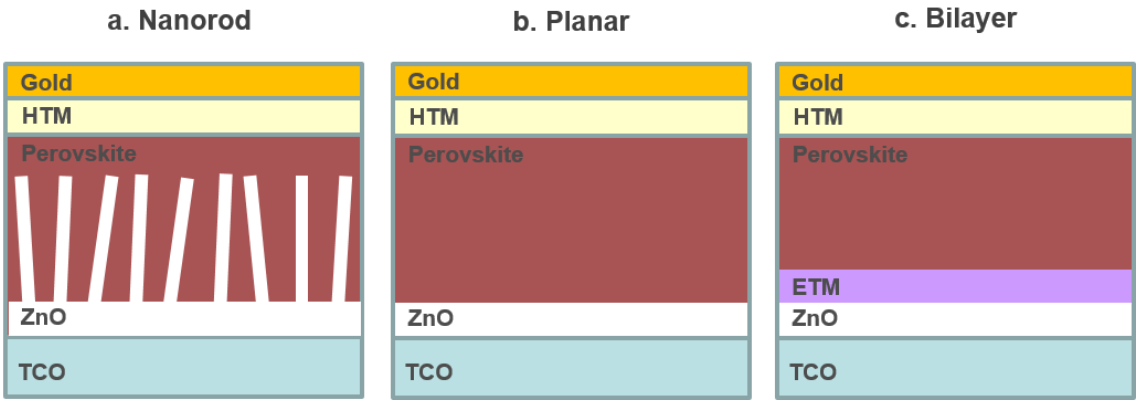

Figure 2.18. Simplified cross-sections of the three main types of perovskite cell structures used with ZnO. HTM = hole transport material, TCO = transparent conducting oxide and ETM = electron transport material. In the case of the bilayer structure, the ETM is typically an organic n-type semiconductor or TiO_2.

This efficiency was improved upon by Son *et al*. who produced a ZnO nanorod perovskite cell with a maximum PCE of 11.13 %.[157] By comparison of the integrated external quantum efficiency with equivalent cells using TiO_2 nanorods it was found that ZnO gave significantly higher J_{sc} values (20 mA cm^{-2} compared to 16 mA cm^{-2} for TiO_2). This was attributed to enhanced electron collection compared to TiO_2, and on this basis it was suggested that ZnO nanorods were an effective charge collection system in perovskite cells. In agreement with the findings of Bi *et al.*, the highest performing cells had nanorods of average length 1000 nm.

Nanorod arrays were also produced by both electrodeposition and plasma enhanced chemical vapour deposition (CVD) and applied within perovskite solar cells.[158, 159] The electrodeposited nanorods were compared to compact ZnO layers also formed by electrodeposition and were found to perform significantly better, achieving power conversion efficiencies of 10.28 %.[158] These optimised efficiencies were achieved after depositing a conformal layer of ZnO with low n-type doping over the surface of the nanorods, which resulted in reduced recombination and improved V_{oc}. In the case of the nanorods deposited by plasma enhanced CVD, a compact TiO_2 layer was used as a hole blocking layer between the nanorod array and the substrate.[159] In this cell configuration maximum efficiencies were found to be relatively low (4.8 %) due to low values of V_{oc} and fill factor.

An effective route to reducing the recombination occurring at the interface between ZnO and the perovskite has been to produce core-shell nanorods, where ZnO acts as the core and is surrounded by another material. Liu *et al*. used CdS as the shell material in cells featuring the

$CH_3NH_3PbBr_3$ perovskite.[160] Using a polymer buffer layer above the perovskite and PEDOT:PSS as the hole conductor they were able to demonstrate cell efficiencies of up to 4.31 %. This was found to be significantly higher than efficiencies gained using ZnO nanorods alone, as significant degradation of the perovskite was observed upon heating in this case, leaving $PbBr_2$. An aluminium-doped ZnO layer has also been found to be an effective shell material to supress recombination.[161] A shell with a 5 % Al doping level was found to effectively raise the conduction band and give rise to increased V_{oc} compared to bare ZnO. Using this approach, maximum power conversion efficiencies of over 10 % were achieved compared to 8.5 % for bare ZnO nanorods.

One of the most commonly used shell materials has been TiO_2, due to its common use as an electron transport material in perovskite solar cells. Dong *et al.* deposited TiO_2 onto ZnO nanorod arrays by atomic layer deposition.[162] They optimised the cell performance on the basis of TiO_2 layer thickness and found that 5 deposition cycles gave the best performances of 13.4 %, with increases coming from the improved fill factors of the cells. TiO_2 shells have also been deposited from solution onto ZnO nanorods with similar improvements in efficiency.[163] Within this study the effect of the ZnO seed layer was also investigated. It was found that nanorod arrays were often damaged or removed from the substrate during subsequent spin coating of the remaining cell layers. This was avoided with the use of a colloidal ZnO seed layer, and when combined with the TiO_2 surface treatment, high efficiencies of 14.35 % were achieved with significantly improved V_{oc} values. Further improvements to the efficiencies of these core-shell devices were made by Mahmood *et al*. who were able to produce nanorod arrays with higher aspect ratio through the addition of a conjugated polyelectrolyte polymer during growth.[164] This higher aspect ratio allowed improved infiltration of the perovskite between the nanorods. When this was combined with the decreased recombination after TiO_2 coating, a maximum efficiency of 15.3 % was obtained.

As an alternative to coating the nanorods in a shell of another material, the doping of the ZnO nanorods themselves has also been explored as a route to higher performances.[165, 166] Doping the nanorods with 5 % Mg has been found to be an effective way of raising the conduction band edge of the nanorods, thereby decreasing recombination and increasing the V_{oc} of the cells to achieve an increase of power conversion efficiency from 14.0 % to 15.3 %.[165] Mahmood *et al*. employed nitrogen doping, together with their previously reported improvements from higher aspect ratios and a thin polyethyleneimine layer, to achieve the highest cell efficiencies to date for ZnO nanorods in perovskite solar cells. These three optimisations allowed them to reach maximum power conversion efficiencies of 16.1 % for cells that also exhibited extremely low hysteresis in the *J-V* curves.[166] These reports have demonstrated that ZnO nanorods can provide an effective electron selective contact, provided that recombination at the interface between ZnO

and perovskite is reduced by means of coating the nanorods with a shell of another material or altering their physical properties.

Table 2.1. The photovoltaic performance of different perovskite solar cells featuring ZnO nanorods reported in the literature. CBD = chemical bath deposition and CVD = chemical vapour deposition.

Cell Structure	Nanorod Deposition Method	J_{sc} (mA cm^{-2})	V_{oc} (V)	FF (%)	PCE (%)	Ref.
Glass/FTO/ZnO/$CH_3NH_3PbI_3$/Spiro-OMeTAD/Ag	Hydrothermal	12.5	0.75	60	5.0	[155]
Glass/FTO/ZnO/$CH_3NH_3PbI_3$/Spiro-OMeTAD/Au	Hydrothermal	20.1	0.99	56	11.1	[157]
Glass/ITO/ZnO/CdS/$CH_3NH_3PbBr_3$/PEDOT:PSS/Au	Hydrothermal	7.2	1.04	57	4.3	[160]
Glass/FTO/ZnO/$CH_3NH_3PbI_3$/Spiro-OMeTAD/Au	Hydrothermal	19.4	1.06	70	14.4	[163]
Glass/ITO/N-doped ZnO/$CH_3NH_3PbI_3$/Spiro-OMeTAD/Ag	Hydrothermal	21.5	0.96	70	16.1	[166]
Glass/FTO/ZnO/TiO_2/$CH_3NH_3PbI_3$/Spiro-OMeTAD/Au	Hydrothermal	21.9	1.00	70	15.3	[164]
Glass/FTO/Mg-doped ZnO/$CH_3NH_3PbI_3$/Spiro-OMeTAD/Au	Hydrothermal	22.7	0.99	68	15.3	[165]
Glass/FTO/ZnO/$CH_3NH_3PbI_3$/Spiro-OMeTAD/Au	CBD	17.0	1.02	51	8.9	[156]
PET/ITO/ZnO/$CH_3NH_3PbI_3$/Spiro-OMeTAD/Au	CBD	7.5	0.80	43	2.6	[156]
Glass/FTO/ZnO/TiO_2/$CH_3NH_3PbI_3$/Spiro-OMeTAD/Au	CBD	21.1	0.98	65	13.4	[162]
Glass/FTO/ZnO/AZO/$CH_3NH_3PbI_3$/Spiro-OMeTAD/Au	Sol-gel	19.8	0.90	60	10.7	[161]
Glass/FTO/ZnO/$CH_3NH_3PbI_3$/Spiro-OMeTAD/Ag	Electrodeposition	21.9	0.99	47	10.3	[158]
Glass/FTO/TiO_2/ZnO/$CH_3NH_3PbI_3$/Spiro-OMeTAD/Au	CVD	16.0	0.72	41	4.8	[167]

ZnO in planar perovskite cells

The first planar perovskite solar cells based on ZnO (Figure 2.18b) came from Liu *et al*., who achieved remarkably high efficiencies using a simple and low temperature cell fabrication procedure that was also compatible with flexible plastic substrates.[151] Critical to their planar cell design was a layer of small (~5 nm diameter) ZnO nanoparticles that functioned as an electron selective contact for the perovskite material. The nanoparticles could be deposited from solution using spin coating and could be used without any annealing prior to perovskite deposition, which greatly simplified cell preparation. $CH_3NH_3PbI_3$ was deposited directly onto these layers via a two-step deposition method with no heating of the perovskite layer. The performance of these cells was optimised on the basis of the thickness of the ZnO nanoparticle layer, with a 25 nm thick layer giving the optimum efficiency of 15.7 %. These efficiencies still remain some of the highest reported for ZnO based perovskite solar cells. Due to the low temperature processing of the ZnO layer, it was possible to also produce cells on flexible PET substrates. These flexible cells exhibited lower efficiencies of 10.2 % due to lower J_{sc} values, but remain as the highest efficiency flexible perovskite cells reported using ZnO electron selective layers.

In a later publication, they then went on to look at the influence of the perovskite layer thickness on the performance of these cells.[168] Significant control over the film thickness was gained by thermally evaporating the PbI_2 layer, rather than depositing from solution. The device performance was found to be strongly dependent on the perovskite layer thickness and layers of ~330 nm were found to be optimum. The efficiencies of cells produced from both thermal evaporation and solution processing were found to give comparable performances for equivalent perovskite film thicknesses. However, it was revealed that both sets of devices suffered from significant hysteresis, which needs to be resolved for reliable efficiency determination.

The use of small ZnO nanoparticles as an electron selective contact has been adopted in a number of more recent reports, however, none have been able to achieve equivalent efficiencies. Song *et al*. reported an almost identical cell structure and achieved optimised efficiencies of 13.4 %, using slightly thinner nanoparticle layers (~20 nm).[169] ZnO nanoparticles have also been applied as the electron selective contact in inverted structure planar cells with an efficiency of 10.5 %, slightly lower than when [6,6]-phenyl C_{61} butyric acid methyl ester (PCBM) was used instead (11.5 %).[170]

Nanoparticle blocking layers have also been employed in devices that make use of carbon electrodes in place of both the hole conductor and conducting contact.[171, 172] These simple cell designs avoid the use of two of the most expensive components of the cell, the hole transport material and metallic contact (typically Au or Ag), and can also be produced at low temperature. Zhou *et al*. deposited a carbon electrode directly onto the perovskite layer and achieved a

remarkable power conversion efficiency of 8 % using this simple cell design on rigid glass substrates and 4 % for flexible substrates.[171] This was improved upon by Jin *et al*., who included an intermediate layer of exfoliated graphite between the perovskite and carbon black to improve the electrical contact.[172] The improved contact greatly enhanced the fill factor of these cells and allowed efficiencies of 10.2 % to be reached.

One of the key advantages demonstrated by the use of ZnO electron selective contacts in planar cell configurations is the ability to avoid high temperature annealing steps and, thereby, complete the whole cell preparation at low temperatures. There are a number of different low temperature deposition techniques in existence for ZnO, and many research efforts have been focussed on the use of these in planar perovskite cell fabrication. Electrospray deposition has been used to produce dense and crack free films of ZnO on FTO coated glass substrates at a high deposition rate.[173] Reasonable efficiencies were achieved (10.8 %) despite fairly thick films of ZnO being used (440 nm). It was found, however, that further increases in ZnO film thickness resulted in significant drops in cell efficiency, likely due to increased resistance through the thick films. A further boost to the cell efficiencies (12.0 %) occurred through Al-doping the ZnO film during deposition.

Sputtering has also been used in the deposition of ZnO layers for perovskite solar cells. Liang *et al*. used magnetron sputtering, a scalable and low temperature technique, to deposit thin (40 nm) ZnO layers onto ITO coated substrates.[174] They produced cells with a maximum power conversion efficiency of 13.1 %, that was largely independent of the ZnO thickness used (up to 160 nm). Key to these high performances was a thin MoO_3 interlayer between the hole conductor and silver contact. Due to the low temperature nature of this technique, they were also able to demonstrate flexible devices based on PET substrates with a maximum efficiency of ~8 %. Sputtering was also used by Tseng *et al*. to deposit 40 nm thick ZnO layers as electron selective contacts.[175] The working gas used during sputtering was found to influence the properties of the ZnO film, including the series resistance, and subsequently the performance of the perovskite solar cells. It was found that a pure Ar working gas gave cells with the highest V_{oc} and J_{sc} and resulted in a maximum efficiency of 15.9 %.

Electrodeposition is another technique that can be used in the formation of high quality ZnO films at low temperature. Zhang *et al*. have been studying the use of electrodeposited ZnO layers within perovskite solar cells.[145, 176] They were able to grow compact ZnO layers with high optical and structural quality at low temperature, and in very short periods of time (2 minutes), using zinc nitrate as the precursor. Despite the ZnO layers formed being quite thick (250-1900 nm), they were able to reach relatively high efficiencies (10.6 %) when applied in planar devices.[176] In a later publication, they were able to demonstrate optimised cell efficiencies

of 15.0 %, using these ZnO layers in conjunction with an improved 1-step perovskite deposition technique involving a very short annealing time (2 minutes).[145]

Modification of the ZnO surface has also been found to be an effective route to improving the efficiency of planar devices.[177] The deposition of a thin molecular monolayer of 3-aminopropanoic acid onto the surface of ZnO was demonstrated recently to greatly alter the crystallization of perovskite on the ZnO surface. Perovskite films with a lower number of pinholes were able to be grown on the modified surface, resulting in a dramatic increase in cell efficiency from 12.0 % to 15.7 %. It is likely that similar simple modifications of the ZnO surface in future might prove to be an effective route to controlling the crystallization of the perovskite film, which has been shown to have dramatic effects on cell performance.

Table 2.2. The photovoltaic performance of different perovskite solar cells featuring planar ZnO layers reported in the literature.

Cell Structure	ZnO Deposition Method	J_{sc} (mA cm^{-2})	V_{oc} (V)	FF (%)	PCE (%)	Ref.
Glass/ITO/ZnO/$CH_3NH_3PbI_3$/Spiro-OMeTAD/Ag	Spin coating NPs	20.4	1.03	75	15.7	[151]
PET/ITO/ZnO/$CH_3NH_3PbI_3$/Spiro-OMeTAD/Ag	Spin coating NPs	13.4	1.03	74	10.2	[151]
Glass/ITO/PEDOT:PSS/$CH_3NH_3PbI_{x-3}Cl_x$/ZnO/Al	Spin coating NPs	17.3	0.89	69	10.5	[170]
Glass/ITO/ZnO/$CH_3NH_3PbI_3$/P3HT/Ag	Spin coating NPs	16.0	0.94	65	11.3	[168]
Glass/FTO/ZnO/$CH_3NH_3PbI_3$/C	Spin coating NPs	18.6	0.77	56	8.1	[171]
PEN/ITO/ZnO/$CH_3NH_3PbI_3$/C	Spin coating NPs	13.4	0.76	42	4.3	[171]
Glass/ITO/ZnO/$CH_3NH_3PbI_3$/Spiro-OMeTAD/Ag	Spin coating NPs	19.9	1.07	1	13.9	[169]
Glass/ITO/ZnO/$CH_3NH_3PbI_3$/Graphite/C	Spin coating NPs	21.3	0.96	50	10.2	[172]
Glass/ITO/ZnO/$CH_3NH_3PbI_3$/Spiro-OMeTAD/Ag	Spin coating	22.5	1.07	65	15.7	[177]
Glass/FTO/ZnO/$CH_3NH_3PbI_{x-3}Cl_x$/Spiro-OMeTAD/Ag	ALD	11.4	0.88	59	6.0	[170]
Glass/FTO/ZnO/$CH_3NH_3PbI_3$/Spiro-OMeTAD/Ag	Electrospray	16.0	1.01	67	10.8	[173]

Glass/FTO/AZO/$CH_3NH_3PbI_3$/Spiro-OMeTAD/Ag	Electrospray	15.1	1.05	76	12.0	[173]
Glass/ITO/ZnO/$CH_3NH_3PbI_3$/Spiro-OMeTAD/Ag	Sputter coating	21.8	1.00	73	15.9	[175]
Glass/ITO/ZnO/$CH_3NH_3PbI_3$/Spiro-OMeTAD/MoO_3/Ag	Sputter coating	22.4	1.04	57	13.4	[174]
PET/ITO/ZnO/$CH_3NH_3PbI_3$/Spiro-OMeTAD/MoO_3/Ag	Sputter coating	18.4	0.87	50	8.0	[174]
Glass/FTO/ZnO/$CH_3NH_3PbI_3$/Spiro-OMeTAD/Ag	Electrodeposition	22.6	0.91	53	10.9	[176]
Glass/FTO/ZnO/$CH_3NH_3PbI_3$/Spiro-OMeTAD/Ag	Electrodeposition	20.0	1.08	69	15.0	[145]

ZnO within bilayer electron selective contacts

An evolution from the simple planar cell design has been to replace the single layer electron selective contact with a bilayer of two different materials (Figure 2.18c). The rationale behind the use of a bilayer contact is to reduce charge recombination occurring at the interface between ZnO and perovskite, improve electron extraction and reduce the chances of pinhole gaps within the electron selective contact.

One of the most common approaches has been to use the n-type organic semiconductor PCBM as an interlayer between ZnO and the perovskite material.[178-181] Due to the solubility of PCBM in polar solvents, such as the dimethylformamide (DMF) or dimethylsulfoxide (DMSO) used in perovskite deposition, it is often employed in inverted planar cell structures on top of the perovskite layer. Qiu *et al*. demonstrated that a PCBM/ZnO bilayer could function as an effective electron selective contact in inverted device structures, achieving power conversion efficiencies of 14.2 %.[179] A short air-aging step after PCBM deposition was found to be critical in obtaining high efficiency cells. The ZnO was found to improve the energy level alignment within the cell and also enhance the air stability of the cells, by preventing reaction between the metal contact and the perovskite. Higher efficiencies of 15.9 % were achieved by Bai *et al*. through optimisation of the perovskite preparation method.[180] In addition to this, larger (1 cm^2) cells were demonstrated with an efficiency of 12.3 %. The efficiencies were boosted further for this cell design by Zhang *et al*. (16.8 %).[181] The production of high quality perovskite films was found to be key to the success of these cells and was achieved through covering the perovskite film with a petri dish during annealing. Covering the film resulted in the slow evaporation of CH_3NH_3Cl from the spin coated precursor solution and the production of high quality perovskite films. The stability of these devices was assessed by storing them in air without encapsulation for two months and then re-measuring the *J-V* curve. The efficiency of the devices was found to fall only by a small

amount, from 13.8 % to 13.1 %, over the two months. However, in the absence of the ZnO interlayer, efficiencies were found to rapidly degrade within just one day. The improved stability caused by the ZnO interlayer was proposed to be caused by either preventing moisture reaching the perovskite, or due to it stopping aluminium diffusing from the metallic contact into the PCBM layer.

The use of PCBM/ZnO bilayers in non-inverted planar structures has yielded relatively less success, likely due to the dissolution of the PCBM in the perovskite precursor solution. Despite these concerns over PCBM dissolution, Kim *et al*. were able to show an increase in efficiency from 8.4 % to 12.2 % upon adding PCBM on top of a ZnO blocking layer, indicating that the layer might not be entirely removed during the subsequent spin coating of the perovskite precursor.[178] They reported a suppression in the trap-assisted charge recombination at the interface of ZnO as a result of the PCBM layer, which increased the V_{oc}. Some improvement upon adding a PCBM layer was also reported by Cheng *et al*., however, they found that the use of poly(ethyleneimine) instead of PCBM resulted in much better cell performance due to its lower solubility in polar solvents.[144]

Another alternative to PCBM for non-inverted cell structures is to use a cross-linkable conjugated polymer, such as poly[9,9-bis(6′-(*N*,*N*-diethylamino)propyl)-fluorene-*alt*-9,9-bis-(3-ethyl(oxetane-3-ethyloxy)-hexyl)-fluorene] (PFN-OX).[182] This polymer shows good solvent resistance to polar solvents such as DMF and DMSO and can, therefore, form a stable bilayer. This approach led to a maximum cell efficiency of 16.2 %. In order to avoid the issue of dissolution entirely, an all inorganic bilayer can be used. Xu *et al*. employed this idea and demonstrated very high efficiencies (17.2 %) for cells featuring a bilayer consisting of ZnO on top of TiO_2. The performance of these bilayer electrodes was much higher than those of ZnO alone (13.0 %) and was attributed to the reduction of pinhole gaps in the bilayer contact. This was effective in reducing interfacial recombination within the cells, resulting in improved V_{oc} and fill factors.

The use of bilayer electron selective contacts has led to many of the highest reported efficiencies for perovskite solar cells featuring ZnO and, therefore, appears to be a promising route to producing planar perovskite solar cells. Although the addition of another layer within the solar cell can add complexity to the production, the fact that the majority of these layers are deposited using simple and low temperature solution processing techniques means that this is not likely to be a significant barrier to its use, particularly given the improvements in efficiency that they give rise to.

Table 2.3. The photovoltaic performance of different perovskite solar cells featuring a bilayer electron selective contact including ZnO reported in the literature.

Cell Structure	J_{sc} (mA cm^{-2})	V_{oc} (V)	FF (%)	PCE (%)	Ref.
Glass/ITO/PEDOT:PSS/$CH_3NH_3PbI_{x-3}Cl_x$/PCBM/ZnO/Al	19.6	0.98	74	14.2	[179]
Glass/ITO/PEDOT:PSS/$CH_3NH_3PbI_{x-3}Cl_x$/PCBM/ZnO/Al	20.5	0.97	80	15.9	[180]
Glass/ITO/PEDOT:PSS/$CH_3NH_3PbI_{x-3}Cl_x$/PCBM/ZnO/Al	22.0	1.03	74	16.8	[181]
Glass/ITO/ZnO/PEI/$CH_3NH_3PbI_3$/Spiro-OMeTAD/Au	16.8	0.88	69	10.2	[144]
Glass/ITO/ZnO/PCBM/$CH_3NH_3PbI_3$/PTB7-Th/MoO_3/Ag	18.2	1.00	67	12.2	[178]
Glass/ITO/ZnO/PFN-OX/$CH_3NH_3PbI_3$/Spiro-OMeTAD/Au	20.7	1.03	76	16.2	[182]
Glass/FTO/ZnO/TiO_2/$CH_3NH_3PbI_3$/Spiro-OMeTAD/Au	21.0	1.08	75	17.2	[183]

Other perovskite solar cell structures featuring ZnO

In addition to the nanorod and planar device architectures that have dominated research in the area of ZnO-based perovskite solar cells, there have been a number of other device structures reported in the literature. In early reports, ZnO was used on several occasions in conjunction with mesoporous scaffolds of other metal oxides. TiO_2 was used as the mesoporous oxide in a study by Juarez *et al*. which examined the role of selective contacts within perovskite solar cells.[184] This mesoporous layer was deposited on top of electron selective contacts formed from either TiO_2, ZnO or CdS and the performance and electrochemical characteristics of the resulting cells were compared. It was found that although the use of ZnO led to very high J_{sc} values, the low fill factors they exhibited made the efficiencies of these cells (7.86 %) intermediate between values obtained for TiO_2 (9.13 %) and CdS (1.53 %). The low fill factor measured with the ZnO electron selective contacts was related to a low recombination resistance, determined from electrochemical impedance spectroscopy. Al_2O_3 was used as the mesoporous material in studies by Dong *et al*. and Chandiran *et al*..[185, 186] In the former of these two reports a thin layer (~30 nm) of ZnO was formed by atomic layer deposition and mesoporous alumina was deposited above it as a scaffold.[185] By infiltrating this scaffold with an all iodide perovskite via 1-step deposition, a maximum efficiency of 13.1 % was achieved. In the latter report, the opposite approach was employed by using atomic layer deposition to form a thin layer (3-6 nm) over the surface of the

mesoporous alumina scaffold.[186] Despite being extremely thin, the ZnO film was found to be able to effectively transport electrons in both dye-sensitized and perovskite solar cells. In the case of perovskite solar cells, the cell efficiency was greatly improved after deposition of the ZnO layer (1.7 % without and 7.0 % with ZnO), largely due to the absence of a blocking layer in the former case.

Some reports have also been made on the use of more unique ZnO morphologies and cell structures within perovskite solar cells. A ZnO double-layer electrode was proposed as an effective structure by Mahmood *et al*.[187] This double layer structure consisted of vertically aligned nanosheets, onto which horizontally aligned nanorods had been grown. Efficiencies of 10.35 % were achieved for devices based on this electrode design and the cells were found to be relatively stable over a period of 240 h in air. Given that higher efficiencies have been obtained for simpler nanorod morphologies, it seems likely that the high surface areas offered by these hierarchical structures are not particularly necessary for efficient cells.

Some interesting flexible perovskite cell designs have also been reported using ZnO. A perovskite solar cell based on stainless steel fibres and fabrics was reported by He *et al*..[188] These cells were produced by first growing 1-D ZnO "obelisks" on the surface of the steel substrates, followed by deposition of both the perovskite and hole conductor by dip coating. The cells were completed by wrapping a transparent carbon nanotube sheet around the wire to act as a conducting contact. These rather unique fibre based cells achieved power conversion efficiencies of 3.8 % and were found to retain 93 % of this efficiency after 200 bending cycles. This method was then further applied to woven stainless steel fabrics, highlighting the opportunity for flexible perovskite cells for a range of niche applications.

Another interesting flexible cell design made use of graphene as the electron selective contact and a mesoporous ZnO scaffold on a flexible conducting substrate.[189] As traditional high temperature sintering of the ZnO was not an option on the flexible substrate, an atmospheric plasma jet treatment was used on the mesoporous film. This treatment greatly improved the performance of cells based on these electrodes from 5.28 % to 9.73 %. This technique could potentially prove to be an interesting route to the low temperature processing of other mesoporous oxides for flexible devices in the future. These unique cell designs show that there is still plenty of room for innovation in cell design and material use in the field of perovskite solar cells. Despite this, the efficiencies obtained for flexible devices can still be seen to lag significantly behind the current state of the art devices on rigid substrates (Figure 2.19).

Table 2.4. The photovoltaic performance of other perovskite solar cell architectures featuring ZnO reported in the literature. CNT = carbon nanotubes.

Cell Structure	J_{sc} (mA cm^{-2})	V_{oc} (V)	FF (%)	PCE (%)	Ref.
Glass/FTO/meso-Al_2O_3/ZnO/$CH_3NH_3PbI_3$/Spiro-OMeTAD/Au	18.5	0.76	50	7.0	[186]
Glass/FTO/ZnO/meso-Al_2O_3/$CH_3NH_3PbI_3$/Spiro-OMeTAD/Ag	20.4	0.98	66	13.1	[185]
Glass/FTO/ZnO/meso-TiO_2/$CH_3NH_3PbI_3$/Spiro-OMeTAD/Au	19.7	0.96	42	7.9	[184]
Glass/FTO/ZnO NW/ZnO NS/$CH_3NH_3PbI_3$/Spiro-OMeTAD/Ag	18.0	0.93	62	10.4	[187]
Stainless Steel Wire/ZnO NW/$CH_3NH_3PbI_3$/Spiro-OMeTAD/CNT	15.2	0.66	37	3.8	[188]
PET/ITO/Graphene/meso-ZnO/$CH_3NH_3PbI_3$/Spiro-OMeTAD/Ag	16.8	0.94	62	9.7	[189]

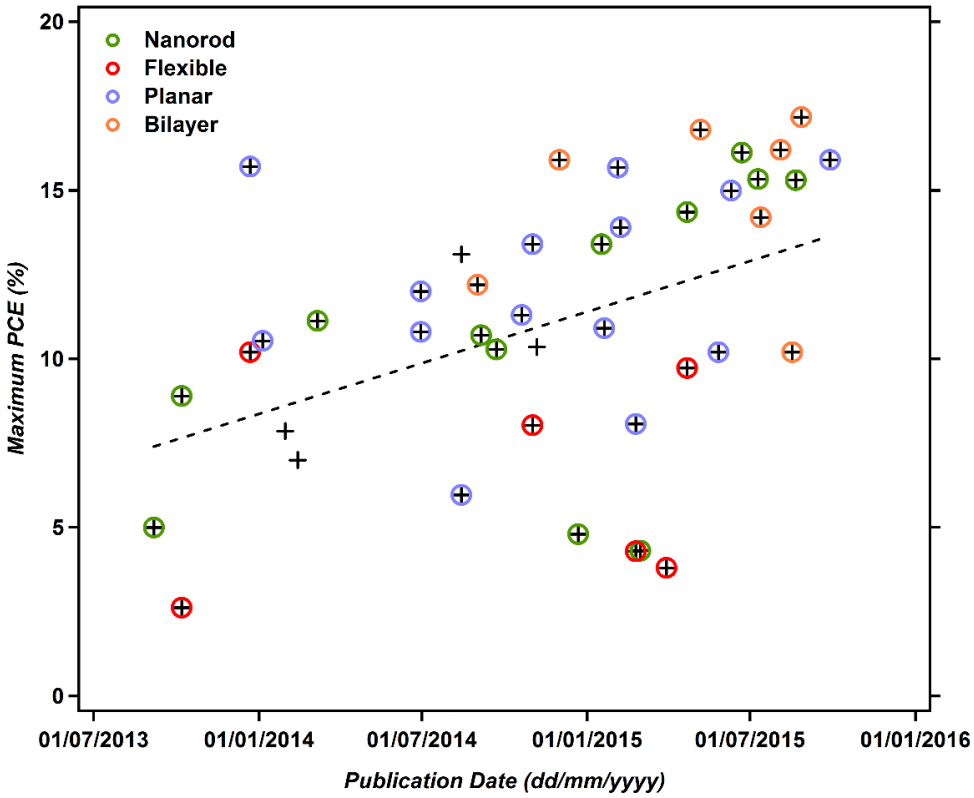

Figure 2.19. Maximum reported power conversion efficiencies *vs.* publication date for all reports to date (11/10/2015) featuring ZnO within perovskite solar cells (black "+" symbols). The dashed line is a linear fit of all values and the main types of device structure are highlighted by the coloured circles. All values were obtained from the references within this section.

Instability issues for perovskite on ZnO

Despite the undoubted progress that has been made within the area of perovskite solar cells featuring ZnO, a major issue has now been highlighted within several recent reports. This issue is the observed thermal instability of perovskite on ZnO contacts. Annealing of the perovskite layer (typically at 70-120 °C) after deposition is a commonly applied technique to improve crystallinity and ensure full conversion to the perovskite. In particular, when the 1-step deposition technique is used, this annealing is absolutely necessary in the case of TiO_2 contacts in order to form the perovskite. It has been noticed, however, that heating the perovskite layer on top of a ZnO layer results in the rapid degradation of the dark brown/black perovskite back to yellow, which is the colour of PbI_2.[144-146] This observation explains why two-step perovskite deposition techniques, with either a short or no annealing step, are most commonly used in conjunction with ZnO electron selective contacts. Although efficient cells have been demonstrated in the absence of perovskite annealing steps, this thermal degradation poses a more serious question for the long term stability of ZnO-containing perovskite solar cells. This is particularly concerning when you consider that solar cells can reach temperatures of around 80 °C under working conditions in warm climates.

The origins of this instability have recently been studied by Yang *et al*. using a combination of *in situ* grazing incidence X-ray diffraction (GIXRD) experiments and density functional theory calculations.[146] They found that annealing films of perovskite on ZnO coated substrates resulted in the degradation to PbI_2, even at temperatures as low as 100 °C. The formation of PbI_2 was confirmed by UV-vis absorption spectroscopy, and powder X-ray diffraction, showing that virtually complete degradation was occurring. In contrast, perovskite films deposited onto TiO_2, PEDOT:PSS, glass and ITO substrates were found to show only very slight degradation, even at 200 °C. An original hypothesis for the reason behind this degradation was that the hygroscopic ZnO was drawing additional moisture into the cell, and as moisture is known to degrade the perovskite this was the source of degradation. However, experiments involving *in situ* absorbance measurements of the films under high humidity revealed that the ZnO actually appears to offer some moisture protection to the perovskite layer. This was proposed to be through the hydrophilic ZnO dehydrating the hydrated perovskite and regenerating the original perovskite material. To further elucidate the decomposition mechanism GIXRD was used to monitor the decomposition in real time. The decomposition was found to occur rapidly at 100 °C (within 13 minutes), indicating a single step decomposition without formation of intermediate phases. These results pointed towards a direct reaction between the perovskite and ZnO, and due to the basic nature of the metal oxide, this was proposed to be via the deprotonation of the methylammonium cation. This hypothesis was validated using density functional theory calculations of an interface between the perovskite and ZnO, and also with TiO_2 as a comparison.

In the case of ZnO, deprotonation of methylammonium ions at the interface was found to occur, forming methylamine as a product, whereas no deprotonation was found for TiO_2. In addition to the degradation of perovskite due to the inherent acid-base chemistry between it and the ZnO, the presence of surface hydroxyl groups and acetate ligands was found to exacerbate this situation. The contribution of these surface groups was found to be reduced by high temperature annealing of the ZnO film, however, some decomposition was still found to occur due to the inherent properties of the ZnO.

This decomposition was also studied by Zhang *et al*. using X-ray diffraction (XRD) on perovskite films deposited on ZnO by a 1-step method.[145] In this case, almost complete decomposition was again observed within short time periods (20 min) of heating at 100 °C. They proposed that the perovskite decomposition was catalysed by the ZnO underlayer according to the reaction:

$$CH_3NH_3PbI_3 \rightarrow PbI_2 + CH_3NH_2 + HI \qquad (2.1)$$

where both the methylamine and HI would be volatile at the annealing temperature and lost to the air, leaving PbI_2. The decomposition in contact with ZnO and the enhancement of this in the presence of surface hydroxide groups was also confirmed by Cheng *et al*..[144] They again showed that annealing the ZnO reduces the rate of perovskite thermal degradation, due to the removal of surface hydroxide groups, and showed that further passivation can be achieved through the use of an organic layer on top of the ZnO. Whilst PCBM provided some improvement, its solubility in DMF and DMSO led to its partial removal. The polymer poly(ethyleneimine) was found to be more suitable and its use allowed the perovskite films to be annealed, leading to improved efficiencies due to higher crystallinity in the perovskite film.

Outlook for ZnO in perovskite solar cells

It therefore seems that the problem of perovskite instability on ZnO might be negated through the use of a bilayer electrode structure. However, until full long-term studies of the stability of such devices are conducted, there remains a big question over the use of ZnO within perovskite solar cells. If this problem of instability can be overcome, ZnO certainly presents an interesting alternative to commonly used materials such as TiO_2. The ability to process ZnO at lower temperatures, making it compatible with flexible substrates, is a big draw of this material and could enable mass production of perovskite devices through roll-to-roll production methods. The range of easily accessible nanostructures is also an interesting opportunity for the use of ZnO within perovskite solar cells, however, due to the apparent lack of requirement for high surface area interfaces within these devices, this is likely to be less of an area of focus compared to the interest it received in DSCs.

Although the current state of the art efficiencies of devices using ZnO electron selective contacts are lagging behind those using TiO_2, efficiencies can still be seen to be on the rise (Figure 2.19). Over the two years since the first report of ZnO within perovskite solar cells an average increase in reported efficiencies of 3 % (PCE) per year has been achieved (see dashed line in Figure 2.19) and there does not appear to be any sign of this trend slowing within the next year. This rate of performance increase might see ZnO devices catch up with TiO_2 based devices, as the efficiency limits of these devices are approached. In particular, it can be seen that the use of bilayer electron selective contacts might prove to be a promising route to focus future efforts. In addition to the higher efficiencies reported for these devices, they are also likely to have improved long-term stabilities due to the separation of ZnO from the perovskite.

2.4 ZnO Nanostructures from Anodization

As has been noted in the previous sections, one of the main merits of ZnO as a material is the wide range of morphologies that can be obtained, using a similarly broad range of synthetic techniques. One of the most interesting nanostructures of ZnO for photovoltaic applications is the nanowire, which is the main focus of this thesis. Ordered arrays of nanowires can be grown on a variety of different substrates using techniques including chemical vapour deposition (CVD), atomic layer deposition (ALD), hydrothermal growth and sol-gel chemistry to name but a few.[190-193] However, growth of nanowires using these techniques typically encounters one of two potential problems:

1. Growth proceeds at high temperatures, limiting the choice of substrate and often requiring costly experimental setups.

2. Growth occurs at a very low rate, thereby requiring reaction times on the scale of hours or even days to gain sufficient nanowire lengths.

The majority of vapour based techniques fit into the first of these categories. Whilst the use of CVD in producing ZnO nanowires for DSCs has been reported, the range of compatible substrates is limited to materials such as FTO-coated glass due to the high temperatures.[194] The experimental setups used in these techniques are also likely to prove to be prohibitively expensive for large-scale manufacturing of photovoltaics, such as DSCs and perovskite solar cells. The second problem relates to the most commonly used techniques for production of ZnO nanowires for photovoltaics, which include hydrothermal growth and chemical bath deposition. Hydrothermal growth typically involves first seeding a substrate with small ZnO nanocrystals, followed by growth of nanostructures from these nucleation sites. Although this procedure can be undertaken at relatively low temperatures (~90 °C), the growth often proceeds very slowly, requiring extremely long reaction times that would make large-scale production in roll-to-roll lines impossible.[195] An example of this is the seminal report of ZnO nanowires within DSCs by Law *et al.*, who used a growth time of up to 50 h to achieve their longest nanowire lengths, and even then found that the lengths were not great enough to achieve sufficient surface area.[68]

One class of techniques that can be used to avoid these two issues is electrochemical growth, which typically occurs at temperatures below 100 °C, and can proceed at a high rate to give aligned nanowire films. Electrodeposition is the primary example of this class of techniques and has been used extensively for the growth of ZnO nanowires; reviews of which can be found in the literature.[196, 197] Over the past few years however, another electrochemical technique has emerged for the production of ZnO nanostructures, based on electrochemical anodization of metallic zinc.

2.4.1 A short background to anodization

Anodization is an electrochemical process used to form an oxide layer on the surface of a metal under an applied voltage. It is a well-established technique and has been used for nearly a century to improve the properties of metal surfaces. Its main applications have been in improving the corrosion and wear resistance of metals, but it has also been used extensively in altering the aesthetic properties of metals. Another application of anodization has been in the production of dielectric materials for electrolytic capacitors.[198]

The name of the technique stems from the fact that the metal to be treated is employed as the anode in the electrochemical cell. During the process, a direct current (DC) is applied through the cell, driving reactions at both electrodes. In a closed circuit, electrons are withdrawn from the anode and drawn towards the positive terminal. This allows the positively charged ions on the anode surface to react with water in the electrolyte to form an oxide layer, which is typically porous in structure. After passing through the circuit, electrons emerge at the cathode where they combine with hydrogen ions to form hydrogen gas, which can be observed as bubbles on the cathode surface.

The electrolytes used are commonly acidic, with sulphuric acid, oxalic acid and phosphoric acid being some of the most extensively used.[199] The use of acidic electrolytes prevents the formation of a barrier oxide layer and allows the electrochemical reaction to continue via transport of the electrolyte through the porous oxide. The typical process of anodization is, therefore, a balance between three processes occurring at the anode: Field assisted oxide growth, field assisted dissolution of the metal oxide, and chemical dissolution of the metal oxide (Figure 2.20).

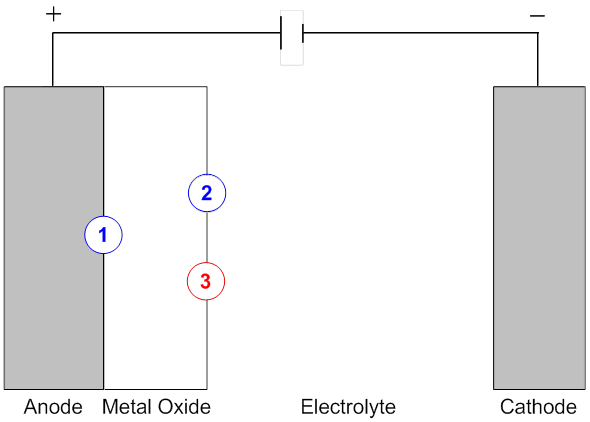

Figure 2.20. The three different processes controlling anodization: Field assisted oxide growth (1), field assisted dissolution of metal oxide (2) and chemical dissolution of metal oxide (3).

Aluminium is by far the most commonly anodized material and there are now many well established methods for gaining films with various different properties.[199] In addition to being widely used for industrial applications, anodic alumina (Al_2O_3) has attracted a large amount of interest from the field of nanoscience, due to the ordered mesoporous films that can be produced. Films with carefully controlled pore diameters and lengths can be produced over relatively large substrates and many detailed studies have investigated the mechanisms behind such phenomena.[199-201]

In addition to being applied by themselves, they have also been used as templates for the production of other types of nanostructures such as nanowires and nanotubes.[202, 203] The success of porous alumina films in nanotechnology has resulted in many other nanostructured metal oxides being produced by anodization. Other metals, such as titanium, zirconium, niobium and hafnium have all been successfully anodized, forming either organised nanoporous or nanotubular morphologies.[15-18] Of these materials, TiO_2 formed by anodization has proven to be particularly interesting in DSC applications, where the TiO_2 nanotube films have been applied in back-illuminated cell configurations, achieving device efficiencies of up to 7 %.[104, 106, 204-206] More recently, similar approaches have been used to apply TiO_2 nanotube arrays within perovskite solar cells, achieving power conversion efficiencies of 6.52 %.[207]

2.4.2 ZnO nanostructures from anodization

The anodization of zinc has received relatively little attention compared to other metals, such as aluminium and titanium. One reason for this is probably the instability of zinc and its oxide form in the acidic electrolytes commonly used when anodizing other metals. It has only been during the past decade that the anodization of zinc has received attention, due to the wide range of easily accessible nanostructures that can be produced, and the many interesting characteristics of ZnO.

The recent interest in the anodization of zinc has seen over twenty new reports on the production of nanostructured ZnO using this technique. Nanostructures including nanostripes,[208] nanowires,[209] nanodots,[210] and nanoflowers[211] have all been produced using electrolytes ranging from basic NaOH solutions to highly protic HF solutions. The majority of investigations have included the study of a range of reaction conditions to identify the changes in surface morphology that result. Within our group, we have recently published a paper combining our own findings with those of previous reports to suggest rational design approaches towards creating different types of ZnO nanostructures from anodization.[212] This study found that the shape of the nanostructures is determined mainly by the type of electrolyte used, whilst the nanostructure surface density typically increases with concentration, voltage and time.

What is, perhaps, most interesting about the anodization of zinc is the ability to use much milder anodization conditions than those required for other metals and still obtain high growth rates of nanostructures. This is particularly true for the choice of electrolyte, where solutions that are only very mildly acidic or basic have been used. One study has even reported the anodization of zinc using water as the electrolyte, although it should be noted that these electrolytes were reported as being mildly acidic, which was attributed to the uptake of atmospheric CO_2.[213] The use of mild conditions makes anodization a very attractive method for the production of nanostructured ZnO films, especially considering the well-established knowledge base of implementing anodization on an industrial scale for other metals.

In some reports, the effects of the anodization conditions on physical properties of the ZnO films have been examined. An example of this is a study by Basu *et al*. who reported a shift in the optical band gap for anodic ZnO films produced under different concentrations of an oxalic acid electrolyte.[214] There was an increase in band gap with decreasing concentrations of oxalic acid, where a bandgap of up to 4.20 eV was obtained by using a 0.05 M oxalic acid electrolyte. In a previous study, they were also able to show that the presence of UV light during the anodization of Zn increases the growth rate as well as the etching rate of ZnO.[215]

ZnO nanomaterials produced by anodization have also been applied in various areas including photocatalysis,[216, 217] photovoltaics,[218] photodetectors [219, 220] and as Schottky diodes.[221] The photocatalytic properties of anodic ZnO films formed of two-dimensional (2-D) plate-like structures were examined in two separate reports. These materials were found to be active in the photodegradation of dyes, such as methylene blue and methyl orange.[216, 217] He *et al*. demonstrated an effective Schottky diode with good rectifying behaviour using a porous film of ZnO grown on a Zn foil by anodization.[221] The success of this device relied upon the improved contact between ZnO and the Zn foil, achieved through a two-step anodization process. An interesting report has also been published recently in which brass foils are anodized to give rise to oxide nanomaterials of both Zn and Cu.[222] This combination of oxides could prove useful in areas such as photovoltaics due to CuO absorbing light within the visible region of the spectrum.

1-D and 2-D ZnO nanostructures

As discussed previously, ordered nanostructures, particularly 1-D or 2-D nanostructures are attractive candidates for DSCs and perovskite solar cells. Two studies have investigated the synthesis of 2-D nanostripe arrays by the anodization of zinc in ethanolic H_2SO_4.[208, 223] It was found that although anodization in aqueous H_2SO_4 leads to largely chemical etching of the metal, anodization in ethanolic solutions leads to the formation of ZnO nanostructures under certain reaction conditions. These nanostructures were the focus of a previous investigation within our group, where it was found that control over nanostructure formation could be achieved by tuning

the anodization conditions. Despite this, it was not possible to obtain nanostructures of significant surface area and it was chosen not to investigate them further for application in DSCs.

Reports of 1-D nanostructures have also been made throughout recent years. Galstyan *et al.* reported the formation of chain-like ZnO nanostructures using a combination of anodization followed by thermal decomposition.[224] They anodized thin layers of zinc, which had been deposited onto alumina, silicon, glass and flexible polymeric substrates, in ethanolic solutions of 0.5 and 2.0 mol dm^{-3} oxalic acid dihydrate. This formed zinc oxalate nanostructures, which were then thermally decomposed to give chain-like ZnO nanostructures, consisting of chains of nanoparticles. Shrestha *et al*. reported the formation of 1-D ZnO nanotube arrays via the anodization of zinc in an aqueous sulphide based electrolyte.[225] These structures are similar to those found for other metals, such as titanium, and had not been obtainable previously for ZnO due to it not forming compact oxide layers, which are required to sustain pore growth. In this case, a compact ZnS layer was reported, which allowed growth of the ZnO nanotubes beneath it. Single-crystalline Zn microtips were demonstrated by Kuan *et al*. by anodizing Zn foil in an NH_4Cl/H_2O_2 solution.[226] These structures could then be annealed to give rise to a thin ZnO layer on the surface of the microtips. Arrays of 1-D nanoneedles of up to 700 nm in length have also been demonstrated via the controlled anodization of Zn foil in NaOH or saturated zincate solutions.[227, 228] The formation of ZnO was proposed to occur via the following electrochemical reactions:

Cathode:

$$2H^+ + 2e^- \rightarrow H_{2(g)} \quad (2.2)$$

Anode:

$$Zn_{(s)} - 2e^- \rightarrow Zn^{2+} \quad (2.3)$$

$$Zn^{2+} + 2OH^- \rightarrow Zn(OH)_{2(s)} \quad (2.4)$$

$$Zn(OH)_{2(s)} + 2OH^- \rightarrow Zn(OH)_4{}^{2-}{}_{(aq)} \quad (2.5)$$

$$Zn(OH)_4{}^{2-}{}_{(aq)} \rightarrow ZnO_{(s)} + 2H_2O + 2OH^- \quad (2.6)$$

Despite the obvious interest of the unique structures formed in these studies, film thicknesses remain quite small and low surface areas would be expected, leading to poor dye loadings in DSCs. One method that has shown promise in the production of high surface area ZnO nanostructures is the anodization of zinc in an aqueous potassium bicarbonate ($KHCO_{3(aq)}$) electrolyte. Using this method, Hu *et al.* described the synthesis of 1-D ZnO nanowires with

aspect ratios exceeding 1000.[209] They investigated the effects of voltage, time and temperature on the morphology of the nanowires and also examined the UV-visible reflectance spectra of the films to show that they can provide efficient light scattering across the visible spectrum. Their investigation showed that the nanowires consisted of polycrystalline ZnO after an annealing treatment, but could not identify the composition of the as-prepared nanostructures. It was suggested that they could consist of some form of zinc hydroxy carbonate, which decomposes upon heating to form the high surface area polycrystalline nanowires of ZnO. Despite the likely presence of carbonate within the nanowire films, growth was still proposed to occur via reactions 2.2 - 2.4 to form $Zn(OH)_2$ which was then decomposed by heating to ZnO.

This report was followed up by Park *et al*. who examined the anodization of Zn foil and sputtered Zn films under galvanostatic or potentiostatic conditions using the $KHCO_3$ electrolyte.[229] Due to the thinness of the sputtered Zn films, the study focussed on the early stages of growth and the differences between potentiostatic and galvanostatic conditions were compared. Galvanostatic growth resulted in significantly more initial growth sites than potentiostatic growth. Nucleation sites continued to appear throughout potenstiostatic growth, resulting in similar numbers of nanowires, with near equal lengths to galvanostatically grown films, by the end of the anodization process. They found that potentiostatic growth on the sputtered films resulted in formation of spherical particle-like structures, as well as nanowires, and that the film started to become detached from the substrate at around 120 s. Conversely, in the case of galvanostatic growth, ordered nanowire arrays of up to 8 μm in length could be grown. This suggests that galvanostatic growth conditions might be more favourable for sputtered Zn films, as more even growth occurs at lower growth times.

Anodized ZnO nanowires grown with $KHCO_3$ electrolytes have also been applied as photodetectors in two separate studies, in which they have shown very high responsivity to light (10 times higher than other reports using ZnO nanorods).[219, 220] These nanostructures also possess many attractive features for application in DSCs, including high aspect ratio, high surface area relative to monocrystalline nanowires, rapid growth, mild synthesis conditions with very low toxicity chemicals, and a flexible conducting substrate. These attractive features have not been unnoticed and have recently been applied in DSCs by Kim *et al*.[218] They used a two-step synthesis comprised of anodization followed by electrodeposition to produce hierarchical structures of large nanowires coated in smaller nanowires. They then removed the nanostructures from the metallic substrate and applied them as a paste in a Grätzel type DSC. Using this technique they were able to gain power conversion efficiencies of 1.63%.

It has, therefore, been shown that ZnO nanostructures produced via the anodization of zinc in a bicarbonate electrolyte can be used within DSCs. However, the efficiencies gained are

still relatively low and not currently competitive with ZnO structures produced using other techniques. The many beneficial characteristics of these nanostructures suggest that higher power conversion efficiencies might be gained and shows that it warrants further investigation. Improvements could be achieved by gaining a greater understanding of the processes controlling nanostructure growth and through optimisation of the nanostructures specifically for DSC application. This, therefore, forms a significant area of focus within this thesis. The optimisation of nanowire growth using anodization is covered in Chapter 4 and has recently been used to form a publication on this area.[230]

2.5 Implications of the Literature

The literature reviewed within this chapter has shown that semiconductor nanowires can act as effective charge transport materials in both dye-sensitized and perovskite solar cells, however, limitations are observed in both cases. In the case of DSCs the limiting factor is the low surface area of nanowire arrays grown using conventional techniques such as chemical bath deposition, which results in a low loading of dye on the semiconductor surface. New synthesis techniques that can give rise to high aspect ratio and high surface area nanowires are, therefore, required in order to determine the full benefits of the use of semiconductor nanowires within DSCs.

Electrochemical anodization of Zn within a bicarbonate electrolyte appears to be a promising technique for achieving the synthesis of high aspect ratio ZnO nanowires required for application in DSCs.[209] The application of these materials in DSCs therefore warrants further examination. In particular, the investigation of a variety of different cell architectures is required so that the full potential benefit of these materials can be determined. The research presented within Chapter 6 aims to answer some of these questions by applying anodic nanowires within a range of different DSC architectures.

In addition to the application of these materials, there still remain many unanswered questions about the chemistry underpinning the growth of ZnO nanowires during anodization and the factors that affect it. No satisfactory mechanisms have been proposed to explain the growth of nanowires in a bicarbonate electrolyte and no quantitative trends have been established to describe the processes that control it. The aim of the research presented in Chapter 4 is to shed light on these currently unanswered questions, so that better control can be gained over the materials produced using this technique.

Over the past five years perovskite solar cells have made a huge impact on the photovoltaic research community. Efficiencies of these devices have increased dramatically as a wide range of different cell architectures have been explored. As in the case of DSCs, the use of ZnO as an electron transport material appears to be less successful than the use of TiO_2, although it is only within recent reports that reasons for this are being suggested. It now appears that perovskite solar cells featuring ZnO contact materials face a fundamental limitation due to the thermal degradation of the perovskite by the relatively basic ZnO.[146] This material incompatibility warrants further research so that the extent of this limitation can be assessed. In particular, reports directly comparing equivalent cell architectures featuring either ZnO or TiO_2 are lacking. To date, the examination of this effect within different porous ZnO scaffolds has also not been reported. This will be explored further within Chapter 7, where perovskite solar cells are prepared using a range of different ZnO morphologies and compared to TiO_2.

Chapter 3 – Materials and Methods

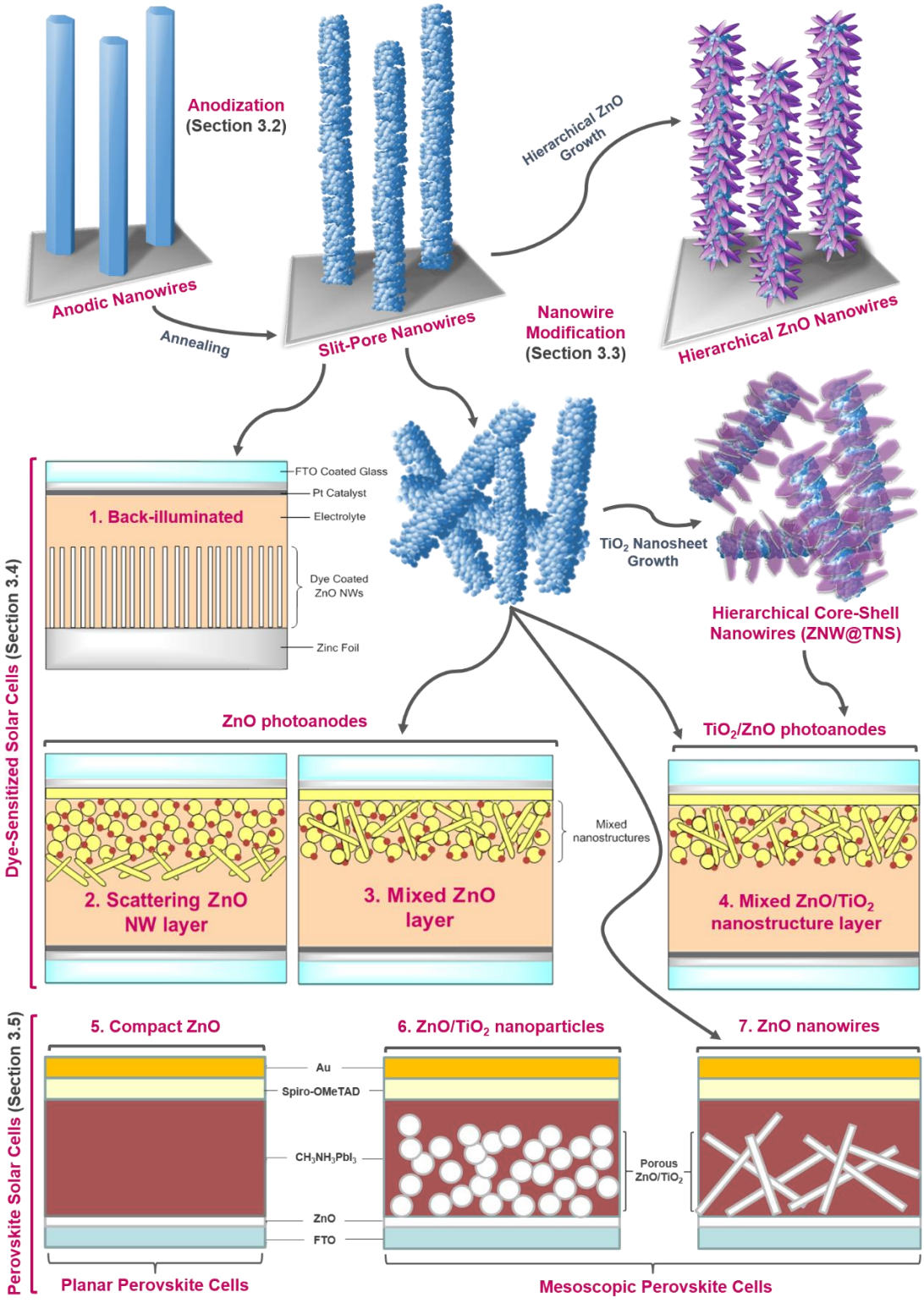

Figure 3.1. Schematic demonstrating the range of nanomaterials and photovoltaic devices produced and the respective sections of Chapter 3 in which the details of production are discussed.

In this Chapter, the experimental details of the fabrication of all of the nanomaterials and photovoltaic devices discussed throughout the thesis (Figure 3.1) are documented. The chapter is split into 6 sections, with Sections 3.2 to 3.5 covering the experimental details associated with the results reported within Chapters 4 to 7 respectively. After fully detailing the materials used (Section 3.1), the experimental methods associated with anodization are discussed (Section 3.2). Section 3.3 then goes on to describe the methods of post-anodization nanowire modification, which was used to obtain hierarchical structures. The steps involved in the production of DSCs is then described in Section 3.4, where the anodic nanowires are applied in four different DSC cell designs (Figure 3.1). Similarly, the experimental details of producing the different perovskite solar cell architectures (Figure 3.1) is discussed in Section 3.5. Finally, Section 3.6 will provide details of the characterisation techniques used throughout Chapters 4 to 7.

3.1 Materials

Ethanol (96 %), ethanol (absolute, >99.8 %), 2-propanol (anhydrous, 99.5 %), 2-propanol (ACS reagent, >99.5 %), sodium bicarbonate (ACS reagent, 99.7-100.3 %), potassium bicarbonate (ACS reagent, 99.7 %), ammonium bicarbonate (ReagentPlus®, ≥99.0 %), acetone (≥99.5 %), fluorine doped tin oxide (FTO) coated glass (2 mm thickness, ~7 Ω sq^{-1}, TEC 7) and (2.3 mm thickness, ~13 Ω sq^{-1}, TEC 15), chloroplatinic acid hexahydrate (ACS reagent, >37.50 % Pt basis), iodine (anhydrous beads, -10 mesh, 99.999 % trace metals basis), lithium iodide (crystalline powder, 99.9 % trace metals basis), guanidine thiocyanate (for molecular biology, >99 %), 4-*tert*-butylpyridine (4-*t*bp, 96 %), acetonitrile (ACS reagent, >99.5 %), valeronitrile (99.5 %), acetic acid (ACS reagent, >99.7 %), terpineol (anhydrous, mixture of isomers), ethyl cellulose (viscosity 10 cP, 5 % in toluene/ethanol 80:20 (lit.), extent of labeling: 48 % ethoxyl), titanium diisopropoxide bis(acetylacetonate) (75 wt% in 2-propanol), poly(vinyl chloride) (PVC, M_w ~ 97,000 g mol^{-1}, M_n ~ 55,000 g mol^{-1}), n-methyl-2-pyrrolidinone (NMP, anhydrous, 99.5 %), poly(oxyethylene methacrylate) (POEM, poly(ethylene glycol) methyl ether methacrylate, M_n 475 g mol^{-1}), CuCl (99 %), 1,1,4,7,10,10-hexamethyltriethylene tetramine (HMTETA, 99 %), methanol (anhydrous, 99.8 %), titanium(IV) isopropoxide (TTIP, >97 %), HCl (ACS reagent, 37 %), $TiCl_4$ (puriss., >99.0 %), toluene (anhydrous, 99.8 %), benzyl alcohol (anhydrous, 99.8 %), poly(ethylene glycol) (M_n 10,000), zinc (purum, powder), zinc acetate dihydrate (ACS reagent, >98 %), KOH (ACS reagent, >85 %, pellets), n-butanol (ACS reagent, >99.4 %), chloroform (ACS reagent, ≥99.8 %, contains 0.5-1.0 % ethanol as stabilizer), ethanolamine (ACS reagent, >99.0 %), zinc nitrate hexahydrate (reagent grade, 98 %), PbI_2 (99 %), *N*,*N*-dimethylformamide (DMF, anhydrous, 99.8 %), dimethyl sulfoxide (DMSO, anhydrous, >99.9 %), bis(trifluoromethane)sulfonimide lithium salt (LiTFSI), chlorobenzene (anhydrous, 99.8 %), $PbCl_2$ (powder, 98 %), $ZnCl_2$ (ACS reagent, >97 %), ZnO nanowires (diam. × L 90 nm × 1 μm) and gold (evaporation slug, diam. × L 0.3 cm × 0.6 cm, 99.99 % trace metals basis) were purchased from Sigma-Aldrich.

$N^2,N^2,N^{2'},N^{2'},N^7,N^7,N^{7'},N^{7'}$-octakis(4-methoxyphenyl)-9,9′-spirobi[9H-fluorene]-2,2′,7,7′-tetramine (Spiro-OMeTAD, 99 %, sublimed grade) (see Chapter 2, Figure 2.11 for the chemical structure) was purchased from Borun Chemical Co. Ltd.. Tetrahydrofuran (THF, butylated hydroxytoluene (BHT) stabilised, HPLC grade) was purchased from Duksan Reagents. Perchloric acid (60-62 %) and zinc foil (0.25 mm thickness, 99.98 %) were purchased from Alfa Aesar. 60 μm and 25 μm thick Surlyn® thermoplastics under the product names of Meltonix 1170-60 and 1170-25, and 1-methyl-3-propylimidazolium iodide (IonLic PMII) were purchased from Solaronix. ZnO nanoparticles (18 nm, 99.95 %) were purchased from US Research Nanomaterials Inc. Deionised water was obtained from a Millipore system at a resistance of >18.2 MΩ cm. *cis*-Diisothiocyanato-bis(2,2'-bipyridyl-4,4'-dicarboxylato) ruthenium(II)

bis(tetrabutylamm-onium) (N719 dye) (see Chapter 2, Figure 2.8 for the chemical structure), methylammonium iodide and 18NR-T transparent titania paste were purchased from Dyesol Ltd..

3.2 Anodization

3.2.1 Electrode preparation

0.25 mm thick zinc foils were cut into strips with approximately 16 mm width and lengths of 50 mm (three films) or 18 mm (single film). The zinc foils were annealed in air at 300 °C for 1 hour in a chamber furnace (Carbolite, CWF 1100). The foils were then degreased with acetone in an ultrasonic bath for 10 minutes and air dried. Prior to anodization, the degreased zinc foils were electropolished in an electrolyte consisting of a 1:4 volumetric ratio of perchloric acid and ethanol at -70 °C. A DC power supply (Agilent, E3620A) was used to provide a constant voltage of 10 V to the electrochemical cell, in which the zinc foil acted as the anode and the stainless steel beaker containing the electrolyte was employed as the cathode. Custom made Teflon® sample holders were used to expose a fixed circular area of the zinc foil to the electrolyte (13 mm diameter). Electropolishing was undertaken for 15 minutes with strong stirring to give the zinc foil a near mirrored appearance. During this time the typical current decreased from ~0.2 A down to ~0.1 A. After removal from the electrolyte, the zinc foil was again washed with ethanol and deionised water to remove any remaining electrolyte from its surface.

3.2.2 Anodization in $KHCO_{3(aq)}$

The electropolished zinc foil (single foil, 16 x 18 mm) was applied as the anode in a two-electrode cell, with a stainless steel plate acting as the cathode which was held parallel to the anode with a separation of 10 mm. The active area of the zinc anode was controlled using a specially designed Teflon® sample holder, which exposed a circular area (10 mm diameter) on one face of the zinc foil (Figure 3.2). The anodization was conducted in an aqueous electrolyte of $KHCO_3$ (50, 15 or 5 x 10^{-3} mol dm^{-3}) with constant stirring. The temperature of the electrolyte was kept constant throughout the anodization (20, 10 or 5 °C) using a refrigerated circulating bath (Thermo Scientific Haake, C10-K10) (Figure 3.3). Anodizations were undertaken for 30, 15 or 5 minutes at a constant voltage of 10 V, 5 V or 1 V provided by a DC power supply (Agilent, E3634A) interfaced to a computer. After anodization, the anodized zinc foils were washed thoroughly with deionised water to remove any excess electrolyte from the surface. The foils were then dried under a flow of argon gas and stored within a desiccator.

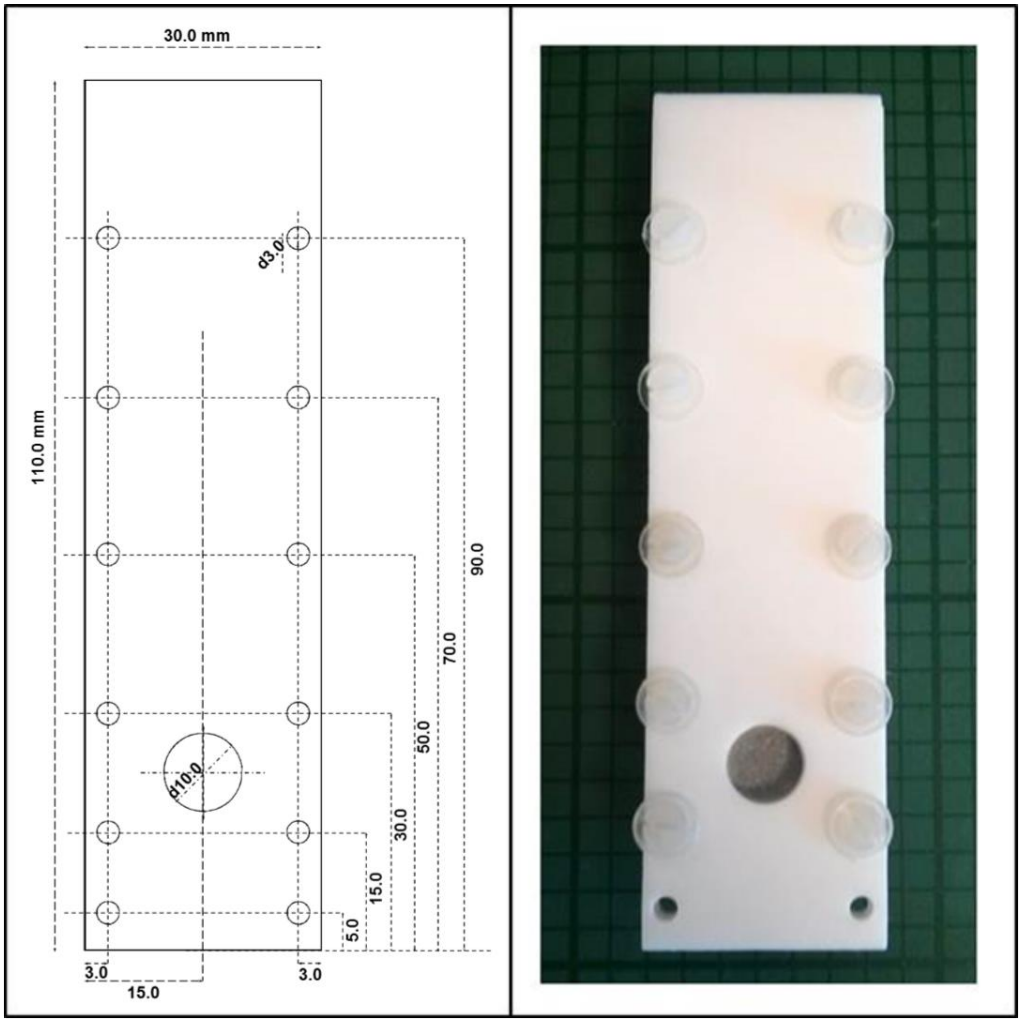

Figure 3.2. Dimensions and picture of the one-hole anode holder used for anodization.

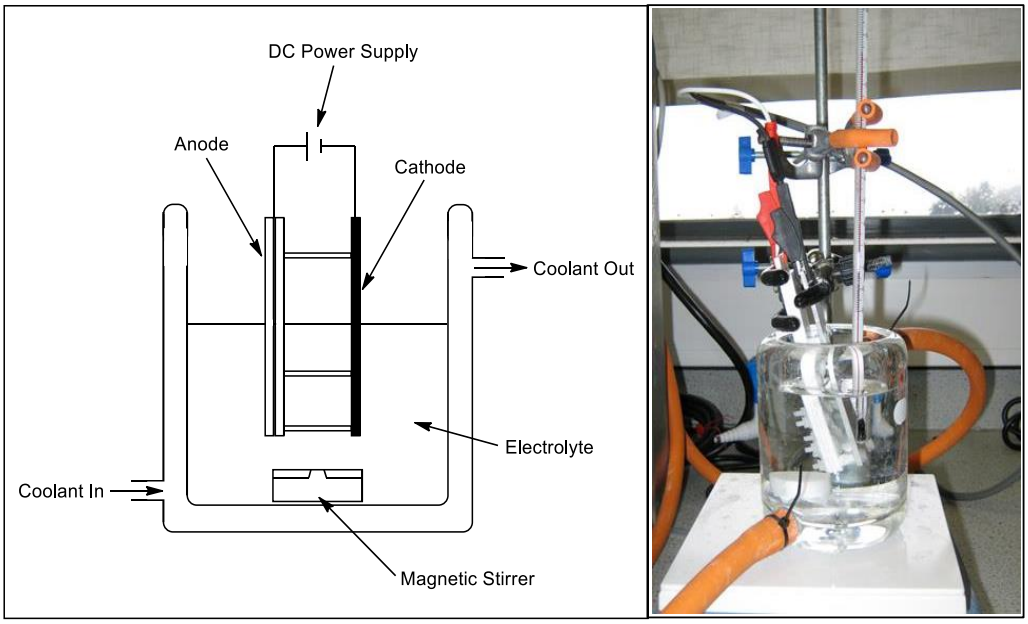

Figure 3.3. Experimental setup for the anodization of electropolished zinc foils.

3.2.3 Anodization in $NaHCO_{3(aq)}$ or $NH_3HCO_{3(aq)}$

The electropolished zinc foil (three film, 16 x 50 mm) was applied as the anode in a two-electrode cell, with a stainless steel plate held parallel to the anode at a distance of 10 mm acting as the cathode. The active area of the zinc anode was controlled using a specially designed Teflon® sample holder which exposed three circular areas (each 12 mm diameter) on one face of the zinc foil (Figure 3.4). The anodization was conducted in an aqueous electrolyte of either $NaHCO_3$ or NH_4HCO_3 (0.2, 0.1 or 0.05 mol dm^{-3}) with constant stirring that was kept consistent throughout all experiments. The temperature of the electrolyte was kept constant throughout the anodization (20, 10 or 5 °C) using a refrigerated circulating bath (Thermo Scientific Haake, C10-K10). Anodizations were undertaken for 120, 60, 30, 15, 5 or 1 min at a constant voltage of 10, 5, 2 or 1 V provided by a DC power supply (Agilent, E3634A) interfaced to a computer. After anodization, the anodized zinc foils were washed thoroughly with deionised water to remove any excess electrolyte from the surface. The foils were then dried under a flow of argon gas and stored within a desiccator.

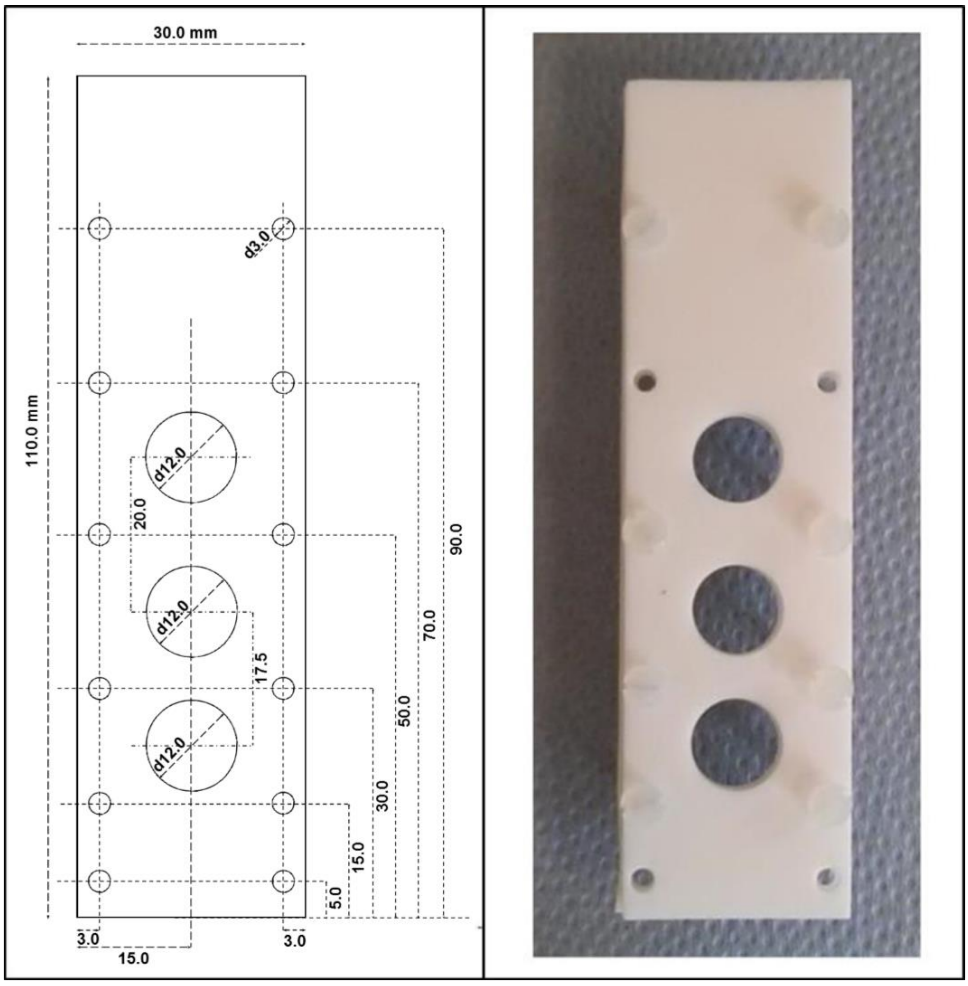

Figure 3.4. Dimensions (left) and picture (right) of the front plate of the Teflon® sample holder used to expose three circular areas (12 mm diameter) of the zinc foil.

3.2.4 Anodization of larger substrates

In order to anodize larger zinc substrates and to produce anodized films in a variety of shapes the use of adhesive masks was implemented instead of the Teflon® sample holders. Kapton® polyimide tape was used as the adhesive mask due to its high chemical stability. The polyimide tape was cut to size and applied to clean zinc foil substrates to expose a rectangular area of 18 x 75 mm (13.5 cm^2) on the front side of the foil (Figure 3.5).

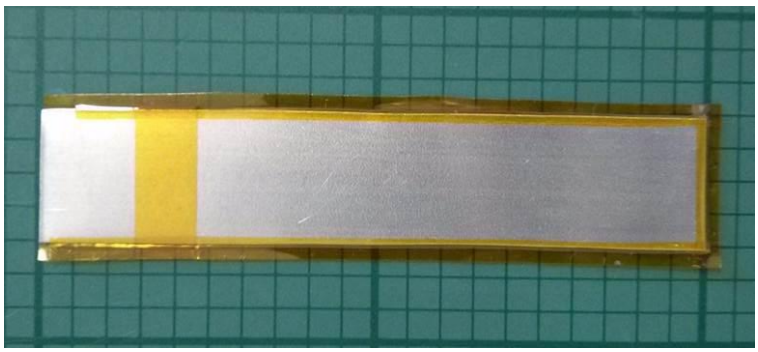

Figure 3.5. Picture of a zinc foil in a rectangular Kapton® mask for anodization of large substrates.

The masked foil was attached to the stainless steel cathode at a fixed distance of 10 mm using nylon screws and nuts as a spacer between the two electrodes. The foils were applied within the anodization setup previously discussed and anodized under optimised conditions of 5 V, 20 °C and 50 mM $NaHCO_{3(aq)}$ electrolyte for 15 minutes. Using the polyimide mask it was possible to anodize the exposed area whilst keeping the masked area unaffected. The tape could be easily removed after anodization without leaving behind any adhesive on the substrate. The morphology of the nanowire films was found to be unchanged compared to those produced under the same conditions using the Teflon® electrode holder, indicating that no significant dissolution of adhesive is occurring which could interfere with nanowire formation. In addition to the formation of rectangular nanowire films, it was also possible to produce more intricate shapes using the masking technique (Figure 3.6). This could be a useful and simple way to control the shape of nanowire films for a variety of applications.

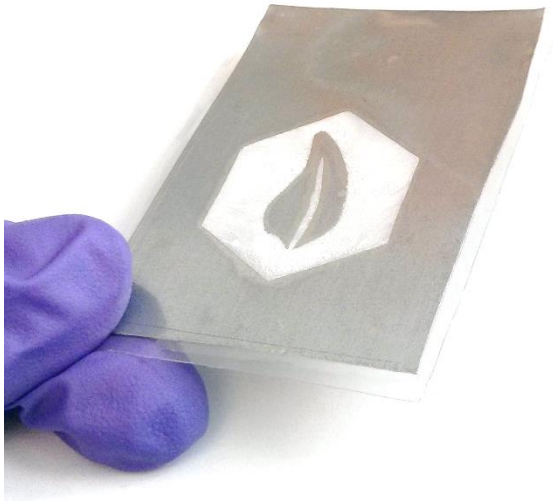

Figure 3.6. Picture demonstrating the potential to anodize intricate shapes into the zinc foil using a Kapton® mask.

3.3 Modification of Nanowires

3.3.1 Nanowire film annealing

In order to convert the films produced directly from anodization into ZnO it was necessary to anneal the films in air. Typically, annealing of films was undertaken at 300 °C in air for 1 h with a controlled ramping rate of 1 °C min^{-1} within a furnace (Carbolite, CWF 1100). These conditions were applied for producing all the nanowires used in solar cells as described in Sections 3.4 and 3.5.

To investigate the effect of annealing on the final nanowire structure, a number of identical nanowire films were produced and heated to different temperatures (200 to 350 °C) for different lengths of time (1 to 24 h). In all cases the nanowire films were produced at anodization conditions of 5 V, 20 °C, 15 min and 50 mM $NaHCO_{3(aq)}$ electrolyte concentration. The rate at which the temperature ramped from room temperature to the programmed maximum was kept constant at 1 °C min^{-1} for all annealing conditions examined.

A NIR annealing system (Adphos Coil Lab LV2, tungsten filament halogen lamps) was also tested to rapidly anneal the nanowire films (Figure 3.7). The NIR system had an output spectrum in the region of 250–2500 nm, peaking between 800 and 1200 nm, and with a maximum power density of 250 kW m^{-2}. Throughout all experiments the lamp to substrate separation was maintained at 10 cm and the sample was passed under the lamp at a rate of 2 m min^{-1} on a conveyor system. Samples were annealed at different lamp powers of 25 %, 35 % and 45 %.

Figure 3.7. Pictures of the NIR rapid annealing system before (left) and during use (right).

3.3.2 Secondary growth on nanowires

Double anodization

Nanowire films were first produced via anodization of a zinc foil under conditions of 5 V, 20 °C, 15 min and 50 mM $NaHCO_{3(aq)}$ electrolyte concentration. The nanowire films were then washed and dried before being annealed at 300 °C for 1 h. After cooling, the ZnO nanowire films were then anodized again under the same conditions, giving rise to a powdery black film which was easily removed from the substrate. The film was washed and dried before annealing again at 300 °C for 1 h.

$Zn(NH_3)_4^{2+}$ treatment

This procedure was based on a method reported by Mukherjee *et al.*[231] A 20 mM $Zn(NH_3)_4^{2+}$ solution was prepared by first dissolving a stoichiometric amount of $ZnCl_2$ in deionised water followed by the drop wise addition of a 10 vol.% solution of ammonia until a pH of 9.5 was achieved. The solution was then made up to 100 mL using deionised water. The annealed ZnO nanowire films were dipped into the solution for 1 min followed by washing in deionised water for 1 minute. This procedure was repeated a further two times. The films were then dried and annealed again at 300 °C for 1 h.

H_2O treatment

Annealed ZnO nanowire films were placed within sealed glass vials containing 20 mL of deionised water. After being stored for 24 h in darkness the films were removed from the vials, washed with deionised water and dried. The films were then annealed again at 300 °C for 1 h.

TiO_2 nanosheet growth

The growth of TiO_2 nanosheets on the anodic ZnO nanowires was attempted in order to form analogous structures to the TiO_2 nanosheet on SnO_2 nanotube (SNT@TNS) structures previously published.[232] These experiments were conducted as part of a collaboration with Yonsei University and were therefore carried out partly by myself and partly by Chang Soo Lee, a PhD student within Yonsei University.

First, ZnO nanowire powder was obtained by scraping away the annealed nanowire films from a large number of zinc substrates (Figure 3.8) using a plastic spatula. For each of the nanosheet growth conditions tested, 50 mg of the nanowire powder was sonicated in 40 mL of 2-propanol for 15 min to fully disperse the nanowires. As it was not certain that the growth conditions used for the SNT@TNS structures would be successful, a number of different syntheses were performed, each using different concentrations of diethylenetriamine (DETA) and titanium(IV) isopropoxide (TTIP) as reactants. In all cases the reactants were added to the

dispersed ZnO nanowires and heated to 200 °C for 24 h within a Teflon® lined autoclave for the reaction to proceed. Details of the reactant quantities used for each experiment are given in Table 3.1.

Figure 3.8. A picture of the anodic nanowire films used for ZnO nanowire powder production.

Table 3.1. Reactant quantities used for each titania nanosheet growth attempt.

Sample	DETA (mL)	TTIP (mL)
1	0.03	0.50
2	0.03	1.00
3	0.03	1.50
4	0.30	0.30
5	0.15	0.30
6	0.30	0.15
7	0.15	0.15

After reaction, a white/yellow precipitate could be observed at the bottom of the solutions and the solvent could be easily removed by pipetting. 5 mL of 2-propanol (IPA) was added to the remaining precipitate and sonicated for 30 mins. The dispersions were then pipetted into clean glass vials and the solvent was allowed to evaporate in a fume hood to obtain a dry solid product. All of the dry solids were then annealed at 450 °C for 30 minutes.

3.4 Dye-Sensitized Solar Cell Fabrication

3.4.1 Back-illuminated dye-sensitized solar cells

In order to produce back-illuminated dye-sensitized solar cells the anodic nanowire films on the zinc foil were employed as the working electrode and flexible conductive substrate, respectively, within the cell architecture demonstrated in Figure 3.9. Nanowire films produced under anodization conditions of 5 V, 20 °C, 50 mM $NaHCO_{3(aq)}$ for 15 minutes, which corresponded to nanowire films of approximately 50 µm in thickness, were used throughout. The nanowire films were dyed for different periods of time between 1 and 4 hours within an ethanolic 0.3 mM N719 dye solution.

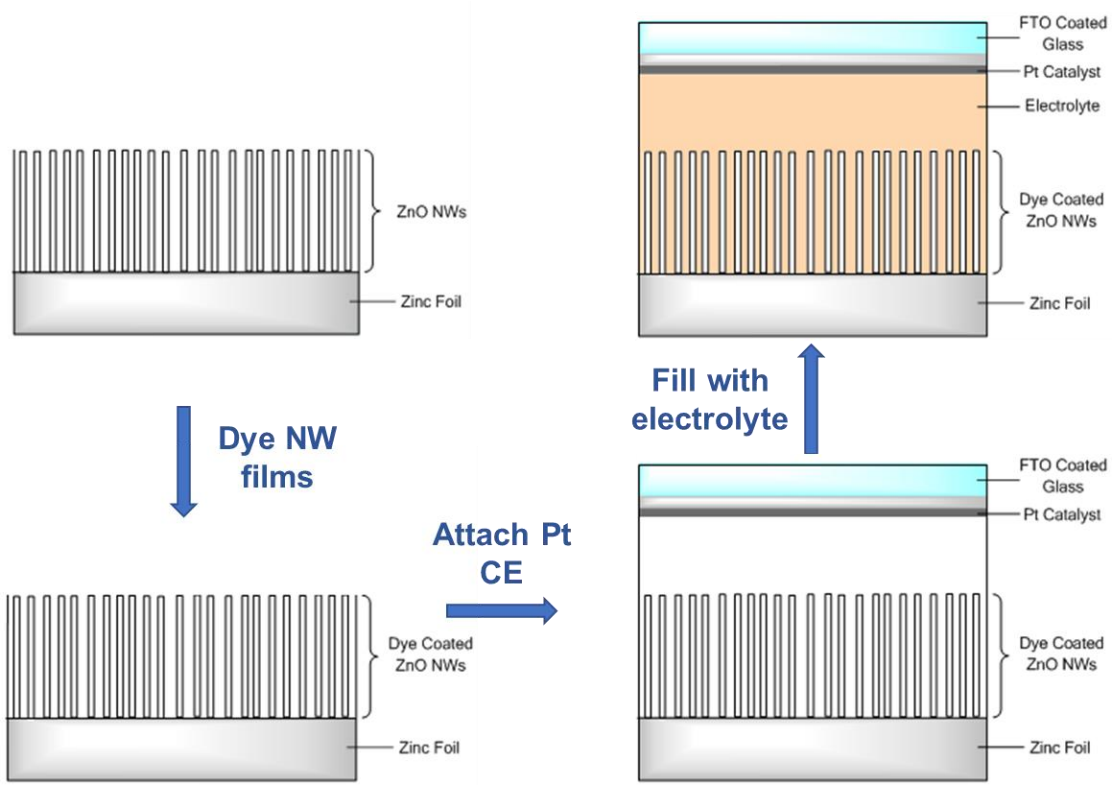

Figure 3.9. Scheme depicting the key stages of back-illuminated DSC production.

To prepare the platinum coated counter electrodes, FTO coated glass (~7 Ω sq^{-1}, TEC 7) was first cut to give substrate sizes of 15 mm x 20 mm. Two small holes with a diameter of ~0.5 mm were then drilled into the glass substrates using a drill with a carbide bur tip (Jota, C1). The substrates were then cleaned by first sonicating in a 10 vol.% solution of Decon90® in deionised water. They were then thoroughly rinsed with deionised water. This sonication and rinsing process was repeated in deionised water, acetone and finally 2-propanol before drying under a flow of nitrogen. Once the substrates were thoroughly cleaned, two drops of a 10 mM solution of chloroplatinic acid hexahydrate in 2-propanol were spin coated onto the substrate at

2000 rpm for 30 s. The substrates coated in the platinum precursor were then annealed at 500 °C for 30 minutes, with a ramping rate of 4 °C min^{-1}, to form a near transparent layer of platinum nanoparticles on the FTO surface.

The counter electrode was sealed to the dye coated working electrode using a 60 µm thick Surlyn® film with an 11 mm diameter hole positioned over the working electrode active area. As the Surlyn® spacer is a heat seal plastic, the sandwiched electrodes were heated on a hotplate to ~100 °C and the electrodes were gently pressed together.

An electrolyte composed of 0.6 M PMII, 0.03 M I_2, 0.5 M 4-*t*bp, 0.1 M guanidine thiocyanate and 0.05 M LiI in a solvent of valeronitrile and acetonitrile in a 15:85 volumetric ratio was introduced via capillary action into the void between the two electrodes through the two drilled holes in the counter electrode. The cell was finally sealed by placing a piece of Surlyn® and a glass microscope cover slide on top the holes in the counter electrode and pressing down with a hot (~100 °C) metal press. Finally, silver conductive paint (RS) was applied to the end of the counter electrode to provide a highly conductive contact and minimise series resistance across the FTO substrate.

3.4.2 Front-illuminated dye-sensitized solar cells

In a typical front illuminated DSC a commercial paste containing TiO_2 nanoparticles, of approximately 20 nm in diameter, is doctor bladed onto a conductive glass substrate. This doctor blading process involves spreading the paste over the substrate using a thin spacer to control the film thickness and shape. The film of paste is then dried and sintered at high temperatures (~450 °C) to form a mesoporous metal oxide film, which after dye adsorption acts as a semi-transparent working electrode within the cell (Figure 3.10).

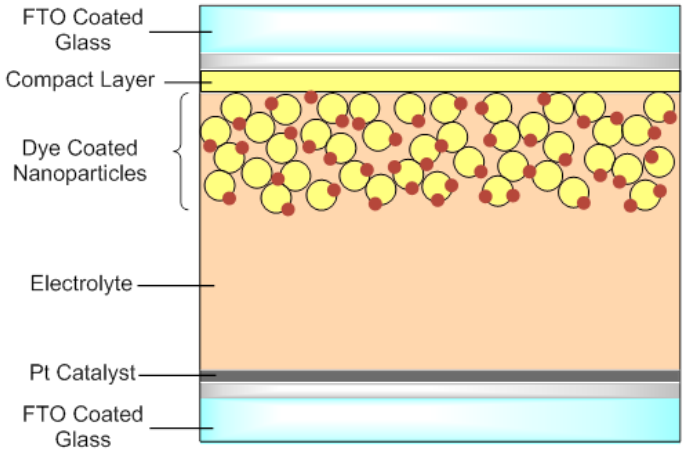

Figure 3.10. Schematic representation of the cross-section of a typical front-illuminated DSC.

As commercially available nanoparticle pastes are only available for TiO_2 (Dyesol, 18NR-T) and not for ZnO, it was first necessary to formulate a ZnO nanoparticle paste that replicates the properties of the commercially available TiO_2 pastes. A DSC nanoparticle paste must effectively disperse the nanoparticles whilst maintaining a high viscosity, so that relatively thick (~10 μm) and even films can be formed by doctor blading onto the substrate. It also must have a sufficiently high organic content so that a mesoporous structure can be formed after annealing the paste. A paste is therefore composed of four main components: (1) the metal oxide nanoparticles, (2) a suitable solvent, (3) a polymer to provide a high viscosity and physical dispersion between particles, and (4) a suitable mild acid for aiding in nanoparticle dispersion.

The first paste to be produced was a ZnO nanoparticle paste designed to be analogous to the most common commercial TiO_2 paste (dyesol, 18NR-T). To ensure reproducibility between batches the ZnO nanoparticles (18 nm, 99.95 %) were purchased from a company (US Research Nanomaterials Inc.) and the same batch of powder was used for all experiments. The first stage in paste production was to initially disperse the nanoparticles. This was completed by adding 19.0 mL of ethanol and 0.2 mL of glacial acetic acid to 1 g of the ZnO nanopowder. The mixture was then sonicated in a sonication bath for 30 minutes. After sonication, 3.5 mL of terpineol and 500 mg of ethyl cellulose was added to the mixture and stirred overnight to fully dissolve and disperse the polymer, forming a smooth paste, free from large aggregates. This paste is referred to within Chapter 6 as “Thin ZnO paste”.

Pastes were also produced using the nanowires from anodization, and also using a commercial nanowire powder (length 1000 nm, diameter 90 nm, Sigma Aldrich). To gain a powder from the annealed anodic nanowire films a plastic spatula was simply used to scrape the nanowires from the substrate and the resultant powder was collected. Care was taken to avoid the use of stainless steel implements throughout the paste and device preparation as it is known that iron contaminants within a DSC device can act as recombination centres, reducing cell performance.[233] Once nanowire powders were obtained, the same paste preparation procedure was used as documented previously for the nanoparticle paste. It was found that after a period of days some sedimentation of larger nanowire aggregates occurred for both the anodic and commercial nanowire pastes. The dispersed paste was therefore separated from the sediment by simply pipetting it into a new glass vial. In this way it was possible to avoid the deposition of large aggregates within working electrodes which could cause significant light scattering and opacity.

A more highly concentrated ZnO nanoparticle paste was also produced in order to obtain greater film thicknesses when doctor bladed, which were more comparable with those of the commercial TiO_2 paste (dyesol, 18NR-T). In order to produce this paste the same procedure was

repeated, but 6.34 mL of ethanol were used for each 1 g of ZnO powder rather than 19.0 mL. This paste is referred to within Chapter 6 as “Thick ZnO paste”. As it was found that the “Thick ZnO paste” resulted in slightly grainy and highly opaque ZnO films, a new method was developed to produce highly concentrated and homogeneous ZnO nanoparticle pastes. This improved method involved first producing a large volume of well dispersed “Thin ZnO paste” (120 mL), followed by removal of the solvent by rotary evaporation. Rotary evaporation was continued until enough solvent was removed to obtain a paste with a ZnO content of 13.7 wt.%, as determined via measurement of the paste mass. This viscous paste is termed “Optimized ZnO paste” within Chapter 6. This paste preparation method was also used to produce mixed pastes containing 1.4 wt.% of ZnO nanowires and 12.3 wt.% of ZnO nanoparticles by controlling the ratios of these nanostructures within the initial Thin ZnO paste. This was completed for mixtures containing either commercial ZnO nanowires or anodic ZnO nanowires.

FTO coated glass (~13 Ω sq^{-1}, TEC 15) was used as the substrate for the front-illuminated DSC working electrodes. A higher resistivity substrate was chosen for the working electrode as it has a higher light transmittance compared to the more conductive FTO TEC 7 coated glass. This is important as the devices will be illuminated through the working electrode. The substrates were cut to sizes of 75 x 40 mm and scored on the glass side to give two columns of five cell size substrates (15 x 20 mm). The scored substrates were then thoroughly cleaned using the procedure documented for the counter electrodes in Section 3.3.1.

The ZnO nanostructure pastes were coated onto the substrates using doctor blading. Scotch® brand magic tape was used as both the mask and spacer for the doctor blading process as it has a known and reliable thickness of ~60 µm and can be easily removed after doctor blading without leaving adhesive residue. In a typical doctor blading, magic tape was stuck along the two longest edges of the 10 cell substrate to mask an area up to 3 mm from edge. The tape was flattened by running a clean, smooth glass rod over the surface. Approximately 300 µL of the paste was pipetted near to the top edge of the substrate and the clean glass rod was drawn over the paste in one smooth motion, to create a film of the paste down the length of the substrate. The magic tape was then removed and the substrate was dried on a hot plate at 100 °C to remove the solvent from the paste. The films were heated in an oven (Carbolite, CWF 1100) at 500 °C for 30 minutes, using a ramping rate of 2 °C min^{-1}, in order to remove any organic components of the paste and to sinter the nanostructures.

Two methods were employed for controlling the film thickness of ZnO resulting from doctor blading: (1) Using different numbers of magic tape layers as a spacer, or (2) completing multiple depositions with one layer of magic tape and drying the films between each deposition.

Using multiple layers of scotch tape was found to be less successful for the more dilute pastes as it often resulted in a large lip in the film where it bordered the magic tape.

After the films had been sintered, the substrates were broken into their individual electrodes (15 x 20 mm) (Figure 3.11a) and any films that appeared inhomogeneous or damaged by visual inspection were discarded. It should be noted that this typically involved discarding the top two electrodes (20 % of the total electrodes) where the nanoparticle paste was first pipetted, as they often had a thick top edge. The active area of the film was controlled to 1 cm^2 by scraping away any excess film using a clean edge of a glass microscope slide. The active area was positioned so that there was a 2.5 mm border surrounding it on three sides and a 7.5 mm border on the edge masked during doctor blading (Figure 3.11b).

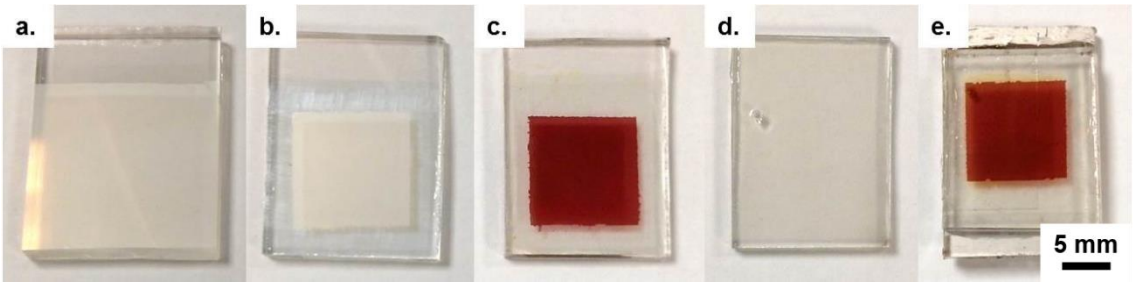

Figure 3.11. Pictures of the main cell preparation stages including after sintering (a), re-sizing (b), dyeing (c), counter electrode preparation (d) and sealing (e).

After controlling the active area, all films were dyed in a 0.5 mM ethanolic solution of N719 dye. N719 dye is the most widely used high efficiency DSC dye, therefore it was chosen to allow the easiest comparison with literature cell performances. Electrodes were typically dyed for 2 h (unless otherwise stated) within a sealed glass container at room temperature and in darkness. After dyeing, the films were washed with ethanol to remove excess dye solution and dried under a gentle flow of nitrogen gas (Figure 3.11c).

Platinum coated FTO counter electrodes were prepared in the same way as documented in Section 3.3.1, however, only one hole was drilled into the substrates in a position that would coincide with the corner of the active electrode area (Figure 3.11d). The working electrode and counter electrode were then sealed together using a 25 µm thick Surlyn® film with a square hole of 1 cm^2 to match the active area of the working electrode (Figure 3.11e).

A liquid electrolyte composed of 0.6 M PMII, 0.05 M I_2, 0.5 M 4-*t*bp and 0.1 M LiI in a solvent of acetonitrile (unless otherwise stated) was filled into the void between the two electrodes via vacuum infilling through the drilled hole in the counter electrode. This first involved placing

a syringe needle containing a small quantity of electrolyte into the hole and placing it inside a vacuum chamber. The chamber was evacuated of air and then slowly opened, causing the liquid inside the needle to be drawn inside the void. This was done until it could be clearly observed that all of the void space was filled with electrolyte. Final sealing of cells was then completed using a piece of Surlyn® and a glass coverslip as described in Section 3.3.1. The contact ends of both the working and counter electrode were painted with silver paint in order to provide a highly conductive contact. A photo of the finished cells and a scheme demonstrating the major steps of cell production are shown in Figure 3.12 and Figure 3.13 respectively.

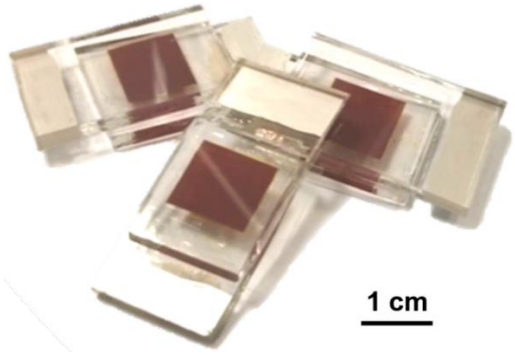

Figure 3.12. Picture of the finished front-illuminated DSCs.

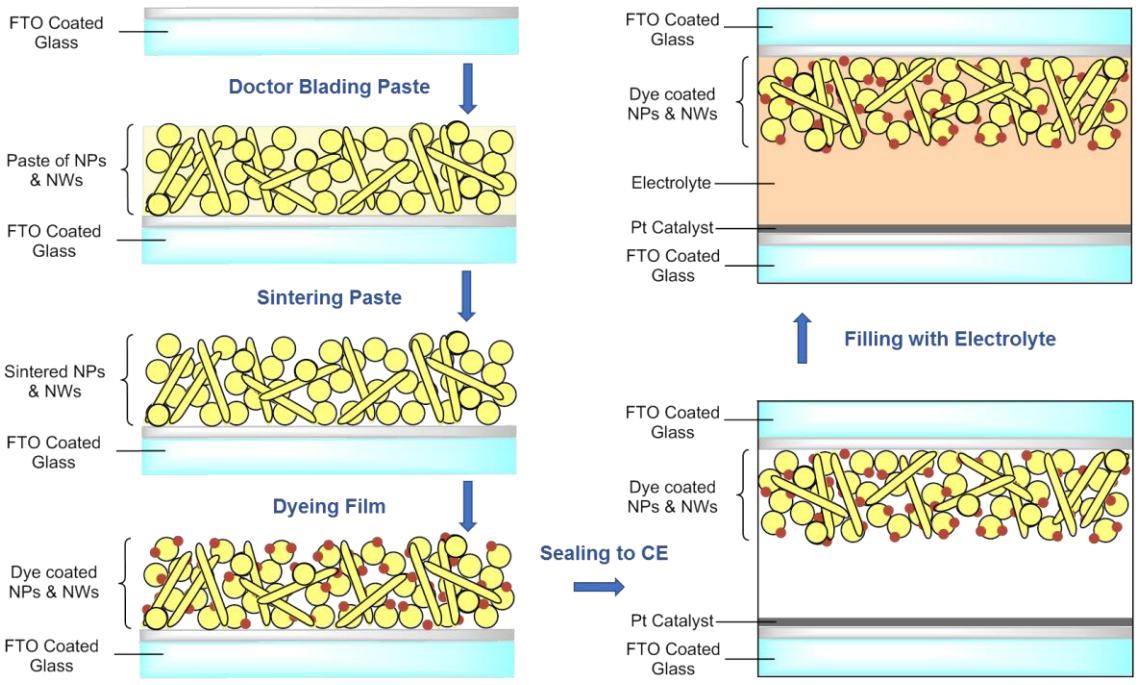

Figure 3.13. Scheme demonstrating the main stages of front-illuminated DSC preparation.

3.4.3 Solid-state dye-sensitized solar cells

This section of research was conducted as part of a collaboration within the group of Professor Jong Hak Kim at Yonsei University in South Korea. Unless otherwise stated, all work was done by me during a six week placement within Yonsei University.

In order to produce efficient solid-state dye-sensitized solar cells (ssDSCs) a suitable pore structure within the metal oxide film is required, enabling infiltration of the viscous electrolyte solutions into the porous working electrode. In order to achieve an ordered porous structure, a graft copolymer was used within the nanoparticle paste, which imparts an ordered porous structure on the resultant mesoporous film via self-assembly. The graft copolymer used consisted of poly(vinyl chloride) (PVC) with poly(oxyethylene methacrylate) (POEM) side chains grafted onto it, which will be referred to as PVC-g-POEM. Synthesis of PVC-g-POEM was completed by students within the group of Professor Kim at Yonsei Univeristy, following a method they had previously published.[234] Briefly, the synthesis involved dissolving 6 g of PVC in 50 mL of n-methyl-2-pyrrolidinone (NMP) by stirring at 90 °C for 4 h. After cooling the solution to room temperature, 9 g of POEM, 0.1 g of CuCl, and 0.23 mL of 1,1,4,7,10,10-hexamethyltriethylenetetramine (HMTETA) were added to the solution. The mixtures were stirred until homogeneous and purged with nitrogen for 30 min. The reaction was carried out at 90 °C for 18 h. After polymerization, the resultant mixtures were diluted with tetrahydrofuran (THF). After passing the solutions through a column with activated Al_2O_3 to remove the catalyst, the solutions were precipitated into methanol. The grafted copolymers were purified by dissolving in THF and reprecipitating into methanol three times. A PVC-g-POEM graft copolymer of composition PVC:POEM=1:1.5 was obtained in the form of a string like polymer (Figure 3.14) and dried in a vacuum oven overnight at room temperature.

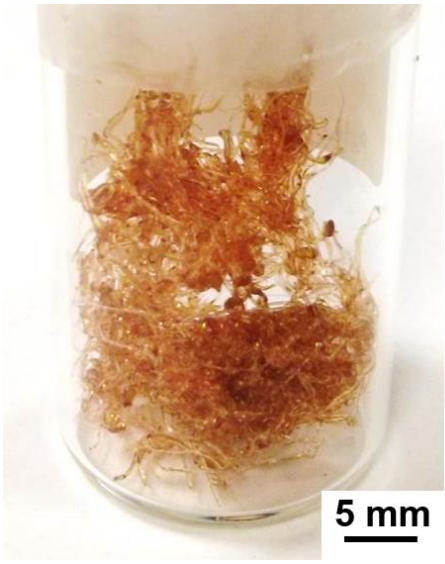

Figure 3.14. Picture of the PVC-g-POEM graft copolymer.

FTO coated glass slides (TEC 7, ~7Ω sq^{-1}) were cut and scribed to give sets of four 15 x 20 mm substrates in a 2 x 2 formation (total dimensions 30 x 40 mm). These substrates were thoroughly cleaned using the cleaning procedures documented in Sections 3.3.1 and 3.3.2.

As an alternative to a compact blocking TiO_2 blocking layer, a porous TiO_2 interfacial layer was used between the FTO and the mesoporous TiO_2 film as previously documented by Kim *et al*..[235] To prepare the interfacial layer 1 mL of titanium(IV) isopropoxide (TTIP) was added to a glass vial under stirring at 1000 rpm provided by a magnetic stirrer bar. 0.5 mL of HCl (37 wt.% in H_2O) was then added dropwise to the vial under stirring at an approximate rate of one drop per two seconds. 0.5 mL of deionised water was also added. The solution was stirred for 15 minutes. Prior to this, a solution of 3 wt.% PVC-g-POEM (1:1.5) in 2.5 mL of THF was prepared by stirring for 2 hours. 0.6 mL of the TTIP solution was then added to the polymer solution and stirred overnight.

A single layer of Scotch® brand magic tape was used to mask the cut and cleaned FTO slide so that a 3 mm strip was masked on the long edges of the substrate. The previously prepared mixture of TTIP and PVC-g-POEM was pipetted onto the substrate and spin coated at 1,500 rpm for 20 s with ramping occurring over 2 s. The magic tape was removed using a razor blade and the films were dried at 50 °C for 15 minutes. The films were then sintered at 450 °C for 30 minutes in air, thereby removing the organic template and leaving an organised porous interfacial layer composed of TiO_2.

Synthesis of nanoparticle pastes

In order to first synthesise the TiO_2 nanoparticles used within the pastes, 1.5 mL of $TiCl_4$ was added drop wise to 10 mL of toluene within a large glass vial under stirring. This caused a colour change from colourless to orange. 50 mL of benzyl alcohol was then added rapidly in one go to the stirred mixture resulting in a colour change to yellow. The mixture was stirred for 30 minutes followed by autoclaving at 70 °C for 15 hours. After 15 hours the solution was removed and it was observed that the solution had gone from a transparent yellow to a cloudy white/yellow. The solution was centrifuged at 12,000 rpm for 30 minutes in order to separate the nanoparticles from solution. The liquid was decanted and the centrifuge tubes were placed upside down on blue roll to allow the remaining solvent to run off. These synthesised nanoparticles will from here on be referred to as preformed TiO_2.

After 30 minutes, 0.35 g of the preformed TiO_2 (waxy solid) was added to a 2 mL solution of PVC-g-POEM (10 wt.%) in THF that had been prepared by stirring the polymer and solvent overnight. The mixture was stirred and 0.1 mL of HCl (37 wt.% in H_2O) was added to disperse the mixture and aid in self-assembly of the graft copolymer. The mixture was stirred overnight to gain a smooth and well mixed paste.

Pastes were also prepared for mixtures of ZnO nanowires and preformed TiO_2 nanoparticles. In order to prepare these pastes, different masses of ZnO nanowire powder (either commercial nanowire powder or powders produced from anodization) ranging between 3.6 mg and 36.8 mg were weighed out into glass vials and 2 mL of THF was added. The mixtures were sonicated for 30 minutes in order to fully disperse the nanowires. 0.2 g of PVC-g-POEM graft copolymer was added to each vial and all vials were stirred overnight to fully dissolve the polymer. 0.35 g of the preformed TiO_2 (waxy solid) was then added to the polymer and nanowire mixture along with 0.1 mL of HCl (37 wt.% in H_2O) and the mixture was stirred overnight to gain a smooth and well mixed paste. The equivalent weight percentages of ZnO nanowires within the pastes relative to the dry weight of preformed TiO_2 is given in Table 3.2 for different masses of ZnO nanowire powder used in paste preparation.

Table 3.2. ZnO nanowire powder mass and equivalent wt.% present within pastes.

ZnO Quantity (wt.%)	ZnO Quantity (mg)
3	3.6
5	6.1
7	8.8
8	10.1
10	13.0
15	20.6
16	22.2
24	36.8

Pastes were also prepared for 0, 3, 5 and 7 wt.% anodic ZnO nanowires in preformed TiO_2, but with replacing the 0.1 mL of HCl with 0.1 mL of DI water. This was done as it was feared that the concentrated HCl added to the paste may cause dissolution of the ZnO nanowires as ZnO is significantly more susceptible to acids than TiO_2.

Cell Preparation

A doctor blading technique, similar to that described in Section 3.3.2, was used to prepare porous anodes in which Scotch® brand magic tape is used as a mask and spacer and a glass pipette is used to spread the paste. The FTO glass substrates coated in a porous TiO_2 interfacial layer were masked along the edges using either 3, 4 or 5 layers of magic tape in order to obtain different film thicknesses. The nanoparticle pastes were applied to the top of the slide and immediately spread down the slide using the side of the glass pipette. The magic tape was removed by cutting with a razor blade to avoid film removal by peeling. The films were dried at 50 °C for 15 minutes in an oven followed by calcination at 450 °C for 30 minutes with ramping from room temperature over

2 hours. Examination of the films after calcination revealed that 3 layers of magic tape is the best, as cracking occurred for films produced with 4 and 5 layers, indicating an overly thick film. Therefore, for all films described herein 3 layers of magic tape were used as a mask and spacer for the doctor blading process.

It was also noted that both after doctor blading and after annealing the films prepared without HCl addition to the paste were less transparent than the films prepared with HCl (including the films prepared only with TiO_2 nanoparticles). This indicated that there might be some aggregation of nanoparticles without HCl or that self-assembly has not successfully occured.

The annealed photoanodes were broken into their cell size pieces (1.5 x 2.0 cm) and the film was scraped away using the clean edge of a glass microscope slide to give an active area of 4 x 4 mm (0.16 mm^2) positioned near the centre of the glass substrate. The photoanodes were immersed in a 0.3 mM ethanolic N719 dye solution within a sealed container and were placed in an oven at 50 °C for two hours in darkness. Platinum counter electrodes were prepared by spin coating a 1 wt.% solution of hexachloroplatinic acid in 2-propanol onto clean FTO coated glass (TEC 7, 15 x 20 mm) at 1500 rpm for 20 s. They were then heated in a furnace at 450 °C for 30 mins.

A viscous “nanogel” (or quasi-solid state) electrolyte was used for the majority of the cells, which offers benefits over conventional liquid electrolytes, such as reduced leakage, due to the presence of a high molecular weight polymer which sets the electrolyte to a near solid state. The nanogel electrolyte was prepared by dissolving the following in 5 mL of acetonitrile: 0.5 g of poly(ethylene glycol) (M_n 10,000), 0.1432 g of 1-methyl-3-propyl imidazolium iodide (PMII), 0.01432 g of iodine and 0.1432 g lithium iodide. The solution was stirred for 30 minutes to fully dissolve the mixture. After this time a small quantity of this solution was pipetted into a new vial and diluted in a 1:4 volume ratio with acetonitrile. The high concentration solution is from now on referred to as HC and the low concentration as LC.

The nanogel electrolyte was cast onto the photoanodes by pipetting two drops of LC over the active area of each, covering with a petri dish and foil and then leaving the solvent to slowly evaporate over one hour. This process was repeated a further 4 times. After the fifth cycle, one drop of HC was pipetted onto each photoanode followed by covering and waiting for one hour. This was repeated once more with HC. After what now totals 7 drop casting cycles, a single drop of HC was pipetted onto both the active area of the photoanode and onto a Pt counter-electrode and the two electrodes were sandwiched together. The electrodes were secured together by clipping them with bulldog clips and allowing the solvent to evaporate overnight at 30 °C in darkness.

For one set of cells a solid-state electrolyte was used that was composed of a polymeric ionic liquid. This solid state electrolyte has the same advantages of no electrolyte leakage but can also be used to obtain higher efficiency devices than the nanogel electrolyte.[236] The main caveat of the higher efficiencies is that the electrolyte is more difficult to cast, resulting in lower reproducibility of the devices. Solid state electrolyte solutions were prepared by students at Yonsei University by dissolving 10 and 2 wt.% of a previously produced polymeric ionic liquid, poly((1-(4-ethenylphenyl)methyl)-3-butyl-imidazolium iodide) (PEBII), in acetonitrile and stirring for 30 minutes.[236] The drop casting method used was the same as for the gel electrolyte except that only one drop of solution was used in each cycle for the low concentration solution. The final assembly with the counter electrode was also identical and the cells were clamped and left overnight to allow the solvent to fully evaporate.

In the case of both electrolytes, the sealing of the sandwiched cells was completed by spreading epoxy resin over the join between the electrodes at the short edges of the cells. The cells were then re-clamped and the epoxy resin was left to dry for 2 hours. After this time, the clamps could be removed and the finished devices were obtained (Figure 3.15).

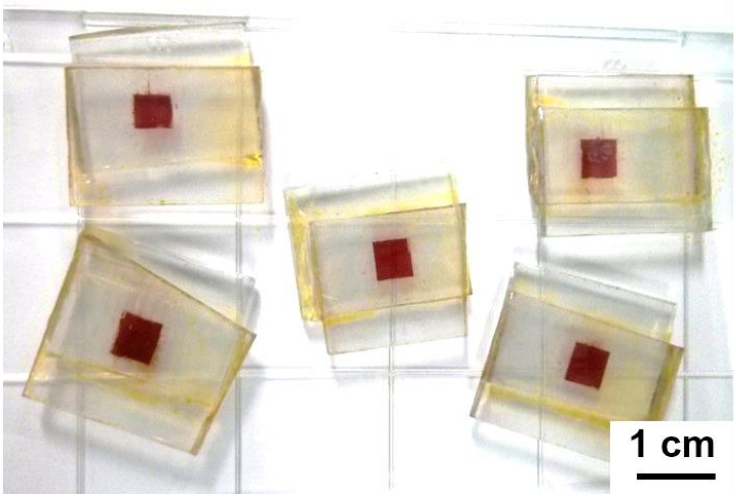

Figure 3.15. Picture of the final solid-state DSCs.

It should be noted that the cells documented in Chapter 6, Section 6.3.3 were prepared and analysed by Chang Soo Lee, a PhD student within the group of Professor Jong Hak Kim at Yonsei University. The cell preparation was based upon the method used for preparation of qssDSCs featuring a “nanogel” electrolyte, as documented previously within this section. The quantities of anodic ZnO nanowires used within the pastes were altered slightly from those documented above to give films containing either 4, 8 or 12 wt.% anodic ZnO nanowires. In addition to the photoanodes containing anodic ZnO nanowires, photoanodes were also prepared

with equal quantities of hierarchical core-shell ZNW@TNS nanostructures (see Section 3.3.2 for details of nanostructure synthesis). Cells were prepared for the photoanodes containing different quantities of both types of nanostructures and their performance was compared.

3.5 Perovskite Solar Cell Fabrication

3.5.1 Substrate and blocking layer preparation

FTO coated glass substrates (~7 Ω sq^{-1}, TEC 7) were first cut to dimensions of 150 x 150 mm. Six strips of 15 mm width were masked down the length of the substrate at regular intervals (10 mm spacing between each) on the FTO coated side using Kapton® polyimide tape. Kapton® tape was selected as it adheres well, can be removed without leaving residue and is chemically resistant. The exposed areas of FTO were coated in zinc powder by gently rubbing it in using a cotton wool bud. A 2 M solution of $HCl_{(aq)}$ was then pipetted over the powder and left to etch for approximately 2 minutes, or until the fizzing resulting from the etching process had subsided. The etched areas were then rubbed away with a cotton wool bud and rinsed thoroughly with water to remove any remaining etchants. After removal of the Kapton® tape it could be clearly observed that the FTO had been removed from the exposed areas, leaving behind six strips of FTO with 15 mm width.

The etched substrates were then scored on the reverse side to give 36 cell size substrates with dimensions of 25 x 25 mm, where the 15 mm wide FTO strip ran down the centre of each cell. Depending on the chosen blocking layer deposition method, the substrates were either broken into sets of 2 x 2 cells (for all spin coated blocking layers), sets of 3 x 1 cells (for spray pyrolysis blocking layers), or 2 x 1 cells (for electrodeposited blocking layers). The substrates were then thoroughly cleaned by first scrubbing with a 2 vol.% solution of Hellmanex® III cleaning concentrate in deionised water followed by thorough rinsing sequentially with deionised water, acetone and 2-propanol. After drying under a clean flow of nitrogen the substrates were cleaned further by treating in an oxygen plasma system (Diener Electronic, Zepto) for 15 minutes at 50 % power output.

The next stage in cell preparation was to deposit a thin, compact blocking layer of either ZnO or TiO_2 onto the clean substrates. The blocking layer acts as a selective contact for electrons, allowing them to travel through to the FTO substrate whilst blocking the transport of electron holes. A suitable blocking layer should therefore be thin, to prevent increased series resistance, and also free of pinholes, which could act as recombination sites between photogenerated electrons and holes. A number of different techniques were therefore tested for the preparation of suitable blocking layers, the preparation procedures of which are presented below.

TiO_2 blocking layer preparation

The first method to be used for preparing TiO_2 blocking layers was one based upon spin coating a TiO_2 precursor solution onto the substrates, followed by annealing.[237] This involved first preparing a solution of titanium(IV) isopropoxide (TTIP, 0.369 mL) in anhydrous 2-propanol

(2.53 mL) and a solution of 2 M HCl (35 µL) in anhydrous 2-propanol (2.53 mL). The acid containing solution was then added drop wise to the TTIP solution under heavy stirring. This solution was then pipetted onto the clean FTO substrates (150 µL per 25 x 25 mm substrate) and spin coated at 2000 rpm for 60 s. The films were then annealed at 500 °C for 30 minutes.

The second method used for the preparation of TiO_2 blocking layers was based upon the spray pyrolysis of a TiO_2 precursor onto hot substrates. Substrates consisting of 3 x 1 cells (75 mm x 25 mm) were fixed inside a custom made aluminium heating block by screwing down a 3 mm wide aluminium strip over the centre of the substrate (Figure 3.16). This strip both prevents the substrate from moving during the spray procedure and masks a central strip of FTO which will be used for a contact at the final stages of cell preparation. The metal block was placed on a hot plate, which had been fitted with a metal surround, and heated to a maximum temperature of approximately 400 °C over a period of at least 40 minutes. A chromatography sprayer was then used to spray a fine mist of a 10 mM solution of diisopropoxytitanium bis(acetyl acetonate) in 2-propanol onto the hot substrates. For each spray cycle two sprays were administered to each set of 3 substrates, one to the upper half and one to the lower half. A wait time of 30 s was then used to allow the substrates to re-heat before repeating the spray cycle. A total of 13 spray cycles were used to ensure complete coverage of the substrate in TiO_2. After these cycles the substrate was kept at the maximum temperature for 15 minutes before cooling to room temperature. Effort was made to maintain a constant distance of 10 cm between the spray nozzle and the substrate at an angle of approximately 45 °, although as this was controlled manually by estimation there will inevitably be some inconsistency present within the process. A future improvement to the blocking layer preparation would therefore be to develop an automated spray system with the nozzle on an x-y stage to ensure that spray cycles were identical each time.

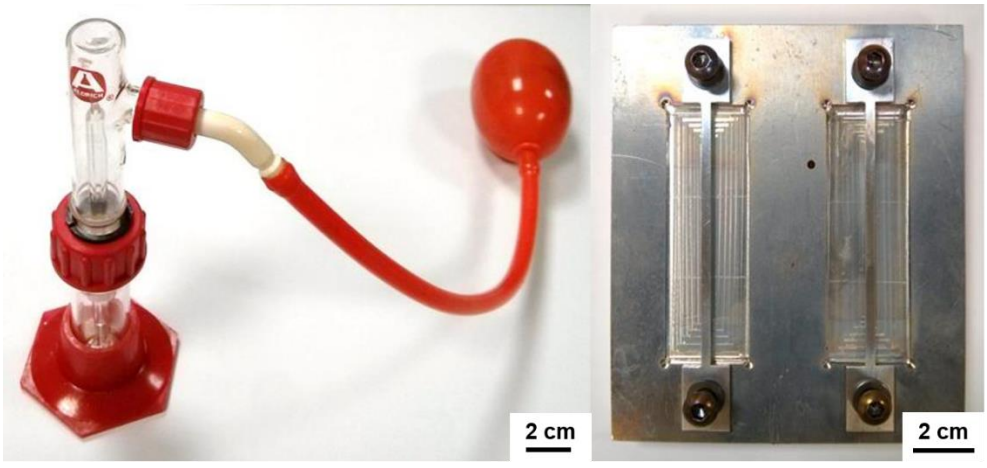

Figure 3.16. Picture of the chromatography sprayer and heating block used for spray pyrolysis.

ZnO blocking layer preparation

The first method tested for the preparation of a ZnO blocking layer was spray pyrolysis of a zinc acetate solution. The spray solution consisted of 0.1 M zinc acetate dihydrate and 0.2 M acetic acid in a 25:75 volumetric mixture of water and ethanol. The substrates were first heated to ~350 °C on a hotplate and maintained at this temperature throughout deposition. The spray was delivered by a gravity feed spray gun (Silverline, HVLP spray gun) with a 100 mL solution reservoir. The tip of the spray gun was secured at a distance of 16 cm from the substrate at an angle of ~45 ° (Figure 3.17). A 0.5 bar argon gas supply was used to complete spray cycles consisting of 1 s of spraying followed by a 9 s wait time. Depositions involved completing either 15, 25 or 35 spray cycles, followed by increasing the hot plate to 400 °C for 30 minutes to decompose any unreacted spray solution.

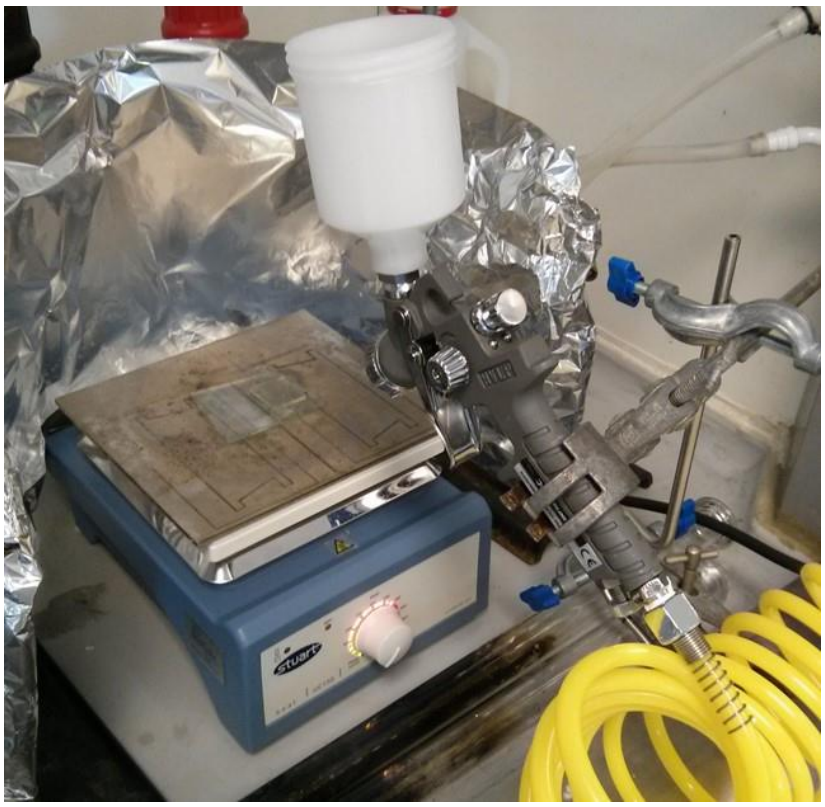

Figure 3.17. Experimental setup used for the spray pyrolysis of ZnO on conducting glass substrates.

The second method tested for the preparation of a ZnO blocking layer was based on a method by Kelly *et al.* in which a thin layer of small (~5 nm) ZnO nanoparticles are spin coated onto the FTO substrates.[151] The nanoparticle solution was synthesized by first dissolving 2.95 g of zinc acetate dihydrate in 125 mL of methanol under stirring at 65 °C. A solution consisting of

1.48 g of KOH in 65 mL of methanol was then added dropwise to this at ~65 °C over a period of 15 min. The reaction mixture was maintained at this temperature and stirred for a further 2.5 h. The mixture was then allowed to cool to room temperature and left overnight for the precipitate to settle out from the solution. The supernatant was decanted and the remaining precipitate was washed twice with methanol. After washing, the nanoparticle precipitate was re-dispersed in a solvent mixture containing 70 mL of n-butanol, 5 mL of methanol and 5 mL of chloroform to form a solution with an approximate ZnO concentration of 6 mg mL^{-1}. This nanoparticle dispersion was then used to spin coat a nanoparticle blocking layer onto the FTO substrates. 150 µL of nanoparticle dispersion was pipetted onto each cell substrate (25 x 25 mm) and spin coated at 3000 rpm for 30 s with ramping from 0 to 3000 rpm occurring over 3 seconds. This process was repeated a further two times to give three layers of ZnO nanoparticles as a blocking layer. This blocking layer was either used as-prepared or after annealing the film at 450 °C for 30 mins.

The third method tested for the preparation of ZnO blocking layers involved spin coating a solution containing a ZnO precursor and annealing to form ZnO. A 250 mM solution of zinc acetate dihydrate in methanol was first prepared. 450 µL of this solution was pipetted onto a set of four cell substrates and spin coated at 1000 rpm for 30 s. The films were then annealed at 500 °C for 30 minutes to form a film of ZnO. The same method was also used but with 100 mM ethanolamine as an additive within the spin coating solution.

The fourth method tested for the production of ZnO blocking layers was the electrodeposition of ZnO. Electrodeposition was undertaken within a three electrode cell setup where FTO coated glass acted as the working electrode, a stainless steel plate acted as counter electrode and a Ag/AgCl electrode was used as a reference electrode. A 3 mm wide strip of Kapton® tape was used to mask a central strip of the FTO working electrode in order to act as a contact point at the end of cell production. The working electrode and counter electrode were held parallel to each other at a distance of 20 mm using nylon screws and nuts. The reference electrode was then held to the side of the working and counter electrodes using a 3-D printed electrode holder. The electrochemical cell was maintained at a constant temperature of 85 °C by keeping it within a heated bath of silicone oil controlled by a temperature probe as shown in Figure 3.18. Electrodeposition was carried out in an electrolyte consisting of 100 mM zinc nitrate hexahydrate in deionised water (pH 4). Electrodepositions were completed at applied voltages between -0.8 and -1.3 V relative to Ag/AgCl, controlled by a potentiostat (µAutolab type II), and stopped after a charge threshold of either 0.1 or 0.15 C cm^{-2} was reached. After electrodeposition the films were quickly removed from the electrolyte and washed thoroughly in deionised water and 2-propanol before drying under a flow of nitrogen.

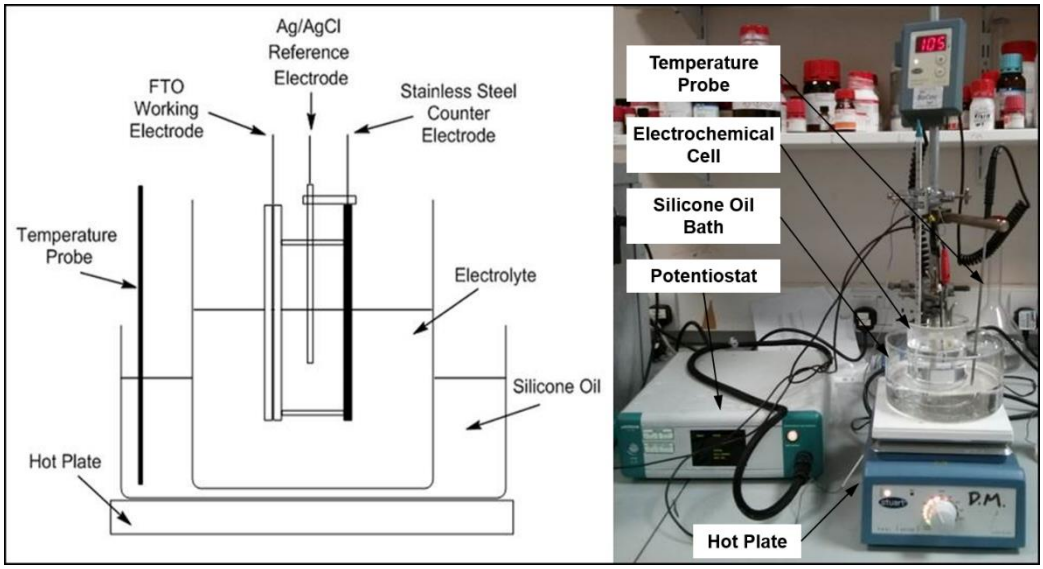

Figure 3.18. Diagram and picture of the electrodeposition experimental setup.

The mechanism of electrodeposition of ZnO first involves the reduction of NO_3^- ions at the cathode to produce OH^- ions (reaction 3.1). These react with Zn^{2+} ions resulting in the precipitation of the solid ZnO product onto the electrode surface (reaction 3.2):[238]

$$NO_3^- + H_2O + 2e^- \rightarrow NO_2^- + 2OH^- \quad (3.1)$$

$$Zn^{2+} + 2OH^- \rightarrow ZnO + H_2O \quad (3.2)$$

3.5.2 Planar cell configurations

For planar perovskite cell configurations (Figure 3.19) the perovskite material is deposited as a thin layer (100-500 nm thick) directly onto the metal oxide blocking layer. For all planar perovskite cells documented within this thesis the perovskite material used is methylammonium lead iodide ($CH_3NH_3PbI_3$). The two main solution based deposition methods for perovskites can be distinguished as either a 1-step deposition or a 2-step (sequential) deposition. The first method to be trialled was the 1-step deposition, in which a DMF based solution containing lead chloride (0.83 M) and methylammonium iodide (MAI, 2.50 M) was pipetted onto the blocking layer (100 µL per cell), left for 20 s and then spin coated at 2000 rpm for 30 s with acceleration occurring within 2 s. The films were then immediately removed from the spin coater and placed on a pre-heated hot plate at 100 °C for 45 minutes. Whilst heating on the hot plate, the film underwent a colour transition from yellow to grey via a red colour corresponding to the chemical reaction:

$$3CH_3NH_3I + PbCl_2 \rightarrow CH_3NH_3PbI_3 + 2CH_3NH_3Cl \quad (3.3)$$

Where the CH_3NH_3Cl is sublimed during the annealing. It could be observed that for all planar perovskite films produced via the one-step method significant de-wetting occurred, resulting in sparse and inhomogeneous perovskite coverage.

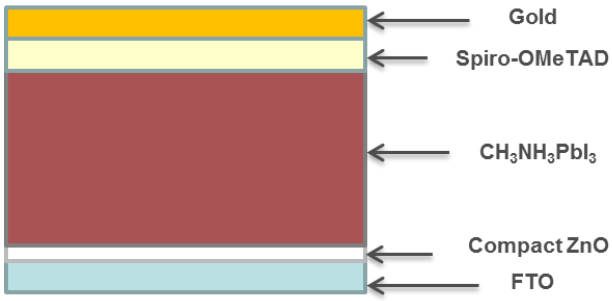

Figure 3.19. Cross-section of a planar perovskite cell structure.

To avoid this unfavourable de-wetting a two-step deposition was then tested. The two step deposition typically involved first spin coating a 1 M solution of PbI_2 in either DMF or DMSO (100 µL per cell) onto the blocking layer coated FTO substrate at 3000 rpm for 15 s, with acceleration to the maximum spin speed occurring over 3 s. The yellow films were then immediately placed on a hot plate at 70 °C for 30 minutes to remove the excess solvent. The films were then dipped into a 10 mg mL^{-1} solution of MAI in 2-propanol (anhydrous) for different time periods ranging from 20 s to 10 min in order to convert the PbI_2 into a layer of $CH_3NH_3PbI_3$ perovskite. This conversion was accompanied by an obvious colour change from yellow to dark brown, which proceeded from the edge of the cells inwards. The films were then removed from the MAI solution, washed with 2-propanol and dried under a short, sharp blast of nitrogen gas. The films were then dried further by placing on a hot plate at 70 °C for 15 minutes.

The films resulting from the two-step deposition did not suffer from de-wetting and good film coverage could be achieved. This two-step technique was therefore used throughout all of the planar perovskite cell preparations. In order to optimise cell performance, various preparation parameters were varied including the spin coating speed, spin coating time, heating time and dipping time in the MAI solution. Where these parameters have been altered compared to the above conditions it will be stated within the results in Chapter 7. It should also be noted that to achieve improved homogeneity both the PbI_2 solution and the substrates were held at 70 °C prior to spin coating to prevent the rapid crystallization of PbI_2.

To complete the perovskite cells a layer of the organic hole transport material spiro-OMeTAD was spin coated on top of the perovskite layer after cooling. The spin coating solution consisted of 142.6 mg spiro-OMeTAD, 17.5 µL 4-tert-butyl pyridine (4-*t*bp) and 37.5 µL of a

170 mg mL^{-1} solution of LiTFSI in acetonitrile, all dissolved in 2 mL of chlorobenzene. 65 µL of the solution was pipetted onto the film, a wait time of 10 s was observed and then the solution was spin coated at 4000 rpm for 30 s. The cell was then stored overnight in a sealed desiccator box which was filled with silica gel to lower the atmospheric water content. A 4 mm wide strip of the perovsite film was scraped away using a razor blade to expose a strip of FTO at the centre of the cell for contacting. Finally, gold contacts were thermally evaporated onto both the exposed FTO strip and onto the perovskite film to provide 10 cell areas, each of 3 x 3 mm, on the one perovskite film (Figure 3.20). Approximately 120 mg of high purity gold (99.99%) was used for each set of evaporations, resulting in a layer thickness of ~100 nm. A laser cut mask was used to control the deposition of gold onto the perovskite cells which could hold up to 16 substrates per deposition (Figure 3.21). A vacuum evaporation system (Emitech, K975) was used with a tungsten boat as a heating element and evaporation was undertaken at a pressure of ~ 3 x 10^{-4} Torr. After evaporation, the cells were immediately placed back within a sealed desiccator box and stored there until used for *I-V* analysis. Although storage within a desiccator box was found to significantly reduce the rate at which the perovskite cells degraded due to moisture, cell performance was found to decrease significantly over a period of days. Therefore, all cell measurements were typically performed on the same day as gold evaporation. The key stages of planar perovskite cell preparation are highlighted in Figure 3.22. It should be noted that all planar perovskite cells were prepared within air under normal laboratory conditions and, therefore, the humidity varied greatly between batches (20-70 % relative humidity) which can lead to poor reproducibility.

Figure 3.20. Picture of the finished perovskite solar cells consisting of 10 separate measurement areas on one substrate.

Figure 3.21. Picture of the gold evaporation mask.

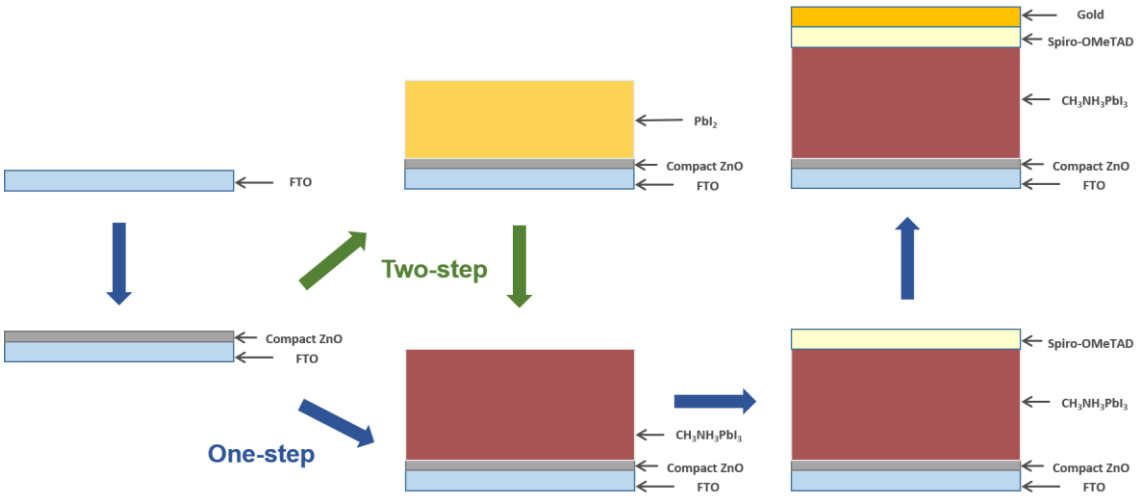

Figure 3.22. Scheme demonstrating the main stages of planar perovskite cell preparation for both one and two-step depositions.

3.5.3 Mesoscopic cell configurations

For mesoscopic perovskite cells a porous layer of nanoparticles, or other nanostructures, is first deposited onto the blocking layer and then filled with a perovskite material (Figure 3.23). The porous layers consisted of either TiO_2 nanoparticles, ZnO nanoparticles, commercial ZnO nanowires or ZnO nanowires produced via anodization. In order to deposit porous layers of the nanomaterials it was first necessary to produce pastes suitable for spin coating. To produce a dilute TiO_2 nanoparticle paste a commercial TiO_2 paste used for creating DSC electrodes (Dyesol,

18-nRT) was diluted in a 2:7 ratio with ethanol and left to stir overnight. For the ZnO nanoparticles and nanowires, the dilute pastes documented in section 3.3.2 were used, which contained 1 g ZnO, 0.5 g ethyl cellulose, 200 µL acetic acid, 19 mL ethanol and 3.5 mL of terpineol. The pastes were spin coated onto either ZnO or TiO_2 blocking layers at various different spin speeds (500 to 6000 rpm) for 30 s using 150 µL of paste for each 25 x 25 mm substrate. After spin coating, the films were dried on a hot plate at 100 °C for 10 minutes followed by sintering at 500 °C in air for 30 minutes with heating from 20 °C at a rate of 2 °C min^{-1}.

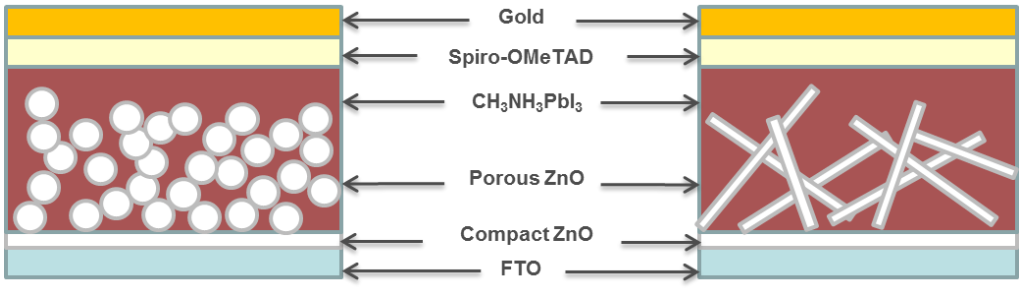

Figure 3.23. Cross-section of the mesoscopic perovskite cells.

Infiltration of the porous layers with a $CH_3NH_3PbI_3$ perovskite was typically performed via a two-step deposition technique, similar to that documented in Section 3.4.2. PbI_2 was first infiltrated into the pores by spin coating a 1 M PbI_2 solution in DMF or DMSO onto the porous film at 3000 rpm for 15 s, with acceleration occurring over 3 seconds. It should be noted that both the substrates and the PbI_2 solution were held at 70 °C prior to spin coating as it was found that smoother more homogeneous films could be obtained in this way. A wait time of 10 s was also used after pipetting the solution onto the porous films to allow infiltration of the solution before spin coating. After spin coating, the films were immediately placed on a hot plate at 70 °C for 30 minutes in order to remove the excess solvent.

Conversion from PbI_2 to $CH_3NH_3PbI_3$ was achieved by dipping the films in a 10 mg mL^{-1} solution of MAI in 2-propanol for a period of time ranging between 20 s and 10 minutes, depending on the specifics of each cell preparation and the rate of conversion. The brown films were then removed from the solution, washed with 2-propanol and blown dry with a short, sharp blast of nitrogen. Further drying was then achieved by drying the films at 70 °C for 15 min. The cells were then completed following the same procedure as documented within section 3.4.2 for the spiro-OMeTAD and gold layers (Figure 3.24).

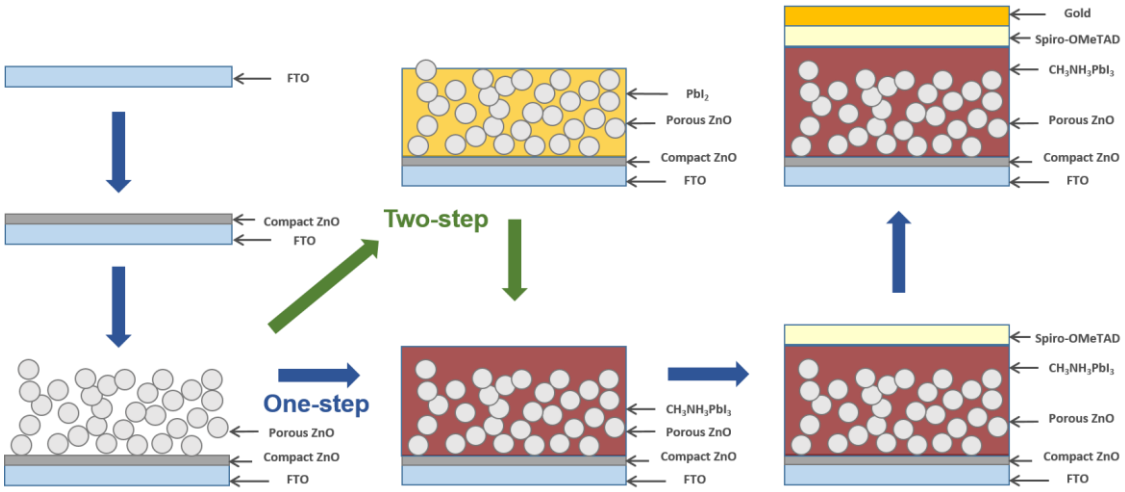

Figure 3.24. Typical cell making stages for mesoscopic perovskite cells.

It should be noted that the conditions stated are those of a typical cell preparation and variations, including different spin coating speeds, spin coating times, heating temperatures and dipping times, were used in order to examine the effect of these parameters and optimize performance. Where different conditions have been used it will be stated within the results section being discussed. It should also be noted that all mesoscopic perovskite cells documented in Chapter 7, Section 7.2.2 were prepared in open air within the laboratory, but the use of a dehumidifier system allowed the humidity to be controlled to < 30 % relative humidity. The cells documented in Section 7.2.3 and Section 7.2.4 were produced within a dry box system (850-NB, Nitrogen Dry Box, Plas-Labs, Inc., USA) which contained a nitrogen atmosphere and a relative humidity below 3 %.

3.6 Characterisation

3.6.1 Materials characterisation

Electron microscopy

Surface and cross-sectional morphologies of the as-prepared anodic films were examined using a field emission scanning electron microscope (FESEM, JEOL, JSM6301F) operating at 3 kV. The anodic films were examined without further treatment and clamping stubs were used to secure the films and provide a conducting pathway. Using the clamping stubs it was possible to avoid the use of carbon tape and thereby preventing the destruction or contamination of the sample. Cross-sections were gained by cutting through the anodic films using a fresh razor blade. This allowed a relatively smooth cut to be made through the nanostructured films, but did not cut completely through the zinc substrate. Sharp scissors were then used to cut through the zinc substrate, taking care not to destroy the smoothly cut edge of the nanostructured films.

Analysis of the FESEM micrographs obtained for films produced in $KHCO_{3(aq)}$ electrolytes was completed by manually measuring nanowire diameters and packing densities within ImageJ. For the determination of the nanowire diameter measurements a minimum of 20 measurements were taken for each film. The measurements were taken over multiple different images in order to gain representative results. Nanowire packing densities were determined by counting the number of different nanowires within a square with an area of 25 μm^2. This was repeated for at least three different squares in order to obtain an average value for the film.

Analysis of the cross-sectional FESEM, obtained for films produced in $NaHCO_{3(aq)}$ and $NH_4HCO_{3(aq)}$ electrolytes, was completed by manually measuring film thicknesses along the cross-sections within ImageJ. For each different sample, five separate measurements were made, at regular length intervals along the film, and average values were gained. Errors displayed for these measurements are standard deviations of the five film thicknesses gained for each film.

Transmission electron microscopy (TEM) was performed using a Philips CM200 FEGTEM at the University of Leeds for the results reported on the slit-type pore nanowires and the hierarchal nanowires within Sections 5.1.2 and 5.2.2. Prior to TEM analysis, the nanowires were scraped from the zinc substrates and dispersed via sonication in ethanol. They were then deposited onto TEM grids (lacey carbon on 400 mesh copper, Agar Scientific) by pipetting and allowing the solvent to evaporate. The TEM micrographs reported in Section 5.4 of the core-shell structures of TiO_2 nanosheets on ZnO nanowires were recorded using a Philips CM30 EF-TEM at Yonsei University.

X-ray diffraction

X-ray diffraction (XRD) measurements were recorded for the as-prepared and annealed anodic films using a Bruker D8-Advance in flat plate mode. This allowed the samples to be examined whilst still attached to the zinc substrate. Measurements were recorded between 2θ values of 20-60° in the case of the films produced in a $KHCO_{3(aq)}$ electrolyte and 10-80° in the case of the films produced in a $NaHCO_{3(aq)}$ electrolyte.

Spectroscopy

Ultraviolet (UV)-visible reflectance spectra of the as-prepared and annealed anodic films were recorded using a UV-visible photospectrometer (Ocean Optics, USB2000+UV-VIS). A reference spectrum was recorded using an untreated piece of zinc foil. This spectrum was subtracted from those of the anodic films to give only the absorbance resulting from the nanostructured film. The resolution is quoted as 1.5 nm for full width at half maximum (FWHM).

Fourier transform infrared (FT-IR) spectra of the anodic nanostructures produced by anodization in $KHCO_{3(aq)}$ were recorded using a Perkin Elmer Spectrum 100 FT-IR spectrometer, equipped with a Universal Attenuated Total Reflectance (UATR) accessory, interfaced to a computer. Measurements were recorded within the range of 4000-600 cm^{-1}. The powders used were produced by the physical abrasion of the nanostructures from the anodic films using a plastic spatula. Spectra were recorded both for powders produced from the as-prepared anodic films and the annealed anodic films. Errors quoted for the Perkin Elmer Spectrum 100 FT-IR spectrometer are ±1.5 cm^{-1}.

X-ray photoelectron spectroscopy (XPS) of the as-prepared and annealed nanowire films was performed using a VG Escalab 250 at the University of Leeds. A 500 μm diameter scan area was used for each measurement. Raman spectroscopy was performed on the nanowire films, as prepared from anodization and after annealing at 300 °C for 1 h, using a Renishaw inVia Raman Microscope. A laser with a wavelength of 532 nm and power of 320 mW was used at 10 % maximum power for acquisition. A minimum of three different areas of the samples were scanned to ensure that the results were reproducible.

Profilometry

Surface profilometry of the spin coated and doctor bladed porous films was performed using a Veeco Dektak surface profilometer operating with a stylus force of 2 mg. Three measurements were made for each film in order to gain an average step height under each deposition condition.

3.6.2 Solar cell characterisation

I-V measurements

Current-voltage (*I-V*) curves of both the dye-sensitized solar cells and perovskite solar cells were carried out under simulated AM 1.5 solar irradiation within a TS Space Systems solar simulator linked to a Keithley 2601A system SourceMeter. Measurements of dye-sensitized solar cells were completed individually by scanning the voltage from short circuit to open circuit using the TSIV software provided with the solar simulator. A non-reflective black mask with a 1 cm^2 square hole was used to control the active area of the cells and ensure overestimation of efficiency did not take place. A minimum of three dye-sensitized solar cells were measured for each cell preparation condition in order to gain average performances and estimate errors.

Measurement of perovskite cell performances were undertaken using a custom automated measurement system that measured each of the ten cell areas in turn. Typical measurements were conducted by sweeping the voltage from 1.2 V to 0 V (backward scan) at a rate of 0.4 V s^{-1} and measuring the current using a custom made script in LabView®. A non-reflective black mask with ten 3 x 3 mm holes was used to control the area of each cell area and prevent overestimation of performance. Measurements for some cells were also recorded by scanning from 0 V to 1.2 V (forward scan) in order to compare with the backward scan data, thereby checking for hysteresis effects. When scans in both directions were recorded, the backward scan always preceded the forward scan.

For the solar cells produced in collaboration with Yonsei University (Section 6.3) a Keithley Model 2400 and a 1,000 W xenon lamp (Oriel, 91193) were used. The light intensity was homogeneous over an 8 in. × 8 in. area and was calibrated using a Si solar cell (Fraunhofer Institute for Solar Energy System, Mono-Si + KG filter, Certificate No. C-ISE269) with a sunlight intensity of one (100 mW cm^{-2}), which was verified by a NREL-calibrated Si solar cell (PV Measurements Inc.). Measurements were recorded by scanning the voltage from short circuit to open circuit and measuring the photocurrent.

For all *I-V* curves recorded, the photocurrents were converted into current densities by dividing by the cell active area, thereby, making all of the results comparable. The current densities were then plotted against the applied voltage to form a *J-V* curve (Figure 3.25). From these plots four cell parameters were extracted: (1.) the short circuit current density (J_{sc}) obtained from the y-axis intercept; (2.) the open circuit voltage (V_{oc}) obtained from the x-axis intercept; (3.) the fill factor (*FF*), which is a measure of ideality obtained from the maximum power point (P_{max}), J_{sc} and V_{oc} (Eq. 3.1); and (4.) the power conversion efficiency (*PCE* or η) which is obtained using Eq. 3.2 in which P_{in} is the solar power incident on the active cell area.

$$FF = \frac{P_{max}}{J_{sc} \cdot V_{oc}} \cdot 100\ \% \qquad \text{Eq. 3.1}$$

$$PCE = \frac{J_{sc} \cdot V_{oc} \cdot FF}{P_{in}} \qquad \text{Eq. 3.2}$$

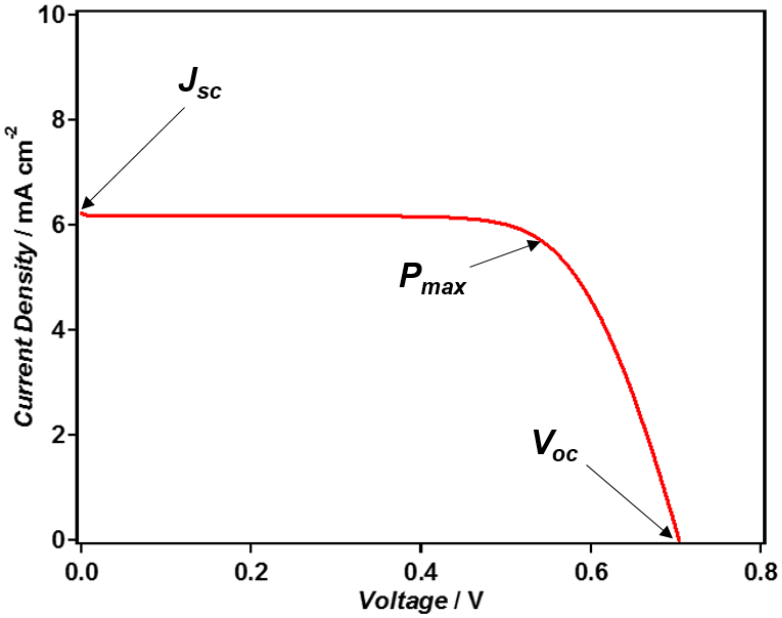

Figure 3.25. Example of a typical *J-V* curve recorded for either a dye-sensitized or perovskite solar cell and the cell parameters that are extracted from it.

IPCE

The incident photon-to-current conversion efficiency (IPCE) measurements were conducted by Chang Soo Lee in Yonsei University. The measurements were taken within the wavelength range of 300 to 800 nm using a Solar Cell IPCE Measurement System (McScience, K3100, Korea).

EIS

Electrochemical impedance spectroscopy (EIS) of the dye-sensitized solar cells produced in Yonsei University was performed at 1 Sun light intensity, provided by a Xenon arc lamp (USHIO Inc., Japan), and open circuit voltage. Measurements were taken within the frequency range of 0.05 Hz to 0.1 MHz with an AC amplitude of 10 mV using a potentiostat (CompactStat, Ivium Technologies, The Netherlands).

Chapter 4 – Controlled Growth of ZnO Nanowires Using Anodization

Anodization has recently been shown to be a promising technique for the production of ZnO nanostructures due to the wide range of possible morphologies that can be obtained and the relatively mild conditions under which growth proceeds.[208, 209, 212] As highlighted in Chapter 2, one of the most interesting reports in this area has been the growth of high aspect ratio nanowires by anodizing zinc within a mild potassium bicarbonate electrolyte.[209] This technique is unique, not only with regard to the nanostructures produced, but also with regard to the high growth rates that have been demonstrated for such mild reaction conditions. These two factors make this anodization reaction an extremely interesting candidate for the production of nanowire arrays to be used within photovoltaic cells.

Although preliminary studies have been conducted on this anodization reaction, there still remain many unanswered questions about the method of nanowire growth on the zinc substrate and the factors that control it.[209, 229] The aim of this chapter is to significantly advance our understanding of this anodization reaction and expand it to cover a range of bicarbonate electrolytes, so that it can be successfully used to produce bespoke nanostructures for application in photovoltaics.

The chapter is split into three main sections. The first section, titled “Understanding the growth process”, will introduce the process of nanowire growth by identifying several key stages of the growth process using electron microscopy. The second section, titled “Control of growth through reaction conditions”, will focus on the many factors that affect the nanowire growth process. Trends will be identified in the changing morphological structure of the nanowires that results from altering parameters, such as the anodization voltage and temperature. The use of alternative bicarbonate electrolytes will also be explored for the first time. The information gained from these experiments is then used to propose the first reaction mechanism for this anodization system. The final section, titled “Conversion to ZnO”, will discuss the annealing of the nanowires after anodization, a process that is found to be a necessary step if ZnO is to be produced, but which can also give rise to novel high surface area nanostructures. Part of the results shown within this chapter have recently been published as a full paper in the Journal of Materials Chemistry A.[230]

4.1 Understanding the Growth Process

In this first section of the chapter the stages of nanowire growth during anodization are explored. Scanning electron microscopy (SEM) was used to examine the morphology of nanostructures formed on the zinc substrate after different time periods of anodization, all the way from a bare zinc foil at the start of anodization to a well aligned array of high aspect ratio nanowires at the end of the process. Detailed description of the morphology at specified time intervals will be given in Section 4.2, where the factors affecting growth are discussed. In this first section, rather, the key stages of nanowire growth are focussed upon. These stages are those that were found to occur for all anodization conditions documented within this chapter.

4.1.1 Growth initiation

In contrast to the process of electrodeposition, where a zinc precursor such as zinc acetate is present within the electrolyte solution, Zn^{+2} ions must first be sourced from the zinc anode in the case of anodization. In the very early stages of anodization this proceeds via the dissolution of the anode to form small, discrete pits over the surface of the metal, which can be observed via SEM (Figure 4.1a). This initial dissolution stage can be observed within the recorded current-time plot as an initial surge in current to what will be the current maximum for the anodization (Figure 4.2). After this stage, the current can be observed to start a steady decrease. It is at this point that nanowire growth commences.

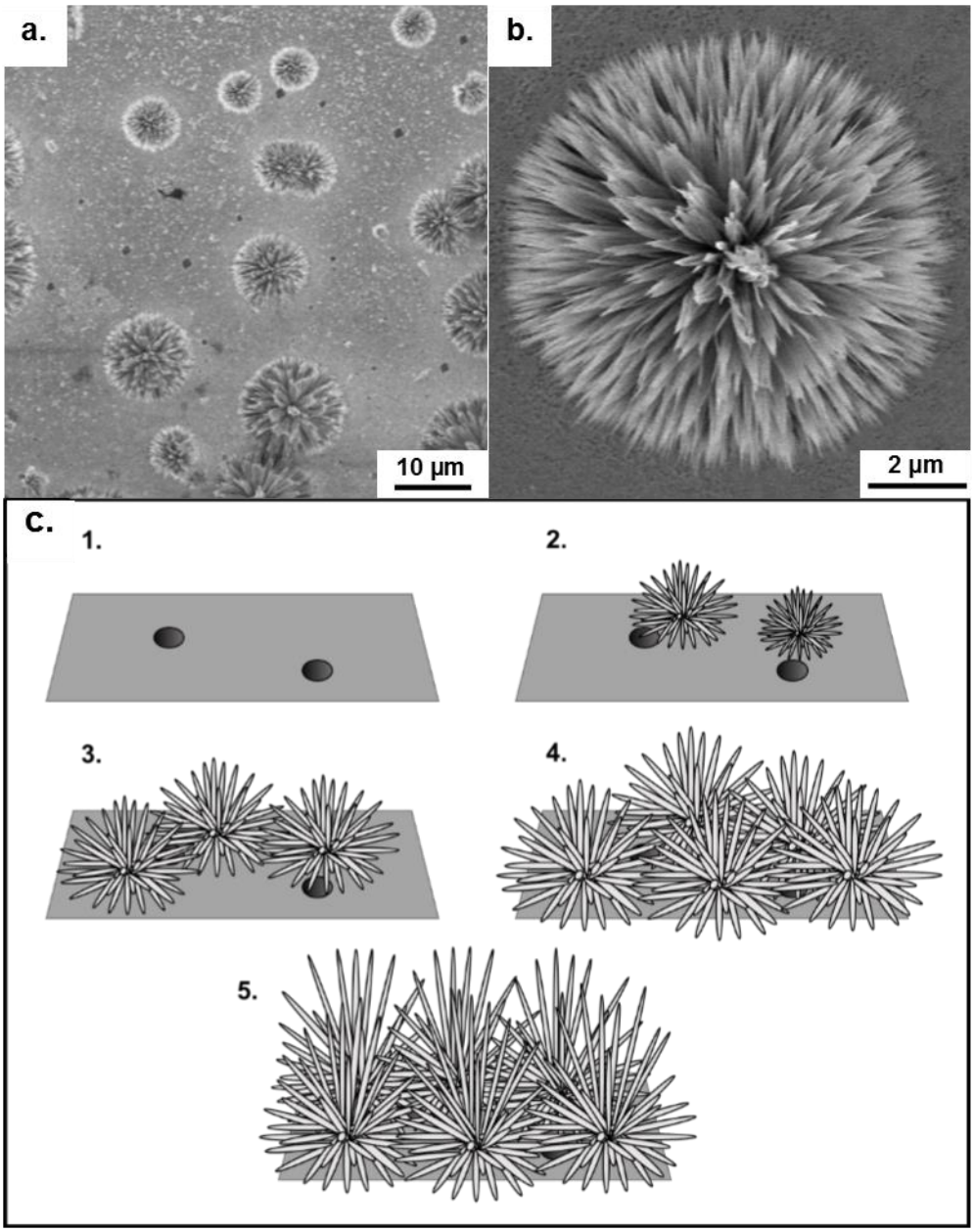

Figure 4.1. FESEM micrographs of multiple (a) and a single nanoflower (b) formed in the early growth stages and a graphical representation of the initial stages of nanowire growth (c). The stages show: (1) formation of pits within the Zn foil, (2) growth of nanoflower structures in regions of close proximity to the pits, (3) increase in both the quantity and size of nanoflowers, (4) full surface coverage of nanoflowers, and (5) inhibition of radial growth resulting in nanowire alignment.

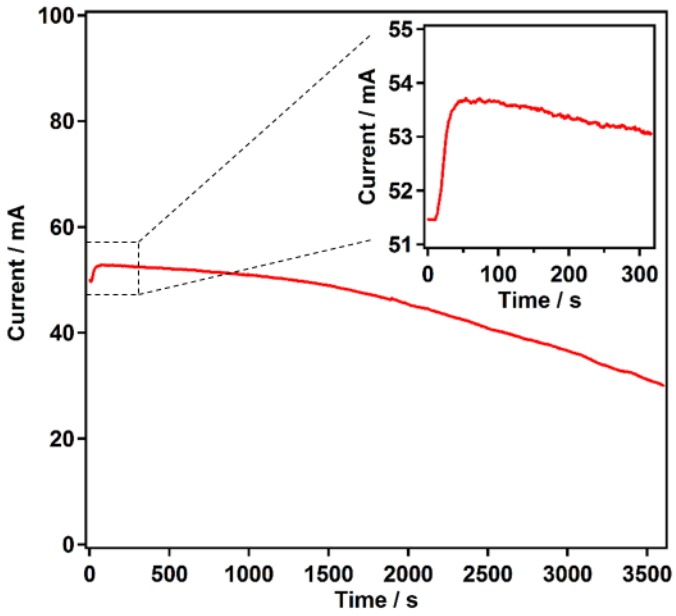

Figure 4.2. Plots of recorded anodization current over time, showing the initial surge in current (inset) followed by a gradual decay over time.

Nanowire growth first proceeds via the formation of discrete bladed structures which are here termed as nanoflowers (Figure 4.1b). Through SEM analysis it appears that nanoflower growth occurs near to, or indeed from within, the number of small pits formed from dissolution, assumedly due to the localized high concentration of Zn^{+2} ions. In these early stages of growth the multiple one-dimensional protrusions that make up the nanoflower more closely resemble blades than nanowires, with tips that taper to a point. Growth continues to proceed, both by the increase in quantity of nanoflowers over the surface and increase in the size of the nanoflowers, with growth proceeding in an ever enlarging hemisphere centred at the point of initiation. This has been demonstrated schematically in stages 1-3 in Figure 4.1c.

4.1.2 Alignment of nanowires

The next phase of growth sees the morphology transform from discrete nanoflower structures to a uniform film of aligned nanowires. SEM analysis reveals that this transition likely occurs simply via inhibited growth of nanowires that are directed parallel, or close to parallel, with the anode surface. This physical inhibition, due to overcrowding and competition for space between neighbouring nanoflowers, can be observed in Figures 4.3a and b where the ideal hemispherical shape of one nanoflower is overlapping with its neighbour. Under these conditions growth is hindered parallel to the substrate, but can proceed freely in a direction perpendicular to the substrate, leading to gradual alignment of nanowires, which is demonstrated in stages 4 and 5

within Figure 4.1c. Further crowding and overlap near to the anode eventually leads to the formation of a relatively dense bottom layer, at which point the morphology can be considered as a uniform nanowire film (Figure 4.3c).

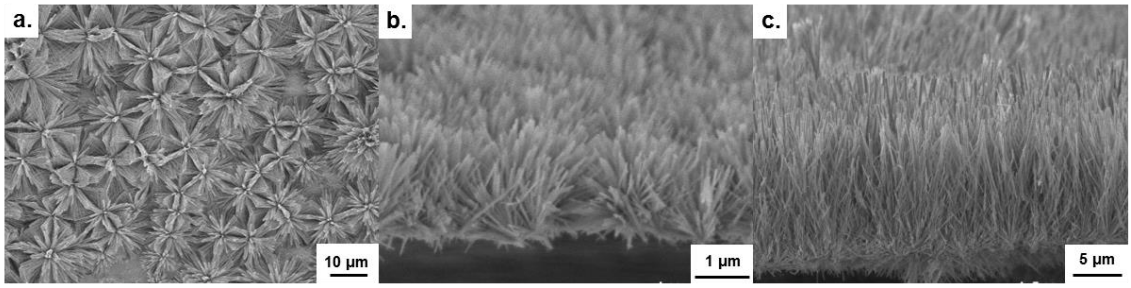

Figure 4.3. FESEM surface morphology (a) and cross-section (b) showing the complete coverage of the zinc surface with nanoflowers (5 min), eventually forming an array of aligned nanowires (c) (15 min).

4.1.3 Formation of layered films

For a period of time following the alignment phase, growth of nanowires proceeds vertically, as might be expected, with little evidence of nanowire widening. Nanowire diameters of approximately 100-150 nm can be observed in Figure 4.4a, which was typical of films in the earlier stages of growth (~5 min). After a time (~15 min), however, it could be clearly observed via SEM that much wider wire structures (300-1000 nm) emerged from the top of the relatively uniform nanowire film. These larger wires displayed a clear hexagonal structure (Figure 4.4c) that was not observed with the smaller nanowires and appeared to grow at a faster rate than the smaller nanowires. This led to the formation of a layered cross-section of the film, with an upper layer of large wires above a more densely packed layer of smaller nanowires (Figure 4.4b).

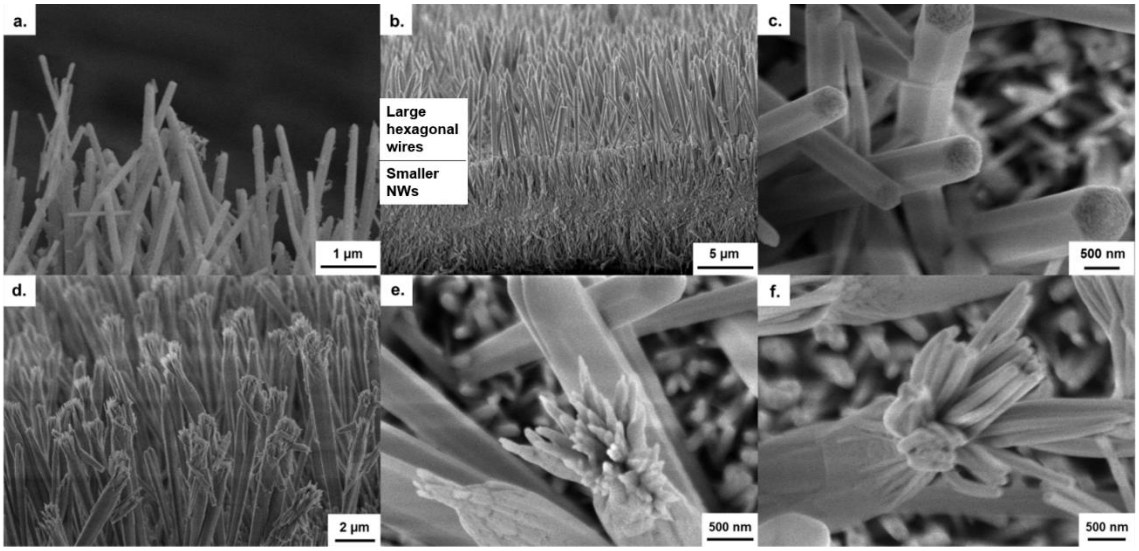

Figure 4.4. FESEM cross-sections and surface morphologies showing the initial (up to 5 min reaction time) formation of thin nanowires (a), the development of a layered structure with large hexagonal wires (b & c) and the formation of hierarchical structures (d-f).

4.1.4 Branching of nanowires

A further peculiarity in the anodization was also observed in the form of hierarchical growth. The initiation of this hierarchical growth process is shown to occur via the branching of a single large, hexagonal wire into several smaller nanowires, with diameters similar to those at the start of nanowire growth (Figure 4.4d-f). These smaller nanowires, together with the underlying nanowires, can continue growing to form very thick nanowire films (>100 µm after 2 h of anodization). At thicknesses in excess of 50 µm, however, complex 3-D networks of nanowires were typically formed rather than aligned nanowires.

The exact reasons for both the formation of layered films of different nanostructures and the formation of hierarchical structures are still currently unknown. This could possibly be related to the increasing distance from the source of Zn^{2+} ions to the nanowire tip, thereby reducing the concentration of Zn^{2+} ions available for reaction as nanowire growth proceeds. It might also be attributed to a decreasing concentration of the already dilute bicarbonate species present in the electrolyte as a function of time.

4.2 Control of Growth through Reaction Conditions

In the initial report on this anodization system by Hu *et al.,* the influence of the temperature, time and voltage on the surface morphology was examined using SEM for the $KHCO_3$ electrolyte.[209] These experiments highlighted some interesting features of the anodic growth, including the formation of spherical and lamellar structures at high temperatures (50-70°C), and also cracking of films at elevated voltages (~40 V) due to oxygen evolution beneath the nanowire films. Although these qualitative insights provided an excellent starting point in understanding this unusual growth, further quantitative measurements of the factors controlling the growth of nanostructures are necessary to be able to design bespoke nanostructures for specific applications.

In this section, the effect of altering the conditions of voltage, temperature and time on nanowire growth is examined in detail, along with the previously unstudied effects of electrolyte concentration and type. Although previous investigations in this area have reported the formation of nanowires in an aqueous $KHCO_3$ electrolyte, it was in fact found that this growth was not only possible when either sodium or ammonium bicarbonate electrolytes were used, but that growth rates were found to be significantly higher than those previously reported for $KHCO_3$.[209, 218] The major steps of growth presented in the previous section were found to be independent of the bicarbonate species used, with only slight variations in growth rates.

In the first part of this section the results from an initial study of anodization within an aqueous potassium bicarbonate electrolyte are documented. This initial study was intended to establish a range of usable reaction conditions and establish what trends in nanowire growth it was possible to investigate. The next part of the section then goes on to look in more detail at the growth of nanowires in alternative bicarbonate electrolytes, which have not previously been studied. In order to gain quantitative information on growth rates under different conditions the cross-sectional film thickness was measured, corresponding to the nanowire length, via FESEM.

4.2.1 Controlled growth in $KHCO_{3(aq)}$ electrolytes

The first stage in this investigation was to expand on the work done by Hu *et al.* on the anodization of zinc foil in an aqueous $KHCO_3$ electrolyte by going beyond qualitative evaluation and applying quantitative trends to the growth process.[209] Electrolyte concentrations of 5-50 mM were used and voltages, temperatures and times were varied. Within this initial investigation the anodization of zinc foil was undertaken under a number of different reaction conditions in order to determine which parameters have the most influence over the nanostructure morphology. The parameters studied were the applied DC voltage (V), the concentration of the aqueous electrolyte (C), the temperature of the electrolyte (T) and the length of time (t) that the anodization was maintained

for. Anodic films were produced at three different values of each parameter in order to gain basic trends in the morphology of the resultant films.

After anodization of the zinc foils it could clearly be observed that anodic growth had occurred, with the presence of a white solid over the exposed area (Figure 4.5). The appearance of the white solid varied depending on the anodization conditions used, ranging from smooth white films to rough or patchy white surfaces. It was discovered early on that the rate of stirring and type of stirrer bar used during the anodization had a significant effect on the appearance of the film and the film morphology (Figure 4.6). Therefore, care was taken throughout all experiments to maintain a constant and consistent stirring rate of approximately 100 rpm using a 30 mm rod shaped stirrer bar.

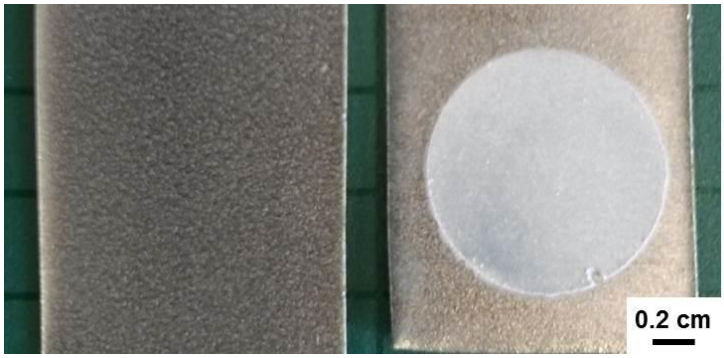

Figure 4.5. Photo of a zinc foil before and after anodization.

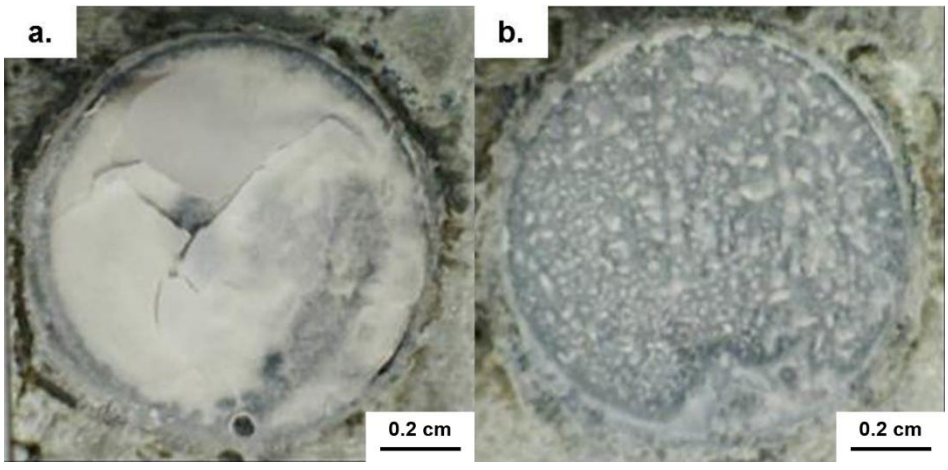

Figure 4.6. Image of an anodic film produced with stirring (a) and an anodic film produced under the same anodization conditions without stirring (b).

FESEM micrographs of the anodic films produced under different reaction conditions are shown in Figure 4.7. It was observed that nanowires were formed on the zinc foil under all of the reaction conditions examined, however the extent of the nanowire coverage and size appeared to be dependent on the reaction conditions used. It could be observed that the nanostructures formed at the lowest voltage (Figure 4.7a) and at the lowest concentration (Figure 4.7g) only partially covered the surface of the zinc foil. This partial coverage was in the form of isolated flowers of nanowires as discussed in Section 4.1.1.

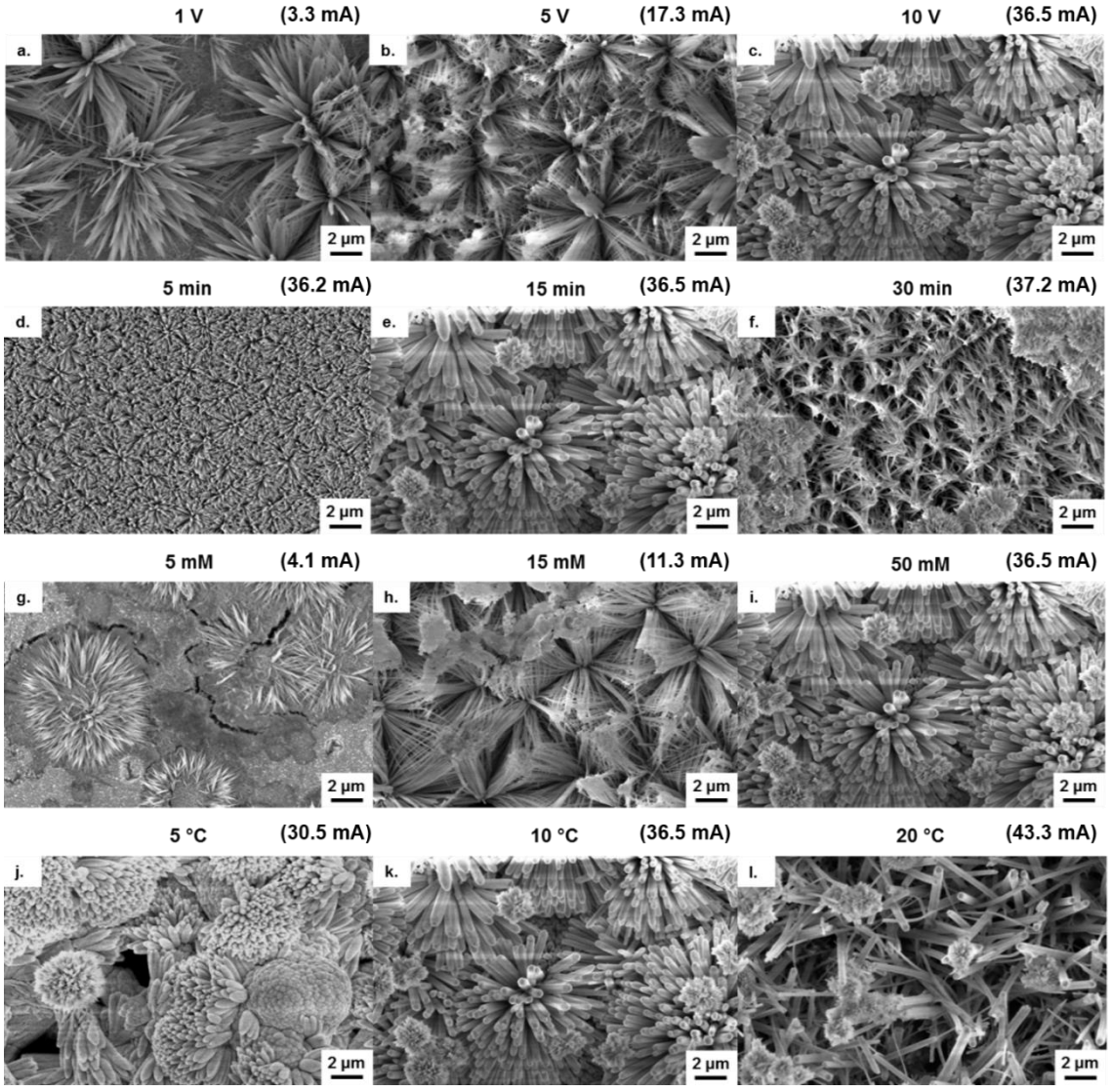

Figure 4.7. FESEM micrographs showing the effect of changing the anodization voltage (a-c), time (d-f), concentration (g-i) and temperature (j-l) on the surface morphology of the anodic films. Unless otherwise stated, the anodization conditions used were 10 V, 15 min, 50 mM $KHCO_{3(aq)}$ electrolyte concentration and 10 °C. The peak currents measured during anodization are shown in brackets.

The micrographs recorded using FESEM were analysed in order to determine any trends in nanowire diameter and also the number of nanowires present per unit area, which will be referred to as the packing density of nanowires (for full details on measurement of packing density see Section 3.6.1). Determination of the nanowire length was also considered originally, however, due to the delamination of many of the samples (Figure 4.8) leading to the formation of multiple layers, such analysis was deemed inappropriate as significant error could arise from measuring a separated layer.

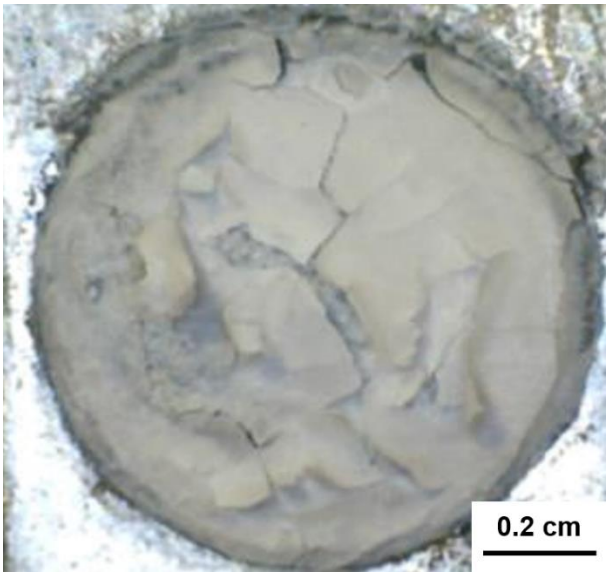

Figure 4.8. Image of the delamination of a film produced at 10 V.

The results obtained from analysis of the electron micrographs can be seen in Figure 4.9. It could be observed that a general increase in nanowire diameter is found at higher voltage, concentration and time. The nanowire diameter is generally of the order of hundreds of nanometers unless a low voltage or low concentration is used during the synthesis, in which case the diameters are of the order of tens of nanometers. When examining the effect that the reaction conditions have on the packing density of nanowires, it could be observed that two different trends occur. In the case of increasing the time or temperature, a steady decrease in packing density occurs. However, in the case of increasing the voltage or concentration a peak is reached at the intermediate value in both cases. This is largely due to the incomplete surface coverage present at both low concentration and low voltage which could be observed by FESEM (Figure 4.7). With the exception of these two results, the decrease in packing density can largely be attributed to the presence of fewer, but larger, nanowires formed at the higher end of the anodization conditions.

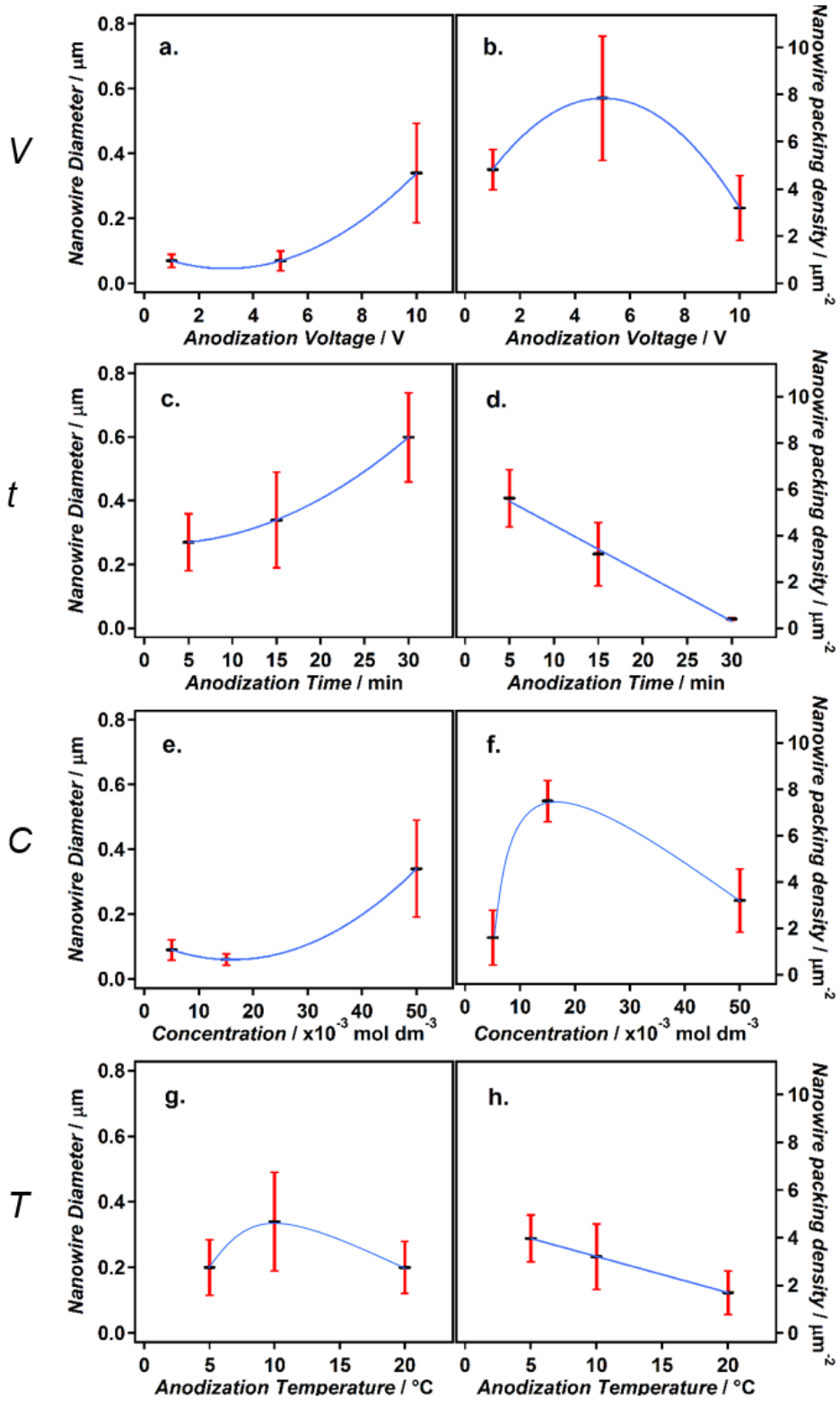

Figure 4.9. The diameters and packing density of nanowires formed at different anodization voltages (a, b), times (c, d), electrolyte concentrations (e, f), and temperatures (g, h) for films formed in a $KHCO_{3(aq)}$ electrolyte. Errors shown are a standard deviation over 20 (diameter) or 3 (packing density) measurements. Unless otherwise stated the anodization conditions used were 10 V, 15 min, 50 mM $KHCO_{3(aq)}$ electrolyte and 10 °C.

This control over both the diameter and packing density of nanostructures on the zinc surface is important, as when combined with control over the nanowire length, this would ultimately allow control over the surface area of the nanostructures. This control over nanostructure surface area is desirable for application in DSCs, where a high surface area is necessary in order to gain a high enough dye loading on the nanostructured film.

From this preliminary study it would seem that the voltage and the electrolyte concentration have very similar effects in controlling the growth of nanostructures during anodization. Changing the length of time for which the anodization is undertaken appears to have a significant effect, with an increase in nanowire diameter and decrease in packing density for longer synthesis times. The effect that the temperature has on nanowire growth, however, appears to be less clear and would require further examination.

It should be noted that although this set of preliminary experiments has been successful in showing how the reaction parameters can influence the formation of nanostructures during anodization, the large majority of films produced were unsuitable for use directly within DSCs due to the delamination of the anodic films (Figure 4.8). This occured largely at high voltages (10 V) and is possibly due to the formation of gas bubbles within the nanostructured films. Indeed, cracks indicative of such behaviour could be observed through FESEM (Figure 4.10). Although smooth films were reported by Hu *et al*. for anodizations at 10 V,[209] the difference in behaviour can likely be attributed to the differences in experimental set up used. Given the very low electrolyte concentrations used, the difference in electrode separation (10 cm for Hu *et al*. and 1 cm for this experimental set up) could make a large difference to the resistance experienced between electrodes and account for the observed differences. It was therefore decided that lower voltages would be used throughout the remainder of the study, with the aim of gaining homogeneous nanostructure coverage without cracking or delamination of the film.

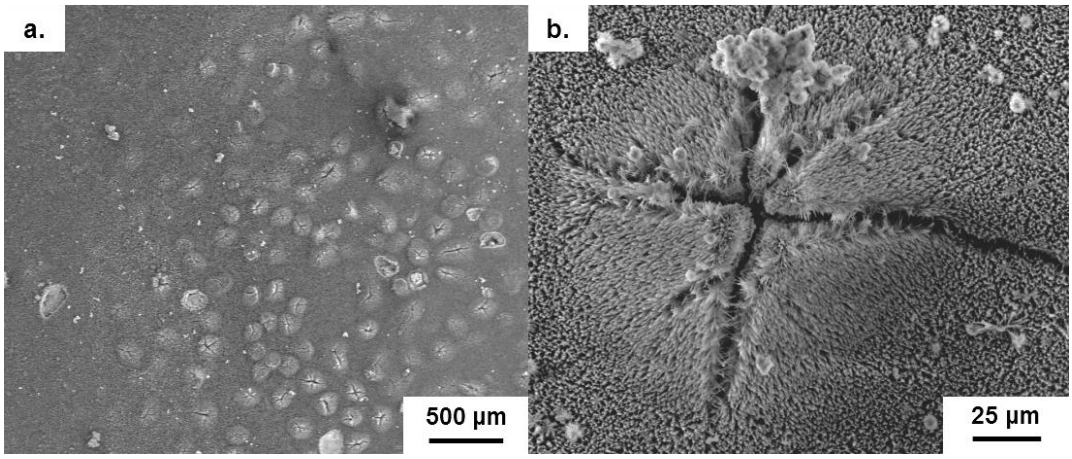

Figure 4.10. Low (a) and high (b) magnification FESEM micrographs of cracks in the nanostructured anodic films.

4.2.2 Growth in other bicarbonate electrolytes

Using the results gained from the preliminary experiments, a further examination into the anodization system was conducted by substituting the $KHCO_{3(aq)}$ electrolyte with $NaHCO_{3(aq)}$ or $NH_4HCO_{3(aq)}$. $NaHCO_3$ was chosen as, although similar to $KHCO_3$, it is a cheaper and more readily available alternative, making it an attractive choice if the synthesis of the anodic films was to be conducted on a larger scale. NH_4HCO_3 was also chosen as an interesting metal-ion free alternative. Although speculative, the possibility of nitrogen incorporation from the ammonium ion into the nanostructures was also attractive for producing doped ZnO. The aim of these experiments was to determine whether nanowire formation occurs regardless of the bicarbonate species used in the electrolyte, and if so, whether there are any differences in the nanostructures formed.

The reaction parameters of voltage, temperature, concentration and time were again examined in order to deduce any resultant trends. However, rather than examining the changes in nanowire diameter and packing density, a focus was put on the change in nanowire length, or film thickness, as a result of changing the reaction parameters. Nanowire length was chosen due to it having a significant impact on the film surface area and also because it is less prone to measurement error, owing to the length scales being significantly larger than those of the nanowire diameter. A focus was also made on identifying suitable films for application in DSCs. Such films would require a high surface area in the form of high aspect ratio nanowires and a homogeneous, defect free surface.

Effect of growth time

The effect of time on nanowire growth was investigated by fixing the voltage, electrolyte concentration and temperature at 5 V, 50 mM and 10 °C respectively whilst anodizing for different lengths of time, between 1 and 120 minutes. As might be expected, longer anodization times led to longer nanowires, as shown in the SEM surface morphologies (Figure 4.11), cross-sections (Figure 4.12) and graphically in Figure 4.13. The evolution of a layered cross-section, with wider nanowires appearing between 5 and 15 minutes, is apparent in the case of both electrolytes, as discussed in Section 4.1.3. Only slight deviations in film thickness are obtained between the two electrolytes, with growth in the NH_4HCO_3 electrolyte appearing to slow over time, perhaps due to slow depletion of the electrolyte species.

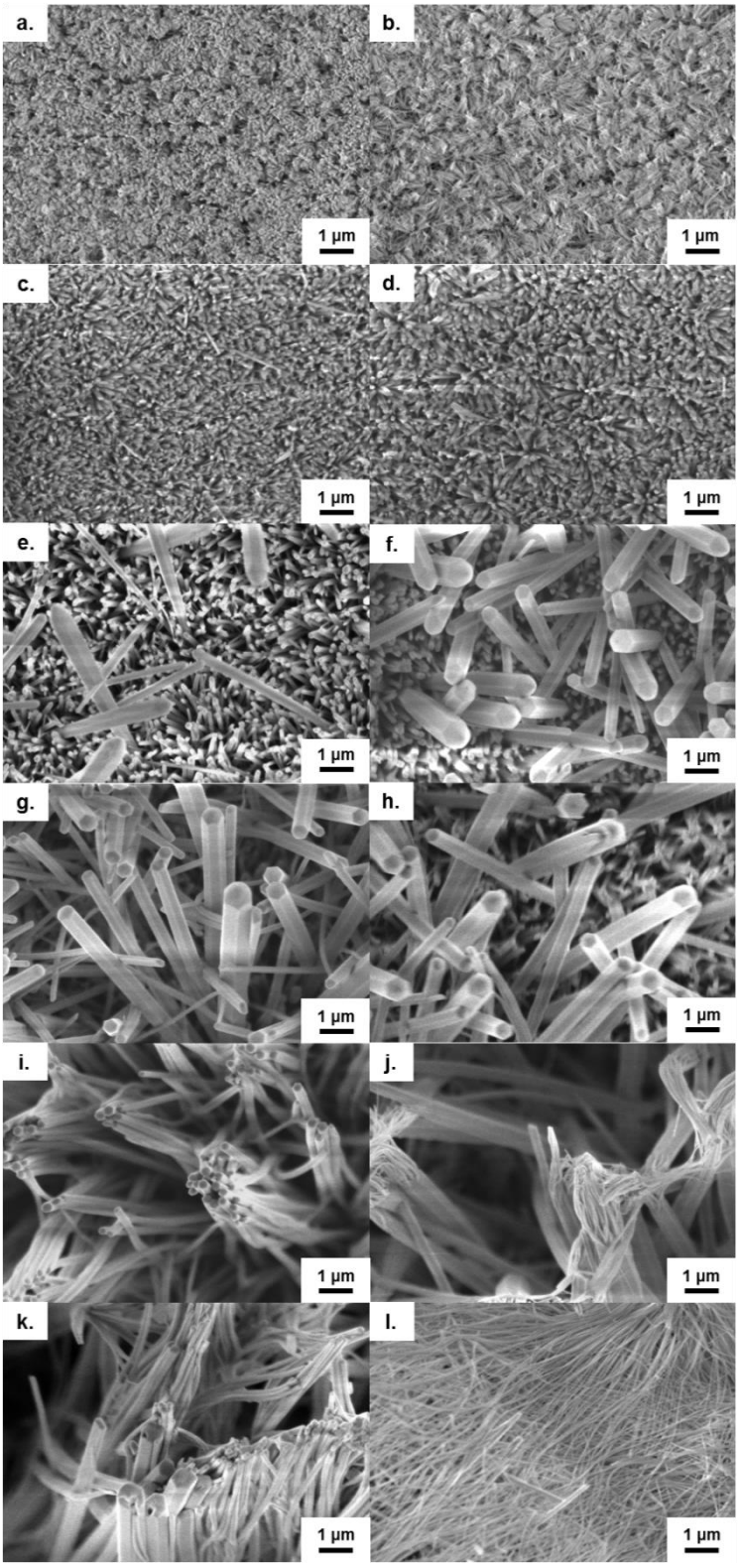

Figure 4.11. FESEM micrographs of the surfaces of nanowire films produced via anodization in aqueous $NaHCO_3$ for times of 1 (a), 5 (c) 15 (e), 30 (g), 60 (i) and 120 min (k). The corresponding films produced in aqueous NH_4HCO_3 are also shown (b, d, f, h, j & l). All films were produced under constant reaction conditions of 5 V, 10 °C and 50 mM electrolyte concentration.

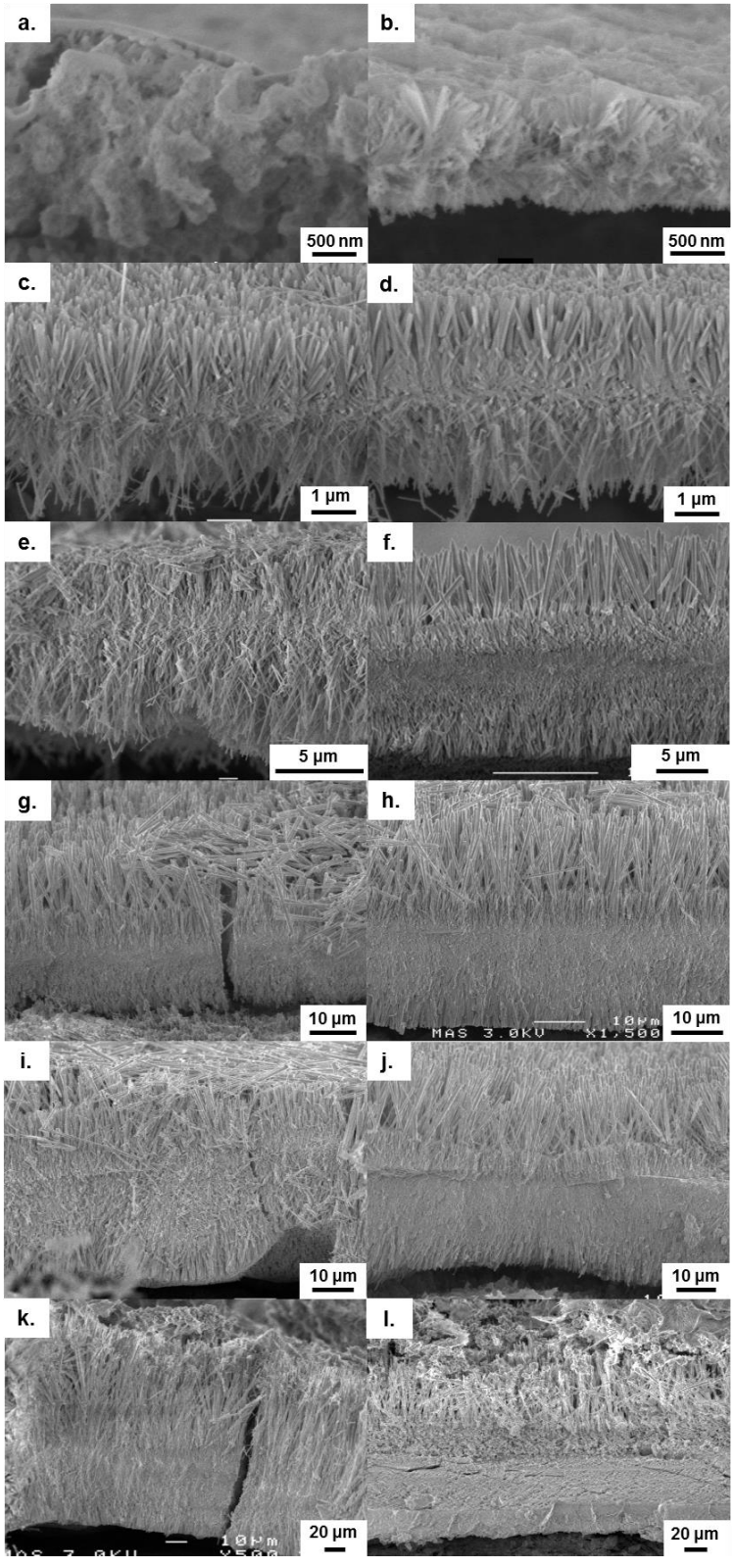

Figure 4.12. Cross-sectional FESEM micrographs of nanowire films produced via anodization in aqueous $NaHCO_3$ for times of 1 (a), 5 (c) 15 (e), 30 (g), 60 (i) and 120 min (k). The corresponding films produced in aqueous NH_4HCO_3 are also shown (b, d, f, h, j & l). All films were produced under constant reaction conditions of 5 V, 10 °C and 50 mM electrolyte concentration.

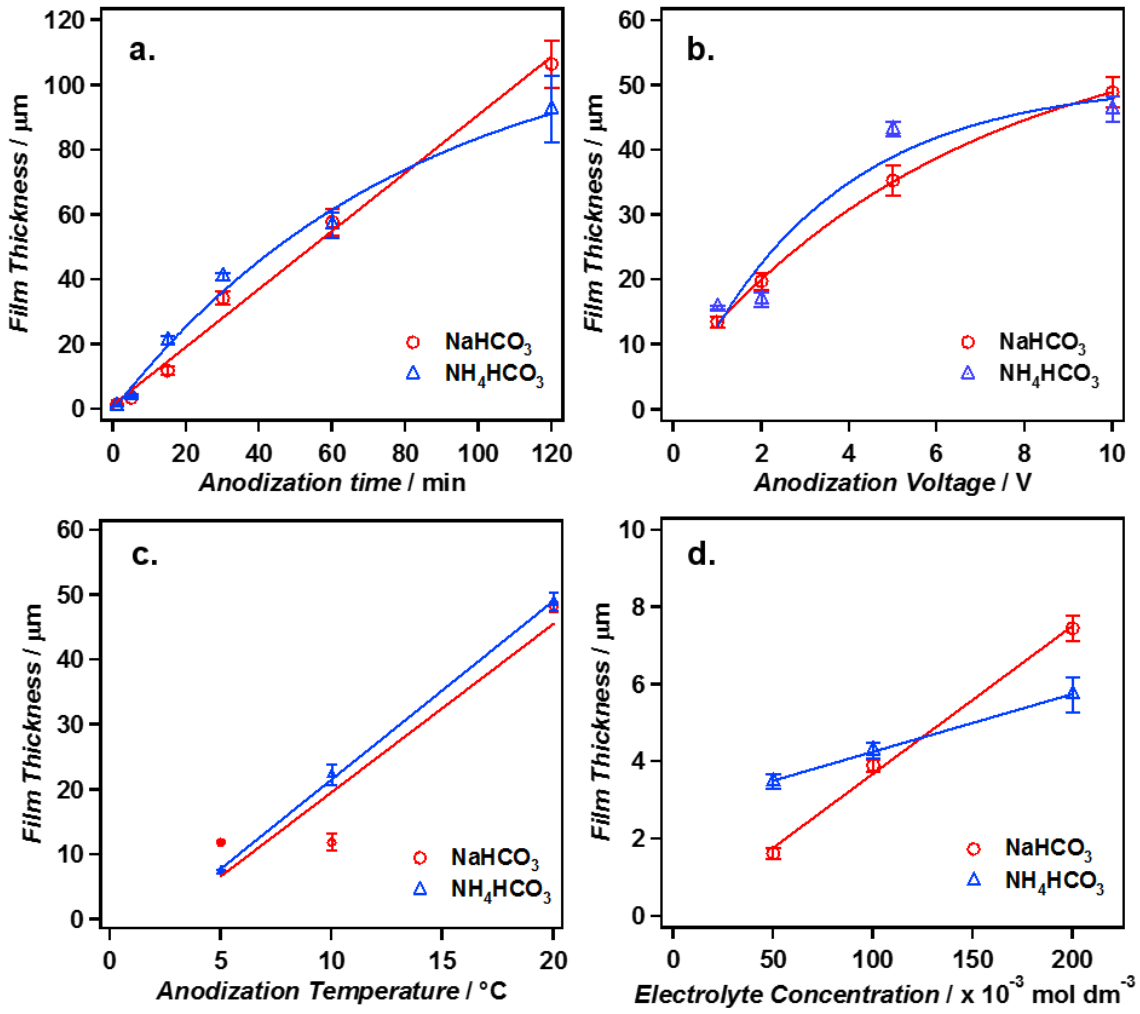

Figure 4.13. Plots of nanowire film thickness, measured through analysis of the cross-sections via FESEM, for different anodization times (a), voltages (b), temperatures (c) and electrolyte concentrations (d) in $NaHCO_3$ or NH_4HCO_3 electrolytes. Unless otherwise stated, anodizations were carried out under conditions of 5 V, 10 °C, 50 mM electrolyte concentration and for 15 min. The error bars represent the standard deviation based upon five measurements at each condition.

By examining the plot of typical film thicknesses versus the anodization time (Figure 4.13a) it can be seen that growth rates are around 1 µm min^{-1} up until 60 minutes. It was found that relatively smooth and homogeneous growth of nanostructures occurred up until 60 minutes. From this point on, further growth appeared to be randomly orientated, with disordered arrays of tangled nanowires on the film surface. This can be seen in more detail in the electron micrographs taken of the film surfaces (Figure 4.11). The point at which larger nanostructures emerge from the layer of smaller nanowires can also be observed in these images (Figure 4.11e & f) at times of approximately 15 minutes. These larger nanostructures appear to split up into a large number of smaller nanowires after ~60 minutes, forming hierarchical structures (Figure 4.11i & j) as discussed previously in Section 4.1.4.

Control of temperature

The next parameter to be examined was the reaction temperature. In the preliminary study using $KHCO_{3(aq)}$, little information could be drawn from the results about the effect of changing the temperature on nanostructure formation. However, by examining the surface morphologies and cross-sections of the films formed at different temperatures for the $NaHCO_{3(aq)}$ and $NH_4HCO_{3(aq)}$ electrolytes (Figures 4.14 and 4.15) it can clearly be observed that the reaction temperature has a significant effect on the rate of nanowire growth. Within the plot of the typical film thicknesses against the reaction temperature (Figure 4.13) it can be seen that growth rate can be increased by approximately five times by a temperature increase of just 15 °C. The results show a linear trend, with the exception of an anomalous result for the $NaHCO_3$ electrolyte at 10 °C. This anomalous result can possibly be attributed to film damage after anodization which can be observed in Figure 4.15c. The use of near ambient temperatures (20 °C) allowed extremely high nanowire growth rates of 3.2 μm min^{-1} to be achieved. These growth rates are significantly higher than those previously reported for anodization of zinc in a $KHCO_3$ electrolyte, which were 0.5 and 1.3 μm min^{-1}.[209, 218]

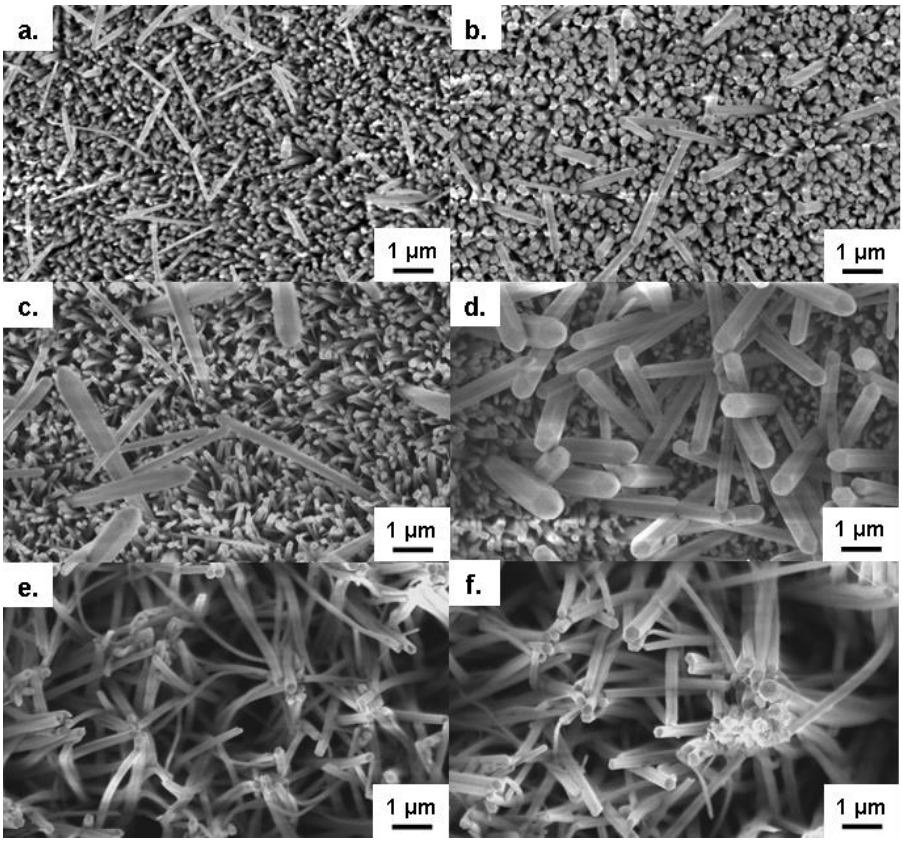

Figure 4.14. FESEM surface morphologies of nanowire films produced via anodization in aqueous $NaHCO_3$ at temperatures of 5 (a), 10 (c) and 20 °C (e). The corresponding films produced in aqueous NH_4HCO_3 are also shown (b, d & f). All films were produced under constant reaction conditions of 15 minutes, 5 V and 50 mM electrolyte concentration.

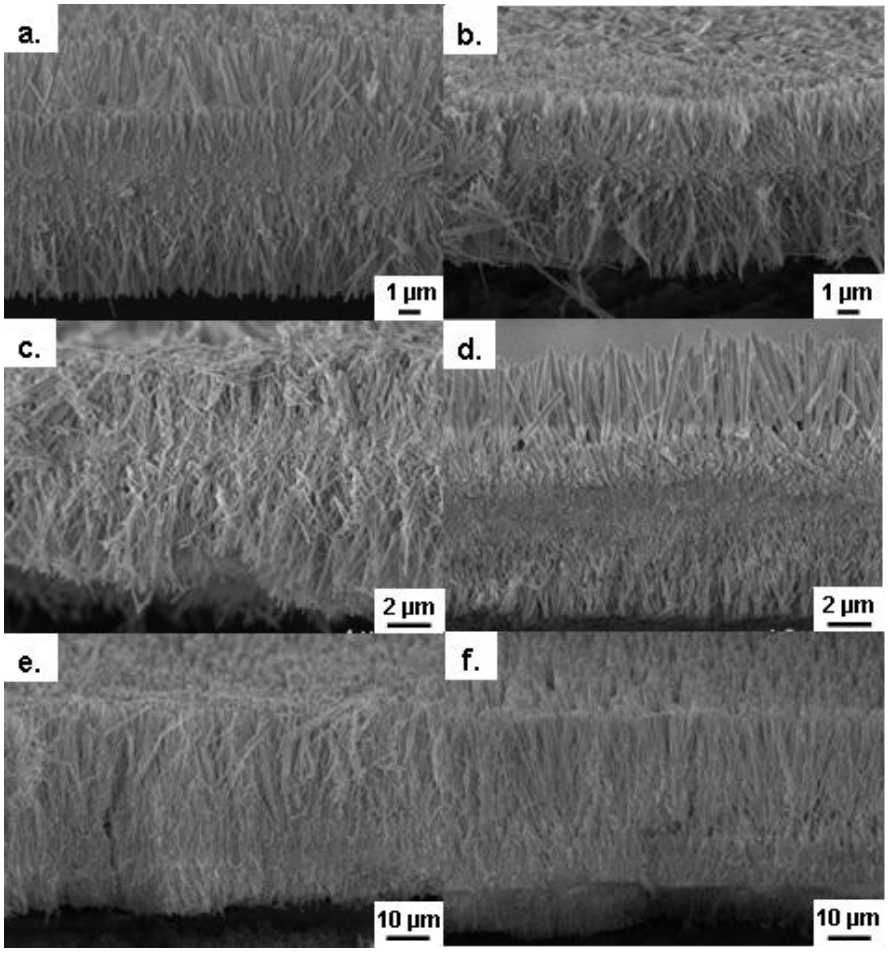

Figure 4.15. Cross-sectional FESEM micrographs of nanowire films produced via anodization in aqueous $NaHCO_3$ at temperatures of 5 (a), 10 (c) and 20 °C (e). The corresponding films produced in aqueous NH_4HCO_3 are also shown (b, d & f). All films were produced under constant reaction conditions of 15 minutes, 5 V and 50 mM electrolyte concentration.

These high growth rates were achieved without causing damage to the film, which is observed when applying high voltages. It is here therefore proposed that the anodization temperature is the most useful parameter to use to control the growth rate of nanowire films. This result is significant as it shows that a large increase in growth rate can be achieved by a minor alteration in temperature. It is also promising if scale-up of production was to be considered, as near room temperature conditions would allow a simpler setup to be used and reduce the energy consumption involved with cooling a large electrolyte bath.

From the plot of nanowire film thickness *vs.* anodization temperature (Figure 4.13c) it was possible to determine the activation energies of the anodizations in each electrolyte from the Arrhenius equation:

$$k = Ae^{\left(\frac{-Ea}{RT}\right)} \qquad \text{Eq. 4.1}$$

Where k is the rate constant (inferred from the nanowire film thickness), A is the pre-exponential factor, E_a is the activation energy, R is the universal gas constant and T is the temperature in Kelvin. By taking the natural logarithm of each side the following expression is obtained:

$$\ln(k) = \frac{-E_a}{R} \cdot \frac{1}{T} + \ln(A) \qquad \text{Eq. 4.2}$$

Using this expression, the activation energy was determined by plotting the natural logarithm of the rate constant against the reciprocal of temperature and calculating the gradient (Figure 4.16). Values of 68 ± 24 kJ mol^{-1} and 81 ± 23 kJ mol^{-1} were gained for the activation energies of nanowire formation in the $NaHCO_3$ and NH_4HCO_3 electrolytes respectively, which are within error of each other. This might indicate that that the nature of the cation in the electrolyte has little influence on the mechanism of nanowire growth.

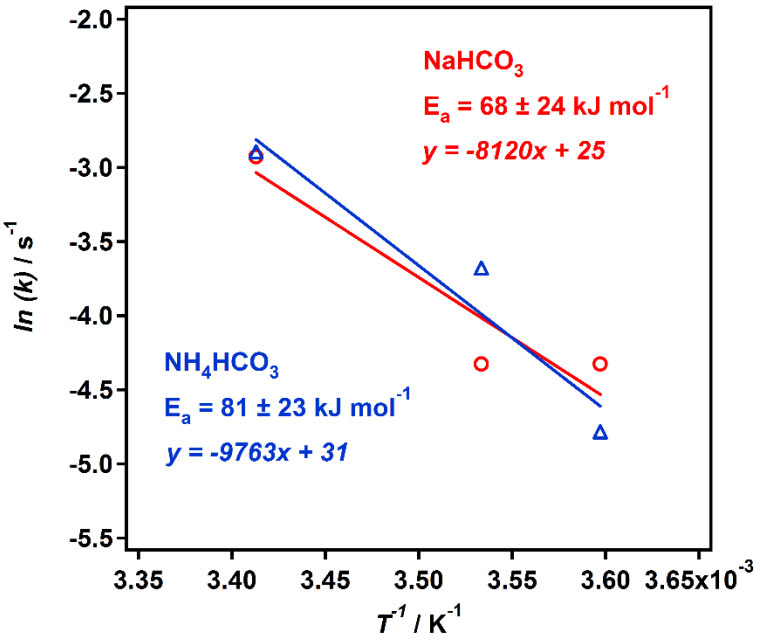

Figure 4.16. Arrhenius plot of the natural logarithm of the rate constant (inferred from the nanowire film thickness) *vs.* the reciprocal of the anodization temperature for anodizations undertaken in either $NaHCO_3$ or NH_4HCO_3 electrolytes.

Control of voltage

In order to examine the effect of the anodization voltage all of the other reaction parameters were kept constant at 30 minutes, 10 °C and 50 mM electrolyte concentration, and films were produced at voltages of 1, 2, 5 and 10 V. It was observed that nanowire formation occurred at all applied voltages for both the $NaHCO_{3(aq)}$ and $NH_4HCO_{3(aq)}$ electrolytes (Figure 4.17). For anodizations conducted at 1 V it was found that incomplete surface coverage occurred, whilst at 10 V rough and inhomogeneous films were formed with severe delamination occurring; a result that is in

agreement with those obtained for the $KHCO_{3(aq)}$ electrolyte. However, films produced at 2 V and 5 V were found to possess smooth anodic films with no cracking present on the surface. As homogeneous nanowire films are typically desired for photovoltaic applications, it is therefore important to select suitable voltages in the range of 2-5 V for nanowire film formation.

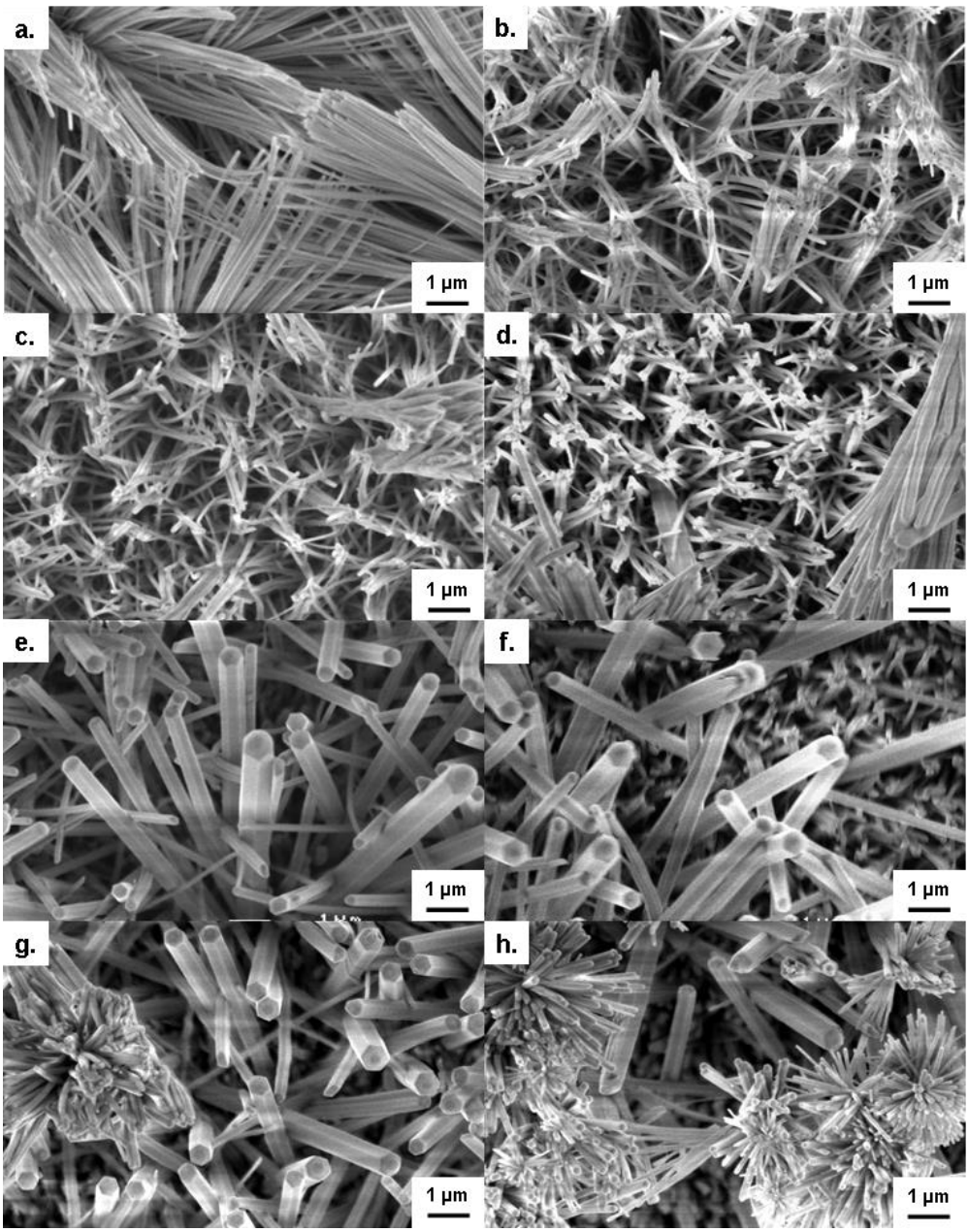

Figure 4.17. FESEM surface morphologies of nanowire films produced via anodization in aqueous $NaHCO_3$ at applied voltages of 1 (a), 2 (c), 5 (e) and 10 V (g). The corresponding films produced in aqueous NH_4HCO_3 are also shown (b, d, f & h). All films were produced under constant reaction conditions of 30 minutes, 10 °C and 50 mM electrolyte concentration.

Cross-sectional electron micrographs of the films produced at different anodization voltages are shown in Figure 4.18. It can be seen that in both the cases longer nanowires are formed at higher anodization voltages. The films formed at 1 V or 2 V appear to be formed entirely of a single layer of thinner nanowires which are aligned perpendicular to the substrate surface. At 5 and 10 V, the films consist of a densely packed lower layer of thinner nanowires with thicker nanowires emerging from this layer to form an upper layer. The reasons for this structuring is not entirely clear, however, the structure arising is attractive for application in DSCs due to the combination of a high surface area layer of densely packed thin nanowires coupled with a layer of thicker nanowires that could provide enhanced light scattering.

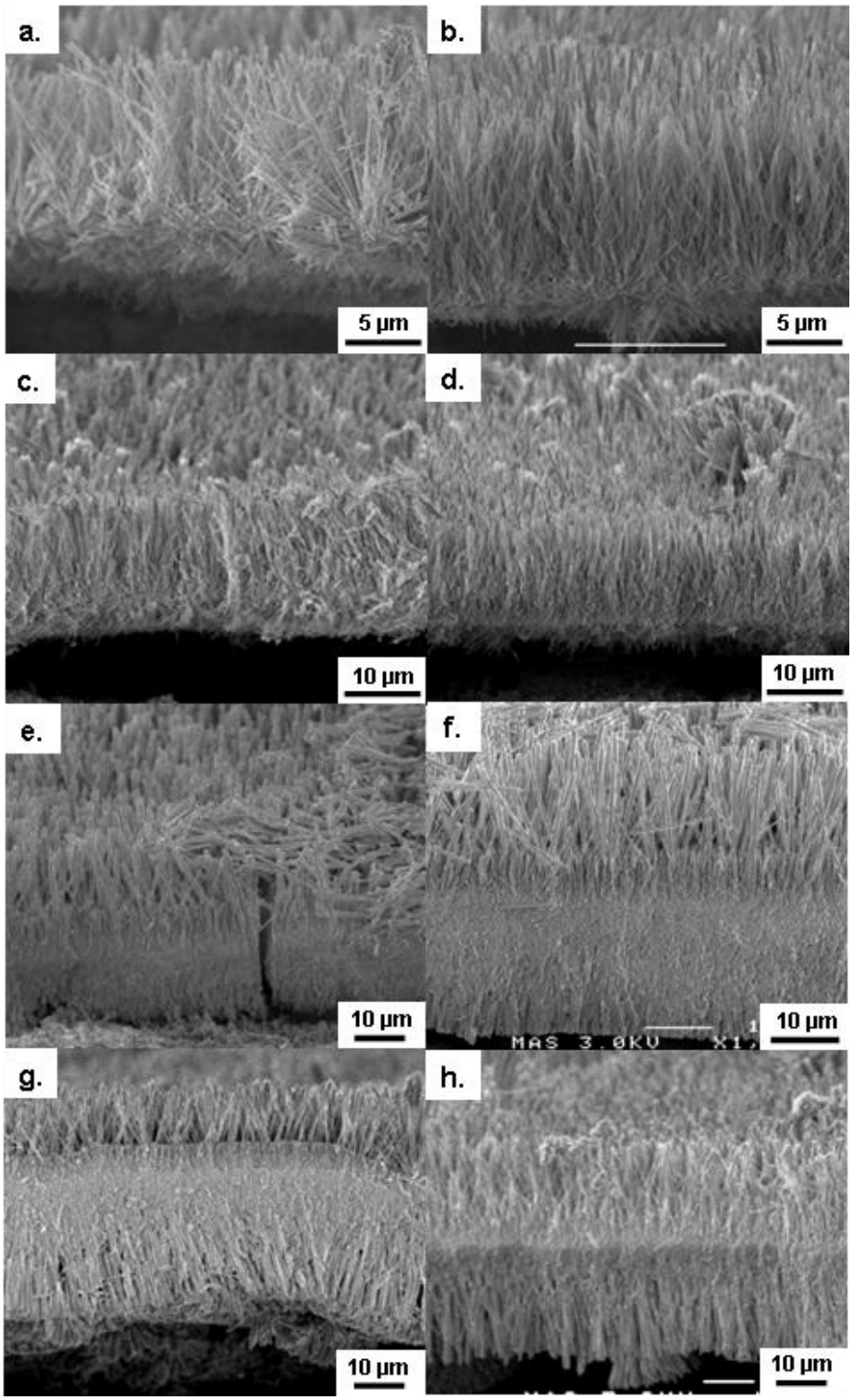

Figure 4.18. Cross-sectional FESEM micrographs of nanowire films produced via anodization in aqueous $NaHCO_3$ at applied voltages of 1 (a), 2 (c), 5 (e) and 10 V (g). The corresponding films produced in aqueous NH_4HCO_3 are also shown (b, d, f & h). All films were produced under constant reaction conditions of 30 minutes, 10 °C and 50 mM electrolyte concentration.

The typical thicknesses of the anodic films produced at different voltages have been plotted for both electrolytes for comparison (Figure 4.13). From this plot it can be observed that the overall growth rate of nanowires in these two electrolytes is relatively similar, with the largest discrepancy occurring for the films produced at 5 V. It can be observed, particularly in $NH_4HCO_{3(aq)}$, that there is a smaller increase in growth rate between 5 and 10 V. This is likely to be due to the delamination observed at the higher of these two voltages, where it can be assumed that growth of nanostructures halts, or at least slows, after detachment of the film from the zinc substrate. Anodic growth would then continue on the newly exposed zinc surface. It was possible to observe the exposure of a new zinc surface in the current-time plots recorded during anodization, where a sharp increase in current would occur during a relatively gentle decrease in current over time which arises from film growth.

Control of concentration

Next, the effect of changing the electrolyte concentration on the formation of nanostructures was examined. Originally a set of experiments were conducted in which the reaction conditions were kept constant at 5 V, 10 °C for 15 minutes and the concentration of the electrolyte was varied. In these experiments it was found that increasing the concentration resulted in significant fracturing and delamination of the anodic films, similarly to what was observed at voltages of 10 V. Due to the difficulty of analysing these films, a new set of experiments were conducted at lower voltage (2 V) and for shorter times (5 minutes) in order to examine the effect of changing the electrolyte concentration within a region of reaction conditions that did not give rise to the extensive fracturing previously observed. Electrolyte concentrations of 50, 100 and 200 mM were examined and nanostructure formation occurred in all three cases (Figure 4.19). Smooth, thin films were gained at the lower two concentrations, whilst some minor delamination occurred at higher concentrations.

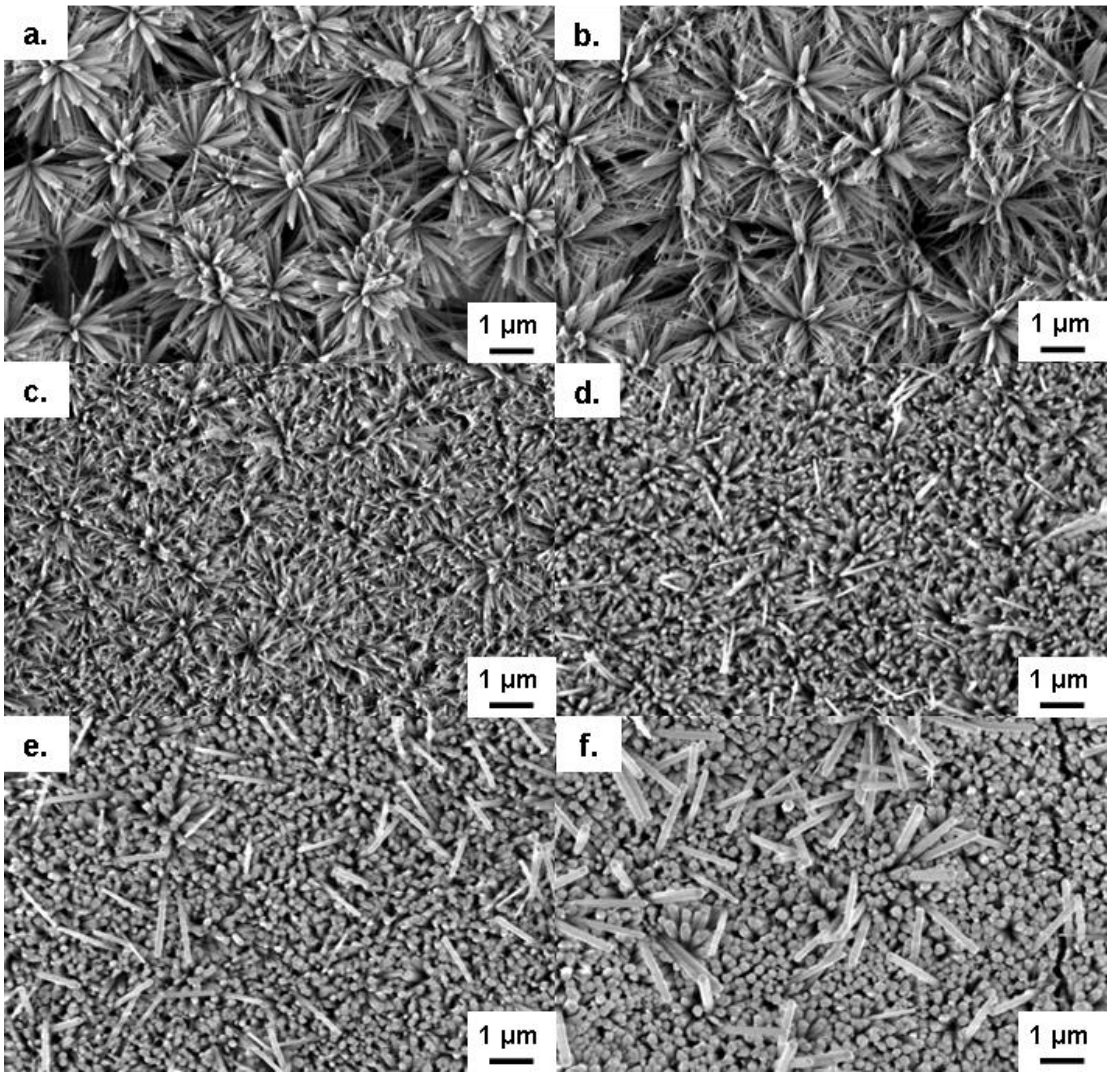

Figure 4.19. FESEM surface morphologies of nanowire films produced via anodization in aqueous $NaHCO_3$ at concentrations of 50 (a), 100 (c) and 200 mM (e). The corresponding films produced in aqueous NH_4HCO_3 are also shown (b, d & f). All films were produced under constant reaction conditions of 5 minutes, 2 V and 10 °C.

Examination of the cross-sections by FESEM (Figure 4.20) revealed that all of the nanostructured films formed were very thin (<10 µm). Despite the films being thin, an increase in film thickness with increasing the electrolyte concentration could be observed in the case of both electrolytes (Figure 4.13). Although a trend clearly exists, it is difficult to compare the extent of the effect concentration has on nanostructure growth with the differences occurring whilst changing the other parameters, due to the low voltages and short times used. From the previous experiments undertaken at higher voltages it appears to be clear that changing the concentration has a significant effect, similarly to changing the voltage. It also seems apparent that gaining homogeneous nanowire arrays with a high growth rate is unlikely to be possible at higher concentrations due to the damage occurring through fracturing and delamination of the films.

Focus would therefore be better placed on using lower concentrations. In light of this, it is again proposed that temperature might be a more useful variable in controlling the growth rate of the nanowire films using this anodization system.

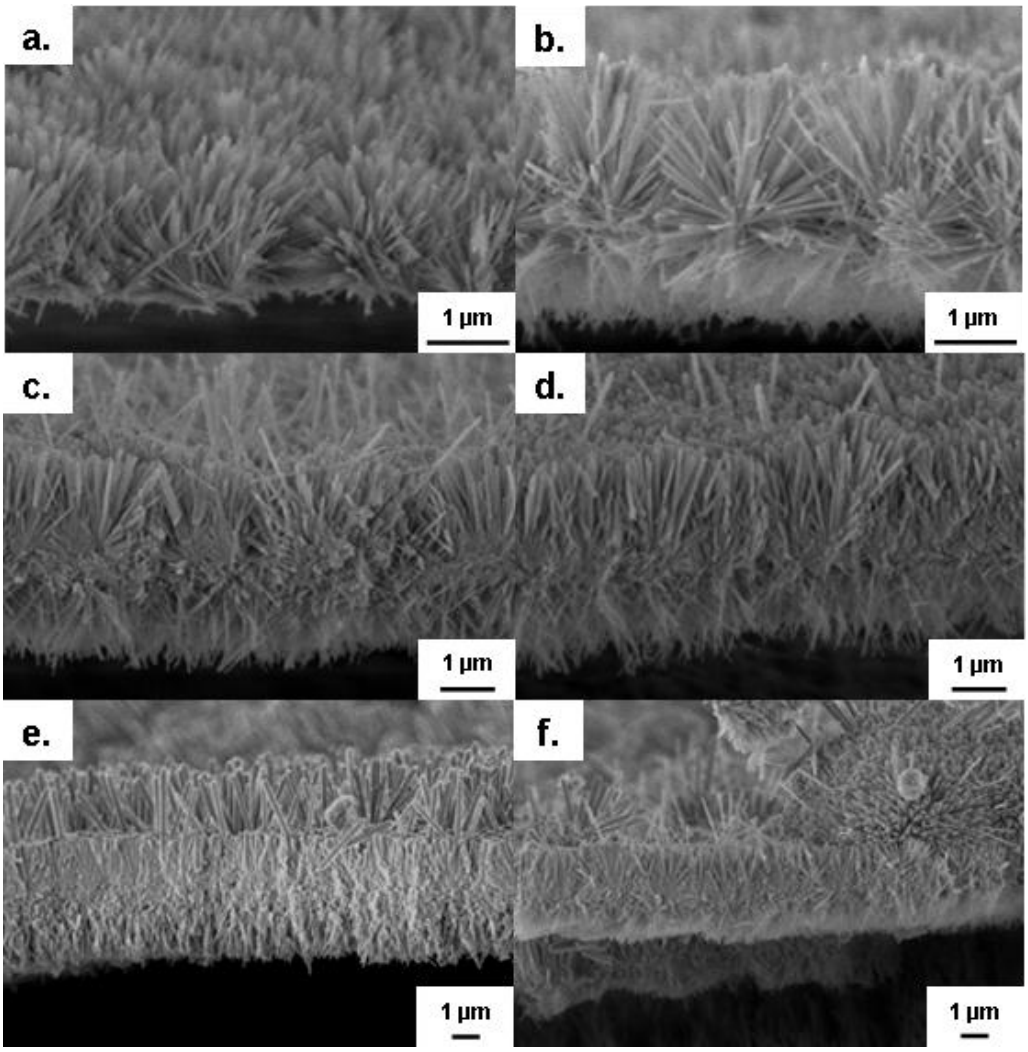

Figure 4.20. Cross-sectional FESEM micrographs of nanowire films produced via anodization in aqueous $NaHCO_3$ at concentrations of 50 (a), 100 (c) and 200 mM (e). The corresponding films produced in aqueous NH_4HCO_3 are also shown (b, d & f). All films were produced under constant reaction conditions of 5 minutes, 2 V and 10 °C.

4.3 Conversion to ZnO

4.3.1 Thermal degradation of nanowires

In the previous report by Hu *et al.* some unusual results were reported for the as-prepared nanowires.[209] Whilst the annealed films were found to consist of polycrystalline ZnO (wurtzite), XRD patterns indicated that the as-prepared nanowire films before annealing consisted of highly crystalline nanowires with a pattern that could not be indexed to a known compound. They suggested that the nanowires might be some form of $Zn(CO_3)_n(OH)_m$, based upon the ions present in the electrolyte, but no further investigation was carried out. Subsequent studies on anodization carried out under similar conditions have described the nanowires prior to annealing as being composed of either $Zn(OH)_2$ or ZnO but with little evidence to support this.[219, 229]

In order to examine the differences between the as-prepared nanostructures and the structures after annealing, a number of different analysis methods were used to characterise films produced under equivalent conditions, both with and without annealing the nanostructures after anodization. In all cases the nanowire films were produced under anodization conditions of 5 V, 20 °C, 15 min and 50 mM $NaHCO_{3(aq)}$ electrolyte. The first method used to examine the two nanowire films was FESEM. Electron micrographs of the surface morphology were recorded for these samples both before and after annealing (Figure 4.21) and little difference in the overall nanostructure could be observed. This confirms that the material maintains its one-dimensional nanowire structure during heating.

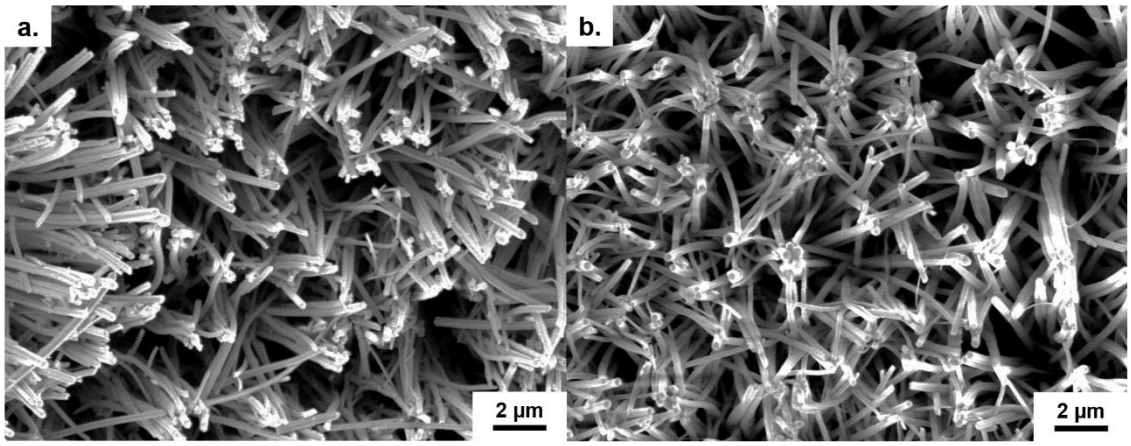

Figure 4.21. FESEM surface morphologies of the anodic nanowire films before (a) and after (b) annealing at 300 °C for 1 h.

The as-prepared and annealed films were then examined by XRD. It could clearly be observed that the patterns produced before and after being annealed were very different (Figure 4.22). Powder x-ray diffraction (pXRD) patterns of the nanowire films prior to annealing display

a complex set of sharp peaks, indicating a highly crystalline material. This is consistent with the observation of smooth hexagonal nanowires via FESEM. The peaks were not found to match with either ZnO, $Zn(OH)_2$ or $ZnCO_3$ and neither were they found to match with known hydroxy carbonates of zinc, $Zn_5(CO_3)_2(OH)_6$ and $Zn_4CO_3(OH)_6 \cdot H_2O$. Given the complex nature of the pattern, it seems possible that a mixture of different unidentified materials of the type $Zn(CO_3)_n(OH)_m$ could be present. Although four of the most dominant peaks are present both before and after annealing, these can be attributed to the zinc substrate that the nanowires are grown on. For the annealed film, broad peaks can be observed which match with the wurtzite structure of ZnO and no trace of the unexplained sharp peaks are present. The broadness of these peaks indicates that these nanowires are in fact polycrystalline after annealing.

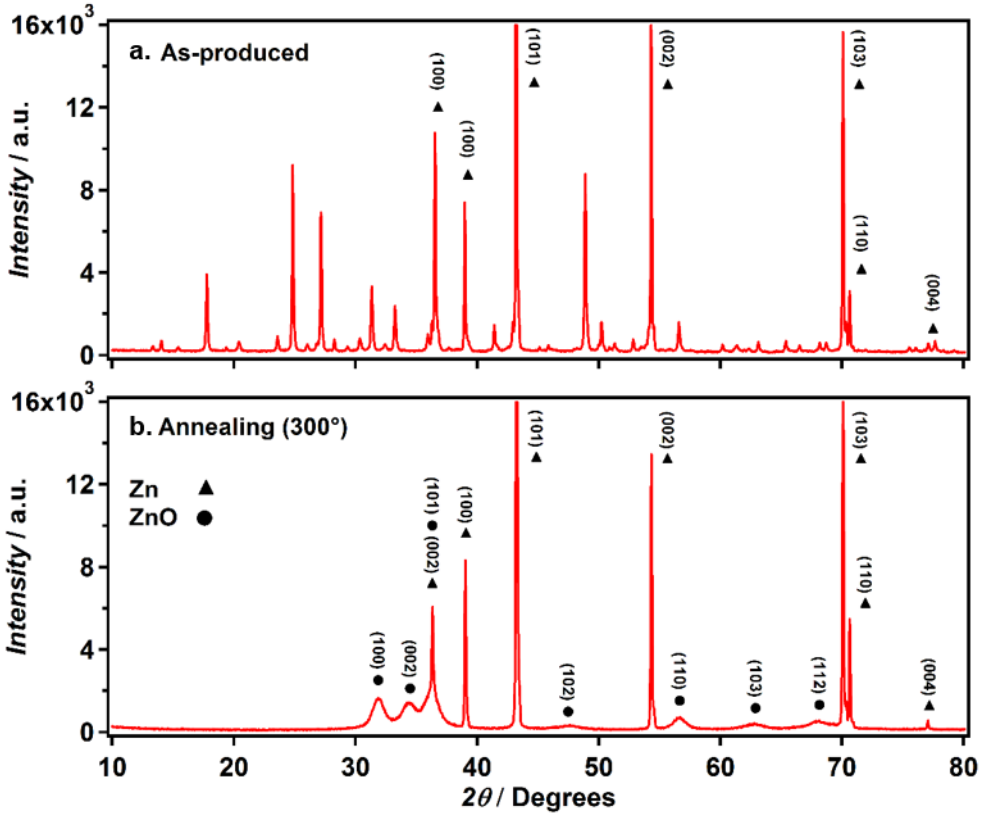

Figure 4.22. Flat plate powder XRD patterns for nanowire films obtained directly from anodization (a) and after annealing at 300 °C for 1 h (b).

In order to gain further information about the structure and chemical composition of the nanowires prior to annealing a range of spectroscopic techniques were applied to analyse the materials. The x-ray photoelectron spectrum (XPS) of the as-prepared nanowire film reveals a significant quantity of carbon present in addition to the expected zinc and oxygen (Figure 4.23). A small quantity of iron could also be detected, which is likely to originate from the stainless steel counter electrode in the anodization setup. Analysis of the C1s region of the x-ray photoelectron

spectrum reveals two peaks: A peak at lower energy attributed to adventitious carbon contamination, and a peak at slightly higher energy within the region often attributed to a metal carbonate. The latter peak is slightly shifted to higher energy compared to a typical metal carbonate which is consistent with a hydrocarbonate species.[239] Since no peaks attributable to Na 1s are present it can be assumed that the hydrocarbonate peak is not due to remaining $NaHCO_3$ from the electrolyte.

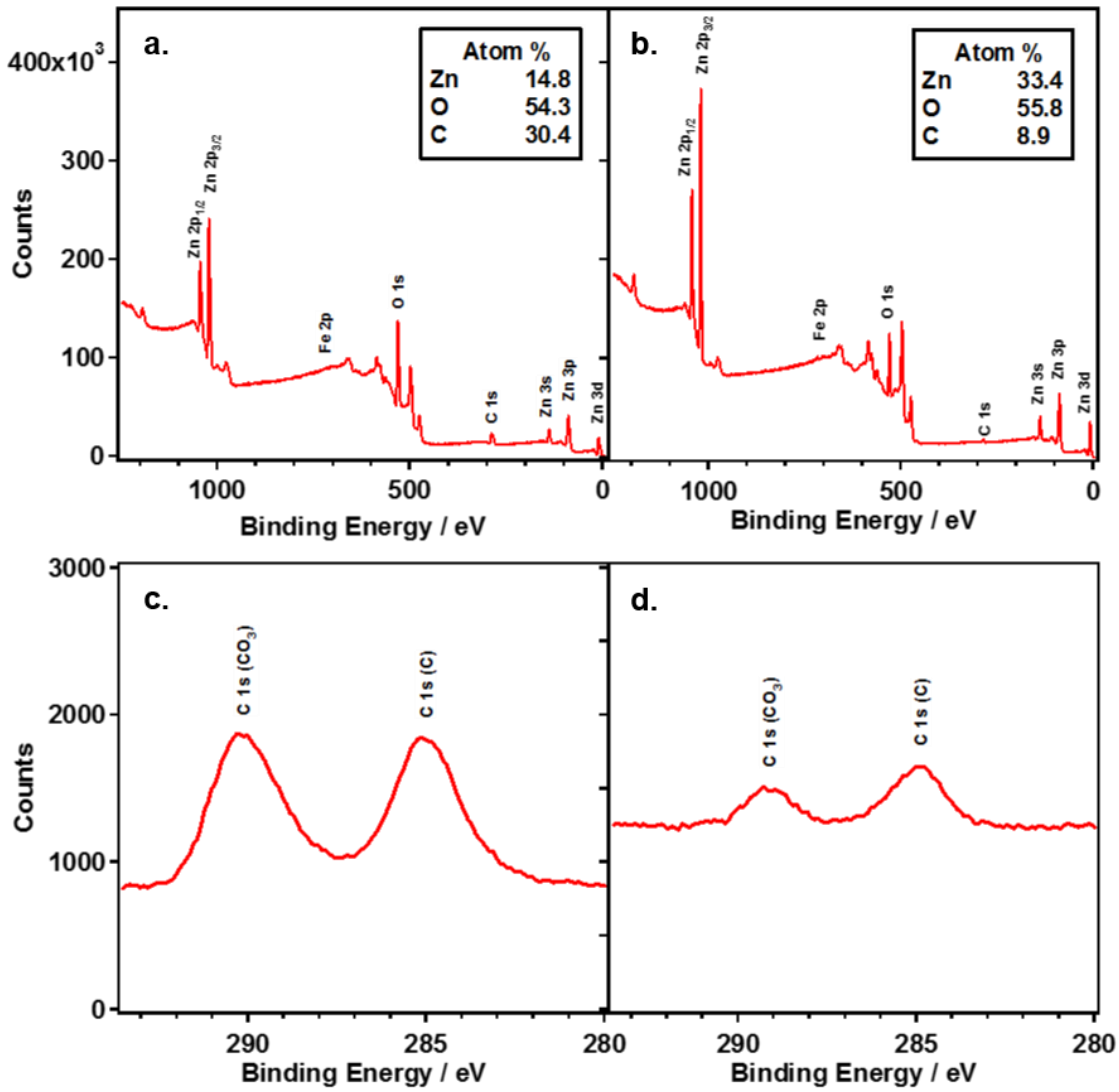

Figure 4.23. XPS survey spectra and C1s region spectra for nanowire films obtained directly from anodization (a & c) and after annealing at 300 °C (b & d)

Fourier transform infrared (FT-IR) spectroscopy was then used to try and determine the presence of carbonate or hydroxide ions within the as-prepared structures. Figure 4.24 shows a broad peak centred at 3218 cm^{-1}, two sharp peaks centred at 1515 cm^{-1} and 1380 cm^{-1}, and a further sharp peak centred at 834 cm^{-1}. Similar results to these have been reported previously by

Kodihalli *et al.* whilst characterising nanoparticles of zinc hydroxy carbonate.[240] They attributed peaks at 1379 and 1511 cm^{-1} to $ZnCO_3$ and bending vibrations of $Zn(OH)_2$. The strong absorption band in the range of 700–1100 cm^{-1} was assigned to the lattice vibration of CO_3^{2-}. The broad peak centred at 3218 cm^{-1} can likely be attributed to stretching modes of water molecules present on the nanostructures. The presence of carbonate and hydroxide ions within the material strengthens the hypothesis that the nanowires consist of a form of zinc hydroxy carbonate.

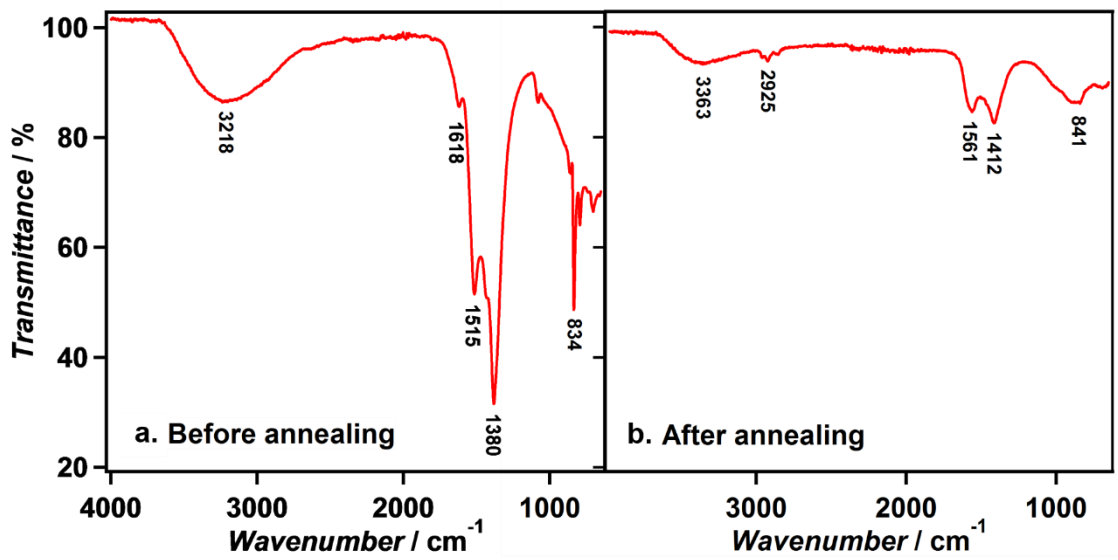

Figure 4.24. FT-IR spectrum of powders produced from nanowire array films before (a) and after (b) a heat treatment at 300 °C for 1 hour in air.

The prediction by Hu *et al.* of the as-prepared nanowires being some form of zinc hydroxy carbonate therefore seems quite possible.[209] However, the fact that the XRD pattern could not be matched to any known zinc hydroxy carbonates still leaves some doubt over the true structure of the nanowires. It is important to note that although the peaks attributed to carbonate and hydroxide groups largely disappear after annealing, their continued presence raises some concerns over the purity of the ZnO nanowires and might require further consideration.

The Raman spectrum of the nanowire array prior to annealing (Figure 4.25a) displays one clear peak at 1100 cm^{-1}. This lies close to the primary phonon mode displayed by smithsonite ($ZnCO_3$) which has been reported previously at 1092 cm^{-1}.[241] Hydrozincite ($Zn_5(CO_3)_2(H_2O)_6$) also displays a similar phonon mode at 1062 cm^{-1} but would be expected to also display multiple smaller modes between 1350 and 1700 cm^{-1}. These modes are not clearly observed within the spectrum, but it is possible they are obscured by the experimental noise. Although the Raman spectrum of the nanowires prior to annealing did not reveal any conclusive identification of the chemical species it seems likely that it is a carbonate material closely related to smithsonite and hydrozincite.

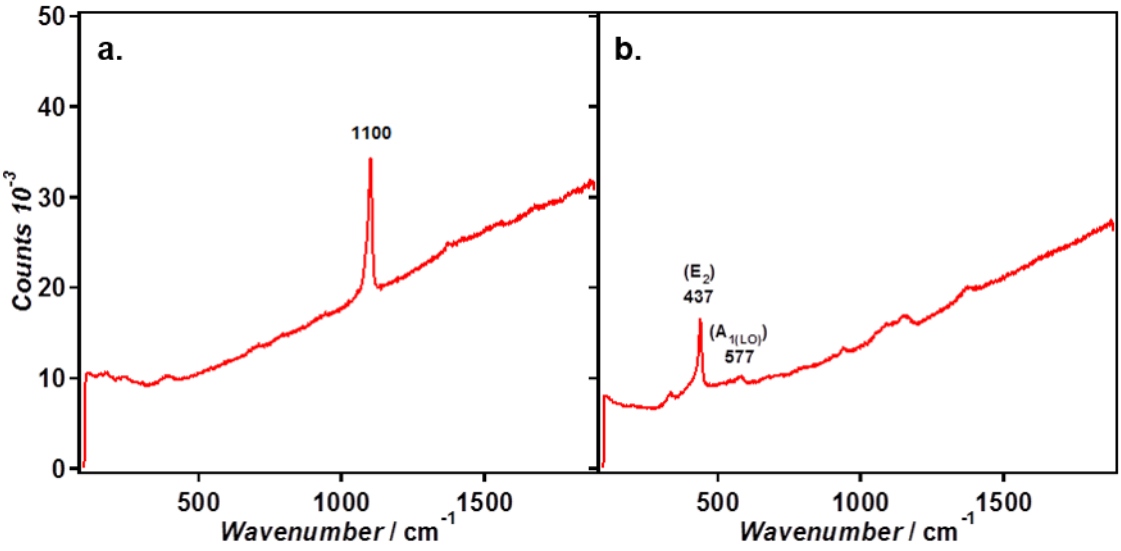

Figure 4.25. Raman spectrum of nanowire array films before (a) and after (b) a heat treatment at 300 °C for 1 hour in air.

The peaks displayed within the Raman spectrum of the annealed nanowires (Figure 4.25b) corresponds closely to the phonon modes displayed by ZnO, further confirming the successful conversion during annealing.[242] Presence of both the E_2(high) and $A_{1(LO)}$ phonon modes, at 437 and 577 cm^{-1} respectively, are indicative of ZnO grown with no preferred orientation which might be expected for a polycrystalline material.[243]

A simple way of discerning whether or not any ZnO is present before the annealing process is by examining its absorbance spectra. ZnO is a wide band gap semiconductor and would be expected to absorb in the UV-region, the presence of a UV absorbance would therefore indicate that the material is, or contains, ZnO. A specular reflectance setup was used to examine the UV absorbance of the films due to the opacity of the zinc substrate and the reflectance spectra for both the as-prepared and annealed films can be seen in Figure 4.26.

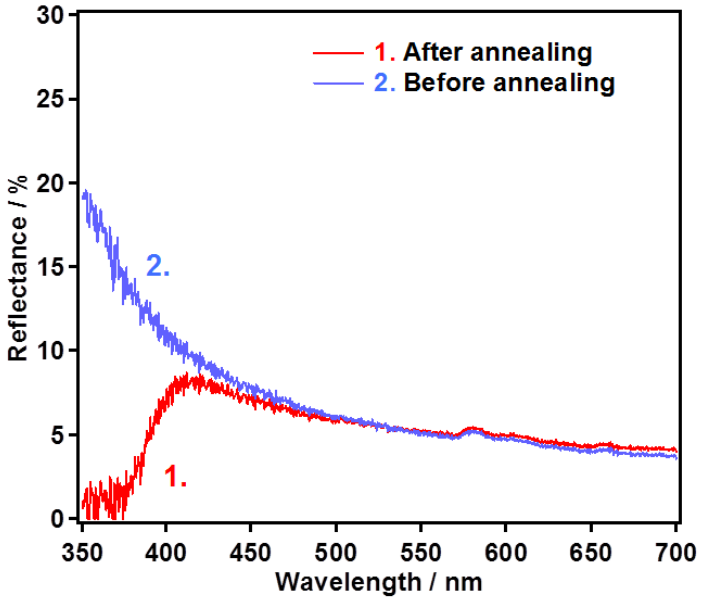

Figure 4.26. UV-Visible reflectance spectrum of a nanowire array film before (blue) and after (red) annealing at 300 °C for 1 hour in air.

It can be seen that absorption of light occurs in the UV-region only for the annealed sample, indicating that the annealed sample consists of ZnO whereas the as-prepared sample does not. The low reflectance in the visible region for both samples should also be noted. This is a result of light scattering from the nanostructures and is advantageous in increasing the path-length of light within a DSC. In addition to the high aspect ratio of nanowires that provide a high surface area for dyes, this feature makes the nanostructured ZnO films produced in this study an attractive candidate for application in these devices.

In order to establish the chemical nature of the as-produced nanowires it is important to consider the reactions that are possible during anodization. The aqueous chemistry of the zinc cation can be relatively complex with dependence on many factors including the pH, temperature, concentration and presence of other anions. The route to zinc hydroxy carbonate formation in aqueous solutions has been previously discussed by Orel *et al.* on the basis of a partial charge model.[244, 245] In water, zinc can form the relatively stable hydrated ions $[Zn(OH_2)_6]^{2+}$ and $[Zn(OH)(OH_2)_5]^{+}$, which can condense to form $[Zn(OH)_2(OH_2)_4]$ via olation and oxolation mechanisms. In the presence of HCO_3^-, either through dissolved CO_2, or in our case through the bicarbonate electrolyte, substitution of up to two water molecules can occur to give $[Zn(OH)(HCO_3)(OH_2)_3]$. Fast condensation of this species via the olation mechanism will then yield a zinc hydroxy carbonate. Based on this, it is proposed that the anodization could be proceeding via the following reactions:

At the anode

$$Zn_{(s)} - 2e^- + 6H_2O_{(l)} \rightarrow [Zn(OH_2)_6]^{2+}_{(aq)} \quad (4.1)$$

$$[Zn(OH_2)_6]^{2+}_{(aq)} \rightleftharpoons [Zn(OH)(OH_2)_5]^{+}_{(aq)} + H^+ \quad (4.2)$$

$$[Zn(OH)(OH_2)_5]^{+}_{(aq)} + HCO_3^-{}_{(aq)} \rightleftharpoons [Zn(OH)(HCO_3)(OH_2)_3]_{(aq)} + 2H_2O_{(l)} \quad (4.3)$$

$$[Zn(OH)(OH_2)_5]^{+}_{(aq)} \rightleftharpoons [Zn(OH)_2(OH_2)_4]_{(aq)} + H^+ \quad (4.4)$$

$$x[Zn(OH)_2(OH_2)_4]_{(aq)} + y[Zn(OH)(HCO_3)(OH_2)_3]_{(aq)} \rightarrow [Zn_{x+y}(OH)_{2x}(CO_3)_y]_{(s)} + 4(x+y)H_2O_{(l)} \quad (4.5)$$

At the cathode

$$2H^+ + 2e^- \rightarrow H_{2(g)} \quad (4.6)$$

Condensation rates via the olation mechanism can proceed rapidly, sometimes being only limited by diffusion.[246] As there is good mixing due to stirring within this experimental setup, it can be assumed that this reaction is not mass transfer limited, leading to rapid nanowire growth. With the reduction of protons at the cathode (reaction 4.6) it would be expected that reaction (4.2) would be driven forwards, accelerating the overall condensation. An increase in concentration of the bicarbonate electrolyte would also be expected to drive forward reaction (4.3), explaining the observed trend of increased growth rate at higher concentrations. This all contributes towards explaining the rapid growth of nanowires observed in this anodization reaction.

4.3.2 Formation of a slit-type pore structure

It has already been established in Section 4.3 that annealing of the nanowire films was found to yield polycrystalline ZnO. This can be observed through the broad peaks in the x-ray diffraction patterns corresponding to the wurzite form of ZnO (Figure 4.22b). Transmission electron microscopy (TEM) analysis revealed that although the overall nanowire form was preserved during annealing, the nanowires' facets were found to no longer be smooth, but instead formed of multiple small crystallites with a radial slit-type porous structure along the length of the nanowires (Figure 4.27c-e). This could also be clearly observed for scanning electron micrographs recorded for annealed nanowires that had been removed from the substrate (Figure 4.28). Under the standard annealing conditions of 300 °C for 1 h, particle sizes were found to be 9 ± 2 nm, as determined by statistical analysis of TEM. This interesting polycrystalline "slit-pore" structure contributes significantly towards a high specific surface area of 54.4 $m^2\ g^{-1}$ as determined

by BET surface area measurements (Figure 4.29). This value is significantly higher than what might be estimated for the smooth hexagonal nanowires prior to annealing (7.4 m^2 g^{-1}, see Appendix 1 for calculation). This high surface area, combined with the one-dimensional structure, makes these materials interesting candidates for applications such as dye-sensitized solar cells.

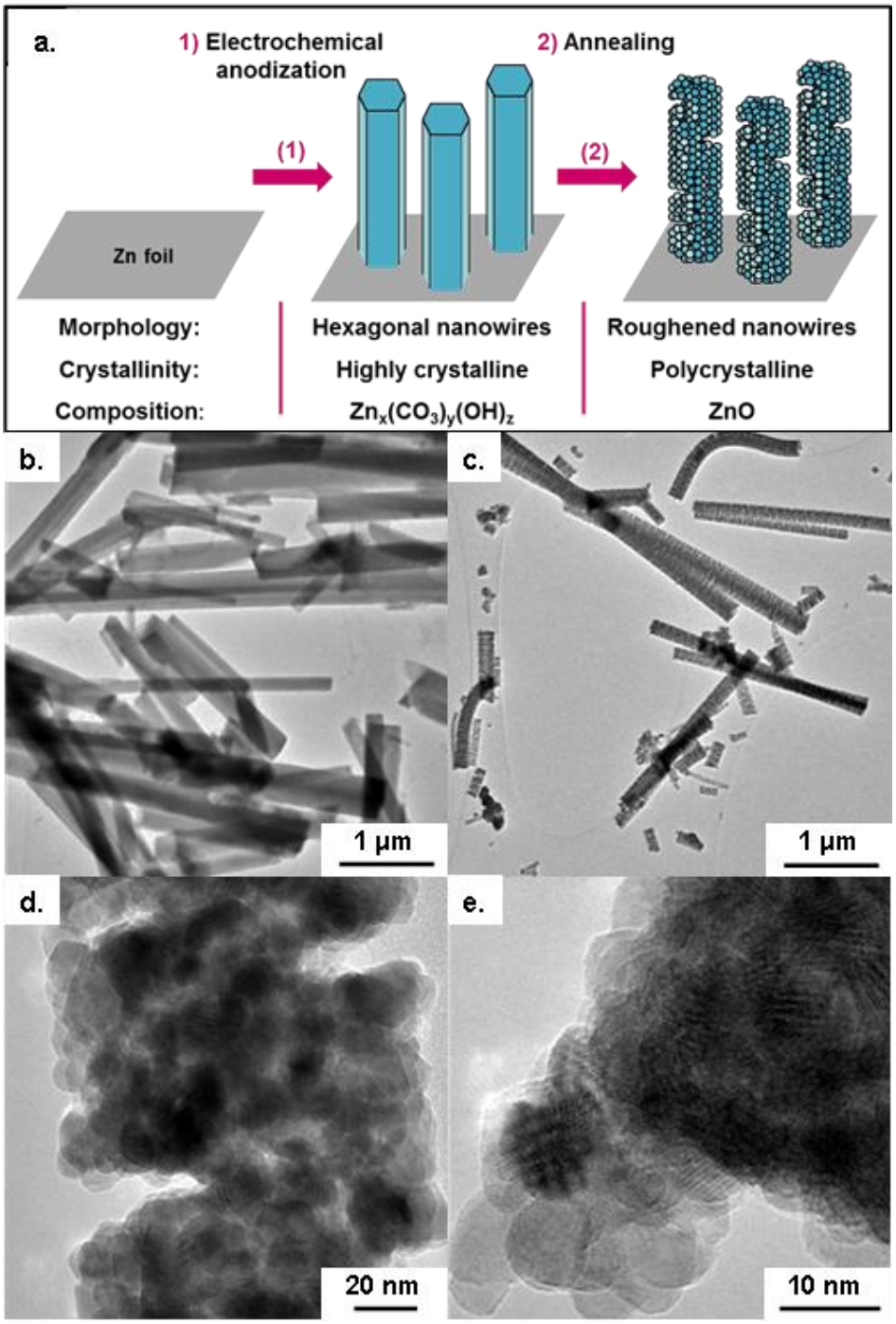

Figure 4.27. Scheme showing the two-step production of polycrystalline ZnO nanowires with a "slit-pore" structure (a), low magnification TEM micrographs of the nanowires before (b) and after (c) annealing, and high magnification micrographs showing the polycrystalline slit-pore structure after annealing (d & e).

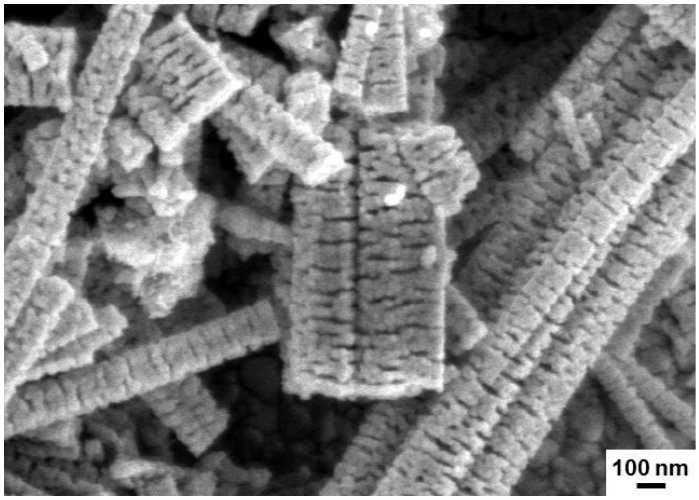

Figure 4.28. FESEM micrographs of annealed nanowires that had been removed from the substrate.

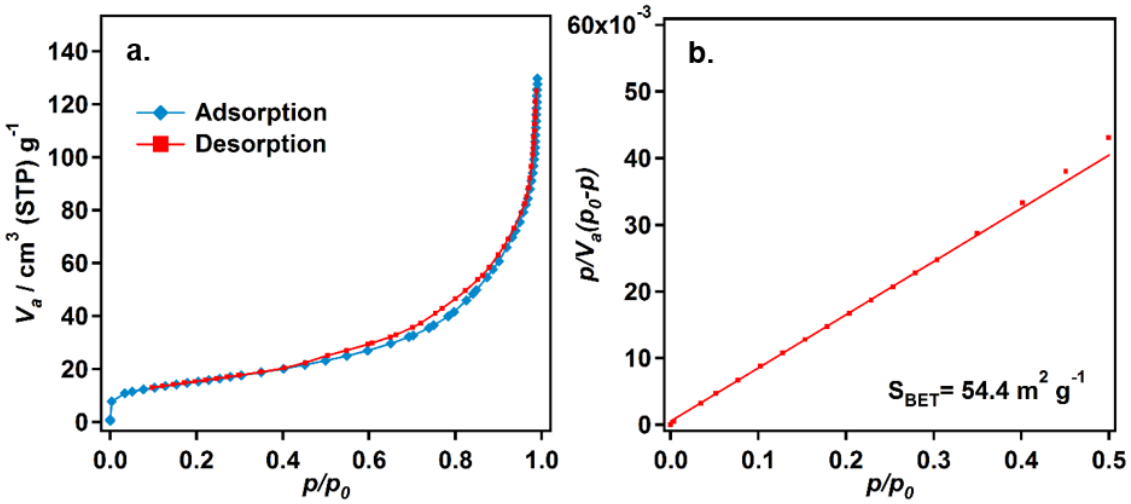

Figure 4.29. Nitrogen adsorption-desorption isotherms for the slit-pore type ZnO nanowires (a) and determination of the BET surface area (b).

In a further effort to identify the chemical species of the nanowires prior to annealing, electron diffraction was attempted on individual nanowires within the TEM. Unfortunately it was found to be impossible to obtain an accurate diffraction pattern as conversion of the nanowires was found to occur during electron beam irradiation (Figure 4.30). The non-annealed nanowires were found to convert within a period of seconds into polycrystalline ZnO. This conversion was accompanied by the apparent production of a liquid on the nanowire surface (Figure 4.30b) which could be water, an expected degradation product of a hydroxy carbonate compound.

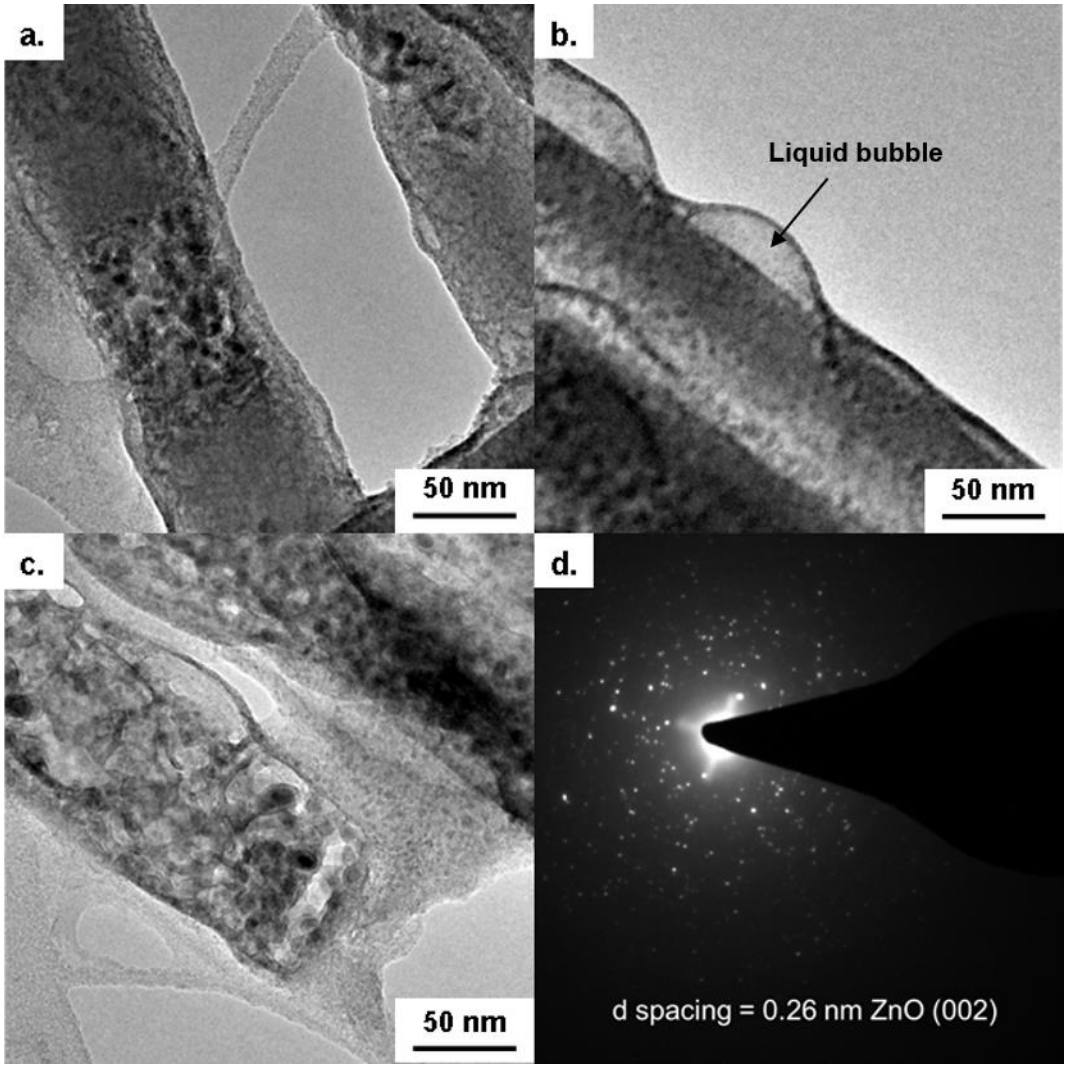

Figure 4.30. TEM micrographs showing the electron beam damage and conversion of the non-annealed nanowires to polycrystalline ZnO (a – c) and the electron diffraction pattern of the resulting ZnO structures (d).

Although electron beam irradiation resulted in the conversion of nanowires at high magnifications, it was found that low magnification imaging of the smooth non-annealed nanowires could still be conducted. By collecting multiple micrographs of the nanowires, both before and after annealing, it was possible to obtain a statistical distribution of nanowire diameters (Figure 4.31). It was found that the average diameter of the nanowires was relatively unchanged during the annealing treatment, falling only slightly from 167 ± 80 nm to 160 ± 61 nm. It therefore seems that conversion to ZnO during annealing does not result in a contraction of the nanowire diameters, but rather converts via a conformal transformation into a porous polycrystalline structure.

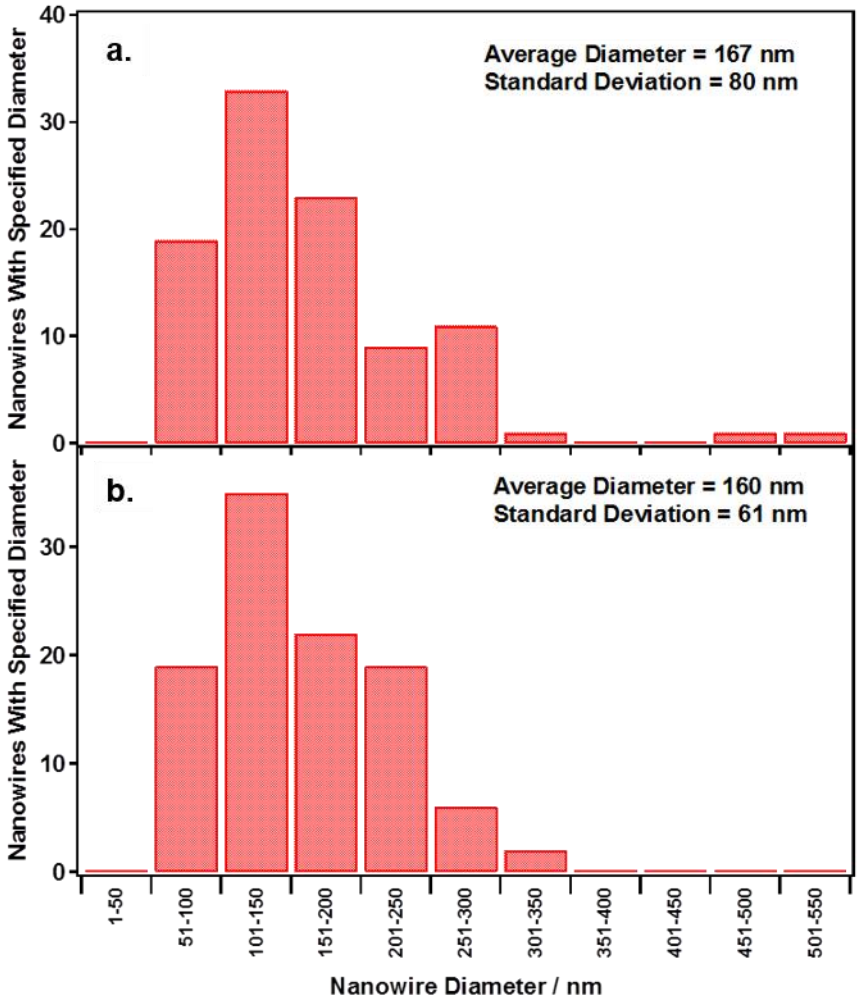

Figure 4.31. Nanowire diameter distributions determined by TEM for nanowires before annealing (a) and after annealing (b).

An insight into the formation of this porous structure can be gained by considering the structural transformation occurring during annealing. Using the assumption that the as-prepared nanowires are a form of zinc hydroxy carbonate then degradation to ZnO will proceed via the loss of H_2O and CO_2.[247] Using the case of hydrozincite ($Zn_5(CO_3)_2(OH)_6$) as an analogy, the decomposition reaction proceeds as:

$$Zn_5(CO_3)_2(OH)_6 \rightarrow 5ZnO + 3H_2O + 2CO_2 \quad (4.7)$$

Loss of these two gases during heating results in a contraction between the plains of the remaining Zn and O atoms to form ZnO. As there is a higher number density of Zn atoms in the ZnO than the hydrozincite, void formation is inevitable. A decomposition such as this can explain the formation of a porous polycrystalline structure as presented here.

4.3.3 Alternative conversion methods

Although it has been demonstrated that interesting polycrystalline nanowires with a slit-type pore structure can be produced by annealing the nanowires, the annealing process itself can add a significant amount of time to the overall production process. As annealing (including heating and cooling) can typically take in excess of 6 h, the benefits of rapid nanowire growth from anodization are lost. This would also prevent the production of nanowire films within a roll-to-roll system, which is typically considered desirable to reduce the manufacturing costs of photovoltaics.

It was, therefore, desirable to determine if this conversion to ZnO could be achieved more rapidly using an alternative technique to traditional annealing within a furnace. One method that has been demonstrated for the rapid thermal heating and annealing of materials is the use of near infra-red (NIR) irradiation.[248] This typically involves illuminating a material with a very high intensity of NIR light for a short period of time. When illuminated, either the material or a substrate that absorbs within the NIR region of the spectrum will rapidly heat up to anneal or thermally degrade the material in question.

In order to determine if NIR heating was a suitable technique for conversion of the nanowires into ZnO, a number of nanowire films were produced by anodization and heated at different NIR lamp powers within a commercial NIR annealing system equipped with a conveyor belt (Figure 4.32). A conveyor belt speed of 2 $m \cdot min^{-1}$ was used for all samples and heating powers of 25, 35 and 45 % were examined. In order to determine if conversion to ZnO was successful the nanowire films were then analysed via powder XRD to detect peaks attributed to ZnO (Figure 4.33).

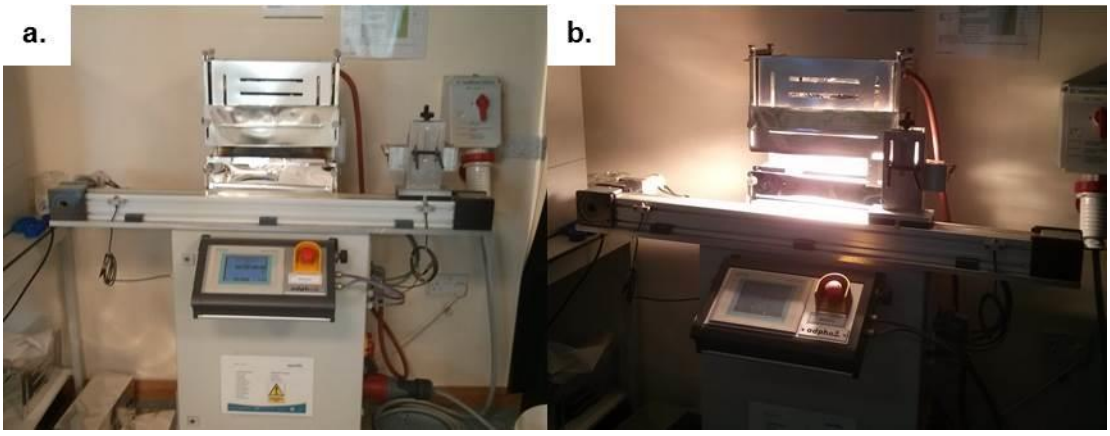

Figure 4.32. Photos of the NIR rapid annealing system used for conversion of the anodic nanowires to ZnO during standby (a) and during operation (b).

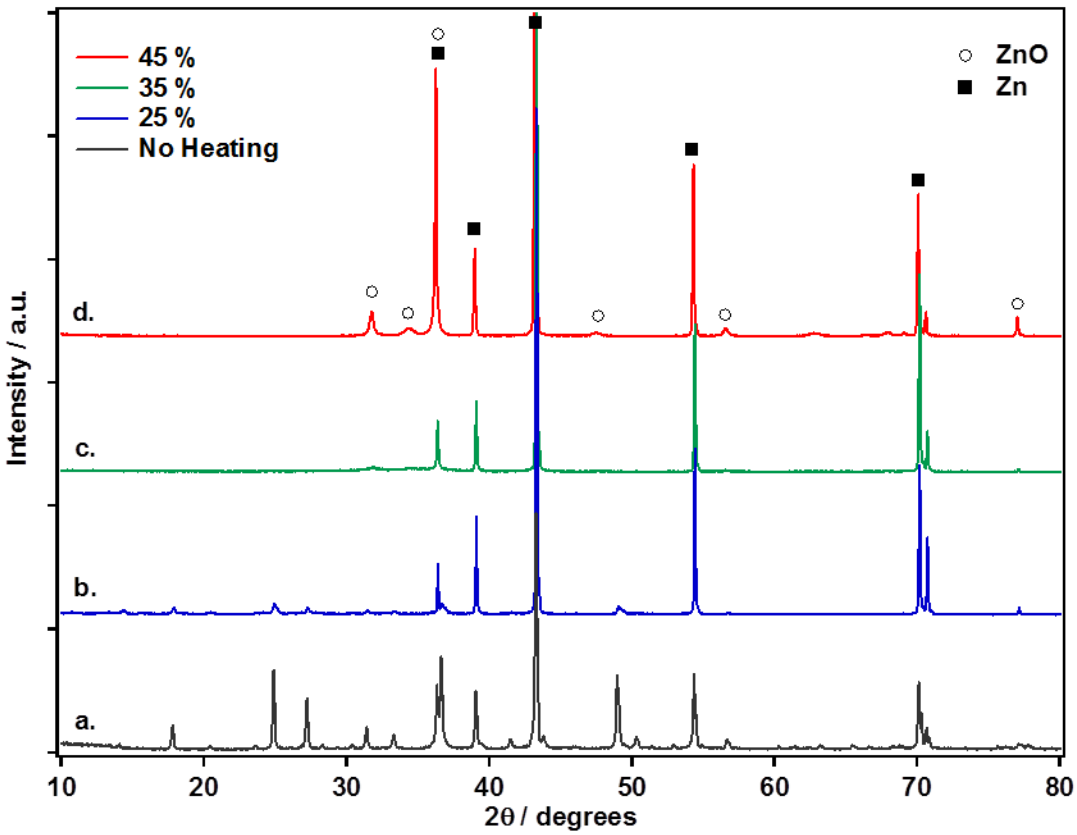

Figure 4.33. Flat plate powder x-ray diffraction patterns of the anodic nanowire films after NIR heating at different heating powers. All heating powers shown are for a conveyor belt speed of 2 m min^{-1}. It should be noted that all Zn peaks occur from the substrate.

At heating powers of 25 % some peaks of the original species can be observed by XRD. These appear to have completely disappeared at heating powers 35 % and further increases in power to 45% results in the clear emergence of ZnO (wurtzite) peaks. Rapid near infrared heating therefore seems to be a promising alternative for the conversion of the nanostructures into ZnO. Based on the conveyor belt speed of 2 m min^{-1}, conversion of the nanowires to ZnO has been successfully demonstrated within 30 s. It should be noted, however, that heating powers in excess of 45 % gave rise to melting of the metallic Zn substrate and, therefore, damage to the nanostructured film (Figure 4.34). It is therefore important to carefully control the heating power so that conversion is achieved whilst maintaining the integrity of the substrate.

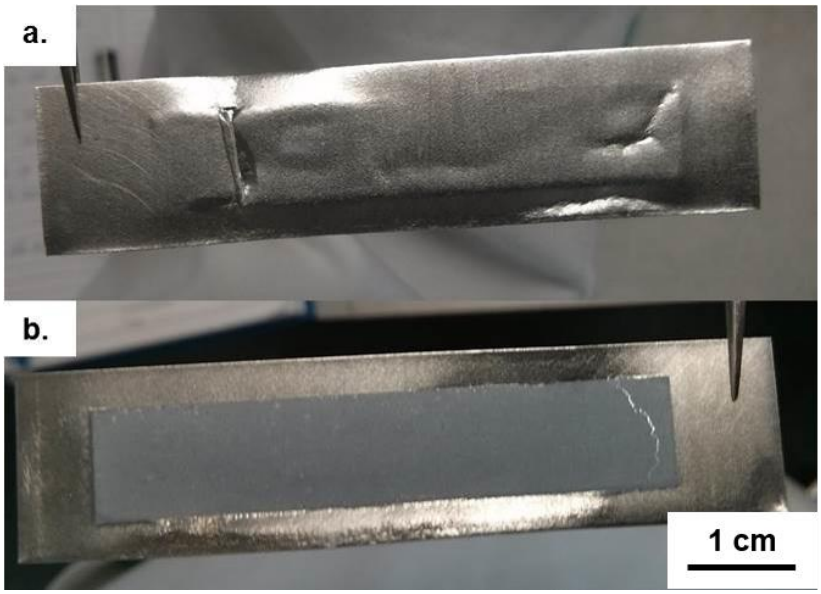

Figure 4.34. Back (a) and front (b) of a nanowire film heated at 50 % power showing signs of substrate melting and nanowire film cracking.

Rapid NIR annealing was also tested on some of the conventional circular nanowire films produced using the Teflon® electrode holders. These samples appeared to exhibit far more significant cracking than the nanowire strips previously tested. One of the key differences between the two sets of films was the use of electropolishing for the circular samples. Therefore, two sets of experiments were run using circular nanowire films that had been produced both with and without an electropolishing pre-treatment. It was found that significantly less cracking occurred after NIR heating for the nanowire films that had not been electropolished compared to those that had (Figure 4.35). This difference in behaviour could be a result of the increased roughness of the substrate providing better anchoring for the nanowire film in the case of the samples without electropolishing. Despite the significant decrease in the extent of cracking for these films, closer examination both by eye and through microscopy revealed that cracking is still present within the films. It therefore would appear that the cracking is an inherent and unavoidable feature of the nanowire conversion during NIR heating.

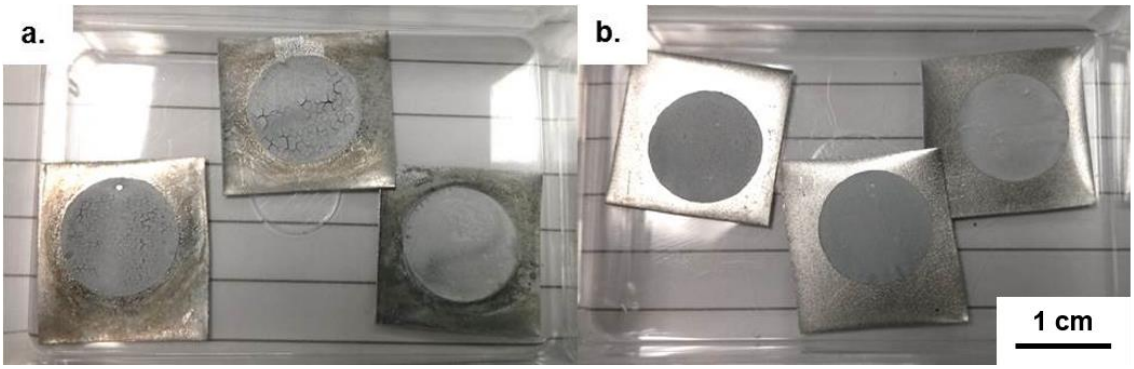

Figure 4.35. (a) electropolished films heated at 35 %, 30 % or 0 % power (left to right). (b) the same but for no electropolishing pretreatment.

4.3.4 Crack formation during heating

As discussed in Section 4.3.2, the conversion to ZnO upon annealing is thought to occur via the loss of water and carbon dioxide (reaction 7) accompanied by a contraction between the Zn plains. This contraction can also be used to explain an often unwanted side-effect of the annealing process, which is cracking of the nanowire films. Cracking of the films during annealing was observed to some extent for all of the anodized films produced, even when low heating and cooling rates were used. This apparently unavoidable feature should be considered, particularly when the application requires a continuous, crack free film. Figure 4.36 is a typical SEM micrograph of the cracking observed after annealing the nanowire films. Cracks with widths on the order of tens of micrometres can be observed over the surface, leaving islands of nanowires. Between the islands, areas of exposed Zn substrate can be observed which would be expected to be extremely disadvantageous for applying the materials directly within photovoltaic devices as recombination and shunting would be expected to occur when contacted with the electrolyte. This cracking is also displayed in a cross-sectional FESEM micrograph of the annealed nanowire film that had been set within a resin (Figure 4.37). It can be seen that a clear route to the zinc substrate is present via the crack, with no barrier layer to stop electron recombination within DSCs or perovskite solar cells. The problems arising from the crack formation will be discussed further within Chapter 6 which discusses the application of the nanowire films within DSCs.

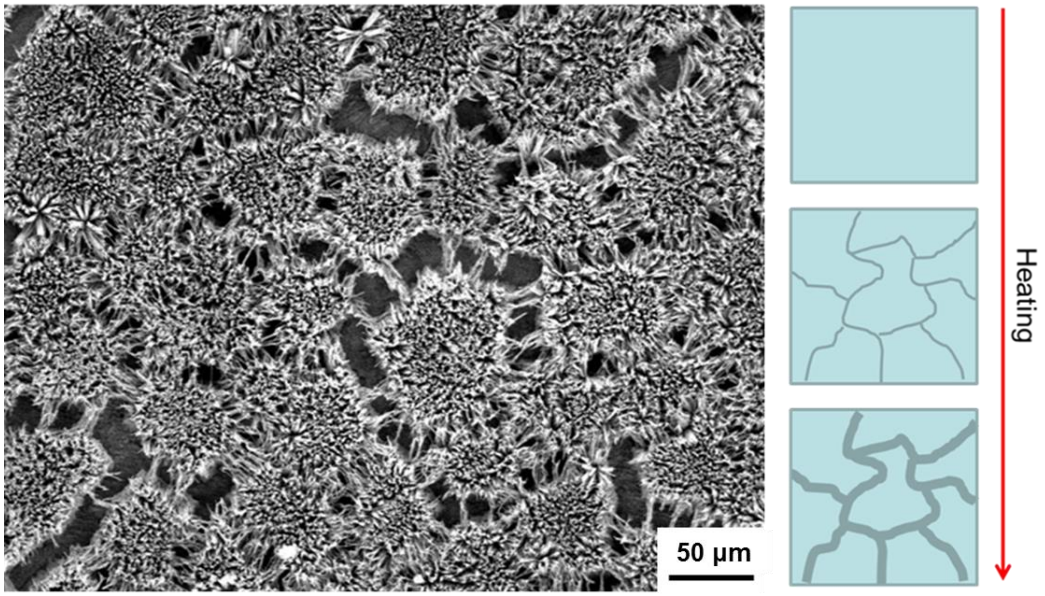

Figure 4.36. FESEM micrograph of a nanowire film surface after annealing at 300 °C for 1 h demonstrating the typical cracking observed as a result of annealing.

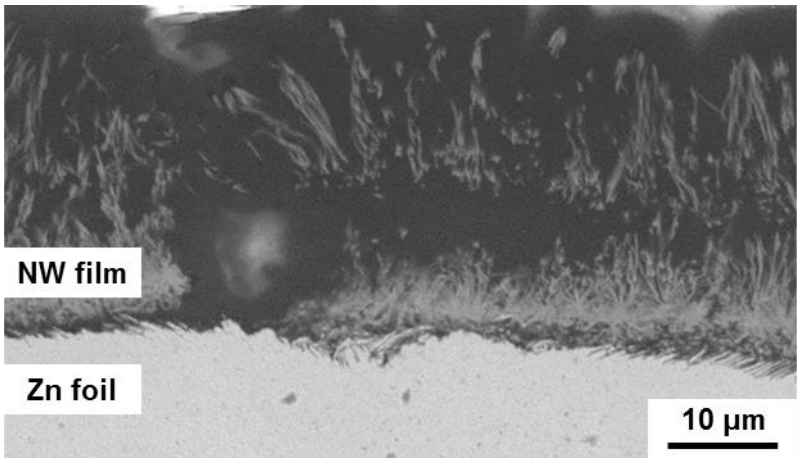

Figure 4.37. FESEM cross-section of an annealed ZnO nanowire film set inside resin, demonstrating the cracking between sections of nanowire film penetrating to the Zn substrate.

4.4 Chapter Summary

In this Chapter, the process of anodization of zinc foil in an aqueous bicarbonate electrolyte has been examined in detail. The growth of nanowire films was found to proceed via four separate growth stages: 1. Growth initiation in the form of discrete nanoflowers, 2. Alignment of the nanowires due to prohibited growth in a direction horizontal to the substrate, 3. The development of a layered structure of larger hexagonal wires emerging through a dense nanowire film, and finally, 4. The hierarchical splitting of the large hexagonal wires into multiple smaller nanowires.

It has been demonstrated for the first time that the growth of high aspect ratio nanowires via the anodization of zinc can be achieved using a range of different bicarbonate electrolytes. It has also been shown quantitatively that the reaction parameters of temperature, voltage, time and electrolyte concentration can significantly alter the nanowire growth rate. By optimising these parameters, remarkably high growth rates in excess of 3 μm min^{-1} can be achieved at room temperature, without destruction of the nanowire films. The nanowire films were found to be formed of ZnO only after annealing. These annealed nanowires were polycrystalline and had a unique slit-type pore structure along their length. Examination of the properties of the nanowire films before and after annealing have allowed an explanation to be proposed, both for the high growth rates achieved, and for the unique porous structure of the annealed ZnO nanowires.

The modification of these anodic nanowires will now be explored in Chapter 5 in order to form novel hierarchical structures, which could further raise the surface areas of these nanostructures. The application of these materials will then be explored further in Chapters 6 and 7, which discuss the application of nanowires within DSCs and perovskite solar cells respectively.

Chapter 5 – Modification of the Nanowire Structure

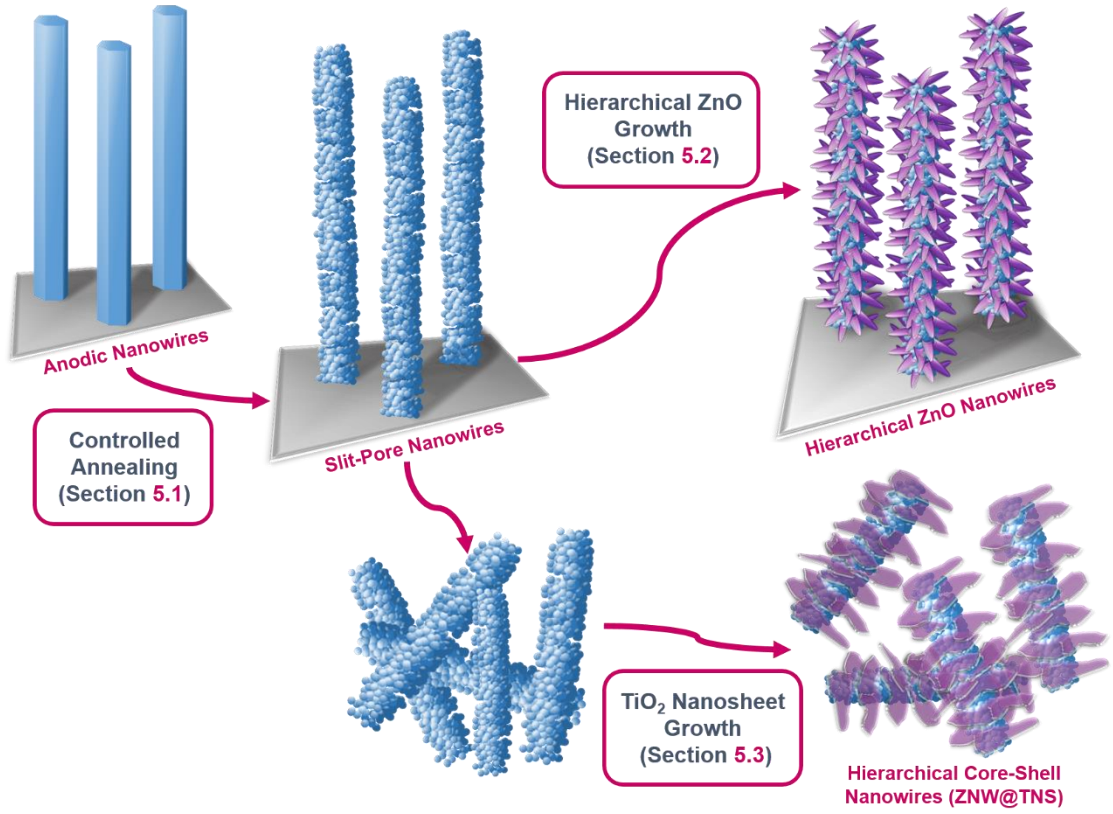

Figure 5.1. Schematic summarising the content and structure of Chapter 5, which focusses on the modification of the nanowire structure after anodization.

In Chapter 4 it was demonstrated how electrochemical anodization can be used to grow high aspect ratio nanowires that can be transformed into polycrystalline ZnO through a simple heat treatment. This gave rise to a beneficial high surface area structure, but also resulted in cracking of the nanowire films.

In this chapter the focus is on a range of treatments - either chemical or physical - that can be performed on the annealed nanowires to impart improved properties for application within the two target technologies of dye-sensitized and perovskite solar cells (Figure 5.1). The first half of the chapter focusses on treatments that might be used to avoid the unwanted exposure of the zinc foil after annealing, thereby allowing the nanowires to be used on the zinc substrate within back-illuminated solar cell configurations. The second half of the chapter goes on to explore the modification of the nanowires with TiO_2, to form what are called core-shell structures. The use of these core-shell structures can allow the combination of the beneficial properties of both the ZnO and TiO_2 materials, thereby, presenting new possibilities within their applications.

It should be noted that Section 5.3 is the result of a collaboration between myself and Chang Soo Lee, a PhD student at Yonsei University. The work was started by myself during a placement within the Department of Chemical and Biological Engineering at Yonsei University and was continued after my return to Bath by Chang Soo Lee. The work presented in Section 5.3 should therefore be viewed as an equal contribution from both parties. The results within section 5.3 have contributed towards a joint first authorship journal article between myself and Chang Soo Lee, which has been submitted to the Journal of Power Sources and is currently under review.

At the end of this chapter, it is hoped that a number of interesting nanostructures will have been demonstrated, together with the routes to forming them. These structures will then be applied in Chapter 6 and Chapter 7 within the applications of dye-sensitized and perovskite solar cells where the benefits or disadvantages of the structures will be explored.

5.1 Structure Modification through Controlled Heating

It has already been shown in Chapter 4 that heating the nanowires formed from anodization results in the formation of polycrystalline ZnO nanowires, with a characteristic slit-type pore structure along their length. This heat treatment had the benefit of imparting a high specific surface area on the nanowires compared to what might be expected for single crystalline nanowires. The surface area of the polycrystalline nanowires is likely to be closely linked to both the crystallite size and the degree of sintering between the neighbouring nanoparticles.

It is well known that the conditions under which a material is annealed can greatly affect the crystallite size of the material.[249] Both the time for which the annealing takes place and the temperature at which the material is annealed can both change the resultant crystallite sizes. It might, therefore, be possible to tune the surface area of the polycrystalline nanowires by controlling the annealing conditions. Such control over the material surface area would be beneficial, particularly within the application of dye-sensitized solar cells where the surface area of the semiconductor support is strongly linked to the cell performance.[27]

In this section, the effect that both the annealing temperature and the annealing time have on the crystallite size of the nanowires is examined using a combination of XRD and TEM. The possible influence that these changes in crystal size are having on the surface area of the nanowires is then examined at the end of the section.

5.1.1 Effect of heating time

The first annealing parameter to be examined was the length of time at which the nanowire films were held at the annealing temperature. A number of nanowire films were produced by anodization under the same conditions and then annealed at 300 °C for different lengths of time ranging from 1 to 24 h. Flat-plate powder XRD patterns were then recorded for films after the annealing treatment to examine what effect this would have on the crystallinity of the ZnO nanowires. The XRD patterns revealed the presence of polycrystalline ZnO in the wurtzite structure for all annealing times, in addition to peaks from the zinc substrate (Figure 5.2). The sharpness of the ZnO peaks was found to increase with increasing annealing times, indicative of larger crystallite sizes for long times.

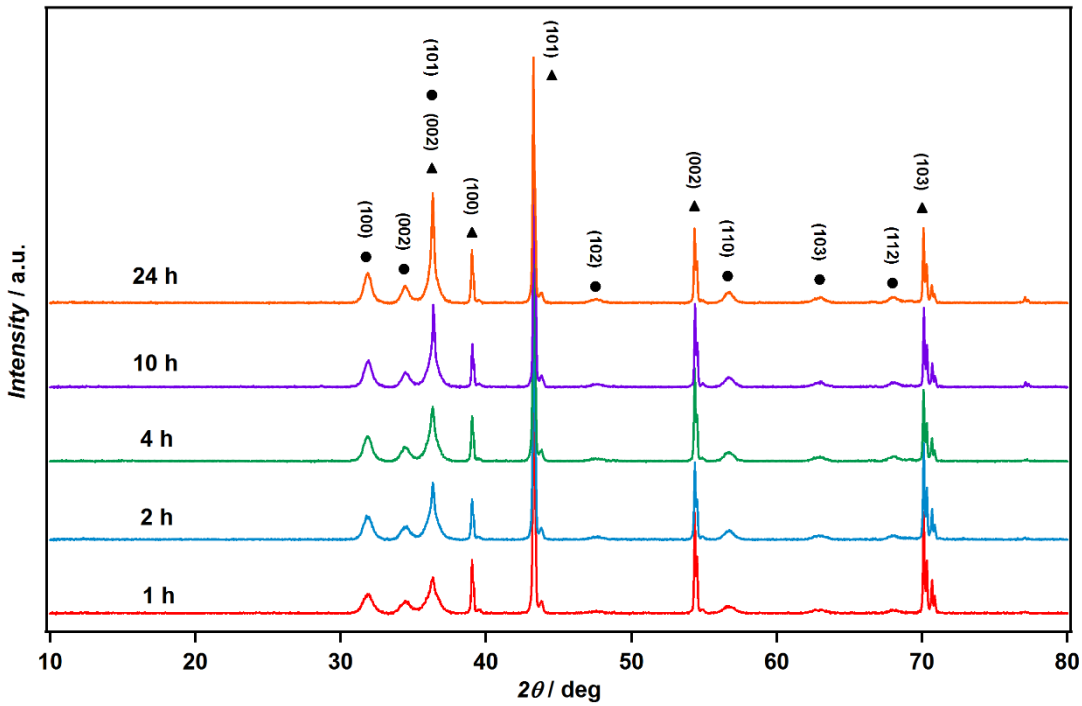

Figure 5.2. Flat plate powder x-ray diffraction patterns of anodic nanowire films annealed at 300 °C for times ranging between 1 and 24 h with ramping at 2 °C min^{-1}. Peaks attributed to the wurtzite form of ZnO (circles) and the Zn substrate (triangles) are shown.

Values for the crystallite sizes could be calculated for each heating time using the Scherrer equation which relates the crystallite size (L) to the peak width at half the maximum intensity for a particular diffraction angle ($B(2\theta)$), the x-ray wavelength (λ), half the diffraction angle (θ) and the Scherrer constant (K) for which the value of 0.94 has been used:[250]

$$B = \frac{K\lambda}{Lcos\theta} \qquad \text{Eq. 5.1}$$

The diffraction peak situated at ~32° was chosen for the crystallite size analysis as it is the most prominent peak corresponding to ZnO within the range of diffraction angles measured. The calculated crystallite sizes for different annealing times (Figure 5.3a) were found to increase with increasing time from ~11 nm in diameter after 1 h to >14 nm after 24 h. The majority of the increase in crystallite size was found to occur within the first 4 h and would then start to plateaux at longer lengths of time.

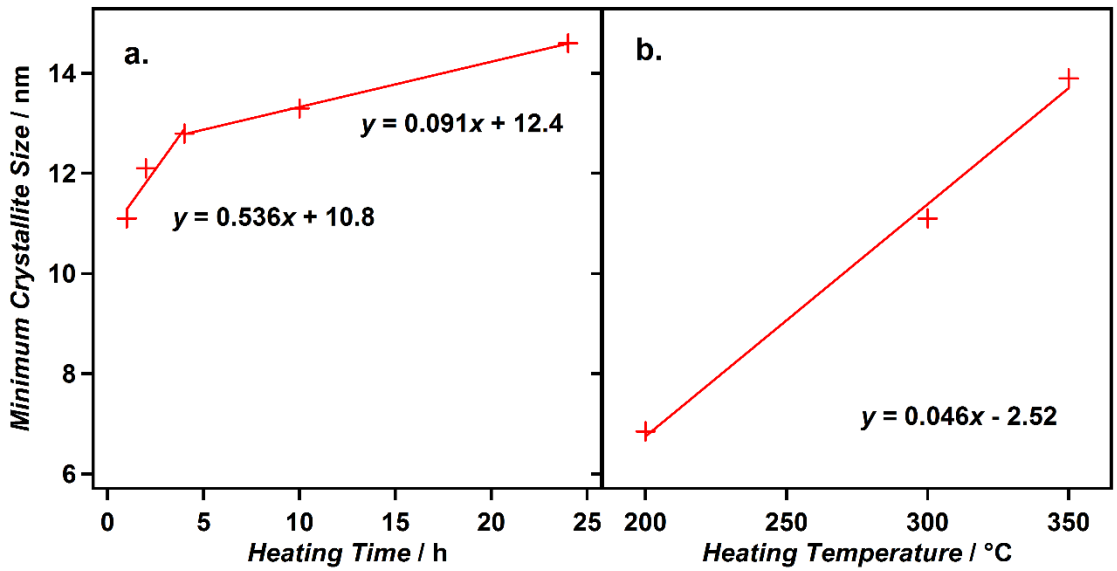

Figure 5.3. Crystallite sizes calculated by applying the Scherrer equation to the (100) ZnO peak in the XRD patterns recorded for nanowire films annealed for different times (a) and at different temperatures (b).

5.1.2 Control of heating temperature

In order to examine what effect the heating temperature has on the crystallinity of the ZnO formed, XRD measurements were carried out on a set of films that had been produced using the same anodization conditions, but annealed at different temperatures afterwards (Figure 5.4). It can be observed that all trace of the sharp peaks present in the as-produced films without heating (WH) have disappeared after heating the film to 200 °C and broad peaks corresponding to the wurtzite structure of ZnO are present. This indicates that decomposition of the as-prepared compound occurs at a relatively low temperature, which is beneficial as it means that high temperatures are not required to obtain the desired ZnO structures. However, the fact that the diffraction peaks are extremely broad indicates that crystallites are very small after heating to this temperature. When higher temperatures were used, sharper peaks corresponding to ZnO could be observed. This is most noticeable for the peaks situated at 2θ values of ~32°, corresponding to the (100) wurtzite peak.

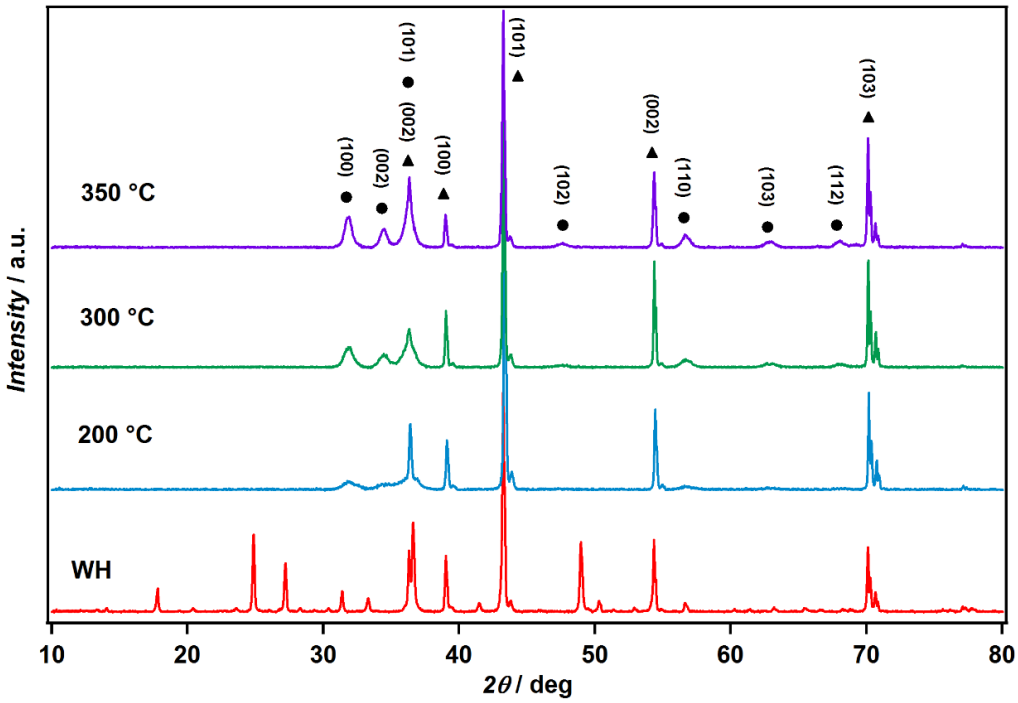

Figure 5.4. Flat plate powder x-ray diffraction patterns of anodic nanowire films annealed for 1 h at temperatures ranging between 200 and 350 °C with ramping at 2 °C min^{-1}. A diffraction pattern of the nanowire film without heating (WH) is also included for comparison. Peaks attributed to the wurtzite form of ZnO (circles) and the Zn substrate (triangles) are shown.

The Scherrer equation was again used to calculate the minimum crystallite sizes present within the nanowires annealed at different temperatures (Figure 5.3b). Within the range of temperatures examined, the increase in crystallite size appeared to scale linearly with the annealing temperature from ~7 nm at 200 °C to ~14 nm at 350 °C. This increase in crystallite size appears to be more significant than the trend found for increasing the annealing time. It might, therefore, be more useful to control the annealing temperature rather than the time for accessing nanowires with a wide range of crystallite sizes.

An understanding of these trends can be gained by considering the mechanisms behind this process. Crystallite growth occurs via different mechanisms including the fusion of different crystals, incorporation into larger crystals and ripening.[251, 252] All of these processes have an activation energy that follows an Arrhenius type curve, which is strongly dependent of temperature. Time can lead to some further ripening of crystallites through processes such as Ostwald ripening, but does not have a direct effect on the activation energy of growth. In this way, it is expected that the crystallite size should have a stronger dependence on the annealing temperature rather than time, as exhibited here.

In order to try and confirm the crystallite sizes calculated using the Scherrer equation, TEM was used to examine the anodic nanowires after annealing at two different temperatures, 300 °C and 350 °C. A large number of micrographs were recorded at high magnification in order to view the small crystallites making up the nanowires (Figure 5.5). By manually measuring the diameters of visible crystallites within ImageJ it was possible to construct particle size distributions for the two different annealing temperatures (Figure 5.6). The average particle diameters obtained from TEM can be seen overlaid onto the values calculated from Scherrer analysis in Figure 5.7. It can be seen that although there is some deviation between the two sets of crystallite diameters, the overall trend of increasing diameter for higher temperatures is true for both measurement methods.

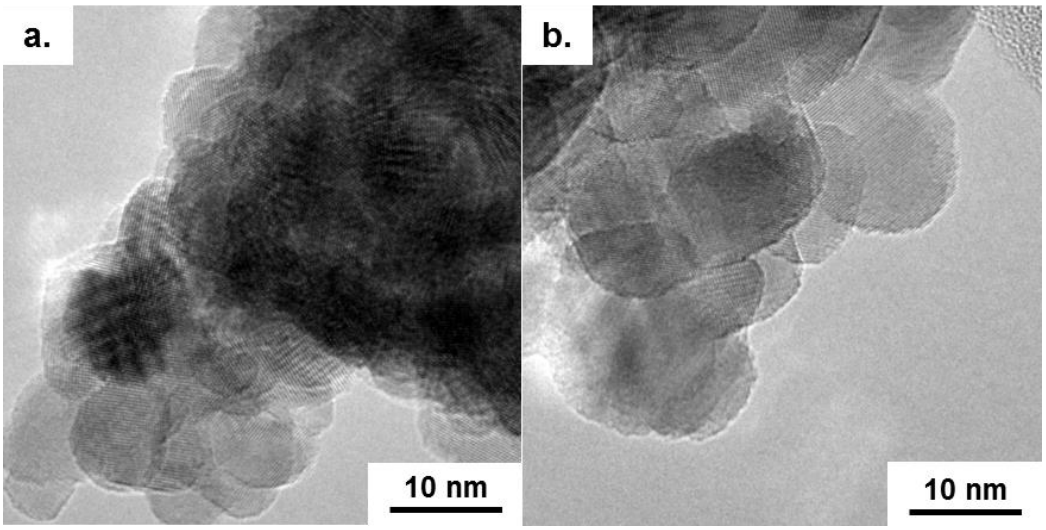

Figure 5.5. TEM micrographs showing the polycrystalline structure of annealed nanowires and the difference in particle size between films annealed at 300 °C (a) and 350 °C (b).

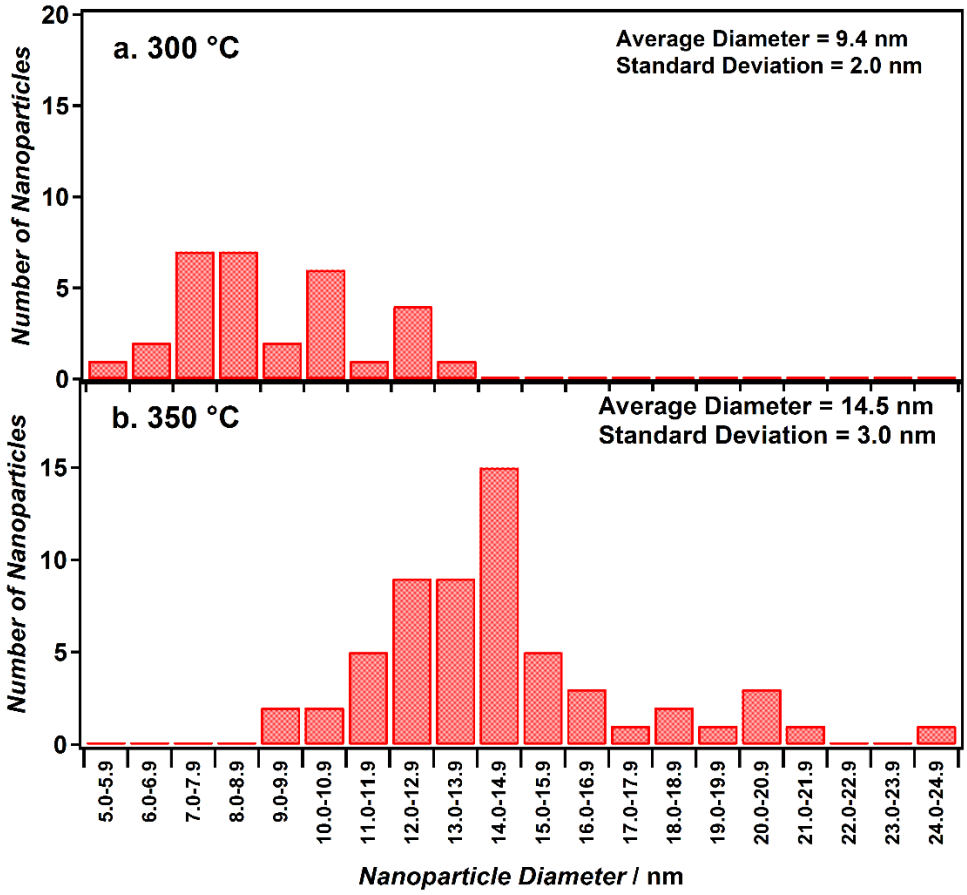

Figure 5.6. Particle size distributions over multiple transmission electron micrographs for anodic nanowires annealed at 300 °C (a) or 350 °C (b) for 1 h.

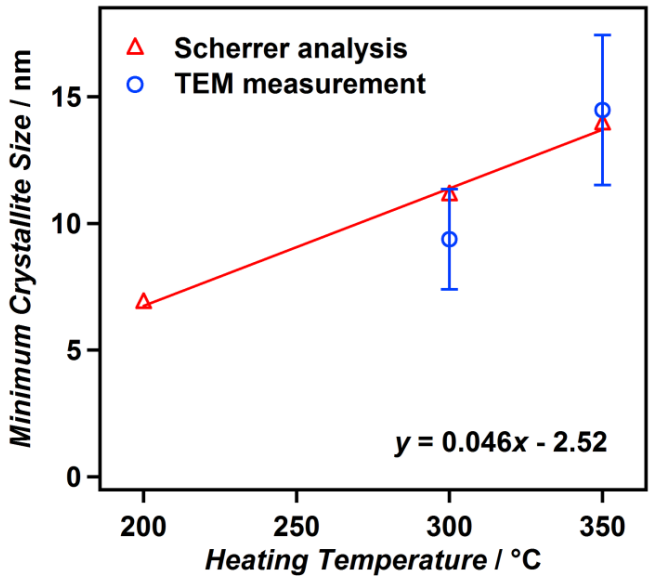

Figure 5.7. Particle sizes determined from TEM analysis overlaid on the values determined by Scherrer analysis of the XRD patterns for nanowires annealed at different temperatures. The error bars show the standard deviation over more than 30 measurements.

5.1.3 Modelling the influence of annealing on nanowire surface area

The surface area of a nanomaterial is of significant importance for applications, such as dye-sensitized solar cells, where it is desirable to maximize the available surface area for chemisorption of the molecular dye. It is, therefore, important to determine what influence changes in crystallite diameter – such as those arising from different annealing conditions – could have on the overall surface area of the nanomaterial.

In order to estimate surface areas of the polycrystalline nanowires a simple model was considered, in which the nanowires are formed of a large number of perfectly spherical nanoparticles of a given diameter. In its simplest form the nanoparticles would be considered as isolated, with no overlap with neighbouring nanoparticles. In this case, the specific surface area can simply be calculated from the nanoparticle diameter, assuming that the density of the ZnO nanoparticle is equal to that of the bulk density of ZnO (5.61 g cm^{-3}) (See Appendix 2 for details of the calculation). Calculated specific surface areas for different nanoparticle diameters using this simple model can be seen in Figure 5.8 as the red circles. It can be observed that the dependence of specific surface area on nanoparticle diameter is strongest for the smallest nanoparticles and decreases as the nanoparticle diameter increases. Within the range of nanoparticle diameters produced via altering the annealing conditions (7-14 nm), a significant change in surface area can arise, which could have large implications for application within dye-sensitized solar cells.

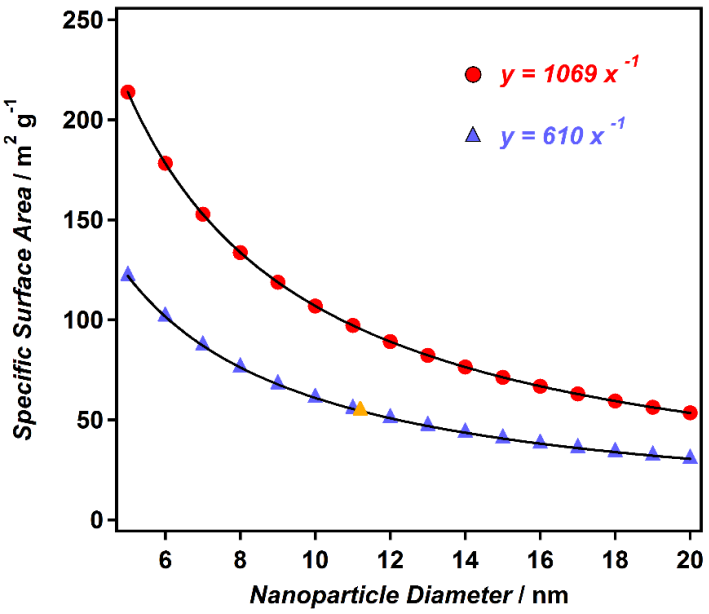

Figure 5.8. Predicted surface areas for polycrystalline nanowires composed of nanoparticles of different diameters, assuming either isolated perfect spheres (red circles) or sintered spheres with a sintering factor of 0.57 (blue triangles). The specific surface area measured for nanowires consisting of 11.2 nm diameter nanoparticles is shown in as a yellow triangle.

The assumption of isolated, non-overlapping nanoparticles is, however, an unrealistic situation within the polycrystalline nanowires. Upon heating, nanoparticles typically undergo a process called sintering in which neighbouring particles fuse, forming necks between them. This process is, indeed, a vital process in forming films for applications such as dye-sensitized solar cells, as in the absence of sintering the conduction of electrons through the nanoparticle film can be extremely low. Sintering does, however, have the effect of surface area reduction due to the overlap of nanoparticles and must therefore be considered in the production of effective photoelectrodes.

In order to correct the estimated specific surface areas for sintering between particles, a sintering factor was calculated using the known nanoparticle diameter and BET surface area of polycrystalline nanowires formed by annealing at 300 °C (11.2 nm and 54.4 $m^2\ g^{-1}$ respectively). The sintering factor can be simply expressed as:

$$Sintering\ Factor = \frac{S_{BET}}{S_{calc}} \qquad \text{Eq. 5.2}$$

Where S_{BET} is the specific surface area, as determined by BET surface area analysis, and S_{calc} is the calculated specific surface area for perfectly spherical, non-overlapping nanoparticles. A sintering factor of 0.57 was obtained, indicating a large reduction of surface area due to sintering of the nanoparticles within the nanowire. By applying this sintering factor, a corrected specific surface area can be calculated for a given nanoparticle diameter which is likely to more closely represent the actual values (blue triangles, Figure 5.8). It should be noted that the extent of sintering would typically be expected to also vary with annealing temperature and time, however, for simplicity this has not been considered.[253]

Although the corrected surface areas show a smaller range of achievable specific surface areas for the nanoparticle diameters reported in this section, the effect of annealing temperature and time have still been demonstrated to have a large influence, with surface areas ranging between 40 and 90 $m^2\ g^{-1}$. This control of annealing conditions could, therefore, be used to form polycrystalline nanowires with tailored surface areas for application in photovoltaic cells, where surface area is an important factor.

5.2 Solution Based Structure Modifications

5.2.1 Attempts at surface passivation

Although a beneficial polycrystalline structure can be obtained from annealing the nanowires, the film cracking that it gives rise to (Section 4.3.4) is expected to be problematic for the application of the films within the two desired applications: dye-sensitized and perovskite solar cells. The presence of exposed areas of the zinc substrate between the cracks in the film would provide sites for rapid recombination of photogenerated electrons and holes and could also lead to shunting within the cell. To prevent these problems it is desirable to passivate the exposed zinc surface by chemically converting it to ZnO, which would allow the transport of electrons, but the blocking of electron holes within the cell.

The first method tested for passivating the zinc substrate was to use a secondary anodization treatment on the nanowire film. This involved first forming a nanowire film by anodization, annealing to form ZnO and then undertaking a second anodization with the aim of reacting any exposed zinc substrate. This method was found to be unsuccessful as the nanowire morphology was destroyed, resulting in areas of porous nanostructures (Figure 5.9a) or heavily fragmented nanowires (Figure 5.9b). The significant damage to the nanowire structure is likely due to fracturing of the nanowires within the stirred electrolyte and also due to the capillary forces acting on the nanowires during subsequent drying. Peculiarly, the nanowire film was found to turn from white to black during the second anodization (Figure 5.9c), the reason for which is still unknown. The flat plate XRD pattern of the film after a secondary anodization treatment revealed that a significant amount of the ZnO structure was lost, but no new crystalline materials were present (Figure 5.10a).

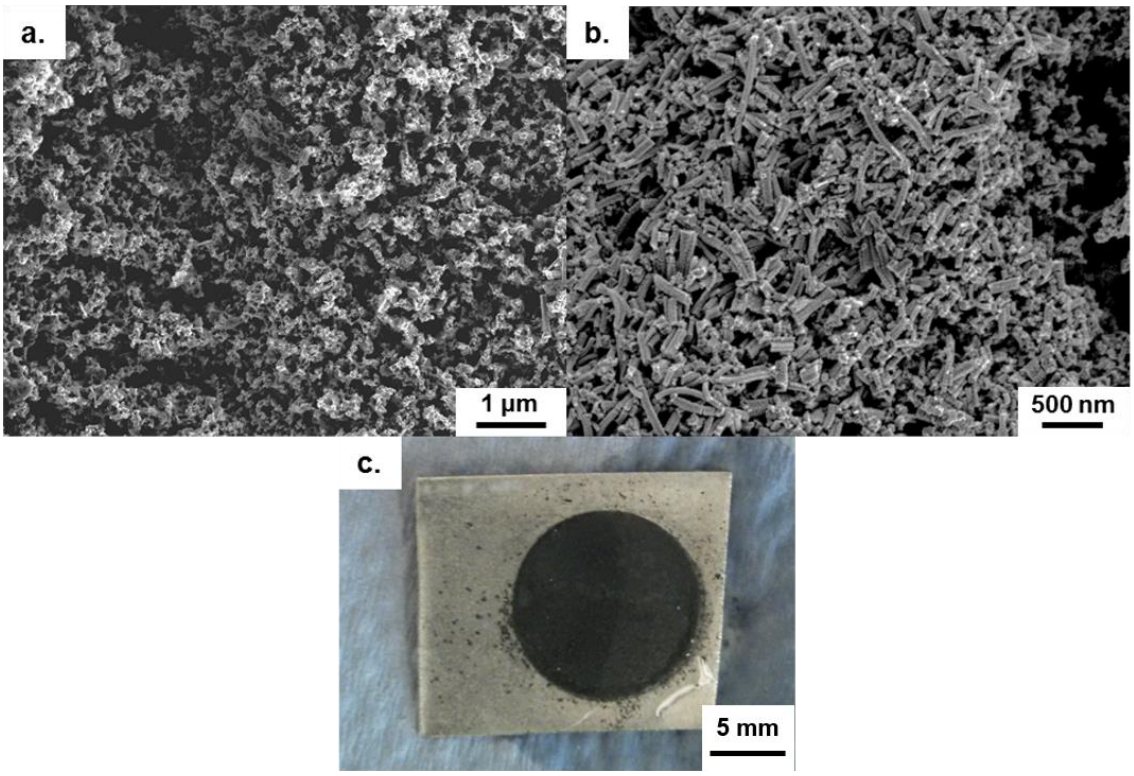

Figure 5.9. FESEM micrograph of the porous (a) and nanowire fragment areas (b) present on the dark surface of the film after a double anodization treatment (c).

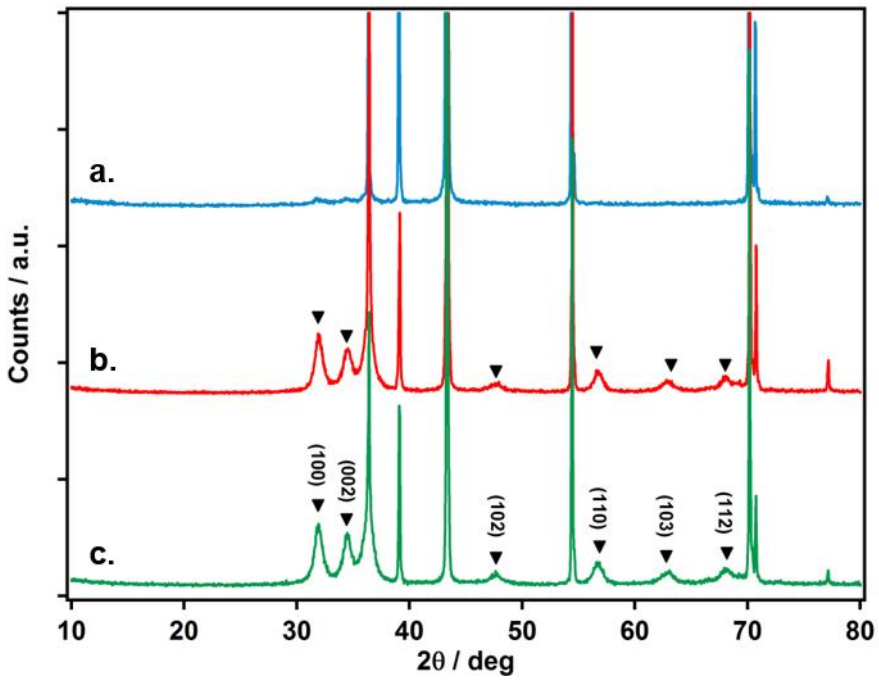

Figure 5.10. Flat plate powder x-ray diffraction patterns of the anodic nanowire films after a second anodization (a), after treatment in a solution of $Zn(NH_3)_4^{2+}$ (b) and after treatment within water (c).

The next method to be tested was the treatment of the annealed nanowire film in a solution of $Zn(NH_3)_4^{2+}$, based on a method reported by Mukherjee *et al*..[231] It was conducted by dipping the film within the solution for 60 s, followed by rinsing in deionised water. This was repeated a further two times and then the film was dried and annealed at 300 °C for 1 h. After treatment, no obvious change in film appearance could be observed by eye and no other materials could be detected by XRD (Figure 5.10b). Upon examination of the surface morphology by FESEM it could be seen that the treatment had resulted in the deposition of patches of material that showed up brightly within the micrographs due to charging (Figure 5.11a). It could also be observed that many of the nanowires had been broken and had bunched together to form bundles of nanowires (Figure 5.11b). This bunching together is likely a result of capillary forces acting on the nanowires when drying the films after treatment. Due to the destruction of the nanostructure, this method was also deemed as unsuitable as a passivation treatment.

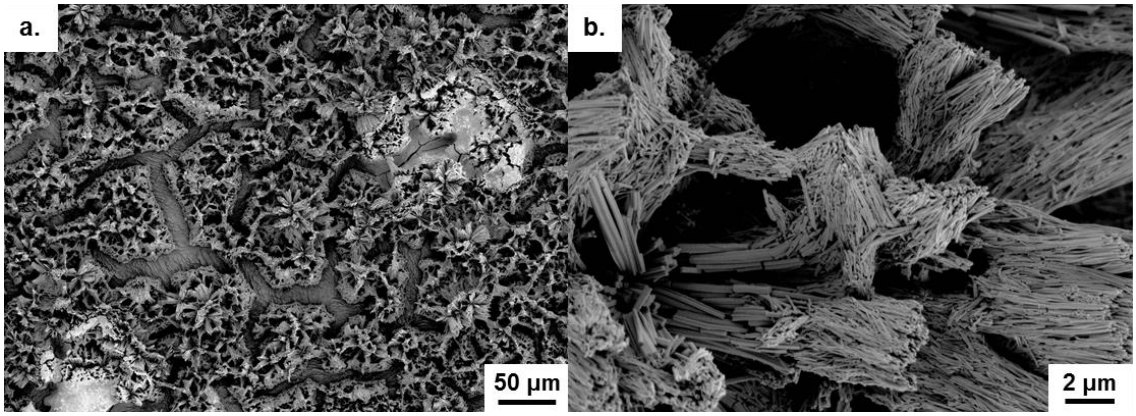

Figure 5.11. Low (a) and high (b) magnification FESEM micrographs of the nanowire film surface after three 1 min treatments in a solution containing $Zn(NH_3)_4^{2+}$ at room temperature followed by annealing in air at 300 °C for 1 h.

5.2.2 Formation of hierarchical ZnO structures

During the investigation into passivation treatments an interesting phenomenon was observed for one of the methods. The method involved simply leaving the annealed nanowire film submerged in a vial of deionised water overnight, followed by rinsing, drying and annealing. Upon examination of the films by FESEM it could be seen that a secondary growth had occurred on the surface of the nanowires to form hierarchical structures (Figure 5.12a and b). The secondary growth was found to be in the form of spikes of a material on the nanowire surface. As the flat plate XRD patterns of the films revealed no other materials than ZnO and the zinc substrate (Figure 5.10c) these spikes were assumed to be formed from ZnO.

In addition to the secondary growth of ZnO on the nanowires, growth was also observed to take place on the zinc substrate (Figure 5.12c). This growth was found to be in the form of small, rounded spikes covering the surface of the foil, with sizes ranging between 50 and 300 nm. This growth on the substrate presents the possibility of passivating the exposed zinc within the cracks of the nanowire film, making the films suitable for application in DSCs.

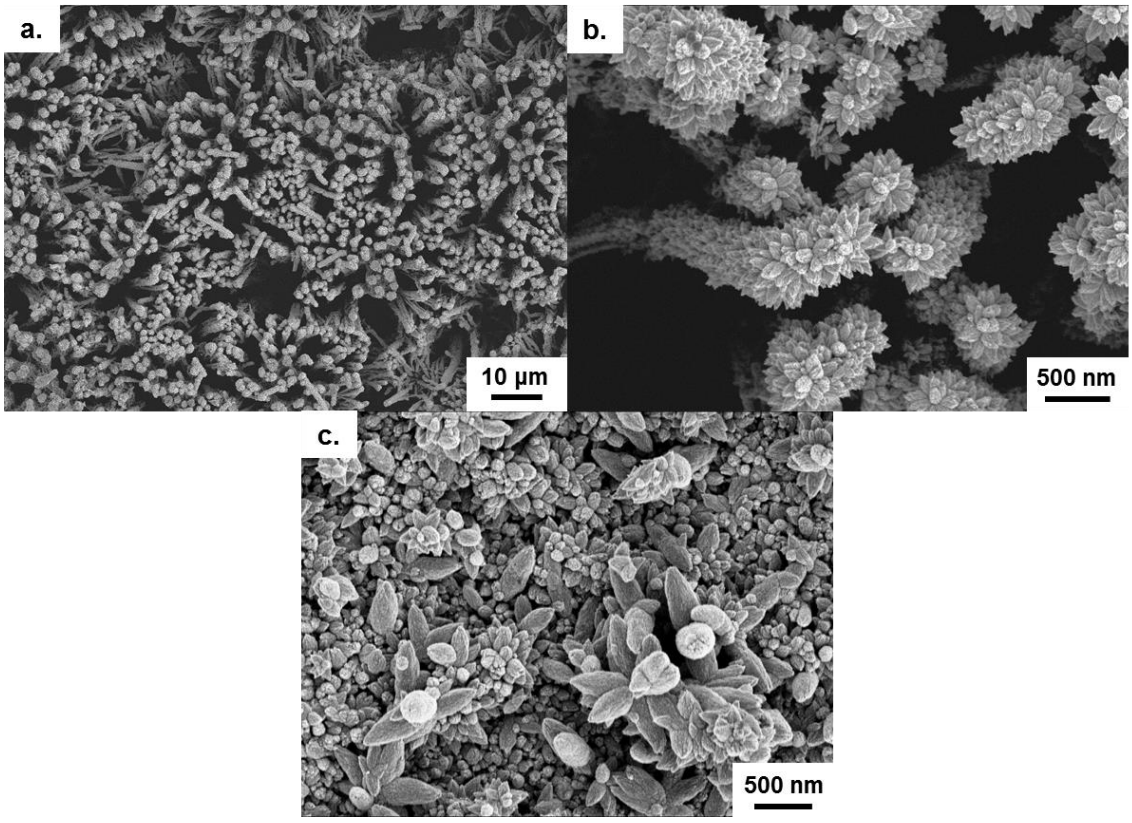

Figure 5.12. Low (a) and high (b) magnification FESEM micrographs of anodic nanowire films after treatment in water for 24 h, followed by annealing in air at 300 °C for 1 h, and FESEM micrograph of the growth on a bare Zn surface after the same treatment in water (c).

A detailed comparison of the nanowire structure before and after this treatment is shown within the TEM micrographs in Figure 5.13. The hierarchical structures consist of spike shaped ZnO crystals of ~40 nm in length surrounding the polycrystalline nanowire. These structures are likely to be the result of a slow secondary growth of ZnO onto the nanowires, with hydrated zinc ions from the substrate as the ion source. The XPS spectrum of the hierarchical structures reveals little difference in composition from the unmodified nanowires, confirming that the structures are formed from ZnO (Figure 5.14). This simple modification method may provide a route to even higher surface area nanostructures than the nanowires with slit-type pores and would therefore

also be promising candidates for application in dye-sensitized solar cells, where the combination of high surface areas and a one-dimensional structure are beneficial.

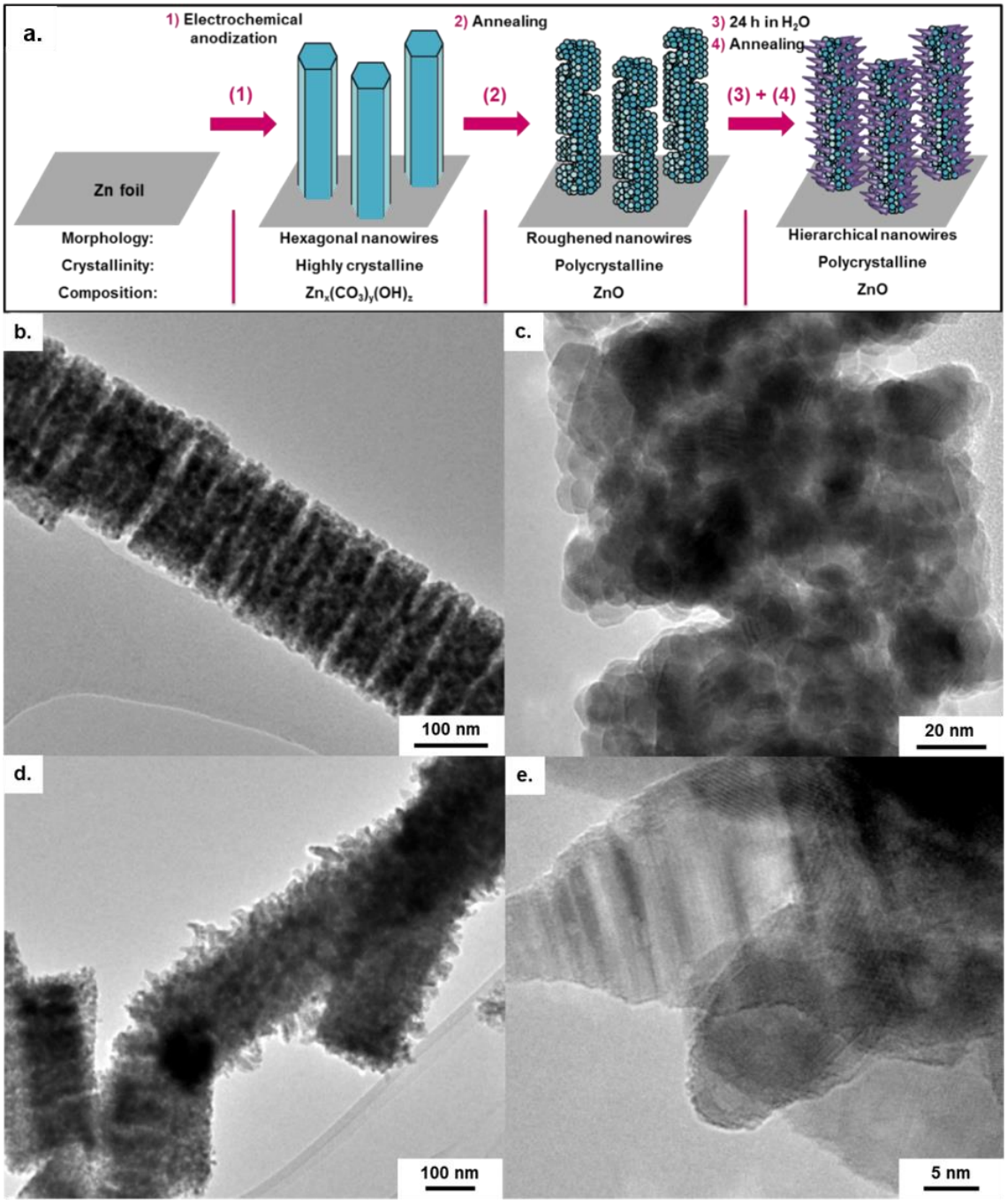

Figure 5.13. Scheme demonstrating the steps in the production of hierarchical ZnO nanowire arrays (a), TEM micrographs of the polycrystalline ZnO nanowires with a slit-pore structure before water treatment (b-c) and with a hierarchical structure featuring spikes after water treatment (d-e).

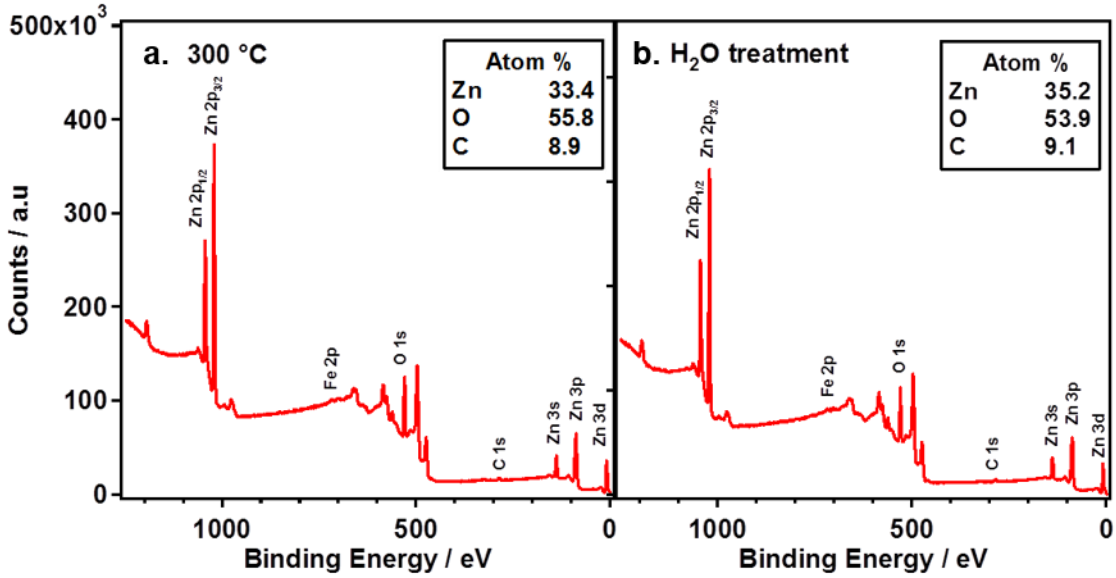

Figure 5.14. Comparison of the XPS spectrum of the anodic nanowire arrays after annealing (a) and after further treating with water and annealing for a second time (b).

5.3 Core-Shell Structures via Solution Based Growth

The modifications documented in Section 5.2 all focussed on the growth of ZnO on the anodic nanowires, however, this need not be the only choice of material. There are multiple reports in the literature of the formation of core-shell structures, where the nanowire acts as a core around which a shell of another material is deposited. For applications in dye-sensitized solar cells TiO_2 is the most obvious shell material to use, due to its chemical stability and compatibility with the highest performing molecular dyes. Indeed, core-shell structures using ZnO nanowire cores and TiO_2 shells have been demonstrated previously and have achieved enhanced performances compared to bare ZnO nanowires.[91]

This section explores the formation of unique core-shell structures, composed of the polycrystalline ZnO nanowires from anodization as the core, surrounded by a shell of nanosheets composed of TiO_2. These will be referred to as ZNW@TNS. This research was conducted as part of a collaboration with the group of Professor Jong Hak Kim at Yonsei University and should therefore be viewed as a joint contribution between myself and Chang Soo Lee, a PhD student within Professor Kim's group. All ZnO nanowires were produced by myself at the University of Bath. Initial attempts at nanosheet growth (as shown in Figure 5.15) were conducted by myself during a one month placement within Yonsei University, after which Chang Soo Lee continued the experiments to successfully form the core-shell structures (as shown in Figure 5.16).

The synthesis technique was based around a method previously reported by Kim *et al*. for the growth of TiO_2 nanosheets on SnO_2 nanotubes.[232] In this case the method involved the addition of anodic ZnO nanowire powder to a 2-propanol based solution containing diethylenetriamine (DETA) and titanium(IV) isopropoxide (TTIP), followed by a solvothermal reaction for 24 h at 200 °C within a Teflon® lined autoclave. The corresponding quantities of DETA and TTIP used in each experiment are detailed within Table 5.1.

Table 5.1. Reagent volumes used for the synthesis of ZNW@TNS under different conditions based on 2-propanol solvent volume of 40 mL.

Condition	DETA (mL)	TTIP (mL)
1	0.03	0.50
2	0.03	1.00
3	0.03	1.50
4	0.30	0.30
5	0.15	0.30
6	0.30	0.15
7	0.15	0.15

The structures formed from the initial set of syntheses (conditions 1-3) can be observed within Figure 5.15. It can be seen that the attempts at TiO_2 nanosheet growth on the ZnO nanowires was unsuccessful in all three cases. For condition 1 the majority product was agglomerates of TiO_2 particles mixed in with uncoated ZnO nanowires. For conditions 2 and 3, however, the majority product was hollow spheres of TiO_2 with typical diameters of 2-6 μm. These TiO_2 hollow spheres have been reported previously by Yang *et al*. under similar reaction conditions and can be attributed to the alcoholysis of the TTIP precursor in low DETA concentrations.[254] Despite the formation of TiO_2 spheres, the ZnO nanowires appeared unaltered and still displayed their characteristic slit-pore structure (Figure 5.15f).

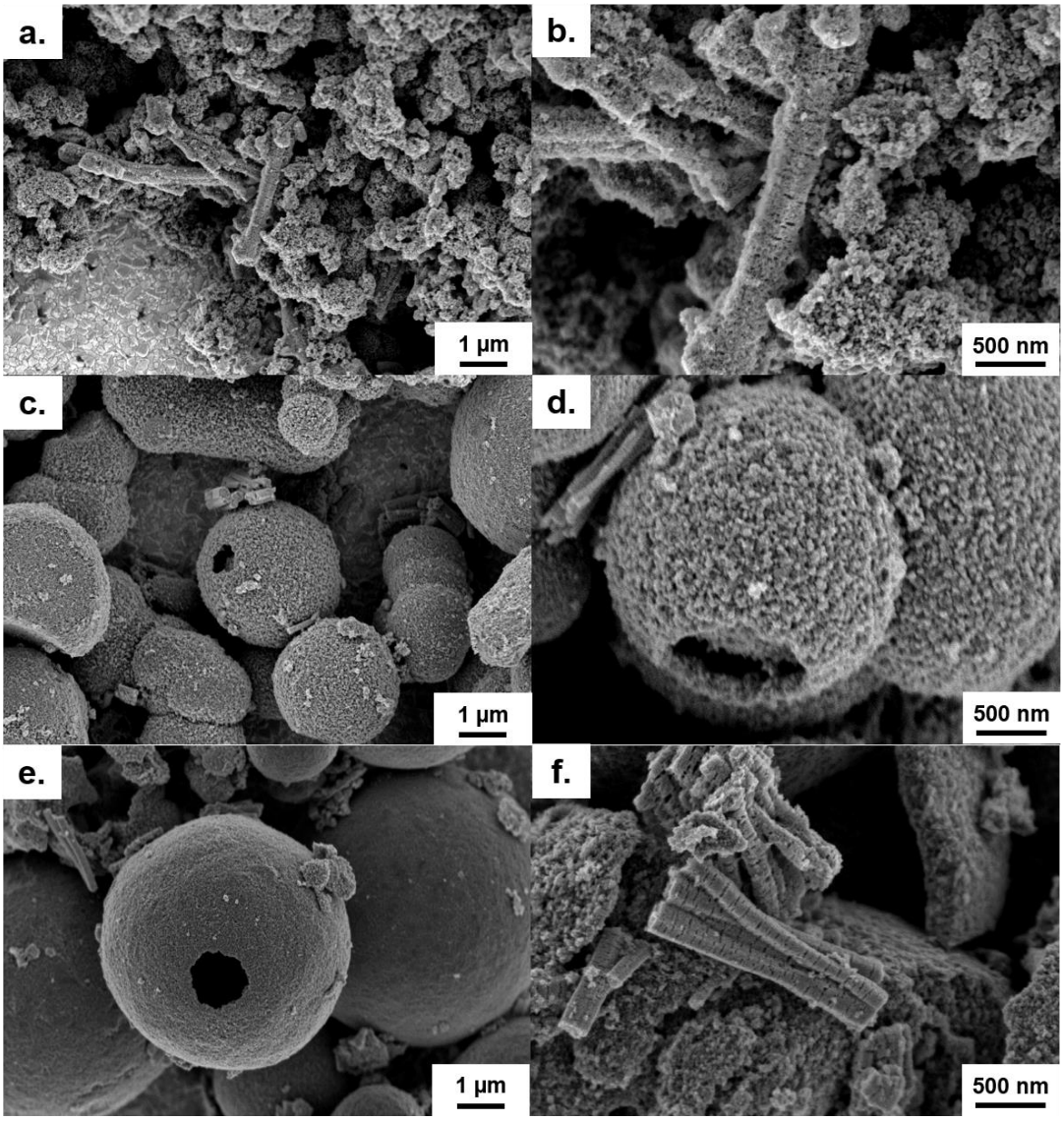

Figure 5.15. FESEM micrographs of the resulting structures formed under conditions 1 (a-b), 2 (c-d) and 3 (e-f).

In the second set of syntheses (conditions 4-7) higher concentrations of DETA and lower concentrations of TTIP were used in an effort to avoid the formation of TiO_2 spheres. This strategy was found to be largely successful, with nanosheet growth occurring under the majority of conditions. Under conditions 4 and 7 the nanowires were observed to be conformally covered with nanosheets, giving them a high surface area core-shell structure (Figure 5.16). Some nanosheet growth was achieved under condition 5, however coverage was found to be inconsistent over the sample, as evidenced in Figure 5.16d where only very minor growth was observed. In contrast, no nanosheet formation was observed for condition 6 and only the formation of TiO_2 particles occurred on the nanowire surface (Figure 5.16f). When relating these results to the reaction conditions, two main outcomes can be deduced: 1. Very low DETA concentrations results in TiO_2 sphere formation rather than nanosheets; and 2. Optimal growth of nanosheets is achieved when equal volumes of DETA and TTIP are present within the reaction mixture.

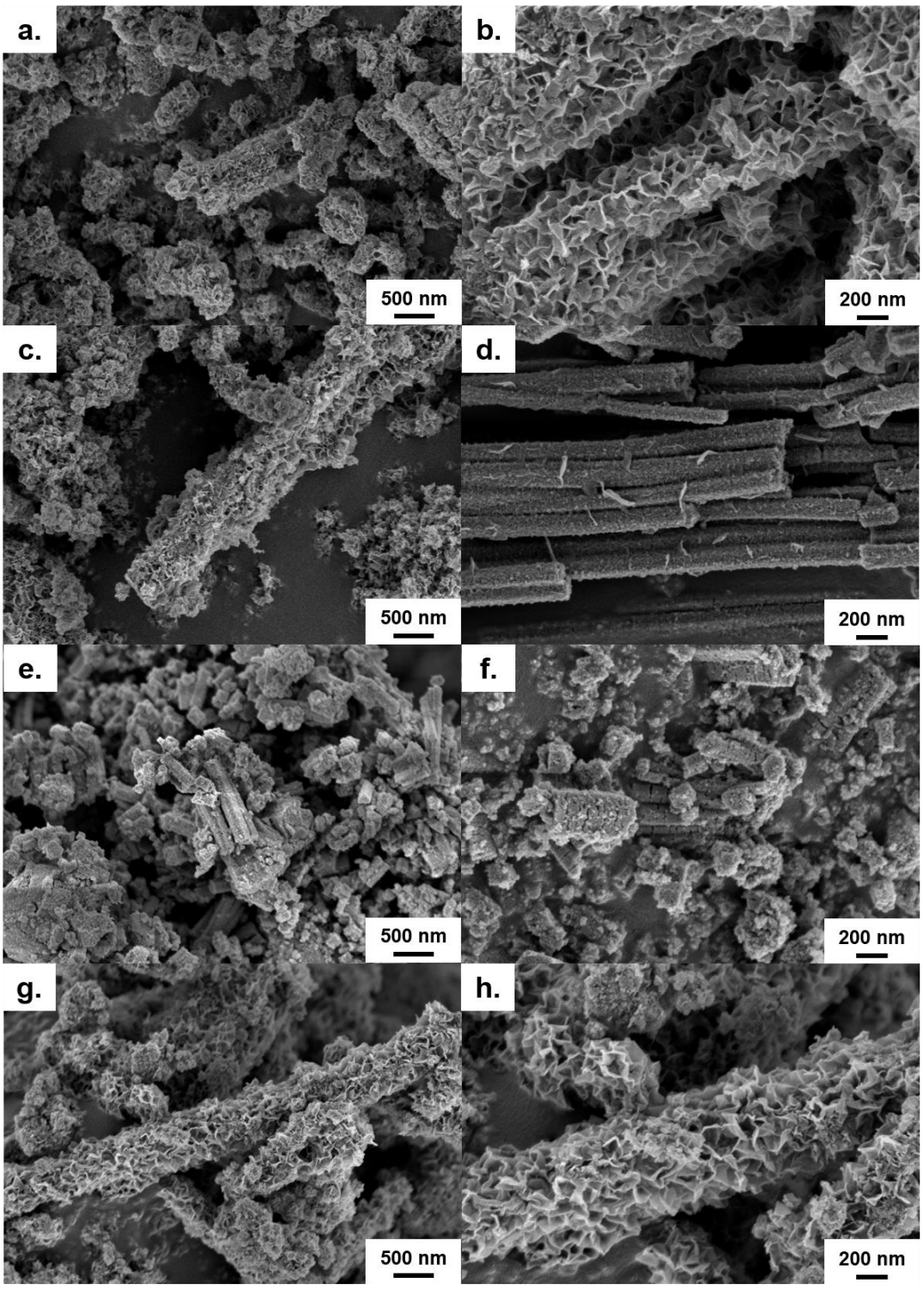

Figure 5.16. FESEM micrographs of the resulting structures formed under conditions 4 (a-b), 5 (c-d), 6 (e-f) and 7 (g-h).

The nanosheets appeared to grow in a random orientation from the nanowire surface (Figure 5.17), which can be viewed in more detail within the high magnification FESEM and TEM micrographs (Figure 5.18). The growth of nanosheets contributed greatly to the diameter of

the nanowires, with diameters of the modified structures typically reaching ~500 nm. Based on an average diameter of ~160 nm for the unmodified nanowires, this allows us to estimate typical nanosheet lengths of ~150-200 nm. As the nanosheets were observed to be extremely thin this modification would be expected to contribute significantly to the surface area of the nanowires, which would be of benefit for application within DSCs.

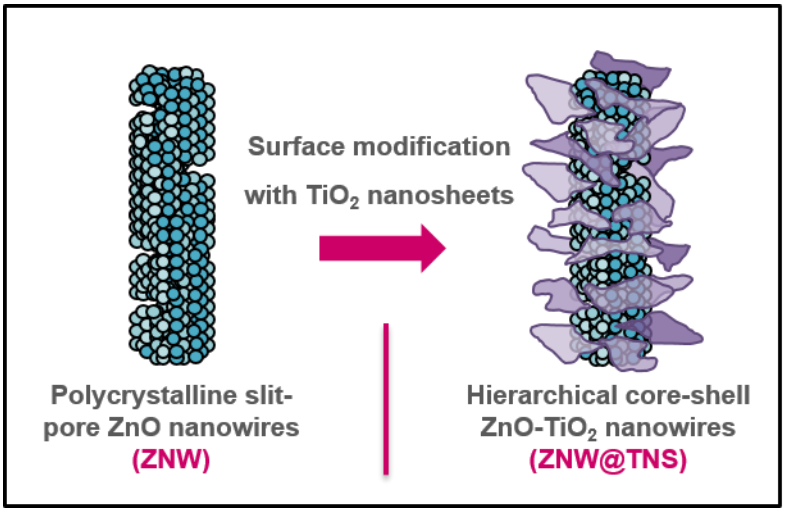

Figure 5.17. Cartoon demonstrating the transformation of structure from polycrystalline ZnO nanowires (ZNW) to hierarchical core-shell nanowires with TiO_2 nanosheets (ZNW@TNS).

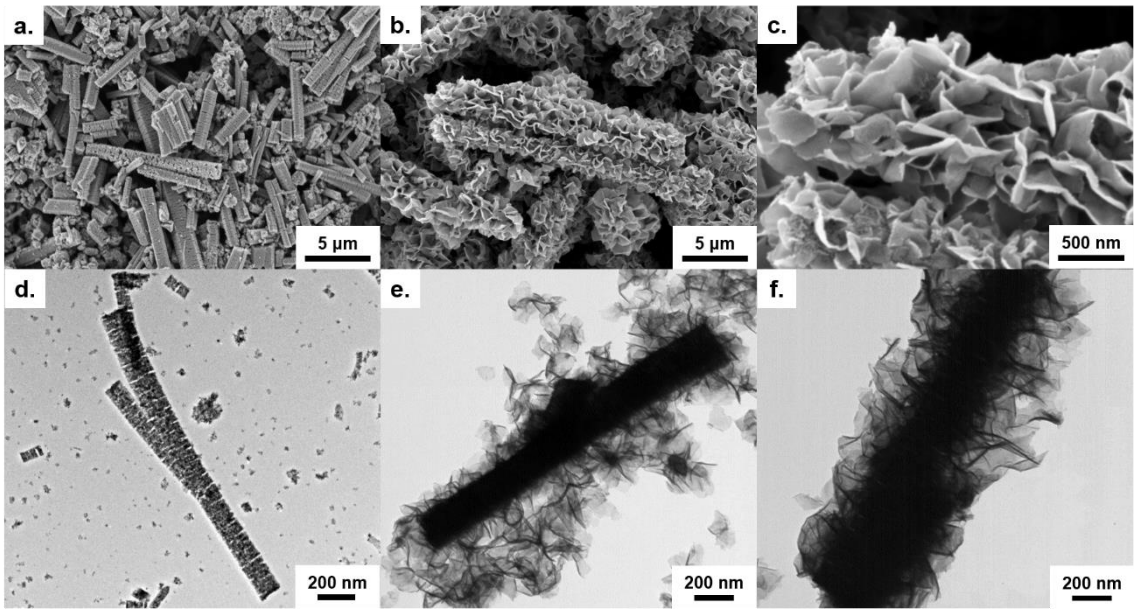

Figure 5.18. FESEM (a-c) and TEM (d-f) micrographs of the ZnO nanowires before modification (ZNW) (a and d) and after modification (ZNW@TNS) with separation by either centrifugation (b and e) or precipitation (c and f).

Despite achieving conformal coverage of nanosheets on the nanowire surface under optimized conditions (condition 4), a number of loose nanosheet agglomerates were also present within the product mixture when separation was achieved via centrifugation (Figure 5.18e). Avoiding the inclusion of these agglomerates within the final product was desirable in order to accurately determine the properties of the core-shell structures. Therefore, different separation techniques were investigated. A successful route was found to be the sonication of the product in 2-propanol, followed by a natural sedimentation. It was found that the larger and heavier core-shell structures slowly separated from the mixture, forming a sediment at the bottom of the vial, whilst the smaller nanosheet agglomerates remained within solution. The solution could then be pipetted away and the sediment re-diluted to give a purer dispersion of the core-shell structures (Figure 5.18f).

The separated ZNW@TNS structures were then characterised using powder XRD and XPS to verify that the nanosheets were formed of TiO_2 and determine in which phase it is formed. The powder XRD pattern of the structures was dominated by peaks corresponding to the wurtzite phase of ZnO, which comes from the underlying ZnO core (Figure 5.19). A small peak at ~25° was observed in addition to the ZnO peaks which corresponds with the (101) plane of TiO_2 in the anatase phase. This is the most desirable phase for application in dye-sensitized solar cells.[255] The relatively small size of the anatase peaks is likely due to the extreme thinness of the nanosheets and also due to overlap with peaks from ZnO including the (102), (103) and (112) wurtzite peaks.

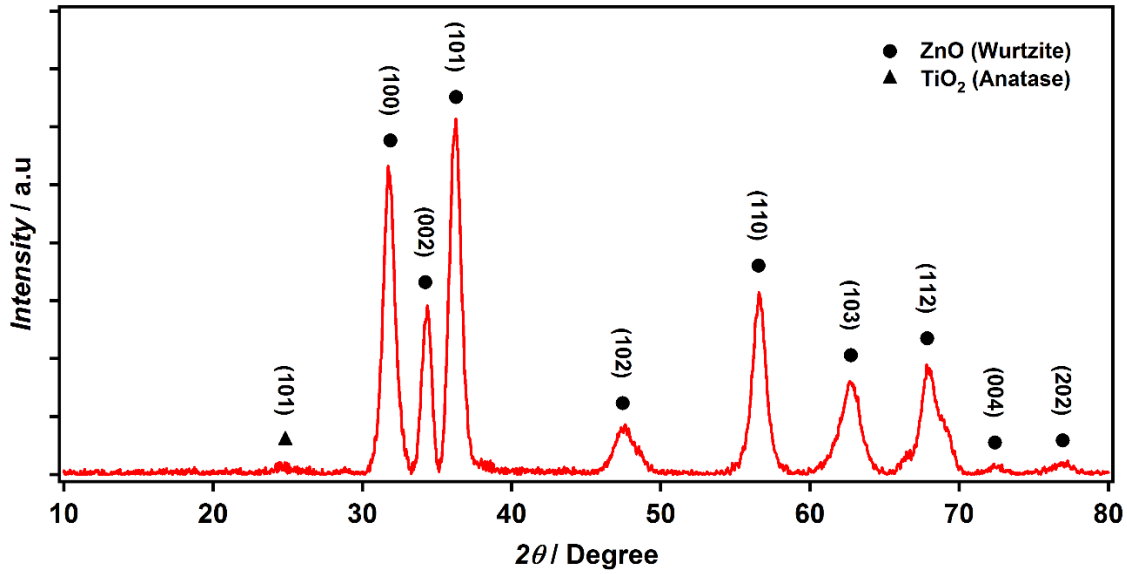

Figure 5.19. Powder XRD pattern of the ZNW@TNS nanowires formed from a solvothermal reaction at 200 °C for 24 h under reaction condition 4.

Whilst the XPS spectra of both the unmodified nanowires (ZNW) and the ZNW@TNS structures displayed peaks within the Zn 2p and O 1s regions, presence of peaks within the Ti 2p region was only achieved after the growth of nanosheets (Figure 5.20). This further supports the formation of TiO_2 during nanosheet growth. It can also be seen that a significant decrease in Zn 2p peak intensity occurs after nanosheet growth due to the exponential decay of signal with depth from the XPS technique, indicating a fairly complete coverage of the nanowire structures with TiO_2. After nanosheet growth it could also be observed that nitrogen was present within the nanostructures. This could possibly indicate nitrogen doping of the TiO_2 nanosheets, with the nitrogen originating from the DETA reactant.

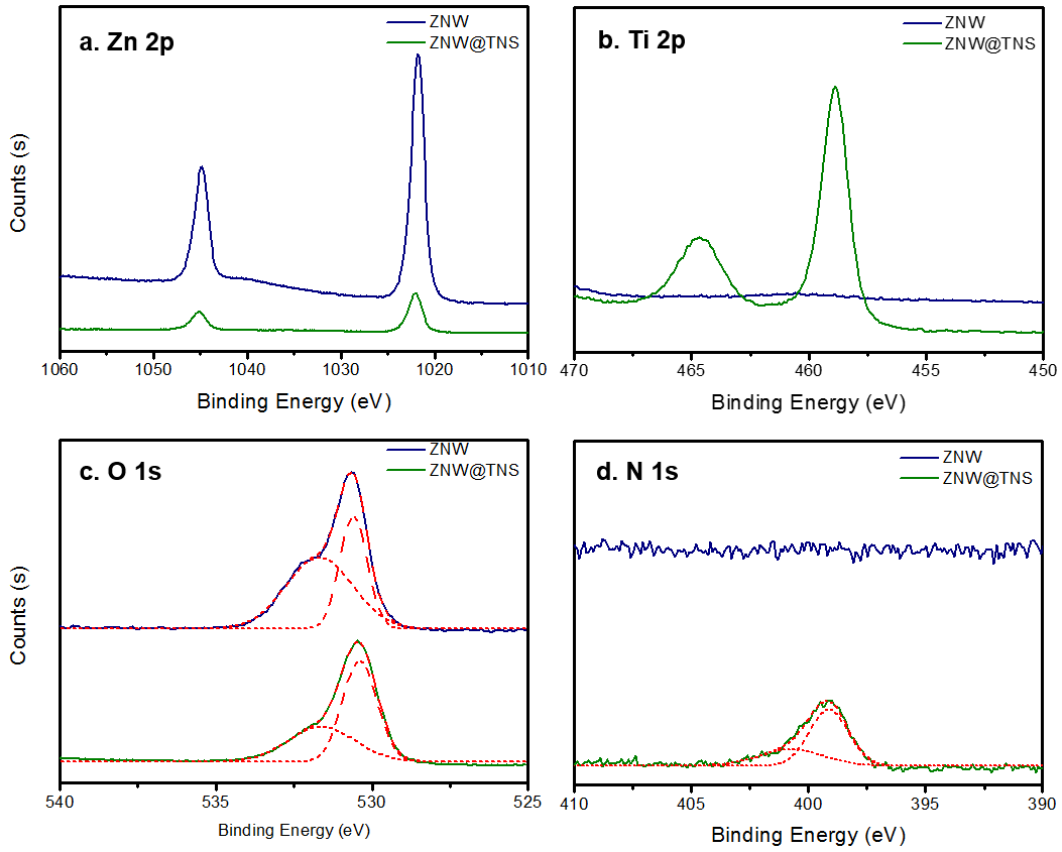

Figure 5.20. Comparison of the XPS spectra of the ZNW and ZNW@TNS structures within the Zn 2p (a), Ti 2p (b), O 1s (c) and N 1s (d) region.

In this section, the production of novel core-shell structures formed from an anodic ZnO core surrounded by a shell of TiO_2 nanosheets (ZNW@TNS) has been demonstrated. These structures present many promising properties for application in DSCs including an overall 1-D structure, high surface areas, a chemically stable TiO_2 shell and a core-shell structure which could reduce electron-hole recombination. In Chapter 6 the application of these promising materials within quasi-solid state DSCs (qssDSCs) will be explored and their performance compared with those of unmodified anodic nanowires (ZNW).

5.4 Chapter Summary

In this chapter, the modification of the nanowires after anodization has been explored. It has been possible to demonstrate that through the use of relatively simple post-treatments a range of nanostructures can be achieved, including polycrystalline nanowires with a slit-type pore structure, hierarchical nanowires formed from ZnO and also unique core-shell structures that could combine the beneficial properties of two different nanomaterials. In the remaining chapters these nanomaterials will be taken and applied in both dye-sensitized solar cells and perovskite solar cells, using a wide range of device architectures that take advantage of the beneficial properties of these nanomaterials. The disadvantages and merits of these nanomaterials within the chosen device architectures will be discussed and it will be demonstrated how some of these unique nanomaterials can be used to improve device performances compared to standard mesoporous films of nanoparticles.

Chapter 6 – Application of ZnO Nanowires in Dye-Sensitized Solar Cells

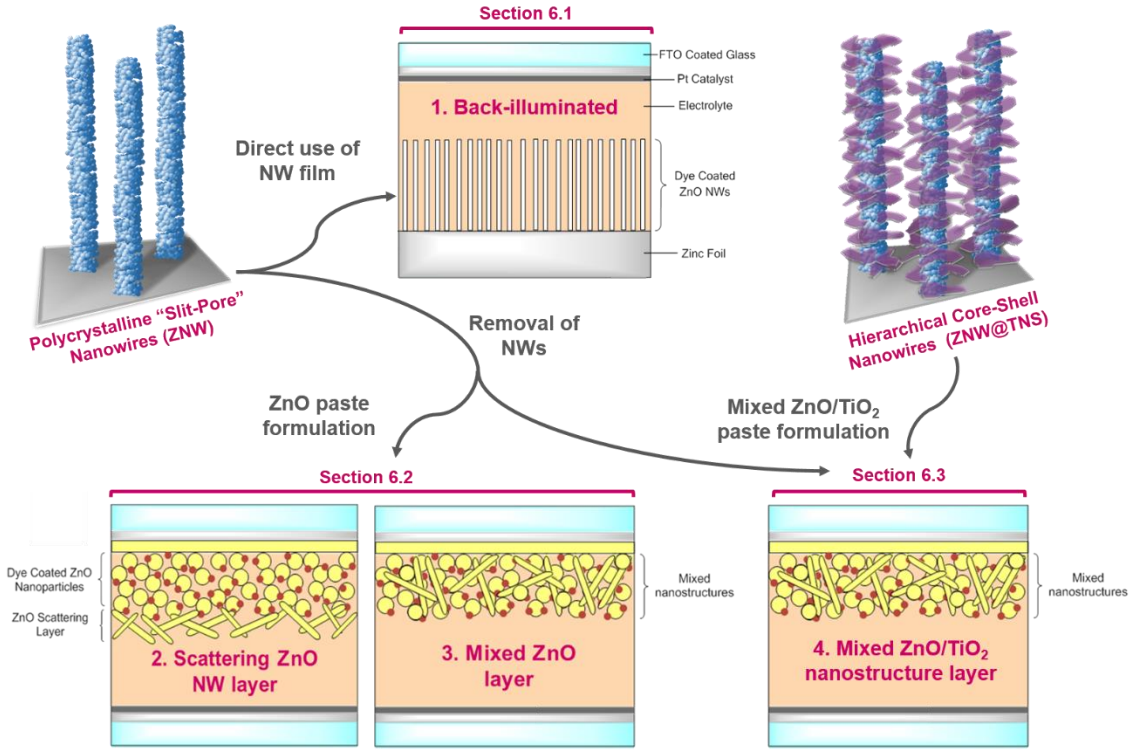

Figure 6.1. Schematic summarising the chapter contents and layout.

In Chapter 5, the production of a range of hierarchical ZnO nanostructures was demonstrated, starting from the nanowires synthesized by anodization. Many of these nanostructures demonstrated the potentially beneficial combination of high surface areas and an overall one-dimensional structure, which is desirable for application in dye-sensitized solar cells (DSCs).

Within this chapter, these nanomaterials will be applied in a range of DSC architectures to assess whether they can bring about improvements to the device performance, compared to the use of simple nanoparticle films. The chapter is split into three main sections, which each focuses on a particular type of DSC architecture, as highlighted in the chapter summary figure (Figure 6.1).

The first section focusses on the direct application of the nanowire films in back-illuminated DSCs, so called due to them being illuminated through the counter electrode. In the second section, various pastes are prepared from the annealed anodic nanowires and are used to prepare different front-illuminated DSC photoanode architectures. These are then used to compare the performance of cells using nanowires to those composed simply of ZnO

nanoparticles. In the final section of the chapter, the hierarchical core-shell structures that were demonstrated in Chapter 5, Section 5.3 are applied within quasi solid state DSCs (qssDSCs), which feature an organised mesoporous TiO_2 photoanode. This final device architecture allows the potential benefits of hierarchical, one-dimensional structures to be combined with a core-shell structure, where the beneficial properties of two different materials can be used.

6.1 Back-Illuminated Dye-Sensitized Solar Cells

The first cell configuration in which the anodic nanowires were tested was what is called a back-illuminated cell configuration (Figure 6.2), so named due to the light entering the cell through the counter electrode (cathode) rather than the photoanode. This cell configuration is ideally suited to the nanowires produced via anodization as the nanowires can be used on the zinc foil substrate, which also acts as a conducting contact. This cell configuration could have a number of benefits as the nanowires would be aligned parallel to the substrate, allowing optimal directed electron transport from the point of generation to the point of collection. The zinc substrate could also be used alongside a flexible counter electrode, giving rise to fully flexible and thin cells, which would be advantageous for a number of portable applications.

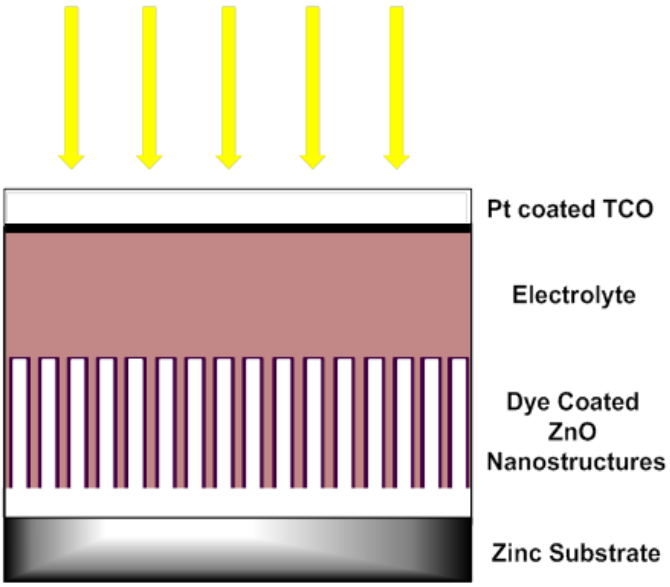

Figure 6.2 Schematic showing the cross-sectional structure of a back-illuminated DSC.

6.1.1 Dye-adsorption on the nanowire films

The first stage in production of back-illuminated DSCs was to dye the nanowire films with a suitable molecular dye. This acts as the light harvester and injects excited electrons into the ZnO during operation. A ruthenium-based molecular dye named N719 (see Chapter 2, Figure 2.8 for the chemical structure) was used for all of the cells reported in this chapter. This dye is the most commonly used dye for application in DSCs and, therefore, provides the biggest scope for comparison of the results with previous literature. The dye has a broad light absorption range within the visible region of the light spectrum and is dark red/purple in colour.[46]

It has been previously reported that there are some compatibility issues between the N719 dye and ZnO photoanodes, due to the instability of ZnO towards corrosion in acidic solutions. Reports have been made of both corrosion of the photoanode and formation of dye agglomerates within pores, due to interactions between the carboxylic acid groups of the N719 dye and Zn^{2+} ions.[98, 99] For these reasons, lower dyeing times are typically used for ZnO photoanodes compared to the times for TiO_2.[256] Despite this compatibility issue, many of the highest reported efficiencies for cells using ZnO photoanodes have been achieved using the N719 dye.[90] It is for this reason that it is used in conjuction with ZnO photoanodes throughout this Chapter.

After a dyeing time of only 2 h in the ethanolic dye solution the anodic nanowire films had become dark red/purple with the darkness of the films depending on the thickness of the nanowire film used (Figure 6.3a). Figure 6.3 shows how the darkness of the dyed films increases for films anodized for longer periods of time, corresponding to thicker nanowire films, as shown in Figure 6.3b-d.

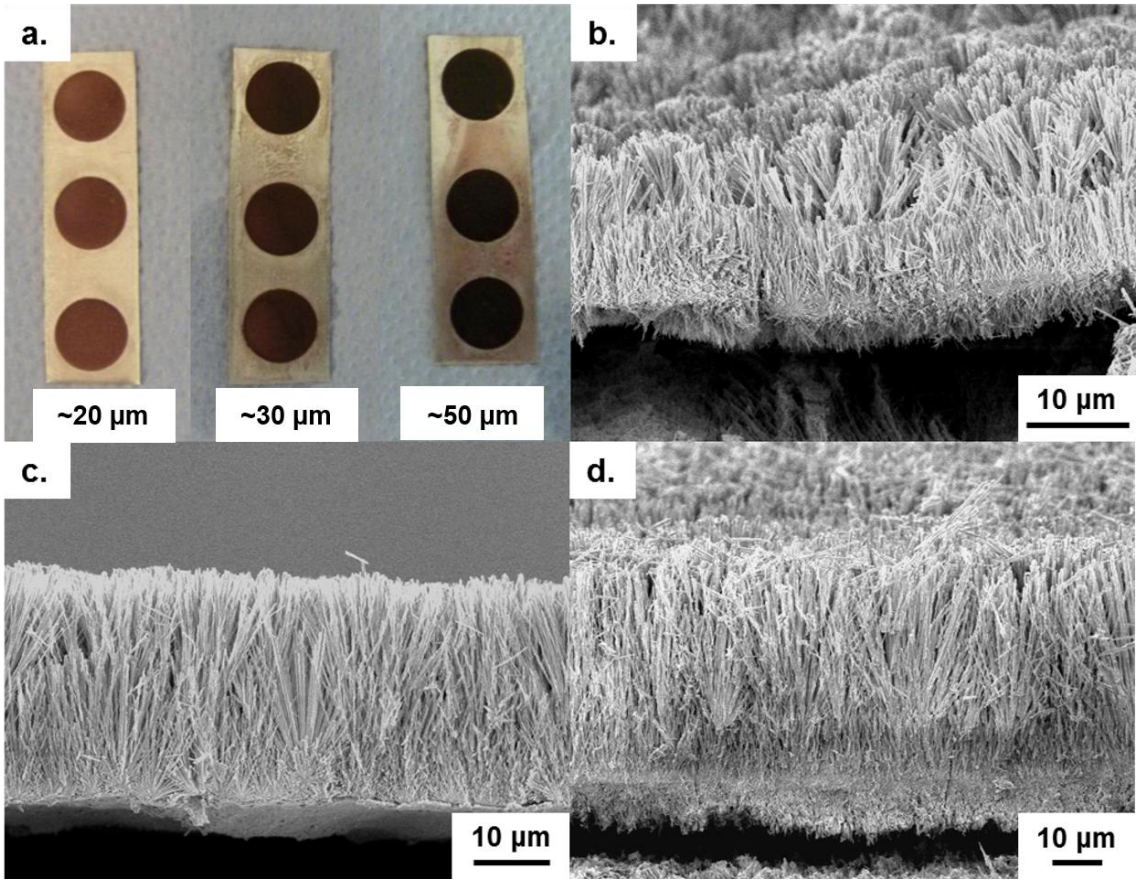

Figure 6.3. Photo of anodic nanowire films formed by anodization for different lengths of time (resulting in different thicknesses) and dyeing in an ethanolic N719 dye solution (a) and cross-sectional FESEM micrographs of the films they correspond to, showing an increase in film thickness (b-d).

In order to quantitatively determine the amount of dye that is loaded onto the nanowire films during the dye treatment, UV-vis absorption spectroscopy was used. A calibration curve was first produced by recording the absorbance intensity at the wavelength of maximum absorbance (λ_{max}, 498 nm) of different known concentrations of the N719 dye (Figure 6.4a). This calibration curve was then used to determine the concentration of N719 dye solutions that had been produced by desorbing the dye from the nanowire films over a period of 24 h using known volume (v) of an ethanolic 0.1 mM KOH solution. Measurements were undertaken for nanowire films of 50 µm in thickness, dyed for lengths of time between 1 and 4 h (Figure 6.4b), and from the concentration (C) measurements the dye loading on the film (D) was calculated according to:

$$D = \frac{C \cdot v}{a} \qquad \text{Eq. 6.1}$$

Where a is the geometric surface area of the nanowire film (1.13 cm^2) (Figure 6.4c).

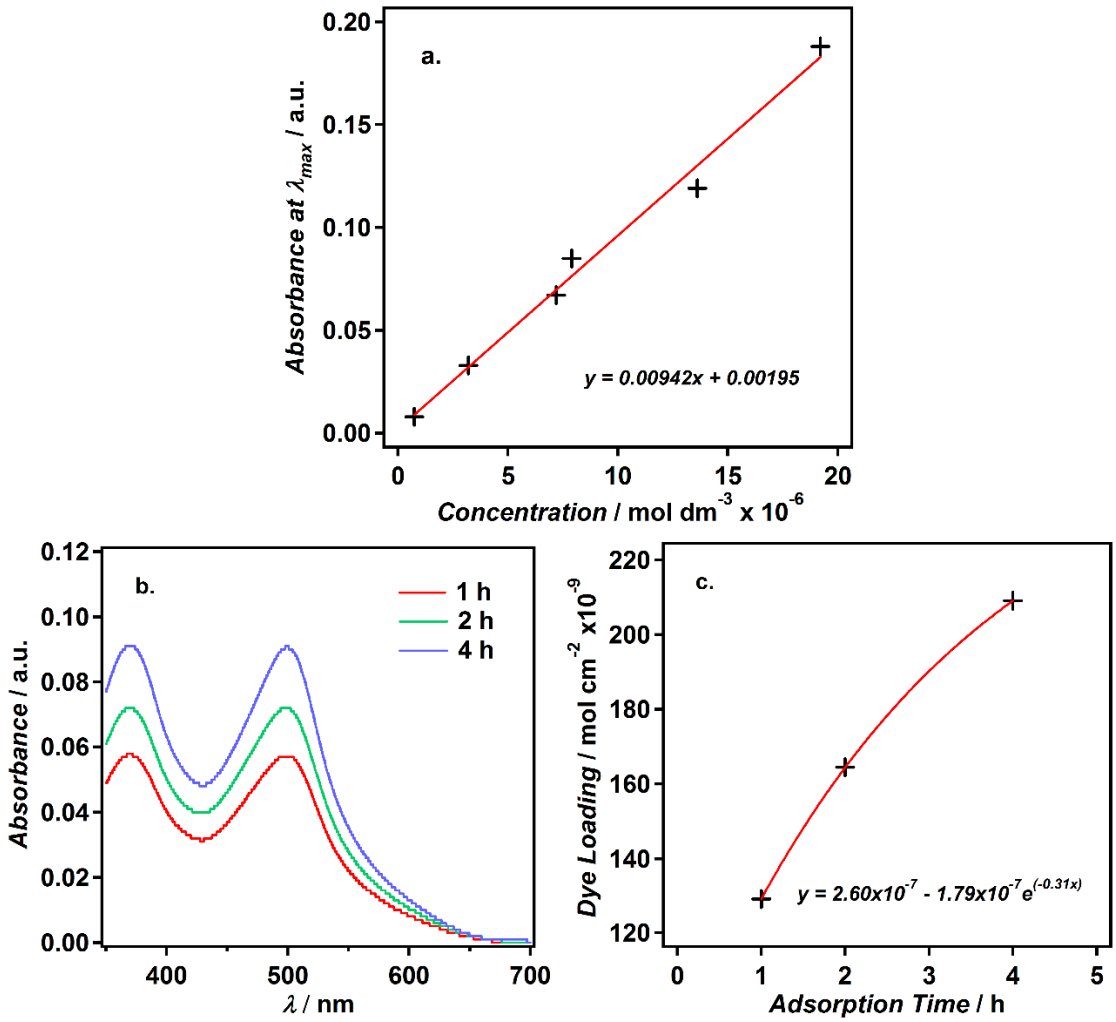

Figure 6.4. Calibration curve of absorbance *vs.* N719 dye concentration (a), UV-Vis absorbance of desorbed dye from nanowire films dyed for different lengths of time (b) and the corresponding loading of dye on the nanowire films (c).

It can be seen that although the dye loading increases with increasing dyeing time, the increase begins to level off towards longer dyeing times. It was chosen not to take measurements for dyeing times longer than 4 h, as beyond this length of time formation of aggregates is known to occur, which would likely give rise to a significant error in the measurement of dye loading.[257] Typical dye loadings for a mesoporous film of TiO_2 nanoparticles with a film thickness of ~5 µm are ~50 x 10^{-9} mol cm^{-2}.[258] Normalising this value for the film thickness gives a value of ~10 x 10^{-9} mol cm^{-2} μm^{-1}. Based on a film thickness of ~50 µm for the anodic nanowire films, a normalised dye loading of ~4 x 10^{-9} mol cm^{-2} μm^{-1} can be calculated, which is less than half of that expected for standard mesoporous TiO_2 films. This is, perhaps, unsurprising considering the considerable amount of void space between nanowires in which there is no dye uptake. However, when the dye uptake of the anodic nanowires is compared to values of 1.3-1.7 x 10^{-9} mol cm^{-2} μm^{-1}, obtained for some of the best performing monocrystalline ZnO nanowires in DSCs, the values of dye loading are promising.[68] These results show that the anodic nanowires could have the potential to overcome the low dye loadings commonly associated with nanowire DSCs, which is generally considered to be the main bottleneck in achieving high efficiencies for these cells.

6.1.2 Cell fabrication and measurement

Cells were fabricated using nanowire films produced from a 15 min anodization (corresponding to a ~50 µm thickness) that had been dyed in an ethanolic N719 dye solution for 2 h. The device performance was assessed by measuring a current-voltage (*I-V*) curve under standard AM 1.5 simulated solar illumination, which was then normalised for the cell area by plotting as a current density-voltage (*J-V*) curve. It was found that in all cases the measured current density and voltage were negligible, despite multiple repeats. A typical *J-V* curve measured for a back-illuminated DSC is shown in Figure 6.5. It can be seen that both the current density and the voltage are approximately three orders of magnitude smaller than what would be typical of a well-performing DSC.[27] The *J-V* curve can also be seen to resemble a straight diagonal line rather than the typical curve shape. This indicates a relationship characteristic of a simple resistor and not of a DSC.

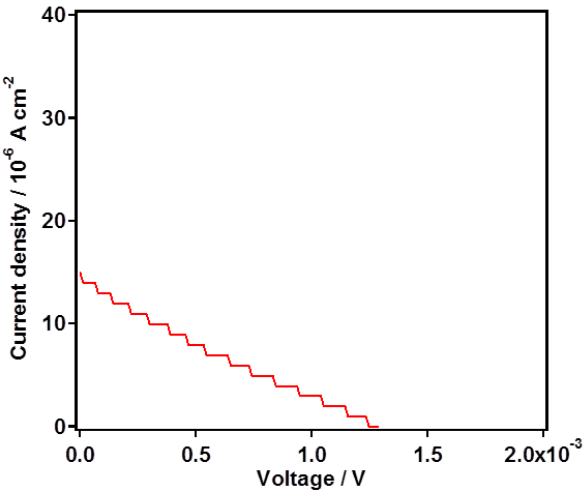

Figure 6.5. Typical *J-V* curve measured under AM 1.5 solar irradiation for a back-illuminated DSC using an anodic nanowire film.

An explanation for the very poor performance of the back-illuminated DSCs might be found in the observations made by FESEM in Chapter 4, Section 4.3.4. FESEM micrographs revealed that the anodic nanowire films were cracked, sometimes severely, after the annealing treatment that was necessary to form ZnO. These cracks exposed bare regions of the zinc substrate beneath the nanowire film. At these points, it is likely that fast recombination of electrons and electron holes occurs between the conducting zinc substrate and the electrolyte, effectively forming a low resistance shunting pathway within the cell (Figure 6.6). This would be expected to lead to an extremely poor cell performance and a straight diagonal line within the *J-V* measurement, indicative of a simple resistance.

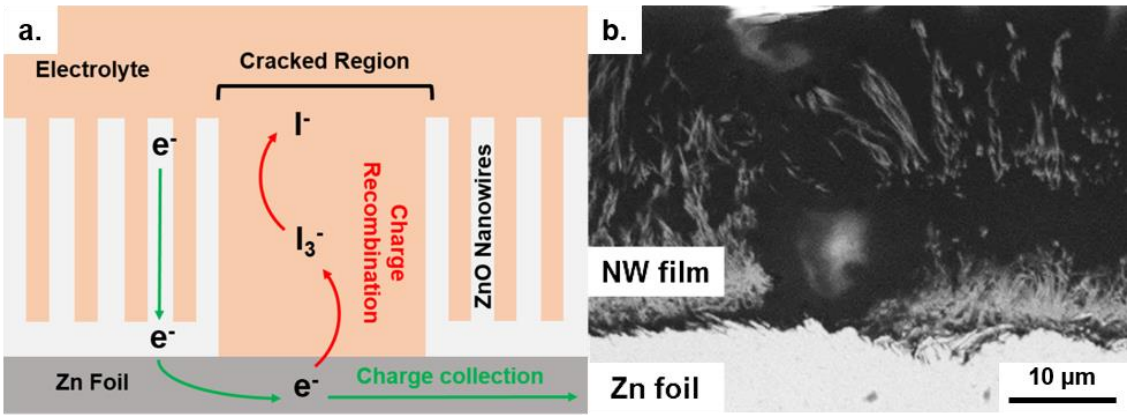

Figure 6.6. Schematic representing the likely route of performance loss within the back-illuminated DSCs (a) and a cross-sectional FESEM micrograph showing cracking in the annealed film (b).

It would, therefore, appear that although in principle the back-illuminated cell configuration has many merits, working cells are not achievable due to the formation of cracks in the nanowire films during annealing. Many efforts were made to passivate the surface of the annealed nanowire films and the exposed zinc substrate through chemical modification and secondary growth (see Chapter 5, Section 5.2 for full details of the modifications). However, it was found that these attempts were unsuccessful in improving the performance of the back-illuminated devices.

It was, therefore, necessary to investigate alternative cell structures in which the anodic nanowires were removed from the zinc substrate that they were grown on. This will be the focus of the remainder of the chapter, with photoanodes formed entirely of ZnO being the focus of Section 6.2 and mixed ZnO-TiO_2 photoanodes being the focus of Section 6.3.

6.2 Front-Illuminated Dye-Sensitized Solar Cells

As an alternative to the back-illuminated cell configurations, front-illuminated DSCs were investigated. This cell configuration is the more typical configuration for a DSC, with the cell being illuminated through the photoanode side of the cell by depositing the photoanode on a transparent conducting electrode (Figure 6.7). To deposit a porous metal oxide film on the transparent electrode it is typical to form a spreadable paste from the nanostructures, which can be deposited by a process called doctor blading. In order to form pastes containing the anodic ZnO nanowires, it was necessary to remove the nanowires from the zinc substrate by scraping to form a nanowire powder. A number of different pastes were formed from ZnO nanoparticles, ZnO nanowires and combinations of the two and applied to form three different photoanode architectures, as shown in Figure 6.7.

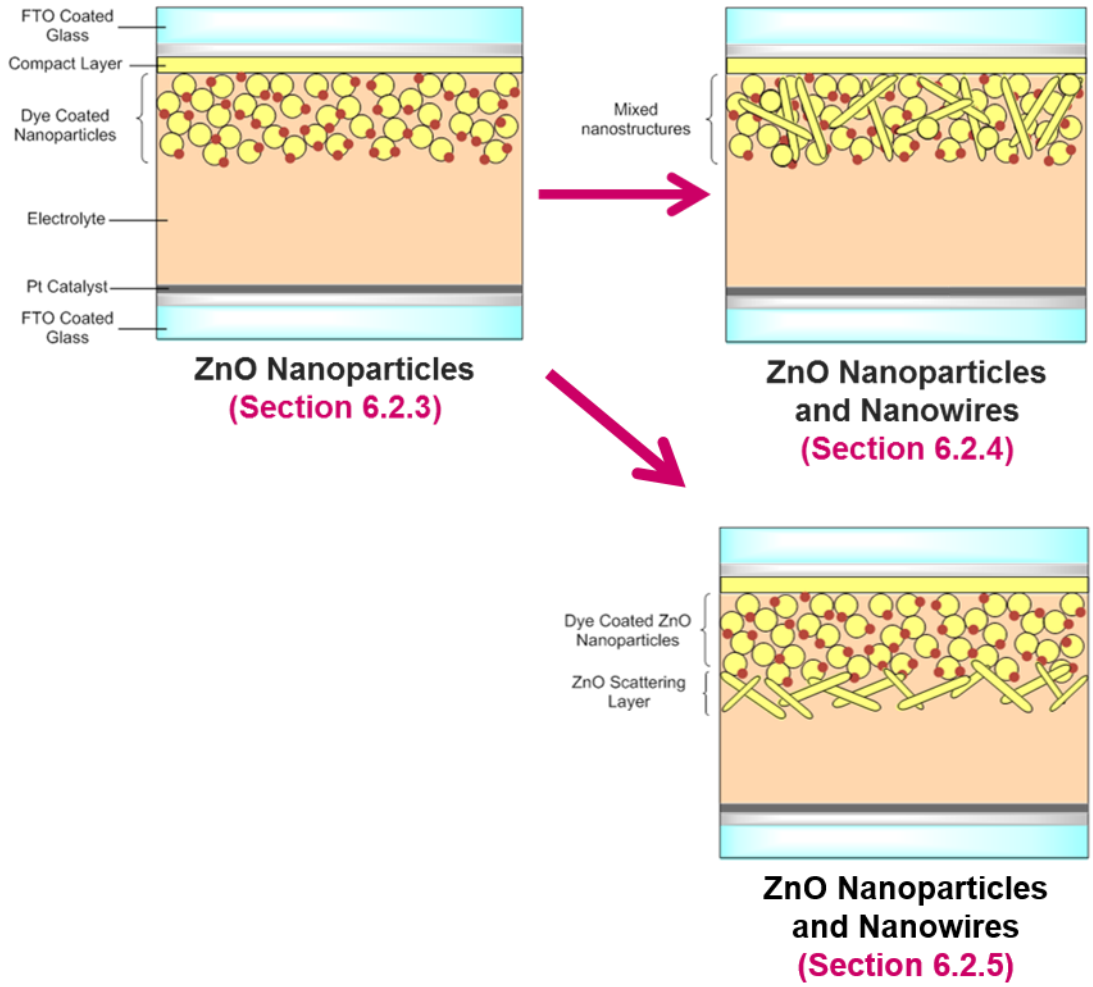

Figure 6.7. Schematic representing the three main photoanode architectures investigated in this section.

6.2.1 Formation of ZnO pastes

In order to form the three types of photoanode structure (Figure 6.7), three main types of ZnO nanostructure pastes were produced. Initial optimization of the paste preparation methods were performed using commercially available ZnO nanoparticle powders, resulting in three main formulations. For the pastes containing anodic ZnO nanowires, in all cases an equivalent paste containing commercially available ZnO nanowires was also produced for comparison. A full list of the pastes formulated, along with their ZnO composition, is provided in Table 6.1 for reference.

Table 6.1. ZnO content of nanostructure pastes produced and used within Section 6.2.

ZnO Paste Type	ZnO Nanoparticle Content (wt.%)	ZnO Nanowire Content (wt.%)
ZnO Nanoparticle Pastes		
Thick ZnO paste	10.0	-
Thin ZnO paste	5.0	-
Optimized ZnO paste	13.7	-
Mixed ZnO Nanowire-Nanoparticle Pastes		
Commercial nanowire and nanoparticle paste	12.3	1.4
Anodic nanowire and nanoparticle paste	12.3	1.4
ZnO Nanowire Pastes		
Commercial nanowire paste	-	5.0
Anodic nanowire paste	-	5.0

6.2.2 ZnO films by doctor blading

Optimization of the ZnO film preparation was performed using the three different ZnO nanoparticle pastes listed in Table 6.1. Films were prepared on FTO coated glass (TEC 15) by doctor blading using Scotch® brand Magic Tape as a mask and spacer. The films were then dried and annealed to sinter the nanoparticles and remove the organic additives present in the paste. Different film thicknesses were obtained by using different paste concentrations, completing different numbers of doctor blading cycles and also by using different numbers of Magic Tape layers as a spacer. Using these controls, it was possible to accurately produce mesoporous ZnO nanoparticle films within the range of 500-2500 nm for the thin ZnO paste (Figure 6.8) and 2-9 µm for the thick ZnO paste (Figure 6.9), as determined by profilometry.

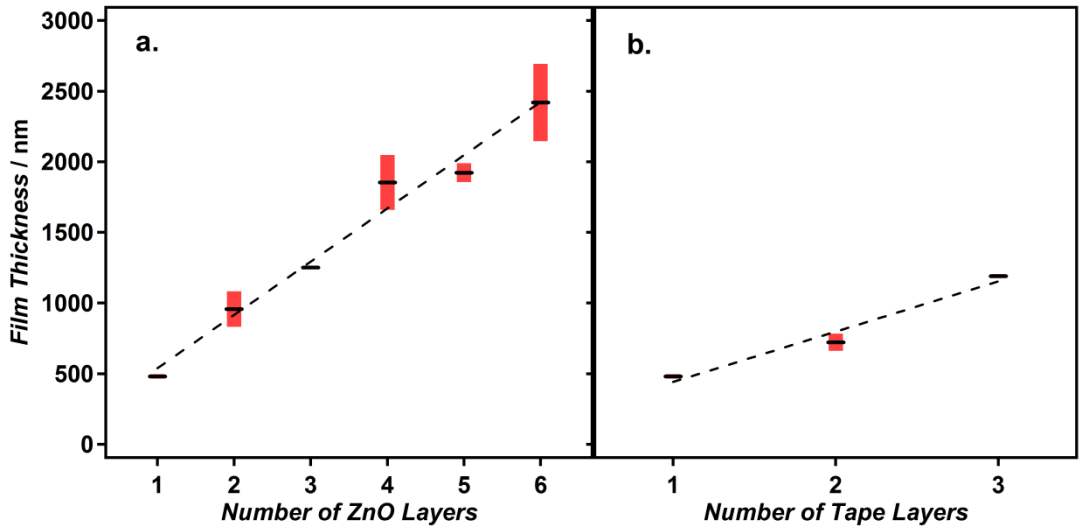

Figure 6.8. Plots of ZnO film thickness *vs.* the number of deposited ZnO layers (a) and the number of tape layers used as a spacer (b) for the thin ZnO paste. The arithmetic mean roughness is shown in the red bars.

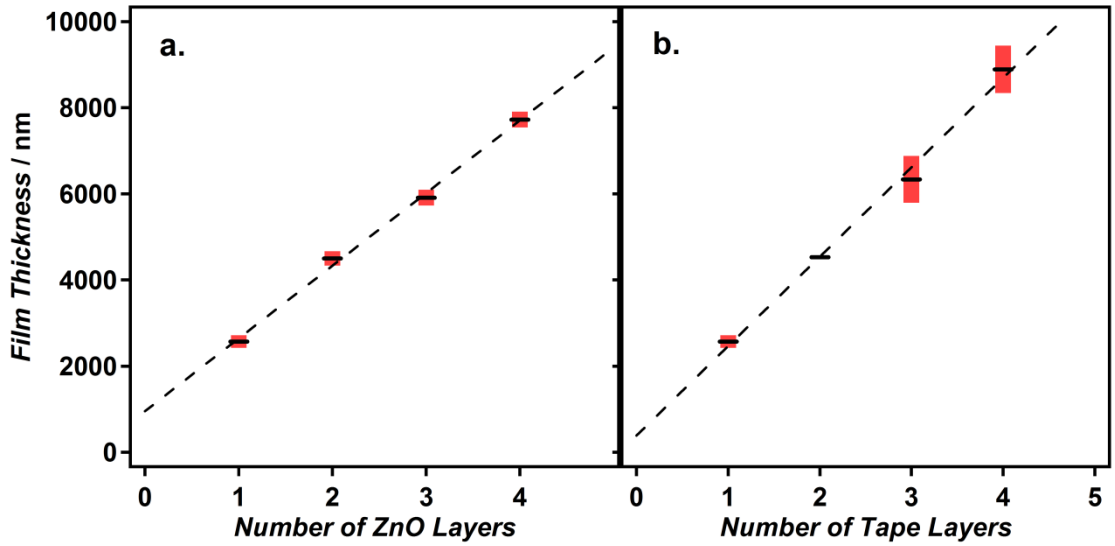

Figure 6.9. Plots of ZnO film thickness *vs.* the number of deposited ZnO layers (a) and the number of tape layers used as a spacer (b) for the thick ZnO paste. The arithmetic mean roughness is shown in the red bars.

Despite being able to obtain a good range of film thicknesses using these two pastes it was observed that the thick ZnO nanoparticle paste gave rise to highly opaque white films, indicative of large light scattering aggregates within the film. Although some degree of light scattering can be beneficial for the cell performance, a highly back-scattering film can lead to reduced light penetration throughout the length film as a whole. For this reason, a new paste

formulation method was employed in which a dilute paste was first formed and subsequently concentrated by rotary evaporation to give a thick paste, which we will call the optimized ZnO nanoparticle paste. By first sonicating the nanoparticle powders in a dilute solution, improved dispersion could be achieved. This paste had a higher transparency than the thick ZnO paste and could form more homogeneous and smooth films as shown by the lower roughness values (red bars) within Figure 6.10a. This paste could be successfully used to form porous ZnO nanoparticle films with thicknesses ranging between 2 and 11 μm, which is comparable to thicknesses that can be obtained using commercially available TiO_2 nanoparticle pastes (Dyesol, 18nr-t) (Figure 6.10b). For thicker ZnO layers it was observed that air bubble formation occurred during the drying stage, which led to inhomogeneous films. Although this might be avoided through the use of a slower drying step, a maximum number of 5 magic tape layers is recommended in order to form homogeneous films.

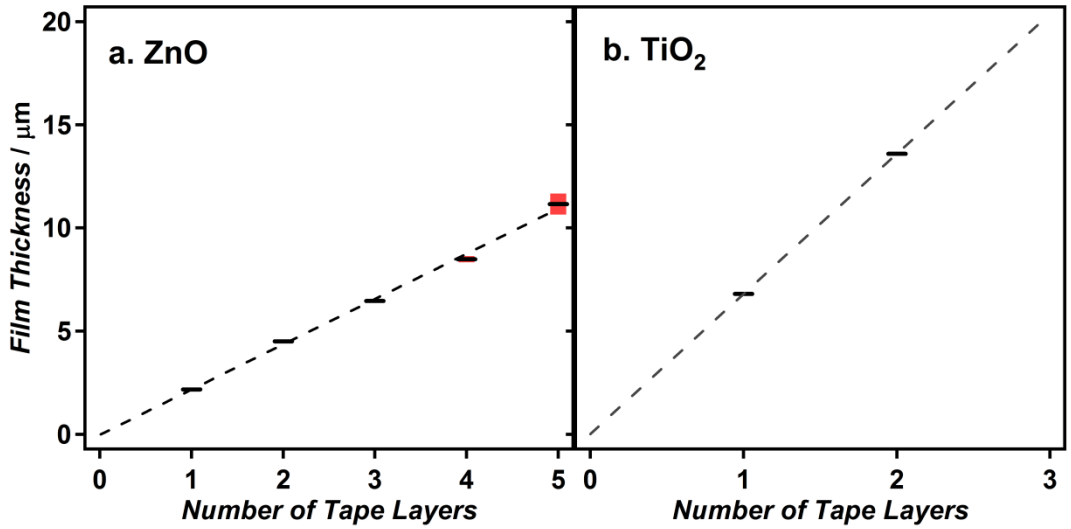

Figure 6.10. Plots of mesoporous film thickness *vs.* the number of tape layers used as a spacer during doctor blading for the optimized ZnO paste (a) and a commercial TiO_2 paste (Dyesol) (b). The arithmetic mean roughness is shown in the red bars.

FESEM was conducted to examine the cross-section of the optimized ZnO paste films and the films formed using commercial TiO_2 paste (Figure 6.11). The thickness of the films in cross-section is in good agreement with the values obtained by profilometry and the film thickness was observed to be relatively uniform along the length of the film. The ZnO films adhered well to the FTO coated substrates, despite a fracturing method being used to prepare the samples, which often resulted in gap formation between the FTO and mesoporous layer in the case of TiO_2 (Figure 6.11b). Closer examination of the film morphology (Figure 6.11c-d) revealed that the

final sintered film was composed of larger nanoparticles in the case of ZnO compared to TiO_2. Despite both pastes being formed of nanoparticles that were specified at equal diameters (~18 nm), it is possible that a greater degree of sintering occurred for the ZnO nanoparticles, resulting in the merging of neighbouring nanoparticles into bigger ones. This might be expected to result in low surface areas of the mesoporous films and, therefore, lower available space for dye loading.

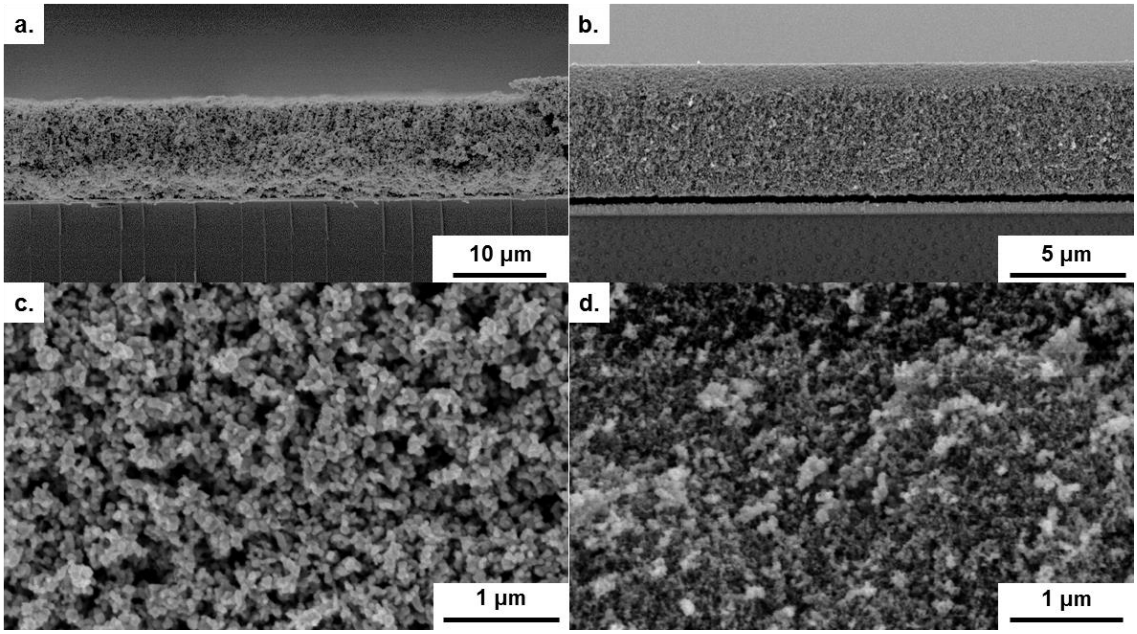

Figure 6.11. Low (a-b) and high (c-d) magnification FESEM micrographs of the cross-section of a ZnO mesoporous film (optimized ZnO paste) (a and c) and a TiO_2 mesoporous film (Dyesol paste) (b and d).

6.2.3 Optimizing device performance

The next stage after production of a suitable ZnO nanoparticle paste was to perform an optimization of DSC performance, using the mesoporous ZnO nanoparticle layers, in order to gain a reasonable baseline performance from which to compare the effects of adding nanowires. Reported efficiencies of cells formed using ZnO nanoparticle photoanodes differ greatly and a wide range of different optimizations have been described, sometimes with conflicting results.[74] It was therefore necessary to perform our own optimization of cell performance. There are many parameters and factors that can affect the final cell performance, so the optimization was narrowed down to four parameters for simplicity.

The first parameter to be examined within the optimization was the type of hole blocking layer used within the DSC. The hole blocking layer can play an important role within the cell,

providing a selective electron acceptor layer above the FTO coated electrode, whilst reducing the recombination of electrons from the FTO with holes in the electrolyte.[259] Three sets of DSCs were produced, all with mesoporous ZnO nanoparticles layer of 11 ± 0.5 μm in thickness, and with either a compact ZnO blocking layer from electrodeposition, a compact TiO_2 blocking layer from spray pyrolysis, or no blocking layer. Three cells of each type were produced and the *J*-*V* characteristics were measured under standard AM 1.5 conditions. Figure 6.12a shows the *J*-*V* curves recorded for the best performing cell of each blocking layer type. It can be easily seen that the blocking layer type has a significant effect on the device performance, with TiO_2 blocking layers causing a drastic decrease in current density compared to both the cells with a ZnO blocking layer and no blocking layer at all. The average values of short circuit current density (J_{sc}), open circuit voltage (V_{oc}), fill factor (*FF*) and power conversion efficiency (*PCE*) for each of the cell types are displayed in Figure 6.12b-e respectively. From these results, it is interesting to observe that there is almost no difference in performance between the cells made with a ZnO blocking layer and without any blocking layer. One possible reason for this could be that the ZnO layer is not fully covering the FTO substrate, leaving areas exposed, as in the case of the cells with no blocking layer. Another explanation for the indifference in performance between these two cell types can be found in previous reports and is due to the large overvoltage required for the reduction of I_3^- on FTO, particularly under high light intensities.[259] The two electron reduction of I_3^- is kinetically very slow on FTO and is, therefore, not a major loss pathway in conventional DSCs. Despite the similar behaviour between the two sets of cells, they are able to achieve a reasonable power conversion efficiency of ~1.8 %.

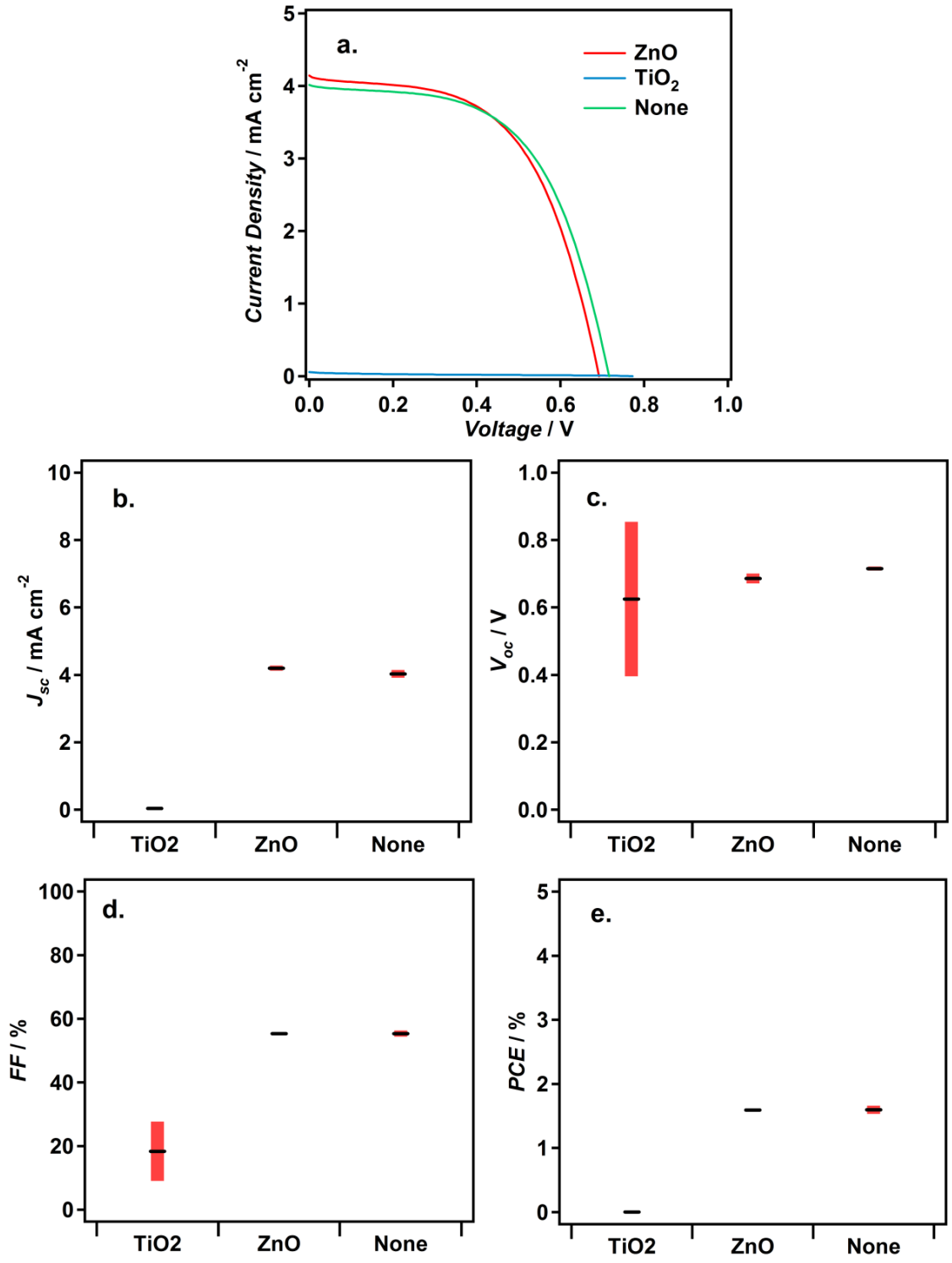

Figure 6.12. *J-V* curves for the best performing cells produced using ZnO mesoporous films and different types of blocking layer (a). Average cell parameters for cells produced using different blocking layers (b-e) with the standard deviation of each set of three cells shown in red.

The significantly lower performance of the cells with a TiO_2 blocking layer is, however, a more difficult result to explain. Given that the band gaps and band edges of bulk ZnO and anatase TiO_2 are almost equal to within ~50 mV, it would be expected that electron transfer would not be hindered between ZnO and the TiO_2 blocking layer.[260] A similar effect, but to a lesser extent, has been observed by Law *et al*. for ZnO nanowires deposited on top of a compact TiO_2 blocking layer.[91] They attributed this phenomenon to an energy barrier formed between the two metal oxides, due to the likely difference in doping levels between the ZnO an TiO_2, hindering the transfer of electrons from ZnO to TiO_2. In the case of Law *et al*. the TiO_2 blocking layer was a thin layer formed by atomic layer deposition (10-50 nm).[91] In our case, the blocking layer, produced by multiple spray pyrolysis cycles, would typically be expected to be thicker, which may account for the more extreme reduction in J_{sc} observed.

In light of the results of the first optimization, all subsequent ZnO photoanodes within Section 6.2 were fabricated directly onto the FTO coated glass substrates without a blocking layer. This both provided the highest cell performance and simplified cell construction by removing one of the cell layers.

The second optimization parameter to be examined was the thickness of the mesoporous ZnO nanoparticle layer. Different thicknesses of ZnO films were produced on FTO coated glass electrodes by using different numbers of Magic Tape layers as a spacer during doctor blading, up to a maximum of five layers for reasons previously discussed. Three cells of each film thickness were produced and the performance was assessed by conducting a *J-V* measurement under AM1.5 simulated sunlight. From the average performance values (Figure 6.13) it can be seen that an increase in ZnO film thickness results in an increase in J_{sc}, fill factor and power conversion efficiency, but a decrease in V_{oc}. The increase in J_{sc} can be explained by an increased light absorbance in the thicker film, giving rise to a greater number of excited electrons being generated. As the film thickness increases it will begin to approach the average electron diffusion length, resulting in an increase in the recombination of photoexcited electrons with the oxidised redox species in the electrolyte. This is typically associated with a decrease of V_{oc}, as is observed here.[91] Overall, the gain in J_{sc} is significant enough to overcome the losses in V_{oc}, resulting in a gain of power conversion efficiency for thicker ZnO nanoparticle films.

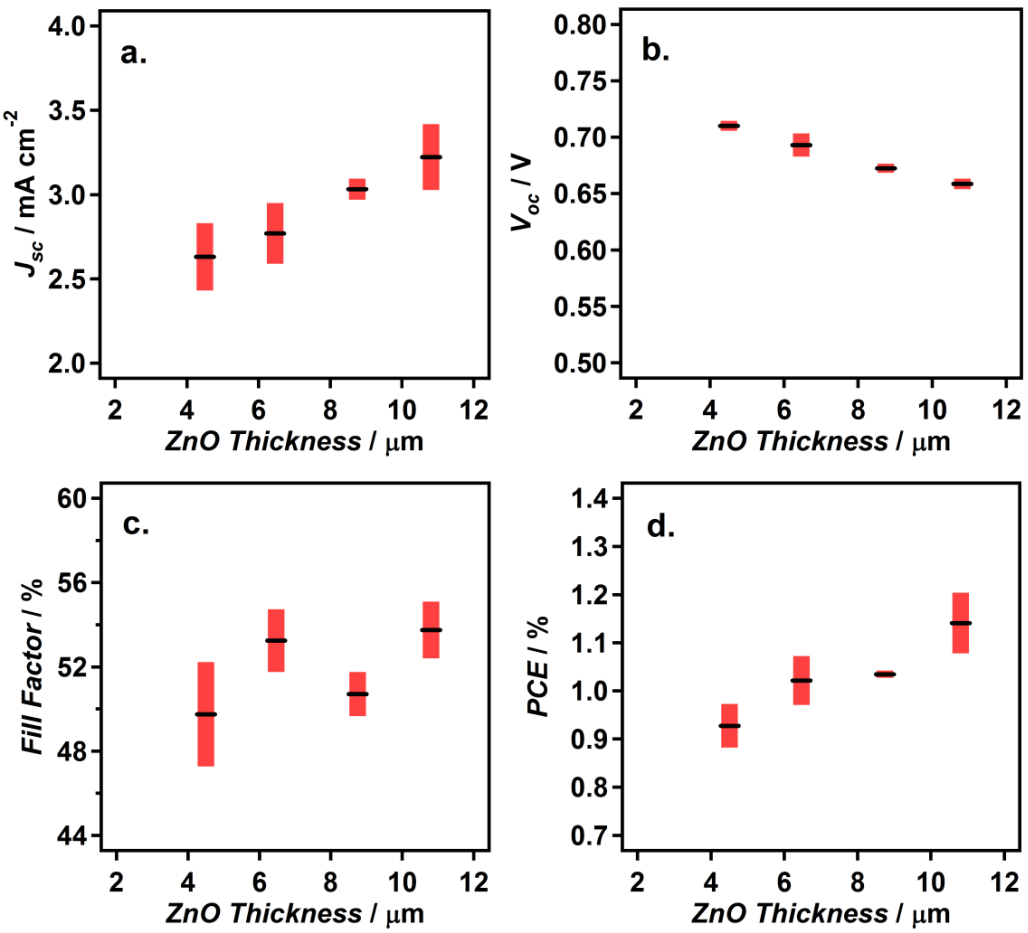

Figure 6.13. Average cell parameters measured for cells using different mesoporous ZnO film thicknesses with the standard deviations for each set of three cells shown in red.

From the trajectory of the slope of *PCE vs.* film thickness, it appears that further increases in cell performance would be possible for thicker films than those investigated in this optimization. However, due to the difficulties of forming homogeneous films at greater thicknesses (as discussed in Section 6.2.2), this was not investigated. It should also be noted that the cell efficiencies of all of the cells produced for the thickness optimisation were consistently lower than those obtained in the blocking layer optimisation, even for the thickest films (~1.2 % *vs.* ~1.8 %). It is believed that this difference is due to older Pt-coated counter electrodes being used in the thickness optimisation. This should be taken into account during cell production and freshly made counter electrodes should always be used in order to gain the maximum possible cell efficiencies. From this optimisation, it can be seen that thicker ZnO nanoparticle films give the best cell performance and, therefore, these were used for all further optimisations.

As a comparison to the results based on ZnO nanoparticle layers, the performance of two sets of DSCs made using different TiO_2 nanoparticle film thicknesses was also assessed (Figure

6.14). Similar trends in J_{sc} and power conversion efficiency were observed for increasing the TiO_2 film thickness to those observed for increasing the ZnO film thickness. However, little change in V_{oc} and fill factor were observed upon changing the TiO_2 film thickness. From these results, it may be the case that an optimum lies somewhere between the two thicknesses examined, however, due to the high concentration and viscosity of the commercial TiO_2 nanoparticle paste, intermediate thicknesses are not readily available without paste modification and were, therefore, not investigated. It can be seen that cell efficiencies for the TiO_2 photoanodes are higher than those for the ZnO photoanodes. This could be attributed to many factors, including a possible lower surface area of the ZnO photoanodes due to the nanoparticle sintering described previously, or also due to the lower compatibility of ZnO with the molecular dye. Such observations of lower efficiencies are generally consistent with those from the literature, where the highest efficiencies have been obtained with TiO_2 photoanodes.[74]

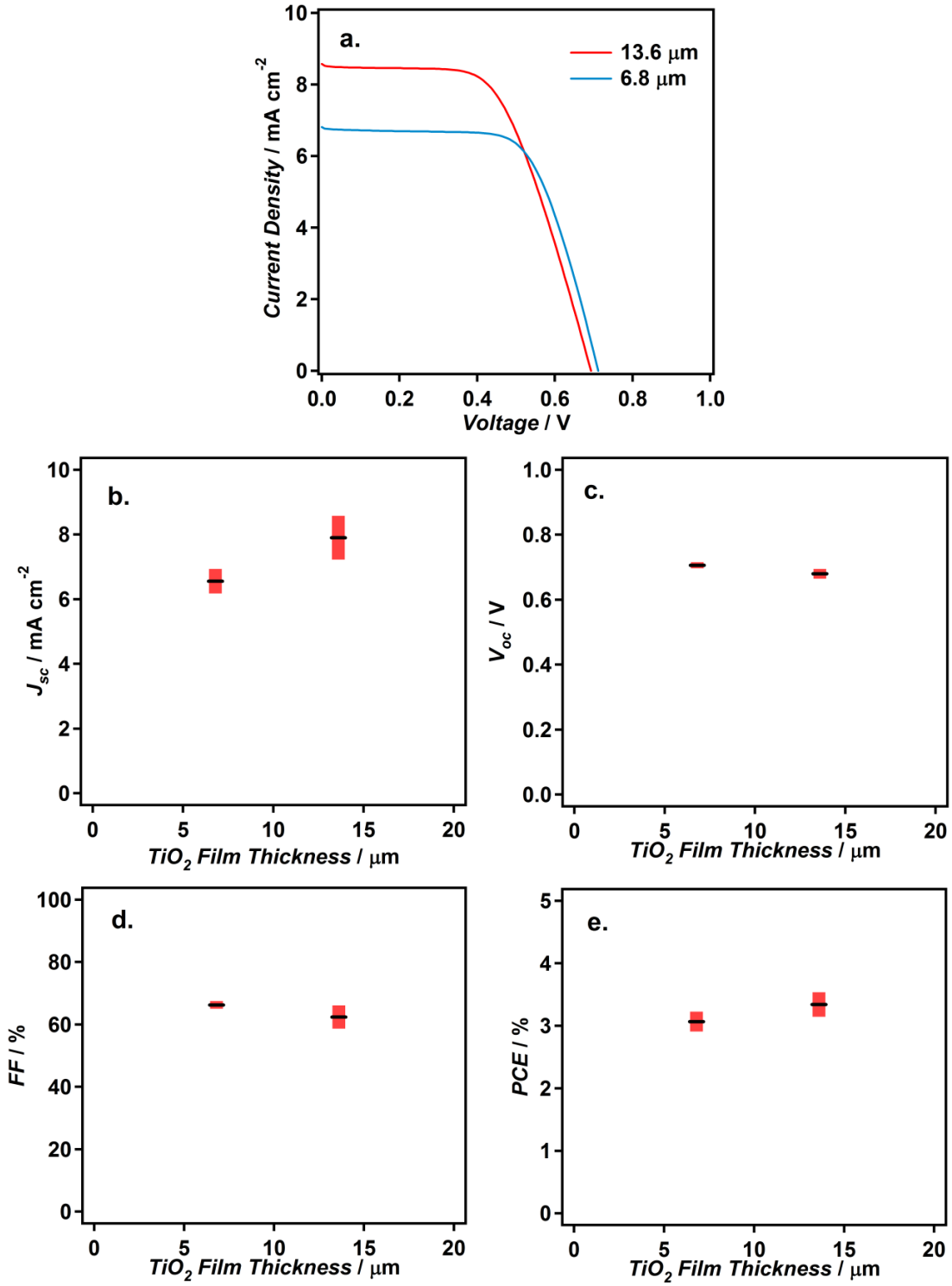

Figure 6.14. *J-V* curves (a) and average cell parameters (b-e) measured for cells using different mesoporous TiO_2 film thicknesses (Dyesol paste) with the standard deviations for each set of three cells shown in red.

The third parameter to be optimized was the electrolyte composition. Cells were prepared using the same ZnO photoanodes (thickness 11 ± 0.5 μm), but different electrolyte compositions based on adaptations of previous literature and research within the group.[78, 90] A list of the electrolyte compositions can be seen in Table 6.2.

Table 6.2. Composition of the different electrolytes tested within the front-illuminated DSCs with ZnO photoanodes, where PMII stands for 1-methyl-3-propylimidazolium iodide and 4-*t*BP is 4-*tert*-butylpyridine.

	Electrolyte components (mol dm^{-3})					
Electrolyte	**LiI**	**I_2**	**PMII**	**4-*t*BP**	**Guanidinium Thiocyanate**	**Solvent**
1	0.10	0.05	0.60	-	-	acetonitrile
2	0.50	0.05	-	0.50	-	acetonitrile
3	0.10	0.05	0.60	0.50	-	acetonitrile
4	0.05	0.03	0.60	0.50	0.10	15:85 valeronitrile and acetonitrile

The *J-V* curves of the cells produced with different electrolytes (Figure 6.15) reveal that electrolyte 3 gave rise to the highest cell efficiency, due to a combination of increased J_{sc}, V_{oc} and fill factor. 4-*t*BP and LiI are generally thought to have opposing effects on the conduction band edge of the metal oxide anode, with 4-*t*BP pushing it towards higher energies and LiI lowering the energy.[261] A movement of the conduction band edge to higher energies would typically be associated with an increase in V_{oc}, whilst a movement to lower energies would result in a lowering of V_{oc}, but a likely increase in J_{sc}. This is demonstrated in the *J-V* curves of electrolytes 1 and 2, where the lack of 4-*t*BP in electrolyte 1 leads to a lower V_{oc}, whilst in electrolyte 2 the high concentration of LiI results in a drop of V_{oc} that is accompanied by an increase in J_{sc}. The balance of additives within the electrolyte is a delicate process, with many competing variables.[45] It can be seen in electrolytes 1 and 2 that the balancing of additives is not correct, due to the low fill factors exhibited by these cells. A more suitable electrolyte mixture was found in electrolyte 3, where a match of higher V_{oc}, J_{sc} and fill factor is achieved.

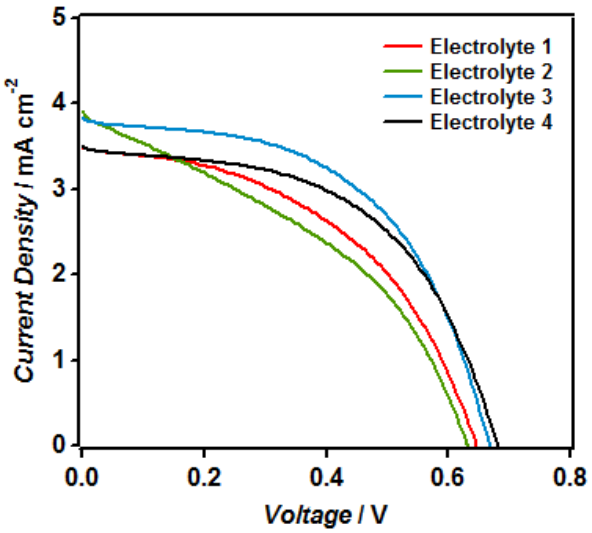

Figure 6.15. *J-V* curves measured for ZnO mesoporous cells using different electrolytes.

Guanidinium thiocyanate has commonly been used as an additive in DSC electrolytes, where it has previously been found to lower the conduction band edge of TiO_2, but at the same time slow electron-hole recombination, resulting in an overall increase in V_{oc}.[262] Electrolyte 4 is a commonly used electrolyte mixture that features this additive. From the *J-V* curve for electrolyte 4, it can be seen that the addition of this additive in the case of DSCs formed from a ZnO photoanode results in a slightly increased V_{oc} but a decrease in J_{sc} and, overall, a lower power conversion efficiency than electrolyte 3. This might be explained by the observed bleaching of the photoanodes in the case of electrolyte 4. This bleaching occurred over a period of hours (Figure 6.16), resulting in a decrease in cell performance with time. This is likely due to the displacement of the molecular dye from the surface of the ZnO.[75] In light of these results, electrolyte 3 was used for the remainder of the experiments on ZnO photoanodes.

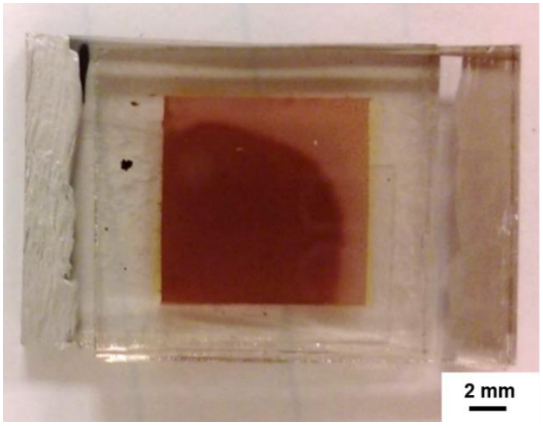

Figure 6.16. Photo of a DSC 2 h after fabrication using a guanidinium thiocyanate containing electrolyte, showing bleaching in the top right corner.

The final parameter to be optimised was the length of time for which the ZnO photoanodes were dyed in the N719 dye solution. This is known to be a more critical parameter for ZnO than for TiO_2, which is typically dyed over a period of 24 h. Long dyeing times can result in corrosion of ZnO and also the formation of dye aggregates, which competitively absorb light but do not inject electrons into the ZnO, thereby, reducing cell performance.[257] Identical ZnO nanoparticle films (thicknesses of 11 ± 0.5 µm) were dyed for lengths of time ranging between 30 mins and 4 h, in darkness and at room temperature, in a sealed vial. Three cells were produced for each dyeing time and the cell performances were assessed via the use of *J-V* measurements under standard AM 1.5 illumination (Figure 6.17).

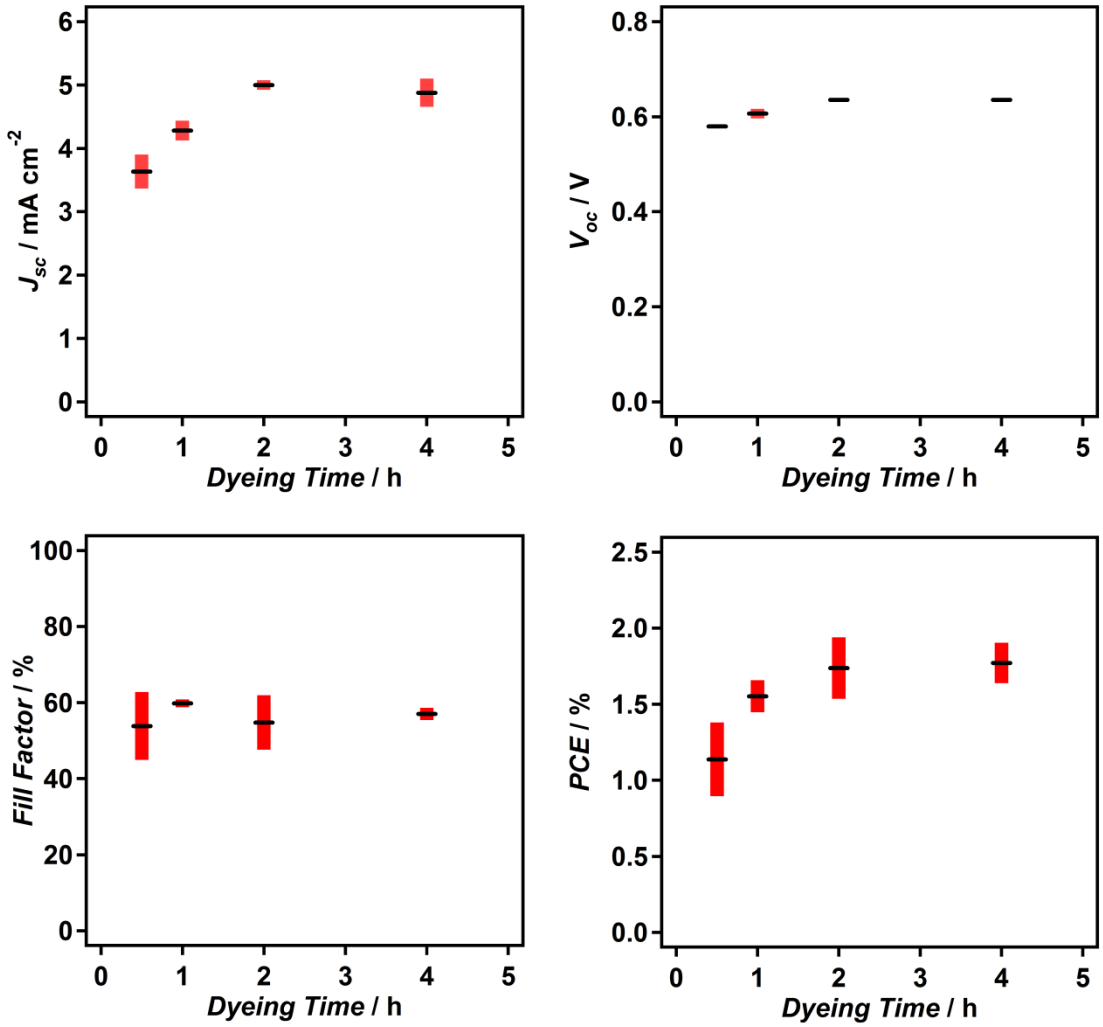

Figure 6.17. Effect of dyeing time in an ethanolic N719 dye solution on average device performance for mesoporous ZnO films. Standard deviations based on three cells are shown in red.

Whilst the fill factor remained relatively consistent for different dyeing times, the J_{sc}, V_{oc} and power conversion efficiency were all found to increase with longer dyeing times up until 2 h, at which point they plateaued until 4 h. Based on previous reports in the literature, cell performances for ZnO photoanodes would be expected to gradually decrease after this plateau due to the degradation of the photoanodes and formation of dye aggregates.[78, 257] A dyeing time of 2 h was, therefore, used for all further cell preparations with ZnO photoanodes.

6.2.4 Addition of nanowires to the mesoporous films

Now that a baseline ZnO-based DSC had been optimized to achieve a reasonable efficiency, it was necessary to test whether addition of anodic ZnO nanowires could provide an efficiency enhancement compared to nanoparticles alone. The first photoanode architecture to be tested was a mixed nanoparticle-nanowire photoanode, where the nanowires were uniformly mixed throughout the photoanode (Figure 6.7). In order to produce these photoanodes, a paste was produced by following the same procedure as for the optimized ZnO nanoparticle paste, but with 10 wt.% of the nanoparticles replaced with either commercially available nanowires with a smooth morphology or anodic nanowires.

Three cells each were produced for photoanodes containing a mixture of anodic nanowires and nanoparticles (A_NW), commercial nanowires and nanoparticles (C_NW) and also photoanodes containing only nanoparticles (NP) as a comparison. In all cases, the optimized cell production procedure documented in Section 6.2.3 was used. *J-V* curves were recorded for all of the cells under AM 1.5 simulated sunlight (Figure 6.18) and the cell performance was assessed (Figure 6.19 and Table 6.3).

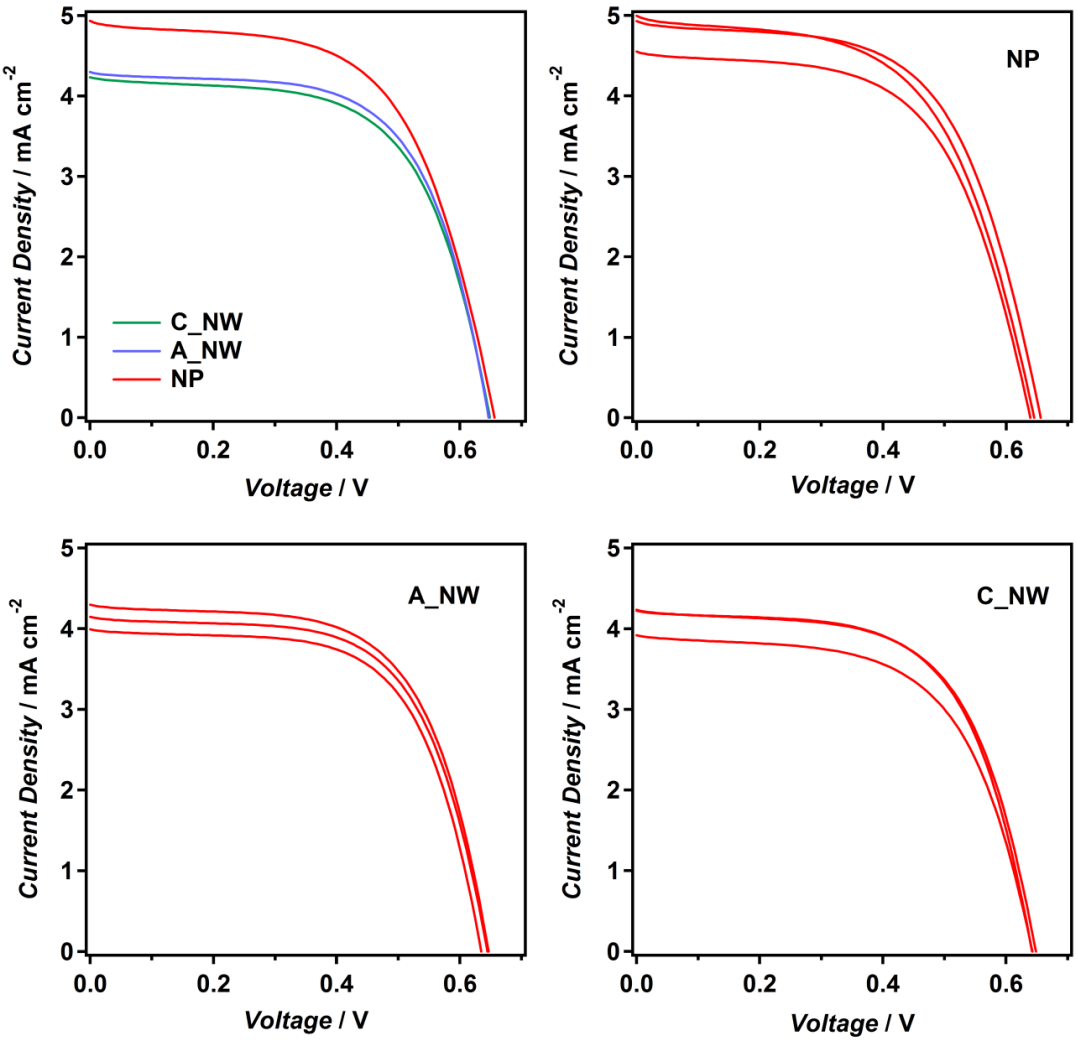

Figure 6.18. *J-V* curves recorded at AM 1.5 solar irradiation for DSCs produced under equivalent conditions, but using photoanodes composed of either ZnO nanoparticles (**NP**), a mixture of anodic ZnO nanowires and nanoparticles (**A_NW**), or a mixture of commercial ZnO nanowires and nanoparticles (**C_NW**). The top-left plot is a comparison of the best cells of each type.

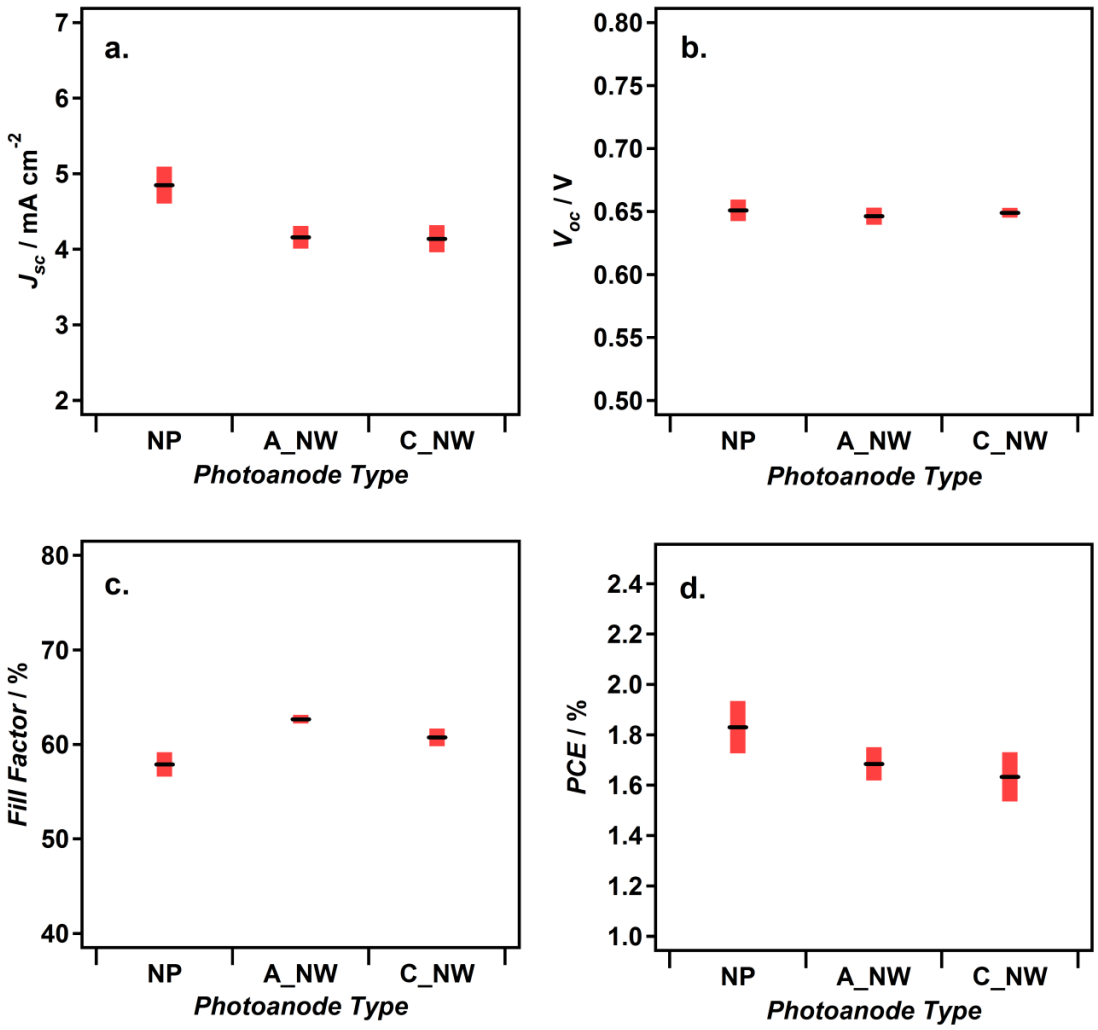

Figure 6.19. Comparison of average short circuit current density (a), open circuit voltage (b), fill factor (c) and power conversion efficiency (d) for DSCs fabricated using different types of photoanodes. The standard deviation over three cells is represented by the red bars.

Table 6.3. Summary of the DSC performance for different photoanode types.

Photoanode Type	J_{sc} (mA cm^{-2})	V_{oc} (V)	*FF* (%)	*PCE* (%)
NP	4.85 ± 0.24	0.651 ± 0.008	57.9 ± 1.3	1.83 ± 0.10
A_NW	4.16 ± 0.15	0.646 ± 0.007	62.7 ± 0.5	1.68 ± 0.07
C_NW	4.14 ± 0.18	0.649 ± 0.004	60.7 ± 0.9	1.63 ± 0.10

It can be seen that although addition of the nanowires resulted in a small increase in the fill factor of the cell, a larger reduction in J_{sc} resulted in an overall decrease in power conversion efficiency compared to the nanoparticle photoanodes. To try and ascertain why this might be the

case, FESEM was undertaken on both the A_NW and C_NW films to check if there were any irregularities compared to the nanoparticle only films (Figure 6.20). The first observation that could be made was that the thickness of the films varied from that of the nanoparticle only photoanodes. Whilst the average thickness of the C_NW film was only slightly lower than that of the NP film (10.16 µm compared to 11.15 µm), the A_NW film was significantly thinner (7.48 µm) (Figure 6.20a-b). This significant discrepancy in film thickness is unexpected, as all pastes contained the same weight percentage of ZnO nanomaterials and were also doctor bladed using the same thickness of spacer. It is possible that the difference in thickness is due to enhanced aggregation of nanoparticles around the larger nanowire structures, resulting in a thinner, denser film. This could give rise to a lower specific surface area after the films are sintered, which in turn would be expected to lower the dye loading and J_{sc} of the cells, as is observed in the *J-V* measurements.

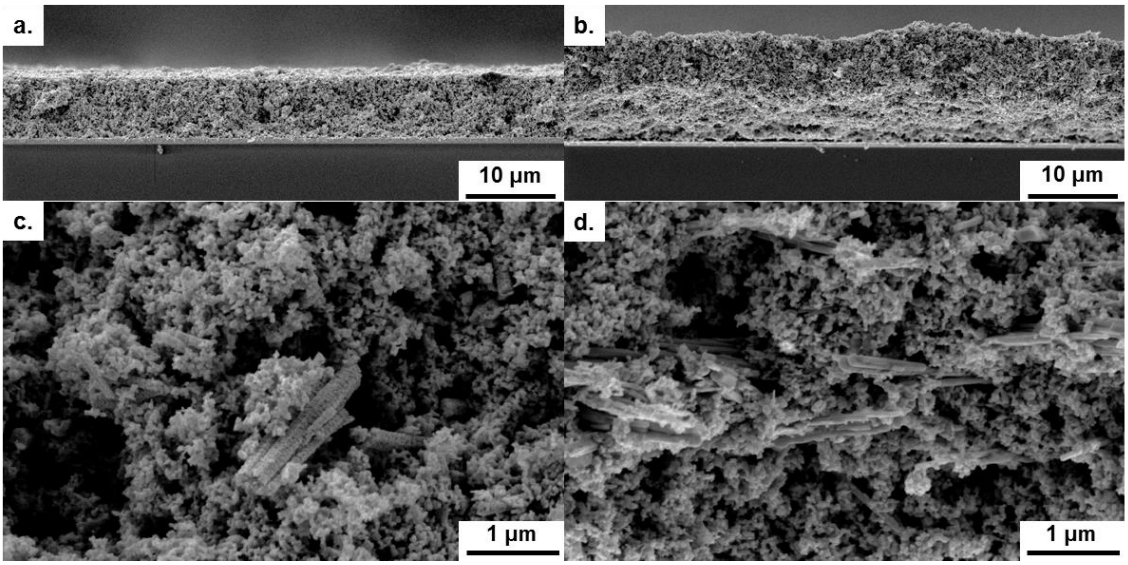

Figure 6.20. Low (a-b) and high (c-d) magnification FESEM micrographs of the cross-section of an A_NW film (a and c) and C_NW film (b and d).

Closer examination of the film cross-sections by FESEM reveals that the nanowires are largely well dispersed throughout the film, with only a few clusters of nanowires observable (Figure 6.20c-d). What was also clearly observable was the overall alignment of the commercial nanowires parallel to the substrate (Figure 6.20d). No obvious alignment of nanowires was observed in the case of the anodic nanowires (Figure 6.20c), therefore, the exact reason for this alignment remains unclear. The alignment could be a result of the doctor blading process in which the paste is drawn out over the substrate in one direction, however, as this is only observed in the case of C_NW there is some doubt over this explanation. The alignment of the nanowires parallel

to the substrate would be expected to be undesirable for enhancing cell efficiency, as one of the main purposes of adding nanowires would be to enhance electron transport in a direction perpendicular to the substrate. This might go some way towards explaining why the C_NW films give similar performance to the A_NW films despite being significantly thicker.

6.2.5 Use of nanowires as light scattering layers

As the nanowires were found to be unsuccessful in improving the cell efficiency when employed within the interior of the ZnO photoanode, they were next employed as a separate layer on top of the ZnO nanoparticles. In this configuration the nanowires would not be expected to enhance electron transport, but would simply be expected to enhance light scattering. Light scattering layers are commonly used on top of mesoporous photoanodes to scatter light back through the photoanode film, thereby increasing the path length of light through the film without significantly increasing film thickness, which would lead to increased recombination.[90] Light scattering layers usually employ larger particles, on the order of hundreds of nanometres, due to their enhanced light scattering ability. As nanowires are large in at least one dimension they should be suitable for light scattering, and the polycrystalline nature of the anodic nanowires may provide further scattering enhancements in a broader wavelength range.

Dilute pastes of both commercial nanowires and anodic nanowires were prepared as documented in Table 6.1. They were then doctor bladed onto mesoporous ZnO photoanodes and annealed once more to remove any organic additives and sinter the scattering layer to the mesoporous layer. Profilometry was used to measure the film thickness of the photoanodes, both with and without scattering layers, in order to determine the thickness of each scattering layer (Figure 6.21). The anodic nanowire scattering layer (ANW) was measured to be 1.1 μm in thickness whilst the commercial nanowire scattering layer (CNW) was 2.5 μm. This trend of the commercial nanowire paste giving rise to thicker films is in agreement with the results obtained in Section 6.2.4 for the mixed nanoparticle-nanowire films. The mass of the photoanodes was also measured by calculating the difference between the substrate mass and the annealed photoanode mass, with or without a scattering layer (Figure 6.21). Comparison of the masses of the two photoanodes which have scattering layers reveals a slight discrepancy between the two types of nanowires (1.56 compared to 1.60 mg cm^{-2} for the photoanodes, or 0.20 *vs*. 0.24 mg cm^{-2} for the scattering layer itself). As the nanowire paste formulations were identical it might be expected that equal masses would also be present. This slight deviation in mass might be a result of increased sedimentation of the anodic nanowires compared to the commercial nanowires during the paste preparation procedure.

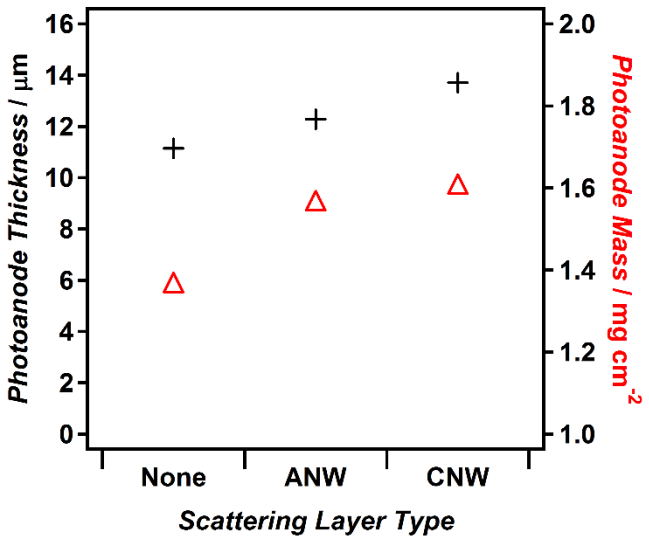

Figure 6.21. Film thicknesses (black plus symbols) and masses (red triangles) for photoanodes without scattering layers and with scattering layers formed of anodic nanowires (ANW) or commercial nanowires (CNW).

The two types of scattering layer photoanodes, along with photoanodes with no scattering layer, were used to prepare DSCs and the performance was tested by measurement of *J*-*V* curves under AM 1.5 solar simulation. Three devices of each photoanode type were measured and the average cell performance was analysed (Figure 6.22). It was found that the two scattering layer types had quite different effects on the cell performance. Whilst the CNW scattering layers improved the J_{sc} and V_{oc} values of the DSCs, the ANW scattering layers improved the fill factor of the DSCs. Overall, this resulted in an improvement in power conversion efficiency for the ANW scattering layers, but no improvement in efficiency for the CNW scattering layers.

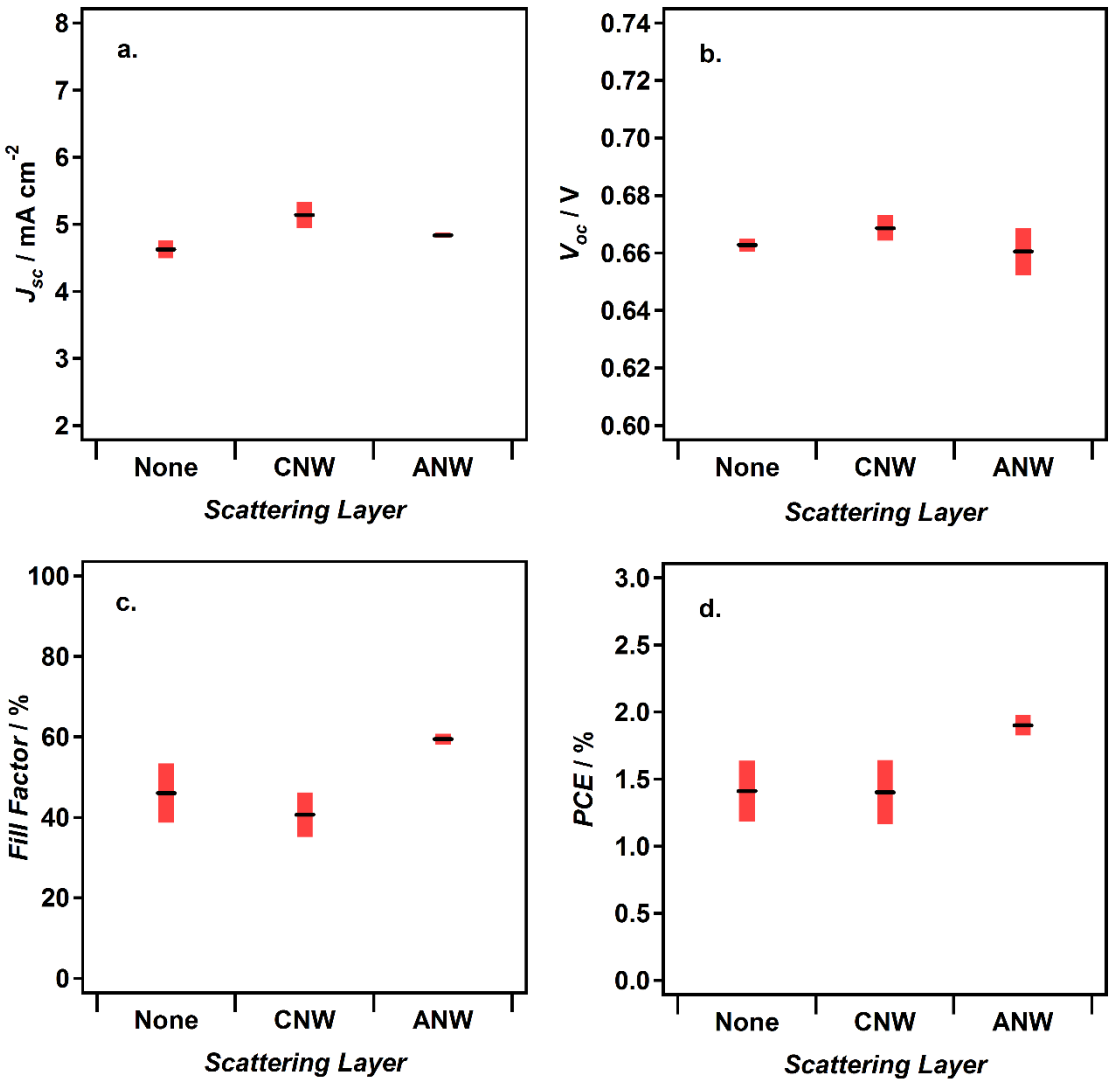

Figure 6.22. Comparison of average short circuit current density (a), open circuit voltage (b), fill factor (c) and power conversion efficiency (d) for DSCs fabricated using different types of scattering layers on ZnO nanoparticle photoanodes. The standard deviation over three cells is represented by the red bars.

6.3 Quasi-Solid State Dye-Sensitized Solar Cells

In this final section of the chapter the use of hierarchical core-shell nanostructures within quasi-solid state DSCs (qssDSCs) will be explored. These devices make use of a highly viscous or gelated electrolyte rather than the conventional electrolytes based on volatile organic solvents. This can have benefits in improving both the stability and safety of DSCs, as electrolyte leakage is minimized and is, therefore, generally deemed as a necessity for commercial DSC systems.[263]

This section of work was completed in collaboration with the group of Professor Jong Hak Kim at Yonsei University. All the research documented in section 6.3.1 and section 6.3.2 was completed by myself during a six week placement at Yonsei University. This research was then continued and expanded to cover hierarchical core-shell structures as a collaboration between myself and Chang Soo Lee, a PhD student within the group of Professor Kim. The results of this collaboration are presented in section 6.3.3 which was subsequently submitted for publication as a joint authorship paper. The photoanode preparation and cell measurements reported in section 6.3.3 were conducted by Chang Soo Lee at Yonsei University and modelling and analysis of the electrochemistry was conducted by myself.

The device architectures make use of an organised mesoporous TiO_2 (OM-TiO_2) photoanode, previously developed by Kim *et al*., to which the ZNW and ZNW@TNS structures demonstrated in Chapter 5 will be incorporated.[264] The work was inspired by a previous report of the use of SnO_2 nanotubes that had been coated with TiO_2 nanosheets (SNT@TNS).[232] In a similar vein to this report, two series' of devices were fabricated and compared; ones with ZNW added to the OM-TiO_2 and ones with ZNW@TNS added to the OM-TiO_2. Sections 6.3.1 and 6.3.2 document the development and assessment of the ZNW series of cells and section 6.3.3 documents the assessment of the ZNW@TNS series of cells in direct comparison with the ZNW series.

6.3.1 Formation of mixed ZnO and TiO_2 films

The first stage of this investigation was to establish a suitable route to incorporating ZNW structures into the OM-TiO_2 photoanode, so that a series of photoanodes with different weight percentages of this nanomaterial could be compared. This method would then be directly adapted for the ZNW@TNS series of photoanodes. For the initial set of film preparations, a method previously reported by Kim *et al*. was directly followed, substituting the SnO_2 nanotubes for the ZNW structures.[232] Briefly, this involved preparing a mixed paste of preformed TiO_2 nanoparticles, ZNW structures and the graft copolymer PVC-g-POEM in THF and doctor blading it onto FTO coated glass slides that had a compact TiO_2 blocking layer deposited on top. The films were then annealed at 450 °C to sinter the nanoparticles and remove any organic constituents.

An initial set of films were prepared in which the weight percentage of ZNW compared to TiO_2 nanoparticles ranged from 8 – 24 wt.%. After annealing these films, significant cracking was clearly visible for films with >8 wt.% ZNW and some minor cracking was even visible for the 8 wt.% sample (Figure 6.23). A clear trend of increased cracking and film damage with increased ZNW content could be observed and it was, therefore, decided that lower ZNW quantities should be used. A second set of films with quantities of ZNW ranging from 3 – 7 wt.% were produced and can be seen in Figure 6.24. All films were found to be highly transparent and crack free, regardless of the ZNW content, with an appearance identical to the OM-TiO_2 photoanode. For comparison, films were also prepared containing 5 wt.% commercial ZnO nanowires (1000 x 90 nm, Sigma-Aldrich).

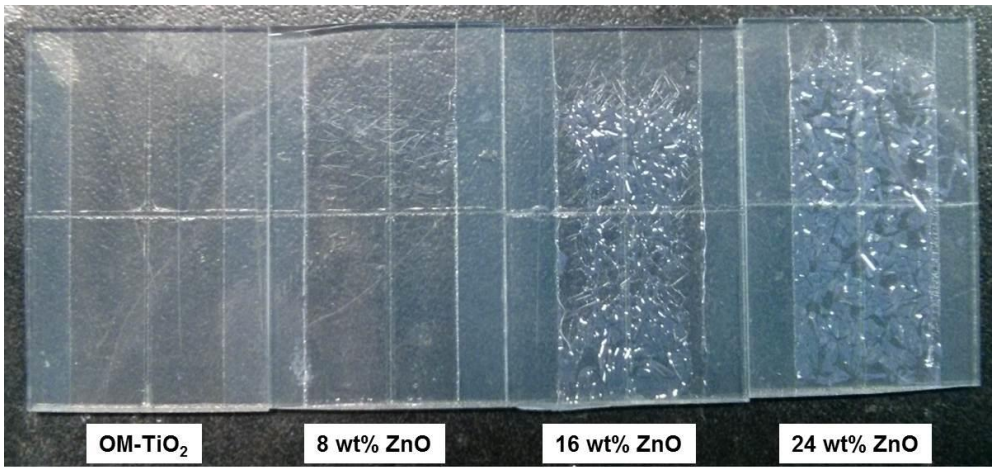

Figure 6.23. Picture of photoanodes prepared with different quantities of ZNW structures added to the OM-TiO_2 film, ranging between 0 and 24 wt.%.

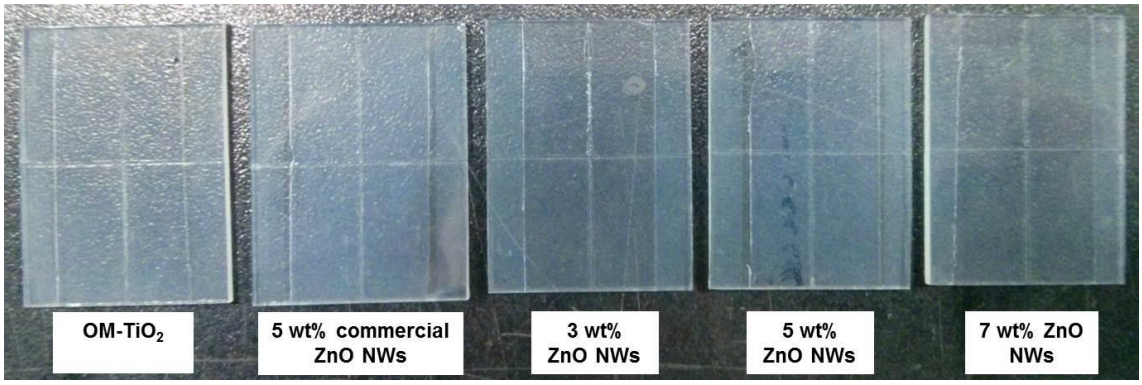

Figure 6.24. Picture of photoanodes prepared with different quantities of ZNW structures added to the OM-TiO_2 film, ranging between 0 and 7 wt.%. Films with 5 wt.% commercial nanowires are shown as a comparison.

These films were then examined by FESEM and were all found to be relatively smooth and crack free, with a typical film thickness of 5.8 ± 1.0 μm (Figure 6.25). The ordered mesoporous (OM) structure of the TiO_2 nanoparticles can be clearly seen in Figure 6.25a, which is brought about by the segregation of the TiO_2 nanoparticles into the hydrophilic POEM domains of the self-assembling PVC-g-POEM graft copolymer.[264] It was found that in the case of the ZNW-containing films, the OM structure was slightly altered, with the nanoparticles seeming to have agglomerated or grown compared to the blank OM films. A more striking observation, however, was that neither the ZNW structures nor the commercial ZnO nanowires could be observed within the films.

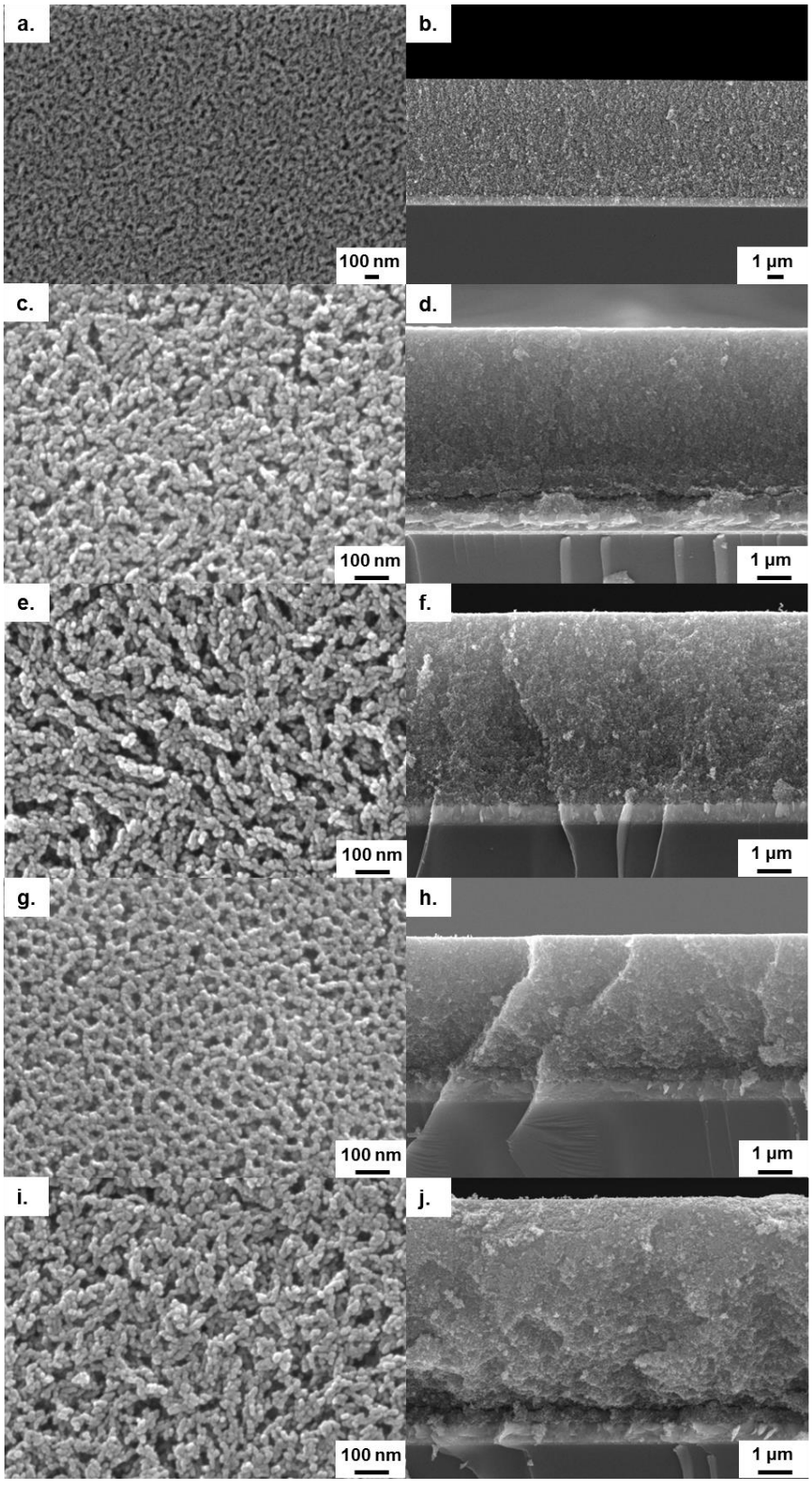

Figure 6.25. FESEM micrographs of the OM-TiO_2 films (a-b), OM-TiO_2 films with 5 wt.% commercial ZnO NWs (c-d) and OM-TiO_2 films with 3 (e-f), 5 (g-h) or 7 wt.% (i-j) ZNW structures. Micrographs shown on the left are of the film surface and cross-sections are shown on the right.

It was proposed that the lack of nanowires observable within the film might be due to dissolution of the ZnO NWs during the paste preparation, which involves the addition of HCl. As ZnO is particularly prone to dissolution in acidic solutions it is possible that the ZNW structures were dissolved, which could help to explain the agglomeration or growth of nanoparticles due to a dissolved Zn source within the paste. Another possible reason for the lack of nanowires appearing within the film is the breakdown of the polycrystalline structures during the sonication of the paste. However, this hypothesis was discarded due to the commercial nanowires also being absent, which were not polycrystalline in structure.

To overcome this problem, a new set of pastes were developed in which the HCl was replaced with water. The new films were found to be far less transparent than the films with the HCl containing paste, indicating poorer dispersion of aggregates and a less organised mesoporous structure (Figure 6.26). Unusually, this increased opacity was most noticeable for the OM film. It then decreased upon the addition of small quantities of ZNW and then slowly increased with the addition of extra ZNW.

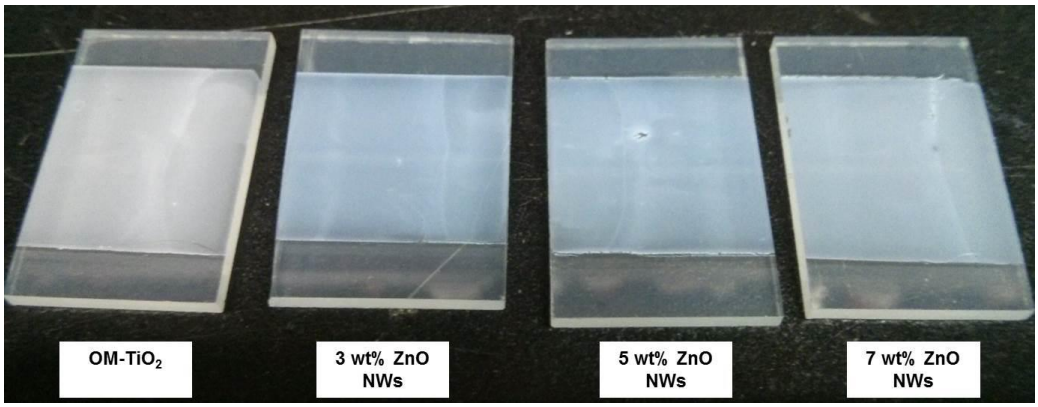

Figure 6.26. Photo of photoanodes formed with different quantities of ZNW nanostructures from pastes where the HCl was replaced by H_2O.

These films were also examined by FESEM (Figure 6.27). Film thicknesses of 5.4 ± 0.4 µm were found in all cases. However, the ordered mesoporous structure present for the films produced with HCl was not evident in these films. Through examination of the cross-sections it was also apparent that the films were not as smooth, due to the presence of agglomerates. Although some cracks can be observed within the film cross-sections, it is believed that these are the result of the film preparation for FESEM and not inherent in the film, as little evidence of cracking could be observed in the surface micrographs.

Unusually, there were also no nanowires observable within the surface and cross-sectional micrographs of these films. It may, therefore, be the case that the nanowires partition into the interior or near the bottom of the films and are difficult to observe due to agglomeration of nanoparticles around them.

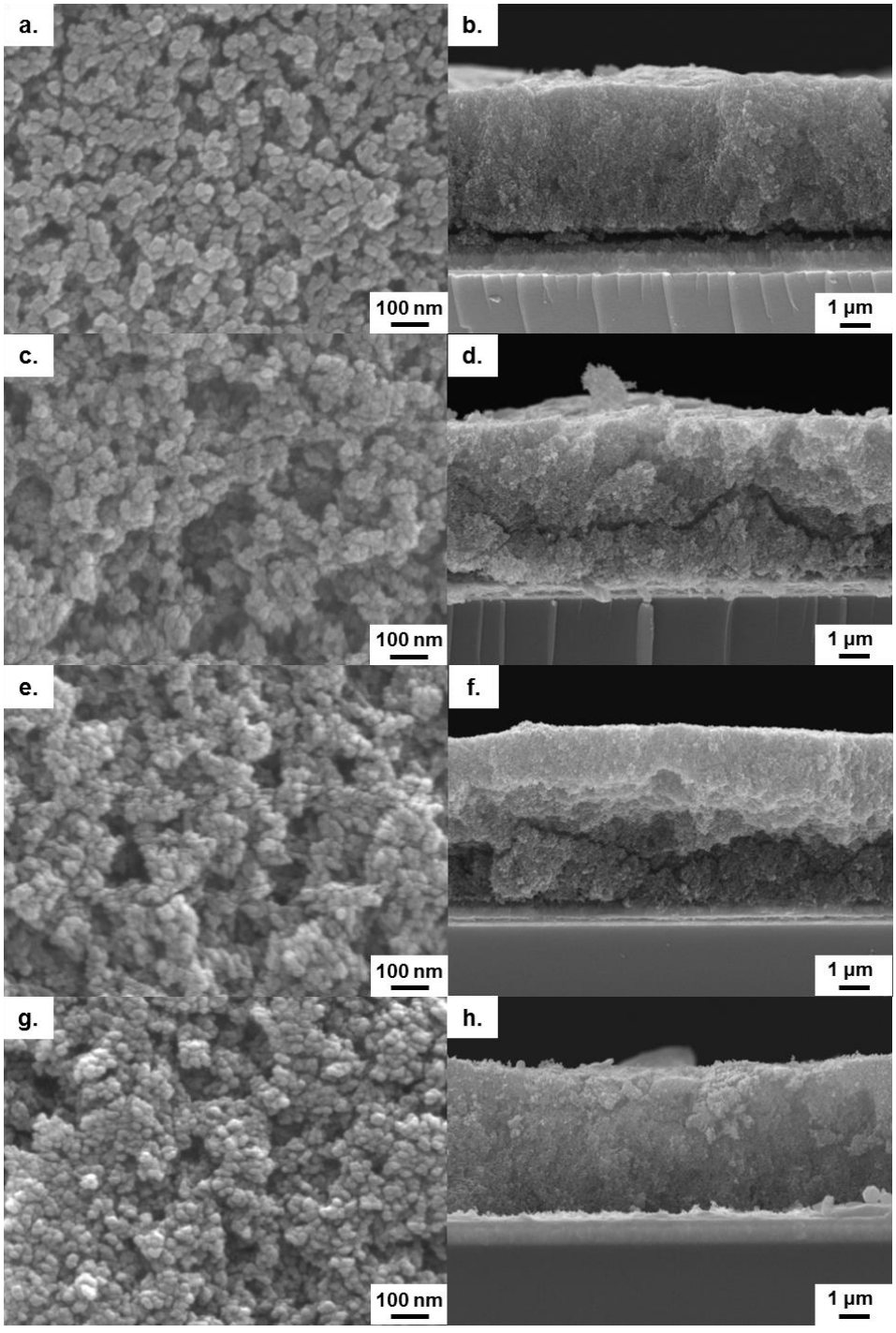

Figure 6.27. FESEM micrographs of the OM-TiO_2 films (a-b) and OM-TiO_2 films with 3 (c-d), 5 (e-f) or 7 wt.% (g-h) ZNW structures for films prepared from pastes in which the HCl had been replaced with H_2O. Micrographs shown on the left are of the film surface and cross-sections are shown on the right.

6.3.2 Device performance

In order to gain further insight into what was happening within the films, it was necessary to produce DSC devices and test their performance to see if the addition of ZNW made any difference. The first films to be tested were the films produced using HCl during the paste formulation. The films were dyed in an N719 solution and used as the photoanodes in solid state DSCs where Pt coated FTO glass was used as the counter electrode and a polymeric ionic liquid (PIL) was used as a solid-state electrolyte, based on previous research within the group of Professor Kim.[232]

Five cells were produced for each photoanode type and tested by *J-V* measurement under 1 Sun AM 1.5 simulated solar illumination (Figure 6.28). It was found that the reproducibility of the cell performances was very poor. This was attributed to the inaccuracies within the complex drop casting technique required to infiltrate the mesoporous film with the PIL. Despite the poor reproducibility of the cell production, some basic trends can tenuously be inferred. It was found that in the case of all cell parameters (J_{sc}, V_{oc}, *FF* and *PCE*) an increase occurred for the addition of small quantities of ZNW (3 wt.%), however this then decreased with the further addition of ZNW, reaching values lower than those of the OM itself (Figure 6.29).

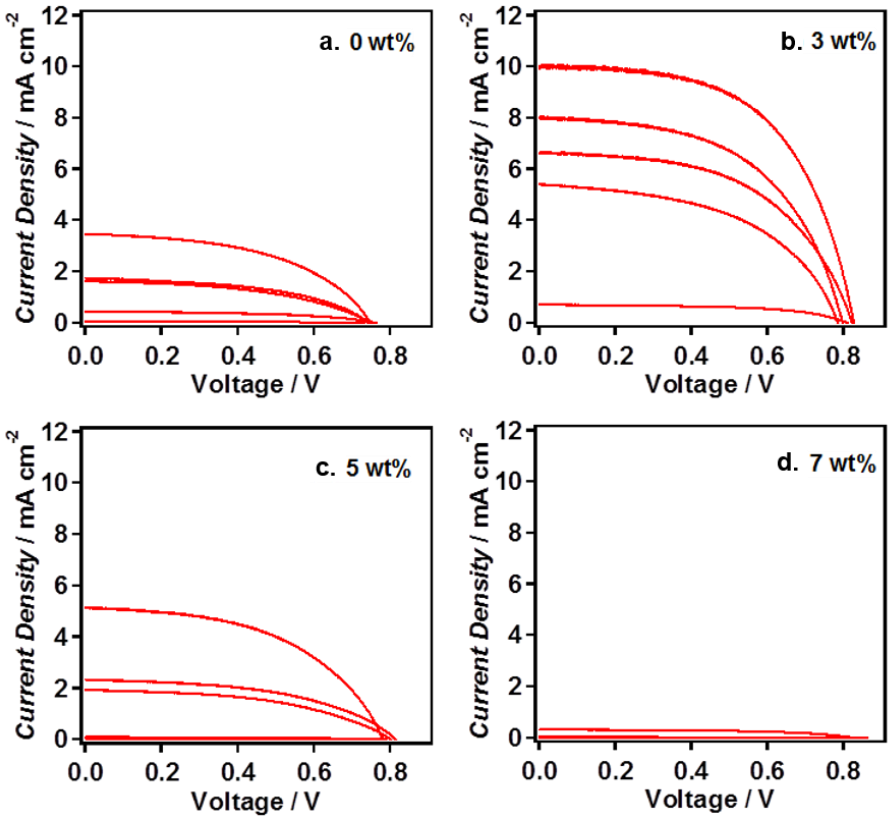

Figure 6.28. *J-V* curves recorded under 1 Sun AM 1.5 simulated sunlight for solid-state DSCs produced using 0 (a), 3 (b), 5 (c) or 7 wt.% (d) ZNW structures in the OM-TiO_2 photoanode.

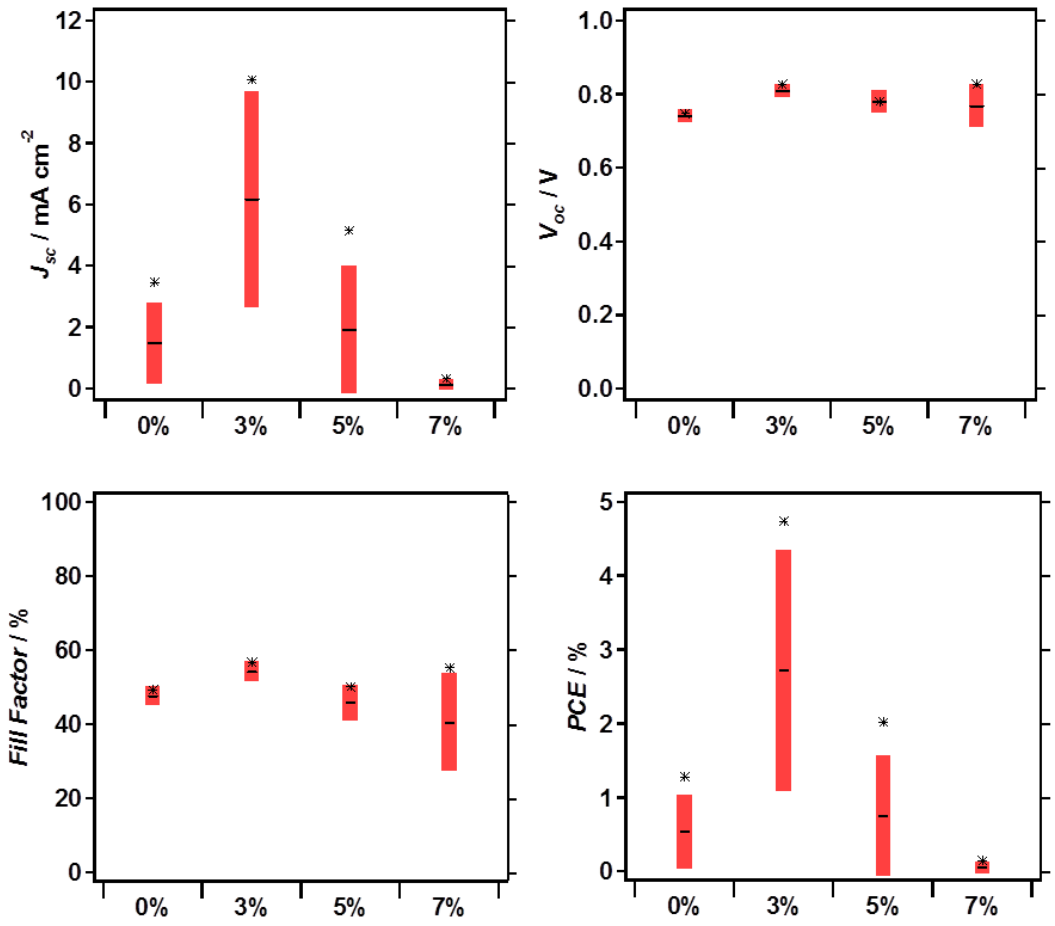

Figure 6.29. Average cell performance parameters extracted from *J-V* curves, recorded under 1 Sun AM 1.5 simulated sunlight, for solid-state DSCs produced using 0, 3, 5 or 7 wt.% ZNW structures in the OM-TiO_2 photoanode. The red error bars represent the standard deviation over five cells and the stars show the values for the highest efficiency cell of each type.

Despite an apparent trend, the poor reproducibility of the results casts some doubt on the accuracy of the findings. It should also be noted that the cell performance of the OM films is significantly lower than those previously achieved within the group of Professor Kim (1.3 % compared to 6.0 %).[232] This casts further doubt on the results, as the different performances may be attributed variation in quality of cell fabrication rather than due to inherent improvements within the photoanodes. Due to these reasons, all further cells were prepared using a quasi-solid state electrolyte, which has a simpler casting methodology and gives rise to more reproducible results.

The next set of films to be tested were the series of photoanodes produced without using HCl in the paste preparation. Four cells were prepared for each of the three different ZNW contents (3, 5 and 7 wt.%) in addition to four blank cells, which contained no ZNW and only TiO_2 nanoparticles. A quasi-solid state electrolyte was used that contained polyethylene glycol to form

a gel upon drying of the solvent. With the exception of the electrolyte and the photoanodes, cell preparation was identical to the cells reported above that used a PIL as the electrolyte. The cells were all tested by *J-V* measurement under simulated 1 Sun AM 1.5 illumination, the results of which can be seen in Figure 6.30. Through analysis of the *J-V* curves, the cell performance parameters could be extracted and are shown as average values in Figure 6.31. Although there was some deviation in cell performance within each batch, the reproducibility was significantly improved compared to when the PIL was used as a solid state electrolyte. This allowed more conclusive trends to be observed in cell performance.

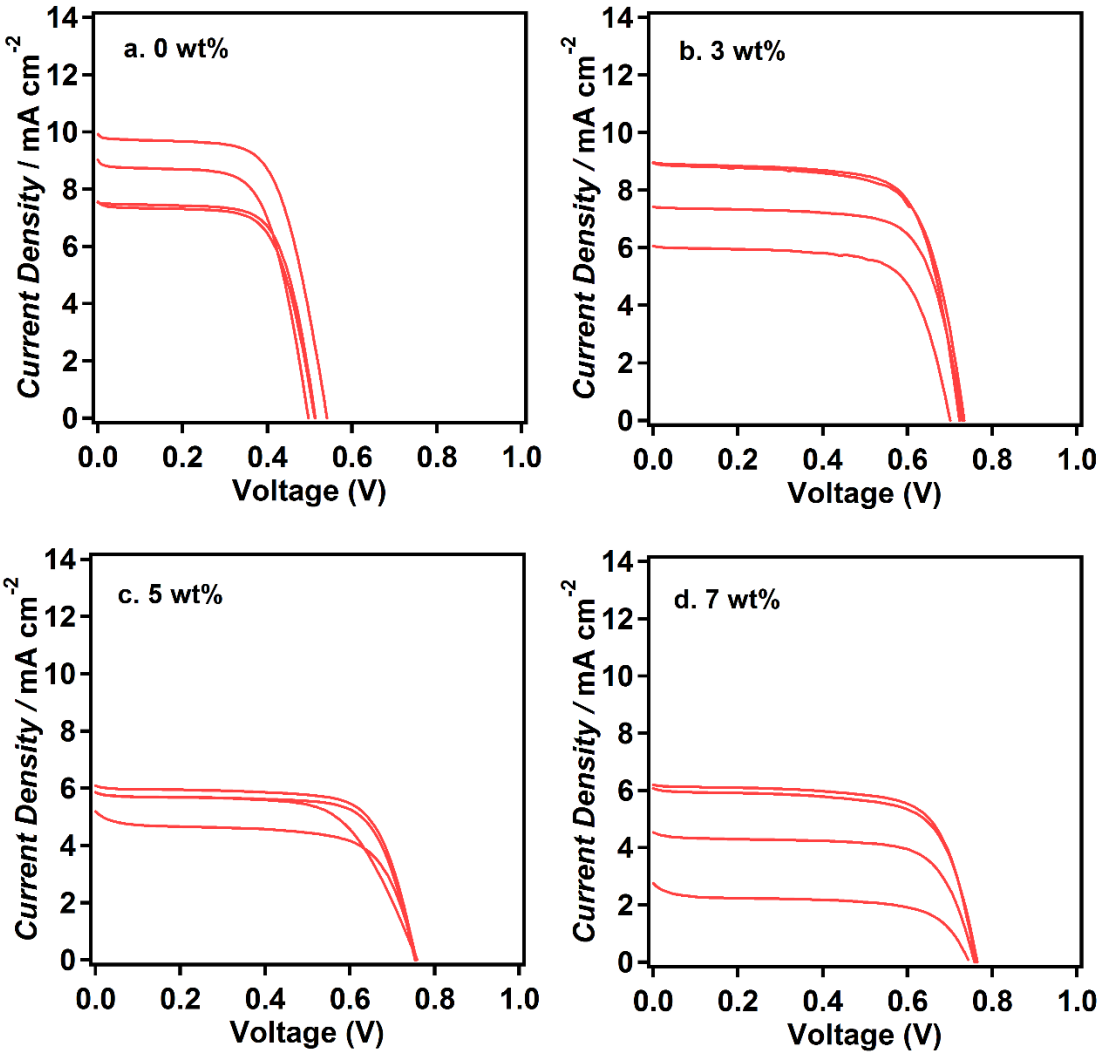

Figure 6.30. *J-V* curves recorded under 1 Sun AM 1.5 simulated sunlight for qssDSCs produced using 0 (a), 3 (b), 5 (c) or 7 wt.% (d) ZNW structures in the OM-TiO_2 photoanode without using HCl in the film preparation. Each plot shows the results of four different cells prepared under the same conditions.

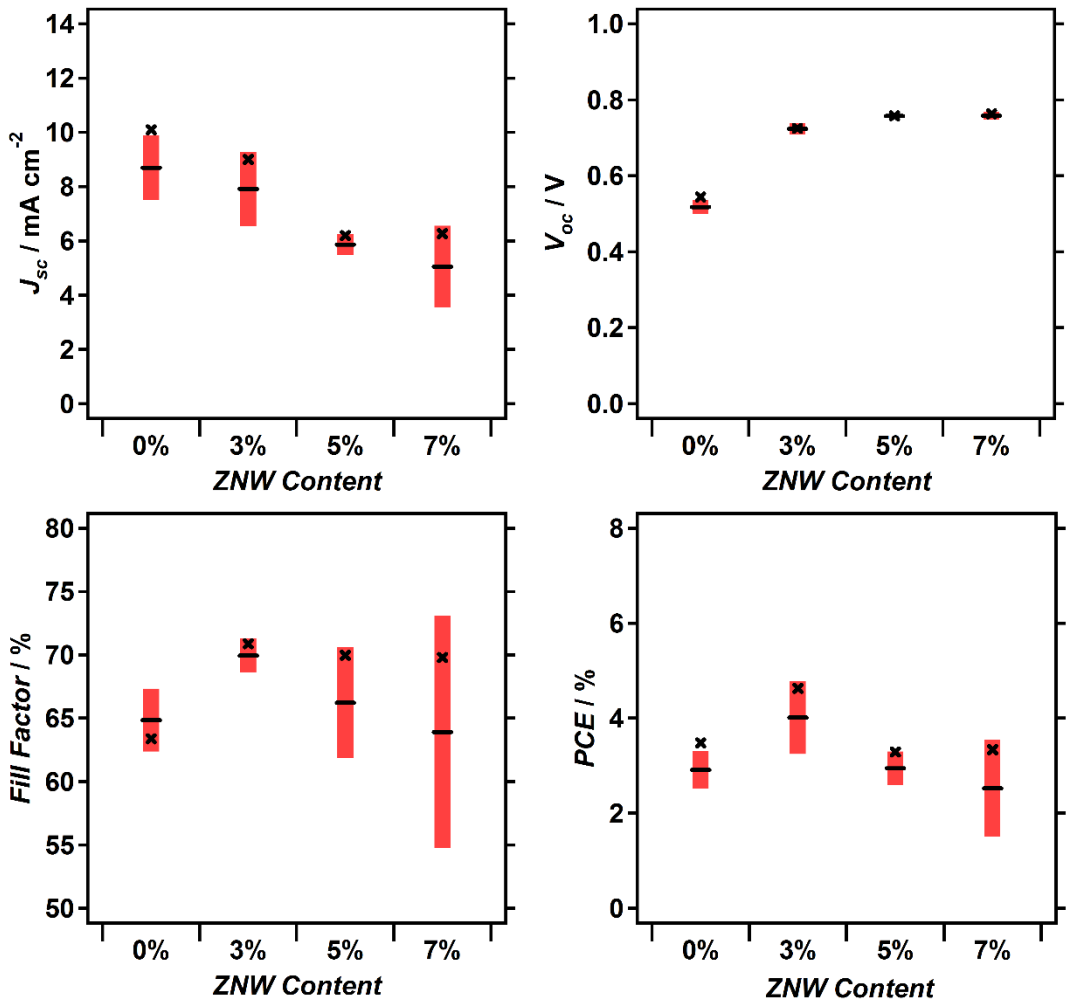

Figure 6.31. Cell performance parameters extracted from *J-V* curves, recorded under 1 Sun AM 1.5 simulated sunlight, for qssDSCs produced using 0, 3, 5 or 7 wt.% ZNW structures in the OM-TiO_2 photoanode without using HCl in the film preparation. The red error bars represent the standard deviation over four cells and the crosses show the values for the highest efficiency cell of each type.

The most obvious difference that can be observed between the *J-V* curves for the ZNW containing cells and the ones without is the significant enhancement in V_{oc}. V_{oc} values were increased by over 200 mV after the addition ZNW to the TiO_2 photoanode, and continues to gradually increase upon increasing the quantity of ZNW present within the photoanode. This might be attributed to a slightly more negative conduction band edge of ZnO compared to TiO_2, or possibly due to a reduction in recombination between the photoexcited electrons in the metal oxide and the oxidised redox species in the electrolyte.[74, 265] In opposition to this increase in $V_{oc,}$ a decrease in J_{sc} is observed with increasing ZNW content. This trend of decreasing J_{sc} appears to correlate roughly linearly with the quantity of ZNW in the film. The J_{sc} of a DSC can be strongly linked to the overall surface area of the photoanode, therefore, the results strongly

suggest that the overall surface area of the photoanodes is reduced by the addition of ZNW.[27] The fill factor of the cells seems to follow a more complex trend by first increasing upon the addition of small quantities of ZNW and then gradually decreasing as the quantity of ZNW is increased. Overall, these trends combine to give rise to a similar trend in power conversion efficiency to that of the fill factor, where the efficiency of the cells is boosted by ~33 % from the addition of small quantities of ZNW structures, but falls gradually as more ZNW is added. It therefore seems that there is a play off between gains in V_{oc}, due to the properties of ZnO, and losses in J_{sc} due to lower surface areas when adding ZNW structures. However, it has been shown that addition of small quantities of ZNW can bring about significant enhancements in power conversion efficiency. It may also be possible to improve efficiencies by performing a further optimisation of the ZNW additive quantity.

6.3.3 Incorporation of hierarchical core-shell ZNW@TNS structures

After showing that the cell performance could be improved by incorporating ZNW structures into the TiO_2 photoanodes, we wanted to determine if further improvements could be made through the use of the novel ZNW@TNS structures described in Chapter 5. These structures are composed of a ZNW core, surrounded by a shell of TiO_2 nanosheets. Core-shell structures have previously been shown to be effective in reducing electron hole recombination in DSCs by providing energy barriers to back electron transfer.[91] This, combined with the likely high surface area of the TNS, makes the ZNW@TNS structures promising materials for incorporation into DSCs.

In this set of experiments, cells containing the ZNW@TNS structures were directly compared with cells containing equivalent amounts of ZNW structures. The weight percentages were slightly altered compared to those used in Section 6.3.2 to 4, 8 and 12 wt.% and film deposition was controlled to give thicknesses of 5.5 ± 0.2 μm.

It was found that the OM-TiO_2 films produced without HCl were heavily cracked (Figure 6.32) in this set of experiments, therefore, OM-TiO_2 films formed from a HCl containing paste were used as the baseline cell performance for all further experiments. Based on the previous performances reported by Kim *et al*. for such cells, this would also provide a more competitive baseline for comparison of our modified photoanodes.[232]

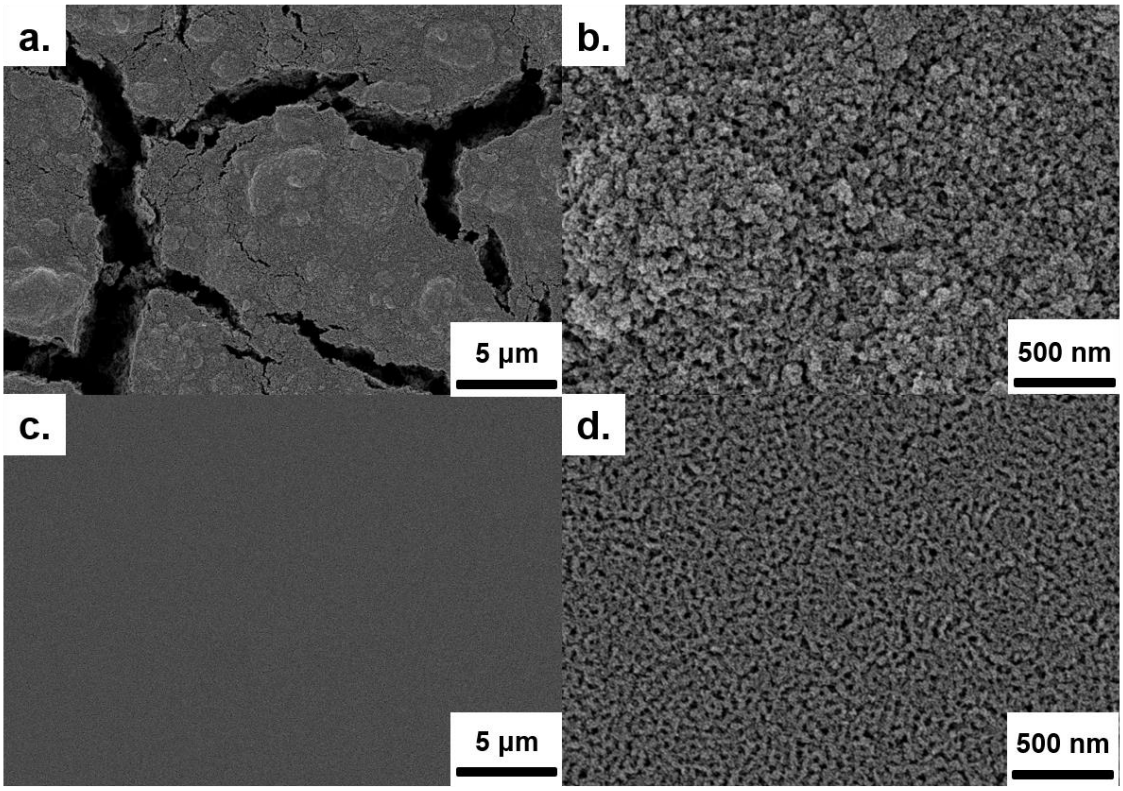

Figure 6.32. Surface SEM micrographs of OM-TiO_2 films without HCl (a-b) and with HCl (c-d) at low (left) and high (right) magnification.

After addition of ZNW structures to the photoanodes, the OM-TiO_2 film structure appeared to improve, without any significant cracking occurring until the addition of 8 wt. % of ZNW particles (Figure 6.33(a), (b), (c) and (d)). 4, 8, and 12 wt. % of ZNW were added in the paste solution and the resulting photoanodes were designated as ZNW1, ZNW2 and ZNW3, respectively. A possible reason for the reduction in cracking is that the hydrophilic POEM domains were well-organized along the hydrophilic –OH functional groups at the surface of ZNW, thereby improving the integrity of the film after annealing. Good film integrity and a well-connected structure is highly important for transferring the photoexcited electrons through the conduction band of the TiO_2. The dye loading ability of the films would also likely be increased as the number of large cracks or voids, where no dye uptake can occur, were reduced for ZNW1 and ZNW2. However, when 12 wt. % of ZNW was added in OM-TiO_2, cracks began to appear. This was attributed to the possible deformation of the polymer, preventing it from fully self-assembling into a more organised structure.

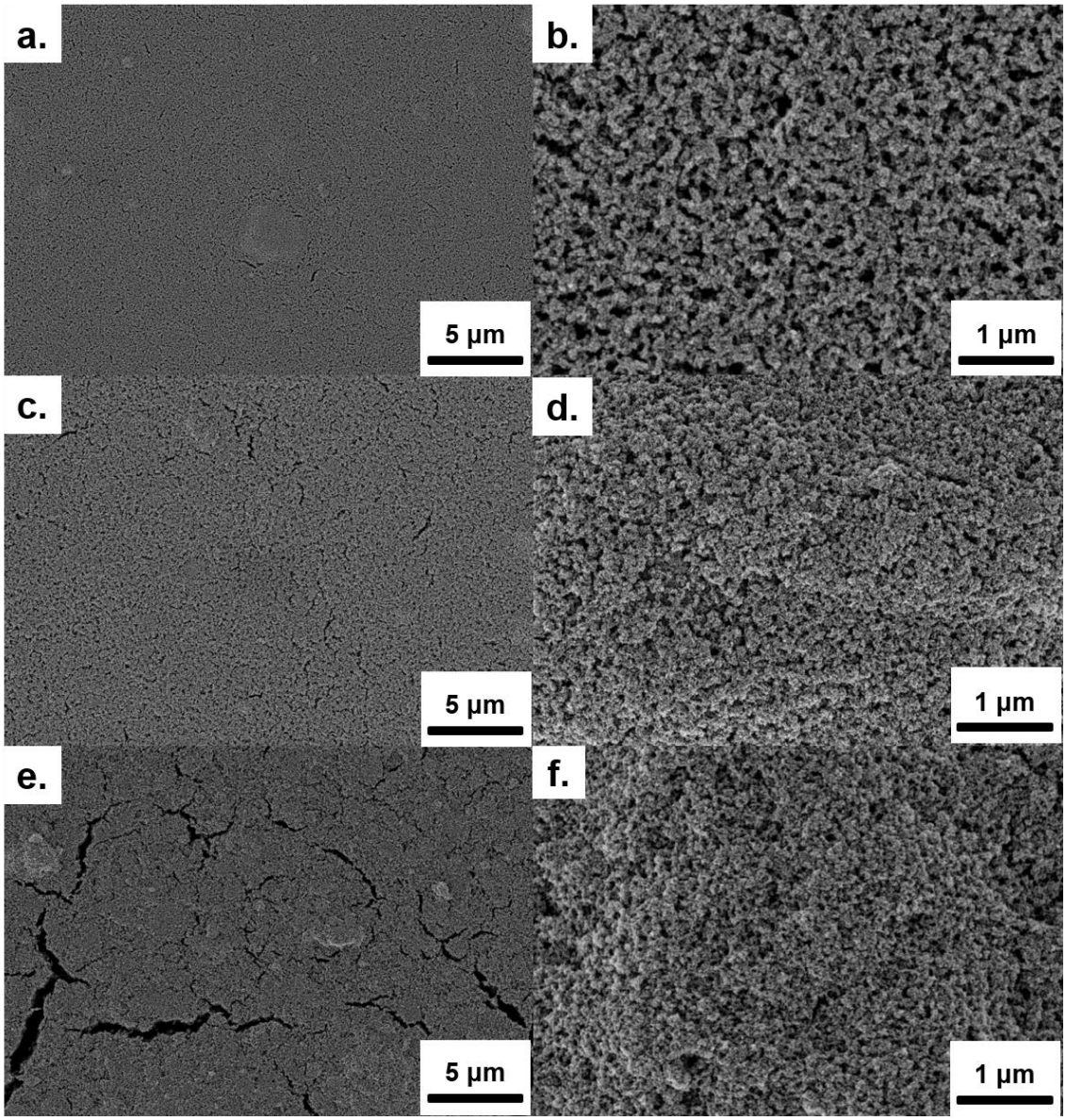

Figure 6.33. Surface SEM micrographs of ZNW1 (a-b), ZNW2 (c-d), and ZNW3 (e-f) photoanodes at low (left) and high (right) magnification.

In order to fabricate the ZNW@TNS containing OM-TiO_2 photoanodes 4, 8 and 12 wt. % of ZNW@TNS were again added in the nanoparticle paste, with the resultant photoanodes named as ZNW@TNS1, ZNW@TNS2 and ZNW@TNS3 respectively. In the case of the ZNW@TNS containing films, it was also found that the film structure was observed to be crack free for these photoanodes up to 12 wt.% (Figure 6.34). This demonstrates that the use of small quantities of larger, one-dimensional structures can benefit the structural integrity of the films when preparation is undertaken without the use of HCl.

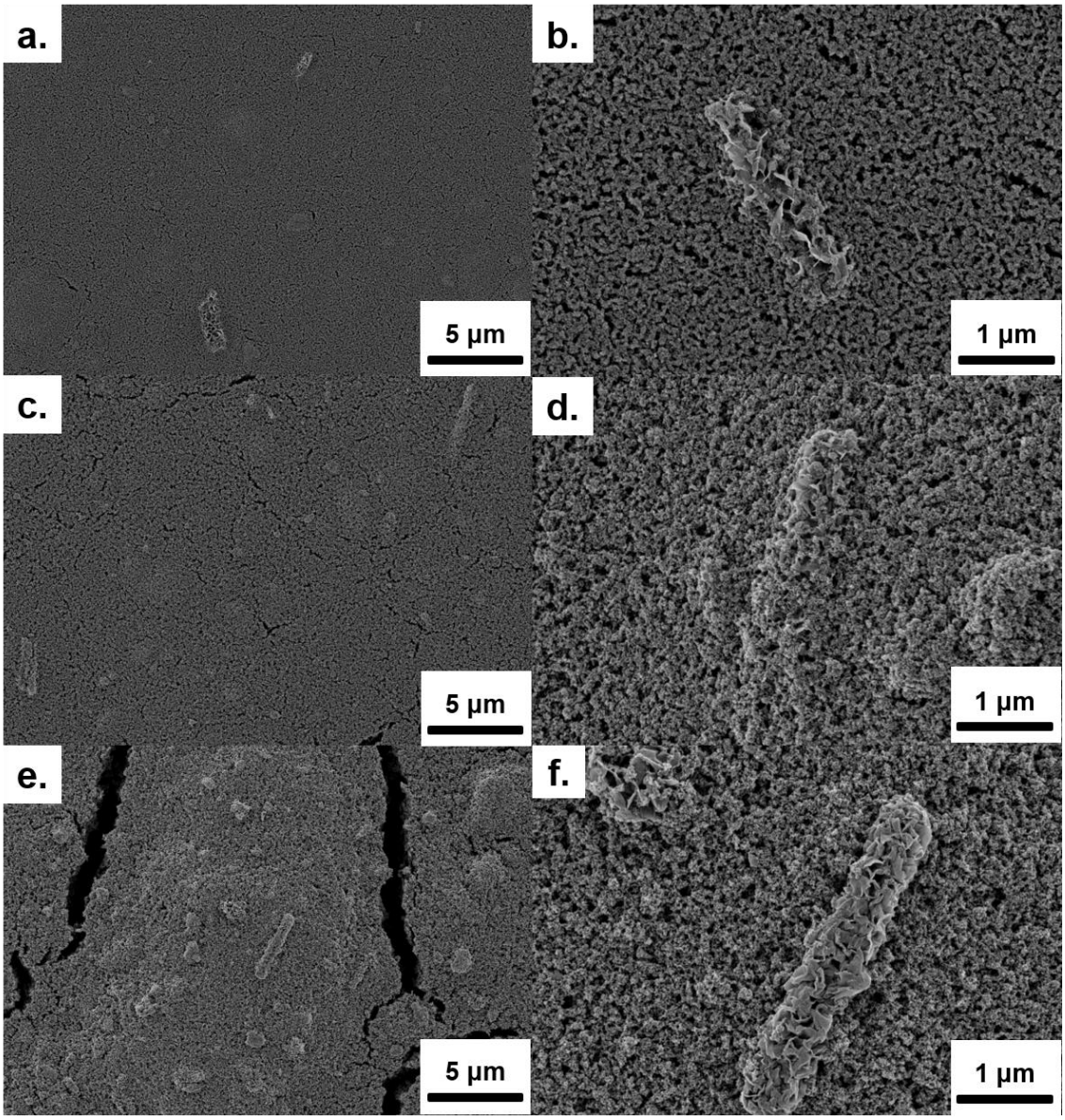

Figure 6.34. Surface SEM micrographs of ZNW@TNS1 (a-b), ZNW@TNS2 (c-d), and ZNW@TNS3 (e-f) photoanodes at low (left) and high (right) magnification.

As both the ZNW and ZNW@TNS structures have at least one dimension on the order of hundreds of nanometers, they would be expected to scatter light significantly more strongly than small nanoparticles typically used within photoanodes. As discussed previously, engineering of the light scattering within a DSC can contribute to improvements in cell performance. Therefore, UV-visible reflectance spectroscopy was employed to measure the light scattering ability of the different ZNW and ZNW@TNS photoanodes (Figure 6.35a). The transparent OM photoanode produced with HCl exhibited a low light reflectance of around 15 % of the maximum value. This low reflectance is expected due to the small nanoparticle size and the well-organized mesoporous structure, without any significant cracks. However, the reflectance of the OM

photoanode produced with H_2O, rather than HCl, was the highest amongst all of the samples due to the severe cracks, less organised structure and aggregation of TiO_2 particles, which can act as scattering centres. Therefore, the OM film produced with HCl was selected as a reference sample for the comparison of the reflectance of the ZNW and ZNW@TNS photoanodes.

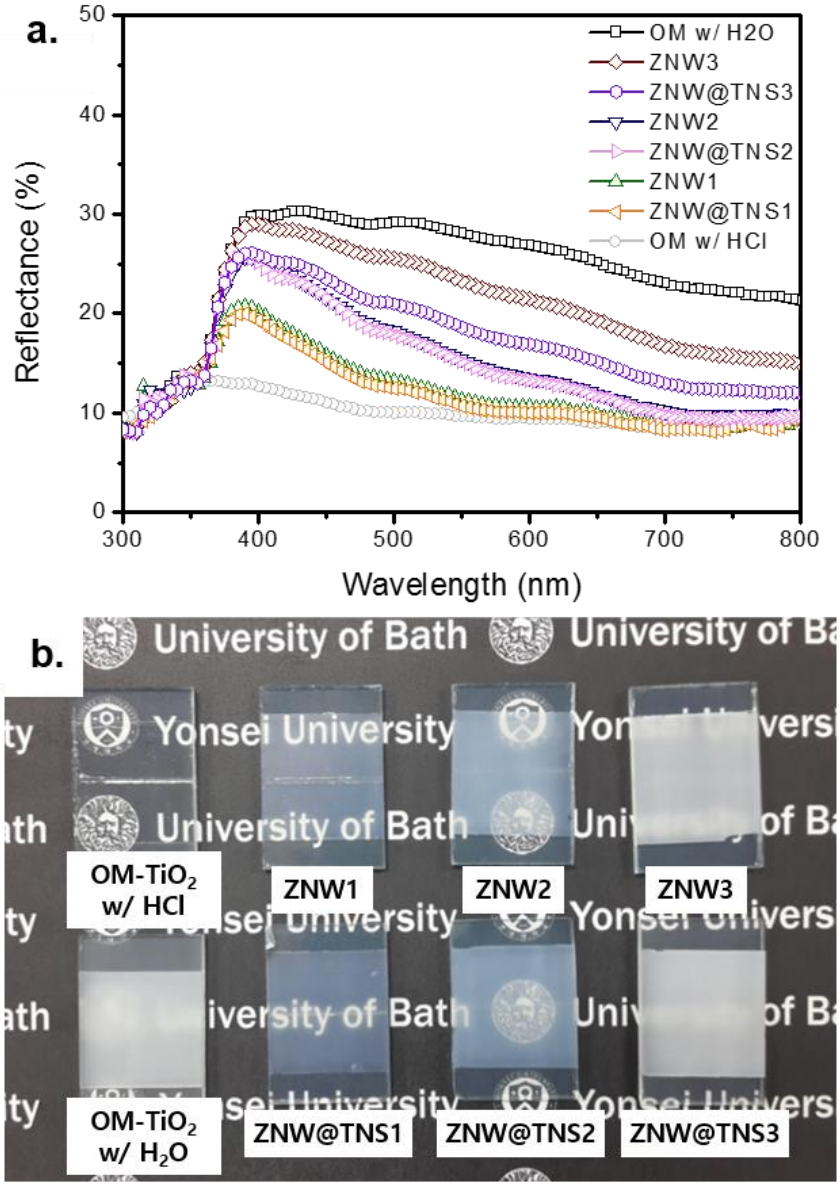

Figure 6.35. UV-visible light reflectance spectra (a) and photograph of OM, ZNW, and ZNW@TNS photoanodes (b).

The ZNW and ZNW@TNS photoanodes all exhibited higher light scattering abilities than the OM photoanode produced with HCl. This was attributed, in part, to the addition of nanostructured ZNW or ZNW@TNS particles, which will scatter light strongly due to the larger size, particularly in one dimension, compared to the smaller TiO_2 nanoparticles. Moreover, the higher light reflectance of the ZNW or ZNW@TNS photoanodes was observed to increase as the

weight percentage of ZNW or ZNW@TNS nanoparticles within the film was increased. This result implies that the addition of ZNW or ZNW@TNS is an important factor in increasing the light scattering ability of the photoanodes, which in turn has the potential to enhance the absorption of light. These trends in the UV-visible reflectance spectra could also be observed by eye in the relative opacity of the films (Figure 6.35b).

The two sets of photoanodes were then assembled into cells by infiltrating with a quasi-solid state electrolyte and then sandwiching with Pt-coated counter electrodes. Photovoltaic parameters of the qssDSCs were analysed by measuring their *J-V* curves under 1 Sun AM 1.5 simulated sunlight (Figure 6.36(a)) and are summarized in Table 6.4. It was found that the conversion efficiency of the qssDSCs using ZNW photoanodes was always lower than that of the baseline OM cells that used HCl in the photoanode preparation. This is in contrast to the results presented in section 6.3.2, which instead used OM films without HCl as the baseline. The lower efficiency of the ZNW series cells than the OM cells results from the lower J_{sc}, which can be linked to the poor dye loading, determined from UV/vis absorbance spectroscopy of dye desorbed from the photoanodes (Table 6.4). However, in all cases the V_{oc} was found to be enhanced when more ZNW nanoparticles were added, compared with bare OM, in agreement with the results obtained in section 6.3.2. This enhancement of V_{oc} can be attributed to the faster electron mobility in bulk phases of ZnO than TiO_2 and to the slightly higher conduction band edge of ZnO compared to TiO_2.[74]

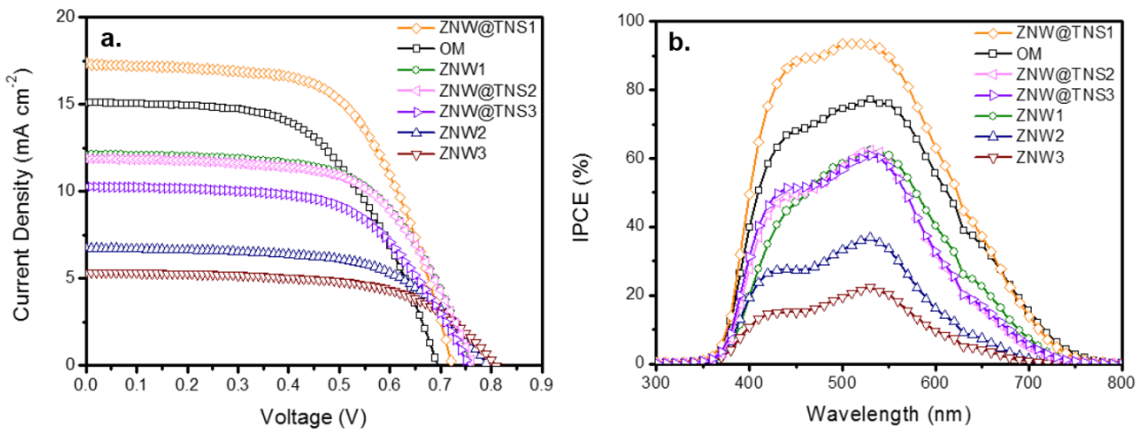

Figure 6.36. *J-V* curves (a) and IPCE spectra (b) of qssDSCs with OM, ZNW, and ZNW@TNS photoanodes.

Table 6.4 Dye loading, specific surface area and qssDSC cell performance for different photoanodes.

Photoanode	Dye Loading (nmol cm^{-2})	Specific Surface Area (m^2 g^{-1})	J_{sc} (mA cm^{-2})	V_{oc} (V)	*FF* (%)	*PCE* (%)
OM	110.2	117	15.34	0.69	55	5.78
ZNW1	94.6	104	12.14	0.76	60	5.54
ZNW2	75.7	98	6.70	0.79	60	3.15
ZNW3	39.3	93	5.31	0.80	60	2.57
ZNW@TNS1	125.5	119	17.36	0.72	60	7.46
ZNW@TNS2	90.4	105	11.92	0.75	60	5.42
ZNW@TNS3	73.5	97	10.36	0.75	58	4.49

In contrast, the cells containing ZNW@TNS gave rise to a significant enhancement in power conversion efficiency compared to OM when small quantities of the nanostructures were used. The J_{sc} of ZNW@TNS1 (17.36 mA cm^{-2}) was the highest among all of the photoanodes tested, which can be attributed to the enhanced dye loading and slightly higher specific surface area compared to both the OM and ZNW containing photoanodes (Table 6.4). The addition of small quantities of ZNW@TNS core-shell structures could achieve the enhancement of J_{sc} in four ways: 1) the increased specific surface area due to TNSs, 2) the faster electron mobility of one-dimensional ZnO than TiO_2 in bulk phases, 3) the suppression of recombination between ZNW/electrolyte due to forming a core-shell structure, and 4) the enhanced light scattering effect. In particular, the recombination rate can be reduced due to the formation of a radial surface field within the core-shell structure, which has been reported for ZnO nanowires with a TiO_2 shell.[91] It should also be noted that the V_{oc} of ZNW@TNS1 was slightly increased from 0.69 to 0.72 V compared to OM. This resulted in a conversion efficiency of 7.46 % for ZNW@TNS1, which is 29 % higher than that of OM (5.78 %).

It therefore seems that the incorporation of ZNW@TNS core-shell nanostructures in OM-TiO_2 can play an important role in enhancing both the J_{sc} and V_{oc}. Despite this, further addition of ZNW@TNS particles in OM-TiO_2 resulted in a lower conversion efficiency. This is likely due to an excessive amount of ZNW@TNS resulting in a less-organized OM-TiO_2 structure, causing cracks in the photoanode that reduce the surface area available for dye adsorption and reducing connectivity within the film for electron transport. It is, therefore, vital to carefully control the quantities of ZNW@TNS structures incorporated into the OM film in order to gain optimal cell performance.

To further investigate the photocurrent density of the OM, ZNW and ZNW@TNS photoanodes, the incident photon-to-current conversion efficiency (IPCE) was measured as a function of wavelength (λ) according to the following relationship:[266]

$$\text{IPCE}\ (\%) = \frac{1240 \times J_{sc}}{\lambda \times P_{in}} \times 100 \qquad \text{Eq. 6.2}$$

Where P_{in} is the incident solar power. Among the samples, the ZNW@TNS1 photoanode exhibited the highest IPCE value from 300 to 800 nm, in good agreement with the trends in J_{sc} value from the *J-V* curves (Figure 6.36b). In particular, the IPCE value in the wavelength range of 450 to 550 nm was greatly increased, which is likely due to the following two factors: 1) the enhanced light scattering effect of ZNW@TNS1 in that region compared with bare OM, and 2) the higher dye loading of ZNW@TNS1 (125.5 nmol cm^{-2}) than that of OM (110.2 nmol cm^{-2}). The IPCE values of the other samples were generally decreased, which can be attributed to the lower dye loadings, severe cracks in the case of ZNW3 and ZNW@TNS3, and an aggregated, less-organized morphology of the photoanodes. These results reinforce the importance of the careful control of ZNW@TNS quantity, as although photocurrent densities were significantly enhanced for small quantities (4 wt.%), further increases in ZNW@TNS quantities resulted in the opposite effect.

The cells were also analysed by electrochemical impedance spectroscopy (EIS), under 1 Sun illumination and open circuit voltages, to determine resistances associated with the various electron transfer processes occurring within the cells. EIS is a frequency domain technique that is commonly employed to analyse DSCs. EIS measures the relationship between an applied modulated voltage and the measured alternating current. This relationship can be represented in the form of a Nyquist plot, which is a plot of the imaginary component of the impedance (*Z''*) *vs*. the real component of the impedance (*Z'*). The Nyquist plots of both the ZNW and ZNW@TNS cell series are shown in Figure 6.37.

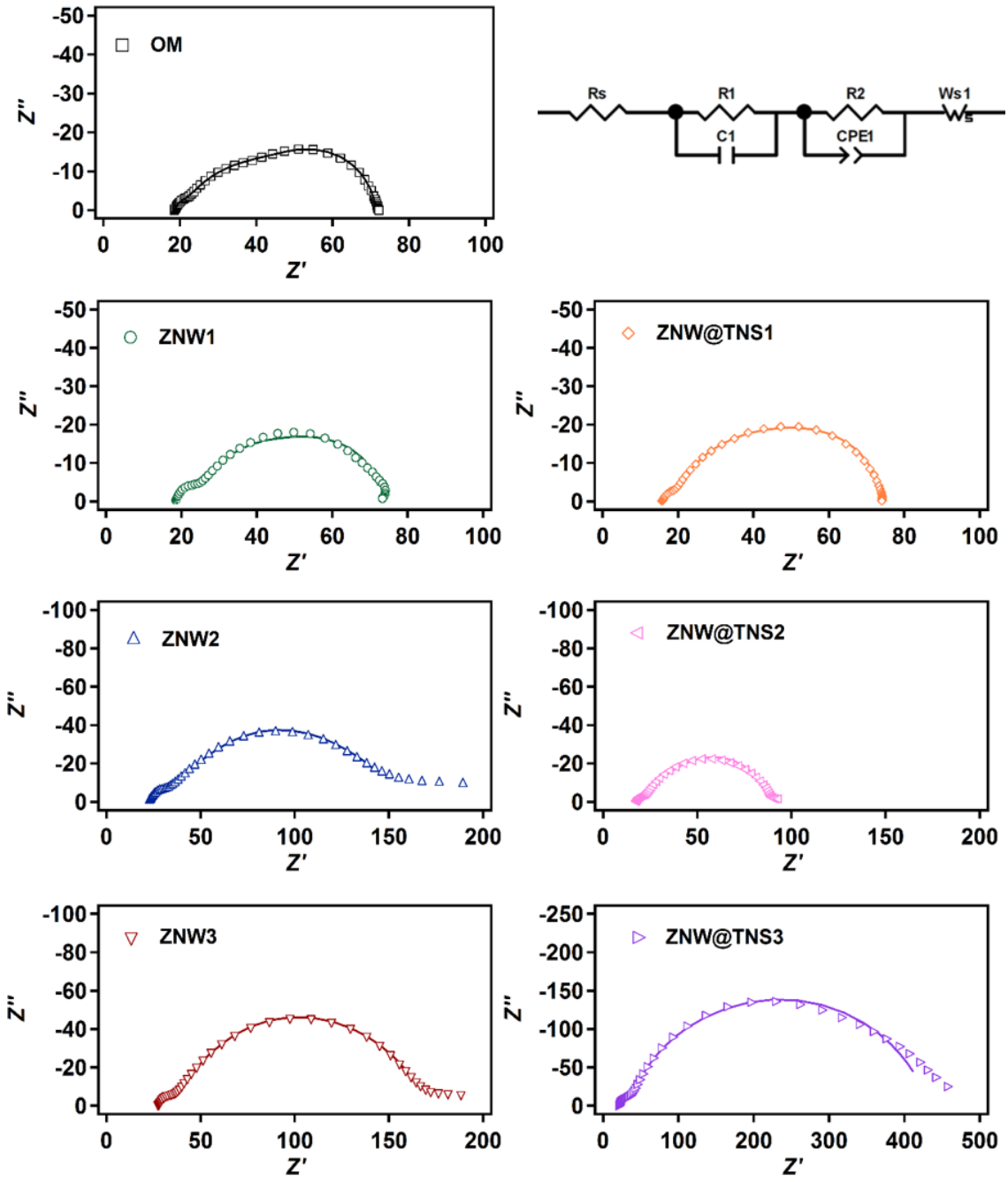

Figure 6.37. Nyquist plots recorded from electrochemical impedance spectroscopy at open circuit voltage and 1 Sun illumination for qssDSCs featuring an OM, ZNW or ZNW@TNS photoanode (symbols) and their equivalent circuit fittings (solid lines). The equivalent circuit used for analysis of the data is also shown at the top right of the figure, where R_S is the series resistance, R1 is the charge transfer resistance at the counter electrode, C1 is the capacitance at the counter electrode, R2 is the charge transfer resistance at the semiconductor/electrolyte interface, CPE1 is a constant phase element used to represent the capacitance at the semiconductor/electrolyte interface and Ws1 is a Warburg impedance associated with diffusion of redox species through the electrolyte.

In the case of the unmodified OM cells, the Nyquist plot was in the form of three overlapping semicircles, which can be attributed to the impedance associated with charge transfer at the counter electrode, charge transfer at the semiconductor/electrolyte interface and diffusion of charge carriers through the electrolyte, from left to right respectively. In the case of the ZNW and ZNW@TNS cells, no clear distinction could be made between the two latter semicircles resulting in single flattened semicircle. This second semicircle was found to be very large in the case ZNW2, ZNW3 and ZNW@TNS3 and may be anomalous due to the cracking that was exhibited in these photoanodes, which is consistent with the lower cell performances observed for these three photoanodes.

Analysis of the impedance spectra was completed by fitting the results to an equivalent circuit (Figure 6.37) based on one previously used in the analysis of DSCs containing viscous electrolytes under high light intensities.[267] Due to the overlap of the second two semicircles in the case of the ZNW and ZNW@TNS samples, analysis was first completed on the OM sample and the obtained value of the Warburg impedance was fixed for the remainder of the cells. This assumes that diffusion through the electrolyte would remain unchanged within the cells. Fitted values of the series resistance (R_S), the resistance of charge transfer at the counter electrode (R_{CE}) and resistance of charge transfer at the semiconductor/electrolyte interface (R_{CT}) for the cells made with different photoanodes can be seen in Table 6.5.

Table 6.5. Calculated values of series and charge transfer resistances obtained from equivalent circuit analysis of qssDSCs based on different photoanodes.

Photoanode	R_S (Ω)	R_{CE} (Ω)	R_{CT} (Ω)
OM	18.6	1.7	26.3
ZNW1	18.6	5.3	23.9
ZNW2	23.0	6.1	102.8
ZNW3	27.5	6.3	111.4
ZNW@TNS1	15.8	2.4	30.8
ZNW@TNS2	17.8	2.5	43.9
ZNW@TNS3	20.2	10.5	377.7

It can be seen that in general the resistance associated with charge transfer at the semiconductor/electrolyte interface (R_{CT}) increases upon adding more ZNW or ZNW@TNS structures to the OM film. These values are particularly large for the ZNW2, ZNW3 and ZNW@TNS3 photoanodes. This trend might indicate some increase in recombination resistance

as a result of adding the nanostructures. It can be seen however that the highest efficiency ZNW and ZNW@TNS devices (ZNW1 and ZNW@TNS1) have R_{CT} values that differ very little from those obtained for the OM photoanodes. Although the value is slightly higher for highest efficiency device (ZNW@TNS1), this difference is likely to be within error for the measurements and further experimentation would be required to confirm an increase in recombination resistance for the core-shell structures. The small deviations in the R_{CT} values between the highest efficiency devices might indicate that the recombination resistance plays a relatively small role in the efficiency enhancement compared to other factors, such as the increased surface areas.

Overall, in Section 6.3 it has been shown that use of novel one-dimensional nanostructures as additives within mesoporous TiO_2 anodes can give rise to improvements in power conversion efficiencies for qssDSCs. It was found that the ZNW structures only gave rise to enhancements in performance when compared to the OM films that had been formed without HCl. However, in the case of the ZNW@TNS hierarchical structures, enhancements in cell performance could be made over the OM films produced without HCl, but also over the higher performing OM films produced with HCl. The difference in the achieved power conversion efficiency between these two structures can be attributed to the higher surface areas and reduced recombination, due to the presence of a TNS shell. In addition to the enhancements in performance, it was also evident that the addition of these one-dimensional nanostructures gave rise to improvements in film integrity when HCl was not used in paste preparation. This effect was, however, only found when small quantities of the materials were used, which stresses the importance of precisely controlling the film composition in order to gain the maximum improvements.

6.4 Chapter Summary

In this chapter, the use of anodic ZnO nanowires has been demonstrated within a range of DSC device architectures. It was found that although direct application of these nanowires within back-illuminated DSCs was unsuccessful, applying them as additives within front-illuminated DSCs could give rise to improvements in cell power conversion efficiencies. In Section 6.2, it was demonstrated that the anodic ZnO nanowires were effective when applied as light-scattering layers, but did not improve cell performance when incorporated within the interior of the mesoporous ZnO film. Despite the increase in cell efficiency obtained for the light-scattering layers, it is notable that overall the cell efficiencies reported in Section 6.2 are relatively low. This is linked with a low J_{sc} exhibited by all of the cells, highlighting the continued issue with ZnO photoanodes in DSCs, which is the incompatibility with the most common sensitizing dyes.[74, 75] Although this can to some degree be negated by the thorough control of sensitizing conditions, there still remains a need for the development of high performance dyes with suitable anchoring groups for ZnO.[78, 257, 268]

In contrast, Section 6.3 demonstrates how efficient cells can be produced by using ZnO as an additive in conjunction with TiO_2, which provides the greatest stability and compatibility with the sensitizing dye. This final section combines the four research strategies of core-shell structuring, high-surface areas, light-scattering enhancement and one-dimensional nanostructures to achieve high efficiencies in qssDSCs. This demonstrates that in order to gain the greatest efficiency improvements through control of the photoanode structure, all of these factors must be taken into account simultaneously. Modified anodic nanowires represent one method of achieving this in a relatively simple way, due to the rapid growth method of the nanowires, the small quantities of additive needed within the photoanode and their easy incorporation into the TiO_2 pastes.

Chapter 7 – Application of ZnO Nanowires in Perovskite Solar Cells

Over the past six years perovskites have emerged as exciting new materials for efficient solar energy conversion. Since their first reported use within solar cells in 2009, efficiencies have risen dramatically and record certified efficiencies of 20.1 % have recently been reported in the literature.[14, 110, 111] Such high efficiencies make these materials competitors with some of the best thin film solar technologies and also with crystalline silicon.[14]

One of the most commonly reported materials for perovskite solar cells is $CH_3NH_3PbI_3$, which will be the material of study throughout this chapter.[110, 126, 129, 151] A wide range of different cell structures and fabrication methods have emerged over recent years, in an effort to raise cell efficiencies and simplify cell production.[269] Two main cell architectures have emerged for perovskite solar cells: 1. Planar perovskite cells,[130] and 2. Mesoscopic perovskite cells.[126] The merits of each of these cell structures is a topic of much debate and it is yet to be seen which will emerge as the most effective cell design. Planar cells benefit from a potentially simplified cell production, due to fewer layers needing to be deposited. They can also be produced at lower temperatures, due to there being no need to anneal a porous metal oxide layer.[151] However, to date, the highest reported efficiencies are still held by cells possessing at least a thin porous oxide layer.[111, 133] The role, and indeed the necessity, of the porous metal oxide is still under debate. Many reports have highlighted the fact that as charge transfer can occur through the perovskite material itself there is little need for an electron conducting porous metal oxide.[124] It may, therefore, be the case that the porous oxide layers are simply acting as a porous anchor for the perovskite material, allowing perovskite films with fewer pinholes and gaps to be formed, which are often routes to efficiency loss via recombination.

In this chapter, the use of ZnO within both planar and mesoscopic perovskite cells will be investigated (Figure 7.1). Upon commencing this research, reports of ZnO within perovskite solar cells were few and far between, with TiO_2 remaining the material of choice due to much of the research originating from DSCs. However, in the course of completing this research, many new reports of ZnO as an electron selective material in perovskite solar cells have emerged, an extensive list of which can be found in Chapter 2.[144-146, 151, 155, 163] The findings in these new reports will be related to the results reported throughout this chapter and aid in the explanation of the observed trends.

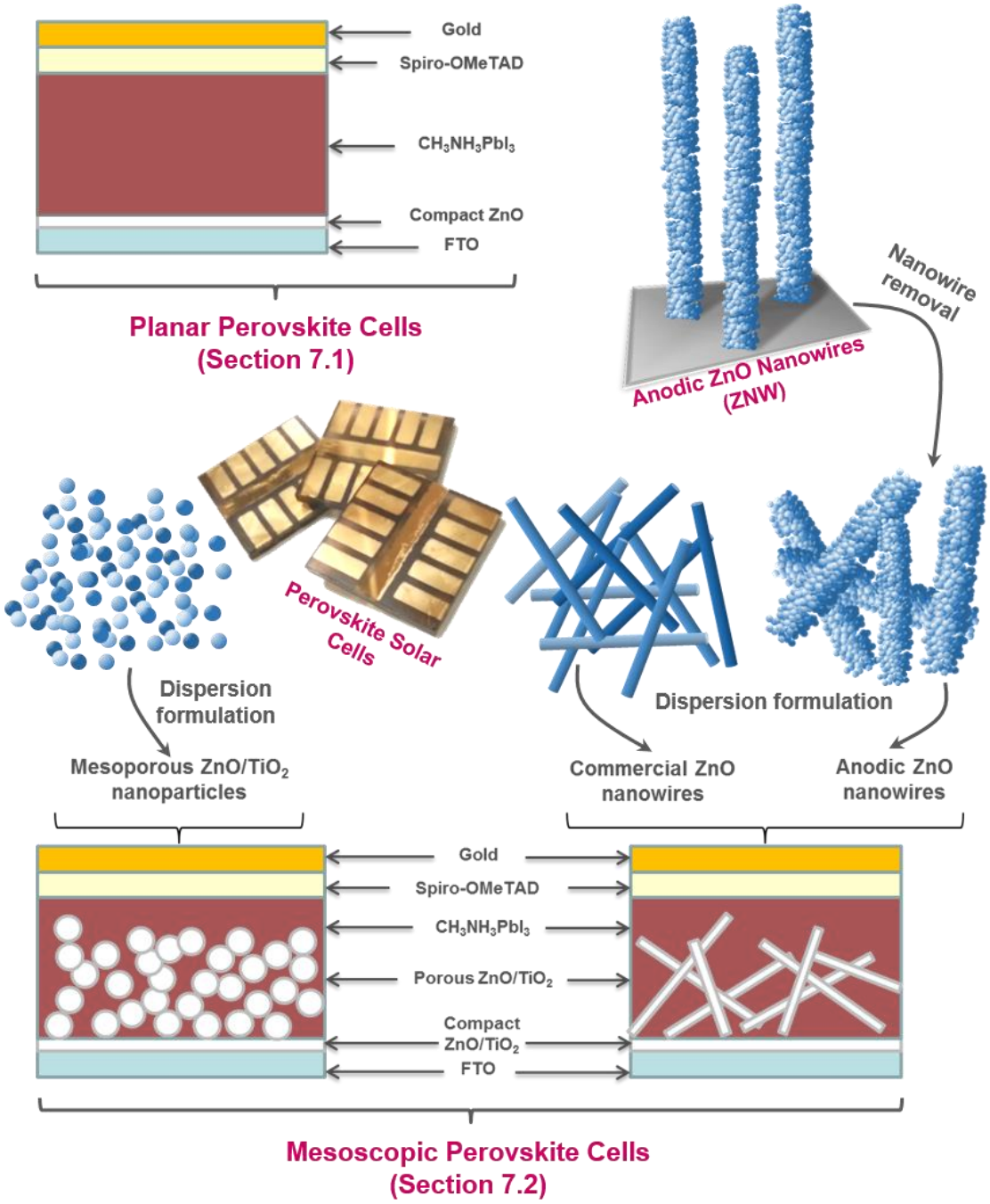

Figure 7.1 Schematic summarising the contents and structure of Chapter 7.

The first section of this chapter will explore the use of ZnO in its simplest form, within planar perovskite cell architectures, where it is used as a thin and flat electron selective contact layer between the perovskite material and the FTO electrode. The second section of this chapter will then move on to look at the use of ZnO nanostructures within mesoscopic perovskite solar cells. Both simple nanoparticle films and porous films of nanowires will be investigated and the results compared to those obtained with mesoporous TiO_2.

7.1 Planar Perovskite Solar Cells

ZnO was first applied within planar perovskite solar cells. These feature a layer of perovskite material sandwiched between two planar contact layers that are selective for accepting electrons (ZnO) and holes (Spiro-OMeTAD) respectively (Figure 7.2). Conducting layers of FTO coated glass and evaporated gold then complete the cell. Within this cell structure, the perovskite material absorbs light and transports both the photoexcited electrons and holes to their respective contacts, rather than charge transport occurring through a porous support.[130]

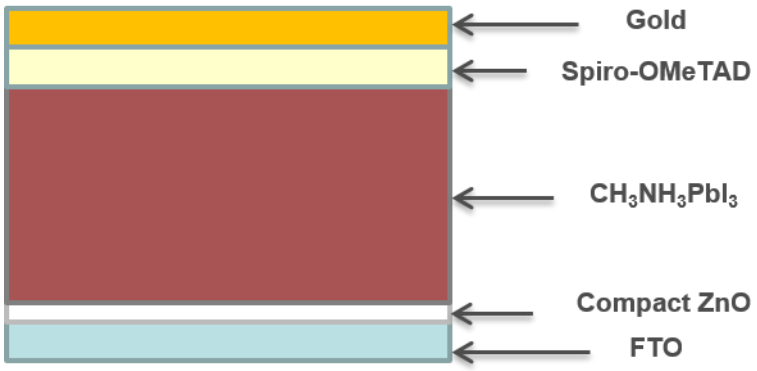

Figure 7.2. Schematic showing the cross-sectional structure of a planar perovskite solar cell featuring a ZnO blocking layer.

Two main solution-based perovskite deposition methods have been reported in the literature: The first method, called the 1-step method, involves dissolving a mixture of all of the required perovskite starting materials in a high boiling point polar aprotic solvent, such as DMF or DMSO. The mixture is then spin coated onto the electron selective layer and annealed to form the perovskite material, typically over a period of ~30-60 minutes. In the second method, called the 2-step method, a lead based precursor (typically a lead halide) is dissolved in a polar aprotic solvent, spin coated and briefly heated to form a thin film of the lead halide. This film is then submerged in a solution of methylammonium iodide (MAI) in order to rapidly convert the lead halide into a perovskite film.

As an initial investigation, the two different deposition methods were compared using ZnO blocking layers that had been formed by the spray pyrolysis of a zinc acetate solution. It was quickly found that the 1-step deposition technique was not suitable for deposition of perovskite onto ZnO. Significant de-wetting occurred, which resulted in very thin and inhomogeneous films of the perovskite material on the substrate (Figure 7.3). This was contrary to findings within the group for blocking layers formed from TiO_2, and could be related to differences in the surface

energy or nanostructure of the two metal oxides. More recent reports in the literature have also documented difficulties in using the 1-step method in conjunction with ZnO substrates.[146]

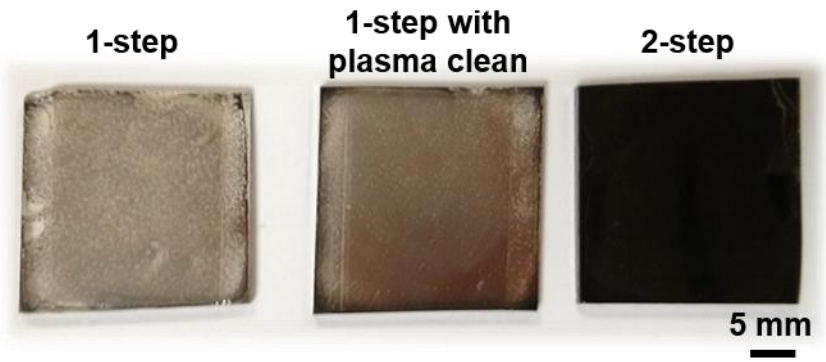

Figure 7.3. Photos comparing the perovskite films obtained using the 1-step and 2-step deposition methods on a ZnO blocking layer.

Oxygen plasma treatment is a well-known technique that can be used in substrate cleaning and also in altering the surface properties of materials, such as ZnO.[270] This treatment was, therefore, used on the ZnO coated substrates, in the hope that by altering the surface properties the 1-step perovskite deposition could be improved. This treatment was successful to some extent, as films deposited after a plasma treatment were darker and more homogeneous, however, it was still apparent that some de-wetting was occurring for these films (Figure 7.3).

In contrast to the films deposited by the 1-step method, the 2-step method gave rise to very dark perovskite films which homogeneously covered the surface of the substrate, with the exception of darker edges and corners, due to the edge effects of the spin coating process (Figure 7.3). The conversion from the PbI_2 film to the perovskite, $CH_3NH_3PbI_3$, during submersion in a MAI solution was found to occur very rapidly, with no sign of the yellow PbI_2 material observable after just 20 s. The 2-step method was, therefore, used throughout the remainder of this chapter as the method of perovskite deposition.

After establishing that the 2-step method was a more suitable perovskite deposition method, the focus was put on the optimisation of the ZnO blocking layer, in order to minimize recombination within the cells whilst maintaining low resistances. This is typically achieved by the deposition of high quality, thin films with no pin-hole gaps that would allow the perovskite layer to contact the underlying FTO. This investigation started with the use of spray pyrolysis as the ZnO deposition technique. In order to optimize this deposition procedure, ZnO films were deposited by spray pyrolysis on FTO coated glass substrates, using different numbers of spray pyrolysis cycles. These coated substrates were then used to produce planar perovskite cells and

their performance was assessed by *J-V* measurement of 10 different sites (pixels) over the cell surface under 1 Sun AM 1.5 simulated sunlight. It should be noted that all *J-V* measurements reported in this section were recorded by scanning the voltage from 1.2 V to 0 V. From the recorded *J-V* curves, the parameters of J_{sc}, V_{oc}, fill factor and *PCE* were calculated for each cell and can be seen in Figure 7.4.

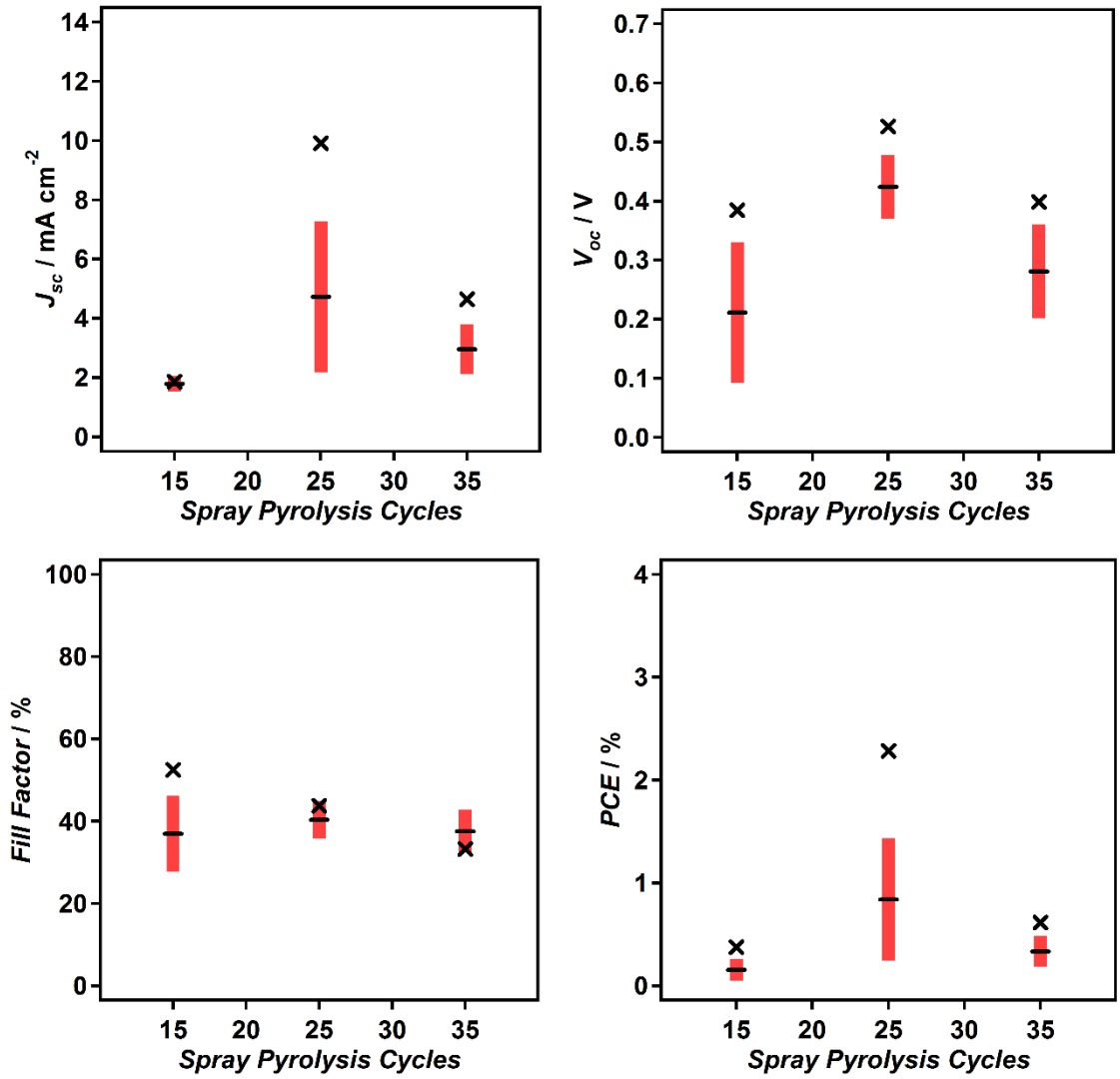

Figure 7.4. Average cell performances and standard deviations (30 cells) for planar perovskite cells, produced on ZnO blocking layers deposited by different numbers of spray pyrolysis cycles. The black crosses represent the values corresponding to the highest efficiency device of each type.

It was found that optimal cell performance was obtained for 25 cycles of ZnO spray deposition. At lower numbers of spray cycles a significant decrease in both J_{sc} and V_{oc} was observed. This is likely due to pinholes within the thin ZnO film that are allowing recombination

between the FTO substrate and the perovskite layer. For ZnO layers deposited over a high number of spray cycles there is also a decrease in performance compared to the intermediate deposition conditions. This might be due to too thick a layer of ZnO being formed, which could lead to increased resistance within the cell.

Despite an optimum being found for 25 spray cycles, performances of these cells were still low, particularly when compared to cell efficiencies obtained within the literature for ZnO blocking layers.[151] It was, therefore, decided that alternative ZnO deposition techniques should be explored in order to improve cell efficiencies. A range of different deposition techniques were examined for producing both ZnO and TiO_2 blocking layers, FESEM micrographs of which can be seen in Figure 7.5.

The bare surface of the FTO-coated glass substrate can be seen to consist of a densely packed film of angular crystallites with diameters of ~150 nm (Figure 7.5a). Two different TiO_2 blocking layer deposition techniques were examined: Spin coating of a TiO_2 precursor followed by annealing (Figure 7.5b) and spray pyrolysis using a TiO_2 precursor solution (Figure 7.5c). In the case of the spin coated TiO_2 precursor the features of the underlying FTO substrate can be seen within the electron micrograph (Figure 7.5b), indicating that the TiO_2 is forming a relatively thin conformal layer over the top of the FTO. The surface features were difficult to resolve, which might also indicate that the TiO_2 layer is filling in a number of the gaps at FTO crystallite boundaries and resulting in a much flatter surface. When spray pyrolysis was used to deposit the TiO_2 no underlying features of the FTO can be observed and the surface can be seen to be densely covered in rounded structures, with typical diameters of <100 nm (Figure 7.5c).

ZnO blocking layers were produced either by electrodeposition from a zinc nitrate solution, spin coating of a zinc acetate solution followed by annealing, or spin coating of a dispersion of small ZnO nanoparticles. The electrodeposited ZnO layers were found to be relatively thick (~400 nm) and formed of densely packed hexagonal structures with diameters of ~200 nm. Films formed from the spin coating of zinc acetate solutions, without or with ethanolamine within the precursor solution, are shown in Figure 7.5e and 7.5f respectively. The films appeared to be formed of very small ZnO crystallites and no features of the underlying FTO could be observed. The films did not appear to be as smooth as the spin coated TiO_2 films and small cracks could be observed on the surface. However, this cracking was reduced to some extent by the addition of ethanolamine to the precursor solution.

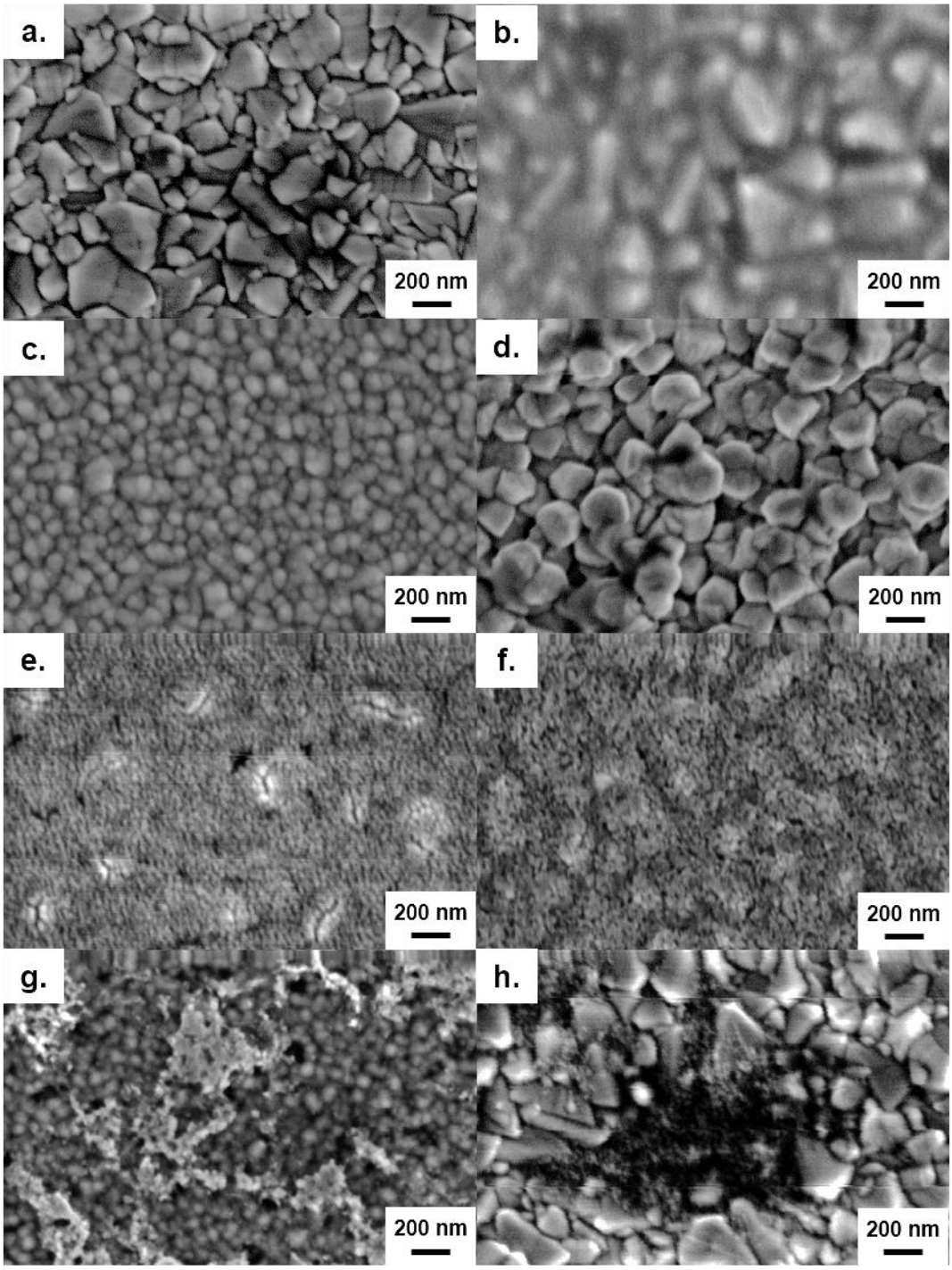

Figure 7.5. FESEM micrographs of clean FTO (a) and blocking layers deposited by TTIP spin coating (b), TiO_2 spray pyrolysis (c), ZnO electrodeposition (d), spin coating of a zinc acetate solution (e), spin coating of a zinc acetate solution containing ethanolamine (f), spin coating ZnO nanoparticles (~5 nm diameter) (g) and spin coating ZnO nanoparticles (~5 nm diameter) followed by annealing (h).

One particularly successful method, that had been recently reported in the literature, was the use of thin films of small (~5 nm) ZnO nanoparticles as electron selective contacts for planar perovskite cells (Figure 7.5g).[151] Using these layers, Kelly *et al*. were able to achieve power conversion efficiencies of up to 15.7 %. This method was, therefore, trialled as an alternative to the deposition of ZnO via spray pyrolysis.

The ZnO nanoparticle dispersion was synthesized following the method previously reported by Kelly *et al*. and was examined using TEM (Figure 7.6).[151] TEM analysis revealed that the nanoparticles had typical diameters of 5-6 nm, in agreement with the results reported by Kelly *et al*..[151] This dispersion was then used to deposit thin layers of ZnO nanoparticles on FTO substrates by spin coating. This spin coating process was repeated different numbers of times (between 1 and 5 cycles), in order to gain different thicknesses of ZnO nanoparticle films. These were then used to produce planar perovskite solar cells, using an identical technique to the method used for the spray coated ZnO films. Figure 7.7 shows the average cell performance parameters calculated from analysis of the *J-V* curves of the cells. From these results, it can be seen that power conversion efficiencies are consistently higher than when a spray deposited ZnO layer was used. This improvement in efficiency is due to increased J_{sc} and V_{oc} values for the cells featuring a nanoparticle blocking layer. Significantly lower performances were obtained when only one layer of ZnO nanoparticles was deposited, which is likely due to incomplete coverage of the FTO substrate. A slight decrease in performance was also observed when 5 spin cycles were used, giving an optimum performance at 3 spin cycles. This result is in agreement with the findings of Kelly *et al*., who also found that 3 spin cycles gave the optimum cell performance.[151]

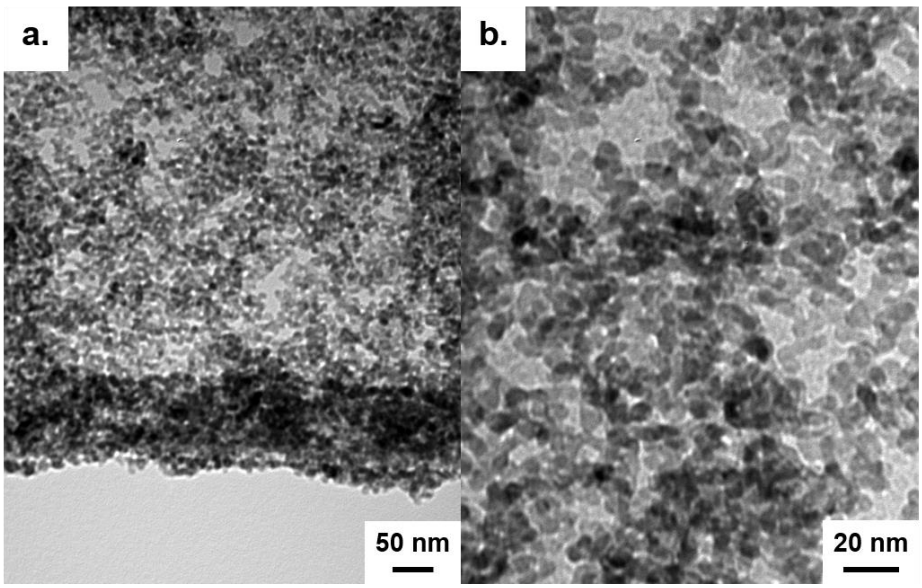

Figure 7.6. TEM micrographs of ZnO nanoparticles, synthesized for deposition of a ZnO blocking layer, on a lacy carbon TEM grid at low (a) and high (b) magnification.

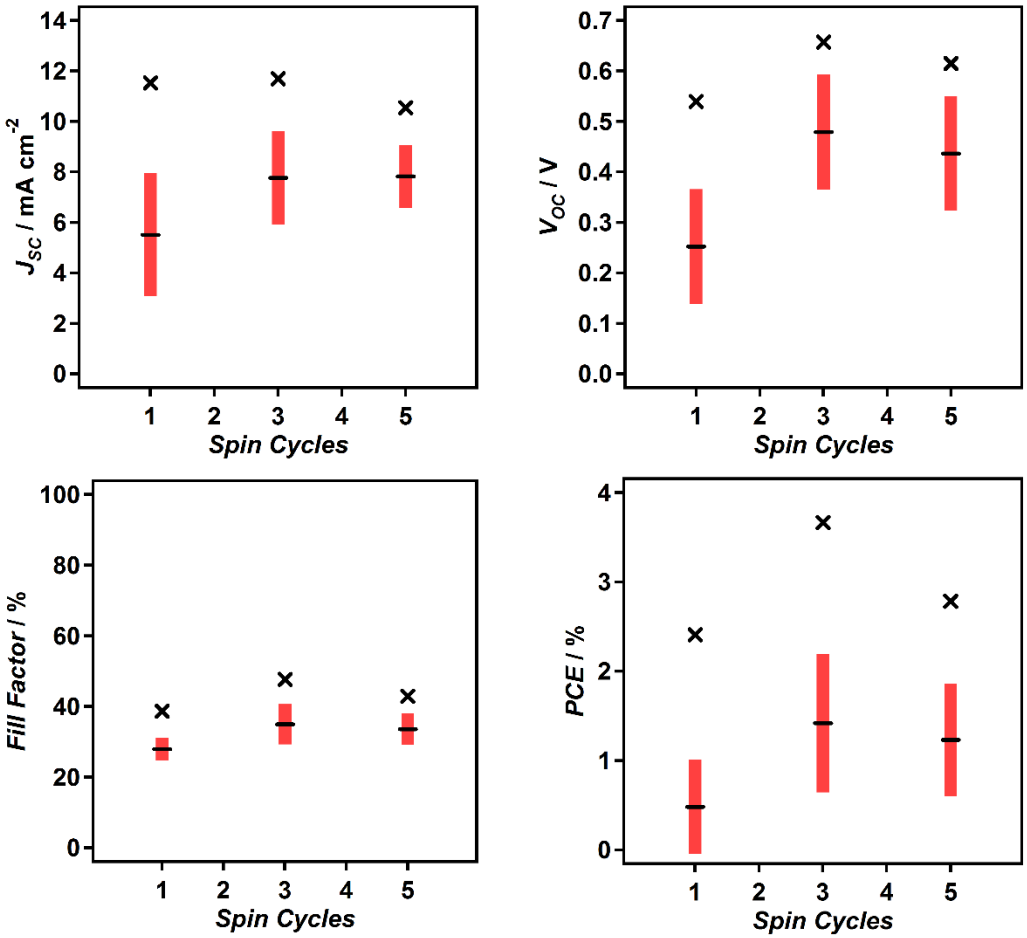

Figure 7.7. Average cell performances for planar perovskite cells produced on ZnO blocking layers, deposited by different numbers of nanoparticle spin coating cycles. The black crosses represent the values corresponding to the highest efficiency device of each type and the red bars show the standard deviation over 30 cells.

Despite an improvement in cell performance compared to the spray deposited ZnO layers, the cell efficiencies were still low and subject to a high degree of error, as exhibited by the error bars. It was hypothesised that these low performances were likely due to the un-optimised perovskite deposition technique and, therefore, time was spent in improving the method of film deposition.

In the initial set of cells fabricated using 2-step deposition, the PbI_2 layer was deposited by first preparing a 1 M solution of PbI_2 in DMF, spin coating the solution onto the substrate and annealing for 30 min at 70 °C. It was observed that dissolving enough PbI_2 within the DMF to reach a 1 M concentration was not possible, even after overnight stirring at 70 °C, therefore, excess solid was filtered from the saturated solution using a 0.45 µm filter. This resulted in a slightly lower concentration of PbI_2 and was, therefore, likely to give rise to thinner PbI_2 films. These thinner PbI_2 films were originally hypothesized to be the source of the low cell

performances, so efforts were made to improve the PbI_2 layer. The first attempt at altering the PbI_2 layer thickness was conducted by repeating the PbI_2 deposition on top of a PbI_2 layer, to give a double layer of PbI_2. These films were a more vibrant shade of yellow/orange than the single layer films and gave rise to much darker perovskite layers after conversion. However, upon testing these cells via *J-V* measurement, it was discovered that only minor improvements in power conversion efficiency were achieved (Figure 7.8). The cells produced using the double PbI_2 layer were effective in improving both the V_{oc} and fill factor of the cells, but resulted in a decreased J_{sc} that counteracted these benefits.

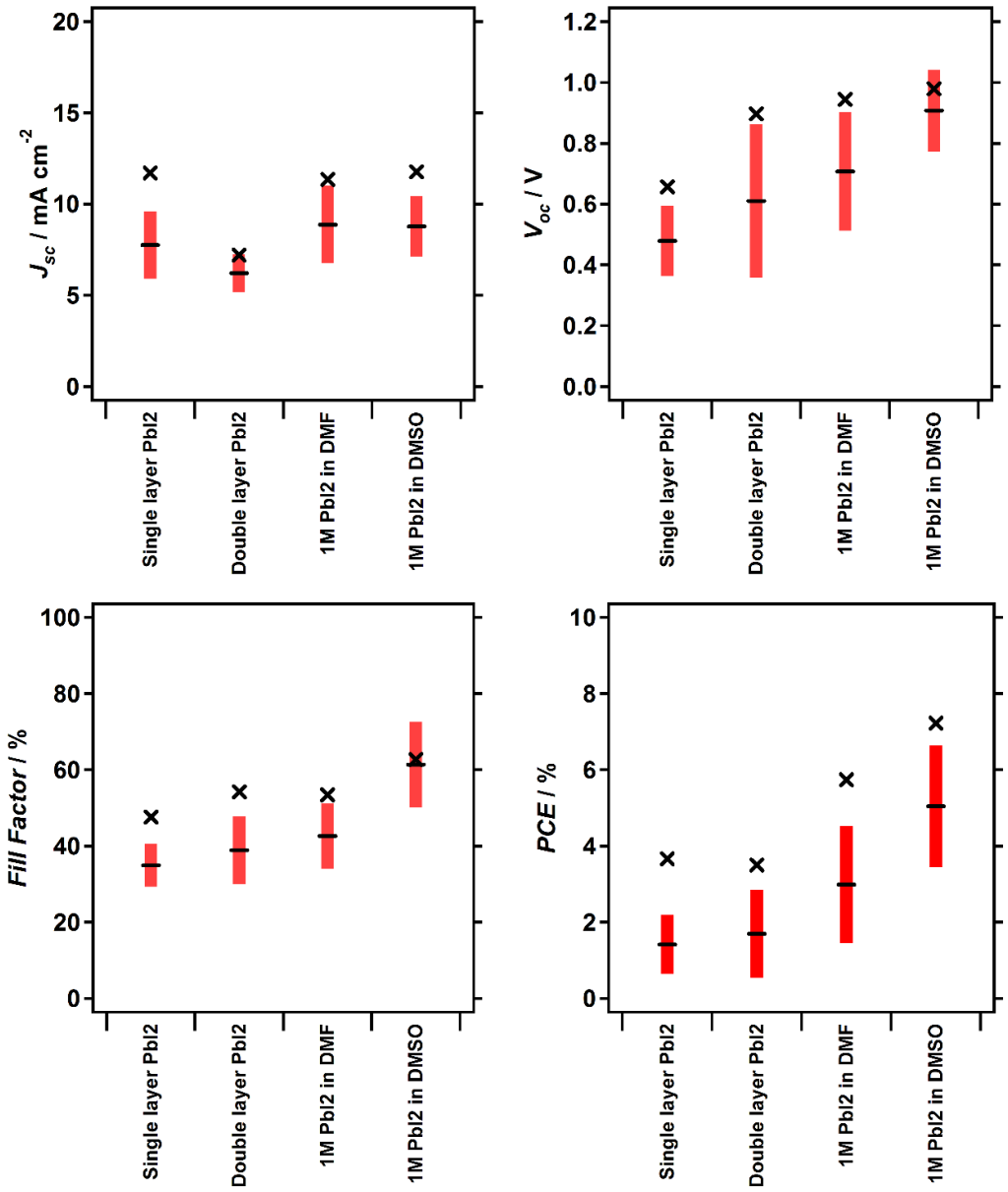

Figure 7.8. Average cell performances for planar perovskite cells produced on ZnO blocking layers using different PbI_2 deposition methods. The black crosses represent the values corresponding to the highest efficiency device of each type and the red bars show the standard deviation over 30 cells.

With minimal improvements being made as a result of the thicker double layer of PbI_2, attention was then brought to the purity of the PbI_2 reagent. A new PbI_2 reagent was purchased in order to ensure that there was no contamination and 1 M PbI_2 solutions were again made in DMF. What was immediately apparent was how easily the new reagent dissolved in DMF. After just 30 minutes of stirring at 70 °C all of the PbI_2 was dissolved within the solvent, negating the need to filter the solution. The insolubility previously observed for the older PbI_2 reagent might be attributed to the gradual hydration of the solid over time, as the hydrated form is known to have a lower solubility.[271] It was found that PbI_2 began to re-crystallize upon cooling to room temperature, so was maintained at 70 °C throughout the deposition process. It was also found that by pre-heating the ZnO coated substrates to ~60 °C before spin coating, PbI_2 with a smoother, glassier appearance could be produced. This method of heating both the solution and substrate was used for the remainder of the cells prepared in this chapter. The cells produced using this method (shown as 1 M PbI_2 in DMF) gave rise to an increase in power conversion efficiency of ~100 % compared to the initial PbI_2 deposition method (Figure 7.8). This increase in efficiency was a result of a combined increase of J_{sc}, V_{oc} and fill factor.

DMSO is another polar aprotic solvent that has been used for the preparation of PbI_2 and perovskite films.[272] DMSO has a higher boiling point than DMF and can also dissolve higher concentrations of PbI_2.[272] Reports have been made in the literature of improved perovskite film quality and increased efficiencies using DMSO as a solvent for the PbI_2 deposition. This has been attributed to the strong coordination of the DMSO to the PbI_2 and the higher boiling point, which both contribute to a slower evaporation during the annealing process that follows spin coating. DMSO was, therefore, trialled as an alternative to DMF for the production of planar cells. The same optimised process was used, as discussed previously, but with the 1 M PbI_2 dissolved in DMSO rather than DMF.

After spin coating the solution, it was observed that the film was a very pale yellow/straw colour, unlike the vibrant yellow when DMF was used. After annealing, the PbI_2 film was a vibrant yellow colour and very smooth and glassy in appearance. Cells fabricated using this method (shown as 1 M PbI_2 in DMSO) were found to perform significantly better, even than the optimised DMF based cells (Figure 7.8). V_{oc} values were significantly increased, reaching values of up to 0.98 V, and fill factors were also greatly increased, up to a maximum of 75 %. This resulted in an average power conversion efficiency of 5.0 % and a maximum efficiency of 7.2 %. These results highlight the importance of carefully controlling the PbI_2 deposition step, as by performing a very simple optimisation the average cell efficiency was increased by over 300 % from its initial value.

A cross-section of one of the optimised planar cells is shown in the FESEM micrograph in Figure 7.9. With the exception of the thin ZnO layer, all layers of the planar cell can be clearly seen. The perovskite layer is 300-400 nm in thickness and can be seen to be formed of multiple large, angular crystallites. Within the cross-section, a pinhole gap can be observed in the perovskite layer, where the Spiro-OMeTAD layer can be seen to directly contact the ZnO blocking layer. Such defects in the perovskite film would be expected to give rise to increased recombination and, therefore, reduced efficiencies for the cell. It is apparent that despite significantly improving the performance of the cells, there is still much room for improving the perovskite film production.

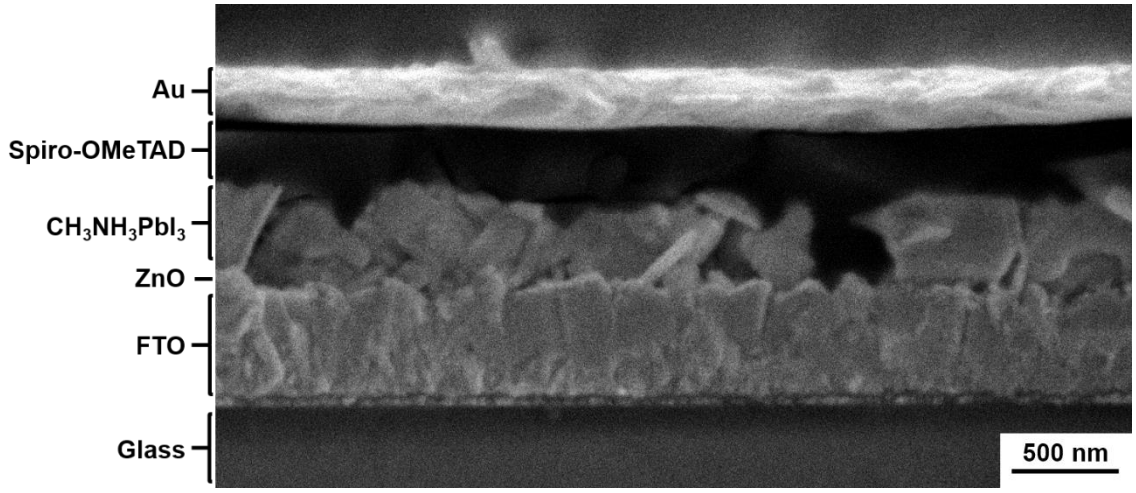

Figure 7.9. FESEM cross-section of a planar perovskite solar cell fabricated on a ZnO NP blocking layer.

7.2 Mesoscopic Perovskite Solar Cells

The next stage in the investigation was to explore the use of ZnO within mesoscopic perovskite solar cells. Mesoscopic cells typically feature a thin layer of a mesoporous metal oxide, such as TiO_2, into which the perovskite material is infiltrated (Figure 7.10). The most efficient devices also feature a capping layer of perovskite above the metal oxide, which acts to prevent contact between the hole conducting and electron conducting materials.[111, 133] In this section, the use of mesoporous ZnO will be compared with the use of mesoporous TiO_2 layers, which are the most commonly used material. To the best of our knowledge, there have been no direct comparisons between mesoscopic perovskite cells featuring equal thickness films of mesoporous ZnO and TiO_2.

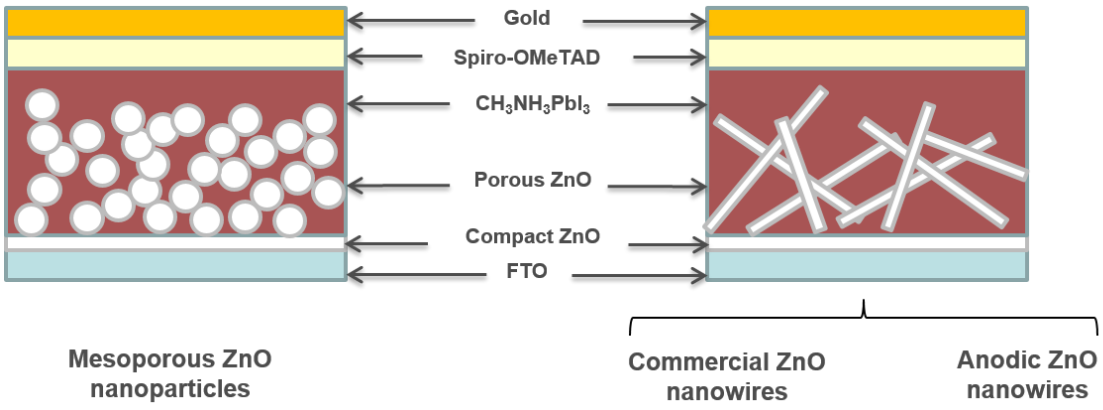

Figure 7.10. Schematic showing the cross-sectional structure of mesoscopic perovskite solar cells featuring either ZnO nanoparticle layers or ZnO nanowire layers.

As high surface areas are not a necessity for the metal oxide layer in perovskite solar cells, the use of more open, porous films will also be explored through the use of randomly oriented nanowire films (Figure 7.10). These films could feature larger void spaces for the infiltration of the perovskite material, whilst still providing an anchoring structure for the formation of pinhole free perovskite films. As in Chapter 6, the use of anodic ZnO nanowires will be compared with commercial ZnO nanowires within these mesoscopic device architectures.

7.2.1 Porous layer preparation

The first stage in the production of mesoscopic perovskite cells was to optimise the deposition of the various porous layers, to gain homogeneous coverage on the substrate and controlled film thicknesses. It should be noted that although ZnO nanoparticle blocking layers (Figure 7.5g) were

effective in planar cells, the morphology was found to change drastically after annealing (Figure 7.5h). After annealing, little evidence of a conformal film of nanoparticles could be observed, and instead only aggregates of nanoparticles could be seen, on what appeared to be, a blank FTO substrate. As annealing is a necessary step in the production of the porous ZnO layers, an alternative ZnO blocking layer was used that was deposited from the spin coating of a zinc acetate solution (Figure 7.5e). The TiO_2 blocking layers used in Sections 7.2.1 and 7.2.2 were formed from spin coating a TiO_2 precursor and annealing (Figure 7.5b). Thereafter, TiO_2 blocking layers were formed from spray pyrolysis, as they were found to give improved reproducibility of results owing to a more conformal coverage of the substrate (Figure 7.5c).

The initial attempts at forming ZnO nanowire and nanoparticle dispersions for spin coating involved simply sonicating the ZnO powders in different solvents or solvent mixtures. The films that resulted from spin coating these dispersions were very grainy in appearance, indicating that a significant quantity of aggregates were still present within the dispersions. These aggregates could be easily observed by FESEM (Figure 7.11) and were found to be multiple microns in diameter. As efficient perovskite films are typically below 1 μm in thickness, the removal of these aggregates was essential for formation of efficient devices. Mesoporous TiO_2 films were deposited by spin coating a dilute commercial paste (Dyesol, 18nr-t) as a comparison. These films were found to be highly transparent and had an extremely homogeneous surface coverage, with no aggregates when examined by FESEM (Figure 7.11b). It was, therefore, apparent that significant improvements in the dispersion formulation were necessary.

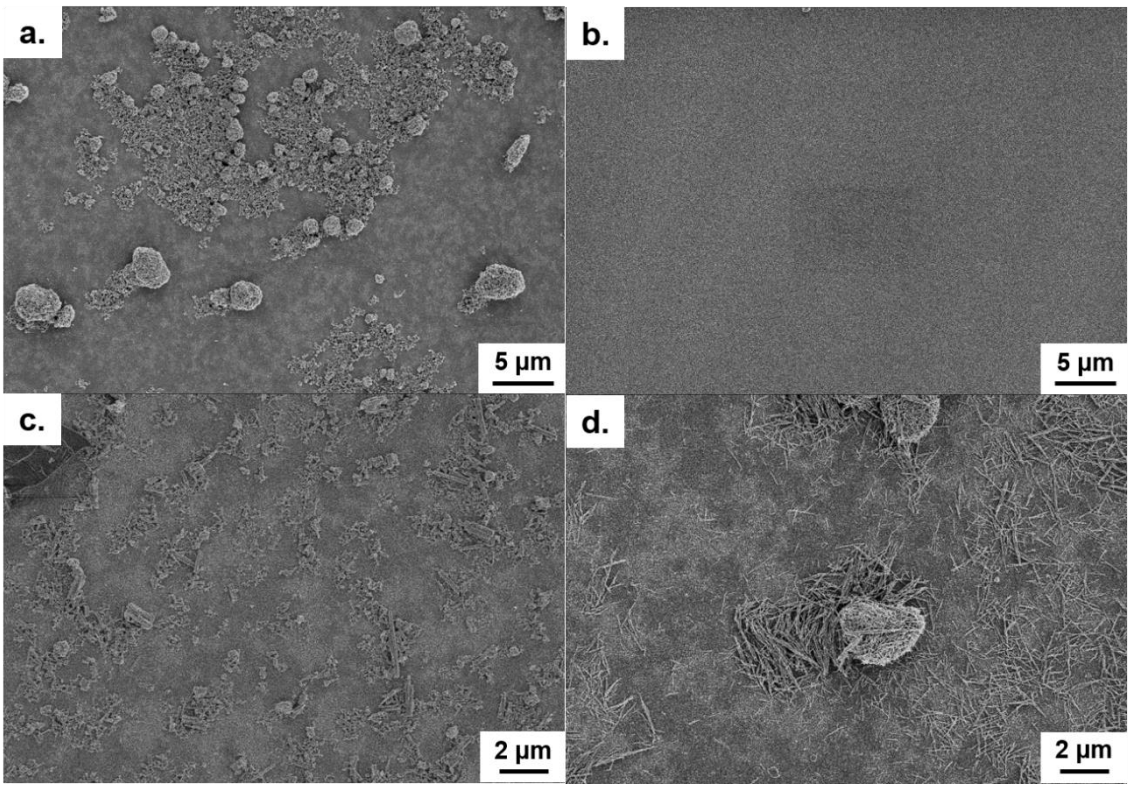

Figure 7.11. FESEM micrographs of the initial annealed ZnO nanoparticle (a), TiO_2 nanoparticle (b), anodic ZnO nanowire (c) and commercial ZnO nanowire (d) layers on FTO coated glass.

A successful route to the formulation of well dispersed nanoparticle solutions was found through the use of a mixture or ethanol, ethyl cellulose, terpineol and acetic acid as a dispersion medium. This provided both steric dispersion, through the ethyl cellulose chains, and electrostatic dispersion from the binding of acetic acid to the ZnO surface.[273] Full details of the formulations can be found within Chapter 3 and a summary of the ZnO compositions of each paste are displayed within Table 6.1 in Chapter 6. In all cases, the ZnO content of the dispersions were calculated to be 5 wt.%.

After spin coating, the newly formulated dispersions were found to give smooth, glassy, translucent films. The dispersions were spin coated onto ZnO coated FTO-glass substrates, at different spin speeds, in order to gain different film thicknesses. After annealing, the thickness of the films was determined by profilometry, using three repeat measurements for each condition. The average film thickness and arithmetic mean roughness of each film is shown in Figure 7.12 for each spin speed. It can be seen that increasing spin speeds result in thinner films, up to a point, at which the film thickness plateaus and ceases to fall further. For the ZnO and TiO_2 nanoparticle layers, homogeneous films could be obtained down to a thickness of ~200 nm, with low roughness values. However, for the two sets of nanowire layers, thicknesses reached a minimum at ~400 nm and roughness values were significantly higher. This is not surprising, considering that the

commercial and anodic nanowires are ~90 and ~160 nm in diameter, respectively, and have lengths of ~1 µm. Regardless of the slight discrepancy in thickness ranges between the nanowire and nanoparticle films, it is possible to produce porous films of all the nanostructures at equal thicknesses of ~400 nm for comparison of their performance within mesoscopic perovskite cells.

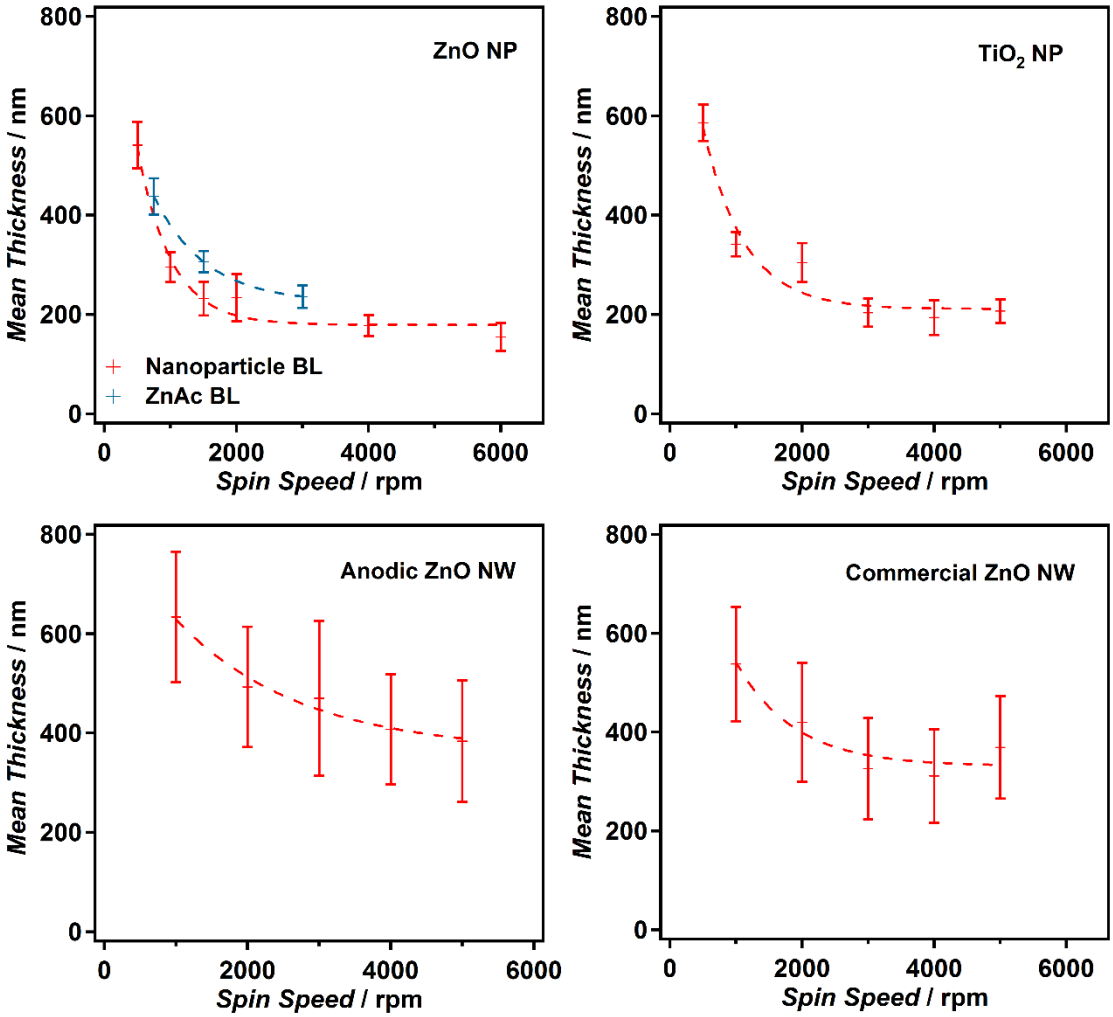

Figure 7.12. Average nanoparticle or nanowire film thicknesses obtained for different spin coating speeds. The error bars show the arithmetic mean roughness of the films calculated from profilometry. For the ZnO NP layers, two sets of thicknesses are shown; one for films deposited on a ZnO nanoparticle blocking layer (Nanoparticle BL, red), and one for films deposited on a ZnO blocking layer formed from spin coating a zinc acetate solution (ZnAc BL, blue). TiO_2 NP layers were deposited on spin coated TiO_2 blocking layers and both nanowire films were deposited on ZnO blocking layer from spin coating a zinc acetate solution.

FESEM micrographs of the improved films show that in all cases the nanostructures cover the entire substrate, with no gaps or large aggregates present within the films that would affect the cell structure and performance (Figure 7.13).

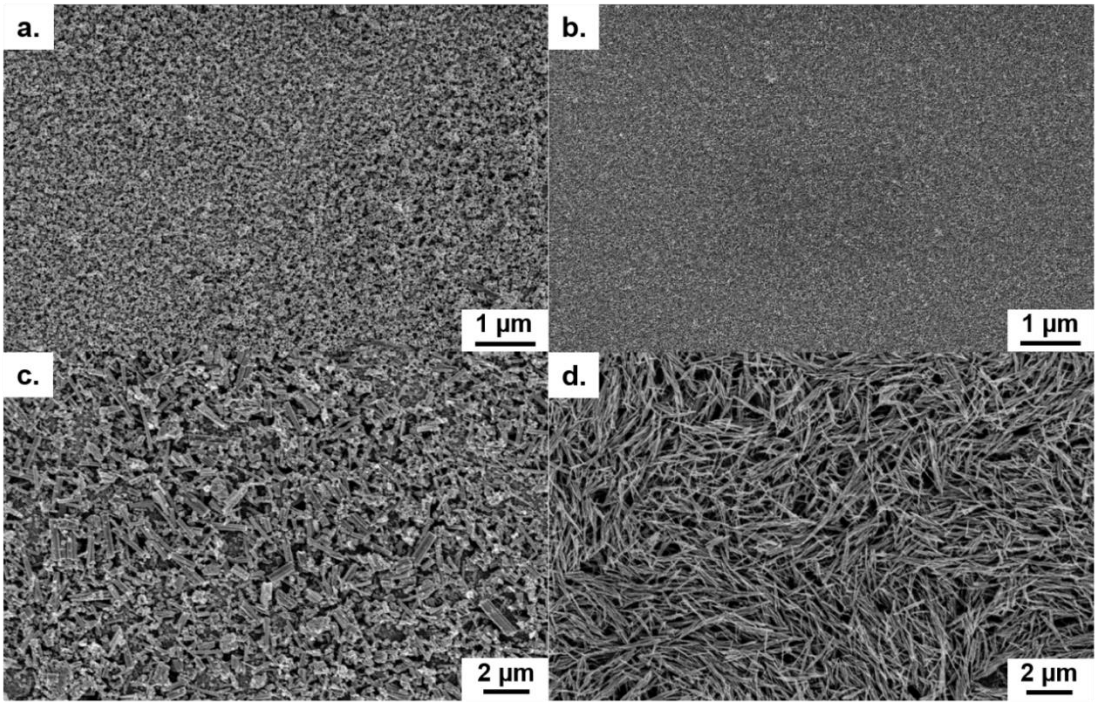

Figure 7.13. FESEM micrographs of annealed ZnO nanoparticle (a), TiO_2 nanoparticle (b), anodic ZnO nanowire (c) and commercial ZnO nanowire (d) layers on FTO coated glass after optimisation of paste preparation.

7.2.2 Fabrication and testing of mesoscopic perovskite solar cells

Now that a suitable method had been developed for the production of porous nanostructured films of equal thickness, it was possible to fabricate mesoscopic perovskite solar cells, using them to compare the performance. Unless otherwise stated, the thickness of the porous oxide layer was fixed to ~400 nm through use of the appropriate spin speed, as shown in Figure 7.12. Cells were fabricated using the 2-step perovskite deposition technique, in which a layer of PbI_2 was first infiltrated into the porous oxide material by spin coating a 1 M DMF-based PbI_2 solution onto the porous film, followed by submerging in a MAI solution to convert to the perovskite. The performance of the cells was assessed by measuring *J-V* curves on ten different sites (pixels) over the surface of the cell under 1 Sun AM 1.5 simulated sunlight. Three cells were measured for each cell type, giving a total of 30 measurements for each. *J-V* curves were measured both in the backward (1.2 to 0 V) and forward (0 to 1.2 V) scan directions in order to assess any differences that might arise due to scan direction, which is commonly referred to hysteresis.

Figure 7.14 shows the *J-V* curves of the best performing pixels of different porous layer types in both the backward (red) and forward (blue) scan directions. The first thing that can be noticed is the significant discrepancy between the current recorded when scanning in different directions. This hysteresis in the cell measurement is a common problem reported for perovskite solar cells and makes accurate determination of the cell efficiency a problem, due to different values being obtained depending on the scan direction. It is interesting to observe that the TiO_2 NP cell does not suffer from a reduction in V_{oc} between the backward and forward scans. This could either be a result of there being no ZnO present within the cell, or due to a TiO_2 blocking layer being used, unlike in the case of the other cells. As the most significant cell hysteresis is observed for the TiO_2 nanoparticle layer on the ZnO blocking layer, this hysteresis is, perhaps, largely attributed to the type of blocking layer used rather than the porous layer material itself.

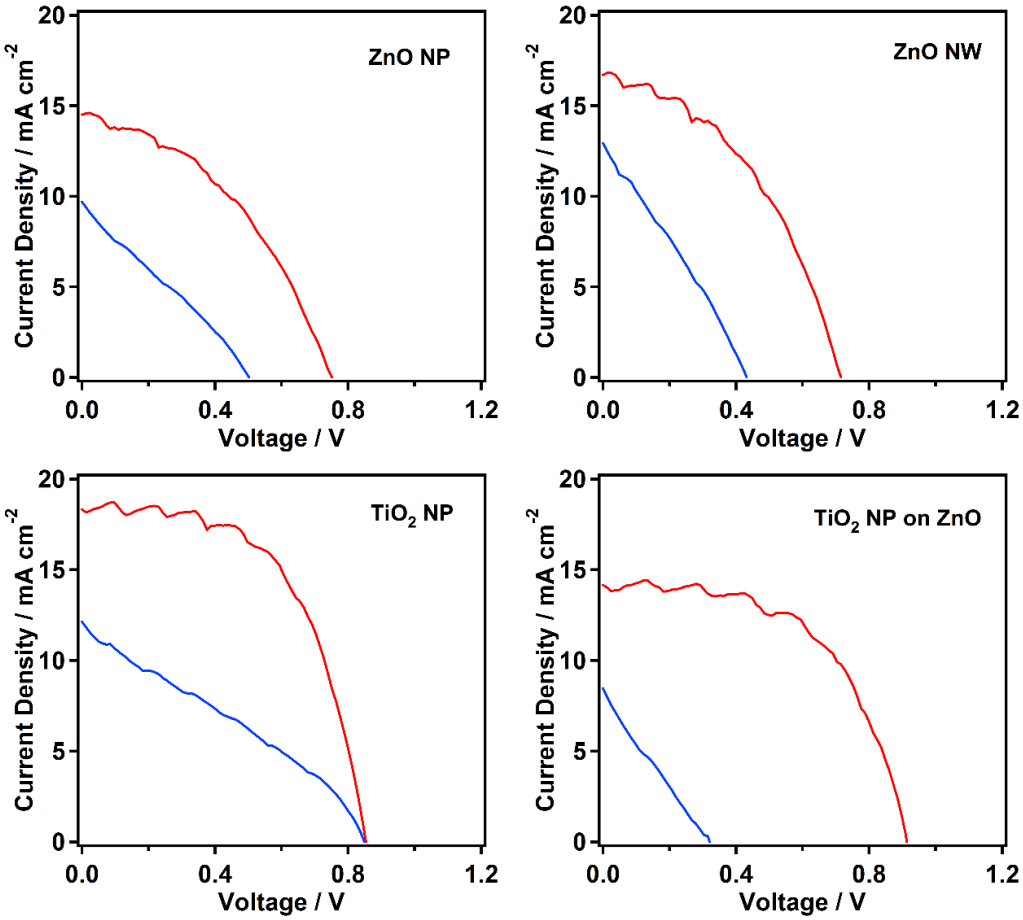

Figure 7.14. *J-V* curves recorded in the backward (red) and forward (blue) scan directions for the highest efficiency pixels for each of the different porous oxide layers. ZnO NW refers to commercial ZnO nanowire layers. All porous layers apart from TiO_2 NP were deposited on ZnO blocking layers. TiO_2 NP layers were deposited on TiO_2 blocking layers.

Average cell performances for both the backward and forward scans are shown in Figure 7.15 for the different porous layer types. Cells featuring a TiO_2 based porous layer were found to give significantly higher power conversion efficiencies when measured in the backward direction, due to a higher V_{oc} and fill factor. In the forward scan direction, however, both the V_{oc} and fill factor values of the TiO_2 nanoparticle film on the ZnO blocking layer dropped significantly, reaching values much closer to those of the ZnO porous cells. Little significant difference in performance can be seen between the cells featuring ZnO nanoparticle and ZnO nanowire porous layers, other than a very slight increase in J_{sc} and V_{oc}. These results seem to indicate that the cell performance is more strongly related to the inherent chemical properties of the porous metal oxide rather than the morphology.

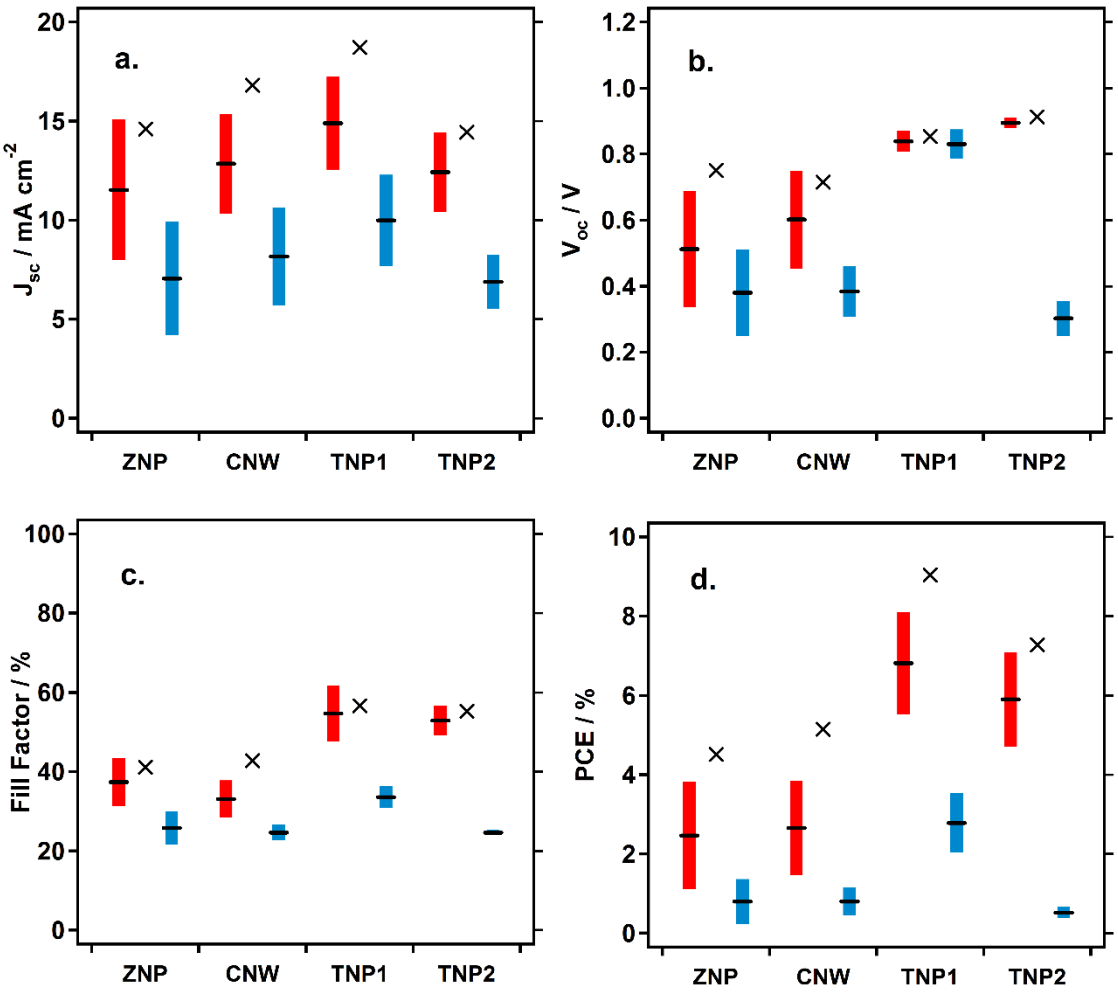

Figure 7.15. Average cell performances and standard deviations (30 cells each) measured for mesoscopic perovskite cells featuring ZnO nanoparticle (ZNP), commercial ZnO nanowire (CNW) or TiO_2 nanoparticle (TNP) porous layers on ZnO (ZNP, CNW and TNP2) or TiO_2 (TNP1) blocking layers. Forward scans are shown in blue and backward scans are shown in red. The values corresponding to the highest efficiency cell on the backwards scan are shown as black crosses.

Some more insights into the reasons for the difference in cell performance between the cells featuring ZnO layers and those featuring TiO_2 can be gained from some more recent reports in the literature.[144-146] These reports all document the decomposition of $CH_3NH_3PbI_3$ on ZnO blocking layers during annealing of the perovskite film. The perovskite was found to convert to PbI_2 upon heating, sometimes within a space of minutes, drastically reducing the cell performance. This was not found when other metal oxide contact layers, such as TiO_2, were employed, suggesting an inherent incompatibility between ZnO and the perovskite. Kelly *et al*. have investigated this instability in detail, using a combination of *in situ* grazing angle X-ray diffraction and density functional theory calculations.[146] They were able to show that the instability was predominantly due to the basic nature of ZnO, which has an isoelectric point of pH >8.7, but was also worsened by the presence of surface hydroxyl groups and residual acetate ligands.[274] Density functional theory calculations showed that the ZnO was capable of deprotonating the methylammonium cation, resulting in the formation of methylamine, which will be released as a gas, leaving PbI_2. Pauporte *et al*. proposed that this might proceed via the following reaction, where both the methylamine and the HI would be lost as gases under the annealing conditions:[145]

$$CH_3NH_3PbI_3 \rightarrow PbI_2 + CH_3NH_2 + HI \quad (7.1)$$

These reports are consistent with observations made during the preparation of the cells, where a yellow hue was observed to form on the underside of the perovskite films in the case of all of the cells prepared on ZnO blocking layers. This would indicate that a layer of PbI_2 is forming near to the perovskite/ZnO interface, which would likely inhibit charge transfer and reduce cell performance. Both Kelly *et al*. and Tsang *et al*. reported that this degradation could be slightly reduced by the annealing of the ZnO layers.[144, 146] This might explain why a full conversion to PbI_2 was not observed throughout the film, but a reduction in performance is still present. Although these reports were made for planar device structures using ZnO, it seems logical that the use of a porous ZnO layer would be even more detrimental to the device performance, owing to the larger surface area of contact between the ZnO and perovskite material. Although high efficiency ZnO-based perovskite cells have been demonstrated in the literature without the use of annealing steps, the long term stability of such devices is likely to be poor, particularly under some of the more extreme operating conditions expected in hotter climates.[146, 151]

Overall, these results are not promising for the application of ZnO within perovskite solar cells, where direct contact is made between these layers. To the best of our knowledge, these are the first results documenting the relative instability of perovskite within porous ZnO layers. As $CH_3NH_3PbI_3$ is well known to also be unstable in contact with moisture, and porous metal oxides would give rise to a large surface area for water adsorption, this source of perovskite instability

cannot be ruled out from these experiments. In the next section, this will be explored further within a dry environment to minimise the contribution of instability arising from adsorbed moisture.

7.2.3 Mesoscopic cell preparation under controlled humidity

Dry boxes or glove boxes have commonly been used to obtain the highest efficiency perovskite solar cells, due to their instability in moisture and the sensitivity of fabrication to the atmospheric conditions.[275] For the remainder of the cells reported within this chapter, a dry box was used for their fabrication, with high temperature annealing of the metal oxides and the final gold evaporation stage being the only stages conducted outside this controlled environment. The dry box was capable of maintaining the humidity to between 1 and 3 % relative humidity throughout the cell preparation. Prior to perovskite deposition, all of the sintered porous layers were heated to 150 °C within the dry box to desorb any water, thereby eliminating the instability of the perovskite due to water adsorbed within the porous film.

The first step was to compare all of the porous metal oxide layers again, within mesoscopic perovskite cells with equivalent film thicknesses. In addition to the commercial nanowire layers tested in section 7.2.2, anodic nanowire layers were also tested, which could provide a higher surface area comparison to the smooth commercial nanowires. If the surface area in contact between the ZnO and the perovskite did play a role in the extent of perovskite degradation, then the anodic nanowire film should provide a good intermediate surface area between the nanoparticle films and the commercial nanowire films. As before, three cells of each type were fabricated, each with ten pixels for *J-V* measurement, giving a total of 30 *J-V* measurements for each condition.

The average cell performances for cells using different porous layers and a ZnO blocking layer can be seen in Figure 7.16. Based on the predicted order of surface areas of ZNP>ANW>CNW and the hypothesis that higher surface areas of ZnO would result in increased degradation and, therefore, lower performance, the results actually show the opposite trend. Average values of all four cell parameters appear to follow the trend of ZNP>ANW>CNW. In addition to this, the performances obtained for the TiO_2 nanoparticle layers are lower than all of the ZnO layers, and significantly lower than those obtained when cells were prepared in open air (Figure 7.15). These results were at first quite puzzling, until the quality of the ZnO blocking layer was called into question. As the general performances of all of the cells were lower than those produced under open air conditions (Figure 7.15), the production of the blocking layers within the dry box was observed more closely. It was found that after initially spin coating the ZnO blocking layers within the dry box they appeared normal, as they would if produced outside

the dry box. However, upon sitting within the dry box it was observed that the films started to become cloudy in appearance, indicating a re-organisation of surface structure within the film. This change is likely due to a build-up of solvent within the dry box during the production of multiple samples, in a similar way to solvent annealing techniques that are commonly used to alter surface morphology.[276] Given the low performances of all of these cells, it seems likely that this surface re-organisation leads to the formation of very poor blocking layers for perovskite solar cells. Any future efforts to repeat these experiments should take this into account and produce the blocking layers in ambient conditions before introducing them to the dry box environment. Unfortunately, this was not found until the end of the investigation. It is, therefore, likely that all cells making use of ZnO blocking layers in the remainder of this chapter suffer from similar issues.

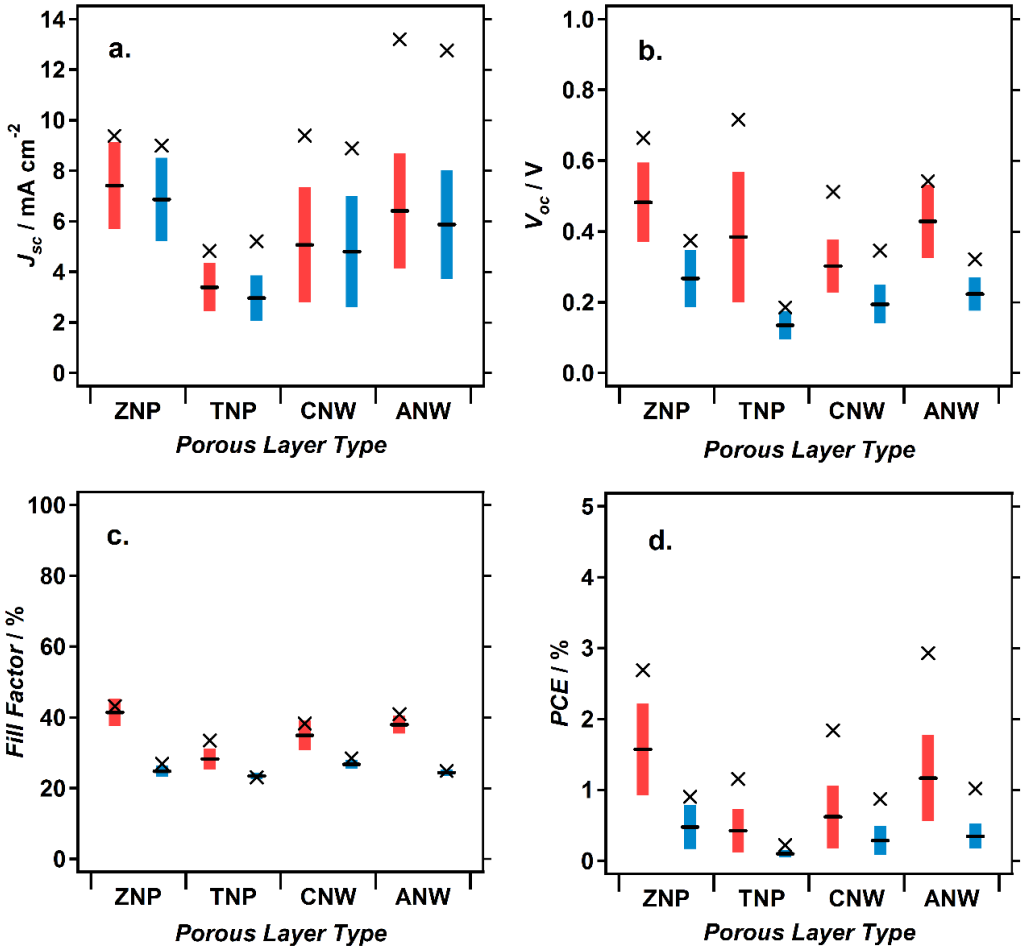

Figure 7.16. Average cell performances and standard deviations (30 cells each) measured for mesoscopic perovskite cells featuring ZnO nanoparticle (ZNP), commercial ZnO nanowire (CNW), anodic ZnO nanowire (ANW) or TiO_2 nanoparticle (TNP) porous layers on ZnO blocking layers. Forward scans are shown in blue and backward scans are shown in red. The values corresponding to the highest efficiency cell are shown as black crosses.

In light of the issues with blocking layer formation, the trend in the results found in Figure 7.16 could be viewed in a different way. Reports have been previously made of the formation of PbI_2 within perovskite solar cells acting as a passivation layer, leading to improved device performances.[277, 278] Somsongkul *et al.* were able to show, using surface photovoltage spectroscopy, that a PbI_2 layer formed between $CH_3NH_3PbI_3$ and TiO_2 allowed the transfer of photoexcited electrons from the perovskite to TiO_2 but prevented the movement of photogenerated holes towards the TiO_2 layer.[279]

Given that the ZnO blocking layer is likely to be performing very poorly, it is possible that the formation of PbI_2 could act as a barrier to recombination within the cells, thereby increasing the performance compared to cells without PbI_2 formation. This explanation would certainly fit in with the trends observed within Figure 7.16, where the higher surface area ZnO films, which would be expected to give rise to more PbI_2, have the highest performance. This would also help to explain why the TiO_2 nanoparticle films give lower performances, as TiO_2 is not active in degrading the perovskite to PbI_2 and would, therefore, result in less of a barrier to recombination.

As a comparison, mesoscopic cells were also produced on TiO_2 blocking layers. These TiO_2 blocking layers were formed by spray pyrolysis (Figure 7.5c), as this method was found to give the highest reproducibility of results within the group. Shown in Figure 7.17 is a comparison of average cell performances obtained using either ZnO or TiO_2 mesoporous layers on TiO_2 blocking layers. It was found that, whenever porous ZnO layers were used on TiO_2 blocking layers, almost negligible currents were measured, giving *J-V* curves similar to those that would be obtained under darkness. In comparison, reasonable efficiencies were obtained when TiO_2 porous layers were used instead. These results are reminiscent of those obtained for DSCs featuring mesoporous ZnO on top of TiO_2 blocking layers, as reported in Chapter 6, Figure 6.12. For the DSCs, this was explained by the possible formation of an energy barrier between the ZnO and TiO_2 due to the likely difference in doping levels between the two materials.[91]

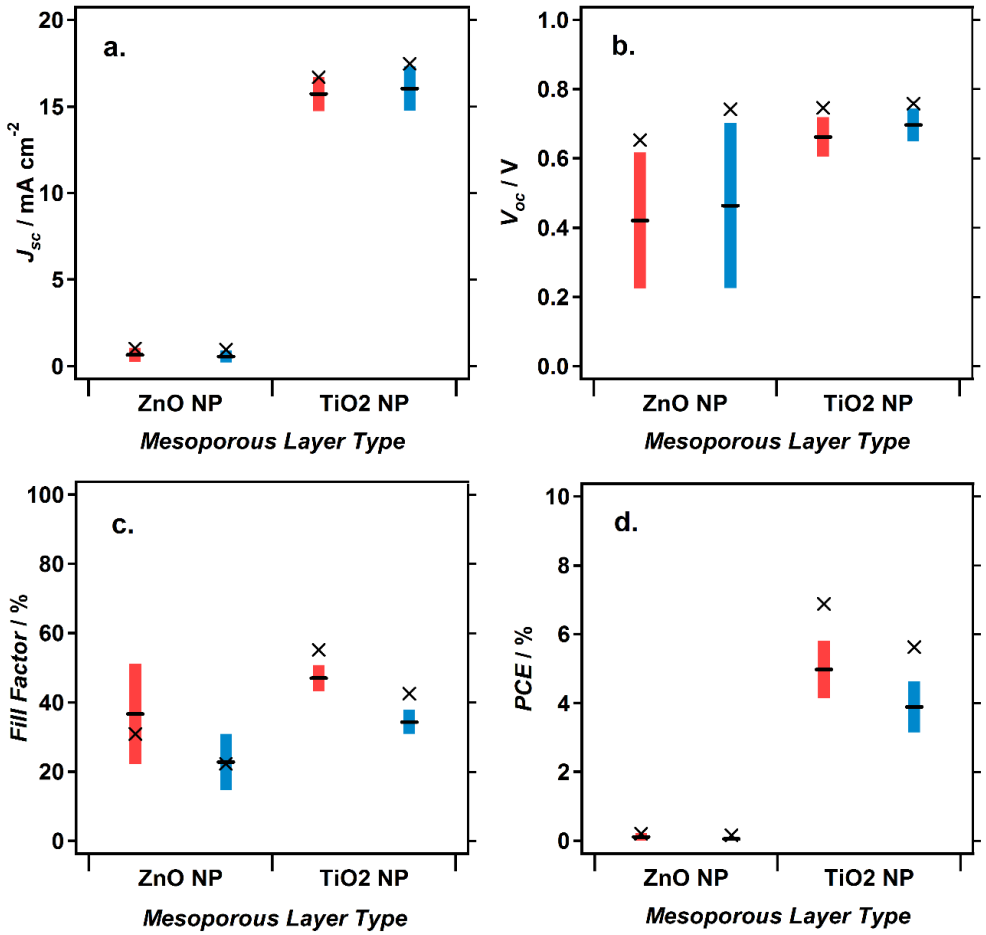

Figure 7.17. Average cell performances and standard deviations (30 cells each) measured for mesoscopic perovskite cells featuring ZnO nanoparticle (ZnO NP) or TiO_2 nanoparticle (TiO2 NP) porous layers on TiO_2 blocking layers. Forward scans are shown in blue and backward scans are shown in red. The values corresponding to the highest efficiency cell are shown as black crosses.

However, this explanation becomes more problematic in the case of perovskite solar cells. Although still under debate, general opinion is that transport of photo-excited electrons occurs through both the perovskite material and the mesoporous oxide, in the case of TiO_2 (Figure 7.18a).[278] If this was the case for mesoporous ZnO, then the collection of photocurrent would still be expected as charge transport could occur through the perovskite material to the TiO_2 blocking layer, bypassing the pathway through the ZnO mesoporous network. In light of the instability of $CH_3NH_3PbI_3$ in contact with ZnO, the reduction of performance due to the formation of PbI_2 would seem like an obvious answer to the difference in performance and, indeed, may play some role in this reduction. However, given that significantly larger currents are observed when a ZnO blocking layer is used in conjunction with a porous ZnO nanoparticle layer (Figure 7.16), it seems unlikely that this can be entirely attributed to PbI_2 formation.

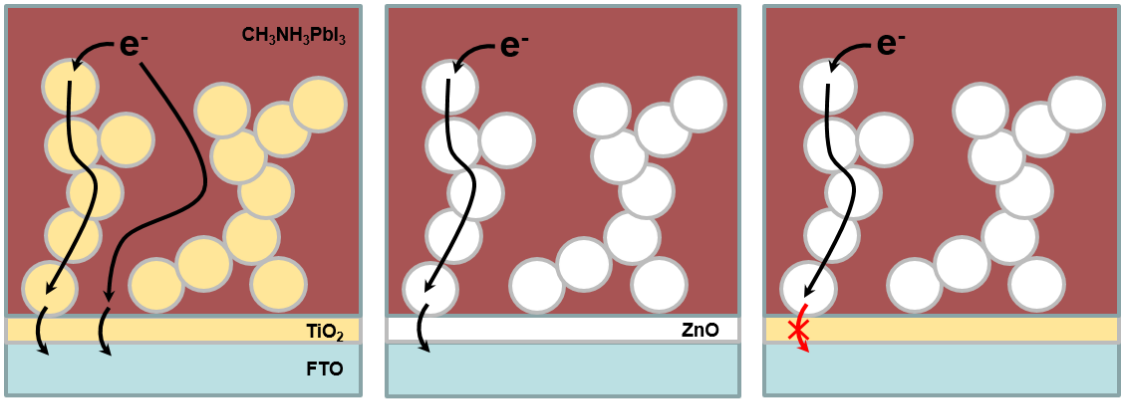

(a.) Mesoporous TiO_2, TiO_2 blocking layer

(b.) Mesoporous ZnO, ZnO blocking layer

(c.) Mesoporous ZnO, TiO_2 blocking layer

Figure 7.18. Schematic demonstrating the proposed routes of electron transport through mesoscopic perovskite solar cells featuring either TiO_2 or ZnO mesoporous layers.

The results, therefore, seem to suggest that, as in the case of DSCs, electrons are transported almost solely through the mesoporous ZnO layer rather than also being transported through the perovskite. In the case of a ZnO blocking layer, electrons would be transferred through the blocking layer to the FTO electrode, resulting in photocurrent (Figure 7.18b). However, in the case of a TiO_2 blocking layer, an energy barrier is reached between the two metal oxides, resulting in the significant reduction in current (Figure 7.18c). If this explanation was correct, then it would form an interesting contribution to the ongoing debate about charge transfer of electrons within perovskite solar cells. A more in depth investigation into the charge transfer processes occurring within these cell architectures would, therefore, be recommended as an area of future work in order to prove this hypothesis.

As an aside, the mesoporous TiO_2 cells based on TiO_2 blocking layers were investigated further, with the aim of establishing a method for producing high efficiency devices. Figure 7.19 shows a FESEM micrograph of the cross-section of a mesoporous TiO_2 cell used in Figure 7.17. The layered structure of the cell can be clearly seen, indicating an effective set of deposition techniques for the various layers. It can be seen that the cell features a perovskite-infiltrated mesoporous TiO_2 layer of ~500 nm in thickness with a 200-300 nm capping layer of larger perovskite crystals above this. This capping layer structure, which forms an intermediate structure between planar and mesoscopic perovskite solar cells, has been demonstrated in the literature to be an effective architecture for the production of efficient devices.[133] The porous layer is slightly thicker than what has been previously been found to be an optimal layer thickness for full pore infiltration in mesoscopic cell architectures (~300 nm).[280] Due to this, efforts were made to reduce the film thickness in order to improve performance.

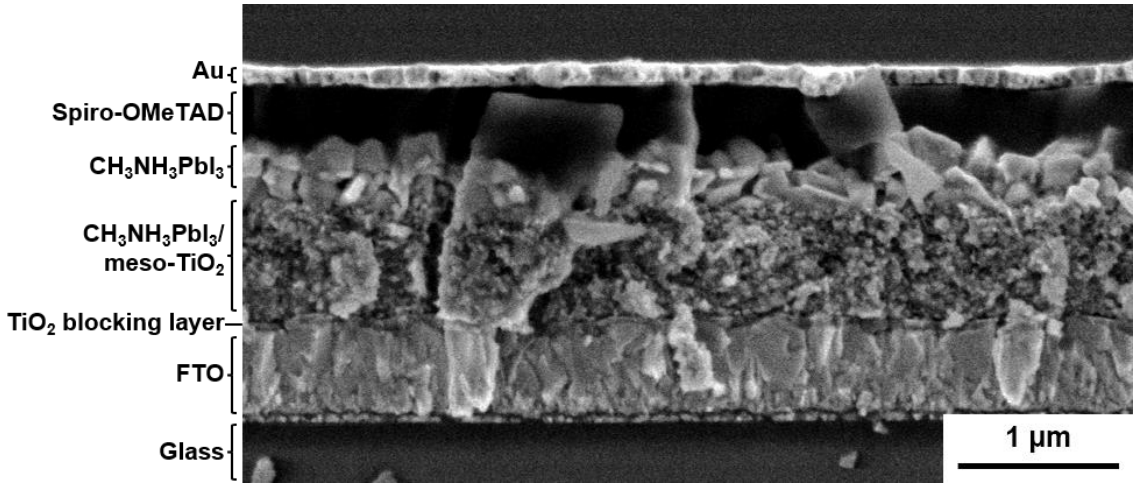

Figure 7.19. FESEM cross-section of a mesoscopic perovskite solar cell featuring a mesoporous TiO_2 layer and a TiO_2 blocking layer.

Mesoporous TiO_2 layers with different thicknesses were fabricated on TiO_2 blocking layers by spin coating, based on the spin speeds reported in Figure 7.12. TiO_2 films with thicknesses of 200, 300 and 400 nm were produced and used in the fabrication of mesoscopic perovskite solar cells. It was found that the highest average cell efficiencies of 7.1 % were obtained for the thinnest TiO_2 layers, however, the highest single pixel efficiency of 9.8 % was recorded for intermediate TiO_2 thicknesses (Figure 7.20). Increasing thickness gave rise to a very small increase in J_{sc}, but a decrease in V_{oc} and *FF* which led to the average cell efficiency decreasing. It, therefore, seems likely that further improvements to cell efficiency might be made in future through the use of an even thinner mesoporous layer. These results may also translate to the ZnO based nanoparticle layers in order to improve their efficiencies in future.

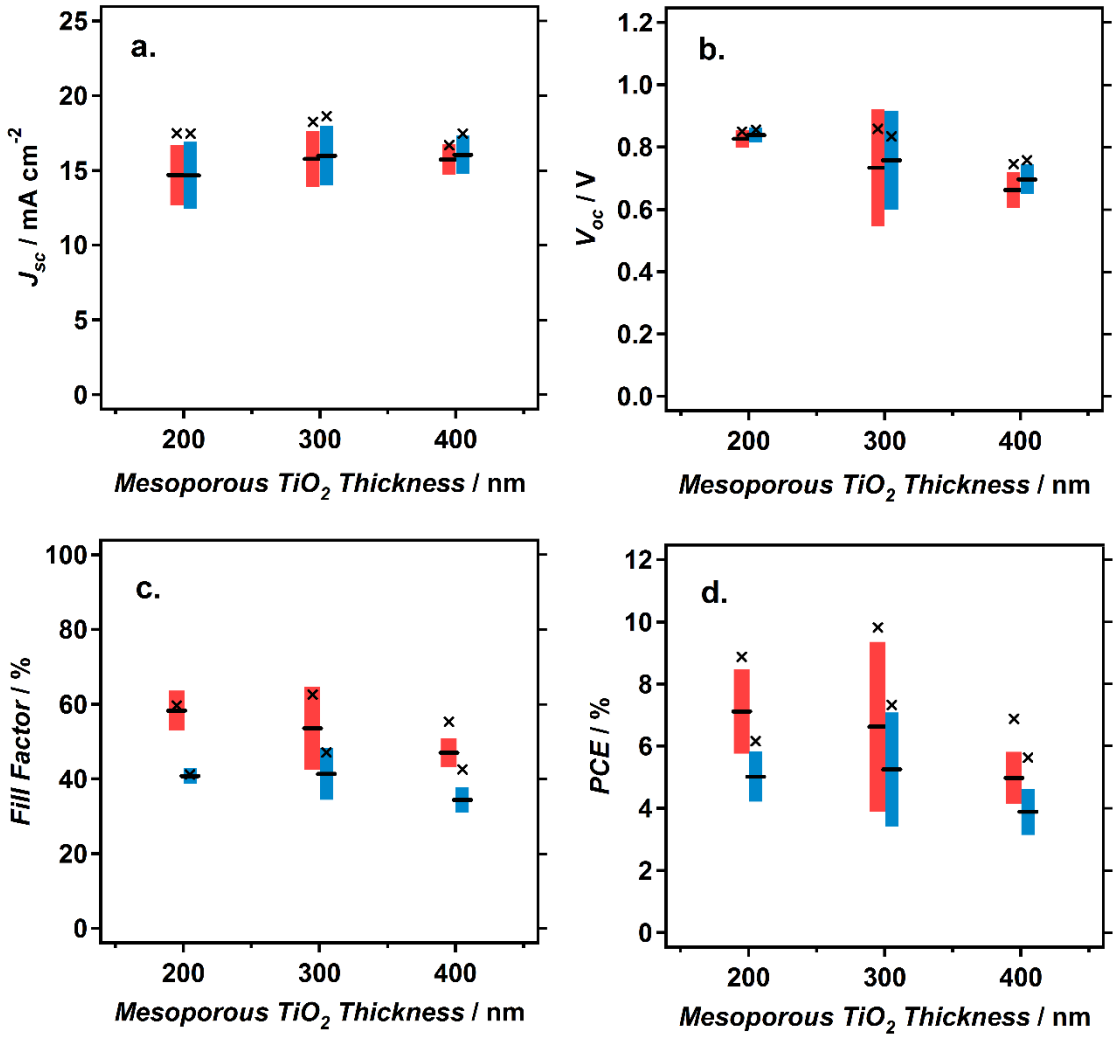

Figure 7.20. Average cell performances and standard deviations (30 cells each) measured for mesoscopic perovskite cells featuring TiO_2 nanoparticle porous layers of different thicknesses on TiO_2 blocking layers. Forward scans are shown in blue and backward scans are shown in red. The values corresponding to the highest efficiency cell are shown as black crosses.

7.2.4 Effect of perovskite annealing time on device performance

As discussed in Section 7.2.2, recent reports in the literature have documented the instability of perovskite on ZnO films. However, as to the best of my knowledge, the degradation within mesoporous ZnO has not been investigated, this was explored in more detail. Mesoporous films of both TiO_2 and ZnO were prepared, on both ZnO and TiO_2 blocking layers, and used in the fabrication of mesoscopic perovskite solar cells. The degradation of the perovskite was investigated by annealing the perovskite films at 70 °C for different time periods, prior to the deposition of the Spiro-OMeTAD layer. It should be noted that, unlike in the previous experiments documented in this chapter, only one cell of each type (10 *J*-*V* measurements) was prepared. It is recommended that further repeats are made in order to gain improved accuracy in

the trends. However, these results suffice in giving a general insight into the processes effecting performance.

The first set of cells to be examined were those formed using a mesoporous TiO_2 layer on a ZnO blocking layer. For these cells, little influence of heating time on the performance can be observed (Figure 7.21). This is likely to be due to the relative stability of the perovskite in contact with TiO_2, which is consistent with findings in the literature.[146] It should be noted that the low performances for these cells are most likely to be attributed to the poor blocking behaviour of the ZnO layer.

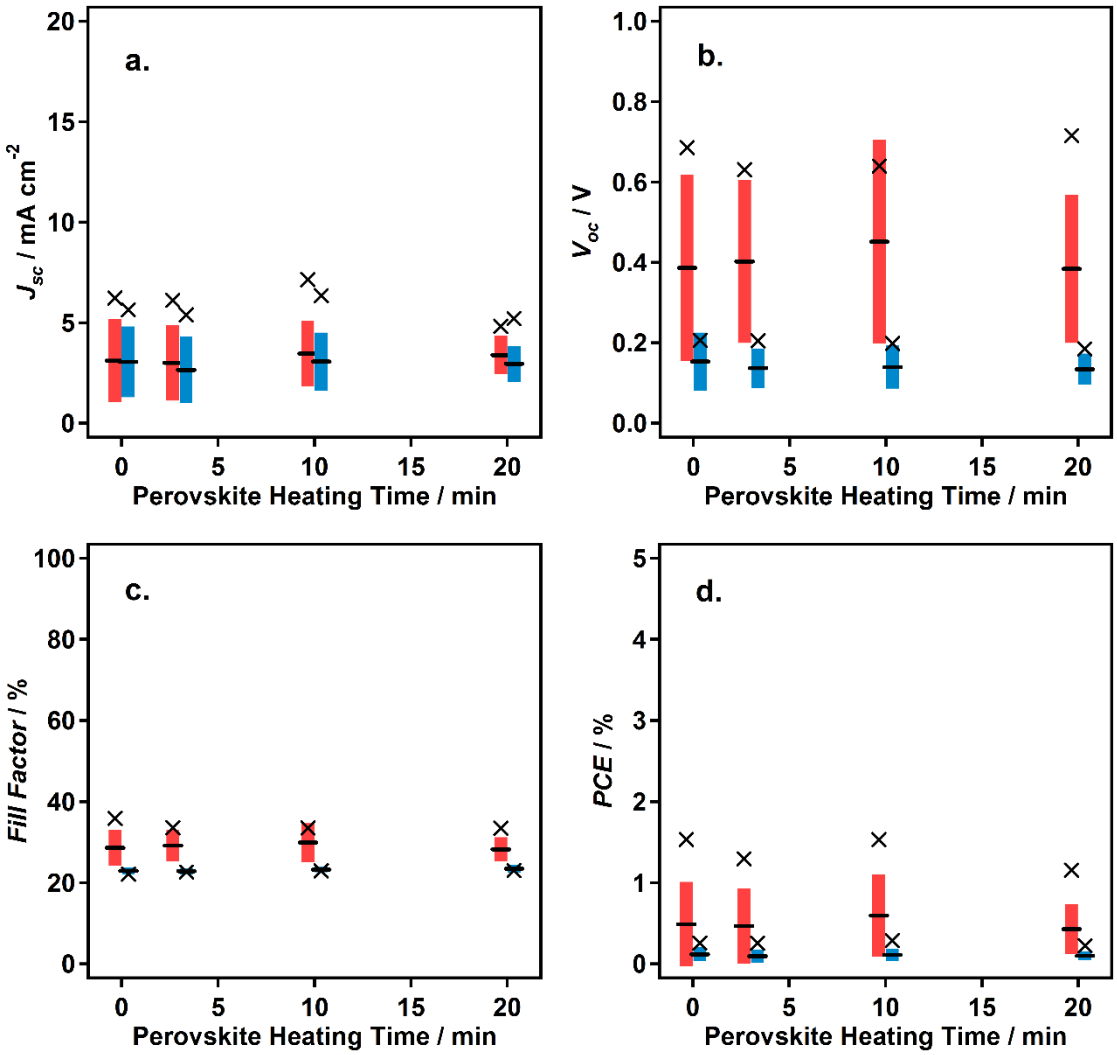

Figure 7.21. Average cell performances and standard deviations (10 cells each) measured for mesoscopic perovskite cells featuring TiO_2 nanoparticle porous layers on ZnO blocking layers, after annealing the perovskite layer at 70°C for different lengths of time. Forward scans are shown in blue and backward scans are shown in red. The values corresponding to the highest efficiency cell are shown as black crosses.

For mesoporous TiO_2 on TiO_2 blocking layers, the cell performance is found to improve in all of J_{sc}, V_{oc}, *FF* and *PCE* as the perovskite annealing time is increased from 0-10 mins, but is then found to decrease slightly at 20 mins (Figure 7.22). This increase in performance can be attributed to the improvement in perovskite crystallinity, which results from annealing, as shown in previous literature.[144, 281] The slight decrease in performance for longer times might be due to the slow degradation of the perovskite within TiO_2, however, further repeats should be completed to ensure this is not an anomalous result. Although TiO_2 has been found to cause significantly less degradation than ZnO, there have been reports of PbI_2 formation due to hydroxyl groups on TiO_2 annealed at low temperatures.[282]

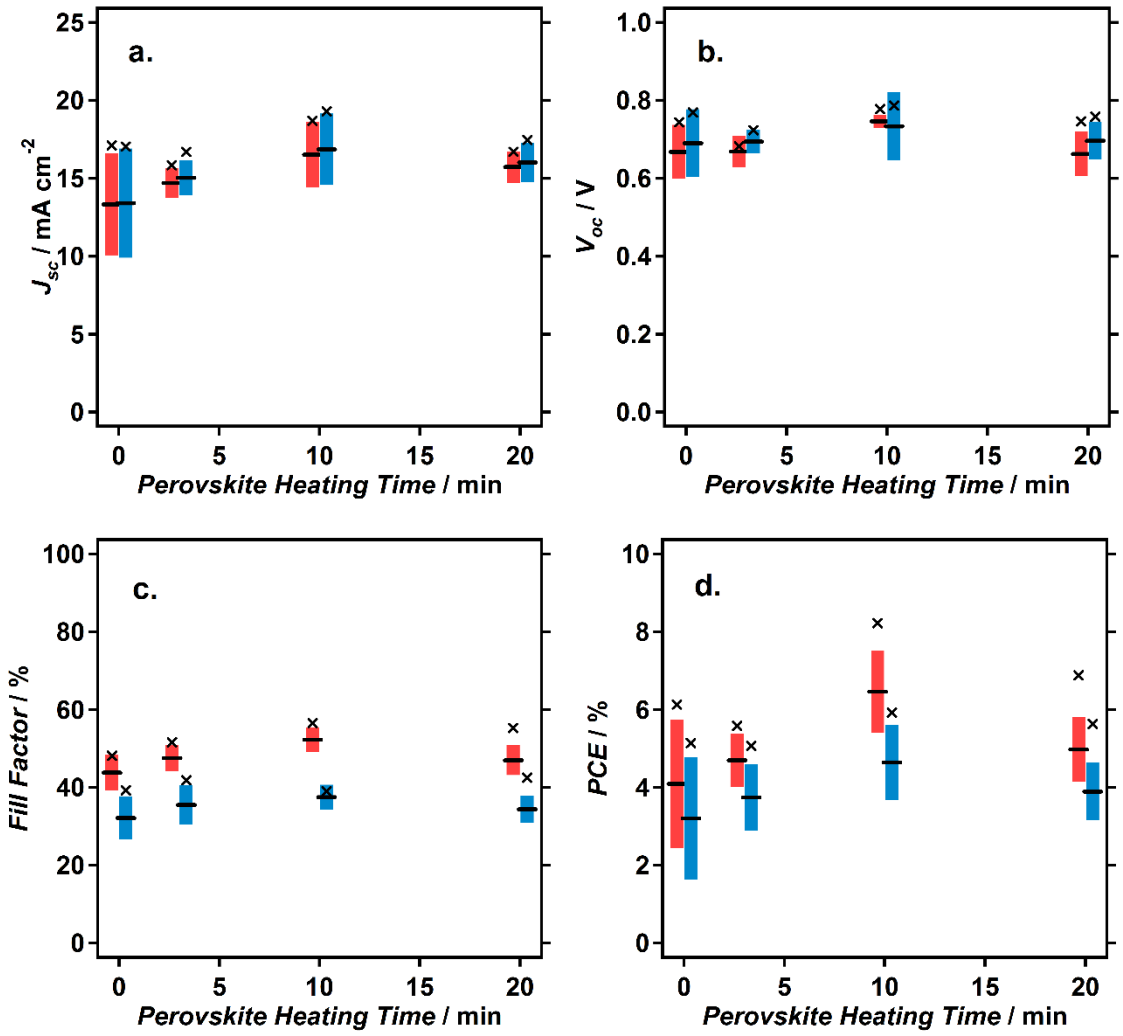

Figure 7.22. Average cell performances and standard deviations (10 cells each) measured for mesoscopic perovskite cells featuring TiO_2 nanoparticle porous layers on TiO_2 blocking layers, after annealing the perovskite layer at 70°C for different lengths of time. Forward scans are shown in blue and backward scans are shown in red. The values corresponding to the highest efficiency cell are shown as black crosses.

Next, mesoporous ZnO layers were investigated on the two blocking layer types. In the case of the ZnO blocking layer the J_{sc}, V_{oc}, and, to a lesser extent, the *FF* are found to decrease as the perovskite annealing time is increased from 0-10 mins, but then increases again at 20 mins (Figure 7.23). This is the opposite trend to what was found for TiO_2 mesoporous layers. The results for 0-10 mins annealing time are in agreement with the hypothesis of ZnO thermally degrading the perovskite into PbI_2, thereby reducing the cell efficiency. This trend appears to be particularly clear when the J_{sc} values are examined (Figure 7.23a), however, the results recorded for 20 minute heating times are yet again at odds with this trend for reasons currently unknown.

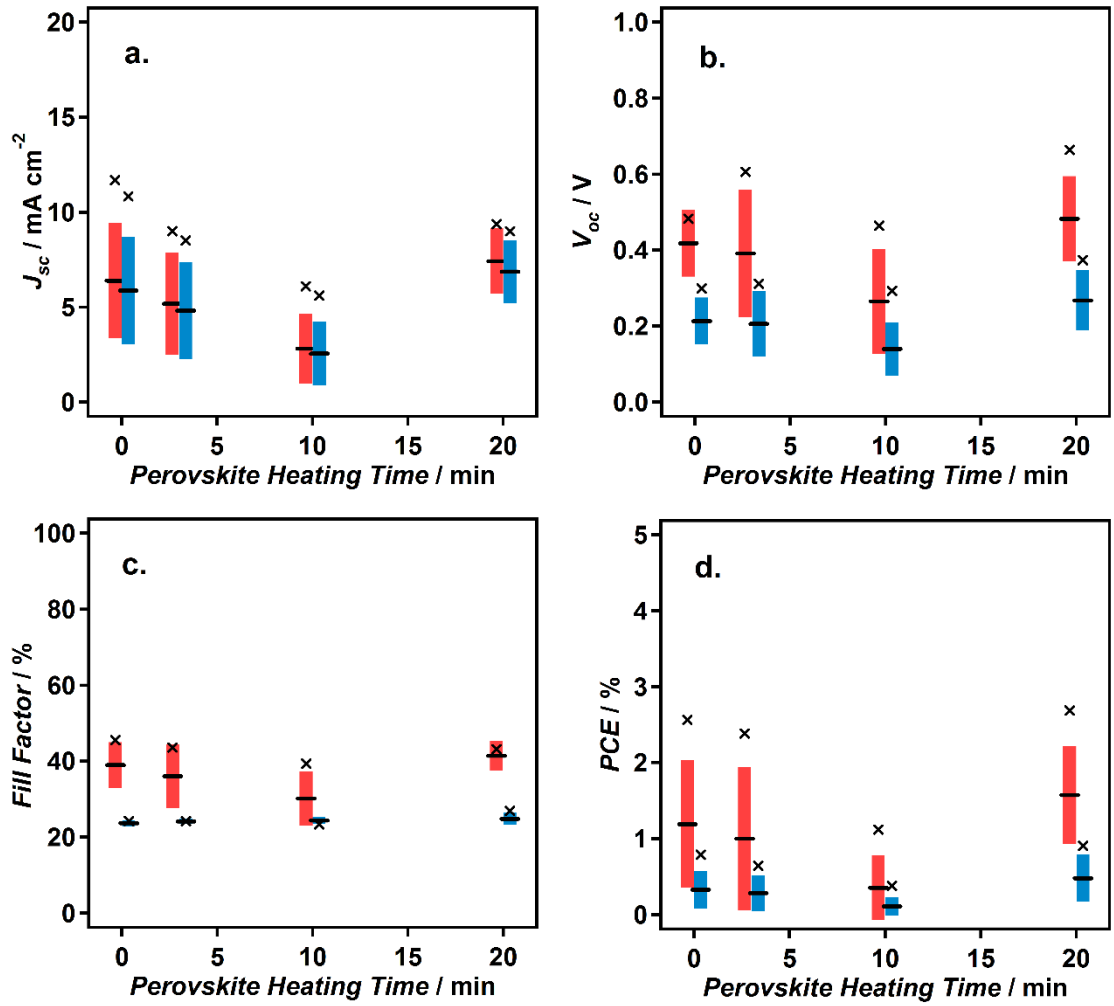

Figure 7.23. Average cell performances and standard deviations (10 cells each) measured for mesoscopic perovskite cells featuring ZnO nanoparticle porous layers on ZnO blocking layers, after annealing the perovskite layer at 70°C for different lengths of time. Forward scans are shown in blue and backward scans are shown in red. The values corresponding to the highest efficiency cell are shown as black crosses.

In comparison, trends in J_{sc} cannot be clearly observed when mesoporous ZnO is used in conjunction with TiO_2 blocking layers (Figure 7.24). As shown previously in Figure 7.17, the current density is almost negligible in this cell configuration, resulting in very low efficiencies. It is interesting to observe, however, that both the V_{oc} and fill factor follow the same trends as when a ZnO blocking layer is used. They are both found to decrease as perovskite annealing times are increased from 0 to 10 mins. These results provide evidence that the ZnO mesoporous layer also contributes significantly towards the degradation of $CH_3NH_3PbI_3$, in addition to the ZnO blocking layer, the latter of which has been shown in previous literature.[144-146]

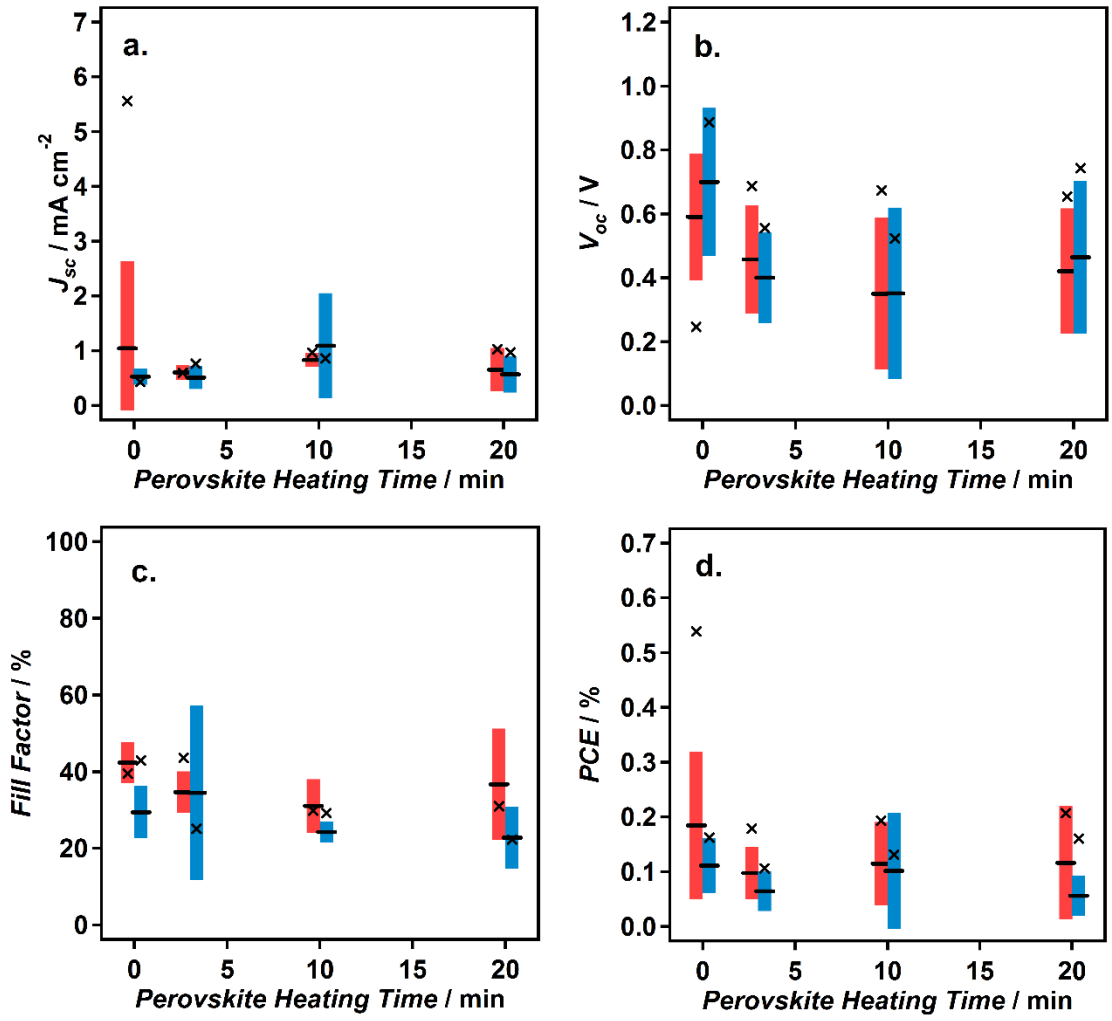

Figure 7.24. Average cell performances and standard deviations (10 cells each) measured for mesoscopic perovskite cells featuring ZnO nanoparticle porous layers on TiO_2 blocking layers, after annealing the perovskite layer at 70°C for different lengths of time. Forward scans are shown in blue and backward scans are shown in red. The values corresponding to the highest efficiency cell are shown as black crosses.

These final results have provided a brief insight into the effect of perovskite heating time on device performance and how this differs based on the porous metal oxide used within the cell, as well as the blocking material used. To fully establish these trends, it is recommended that the results are repeated as future work in order to improve the accuracy of the findings, particularly with respect to the unexplained change in trend for the 20 minute heating times. It would also be beneficial to repeat the experiments using the ZnO blocking layer, but with ZnO blocking layers produced outside the dry box in order to improve the cell performance.

7.3 Chapter Summary

In this chapter, the use of ZnO nanostructures within both planar and mesoscopic perovskite solar cells has been presented. For planar cell configurations, device efficiencies were found to be highly dependent on the preparation methods of both the electron selective contact and the PbI_2 layer. Despite undertaking some optimisation on these depositions, cell efficiencies were still far below those reported within the literature for ZnO blocking layers.[151] It seems clear that further optimisation of the remaining stages of cell preparation would be required in order to boost efficiencies further.

In the case of mesoscopic perovskite solar cells, the findings obtained were far more complex. Initial experiments, conducted in normal atmospheric conditions, revealed a significant disparity in performance between cells based on TiO_2 and cells based on ZnO. The mesoporous ZnO based cells exhibited consistently lower performances. The use of ZnO blocking layers, even with a TiO_2 mesoporous layer, was also found to significantly increase the hysteresis in the *J-V* measurement. It appears highly likely that the poor performance is related to the degradation of $CH_3NH_3PbI_3$ to PbI_2, upon contact with ZnO. This was observed by the discolouration of the perovskite film and is consistent with previous studies on ZnO within planar cell structures.[144-146]

Through further examination of the influence of degradation for cells produced within dry atmospheres, it seems possible that the formation of PbI_2 can, in some cases, be beneficial to cell performance. This seems true for the case of when poor performing blocking layers are used. These results also led to some interesting questions concerning electron transport within perovskite solar cells featuring mesoporous ZnO. Although further investigation is required, initial results seem to indicate that electron transport occurs predominantly through the ZnO, rather than the perovskite material, in this device architecture.

Finally, an investigation into the effect of perovskite annealing time on performance was found to yield opposite trends when either TiO_2 or ZnO mesoporous layers were used. In the case of ZnO, efficiencies were found to drop as a result of annealing the perovskite layer, which is in agreement with the hypothesis of PbI_2 formation. In contrast, efficiencies were found to increase in the case of TiO_2, which is likely due to the enlargement of perovskite crystals during annealing.

Overall, the future of ZnO within perovskite solar cells seems relatively bleak. The degradation of the perovskite to PbI_2 is a significant issue that will, inevitably, lead to the poor long term stability of these cells. Although it seems that the use of interlayers between the ZnO and perovskite might improve the situation in the case of planar cells, it is hard to foresee this problem being overcome within mesoscopic architectures, where there is a significantly higher

contact area between the two materials.[144] Efforts might, therefore, be better spent on the use of other metal oxides or organic materials as electron selective layers in perovskite solar cells.

Chapter 8 – Conclusions and Future Work

8.1 Conclusions

In this thesis, the production of novel ZnO nanomaterials and their application in two photovoltaic technologies has been presented. Overall, the anodization of zinc has been shown to be a promising technique for the rapid production of high aspect ratio ZnO nanowires under relatively mild conditions. It has been demonstrated that the morphological properties of these nanowires can be tuned towards their desired application in photovoltaics, either through control of the anodization conditions or through a simple synthetic modification after anodization. This approach could also be adopted to produce bespoke nanomaterials for a wide range of applications in the future. When applied within DSCs, the benefits of using 1-D nanostructures are evident from increased power conversion efficiencies, particularly when hierarchical core-shell structures are employed. For perovskite cells however, the potential benefits gained from using nanowires rather than nanoparticles still remains unclear. The following sections will summarise the key findings from each of the results chapters within this thesis.

Controlled growth of ZnO nanowires using anodization

In Chapter 4, the process of anodization of zinc foil in an aqueous bicarbonate electrolyte was examined in detail. The growth of nanowire films was found to proceed via four separate growth stages: 1. Growth initiation in the form of discrete nanoflowers, 2. Alignment of the nanowires due to prohibited growth in a direction horizontal to the substrate, 3. The development of a layered structure of larger hexagonal wires emerging through a dense nanowire film, and finally, 4. The hierarchical splitting of the large hexagonal wires into multiple smaller nanowires.

It was demonstrated for the first time that the growth of high aspect ratio nanowires via the anodization of zinc can be achieved using a range of different bicarbonate electrolytes, not just in the case of $KHCO_3$. It was shown quantitatively that the reaction parameters of temperature, voltage, time and electrolyte concentration can significantly alter the nanowire growth rate and can be used to control the morphological properties of the nanowires, such as diameter (70-600 nm), packing density (0.5-8.0 μm^{-2}) and length (1-100 μm). By optimising these parameters, remarkably high growth rates in excess of 3 μm min^{-1} can be achieved at room temperature. These growth rates were significantly higher those previously reported in the literature (0.5 and 1.3 μm min^{-1}) .[209, 218]

Annealing was found to be a necessary process in converting the as-prepared anodic nanowires into ZnO. Although this annealing step could potentially counteract the benefits rapid nanowire growth during anodization, it was shown that rapid NIR annealing could be used to convert the nanowires to ZnO within a matter of seconds. The annealed nanowires were

polycrystalline and had a unique slit-type pore structure along their length, which gave rise to a high surface area (54.4 m^2 g^{-1}) compared to what would be expected for conventional monocrystalline nanowires (7.4 m^2 g^{-1}). Examination of the properties of the nanowire films before and after annealing have allowed an explanation to be proposed, both for the high growth rates achieved, and for the unique porous structure of the annealed ZnO nanowires. This involves the rapid formation of a zinc hydroxy carbonate species during anodization, which can be degraded at temperatures above 200 °C to give polycrystalline ZnO.

Modification of the nanowire structure

In Chapter 5, the modification of the nanowires after anodization was explored. It was possible to demonstrate that through the use of relatively simple post-treatments a range of interesting nanostructures could be achieved. The use of controlled heating was used to give rise to different nanocrystallite sizes within the nanowires (7-14 nm), which could potentially be used as a method of controlling the surface areas of the polycrystalline nanowires. Hierarchical ZnO nanowires could be obtained through a simple water treatment, which resulted in the growth of small ZnO spikes on the outer surface of the nanowires. Finally, unique core-shell structures were demonstrated by growing TiO_2 nanosheets on the surface of the anodic nanowires. These materials had a high surface area owing to the hierarchical structure.

Application of ZnO nanowires in DSCs

In Chapter 6, the use of anodic ZnO nanowires was demonstrated within a range of DSC device architectures. It was found that direct application of these nanowire films within back-illuminated DSCs was unsuccessful. This was related to the cracking of the anodic film that occurred during the annealing process. However, it was found that removing the nanowires and applying them as additives within front-illuminated DSCs could give rise to improvements in cell power conversion efficiencies. It was demonstrated that the anodic ZnO nanowires were effective when applied as light-scattering layers on top of a ZnO nanoparticle photoanode and increased the power conversion efficiency from 1.4 % to 1.9 %. However, when incorporated within the interior of the mesoporous ZnO film, no improvement in cell efficiency was observed.

Despite the increase in cell efficiency obtained using the light-scattering layers, it is notable that overall the cell efficiencies reported when using ZnO photoanodes were typically ~50 % lower than when TiO_2 photoanodes were used. This is linked with a low J_{sc} exhibited by all of the cells, highlighting the continued issue with ZnO photoanodes in DSCs, which is the incompatibility with the most common sensitizing dyes.[74, 75] Although this can, to some degree, be negated by the thorough control of sensitizing conditions, there still remains a need for the development of high performance dyes with suitable anchoring groups for ZnO.[78, 257, 268] Until this

issue is resolved, it seems likely that this will remain the main limitation on power conversion efficiencies, rather than the photoanode design, in ZnO-based DSCs.

In contrast, the final section of the chapter demonstrated how efficient cells can be produced by using ZnO as an additive in conjunction with TiO_2. The inclusion of small quantities of hierarchical ZNW@TNS structures within the mesoporous TiO_2 resulted in a significant enhancement in power conversion efficiency from 5.8 % to 7.5 % for qssDSCs. The use of these nanostructures combines the four research strategies of core-shell structuring, high-surface areas, light-scattering enhancement and one-dimensional structure to achieve these high efficiencies. This demonstrates that in order to gain the greatest efficiency improvements through control of the photoanode structure, all of these factors must be taken into account simultaneously. Modified anodic nanowires represent one method of achieving this in a relatively simple way, due to the rapid growth method of the nanowires, the small quantities of additive needed within the photoanode and their easy incorporation into the TiO_2 pastes.

Application of ZnO nanowires in perovskite solar cells

In the final results Chapter of this thesis, the use of ZnO nanostructures within both planar and mesoscopic perovskite solar cells has been presented. For planar cell configurations, device efficiencies were found to be highly dependent on the preparation methods of both the electron selective contact and the PbI_2 layer. Despite undertaking some optimisation on these depositions, cell efficiencies were still far below those reported within the literature for ZnO blocking layers (7.2 % compared to 15.7 %).[151] It seems clear that further optimisation of the remaining stages of cell preparation would be required in order to boost efficiencies further.

In the case of mesoscopic perovskite solar cells, the findings obtained were far more complex. Initial experiments, conducted in normal atmospheric conditions, revealed a significant disparity in performance between cells based on TiO_2 nanoparticles and cells based on ZnO nanoparticles. The mesoporous ZnO-based cells exhibited consistently lower performances, with power conversion efficiencies ~50 % lower than for equivalent TiO_2 cells. The use of ZnO blocking layers, even with a TiO_2 mesoporous layer, was also found to significantly increase the hysteresis in the *J-V* measurement. It seems highly likely that the poor performance is related to the degradation of $CH_3NH_3PbI_3$ to PbI_2, upon contact with ZnO, through acid-base chemistry. Furthermore, it was found that no significant difference in power conversion efficiency was exhibited between cells featuring a nanoparticle or nanowire porous layer. This result seems to indicate that in the case of perovskite solar cells, it is the control of the perovskite deposition and properties that has the dominant effect on the overall cell performance.

Through further examination of the influence of degradation for cells produced within dry atmospheres, it seems possible that the formation of PbI_2 can, in some cases, be beneficial to

cell performance. This seems true for when poor performing blocking layers are used. These results also led to some interesting questions concerning electron transport within perovskite solar cells featuring mesoporous ZnO. Although further investigation is required, initial results seem to indicate that electron transport occurs predominantly through the ZnO, rather than the perovskite material, in this device architecture.

Finally, an investigation into the effect of perovskite annealing time on performance was found to yield opposite trends when either TiO_2 or ZnO mesoporous layers were used. In the case of ZnO, efficiencies were found to drop as a result of annealing the perovskite layer, which is in agreement with the hypothesis of PbI_2 formation. In contrast, efficiencies were found to increase in the case of TiO_2, which is likely due to the enlargement of perovskite crystals during annealing. This results indicates that the use of heating steps should be avoided in the production of efficient perovskite solar cells featuring ZnO.

Overall, it seems that the degradation of the perovskite when in contact with ZnO is a significant issue that will, inevitably, lead to the poor long term stability of these cells. The use of interlayers between the ZnO and perovskite might improve the situation in the case of planar cells, but it is hard to foresee this problem being overcome within mesoscopic architectures, where there is a significantly higher contact area between the two materials.[144] Efforts might, therefore, be better spent on the use of other metal oxides or organic materials as electron selective layers in perovskite solar cells.

8.2 Future Work

Although the research presented in this thesis provides many insights into the production of ZnO nanowires by anodization, and also into their application within DSCs and perovskite solar cells, there still remains many areas into which this investigation could be expanded. The following sections highlight some suggested areas of future research in the areas of anodization, ZnO-based DSCs and also ZnO-based perovskite solar cells.

ZnO from anodization

As discussed in Chapter 4, the anodization of zinc in a bicarbonate electrolyte can be used to rapidly grow long nanowire arrays on zinc substrates. This can also be scaled up simply through the use of larger foils and adhesive Kapton® films to act as a mask in a variety of different shapes (see Chapter 3, Section 3.2.4 for examples). However, when nanowire powders are required, this can be a very ineffective method to produce large quantities. An anodic nanowire film was typically found to yield little more than 1 mg of nanowire powder per square centimetre of film area, therefore, many anodizations were required in order to gain a sufficient quantity for further use. In the case of the powders produced for application in DSCs and perovskite solar cells this required repeating the anodization reaction many hundreds of times.

It is, therefore, necessary to alter this anodization method if large scale nanowire powder production was required. One way that might be envisaged for achieving this is to perform a prolonged anodization procedure, whilst periodically removing the nanowires from the substrate. During the investigation of these materials it was found that sonication could be used to remove nanowires from the substrate. It may, therefore, be possible to periodically remove the nanowires from the substrate using a pulse from a sonication probe. At the end of an extended anodization reaction, involving multiple pulsing cycles, the nanowires could then be extracted from the electrolyte via filtration. Alternatively, a more continuous experimental setup could be developed in which the electrolyte is recirculated and the nanowires are filtered out from the electrolyte during the process (Figure 8.1). This setup would have the advantage of being able to replenish the electrolyte during the process as well as reducing further fragmentation of the removed nanowires by the sonication probe. Using the growth rates reported in Chapter 4, it might be possible to time the periods between sonication pulses in order to obtain specific nanowire lengths.

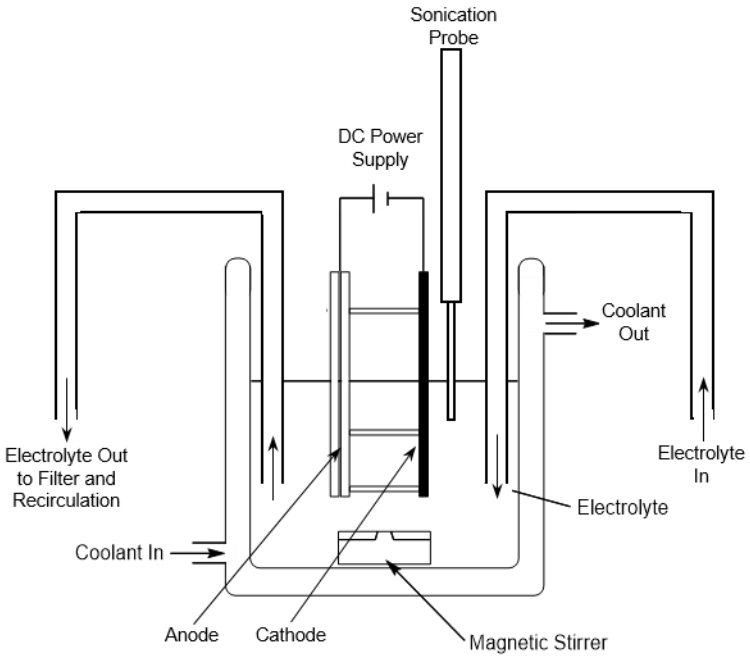

Figure 8.1 Diagram of a possible experimental setup for continuous nanowire production using anodization.

Another area that could be investigated is the use of additives within the anodization electrolyte. These could act as either structure directing additives or give rise to doping within the nanomaterials, thereby changing their physical properties. Both of these things have been demonstrated for ZnO produced via electrodeposition, however, little or no research has been conducted on its use in the production of ZnO by anodization.[197] In the case of producing doped ZnO, a nitrogen containing anion, such as a nitrate, would likely be drawn towards the anode during the anodization process and possibly become incorporated into the material, giving rise to nitrogen doping. Incorporation of other metals as dopants within ZnO would be harder, as it would need to be present within the electrolyte in the form of an anion. Although speculative, the use of an oxyanion of aluminium, such as sodium aluminate, as an additive might provide a route to Al-doped ZnO from anodization.

ZnO in dye-sensitized solar cells

The use of ZnO nanostructures within DSCs seems to be ultimately limited by the poorer interaction and electron injection between the sensitizing dye and ZnO. If ZnO is ever going to compete with TiO_2 as the semiconductor of choice within DSCs then further research into the interactions between ZnO and alternative dyes needs to be conducted. This should be focussed on the dyes featuring binding groups other than carboxylate, which is known to interact unfavourably with the ZnO surface.[75]

An experiment more specific to the subject matter of this thesis would be to try and grow TiO_2 nanosheets on the nanowire films produced by anodization. Although nanosheet growth was successful on the anodic ZnO nanowire powder, no attempts were made to grow the nanosheets on the aligned nanowire films. If this was successful, it might allow back-illuminated DSCs to be fabricated using the nanowire films on the zinc substrate.

ZnO in perovskite solar cells

Although many interesting findings were reported for the application of ZnO in perovskite solar cells in Chapter 7, there still remains many unanswered questions and areas that would need further confirmation. A starting point would be to repeat the experiments shown in Figure 7.16, but using ZnO blocking layers that had been prepared outside of the dry box. This would allow higher efficiency devices to be produced and allow a more accurate comparison between the different ZnO porous layers to be made. In this way, it would be possible to see if the ZnO morphology makes a significant difference to the overall cell performance. Alternatively a different ZnO blocking layer preparation method could be used.

The results reported in Figure 7.17 also warrant follow-up experiments in order to determine if electron transport does indeed occur almost solely through the ZnO, rather than through the perovskite material. If charge transport does occur almost solely through the ZnO then this could form an interesting contribution towards the understanding of charge transport within these devices.

Repeats of the initial experiments reported in Figures 7.21 to 7.24 would also be useful in confirming the observed trends. These results seem to suggest that longer perovskite heating times result in decreased performance in the case of mesoporous ZnO photoanodes. Although the degradation of the perovskite material in contact with planar ZnO films has previously been reported, no such studies on mesoporous ZnO films have been reported, and neither have the cell performances been correlated to this degradation process. This would, therefore, help in establishing whether or not porous ZnO layers can be used in efficient perovskite solar cells, in cases where heating of the perovskite is unavoidable.

In addition to following up some of the experiments reported in Chapter 7, the application of anodic ZnO nanostructures in back-illuminated or inverted structure perovskite solar cells could also be explored. The nanowire arrays demonstrated within Chapter 4 are likely to be too thick to form efficient perovskite cells, but many other ZnO nanostructures with lower aspect ratios have been demonstrated using anodization. One example is 2-D nanosheets that can be produced by anodizing zinc in an ethanolic H_2SO_4 electrolyte.[208] These materials were the subject of a previous MRes project, but were dismissed for application in DSCs due to their low aspect ratios. These materials might be more suited to application in perovskite solar cells, where high

surface areas are not necessary. Perovskite could be deposited onto the nanosheet film and, if used in conjunction with a flexible conducting cathode, flexible perovskite solar cells could be produced. This could potentially reduce cell production costs due to removing the expensive conducting glass laminate.

Dissemination

Journal Publications

D. O. Miles, C. S. Lee, P. J. Cameron, D. Mattia and J. H. Kim, "*Hierarchical growth of TiO_2 nanosheets on anodic ZnO nanowires for high efficiency dye-sensitized solar cells*", 2015, Submitted to Nanoscale.

D. O. Miles, P. J. Cameron & D. Mattia, "*Hierarchical 3D ZnO nanowire structures via fast anodization of zinc*", 2015, Journal of Materials Chemistry A, 3, p. 17569-17577. (Front Cover)

A. Ramirez-Canon, D. O. Miles, P. J. Cameron & D. Mattia, "*Zinc oxide nanostructured films produced via anodization: A rational design approach*", 2013, RSC Advances, 3, 47, p. 25323-25330.

Conference Presentations

D. O. Miles, P. J. Cameron, D. Mattia, Sept 2015, *ISACS17: Challenges in Chemical Renewable Energy*, Rio de Janeiro, Brazil, (Flash Presentation and Poster).

D. O. Miles, P. J. Cameron, D. Mattia, Jul 2015, *CSCT Summer Showcase 2015*, Bath, UK, (Poster Presentation).

D. O. Miles, P. J. Cameron, D. Mattia, April 2015, *University of Bath ChemEngDay 2015*, Bath, UK, (Speaker and Poster Presentation).

D. O. Miles, P. J. Cameron, D. Mattia, Oct 2014, *1st Yonsei-Bath International Workshop on Energy, Environment and Sustainability*, Seoul, Republic of Korea, (Speaker and Poster Presentation).

D. O. Miles, P. J. Cameron, D. Mattia, Jul 2014, *CSCT Summer Showcase 2014*, Bath, UK, (Speaker and Poster Presentation).

D. O. Miles, P. J. Cameron, D. Mattia, Apr 2014, *Materials Research Society (MRS) Spring Meeting 2014*, San Francisco, USA, (Speaker).

D. O. Miles, P. J. Cameron, D. Mattia, Sep 2013, *Energy Futures Research Conference*, London, UK, (Speaker).

D. O. Miles, P. J. Cameron, D. Mattia, Sep 2013, *DTC in Sustainable Chemical Technologies Summer Showcase 2013*, Bath, UK, (Poster Presentation).

D. O. Miles, P. J. Cameron, D. Mattia, Jul 2012, *DTC in Sustainable Chemical Technologies Summer Showcase 2012*, Bath, UK, (Poster Presentation).

Prizes

Presentation prize, Second year PhD student, Department of chemical engineering seminar series, 2014, University of Bath, UK.

Presentation prize, Final year PhD student, Department of chemical engineering seminar series, 2015, University of Bath, UK.

Poster prize, Centre for sustainable chemical technologies Summer Showcase, 2014, University of Bath, UK.

Poster prize, Centre for sustainable chemical technologies Summer Showcase, 2015, University of Bath, UK.

Poster prize, University of Bath ChemEngDay, 2015, University of Bath, UK.

References

1. WEC, *World Energy Resources 2013 Survey*, World Energy Council, London, UK, 2013.
2. R. F. Keeling, S. C. Piper, A. F. Bollenbacher and J. S. Walker, *Atmospheric CO_2 records from sites in the SIO air sampling network*, U.S. Department of Energy, Oak Ridge, Tennessee, USA, 2009.
3. A. Neftel, H. Friedli, E. Moor, H. Lotscher, H. Oeschger, U. Siegenthaler and B. Stauffer, *Historical CO_2 record from the Siple Station ice core*, U.S. Department of Energy, Oak Ridge, Tennessee, USA, 1994.
4. D. M. Etheridge, L. P. Steele, R. L. Langenfelds, R. J. Francey, J. M. Barnola and V. I. Morgan, *Historical CO_2 records from the Law Dome DE08, DE08-2, and DSS ice cores*, U.S Department of Energy, Oak Ridge, Tennessee, USA, 1998.
5. T. F. Stocker, D. Qin, G. K. Plattner, M. Tignor, S. K. Allen, J. Boschung, A. Nauels, Y. Xia, V. Bex and P. M. Midgley, *IPCC, 2013: Climate Change 2013: The Physical Science Basis. Contribution of Working Group I to the Fifth Assessment Report of the Intergovernmental Panel on Climate Change*, IPCC, Cambridge, United Kingdom and New York, NY, USA, 2013.
6. J. D. Figueroa, T. Fout, S. Plasynski, H. McIlvried and R. D. Srivastava, *International Journal of Greenhouse Gas Control*, 2008, **2**, 9-20.
7. BP, *BP Statistical Review of World Energy 2015*, London UK, 2015.
8. V. Smil, *Energy in nature and society general energetics of complex systems*, MIT Press, Cambridge, Mass., 2008.
9. N. S. Lewis and D. G. Nocera, *Proceedings of the National Academy of Sciences of the United States of America*, 2006, **103**, 15729-15735.
10. W. C. Turkenburg, in *World energy assessment: Energy and the challenge of sustainability*, UNDP, New York, USA, 2000, ch. 7.
11. S. A. Kalogirou, *Progress in Energy and Combustion Science*, 2004, **30**, 231-295.
12. E. Becquerel, *Comptes Rendus*, 1839, **9**, 561-567.
13. D. M. Chapin, C. S. Fuller and G. L. Pearson, *Journal of Applied Physics*, 1954, **25**, 676-677.
14. M. A. Green, K. Emery, Y. Hishikawa, W. Warta and E. D. Dunlop, *Progress in Photovoltaics*, 2015, **23**, 1-9.
15. W. Shockley and H. J. Queisser, *Journal of Applied Physics*, 1961, **32**, 510-519.
16. T. Saga, *Npg Asia Materials*, 2010, **2**, 96-102.
17. J. Hernandez-Moro and J. M. Martinez-Duart, *Renewable & Sustainable Energy Reviews*, 2015, **41**, 1288-1297.
18. J. Hernandez-Moro and J. M. Martinez-Duart, *Renewable & Sustainable Energy Reviews*, 2013, **20**, 119-132.
19. M. Afzaal and P. O'Brien, *Journal of Materials Chemistry*, 2006, **16**, 1597-1602.
20. L. M. Peter, *Philosophical Transactions of the Royal Society a-Mathematical Physical and Engineering Sciences*, 2011, **369**, 1840-1856.
21. R. J. Ellingson, M. C. Beard, J. C. Johnson, P. R. Yu, O. I. Micic, A. J. Nozik, A. Shabaev and A. L. Efros, *Nano Letters*, 2005, **5**, 865-871.
22. A. Shalav, B. S. Richards and M. A. Green, *Solar Energy Materials and Solar Cells*, 2007, **91**, 829-842.
23. D. B. Mitzi, O. Gunawan, T. K. Todorov, K. Wang and S. Guha, *Solar Energy Materials and Solar Cells*, 2011, **95**, 1421-1436.
24. W. Wang, M. T. Winkler, O. Gunawan, T. Gokmen, T. K. Todorov, Y. Zhu and D. B. Mitzi, *Advanced Energy Materials*, 2014, **4,** 1301465.
25. M. C. Scharber and N. S. Sariciftci, *Progress in Polymer Science*, 2013, **38**, 1929-1940.
26. M. A. Green, K. Emery, Y. Hishikawa, W. Warta and E. D. Dunlop, *Progress in Photovoltaics*, 2015, **23**, 805-812.
27. B. Oregan and M. Gratzel, *Nature*, 1991, **353**, 737-740.
28. M. A. Green, *Progress in Photovoltaics*, 2001, **9**, 123-135.

29. A. Shah, P. Torres, R. Tscharner, N. Wyrsch and H. Keppner, *Science*, 1999, **285**, 692-698.
30. L. M. Goncalves, V. d. Z. Bermudez, H. A. Ribeiro and A. M. Mendes, *Energy & Environmental Science*, 2008, **1**, 655-667.
31. H. S. Jung and J.-K. Lee, *Journal of Physical Chemistry Letters*, 2013, **4**, 1682-1693.
32. M. D. Archer and A. J. Nozik, *Nanostructured and photoelectrochemical systems for solar photon conversion*, Imperial College Press, London, 2008.
33. M. K. Nazeeruddin, P. Pechy, T. Renouard, S. M. Zakeeruddin, R. Humphry-Baker, P. Comte, P. Liska, L. Cevey, E. Costa, V. Shklover, L. Spiccia, G. B. Deacon, C. A. Bignozzi and M. Gratzel, *Journal of the American Chemical Society*, 2001, **123**, 1613-1624.
34. M. K. Nazeeruddin, A. Kay, I. Rodicio, R. Humphrybaker, E. Muller, P. Liska, N. Vlachopoulos and M. Gratzel, *Journal of the American Chemical Society*, 1993, **115**, 6382-6390.
35. M. K. Nazeeruddin, P. Pechy and M. Gratzel, *Chemical Communications*, 1997, 1705-1706.
36. M. K. Nazeeruddin, F. De Angelis, S. Fantacci, A. Selloni, G. Viscardi, P. Liska, S. Ito, T. Bessho and M. Gratzel, *Journal of the American Chemical Society*, 2005, **127**, 16835-16847.
37. F. Gao, Y. Wang, D. Shi, J. Zhang, M. Wang, X. Jing, R. Humphry-Baker, P. Wang, S. M. Zakeeruddin and M. Graetzel, *Journal of the American Chemical Society*, 2008, **130**, 10720-10728.
38. C.-Y. Chen, M. Wang, J.-Y. Li, N. Pootrakulchote, L. Alibabaei, C.-h. Ngoc-le, J.-D. Decoppet, J.-H. Tsai, C. Graetzel, C.-G. Wu, S. M. Zakeeruddin and M. Graetzel, *ACS Nano*, 2009, **3**, 3103-3109.
39. A. Yella, H.-W. Lee, H. N. Tsao, C. Yi, A. K. Chandiran, M. K. Nazeeruddin, E. W.-G. Diau, C.-Y. Yeh, S. M. Zakeeruddin and M. Graetzel, *Science*, 2011, **334**, 629-634.
40. S. Mathew, A. Yella, P. Gao, R. Humphry-Baker, B. F. E. Curchod, N. Ashari-Astani, I. Tavernelli, U. Rothlisberger, M. K. Nazeeruddin and M. Graetzel, *Nature Chemistry*, 2014, **6**, 242-247.
41. K. Kakiage, Y. Aoyama, T. Yano, K. Oya, J. Fujisawa and M. Hanaya, *Chemical Communications*, 2015, **51**, 15894-15897.
42. B. E. Hardin, H. J. Snaith and M. D. McGehee, *Nature Photonics*, 2012, **6**, 162-169.
43. H. J. Snaith, *Advanced Functional Materials*, 2010, **20**, 13-19.
44. K. Kakiage, Y. Aoyama, T. Yano, K. Oya, J. Fujisawa and M. Hanaya, *Chemical Communications*, 2015, **Advance Article**.
45. A. Hagfeldt, G. Boschloo, L. C. Sun, L. Kloo and H. Pettersson, *Chemical Reviews*, 2010, **110**, 6595-6663.
46. M. K. Nazeeruddin, S. M. Zakeeruddin, R. Humphry-Baker, M. Jirousek, P. Liska, N. Vlachopoulos, V. Shklover, C. H. Fischer and M. Gratzel, *Inorganic Chemistry*, 1999, **38**, 6298-6305.
47. S. Ardo and G. J. Meyer, *Chemical Society Reviews*, 2009, **38**, 115-164.
48. M. Sandroni, L. Favereau, A. Planchat, H. Akdas-Kilig, N. Szuwarski, Y. Pellegrin, E. Blart, H. Le Bozec, M. Boujtita and F. Odobel, *Journal of Materials Chemistry A*, 2014, **2**, 9944-9947.
49. T. Horiuchi, H. Miura, K. Sumioka and S. Uchida, *Journal of the American Chemical Society*, 2004, **126**, 12218-12219.
50. P. Wang, C. Klein, R. Humphry-Baker, S. M. Zakeeruddin and M. Gratzel, *Applied Physics Letters*, 2005, **86**, 3, 123508.
51. Y. Liu, A. Hagfeldt, X. R. Xiao and S. E. Lindquist, *Solar Energy Materials and Solar Cells*, 1998, **55**, 267-281.
52. B. Xu, E. Gabrielsson, M. Safdari, M. Cheng, Y. Hua, H. Tian, J. M. Gardner, L. Kloo and L. Sun, *Advanced Energy Materials*, 2015, **5**, 1402340.
53. B. O'Regan, F. Lenzmann, R. Muis and J. Wienke, *Chemistry of Materials*, 2002, **14**, 5023-5029.

54. I. Chung, B. Lee, J. He, R. P. H. Chang and M. G. Kanatzidis, *Nature*, 2012, **485**, 486-494.
55. W. Kubo, K. Murakoshi, T. Kitamura, Y. Wada, K. Hanabusa, H. Shirai and S. Yanagida, *Chemistry Letters*, 1998, 1241-1242.
56. Q. J. Yu, C. L. Yu, F. Y. Guo, J. Z. Wang, S. J. Jiao, S. Y. Gao, H. T. Li and L. C. Zhao, *Energy & Environmental Science*, 2012, **5**, 6151-6155.
57. S. M. Zakeeruddin and M. Graetzel, *Advanced Functional Materials*, 2009, **19**, 2187-2202.
58. M. Gorlov and L. Kloo, *Dalton Transactions*, 2008, 2655-2666.
59. Y. Bai, Y. Cao, J. Zhang, M. Wang, R. Li, P. Wang, S. M. Zakeeruddin and M. Graetzel, *Nature Materials*, 2008, **7**, 626-630.
60. S. E. Koops, B. C. O'Regan, P. R. F. Barnes and J. R. Durrant, *Journal of the American Chemical Society*, 2009, **131**, 4808-4818.
61. H. Tang, K. Prasad, R. Sanjines, P. E. Schmid and F. Levy, *Journal of Applied Physics*, 1994, **75**, 2042-2047.
62. L. M. Peter, *Journal of Physical Chemistry Letters*, 2011, **2**, 1861-1867.
63. S. M. Feldt, E. A. Gibson, E. Gabrielsson, L. Sun, G. Boschloo and A. Hagfeldt, *Journal of the American Chemical Society*, 2010, **132**, 16714-16724.
64. J. Melas-Kyriazi, I. K. Ding, A. Marchioro, A. Punzi, B. E. Hardin, G. F. Burkhard, N. Tetreault, M. Graetzel, J.-E. Moser and M. D. McGehee, *Advanced Energy Materials*, 2011, **1**, 407-414.
65. T. P. Chou, Q. Zhang, B. Russo, G. E. Fryxell and G. Cao, *Journal of Physical Chemistry C*, 2007, **111**, 6296-6302.
66. P. Wang, S. M. Zakeeruddin, J. E. Moser and M. Gratzel, *Journal of Physical Chemistry B*, 2003, **107**, 13280-13285.
67. Q. Zhang, T. R. Chou, B. Russo, S. A. Jenekhe and G. Cao, *Angewandte Chemie-International Edition*, 2008, **47**, 2402-2406.
68. M. Law, L. E. Greene, J. C. Johnson, R. Saykally and P. D. Yang, *Nature Matererials*, 2005, **4**, 455-459.
69. B. Onwona-Agyeman, S. Kaneko, A. Kumara, M. Okuya, K. Murakami, A. Konno and K. Tennakone, *Japanese Journal of Applied Physics Part 2-Letters & Express Letters*, 2005, **44**, L731-L733.
70. A. Kay and M. Gratzel, *Chemistry of Materials*, 2002, **14**, 2930-2935.
71. D. C. Look, D. C. Reynolds, J. R. Sizelove, R. L. Jones, C. W. Litton, G. Cantwell and W. C. Harsch, *Solid State Communications*, 1998, **105**, 399-401.
72. L. Forro, O. Chauvet, D. Emin, L. Zuppiroli, H. Berger and F. Levy, *Journal of Applied Physics*, 1994, **75**, 633-635.
73. C. Klingshirn, J. Fallert, H. Zhou, J. Sartor, C. Thiele, F. Maier-Flaig, D. Schneider and H. Kalt, *Physica Status Solidi B-Basic Solid State Physics*, 2010, **247**, 1424-1447.
74. Q. F. Zhang, C. S. Dandeneau, X. Y. Zhou and G. Z. Cao, *Advanced Materials*, 2009, **21**, 4087-4108.
75. J. A. Anta, E. Guillen and R. Tena-Zaera, *Journal of Physical Chemistry C*, 2012, **116**, 11413-11425.
76. I. Concina and A. Vomiero, *Small*, 2015, **11**, 1744-1774.
77. M. Saito and S. Fujihara, *Energy & Environmental Science*, 2008, **1**, 280-283.
78. K. Keis, E. Magnusson, H. Lindstrom, S. E. Lindquist and A. Hagfeldt, *Solar Energy Materials and Solar Cells*, 2002, **73**, 51-58.
79. E. Guillen, E. Azaceta, L. M. Peter, A. Zukal, R. Tena-Zaera and J. A. Anta, *Energy & Environmental Science*, 2011, **4**, 3400-3407.
80. K. S. Kim, Y. S. Kang, J. H. Lee, Y. J. Shin, N. G. Park, K. S. Ryu and S. H. Chang, *Bulletin of the Korean Chemical Society*, 2006, **27**, 295-298.
81. W. J. Lee, A. Suzuki, K. Imaeda, H. Okada, A. Wakahara and A. Yoshida, *Japanese Journal of Applied Physics Part 1-Regular Papers Short Notes & Review Papers*, 2004, **43**, 152-155.

82. T. Yoshida, J. B. Zhang, D. Komatsu, S. Sawatani, H. Minoura, T. Pauporte, D. Lincot, T. Oekermann, D. Schlettwein, H. Tada, D. Wohrle, K. Funabiki, M. Matsui, H. Miura and H. Yanagi, *Advanced Functional Materials*, 2009, **19**, 17-43.
83. A. Sacco, A. Lamberti, R. Gazia, S. Bianco, D. Manfredi, N. Shahzad, F. Cappelluti, S. Ma and E. Tresso, *Physical Chemistry Chemical Physics*, 2012, **14**, 16203-16208.
84. M. S. Akhtar, M. A. Khan, M. S. Jeon and O. B. Yang, *Electrochimica Acta*, 2008, **53**, 7869-7874.
85. C. F. Lin, H. Lin, J. B. Li and X. Li, *Journal of Alloys and Compounds*, 2008, **462**, 175-180.
86. Y. Shi, C. Zhu, L. Wang, W. Li, K. K. Fung and N. Wang, *Chemistry-a European Journal*, 2013, **19**, 282-287.
87. K. Mahmood and S. B. Park, *Journal of Materials Chemistry A*, 2013, **1**, 4826-4835.
88. Z. S. Wang, H. Kawauchi, T. Kashima and H. Arakawa, *Coordination Chemistry Reviews*, 2004, **248**, 1381-1389.
89. Q. Zhang, T. P. Chou, B. Russo, S. A. Jenekhe and G. Cao, *Advanced Functional Materials*, 2008, **18**, 1654-1660.
90. N. Memarian, I. Concina, A. Braga, S. M. Rozati, A. Vomiero and G. Sberveglieri, *Angewandte Chemie International Edition*, 2011, **50**, 12321-12325.
91. M. Law, L. E. Greene, A. Radenovic, T. Kuykendall, J. Liphardt and P. Yang, *Journal of Physical Chemistry B*, 2006, **110**, 22652-22663.
92. H.-Y. Chen, D.-B. Kuang and C.-Y. Su, *Journal of Materials Chemistry*, 2012, **22**, 15475-15489.
93. C. K. Xu, J. M. Wu, U. V. Desai and D. Gao, *Journal of the American Chemical Society*, 2011, **133**, 8122-8125.
94. S. H. Ko, D. Lee, H. W. Kang, K. H. Nam, J. Y. Yeo, S. J. Hong, C. P. Grigoropoulos and H. J. Sung, *Nano Letters*, 2011, **11**, 666-671.
95. V.-M. Guerin and T. Pauporte, *Energy & Environmental Science*, 2011, **4**, 2971-2979.
96. E. Puyoo, G. Rey, E. Appert, V. Consonni and D. Bellet, *Journal of Physical Chemistry C*, 2012, **116**, 18117-18123.
97. Y. Bai, H. Yu, Z. Li, R. Amal, G. Q. Lu and L. Wang, *Advanced Materials*, 2012, **24**, 5850-5856.
98. Z. Qin, Y. Huang, J. Qi, Q. Liao, W. Wang and Y. Zhang, *Materials Letters*, 2011, **65**, 3506-3508.
99. F. P. Yan, L. H. Huang, J. S. Zheng, J. Huang, Z. Lin, F. Huang and M. D. Wei, *Langmuir*, 2010, **26**, 7153-7156.
100. E. Guillen, F. Casanueva, J. A. Anta, A. Vega-Poot, G. Oskam, R. Alcantara, C. Fernandez-Lorenzo and J. Martin-Calleja, *Journal of Photochemistry and Photobiology a-Chemistry*, 2008, **200**, 364-370.
101. B. M. Klahr and T. W. Hamann, *Journal of Physical Chemistry C*, 2009, **113**, 14040-14045.
102. J. J. Nelson, T. J. Amick and C. M. Elliott, *Journal of Physical Chemistry C*, 2008, **112**, 18255-18263.
103. S. Ito, N. L. C. Ha, G. Rothenberger, P. Liska, P. Comte, S. M. Zakeeruddin, P. Pechy, M. K. Nazeeruddin and M. Gratzel, *Chemical Communications*, 2006, 4004-4006.
104. M. Paulose, K. Shankar, O. K. Varghese, G. K. Mor, B. Hardin and C. A. Grimes, *Nanotechnology*, 2006, **17**, 1446-1448.
105. D. S. Zhang, T. Yoshida, T. Oekermann, K. Furuta and H. Minoura, *Advanced Functional Materials*, 2006, **16**, 1228-1234.
106. D. Kuang, J. Brillet, P. Chen, M. Takata, S. Uchida, H. Miura, K. Sumioka, S. M. Zakeeruddin and M. Graetzel, *ACS Nano*, 2008, **2**, 1113-1116.
107. X. Liu, Y. Luo, H. Li, Y. Fan, Z. Yu, Y. Lin, L. Chen and Q. Meng, *Chemical Communications*, 2007, 2847-2849.
108. N. G. Park, K. M. Kim, M. G. Kang, K. S. Ryu, S. H. Chang and Y. J. Shin, *Advanced Materials*, 2005, **17**, 2349-2353.

109. T. Yoshida, J. Zhang, D. Komatsu, S. Sawatani, H. Minoura, T. Pauporte, D. Lincot, T. Oekermann, D. Schlettwein, H. Tada, D. Wohrle, K. Funabiki, M. Matsui, H. Miura and H. Yanagi, *Advanced Functional Materials*, 2009, **19**, 17-43.
110. A. Kojima, K. Teshima, Y. Shirai and T. Miyasaka, *Journal of the American Chemical Society*, 2009, **131**, 6050-6051.
111. W. S. Yang, J. H. Noh, N. J. Jeon, Y. C. Kim, S. Ryu, J. Seo and S. I. Seok, *Science*, 2015, **348**, 1234-1237.
112. H.-S. Kim, S. H. Im and N.-G. Park, *Journal of Physical Chemistry C*, 2014, **118**, 5615-5625.
113. D. Weber, *Z. Naturforsch.*, 1978, **33b**, 1443.
114. D. Weber, *Z. Naturforsch.*, 1978, **33b**, 862.
115. D. B. Mitzi, C. A. Feild, W. T. A. Harrison and A. M. Guloy, *Nature*, 1994, **369**, 467-469.
116. F. Brivio, K. T. Butler, A. Walsh and M. van Schilfgaarde, *Physical Review B*, 2014, **89**, 6.
117. A. Poglitsch and D. Weber, *Journal of Chemical Physics*, 1987, **87**, 6373-6378.
118. S. De Wolf, J. Holovsky, S.-J. Moon, P. Loeper, B. Niesen, M. Ledinsky, F.-J. Haug, J.-H. Yum and C. Ballif, *Journal of Physical Chemistry Letters*, 2014, **5**, 1035-1039.
119. H. S. Kim, C. R. Lee, J. H. Im, K. B. Lee, T. Moehl, A. Marchioro, S. J. Moon, R. Humphry-Baker, J. H. Yum, J. E. Moser, M. Gratzel and N. G. Park, *Scientific Reports*, 2012, **2**, 7.
120. S. D. Stranks, G. E. Eperon, G. Grancini, C. Menelaou, M. J. P. Alcocer, T. Leijtens, L. M. Herz, A. Petrozza and H. J. Snaith, *Science*, 2013, **342**, 341-344.
121. F. Hao, C. C. Stoumpos, R. P. H. Chang and M. G. Kanatzidis, *Journal of the American Chemical Society*, 2014, **136**, 8094-8099.
122. C. C. Stoumpos, C. D. Malliakas and M. G. Kanatzidis, *Inorganic Chemistry*, 2013, **52**, 9019-9038.
123. J.-H. Im, C.-R. Lee, J.-W. Lee, S.-W. Park and N.-G. Park, *Nanoscale*, 2011, **3**, 4088-4093.
124. M. M. Lee, J. Teuscher, T. Miyasaka, T. N. Murakami and H. J. Snaith, *Science*, 2012, **338**, 643-647.
125. L. Etgar, P. Gao, Z. Xue, Q. Peng, A. K. Chandiran, B. Liu, M. K. Nazeeruddin and M. Graetzel, *Journal of the American Chemical Society*, 2012, **134**, 17396-17399.
126. J. H. Heo, S. H. Im, J. H. Noh, T. N. Mandal, C.-S. Lim, J. A. Chang, Y. H. Lee, H.-j. Kim, A. Sarkar, M. K. Nazeeruddin, M. Graetzel and S. I. Seok, *Nature Photonics*, 2013, **7**, 487-492.
127. J. H. Noh, S. H. Im, J. H. Heo, T. N. Mandal and S. I. Seok, *Nano Letters*, 2013, **13**, 1764-1769.
128. J. M. Ball, M. M. Lee, A. Hey and H. J. Snaith, *Energy & Environmental Science*, 2013, **6**, 1739-1743.
129. J. Burschka, N. Pellet, S.-J. Moon, R. Humphry-Baker, P. Gao, M. K. Nazeeruddin and M. Graetzel, *Nature*, 2013, **499**, 316-319.
130. M. Liu, M. B. Johnston and H. J. Snaith, *Nature*, 2013, **501**, 395-398.
131. G. E. Eperon, V. M. Burlakov, P. Docampo, A. Goriely and H. J. Snaith, *Advanced Functional Materials*, 2014, **24**, 151-157.
132. D. Liu, J. Yang and T. L. Kelly, *Journal of the American Chemical Society*, 2014, **136**, 17116-17122.
133. N. J. Jeon, J. H. Noh, W. S. Yang, Y. C. Kim, S. Ryu, J. Seo and S. I. Seok, *Nature*, 2015, **517**, 476-480.
134. N. J. Jeon, J. H. Noh, Y. C. Kim, W. S. Yang, S. Ryu and S. Il Seol, *Nature Materials*, 2014, **13**, 897-903.
135. J.-H. Im, I.-H. Jang, N. Pellet, M. Graetzel and N.-G. Park, *Nature Nanotechnology*, 2014, **9**, 927-932.
136. H. Zhou, Q. Chen, G. Li, S. Luo, T.-b. Song, H.-S. Duan, Z. Hong, J. You, Y. Liu and Y. Yang, *Science*, 2014, **345**, 542-546.

137. W. Nie, H. Tsai, R. Asadpour, J.-C. Blancon, A. J. Neukirch, G. Gupta, J. J. Crochet, M. Chhowalla, S. Tretiak, M. A. Alam, H.-L. Wang and A. D. Mohite, *Science*, 2015, **347**, 522-525.
138. B. Hailegnaw, S. Kirmayer, E. Edri, G. Hodes and D. Cahen, *Journal of Physical Chemistry Letters*, 2015, **6**, 1543-1547.
139. D. Fabini, *Journal of Physical Chemistry Letters*, 2015, **6**, 3546-3548.
140. J. Gong, S. B. Darling and F. You, *Energy & Environmental Science*, 2015, **8**, 1953-1968.
141. F. Hao, C. C. Stoumpos, C. Duyen Hanh, R. P. H. Chang and M. G. Kanatzidis, *Nature Photonics*, 2014, **8**, 489-494.
142. N. K. Noel, S. D. Stranks, A. Abate, C. Wehrenfennig, S. Guarnera, A.-A. Haghighirad, A. Sadhanala, G. E. Eperon, S. K. Pathak, M. B. Johnston, A. Petrozza, L. M. Herz and H. J. Snaith, *Energy & Environmental Science*, 2014, **7**, 3061-3068.
143. T. Leijtens, G. E. Eperon, S. Pathak, A. Abate, M. M. Lee and H. J. Snaith, *Nature Communications*, 2013, **4**, 2885.
144. Y. Cheng, Q.-D. Yang, J. Xiao, Q. Xue, H.-W. Li, Z. Guan, H.-L. Yip and S.-W. Tsang, *ACS applied materials & interfaces*, 2015, **7**, 19986-19993.
145. J. Zhang and T. Pauporte, *Journal of Physical Chemistry C*, 2015, **119**, 14919-14928.
146. J. Yang, B. D. Siempelkamp, E. Mosconi, F. De Angelis and T. L. Kelly, *Chemistry of Materials*, 2015, **27**, 4229-4236.
147. H. J. Snaith, A. Abate, J. M. Ball, G. E. Eperon, T. Leijtens, N. K. Noel, S. D. Stranks, J. T.-W. Wang, K. Wojciechowski and W. Zhang, *Journal of Physical Chemistry Letters*, 2014, **5**, 1511-1515.
148. M. Herman, M. Jankovec and M. Topic, *International Journal of Photoenergy*, 2012, 151452.
149. Y. Zhang, M. Liu, G. E. Eperon, T. C. Leijtens, D. McMeekin, M. Saliba, W. Zhang, M. de Bastiani, A. Petrozza, L. M. Herz, M. B. Johnston, H. Lin and H. J. Snaith, *Materials Horizons*, 2015, **2**, 315-322.
150. J. M. Frost, K. T. Butler, F. Brivio, C. H. Hendon, M. van Schilfgaarde and A. Walsh, *Nano Letters*, 2014, **14**, 2584-2590.
151. D. Y. Liu and T. L. Kelly, *Nature Photonics*, 2014, **8**, 133-138.
152. A. Bera, K. Wu, A. Sheikh, E. Alarousu, O. F. Mohammed and T. Wu, *Journal of Physical Chemistry C*, 2014, **118**, 28494-28501.
153. S. S. Shin, W. S. Yang, J. H. Noh, J. H. Suk, N. J. Jeon, J. H. Park, J. S. Kim, W. M. Seong and S. Il Seok, *Nature Communications*, 2015, **6**, 7410.
154. U. Ozgur, Y. I. Alivov, C. Liu, A. Teke, M. A. Reshchikov, S. Dogan, V. Avrutin, S. J. Cho and H. Morkoc, *Journal of Applied Physics*, 2005, **98**, 41310.
155. D. Bi, G. Boschloo, S. Schwarzmueller, L. Yang, E. M. J. Johansson and A. Hagfeldt, *Nanoscale*, 2013, **5**, 11686-11691.
156. M. H. Kumar, N. Yantara, S. Dharani, M. Graetzel, S. Mhaisalkar, P. P. Boix and N. Mathews, *Chemical Communications*, 2013, **49**, 11089-11091.
157. D.-Y. Son, J.-H. Im, H.-S. Kim and N.-G. Park, *Journal of Physical Chemistry C*, 2014, **118**, 16567-16573.
158. J. Zhang, P. Barboux and T. Pauporte, *Advanced Energy Materials*, 2014, **4**, 1400932.
159. F. J. Ramos, M. C. Lopez-Santos, E. Guillen, M. K. Nazeeruddin, M. Graetzel, A. R. Gonzalez-Elipe and S. Ahmad, *Chemphyschem*, 2014, **15**, 1148-1153.
160. C. Liu, Z. Qiu, W. Meng, J. Chen, J. Qi, C. Dong and M. Wang, *Nano Energy*, 2015, **12**, 59-68.
161. J. Dong, Y. Zhao, J. Shi, H. Wei, J. Xiao, X. Xu, J. Luo, J. Xu, D. Li, Y. Luo and Q. Meng, *Chemical Communications*, 2014, **50**, 13381-13384.
162. J. Dong, X. Xu, J.-J. Shi, D.-M. Li, Y.-H. Luo, Q.-B. Meng and Q. Chen, *Chinese Physics Letters*, 2015, **32**.
163. D.-Y. Son, K.-H. Bae, H.-S. Kim and N.-G. Park, *Journal of Physical Chemistry C*, 2015, **119**, 10321-10328.
164. K. Mahmood, B. S. Swain and A. Amassian, *Nanoscale*, 2015, **7**, 12812-12819.
165. J. Dong, J. Shi, D. Li, Y. Luo and Q. Meng, *Applied Physics Letters*, 2015, **107**, 73507.

166. K. Mahmood, B. S. Swain and A. Amassian, *Advanced Energy Materials*, 2015, **5**, 1500568.
167. F. J. Ramos, M. C. Lopez-Santos, E. Guillen, M. K. Nazeeruddin, M. Gratzel, A. R. Gonzalez-Elipe and S. Ahmad, *Chemphyschem : a European journal of chemical physics and physical chemistry*, 2014, **15**, 1148-1153.
168. D. Liu, M. K. Gangishetty and T. L. Kelly, *Journal of Materials Chemistry A*, 2014, **2**, 19873-19881.
169. J. Song, J. Bian, E. Zheng, X.-F. Wang, W. Tian and T. Miyasaka, *Chemistry Letters*, 2015, **44**, 610-612.
170. J. You, Z. Hong, Y. Yang, Q. Chen, M. Cai, T.-B. Song, C.-C. Chen, S. Lu, Y. Liu and H. Zhou, *ACS Nano*, 2014, **8**, 1674-1680.
171. H. Zhou, Y. Shi, K. Wang, Q. Dong, X. Bai, Y. Xing, Y. Du and T. Ma, *Journal of Physical Chemistry C*, 2015, **119**, 4600-4605.
172. Y. Jin and G. Chumanov, *ACS Applied Materials & Interfaces*, 2015, **7**, 12015-12021.
173. K. Mahmood, B. S. Swain and H. S. Jung, *Nanoscale*, 2014, **6**, 9127-9138.
174. L. Liang, Z. Huang, L. Cai, W. Chen, B. Wang, K. Chen, H. Bai, Q. Tian and B. Fan, *Acs Applied Materials & Interfaces*, 2014, **6**, 20585-20589.
175. Z.-L. Tseng, C.-H. Chiang and C.-G. Wu, *Scientific Reports*, 2015, **5**, 13211-13211.
176. J. Zhang, E. J. Juarez-Perez, I. Mora-Sero, B. Viana and T. Pauporte, *Journal of Materials Chemistry A*, 2015, **3**, 4909-4915.
177. L. Zuo, Z. Gu, T. Ye, W. Fu, G. Wu, H. Li and H. Chen, *Journal of the American Chemical Society*, 2015, **137**, 2674-2679.
178. J. Kim, G. Kim, T. K. Kim, S. Kwon, H. Back, J. Lee, S. H. Lee, H. Kang and K. Lee, *Journal of Materials Chemistry A*, 2014, **2**, 17291-17296.
179. W. Qiu, M. Buffiere, G. Brammertz, U. W. Paetzold, L. Froyen, P. Heremans and D. Cheyns, *Organic Electronics*, 2015, **26**, 30-35.
180. S. Bai, Z. W. Wu, X. J. Wu, Y. Z. Jin, N. Zhao, Z. H. Chen, Q. Q. Mei, X. Z. Wang, Z. Ye, T. Y. Song, R. Y. Liu, S. T. Lee and B. Q. Sun, *Nano Research*, 2014, **7**, 1749-1758.
181. L. Q. Zhang, X. W. Zhang, Z. G. Yin, Q. Jiang, X. Liu, J. H. Meng, Y. J. Zhao and H. L. Wang, *Journal of Materials Chemistry A*, 2015, **3**, 12133-12138.
182. Q. Hu, Y. Liu, Y. Li, L. Ying, T. Liu, F. Huang, S. Wang, W. Huang, R. Zhu and Q. Gong, *Journal of Materials Chemistry A*, 2015, **3**, 18483-18491.
183. X. Xu, H. Zhang, J. Shi, J. Dong, Y. Luo, D. Li and Q. Meng, *Journal of Materials Chemistry A*, 2015, **3**, 19288-19293.
184. E. J. Juarez-Perez, M. Wussler, F. Fabregat-Santiago, K. Lakus-Wollny, E. Mankel, T. Mayer, W. Jaegermann and I. Mora-Sero, *Journal of Physical Chemistry Letters*, 2014, **5**, 680-685.
185. X. Dong, H. Hu, B. Lin, J. Ding and N. Yuan, *Chemical Communications*, 2014, **50**, 14405-14408.
186. A. K. Chandiran, M. Abdi-Jalebi, A. Yella, M. I. Dar, C. Y. Yi, S. A. Shivashankar, M. K. Nazeeruddin and M. Gratzel, *Nano Letters*, 2014, **14**, 1190-1195.
187. K. Mahmood, B. S. Swain and A. Amassian, *Nanoscale*, 2014, **6**, 14674-14678.
188. S. He, L. Qiu, X. Fang, G. Guan, P. Chen, Z. Zhang and H. Peng, *Journal of Materials Chemistry A*, 2015, **3**, 9406-9410.
189. S. Ameen, M. S. Akhtar, H.-K. Seo, M. K. Nazeeruddin and H.-S. Shin, *Journal of Physical Chemistry C*, 2015, **119**, 10379-10390.
190. E. Galoppini, J. Rochford, H. Chen, G. Saraf, Y. Lu, A. Hagfeldt and G. Boschloo, *Journal of Physical Chemistry B*, 2006, **110**, 16159-16161.
191. K. Subannajui, F. Guder, J. Danhof, A. Menzel, Y. Yang, L. Kirste, C. Y. Wang, V. Cimalla, U. Schwarz and M. Zacharias, *Nanotechnology*, 2012, **23**, 7.
192. L. E. Greene, M. Law, J. Goldberger, F. Kim, J. C. Johnson, Y. F. Zhang, R. J. Saykally and P. D. Yang, *Angewandte Chemie-International Edition*, 2003, **42**, 3031-3034.
193. S. E. Ahn, J. S. Lee, H. Kim, S. Kim, B. H. Kang, K. H. Kim and G. T. Kim, *Applied Physics Letters*, 2004, **84**, 5022-5024.

194. A.-J. Cheng, Y. Tzeng, Y. Zhou, M. Park, T.-h. Wu, C. Shannon, D. Wang and W. Lee, *Applied Physics Letters*, 2008, **92**, 92113.
195. L. E. Greene, M. Law, D. H. Tan, M. Montano, J. Goldberger, G. Somorjai and P. D. Yang, *Nano Letters*, 2005, **5**, 1231-1236.
196. H. Zeng, J. Cui, B. Cao, U. Gibson, Y. Bando and D. Golberg, *Science of Advanced Materials*, 2010, **2**, 336-358.
197. M. Skompska and K. Zarebska, *Electrochimica Acta*, 2014, **127**, 467-488.
198. I. Sieber, H. Hildebrand, A. Friedrich and P. Schmuki, *Electrochemistry Communications*, 2005, **7**, 97-100.
199. J. P. O'Sullivan and G. C. Wood, *Proceedings of the Royal Society of London Series a-Mathematical and Physical Sciences*, 1970, **317**, 511-543.
200. M. Pashchanka and J. J. Schneider, *Journal of Materials Chemistry*, 2011, **21**, 18761-18767.
201. M. L. Wang, Y. N. Liu and H. Yang, *Electrochimica Acta*, 2012, **62**, 424-432.
202. A. B. F. Martinson, J. W. Elam, J. T. Hupp and M. J. Pellin, *Nano Letters*, 2007, **7**, 2183-2187.
203. A. J. Yin, J. Li, W. Jian, A. J. Bennett and J. M. Xu, *Applied Physics Letters*, 2001, **79**, 1039-1041.
204. C.-C. Chen, H.-W. Chung, C.-H. Chen, H.-P. Lu, C.-M. Lan, S.-F. Chen, L. Luo, C.-S. Hung and E. W.-G. Diau, *Journal of Physical Chemistry C*, 2008, **112**, 19151-19157.
205. J. R. Jennings, A. Ghicov, L. M. Peter, P. Schmuki and A. B. Walker, *Journal of the American Chemical Society*, 2008, **130**, 13364-13372.
206. G. K. Mor, K. Shankar, M. Paulose, O. K. Varghese and C. A. Grimes, *Nano Letters*, 2006, **6**, 215-218.
207. X. Gao, J. Li, J. Baker, Y. Hou, D. Guan, J. Chen and C. Yuan, *Chemical Communications*, 2014, **50**, 6368-6371.
208. S. J. Kim and J. Choi, *Electrochemistry Communications*, 2008, **10**, 175-179.
209. Z. Hu, Q. Chen, Z. Li, Y. Yu and L.-M. Peng, *Journal of Physical Chemistry C*, 2010, **114**, 881-889.
210. S. He, M. Zheng, L. Yao, X. Yuan, M. Li, L. Ma and W. Shen, *Applied Surface Science*, 2010, **256**, 2557-2562.
211. J. L. Zhao, X. X. Wang, J. J. Liu, Y. C. Meng, X. W. Xu and C. C. Tang, *Materials Chemistry and Physics*, 2011, **126**, 555-559.
212. A. Ramirez-Canon, D. O. Miles, P. J. Cameron and D. Mattia, *RSC Advances*, 2013, **3**, 25323-25330.
213. A. Shetty and K. K. Nanda, *Applied Physics a-Materials Science & Processing*, 2012, **109**.
214. P. K. Basu, E. Bontempi, S. Maji, H. Saha and S. Basu, *Journal of Materials Science-Materials in Electronics*, 2009, **20**, 1203-1207.
215. P. K. Basu, N. Saha, S. Maji, H. Saha and S. Basu, *Journal of Materials Science-Materials in Electronics*, 2008, **19**, 493-499.
216. M. A. Farrukh, C.-K. Thong, R. Adnan and M. A. Kamarulzaman, *Russian Journal of Physical Chemistry A*, 2012, **86**, 2041-2048.
217. H.-S. Goh, R. Adnan and M. A. Farrukh, *Turkish Journal of Chemistry*, 2011, **35**, 375-391.
218. Y.-T. Kim, J. Park, S. Kim, D. W. Park and J. Choi, *Electrochimica Acta*, 2012, **78**, 417-421.
219. S.-T. Ren, Q. Wang, F. Zhao and S.-L. Qu, *Chinese Physics B*, 2012, **21**, 18502.
220. N. Samir, D. S. Eissa and N. K. Allam, *Materials Letters*, 2014, **137**, 45-48.
221. L. R. He and F. Y. Chen, *ECS Solid State Letters*, 2014, **3**, 41-44.
222. M. Dezfoolian, F. Rashchi and R. K. Nekouei, *Surface & Coatings Technology*, 2015, **275**, 245-251.
223. S. W. Ng, F. K. Yam, L. L. Low, K. P. Beh, M. F. Mustapha, E. N. Sota, S. S. Tneh and Z. Hassan, *Optoelectronics and Advanced Materials-Rapid Communications*, 2011, **5**, 89-91.

224. V. Galstyan, E. Comini, C. Baratto, A. Ponzoni, E. Bontempi, M. Brisotto, G. Faglia and G. Sberveglieri, *Crystengcomm*, 2013, **15**, 2881-2887.
225. N. K. Shrestha, K. Lee, R. Hahn and P. Schmuki, *Electrochemistry Communications*, 2013, **34**, 9-13.
226. C. Y. Kuan, J. M. Chou, I. C. Leu and M. H. Hon, *Electrochemistry Communications*, 2007, **9**, 2093-2097.
227. S. Sreekantan, L. R. Gee and Z. Lockman, *Journal of Alloys and Compounds*, 2009, **476**, 513-518.
228. X. F. Wu, G. W. Lu, C. Li and G. Q. Shi, *Nanotechnology*, 2006, **17**, 4936-4940.
229. J. Park, K. Kim and J. Choi, *Current Applied Physics*, 2013, **13**, 1370-1375.
230. D. O. Miles, P. J. Cameron and D. Mattia, *Journal of Materials Chemistry A*, 2015, **3**, 17569-17577.
231. B. Mukherjee, W. Wilson and V. Subramanian, *Nanoscale*, 2013, **5**, 269-274.
232. S. H. Ahn, D. J. Kim, W. S. Chi and J. H. Kim, *Advanced Materials*, 2013, **25**, 4893-4897.
233. K. Miettunen, J. Halme, M. Toivola and P. Lund, *Journal of Physical Chemistry C*, 2008, **112**, 4011-4017.
234. S. H. Ahn, W. S. Chi, J. T. Park, J. K. Koh, D. K. Roh and J. H. Kim, *Advanced Materials*, 2012, **24**, 519-522.
235. S. H. Ahn, H. Jeon, K. J. Son, H. Ahn, W.-G. Koh, D. Y. Ryu and J. H. Kim, *Journal of Materials Chemistry*, 2011, **21**, 1772-1779.
236. W. S. Chi, J. K. Koh, S. H. Ahn, J.-S. Shin, H. Ahn, D. Y. Ryu and J. H. Kim, *Electrochemistry Communications*, 2011, **13**, 1349-1352.
237. P. Docampo, J. M. Ball, M. Darwich, G. E. Eperon and H. J. Snaith, *Nature Communications*, 2013, **4**, 2761.
238. B. N. Illy, A. C. Cruickshank, S. Schumann, R. Da Campo, T. S. Jones, S. Heutz, M. A. McLachlan, D. W. McComb, D. J. Riley and M. P. Ryan, *Journal of Materials Chemistry*, 2011, **21**, 12949-12957.
239. A. V. Shchukarev and D. V. Korolkov, *Central European Journal of Chemistry*, 2004, **2**, 347-362.
240. K. G. Chandrappa, T. V. Venkatesha, K. Vathsala and C. Shivakumara, *Journal of Nanoparticle Research*, 2010, **12**, 2667-2678.
241. M. C. Hales and R. L. Frost, *Polyhedron*, 2007, **26**, 4955-4962.
242. R. Cusco, E. Alarcon-Llado, J. Ibanez, L. Artus, J. Jimenez, B. Wang and M. J. Callahan, *Physical Review B*, 2007, **75**, 165202.
243. Y. Q. Huang, M. D. Liu, Z. Li, Y. K. Zeng and S. B. Liu, *Materials Science and Engineering B-Solid State Materials for Advanced Technology*, 2003, **97**, 111-116.
244. M. Bitenc, P. Podbrscek, P. Dubcek, S. Bernstorff, G. Drazic, B. Orel, S. Pejovnik and Z. C. Orel, *Chemistry-a European Journal*, 2010, **16**, 11481-11488.
245. M. Bitenc, P. Podbrscek, P. Dubcek, S. Bernstorff, G. Drazic, B. Orel and Z. C. Orel, *Crystengcomm*, 2012, **14**, 3080-3088.
246. J. Livage, M. Henry and C. Sanchez, *Progress in Solid State Chemistry*, 1988, **18**, 259-341.
247. X. Wang, W. Cai, Y. Lin, G. Wang and C. Liang, *Journal of Materials Chemistry*, 2010, **20**, 8582-8590.
248. K. Hooper, M. Carnie, C. Charbonneau and T. Watson, *International Journal of Photoenergy*, 2014.
249. Z. B. Fang, Z. J. Yan, Y. S. Tan, X. Q. Liu and Y. Y. Wang, *Applied Surface Science*, 2005, **241**, 303-308.
250. A. L. Patterson, *Physical Review*, 1939, **56**, 978-982.
251. B. N. Kim, K. Hiraga and K. Morita, *Materials Transactions*, 2003, **44**, 2239-2244.
252. M. Hillert, *Acta Metallurgica*, 1965, **13**, 227-238.
253. T. J. Gray, *Journal of the American Ceramic Society*, 1954, **37**, 534-538.
254. W. Q. Fang, X. H. Yang, H. Zhu, Z. Li, H. Zhao, X. Yao and H. G. Yang, *Journal of Materials Chemistry*, 2012, **22**, 22082-22089.

255. G. Li, C. P. Richter, R. L. Milot, L. Cai, C. A. Schmuttenmaer, R. H. Crabtree, G. W. Brudvig and V. S. Batista, *Dalton Transactions*, 2009, 10078-10085.
256. W.-C. Chang, C.-H. Lee, W.-C. Yu and C.-M. Lin, *Nanoscale Research Letters*, 2012, **7**.
257. T. P. Chou, Q. Zhang and G. Cao, *Journal of Physical Chemistry C*, 2007, **111**, 6296-6302.
258. E. Dell'Orto, L. Raimondo, A. Sassella and A. Abbotto, *Journal of Materials Chemistry*, 2012, **22**, 11364-11369.
259. P. J. Cameron, L. M. Peter and S. Hore, *Journal of Physical Chemistry B*, 2005, **109**, 930-936.
260. M. Gratzel, *Nature*, 2001, **414**, 338-344.
261. G. Schlichthorl, S. Y. Huang, J. Sprague and A. J. Frank, *Journal of Physical Chemistry B*, 1997, **101**, 8141-8155.
262. N. Kopidakis, N. R. Neale and A. J. Frank, *Journal of Physical Chemistry B*, 2006, **110**, 12485-12489.
263. J. B. Baxter, *Journal of Vacuum Science & Technology A*, 2012, **30**, 19, 21201.
264. S. H. Ahn, W. S. Chi, J. T. Park, J. K. Koh, D. K. Roh and J. H. Kim, *Advanced Materials*, 2012, **24**, 519-522.
265. S.-J. Roh, R. S. Mane, S.-K. Min, W.-J. Lee, C. D. Lokhande and S.-H. Han, *Applied Physics Letters*, 2006, **89**, 253512.
266. A. J. McEvoy, T. Markvart, L. Castaeaner, Practical handbook of photovoltaics: fundamentals and applications, Academic Press, MA, USA, 2012.
267. F. Fabregat-Santiago, J. Bisquert, E. Palomares, L. Otero, D. Kuang, S. M. Zakeeruddin and M. Gratzel, *Journal of Physical Chemistry C*, 2007, **111**, 6550-6560.
268. R. Scholin, M. Quintana, E. M. J. Johansson, M. Hahlin, T. Marinado, A. Hagfeldt and H. Rensmo, *Journal of Physical Chemistry C*, 2011, **115**, 19274-19279.
269. T. Salim, S. Sun, Y. Abe, A. Krishna, A. C. Grimsdale and Y. M. Lam, *Journal of Materials Chemistry A*, 2015, **3**, 8943-8969.
270. J. S. Meena, M.-C. Chu, Y.-C. Chang, H.-C. You, R. Singh, P.-T. Liu, H.-P. D. Shieh, F.-C. Chang and F.-H. Ko, *Journal of Materials Chemistry C*, 2013, **1**, 6613-6622.
271. A. Wakamiya, M. Endo, T. Sasamori, N. Tokitoh, Y. Ogomi, S. Hayase and Y. Murata, *Chemistry Letters*, 2014, **43**, 711-713.
272. Y. Wu, A. Islam, X. Yang, C. Qin, J. Liu, K. Zhang, W. Peng and L. Han, *Energy & Environmental Science*, 2014, **7**, 2934-2938.
273. B. Faure, G. Salazar-Alvarez, A. Ahniyaz, I. Villaluenga, G. Berriozabal, Y. R. De Miguel and L. Bergstrom, *Science and Technology of Advanced Materials*, 2013, **14**.
274. M. Kosmulski, *Chemical Properties of Material Surfaces*, Marcel Dekker, New York, 2001.
275. G. Niu, X. Guo and L. Wang, *Journal of Materials Chemistry A*, 2015, **3**, 8970-8980.
276. Z. Xiao, Q. Dong, C. Bi, Y. Shao, Y. Yuan and J. Huang, *Advanced Materials*, 2014, **26**, 6503-6509.
277. L. Wang, C. McCleese, A. Kovalsky, Y. Zhao and C. Burda, *Journal of the American Chemical Society*, 2014, **136**, 12205-12208.
278. Q. Chen, H. Zhou, T.-B. Song, S. Luo, Z. Hong, H.-S. Duan, L. Dou, Y. Liu and Y. Yang, *Nano Letters*, 2014, **14**, 4158-4163.
279. V. Somsongkul, F. Lang, A. R. Jeong, M. Rusu, M. Arunchaiya and T. Dittrich, *Physica Status Solidi-Rapid Research Letters*, 2014, **8**, 763-766.
280. T. Leijtens, B. Lauber, G. E. Eperon, S. D. Stranks and H. J. Snaith, *Journal of Physical Chemistry Letters*, 2014, **5**, 1096-1102.
281. A. Dualeh, N. Tetreault, T. Moehl, P. Gao, M. K. Nazeeruddin and M. Graetzel, *Advanced Functional Materials*, 2014, **24**, 3250-3258.
282. H. K. Adli, T. Harada, W. Septina, S. Hozan, S. Ito and S. Ikeda, *Journal of Physical Chemistry C*, 2015, **119**, 22304-22309.

Appendix 1 – Estimation of the Specific Surface Area of Hexagonal Nanowires

This estimation of the specific surface area of the as-prepared nanowires from anodization assumes that the nanowires are perfectly smooth with a hexagonal cross-section. As the exact identity of the material is not known the density of the material hydrozincite will be used during the calculation as the closest analogue.

Values used in this calculation are:

Average Nanowire Radius (r)= 83.5 nm

Average Density of Hydrozincite (ρ)= 3.5 g cm^{-3}

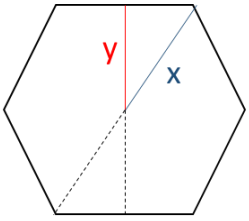

$$y = x \cdot \cos(30)$$

$$y = x \cdot 0.866$$

Assuming the average nanowire radius corresponds to the mean value of x and y:

$$r = \frac{x + y}{2}$$

$$r = \frac{1.866 \cdot x}{2}$$

$$\therefore x = 89.5\,nm \;\; and \;\; y = 77.5\,nm$$

The circumference of a hexagon (C) is given by:

$$C = 6x$$

And the area (A) is given by:

$$A = 3xy$$

The specific surface area (SSA) can be determined as the ratio of the surface area to volume divided by the material density

$$\therefore SSA = \frac{C \cdot L}{\rho \cdot A \cdot L}$$

Where L is the nanowire length. Substituting in for C and A, we obtain:

$$SSA = \frac{6x \cdot L}{3\rho \cdot x \cdot y \cdot L}$$

$$SSA = \frac{2}{\rho \cdot y}$$

Substituting in the values for ρ and y and calculating gives:

$$SSA = 7.4\, m^2 g^{-1}$$

Appendix 2 – Estimation of the Specific Surface Area of Spheroidal ZnO Nanoparticles

The specific surface area of the polycrystalline ZnO nanowires was estimated by treating the nanowires as being composed solely of perfectly spheroidal nanoparticles with no overlap between neighbouring nanoparticles.

The surface area of a sphere (*A*) is given by:

$$A = 4\pi r^2$$

Where *r* is the radius of the sphere.

The volume of a sphere (*V*) is given by:

$$V = \frac{4}{3}\pi r^3$$

The calculated specific surface area (S_{calc}) for a material formed of perfectly spherical, non-overlapping spheres can therefore be determined using:

$$S_{calc} = \frac{A}{V \cdot \rho}$$

Where ρ is the density of the material.

Substituting in for *A* and *V* we obtain:

$$S_{calc} = \frac{12\pi r^2}{4\pi r^3 \cdot \rho}$$

This then cancels down to give the relationship of:

$$S_{calc} = \frac{3}{\rho} \cdot r^{-1}$$

Using the bulk density of ZnO the specific surface areas of the materials can then be estimated.